



NATIONAL RESEARCH CENTER
"KURCHATOV INSTITUTE"

Petersburg Nuclear Physics Institute
named by B.P. Konstantinov



PNPI



High Energy Physics Division



MAIN SCIENTIFIC ACTIVITIES
2018–2022

GATCHINA
2023

Editor G.D. Alkhazov

ISBN 978-5-86763-483-4

© NRC “Kurchatov Institute” – PNPI, 2023

PREFACE

This edition presents a summary of the scientific activities of the High Energy Physics Division (HEPD) in the period 2018–2022. It can be considered as a continuation of the previous editions:

High Energy Physics Division. Main Scientific Activities 1971–1996, Gatchina (1997);
High Energy Physics Division. Main Scientific Activities 1997–2001, Gatchina (2002);
High Energy Physics Division. Main Scientific Activities 2002–2006, Gatchina (2007);
High Energy Physics Division. Main Scientific Activities 2007–2012, Gatchina (2013);
High Energy Physics Division. Main Scientific Activities 2013–2018, Gatchina (2019).

The main directions of the HEPD scientific activities are experimental studies in nuclear and particle physics at accelerators, as well as some applications of the nuclear methods, in medicine in particular. As in the previous years, the HEPD strategy was, on the one hand, to exploit in a maximal possible way the accelerator facilities available at NRC “Kurchatov Institute” – PNPI (PNPI) and, on the other hand, to maintain active international cooperation in fundamental research in the world’s most advanced accelerator centres. The PNPI 1-GeV proton synchrocyclotron with its proton, neutron, pion, and muon beams remains a valuable instrument for nuclear physics, for solid state physics, for medical applications, as well as for radiation studies of various materials and equipment. An important step in medical applications is related to the construction at PNPI of a new 80-MeV high-intensity proton cyclotron. This accelerator will be specialized on production of various radioactive isotopes (project “Isotope” implemented at PNPI), including production of generators of positron emitting isotopes for applications in the positron emission tomography. The HEPD participated in the development of methods for obtaining isotopes. A new innovative method for obtaining radioactive isotopes using a mass separator and new high temperature methods have been developed at the HEPD.

During the reviewed period, the HEPD participated in experiments at the leading accelerator centres: European Organization for Nuclear Research (CERN), Paul Scherrer Institute (PSI, Switzerland), Helmholtz Centre for Heavy Ion Research (GSI, Germany), as well as at the accelerators in the Universities in Bonn (Germany), in Mainz (Germany), and at the accelerator at IHEP (Protvino). Our main efforts were concentrated on experiments at the Large Hadron Collider (LHC) at CERN. PNPI participates in all major collider experiments at the LHC: CMS, ATLAS, LHCb, ALICE with essential contributions to the design, construction, and maintenance of these experiments. A tremendous success of the LHC experiments is well known. More than 3 000 physics papers were published by the end of 2022 starting from the first publications in 2008 that describe the detector design. A large number of new results were obtained, including predicted by PNPI theorists the quantum chromodynamics dead cone effect – an angular region of suppressed gluon bremsstrahlung surrounding an emitting heavy quark – which was confirmed by results of the ALICE experiment. At present, PNPI participates in preparations for further studies at the LHC with the increased energy and intensity of the colliding beams. The first upgrade stage Phase-1 LHC detectors was successfully completed in early 2022. The PNPI was strongly involved in the LHC detectors upgrade program. On July 5, 2022, the LHC delivered proton–proton collisions at the energy of 13.6 TeV for the first time, setting a new world record. Thus began a new stage of data taking in the experiments at the LHC – Run-3.

Very successful was also our traditional cooperation with the nuclear centre PSI in Switzerland, where we have a possibility to use the world’s best muon beams of the “meson factory”. Deep studies of the muon catalyzed dd -, dt - and $d^3\text{He}$ -fusion, were followed by high precision measurements of the muon capture by protons and by light nuclei.

Future plans of the HEPD are aimed at the development of advanced scientific research and broad international cooperation.

Also we plan to create a special complex (project IRINA) at the high flux neutron reactor PIK, which will start to operate at PNPI, for studies of neutron-rich nuclei far from the stability region.

Oleg Fedin, Head of the HEPD



Status of the Accelerator
Facilities at PNPI

STATUS OF THE PNPI ACCELERATOR COMPLEX

D.A. Amerkanov, S.A. Artamonov, E.M. Ivanov, L.A. Sukhorukov

1. PNPI synchrocyclotron

The synchrocyclotron SC-1000 of the PNPI (Fig. 1) with the energy of the extracted proton beam of 1 000 MeV is a basic experimental facility of the Institute. The physical launch of the synchrocyclotron took place on November 4, 1967; it was put into operation in 1970.



Fig. 1. Synchrocyclotron PNPI

Main parameters of the synchrocyclotron are given in Table 1.

Table 1

Main parameters of the synchrocyclotron of the PNPI

Energy of the extracted beam	1 000 MeV (const.)
Uniformity of energy	1%
Beam intensity inside the chamber	$\leq 3 \mu\text{A}$ (var.)
Extracted beam intensity	$\leq 1 \mu\text{A}$ (var.)
Efficiency	30%
Macropulse repetition rate	45–60 Hz
Macropulse duration	300 μs – 20 ms

Parameters of the proton beams of the synchrocyclotron with the energy $E = 1\,000$ MeV are given in Table 2.

Table 2

Parameters of proton beams of the synchrocyclotron

$\Delta E/E$, %	Intensity, s^{-1}	Application
1	$< 6 \cdot 10^{12}$	Main proton beam
1	10^8	Medical beam of the size 3–5 mm ²
10^{-3}	10^{10}	Spectrometric beam
1	10^{10}	Second proton beam

A widely developed system of secondary beams expands the boundaries of the experimental possibilities of the accelerator complex. Main parameters of the secondary beams are given in Table 3.

Table 3

Main parameters of secondary beams of the synchrocyclotron at the PNPI

Particle	Momentum, MeV/c	$\Delta p/p$, %	Intensity (at 1 $\mu A p^+$), s^{-1}	Channel
π^+	450	6	10^6	$\pi 1$ -channel
π^-	450	6	$3 \cdot 10^5$	
π^-	250	2.5–12	$10^5 - 5 \cdot 10^6$	$\pi 2$ -channel
π^+	250	2.5–12	$3 \cdot 10^5 - 1.6 \cdot 10^7$	
μ^+	29	12	$3 \cdot 10^4$	$\pi 2$ -channel
μ^-	160	10	$9 \cdot 10^4$	μ -channel
μ^+	175	10	$3 \cdot 10^5$	

Neutron beam:

- Energy – 10^{-2} –1 000 MeV,
- Intensity – $3 \cdot 10^{14}$,
- Pulse width – 10 ns,
- Frequency – 50 Hz.

The uniqueness of the accelerator base of the PNPI is determined both by the parameters of the synchrocyclotron itself – energy, intensity, time structure of the beam, and by the created experimental facilities and complexes:

- Muon channel (μ SR-facility),
- $\pi 1$ -meson high energy channel,
- $\pi 2$ -meson low energy channel,
- Mass-separator complex IRIS (investigation of radioactive isotopes of the synchrocyclotron),
- Neutron time-of-flight spectrometer GNEIS (Gatchina neutron time-of-flight spectrometer),
- MAP (magnetic analyser of protons),
- The complex of radiation tests of the electronic component base for radiation resistance in proton and neutron beams.

2. Accelerator complex staff

Currently, there are 44 employees in the accelerator department of the Advanced Development Division (ADD). The diagrams (Fig. 2) show the age and qualification composition of the accelerator department for January 2023.

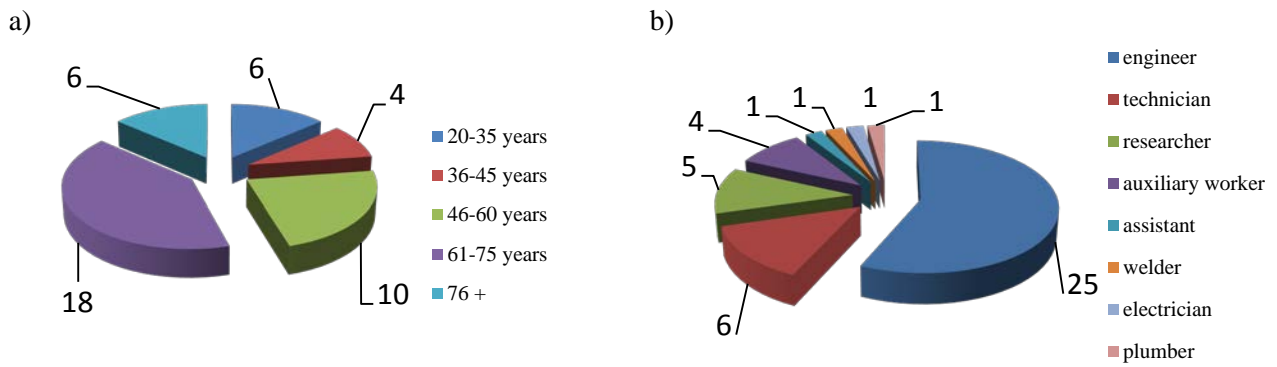


Fig. 2. Age (a) and qualification (b) composition of the accelerator department

3. The dynamics of the synchrocyclotron operation

Figure 3 shows the dynamics of the synchrocyclotron operation in hours since 2016.

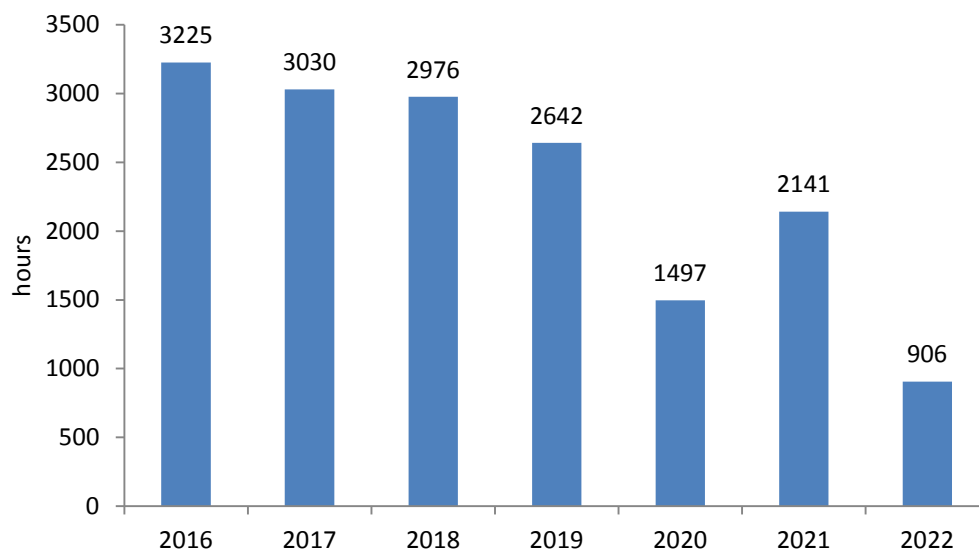


Fig. 3. The dynamics of the synchrocyclotron operation in hours since 2016

The decrease in the operating time of the synchrocyclotron in 2022 is associated with the forced shutdown of the accelerator. It was necessary to carry out work on fixing shims on the poles of the synchrocyclotron magnet (Fig. 4). This work was carried out from April to December 2022.

Reducing the working time of the synchrocyclotron in the period 2020–2021 is due to the pandemic. During this period of time, the users activity dropped sharply. Reducing the working time of the synchrocyclotron in the period 2016–2019 is associated with both minor accidents in the accelerator systems and a shortage of personnel in the synchrocyclotron control service. At present, the SC-1000 control service is equipped with only three shifts, consisting of: a shift supervisor, an operator and a technician. With this situation, 3 500 h of continuous work per year is under question.

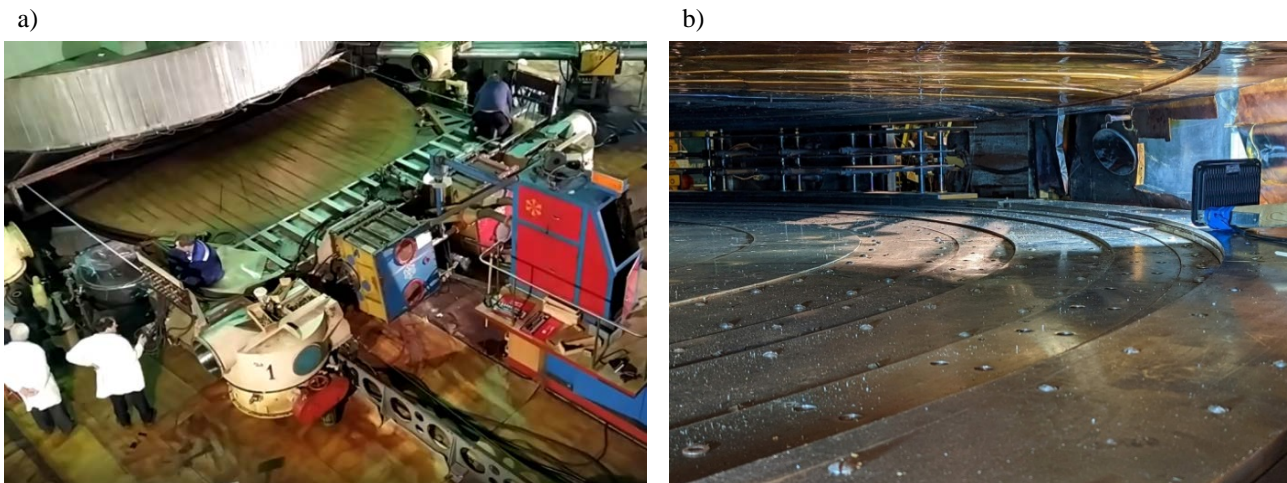


Fig. 4. Shims: *a* – fixing (the duant is out); *b* – bottom pole of the magnet

In the period 2019–2022, for the maintenance of the accelerator department and for the operation of the synchrocyclotron, services, materials and equipment were purchased in the amount of 9 652 153 ₺. More detailed funding of the department is given in Table 4.

Table 4

Financing of the accelerator department

Source of financing	Year			
	2019	2020	2021	2022
Branch (ADD)	2 467 105 ₺	2 348 613 ₺	2 499 228 ₺	2 332 167 ₺
Centre	5 040 ₺	–	–	–
Total	2 472 145 ₺	2 348 613 ₺	2 499 228 ₺	2 332 167 ₺

Distribution of the work time of groups at the synchrocyclotron in the period 2019–2022 is shown in Fig. 5.

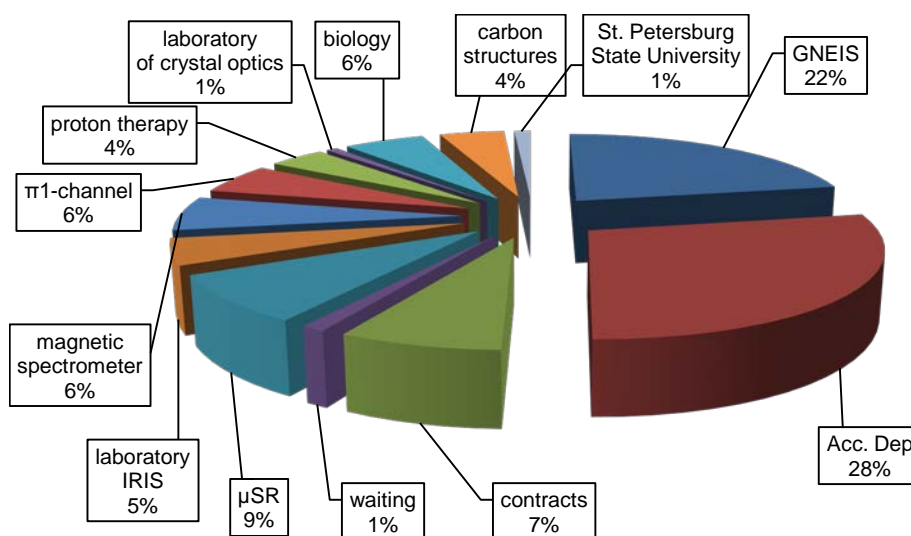


Fig. 5. Distribution of work time at the synchrocyclotron

4. Physics research at the PNPI synchrocyclotron

Along with traditional research in the field of nuclear physics at the PNPI synchrocyclotron, the need arose for new experimental studies.

The Molecular and Radiation Biophysics Division of PNPI is conducting a series of experiments on the topic “Approbation on Biomodels of Potential Sensitizing Compounds to Improve the Efficiency and Safety of Radiation Therapy”. The works were supported within the framework of research work on the complex topic “Biomedical Technologies” of the NRC “Kurchatov Institute” in the period 2019–2022. (The order of the NRC “Kurchatov Institute” dated June 25, 2019 No. 1363.)

The main results of the work are presented in Ref. [1–7].

Success in the field of biomedical research is closely related to the use of new pharmaceuticals in clinical practice. The Laboratory of Chemistry and Spectroscopy of Carbon Materials is conducting a series of experiments to study the use of proton irradiation for the synthesis of new pharmaceuticals based on endofullerenes for the diagnosis and treatment of processes with different pharmacokinetics. At the synchrocyclotron SC-1000, work was carried out to study the radiation resistance of fullerenes and their derivatives, namely C_{60} , C_{70} , fullereneols $C_{60}(OH)_{30}$, $Fe@C_{60}(OH)_{30}$ and $Me@C_{82}(OH)_{38-40}$ ($Me = Sm, Eu, Gd, Tb, Ho$) and $Sm@C_{82}(C_6H_9NO)_n$, $Gd@C_{82}(C_6H_9NO)_n$, $Fe@C_{60}(C_6H_9NO)_n$, $Fe@C_{60}(C_6H_{10}O_5)_n$ complexes. The relevance of these studies is due to the fact that currently existing chemotherapy methods do not provide selective delivery and adequate concentration of therapeutic agents in tumor tissue with limited monitoring of the result of treatment procedures, which often leads to complications and also reduces the therapeutic effect. In turn, irradiation of endometallofullerenes in a stream of ionizing radiation opens up the possibility of creating radiopharmaceuticals for the diagnosis and treatment of oncological diseases using endometallofullerenes. We also studied the effect of proton irradiation with an energy of 1 000, 500 and 100 MeV on preparations $Ho@C_{2n}(OH)_x$, $Sm@C_{2n}(OH)_x$, $Tb@C_{2n}(OH)_x$, and complexes of endofullerenes with biocompatible polymers dextrin $(C_6H_{10}O_5)_n$ and low molecular weight polyvinylpyrrolidone $(C_6H_9NO)_n$. The main results of the work were published in Ref. [8–9].

The activities of the employees of the Saint Petersburg State University are related to the study of the characteristics of the latest pixel detectors for their use in the creation of vertex detectors in experiments at the NICA (nuclotron-based ion collider facility) collider. Work is carried out in three directions:

- Testing on proton beams of the SC-1000 synchrocyclotron of an experimental set-up for researching the characteristics of silicon pixel sensors based on complimentary metal–oxide–semiconductor (CMOS) technology for vertex detectors in high energy physics,
- Development and testing on the beams of the SC-1000 synchrocyclotron of an experimental bench for research with new pixel detectors and ultralight carbon composite materials to create new diagnostic systems for proton tomography (250 MeV protons) used in nuclear medicine,
- Development of systems for diagnosing charged particle beams using telescopes of silicon pixel detectors.

The experimental set-up of the Saint Petersburg State University is shown in Fig. 6. Figure 7 shows the emittance of the proton beam with the energy $E = 1\ 000$ MeV at the entrance to the facility.



Fig. 6. The experimental set-up of the Saint Petersburg State University at the SC-1000 proton beam

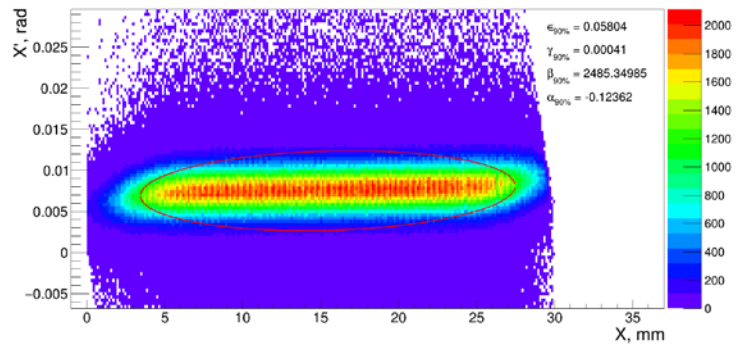


Fig. 7. The emittance of the $E = 1\,000$ MeV proton beam at the entrance to the facility

It is planned to continue the analysis of data for the 200 and 400 MeV proton beams. The results of the work were reported at conferences and published in Ref. [10–14].

As part of the development of methods for conducting tests at the PNPI CMOS (BiCMOS) of specialized integrated circuits for nuclear physics equipment at charged particle accelerators, primarily for experiments at the NICA, within the framework of the agreement concluded with the National Research Nuclear University (Moscow Engineering Physics Institute) work was done on the topic: “Carrying Out Radiation Tests and Studies of Experimental Samples of Specialized Integrated Circuits on Proton Beams at the Synchrocyclotron”.

The National Research Technological University MISiS (Moscow Institute of Steel and Alloys) performed irradiation of Ga_2O_3 structures with a 1 GeV proton beam in order to obtain defects in the crystal lattice in structures based on gallium oxide. The results obtained will be used to study new radiation phenomena in gallium oxide, to assess the prospects for their application in the development and production of new semiconductor devices with improved properties. The work will continue.

5. Operation life of the PNPI synchrocyclotron

In 2020, the staff of the Accelerator Department and the Nuclear Safety Administration carried out work to extend the operation life of the synchrocyclotron complex as part of the SC-1000 synchrocyclotron, the IRIS complex and the GNEIS neutron spectrometer.

Based on the results of a comprehensive examination of the synchrocyclotron complex, a conclusion was made, which was approved by the Ministry of Science and Higher Education of the Russian Federation, about the possibility of extending its service life beyond the appointed one by 10 years – until 01.04.2030, provided that the specified comments are met by 01.04.2024.

Specific comments, measures and deadlines for their implementation are given in Table 5.

Table 5

Comments, measures and deadlines for their implementations

No.	Name of the event	The timing or frequency of not later / not less than
1	Inspection of building structures of building No. 2, the IRIS complex and the GNEIS hangar	Once a year
2	Carrying out repair and restoration work of the brick walls of building No. 2	01.04.2024
3	Carrying out repair and restoration works of roll roofing of building No. 2	01.04.2024
4	Carrying out repair and restoration work of the brick walls of the IRIS complex	01.04.2024
5	Carrying out repair and restoration work of reinforced concrete floor slabs and coatings of the IRIS complex	01.04.2024
6	Carrying out repair and restoration work of the rolled roof of the IRIS complex	01.04.2024
7	Carrying out repair and restoration work of the metal walls of the GNEIS hangar	01.04.2024
8	Carrying out repair and restoration work of the roof, ceiling and coating of the GNEIS hangar	01.04.2024
9	Maintenance and scheduled preventive (restorative) repair of systems and their elements	In accordance with the scheduled preventive maintenance schedules
10	Testing systems and their elements	Once a year
11	Replacement of elements of the radiation monitoring system that have exhausted their resource	31.12.2022
12	Replacement of elements of the ventilation system, the operating time of which is approaching 30 years	As the operating time approaches 30 years
13	Replacement of VMG-133 oil circuit breakers with PS-10 drives	31.12.2022
14	Filling technological openings (passages) in the ceiling above the basement of building No. 2 with materials with a fire resistance limit of at least EI30	31.12.2023
15	Retrofitting the basement of the experimental hall of building No. 2 with automatic fire extinguishing installations	31.12.2023
16	Installation of an additional door to the experimental room equipped with a physical access control system	31.12.2021

6. C-80 based projects

At present, the PNPI is ready to implement the “Isotope” and “Okol” projects on the basis of the existing C-80 isochronous cyclotron [15]. Within the framework of these projects, the accelerator department indicated and justified the construction site of new buildings and their configuration (Fig. 8a).

In the initial version, one proton beam is extracted from the C-80 cyclotron. In accordance with the projects and configuration of the buildings, it became necessary to output a second proton beam for proton therapy, and these two beams should be output both separately and simultaneously. Taking into account the accepted geometry of the buildings, the point of installation of the charge exchange foil in the cyclotron chamber (Fig. 8b) was found by calculation to extract the second beam [16]. A proton beam transport path for radionuclide production was designed and optimized (Fig. 9a). For this, the newly created Proton_MK program was used [17].

For proton therapy, the $E = 70$ MeV beam extracted from the C-80 was used. It is transported using the Proton_MK program to a Ta-foil used as a diffuser, on which a beam size of $\sim \varnothing 30$ mm is formed by a triplet of lenses. The results of the passage of protons through a Ta-foil $300 \mu\text{m}$ thick were obtained using the GEANT4 program. They were the initial conditions of the Proton_MK program for further transport of the diverging proton beam in free space ~ 3.7 m to the collimator. As a result, according to the requirements, a beam was formed at the entrance to the irradiation room with a diameter of 60 mm. In this case, the minimum possible divergence angle (0.3°) was obtained, and the homogeneity of the beam was 95% (Fig. 9b).

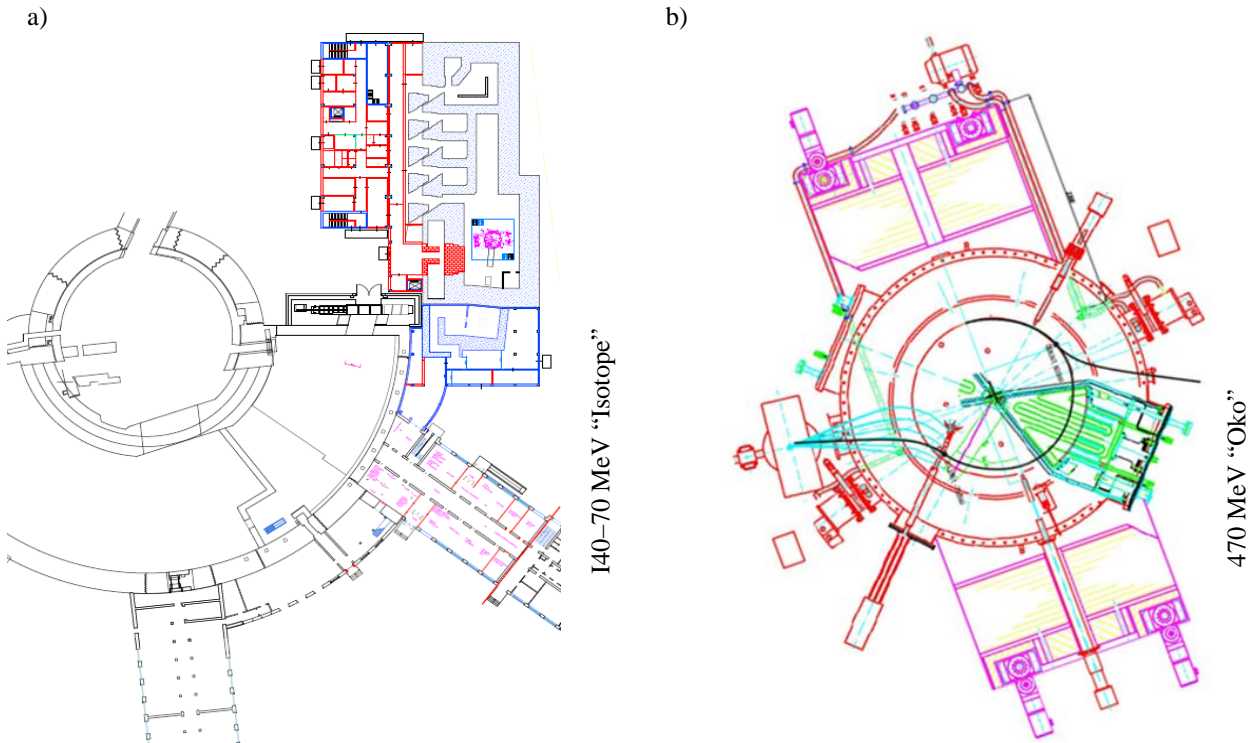


Fig. 8. Location and geometry of buildings (a); location of the beam extraction system for proton therapy (b)

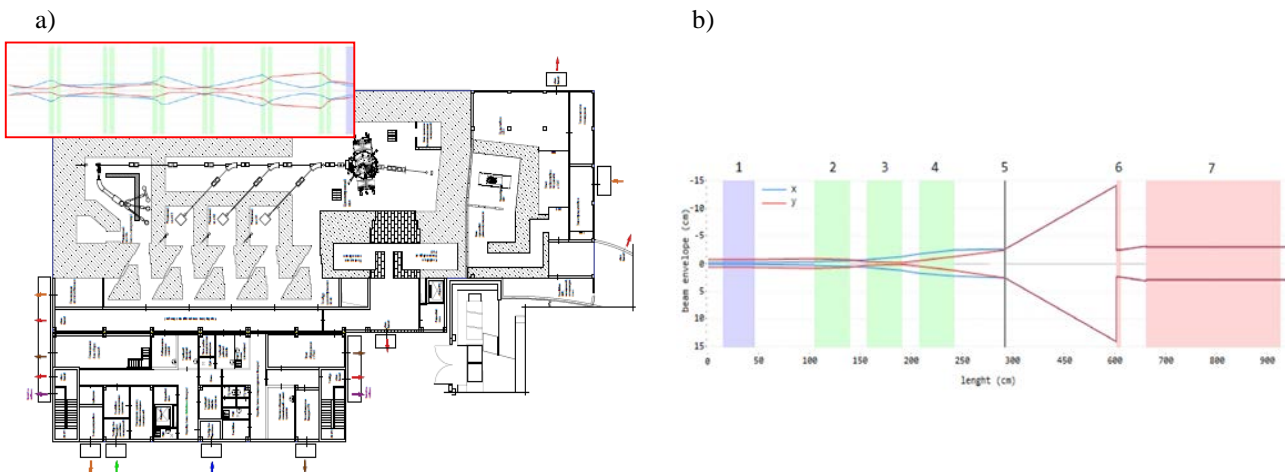


Fig. 9. Geometry of the path for isotope production and beam envelopes (a); geometry of the tract for proton therapy and beam envelopes (b): 1 – corrective magnet; 2–4 – triplet lenses; 5 – scattering Ta-foil of $300 \mu\text{m}$; 6 – collimator $\varnothing 50$ mm; 7 – biological protection

In addition to the works [1–17] mentioned above, the staff of the Accelerator Department and the Laboratory of Physics and Technology of Accelerators published 55 papers of various significance in 2019–2022.

References

1. T. Shtam, V. Burdakov, A. Garina *et al.*, Experimental Validation of Proton Boron Capture Therapy for Glioma Cells. Sci. Rep., Under Review.
2. D. Lebedev, L. Garaeva, V. Burdakov *et al.*, in *RAD Conf. Proc.* **4**, 60–65 (2020). DOI: 10.21175/Rad.Proc.2020.12.
3. T. Shtam, N. Razgildina, L. Garaeva *et al.*, in *Collection of Sci. Papers of the VI St. Petersburg Int. Oncological Forum “White Nights”*, 546 (2020).
4. L. Garaeva, V. Burdakov, A. Volnitskiy *et al.*, in *Book of Abstr. of the Eighth Int. Conf. on Radiation in Various Fields of Research 2020*, 118 (2020).
5. L. Garaeva, V. Burdakov, E. Kuus *et al.*, in *Book of Abstr. of the Eighth Int. Conf. on Radiation in Various Fields of Research “RAD 2021 Conference”*, 118 (2021).
6. A.V. Volnitskii, A.V. Garina, V.S. Burdakov *et al.*, *Advances in Molecular Oncology* **8**, Appendix 4, 123 (2021).
7. A.V. Garina, V.S. Burdakov, L.A. Garaeva *et al.*, in *Proc. of the 64th All-Rus. Sci. Conf. of the Moscow Institute of Physics and Technology. Biological and Medical Physics*, 69–70 (2021).
8. M.V. Suyasova, A.A. Borisenkova, V.A. Shilin *et al.*, *Nanosyst.: Phys. Chem. Math.* **10** (4), 447 (2019). DOI 10.17586/2220-8054-2019-10-4-447-455.
9. M.V. Suyasova, A.A. Borisenkova, V.A. Shilin *et al.*, in *Proc. of the Conf. “VII Annual All-Rus. Youth Sci. Forum Open Science 2019”* (2019).
10. V. Zhrebchevsky, New Technologies for the Vertex Detectors at the NICA Collider Experiments: Oral Report, *LXXI Int. Conf. “NUCLEUS-2021. Nuclear Physics and Elementary Particle Physics. Nuclear Physics Technologies”* (2021).
11. D. Nesterov, New Mechanic and Cooling Systems for the Silicone Detectors Used in High Energy Physics Experiments: Oral Report, *LXXI Int. Conf. “NUCLEUS-2021. Nuclear Physics and Elementary Particle Physics. Nuclear Physics Technologies”* (2021).
12. D. Nesterov, Cooling Systems for the Novel Pixel Detectors: Oral Report, *LXX Int. Conf. “NUCLEUS-2020. Nuclear Physics and Elementary Particle Physics. Nuclear Physics Technologies”* (2020).
13. V. Zhrebchevsky, Silicon Pixel Detectors for the Inner Tracking System of MPD Experiment at the NICA Collider: Oral Report, *LXX Int. Conf. “NUCLEUS-2020. Nuclear Physics and Elementary Particle Physics. Nuclear Physics Technologies”* (2020).
14. V.I. Zhrebchevsky, V.V. Vechernin, S.N. Igolkin *et al.*, *Bull. Rus. Acad. Sci.: Phys.* **85** (5), 541 (2021).
15. D.A. Amerkanov, S.A. Artamonov, E.M. Ivanov *et al.*, in *Proc. 27th Rus. Particle Accelerator Conf. (RuPAC’21)* 189–191 (2021). DOI:10.18429/JACoW-RuPAC2021-MOPSA44.
16. E.M. Ivanov, V.I. Maksimov, G.F. Mikhev, G.A. Ryabov, Method of Simultaneously Extracting Two Proton Beams from a Cyclotron: Main and Medical for Ophthalmology: Patent for Invention No. 2738954, Application No. 2020127023, Invention Priority: 11.08.2020.
17. D.A. Amerkanov, E.M. Ivanov, G.A. Riabov, V.A. Tonkikh, in *Proc. 27th Rus. Particle Accelerator Conf. (RuPAC’21)* 262–264 (2021). DOI:10.18429/JACoW-RuPAC2021-TUPSB16.



Elementary Particles Physics

HIGGS BOSON AND STANDARD MODEL STUDY WITH CMS AT THE LARGE HADRON COLLIDER

PNPI participants of the CMS Collaboration: **A.A. Vorobyev**, V.T. Kim, Yu.M. Ivanov, V.L. Golovtsov, E.V. Kuznetsova, P.M. Levchenko, A.Iu. Egorov, V.A. Murzin, V.A. Oreshkin, L.A. Shchipunov, I.B. Smirnov, D.E. Sosnov, V.V. Sulimov, L.N. Uvarov, S.A. Vavilov, S.S. Volkov, An.A. Vorobyev

1. Introduction

The compact muon solenoid (CMS) experiment [1] is one of the largest international scientific collaborations in history, involving about 4 300 particle physicists, engineers, technicians, students and support staff from 182 institutes in 42 countries.

During 2019–2022, CMS obtained a big amount of physics results based on data from the Large Hadron Collider (LHC) Run-2 and the beginning of Run-3, which started in July 2022 after Long Shutdown 2 (LS2). Run-2 included the data taken at $\sqrt{s} = 13$ TeV with the recorded integrated luminosity of 140 fb^{-1} .

Starting after LS2, Run-3 features the c. m. energy increased to 13.6 TeV and a higher average instantaneous luminosity thanks to the luminosity leveling. Significant enhancements are made to the subdetectors. Data acquisition (DAQ) and trigger systems during LS2 allow for extensive improvements in physics objects reconstruction. For example, the muon subsystem of cathode strip chambers (CSC) underwent a read-out electronics upgrade in all the 180 CSC muon chambers during LS2. Other improvements include an increased geometric coverage for the resistive plate chambers (RPC), introduction of a new subsystem of the gas electron multiplier (GEM) chambers, and enhanced CSC data taking bandwidth timing. Accordingly, the muon trigger was modernized to take into account the newly added chambers and the muon subsystem enhancements. The Run-2 data taking ended in December 2018, accumulating the total integrated luminosity of 150 fb^{-1} , as shown in Fig. 1. Run-3 started in July 2022 and collected data with an integrated luminosity of around 33.3 fb^{-1} . Run-3 is expected to double the integrated luminosity of Run-2.

The results cover a wide assortment of topics and range from precision measurements of the Higgs boson and the Standard Model (SM) processes to searches for rare decays and exotic phenomena. Some selected results are presented below: measurement of the Higgs boson properties, its production and decay modes, newly obtained results on Higgs coupling to second generation fermions, Higgs width measurement, self-interaction, as well as precision measurements of some SM parameters such as the top mass, vector boson decay widths. Two other crucial topics, dijets with large rapidity separation as a probe of BFKL (Balitsky–Fadin–Kuraev–Lipatov) effects and diffractive proton–nucleus collisions [2, 3], are separately covered elsewhere in this volume.

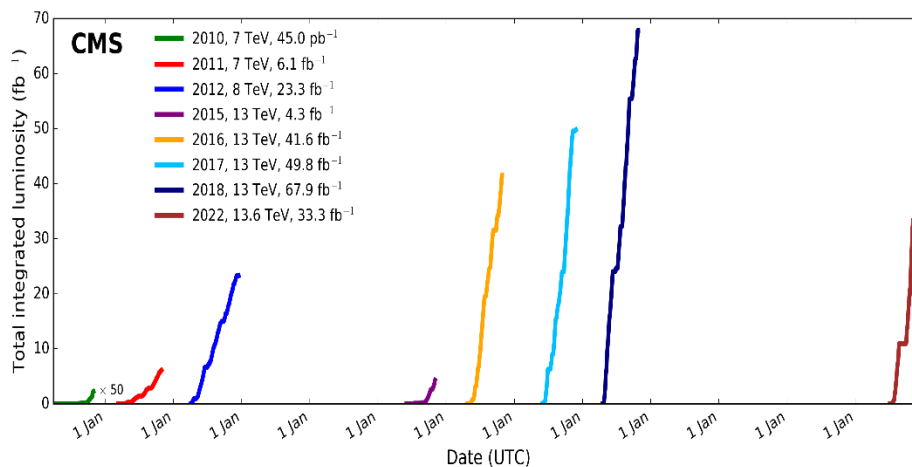


Fig. 1. Integrated proton–proton luminosity for LHC Run-1 (7 TeV), Run-2 (13 TeV) and first months of Run-3 (13.6 TeV)

2. Properties of the Higgs boson

By taking the benefit of all collected Run-2 data, a large set of measurements were performed aimed at further checking the consistency of the Higgs boson with the SM. The Higgs boson mass was measured to be 125.38 ± 0.14 GeV by the CMS Collaboration [4] with an unprecedented precision (0.11% uncertainty) as a result of a single experiment. The measurement was based on Run-2 and Run-1 data and on a combination of the $H \rightarrow ZZ$ and $H \rightarrow \gamma\gamma$ processes. This value of the Higgs mass was used as a parameter of the SM, in order to obtain the SM predictions. To quantify the properties of the Higgs boson, CMS performed various measurements of signal strength parameters μ , which are defined as ratios of the measured cross section multiplied by a branching fraction over the corresponding SM prediction or, more briefly, the observed rate normalized by an SM prediction. For the inclusive Higgs production, where an equal value of μ was assigned for each process, μ was measured to be 1.002 ± 0.057 [5]. This is a fourfold improvement in precision since the analogous result of 0.87 ± 0.23 obtained at the time of the Higgs boson discovery, and it is in excellent agreement with the SM expectation. The theoretical uncertainties in the signal prediction, the experimental statistical, and the systematic uncertainties being 0.036, 0.029 and 0.033 [5], respectively, contribute to the total uncertainty at a similar level.

A more detailed picture was obtained by relaxing the assumption of a common signal strength parameter, and introducing different μ_i and μ_f (where i and f designate initial and final states) in a combination of several analyses targeting different production and decay mechanisms of the Higgs boson. All main production modes ggH , VBF (vector boson fusion), WH , ZH , and ttH were observed with a significance of 5 s. d. (standard deviations) or larger, except for the Higgs associated with the single top (tH) production mode. It should be noted that large quantum chromodynamics (QCD) corrections to bb decay change the total SM Higgs decay width by a factor of ~ 1.5 – 2 . [6–14]. All main decays, $\gamma\gamma$, ZZ , WW , $\tau\tau$, bb , $\mu\mu$, were observed with significances of more than 5 s. d., except for the newly observed Higgs decay to a pair of muons which was observed with a significance of 3 s. d., and the $H \rightarrow Z\gamma$ decay [15] with a significance of 2.7 s. d. (2.1 s. d. expected).

Another set of measurements were done in the κ -framework [16] for coupling modifiers κ , which are defined as multipliers of the process strength at the amplitude level (or, equivalently, in the SM Lagrangian). In this framework a set of coupling modifiers κ alter the signal strength, without affecting the kinematic distributions. Among the advantages of the κ -framework is the ability to take into account the interference effects in loops, such as negative interference between the top (or bottom) quark loop diagrams and W boson diagrams in the Higgs decay. The κ_f , κ_V values for the Higgs couplings to fermions and bosons were measured for the full Run-2 dataset (Fig. 2). The sensitivity with present data is much improved, and both coupling modifiers are measured to be in agreement, within an uncertainty of 10%, with the predictions from the SM. By taking more detailed parameterizations, each of the coupling modifiers κ_t , κ_W , κ_Z , κ_b , κ_τ , κ_μ , $\kappa_{Z\gamma}$, κ_g , κ_γ , was also measured by performing a fit to data. For all the couplings, the results indicate agreement with the SM, and a significant improvement in precision as compared to the previous measurements, as shown in Fig. 3. The κ -framework can also accommodate any non-SM invisible or undetected component. To probe decays of the Higgs boson to invisible particles, including unknown non-SM particles, such as new neutral long-lived particles or dark matter particles, other two floating parameters were added to the fit: the Higgs invisible decay branching fraction, \mathcal{B}_{inv} , and the Higgs undetected decay branching fraction, $\mathcal{B}_{\text{undet}}$. The $\mathcal{B}_{\text{undet}}$ branching ratio corresponds to undetected particles, a species of particles that may optionally leave a trace in the detector. Although, CMS has no experimental signature to reconstruct such particles, they contribute to the total width and thus can be inferred indirectly. The fitting procedure allowed CMS to find \mathcal{B}_{inv} , and $\mathcal{B}_{\text{undet}}$ to be consistent with zero, provided that the upper bounds on κ_W , κ_Z are set to their SM values. The 95% CL (confidence level) upper limit on \mathcal{B}_{inv} is found to be $\mathcal{B}_{\text{inv}} < 0.18$ (with 0.10 expected value) [17]. To constrain these quantities without imposing bounds on κ_W and κ_Z , an independent total Higgs width measurement should be performed.

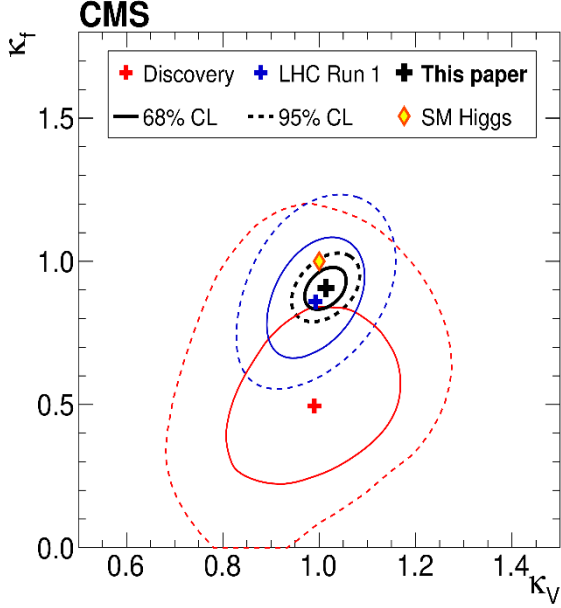


Fig. 2. Constraints on the Higgs boson coupling modifiers to fermions (κ_f) and heavy gauge bosons (κ_V)

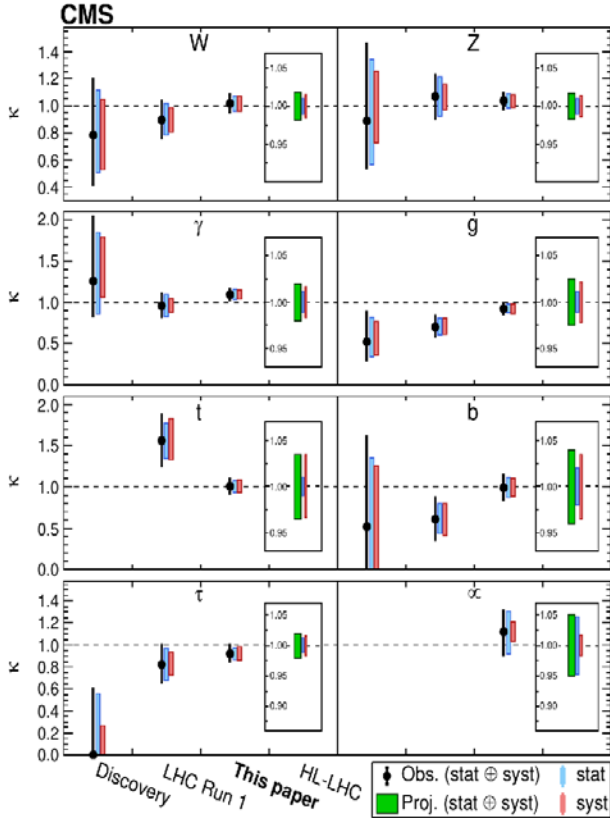


Fig. 3. Coupling modifiers κ in different data sets: at the time of the Higgs boson discovery, using the full Run-1 data, the data used in paper [5], and the expected uncertainty at the HL (high luminosity) – LHC for $L = 3\,000\text{ fb}$

While in Run-1 only the interactions with the three heaviest fermions (third generation fermions) began to be established by observing the decay to tau particles, the heaviest leptons, only in combination of ATLAS and CMS results, an increase in the centre-of-mass energy to 13 TeV and larger datasets ($36.5, 140\text{ fb}^{-1}$) in Run-2 allowed further channels to be probed and further study of the already observed processes. For example, in the analysis of all Run-2 data, CMS measured differential cross sections for processes of Higgs decaying to a pair of tau leptons [18, 19] as functions of the Higgs boson transverse momentum, jet multiplicity, and transverse momentum of the leading jet. This is the first measurement in the Higgs to tau decay channel, which was performed in a fiducial volume defined by the kinematics of the visible tau decay products. In this analysis, CMS measured a fiducial cross section of $426 \pm 102\text{ fb}$, in good agreement with the SM prediction of $408 \pm 27\text{ fb}$. Also, the $H \rightarrow \tau\tau$ channel provides sensitivity to the charge parity (CP) structure of the Higgs boson *via* the angle φ_{CP} between the reconstructed τ -lepton decay planes. So, the tau lepton Yukawa [20] CP -structure was probed by CMS. The angle was found to be $-1 \pm 19^\circ$, and the pure CP -odd coupling was excluded with a significance of 3 s. d. Similarly, the pure CP -odd coupling of tau lepton was excluded at 3.2σ . Besides, in the fermion sector the pure CP -odd Higgs coupling was disfavoured [21] with a statistical significance of 3.7σ for the top-quark Yukawa interaction by targeting a process where a Higgs boson is produced in association with a pair of top quarks ($t\bar{t}H$). Kinematic differences between the $t\bar{t}H$ CP -even component and a potential $t\bar{t}H$ CP -odd component are exploited to put constraints on the mixing angle by means of an additional multivariate discriminator based on boosted decision trees (BDT). In this analysis, CMS employed all-hadronic and semi-leptonic final states and combined multiple channels of the Higgs boson decay: $H \rightarrow \gamma\gamma$, $H \rightarrow 4\ell$ and $H \rightarrow \tau\tau$. A new tau lepton identification tagger called DeepTau [22] based on a convolutional deep neural network was used in the above analysis. It combines information from the high-level reconstructed tau lepton features together with the low-level information from the inner tracker, calorimeters and muon sub-detectors to reduce the fraction of quark and gluon jets, electrons and muons misidentified as τ .

But a major breakthrough in the study of Yukawa couplings was that the Higgs couplings to the second-generation fermions were probed for the first time. An evidence for the $H \rightarrow \mu\bar{\mu}$ decay with a significance of three standard deviations was obtained [23] by CMS. The corresponding Yukawa coupling, y_μ , confirms the linear dependence on particle masses, as shown in Fig. 4, which is tested now over four orders of magnitude. The coupling to another 2nd generation fermion, c quark, was harder to study due to 20 times less branching fraction than that of the b -quark Higgs decay and a less prominent experimental signature of c -quark jets. A constraint on the charm quark interaction coupling modifier was found to be $1.1 < |\kappa_c| < 5.5$ (with the expected $|\kappa_c| < 3.40$) [24] at 95% CL. This is the most stringent constraint on the charm–Higgs interaction to date, thanks to the increased amount of data (full Run-2 data were analysed) and improved machine learning techniques for the charm-jet identification [25], which aids in discrimination of a charm-flavoured jet both from a light-quark jet and a b -quark jet. CMS constraints on Yukawa charm-Higgs interaction, y_c , are comparable to what had previously been expected at the end of the HL–LHC. This measurement was done in the VH production channel, $VH (H \rightarrow c\bar{c})$ and V decaying leptonically. The leptonic decay of the associated vector boson allows to tag an event, independently of the H boson decay, and helps to eliminate the contribution of the multijet background. Simultaneously, to validate the method, the analogous process with a vector boson instead of H , $VZ (Z \rightarrow c\bar{c})$ production, was observed with a significance of 5.7σ , for the first time. From the experimental point of view this process is very similar to $VH(cc)$, except for the mass of the $Z(H)$ boson.

Besides its couplings, another important property of the Higgs is its natural decay width. Although it can be indirectly constrained in coupling fits, its direct measurement is a sensitive probe of beyond the Standard Model (BSM) processes and it is interesting to compare it with predictions from the SM. However, the CMS measurement resolution is of about 1 GeV, which is much larger than, *e. g.* 4.1 MeV, where $\Gamma_H = 4.1$ MeV is the Higgs width prediction at Born level. On the other hand, the time-of-flight measurement, performed by searching for Higgs bosons that traveled measurable distances before decaying, gives a too loose constraint of $\Gamma_H < 46$ MeV [26]. To overcome the resolution limitation, the CMS utilized the off-shell Higgs production (an evidence for which was found with a significance of 3.6σ for the first time) to indirectly measure [27] the Higgs width by using the fact that it is proportional to the ratio of the off-shell over the on-shell production rate. The result of the measurement, $\Gamma_H = 3.2^{+2.4}_{-1.7}$ MeV is the new two-sided limit on the Higgs natural width at 95% CL (or equivalently the Higgs lifetime $7.71 \cdot 10^{-23}\text{s} < \tau_H < 1.31 \cdot 10^{-31}\text{s}$). This is a significant improvement of the upper limit $\Gamma_H < 28$ MeV at 95% CL obtained in the previous CMS study [28]. Compared to the previous study, this work makes use of a much larger sample of collision data and reconstructs the ZZ in an additional final state $ZZ \rightarrow 2\ell 2\nu$, besides $ZZ \rightarrow 4\ell$. The new result is in good agreement with the predicted SM value at Born level of 4.1 MeV [29], as well as with predictions that take into account higher-order next-to-leading order (NLO) QCD corrections [12, 14] which predict, as we noted earlier, approximately two times lower value of the Higgs width.

One of the most important open questions in Higgs physics is whether the potential written in the SM is the one chosen by nature. A specific shape of the potential in the immediate vicinity of the minimum determines the probability of an important process (coupling), the splitting of a Higgs boson into two (or even three) Higgs bosons. The Higgs boson pair production is an interesting process due to its potential to access the trilinear Higgs boson self-coupling, which is one of a few SM parameters being still largely unconstrained. Several CMS analyses [5] were devoted to study the Higgs pair production. Each of the analyses dealt with its

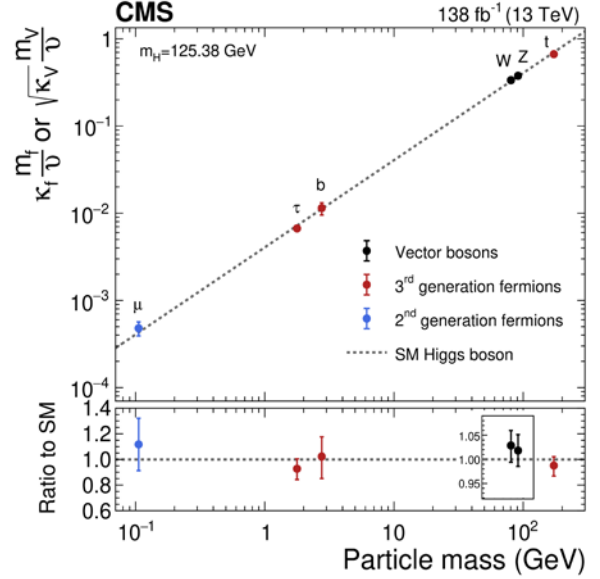


Fig. 4. The measured coupling modifiers of the Higgs boson to fermions and heavy gauge bosons, as functions of fermion or gauge boson mass

own type of final states. The final states are categorized by the decay type of each of the two Higgs bosons (bb , $\tau\tau$, WW , ZZ , or $\gamma\gamma$) or whether a pair of b -quarks decays into two separate jets or, being highly boosted, merge into a single jet. In the combination of these analyses, the Higgs boson pair production is found to be less than 3.4 times the SM expectation at 95% CL. This is a significant improvement over the 2016 analysis combination [30] for 36.5 fb^{-1} , which claimed an upper limit of $\sigma_{HH} < 22.2 \sigma_{HH}^{\text{SM}}$. Moreover, combined coupling modifier constraints for the Higgs trilinear coupling were significantly improved: $-1.24 < \kappa_\lambda < 6.49$, given that for the 2016 analysis it was found to be $-11.8(-7.1) < \kappa_\lambda < 18.8(13.6)$. Also, for the quartic coupling ($VVHH$), a constraint was found to be $0.67 < \kappa_{2V} < 1.38$, excluding for the first time a zero value of κ_{2V} at a 6.6 s. d. CL.

3. Standard Model

Besides the Higgs properties, CMS progressed towards precise determination of other parameters of the SM. Parameters of weak and strong interaction were extensively studied using Run-2 data at 13 TeV, but one of the recent results is obtained at new energy of 13.6 TeV with the Run-3 data. It is the first observation [31] of the top-antitop production, and its cross section measurement required detailed state-of-the-art simulation of electroweak processes and of QCD processes at the next-to-next-to-leading order (NNLO) at the new energy. The inclusive $t\bar{t}$ cross section was measured to be $887_{-41}^{+43}(\text{stat} + \text{syst}) \pm 53(\text{lumi}) \text{ pb}$, which is in good agreement with the SM prediction of $921_{-37}^{+29} \text{ pb}$ and about 10% higher than at 13 TeV. The top quark occupies a special place in the SM, because its mass together with the Higgs boson mass and the Higgs boson potential determines the stability of the vacuum. A direct top mass measurement was performed by CMS using Run-2 data [32]. The obtained result $m_t = 171.77 \pm 0.38 \text{ GeV}$ has the best accuracy ever reached (0.22%). The mass was reconstructed from a kinematic fit. In contrast to the previous analyses, a novel approach of determination of the uncertainties was used, where the jet energy scale, resolution and other uncertainties were determined directly from the maximal likelihood estimate (MLE) fitting procedure, with the likelihood function scans with respect to the nuisance parameters. Thus, the precision was significantly improved over the previous measurements [33, 34]. Also, five kinematic variables, instead of three, were employed in the measurement, and the jet energy scale uncertainty was constrained *in situ* using hadronic W boson decays.

A competitive and complementary way to study the top mass was based on the measurement of the mass of a jet, originating from a top quark [35]. The mass was found to be $m_t = 172.76 \pm 0.81 \text{ GeV}$. The pole top mass was also measured by CMS, exploiting the mass sensitivity of $t\bar{t}$ production with at least one additional jet ($t\bar{t} + \text{jet}$) [36]. The normalized differential cross section as a function of the ρ observable defined as $340 \text{ GeV}/m_{t\bar{t} + \text{jet}}$ is measured at the parton level using a profiled likelihood unfolding approach. Machine learning methods are used for the reconstruction of the ρ and pole event classification. The top pole mass was found to be $m_t^{\text{pole}} = 172_{-1.34}^{+1.37} \text{ GeV}$ from a comparison to NLO predictions with the ABMP16NLO parton distribution function (PDF). Another PDF CT18NLO was also used with the result $m_t^{\text{pole}} = 172.16_{-1.41}^{+1.44} \text{ GeV}$. With respect to previous measurements, the result is improved by a factor of two. This is mainly due to dedicated calibrations of the jet mass scale and tuning of the final state radiation scale in the Monte Carlo.

On the other hand, as the top quark decays before it hadronizes, its spin properties are transferred to the decay products, and the spin and polarization properties can be studied using the decay products. The measurement of the top quark spin asymmetry, which is sensitive to the top quark polarization [37], uses the full Run-2 dataset corresponding to 139 fb^{-1} of the recorded integrated luminosity and targets the production of a single top quark in association with a Z boson (tZq), with the top quark and the Z boson decaying leptonically. The result $A_\rho = 0.54 \pm 0.16(\text{stat}) \pm 0.06(\text{syst})$ is extracted from the differential cross section of the cosine of the polarization angle. The ratio of the observed cross section to the SM prediction is $\mu_{tZq} = 0.933_{-0.077}^{+0.080}(\text{stat})_{-0.064}^{+0.078}(\text{syst})$, making it the most precise inclusive measurement to-date of the rare tZq processes in final states with three leptons. This and other top measurements [38, 39], are compared to SM predictions of Monte Carlo generators with NLO accuracy and also beyond NLO. Largest deviations were found for the multidifferential cross-sections [39], and the nominal predictions from all calculations do not describe well several of the measured cross sections.

Another heavy quark study is related to indirect searches of BSM physics *via* rare B -meson decays. Rare decays of neutral B_s mesons to muon and antimuon pair were studied by CMS. Rare B meson decays can be sensitive to new physics, because in the SM they proceed only *via* flavour changing neutral currents (FCNC) and, therefore, are highly suppressed. A new measurement result $\mathcal{B}(B_s^0 \rightarrow \mu\mu) = 3.95^{+0.39}_{-0.37}(\text{stat})^{+0.29}_{-0.24}(\text{syst}) 10^{-9}$ [40] is the most precise single experiment measurement to date. It is much closer to the theoretical predictions than the previous analogous measurement by CMS, as well than the most recent LHCb result. This decreases the overall tension in the present B decay anomalies, related to electron/muon lepton flavour universality (LFU). Several hints of departure from LFU and SM constants may also be derived from W boson branching ratios. Thus, another test of LFU was also performed by CMS [41]. Figure 5 shows the measured W fully leptonic branching ratios [41] compared with the corresponding LEP result. The CMS results are in good agreement with LFU, and remove the tension that was present in the LEP measurements for $W \rightarrow \tau\nu$ decays (see Fig. 5). This is further illustrated in Fig. 6, which presents the two-dimensional distribution of the ratios of the $W \rightarrow \tau\nu$ branching fraction to their counterparts for decays into electrons or muons. It is interesting to observe that the precision achieved by CMS for the $W \rightarrow \mu\nu$ and $W \rightarrow e\nu$ branching ratio is better than the LEP one. This is primarily due to the much smaller statistical uncertainty in CMS thanks to large sizes of vector boson samples. In the same analysis [41], CMS also studied the hadronic decays of the W boson. The hadronic width of the W boson depends on other SM parameters, such as strong coupling constant at the W boson mass, $\alpha(m_W^2)$, or the elements V_{ij} of the Cabibbo–Kobayashi–Maskawa (CKM) matrix. By fixing other parameters to their world averages, the CKM element, V_{cs} , which currently has the largest absolute uncertainty among the elements of the first two rows of the CKM matrix, was better constrained $|V_{cs}| = 0.967 \pm 0.011$. CMS also checked the unitarity of the CKM matrix by extracting the sum of squared elements in the first two rows, the uncertainty in the sum being dominated by the uncertainty of $|V_{cs}|$. The sum was found to be $\sum_{i=(u,c), j=(d,s,b)} |V_{ij}|^2 = 1.984 \pm 0.021$. This result provides a more precise constraint than in previous analyses. The strong coupling constant, the worst known of all fundamental couplings in nature, was also extracted to be $\alpha_s(m_W^2) = 0.095 \pm 0.033$. The result cannot compete with other extractions based on data combined from ee , ep and pp collisions, such as the world-average QCD coupling constant, which amounts to $\alpha_s(m_W^2) = 0.1202 \pm 0.0010$ [42], as shown in Fig. 7 together with other measurements, including nine (in *red colour*) measurements by CMS. However, it confirms the usefulness of this approach to extract this fundamental parameter at future e^+e^- colliders, where the W boson branching fractions can be measured much more precisely.

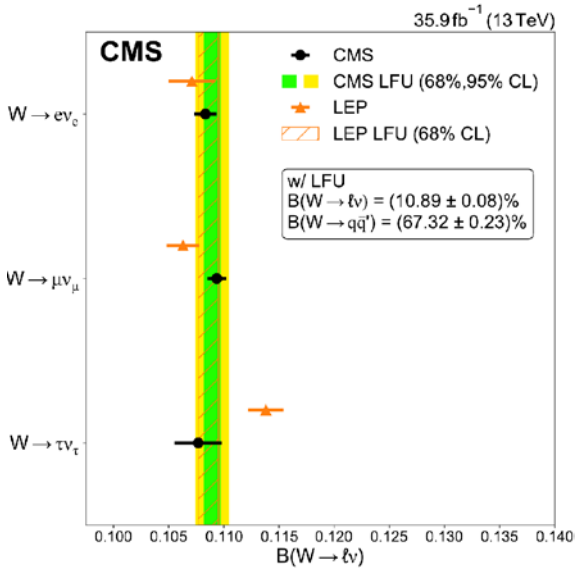


Fig. 5. Measured W leptonic branching fractions, compared to the SM prediction and analogous results from LEP

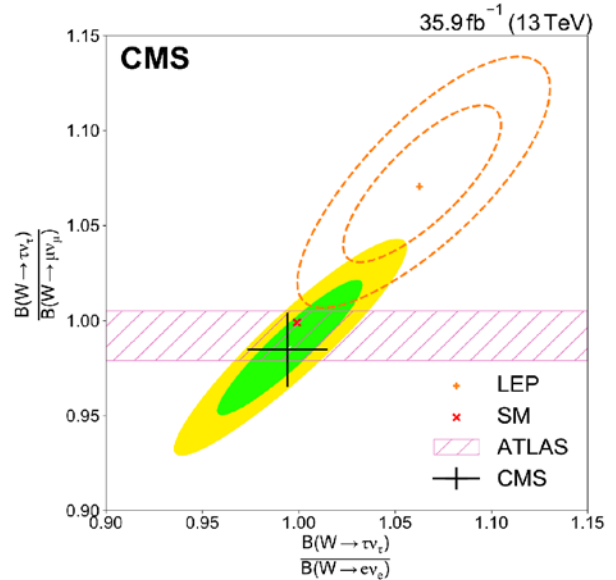


Fig. 6. Two-dimensional distribution of the ratios of the $W \rightarrow \tau\nu$ to $W \rightarrow \mu\nu$ or $W \rightarrow e\nu$ branching fractions

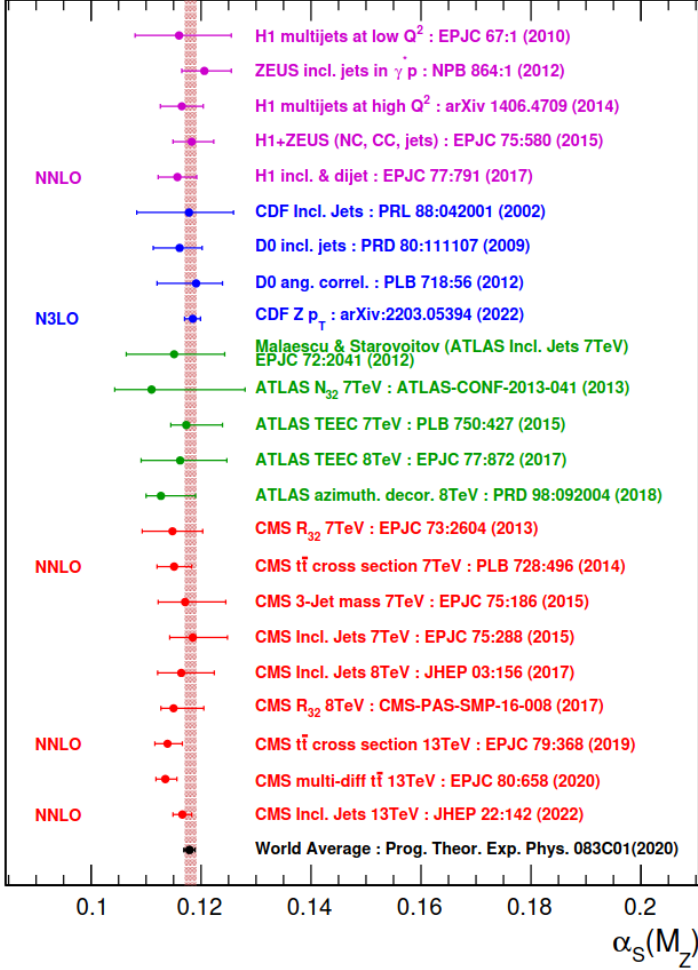


Fig. 7. An overview of $\alpha_s(M_Z^2)$ measurements using hadrons. Nine CMS measurements (in red) are shown [43, 44]

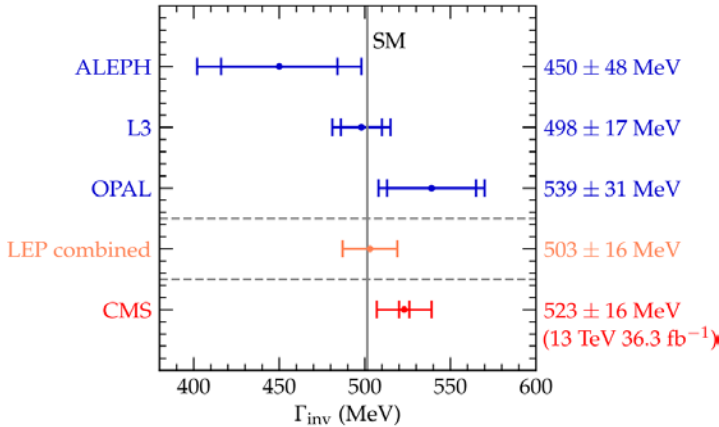


Fig. 8. Direct measurements of the Z invisible width by the LEP experiments and the result from the CMS experiment presented here. Also shown is the prediction from the SM. The inner (outer) error bars show the statistical (total) uncertainty

A large sample size of vector boson production at the LHC also allowed CMS to study in detail the $Z(p_T)$ distribution using decays of the Z boson into muons or electrons, and both inclusively in the number of jets, and in events with at least one jet [45]. These results extend the previous CMS 13 TeV measurement from the dataset collected in 2015 using a 16 times larger dataset acquired during the year 2016 and representing 36.3 fb⁻¹ of the integrated luminosity. The measurement of the Z boson p_T distribution was performed differentially in the dilepton pair mass $m_{\ell\ell}$. This direct measurement permits the validation of the resummation approach while also testing the precision of different predictions. Generators such as arTemide, include resummation to next-to-next-to-next-to leading logarithmic (N³LL) accuracy and thus show very good agreement with data at low p_T , while the high- p_T region is poorly described because higher-order matrix element contributions are missing. On the contrary, generators, that employ matrix element calculations at higher orders such as MG5_aMC, correctly describe the spectrum at high p_T , but are less accurate at low p_T because of the lack of NLL corrections.

A nice example of the high potential of electro-weak physics at hadron colliders is given by the CMS measurement of the invisible width of the Z boson, which was measured by CMS [46] for the first time at a hadron collider. The measurement was performed based on the ratio of the $Z(\rightarrow \bar{\nu}\nu) + \text{jets}$ over the $Z(\rightarrow \bar{\ell}\ell) + \text{jets}$ production cross section. The result is obtained from a simultaneous fit to the recoil distribution for two data samples: one enriched in Z boson decays to invisible particles and the other dominated by Z boson decays to muon and electron pairs. The resulting width of $523 \pm 3(\text{stat}) \pm 16(\text{syst})$ MeV has an accuracy similar to the measurement at LEP (combined) as shown in Fig. 8, which remained the most precise measurement of the invisible Z width for two decades.

The experimental review of the Higgs boson and SM would not be complete, without the measurement of the vector boson scattering (VBS) processes. VBS Feynman diagrams include four- and three-boson non-Abelian vertices, corresponding to

quartic (QGC) and triple gauge couplings (TGC). Study of these vertices can shed light on existence of anomalous vector boson couplings sensitive to new physics BSM. VBS processes are extensively studied at the LHC, in several flavours of production modes and final states, because the measurement of VBS is also important to probe the nature of the Higgs sector, since the precise cancellation of direct vector boson interactions from counterbalancing diagrams, involving the Higgs boson, prevents its unitarity violation.

However, VBS is experimentally challenging, being a very rare process, and having a large $t\bar{t}$ background. A recent CMS analysis [47] was devoted to the study of opposite-sign W^+W^- scattering, where the experimental signature was two leptons (e or μ) and two jets with a large pseudorapidity gap and a large invariant mass. The differential distributions were measured for the first time. The observed significance for the signal is 5.6σ (with 5.2σ expected) with respect to the background-only hypothesis. The distributions may be sensitive to potentially new physics phenomena affecting the Higgs boson coupling to the W boson. So, the limits were obtained on anomalous quartic gauge couplings. The main difficulty was irreducible background from $t\bar{t}$ production.

Complementary to the VBS measurement is the first observation by CMS of the simultaneous production of three heavy bosons [48], a set of processes with final states of the type VVV , where $V = Z, W^+$ or W^- boson. The analysis used the 2016–2018 dataset with an integrated luminosity of 137 fb^{-1} . Triple gauge boson production can shed light on the quartic and triple gauge vector boson couplings, and also gives access to the Yukawa couplings of the Higgs boson to light quarks. The production cross section of these processes is small, *e. g.* the triple vector boson production is 50 times rarer than the production of the Higgs boson. Furthermore, despite the majority of triboson decays are hadronic, CMS restricted the analysis only to leptonic boson decays shrinking the dataset even more. The strategy of the analysis was to isolate this very rare process from backgrounds, where multiple vector bosons are not produced and thus, the number of electrons and muons are low. Thus, CMS used the clearest experimental signature, defined by the presence of multiple high momentum electrons and muons. The more Z bosons are in VVV , the more leptons in the final state are to be registered by CMS, which is known to be a best instrument for electron and muon detection. Separate lepton identification criteria and BDT discriminants were used for each event category in the fit to data. The signal strengths are shown in Fig. 9 for all four final states. For the ZZZ production, a 95% CL upper limit is shown. The combined signal strength of $1.02^{+0.46}_{-0.23}$ corresponds to a cross section of $1010^{+210}_{-200}(\text{stat})^{+150}_{-120}(\text{syst}) \text{ fb}$, which is in good agreement with SM predictions.

4. Conclusion

Thanks to excellent performance of the LHC and the CMS detector, a large number of important and unique physics results were obtained in 2019–2022. Higgs boson properties, precision measurements of the Higgs mass, couplings to the 3rd and 2nd generation fermions were established. Also, the Higgs decay width was constrained. Other important standard model parameters such as the top quark mass, invisible Z boson decay widths were measured. Also, rare decays of B mesons were measured, and tests of LFU were performed. The knowledge about the nature of the Higgs boson couplings and other SM parameters is significantly improved compared to Run-1 results.

The PNPI team was involved in the CMS project through design, production, maintenance and upgrade [49] of the CMS endcap muon system, as well as in the data physics analysis, including the QCD, electroweak and Higgs boson physics studies.

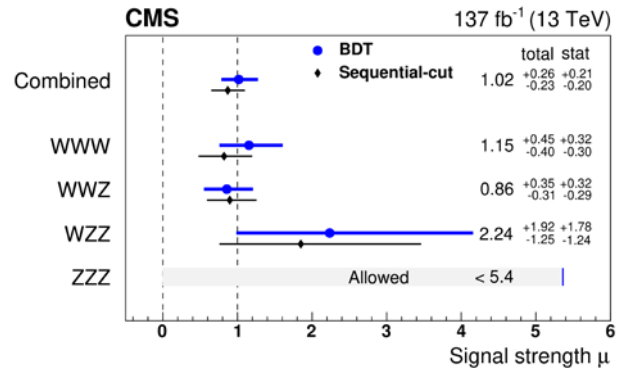


Fig. 9. Best fit values of the signal strength associated with each VVV process for the BDT-based (blue circles) and the cut-based (black diamonds) analyses

References

1. CMS Collab., JINST **3**, S08004 (2008).
2. A.Iu. Egorov *et al.*, Dijets with Large Rapidity Separation at CMS as a Probe for BFKL Effects, This Vol.
3. E.V. Kuznetsova *et al.*, First Measurement of Diffractive Proton–Nucleus Collisions with CMS at the LHC, This Vol.
4. CMS Collab., Phys. Lett. B **805**, 135425 (2020), arXiv:2002.06398.
5. CMS Collab., Nature **607** (60), 7917 (2022), arXiv:2207.00043.
6. E. Braaten, J.P. Leveille, Phys. Rev. D **22**, 715 (1980).
7. N. Sakai, Phys. Rev. D **22**, 2220 (1980).
8. T. Inami, T. Kubota, Nucl. Phys. B **179**, 171 (1981).
9. S.G. Gorishnii, A.L. Kataev, S.A. Larin, Sov. J. Nucl. Phys. **40**, 329 (1984); Yad. Fiz. **40**, 517 (1984).
10. M. Drees, K. Hikasa, Phys. Lett. B **240**, 455 (1990); Phys. Lett. B **262**, 497 (1991).
11. D.Yu. Bardin, B.M. Vilensky, P.Kh. Khristova, Sov. J. Nucl. Phys. **53**, 152 (1991); Yad. Fiz. **53**, 240 (1991).
12. A.L. Kataev, V.T. Kim, Mod. Phys. Lett. A **9**, 1309 (1994).
13. K.G. Chetyrkin, A. Kwiatkowski, Nucl. Phys. B **461**, 3 (1996), arXiv:hep-ph/9505358.
14. V.T. Kim, Nucl. Phys. B Proc. Suppl. **198**, 223 (2010), arXiv:0912.0489.
15. CMS Collab., arXiv:2204.12945.
16. LHC Higgs Cross Section Working Group Collab., LHC HXSWG Interim Recommendations to Explore the Coupling Structure of a Higgs-Like Particle, arXiv:1209.0040.
17. CMS Collab., Phys. Rev. D **105**, 092007 (2022), arXiv:2201.11585.
18. CMS Collab., arXiv:2204.12957.
19. CMS Collab., Phys. Rev. Lett. **128**, 081805 (2022).
20. CMS Collab., JHEP **06**, 012 (2022), arXiv:2110.04836.
21. CMS Collab., arXiv:2208.02686.
22. CMS Collab., JINST **17**, P07023 (2022), arXiv:2201.08458.
23. CMS Collab., JHEP **01**, 148 (2021), arXiv:2009.04363.
24. CMS Collab., arXiv:2205.05550.
25. CMS Collab., JINST **17**, P03014 (2022), arXiv:2111.03027.
26. CMS Collab., Phys. Rev. D **92** (7), 072010 (2015), arXiv:1507.06656.
27. CMS Collab., Nature Physics **18**, 1329 (2022), arXiv:2202.06923.
28. CMS Collab., Phys. Rev. D **99**, 112003 (2019), arXiv:1901.00174.
29. LHC Higgs Cross Section Working Group, Handbook of LHC Higgs Cross Sections: 4. Deciphering the Nature of the Higgs Sector, CERN Yellow Reports: Monographs (2017), arXiv:1610.07922.
30. CMS Collab., Phys. Rev. Lett. **122**, 121803 (2019), arXiv:1811.09689.
31. CMS Collab., CMS Physics Analysis Summary CMS-PAS-TOP-22-012 (2022).
32. CMS Collab., arXiv:2302.01967.
33. CMS Collab., JHEP **12**, 161 (2021), arXiv:2108.10407.
34. CMS Collab., Phys. Rev. D **93**, 072004 (2016), arXiv:1509.04044.
35. CMS Collab., arXiv:2211.01456.
36. CMS Collab., arXiv:2207.02270.
37. CMS Collab., JHEP **02**, 107 (2022), arXiv:2111.02860.
38. CMS Collab., Eur. Phys. J. C **80** (5), 370 (2020), arXiv:1907.08330.
39. CMS Collab., CMS Physics Analysis Summary CMS-PAS-TOP-20-006 (2022).
40. CMS Collab., arXiv:2212.10311.
41. CMS Collab., Phys. Rev. D **105**, 072008 (2022), arXiv:2201.07861.
42. Particle Data Group, Review of Particle Physics, Prog. Theor. Exp. Phys. **2020**, 083C01 (2020).
43. CMS Collab., Eur. Phys. J. C **79**, 368 (2019), arXiv:1812.10505.
44. CMS Collab., JHEP **02**, 142 (2022); JHEP **12**, 035 (2022), arXiv:2111.10431.
45. CMS Collab., arXiv:2205.04897.

46. CMS Collab., arXiv:2206.07110.
47. CMS Collab., arXiv:2205.05711.
48. CMS Collab., Phys. Rev. Lett. **125**, 151802 (2020).
49. A.A. Vorobyev *et al.*, CMS Endcap Muon System Upgrade, This Vol.

OVERVIEW OF RECENT ATLAS RESULTS

PNPI participants of the ATLAS Collaboration: S.G. Barsov, A.E. Ezhilov, O.L. Fedin, V.T. Grachev, M.P. Levchenko, V.P. Maleev, Yu.G. Naryshkin, D. Pudzha, V.A. Schegelsky, V.M. Solovyev

1. Introduction

ATLAS is one of the largest particle physics experiments operating at the Large Hadron Collider (LHC) at CERN since 2010. The international collaboration exploiting the ATLAS detector [1] involves about 3 000 scientists from 182 institutions and 38 countries. They are aimed to investigate a wide range of physics including studies of the Standard Model (SM), searches for new physics beyond the SM (BSM), like supersymmetry (SUSY), dark matter (DM), extra dimensions of space, new particles from the extended Higgs sector, study of hot and dense matter created in relativistic ion–ion collisions (quark–gluon plasma), *etc.* The PNPI participates in the ATLAS Collaboration from the very beginning, starting with the conceptual detector design. Since the ATLAS detector has started recording data, PNPI physicists have been involved in many physics analyses performed by the collaboration.

During the LHC Run-2 data taking period (2015–2018) the ATLAS experiment has been operating at unprecedented high energy of proton–proton collisions $\sqrt{s} = 13$ TeV. A huge amount of experimental data corresponding to the integral luminosity of 139 fb^{-1} have then been collected. More than 400 papers were already published by the ATLAS Collaboration last five years. Since it is impossible to overview all these results in a short article, only a few selected results are presented here.

2. Higgs boson measurements

Due to higher proton–proton collision energy leading to an increase of the Higgs boson production cross section and higher luminosity delivered by the LHC, during Run-2 ATLAS has collected about 30 times larger sample of data than it had been available when ATLAS and CMS reported the discovery of the Higgs boson [2, 3]. This allowed more detailed studies of Higgs boson properties. A number of production cross sections and Higgs boson decay rates were measured which allowed us to improve our knowledge about couplings between the Higgs boson and particles involved. In particular, such a rare decay mode as the $H \rightarrow \mu\mu$ [4] and the very difficult for identification channel $H \rightarrow c\bar{c}$ [5] were investigated. The most of studies concerned the Higgs boson performed at ATLAS are presented in a more detailed overview [6], which will be only briefly discussed in section 2.3 below.

2.1. $H \rightarrow b\bar{b}$ decay

While the SM Higgs boson of mass 125 GeV decays to $b\bar{b}$ pair with a branching ratio of about 58%, this channel remains the most poorly measured Higgs boson decay channel due to huge quantum chromodynamics (QCD) background. Nevertheless, it has been already observed [7] with a significance of 6.7σ for the most sensitive cases where the Higgs boson is produced in association with a vector boson (VH , $V = W, Z$), which provides sufficient discrimination against QCD background processes despite its small cross-section.

The ATLAS Collaboration also significantly improved a measurement of the SM Higgs boson decaying to b -quark pairs in the vector boson fusion (VBF) production mode [8] relative to the previous analysis. The VBF Higgs boson production in $b\bar{b}$ decay mode is measured with a significance of 2.6σ relative to the background-only hypothesis, with an observed signal strength of $\mu_{VBF} = 0.95_{-0.32}^{+0.32}(\text{stat})_{-0.17}^{+0.20}(\text{syst})$, compared to the expected value of $1.00_{-0.32}^{+0.32}(\text{stat})_{-0.17}^{+0.21}(\text{syst})$.

Improvements of the analysis include the usage of an adversarial neural network for event classification to define if the event is signal- or background-like, and to determine the value of m_{bb} in terms of binned m_{bb} . Additionally, for estimation of the $Z \rightarrow b\bar{b}$ resonant background the embedding method in Monte Carlo events is applied. In this method $Z \rightarrow \mu\mu$ events are selected in data and the muons are replaced with b -jets

from simulation. Then analysis selections are applied to determine the number of selected $Z \rightarrow b\bar{b}$ events. This procedure results in significantly less uncertainty on the Z boson background contribution to the fit.

The measured μ_{VBF} corresponds to a cross-section $\sigma_{VBF} \times B_{H \rightarrow b\bar{b}} = 2.07^{+0.70}_{-0.70}(\text{stat}) \ ^{+0.46}_{-0.37}(\text{syst})$ fb, and assuming the branching fraction $B_{H \rightarrow b\bar{b}} = 0.5809$ leads to the inclusive VBF cross-section $\sigma_{VBF} = 3.56^{+1.21}_{-1.21}(\text{stat}) \ ^{+0.80}_{-0.64}(\text{syst})$ fb. A fiducial cross-section for the rapidity range $|y_H| < 2.5$ is measured to be $\sigma_{VBF \text{fid}} = 3.31^{+1.12}_{-1.12}(\text{stat}) \ ^{+0.74}_{-0.64}(\text{syst})$ fb. These results are combined with a complementary measurement of the $VBF H \rightarrow b\bar{b}$ production in association with a photon, leading to a 2.9σ measurement of the $VBF H \rightarrow b\bar{b}$ production.

2.2. $H \rightarrow c\bar{c}$ decay

The ATLAS Collaboration has performed a measurement of the SM Higgs boson decay to c -quark pairs ($H \rightarrow c\bar{c}$) when the Higgs boson is produced in association with a vector boson (W, Z) making use of the full Run-2 dataset taken at $\sqrt{s} = 13$ TeV [5]. The search uses three channels, $ZH \rightarrow \nu\nu c\bar{c}$, $WH \rightarrow \ell\nu c\bar{c}$ and $ZH \rightarrow \ell\ell c\bar{c}$, where $\ell = e, \mu$. In this mode the leptonic decay of the weak gauge boson allows efficient triggering and background rejection. However, there are additional difficulties compared to $H \rightarrow b\bar{b}$ measurements, discussed above. First, the branching $\mathcal{B}(H \rightarrow c\bar{c})$ is about 3%, *i. e.* 20 times smaller than the branching $\mathcal{B}(H \rightarrow b\bar{b})$. Another problem is that charm tagging is less effective than b -tagging. Separating charm-jets from b -jets is particularly challenging; this is addressed by a dedicated charm tagging algorithm, which requires the jets to have a high c -tagging score as well as vetoing jets with high b -tagging scores. This veto makes the signal events in $H \rightarrow c\bar{c}$ and $H \rightarrow b\bar{b}$ analyses orthogonal and enables their combination.

The analysis method is validated by the simultaneous measurement of diboson production processes WW, WZ and ZZ in which one of the bosons decays to at least one charm quark, $VW(\rightarrow cq)$ and $VZ(\rightarrow c\bar{c})$, where q is a down type quark. The measurement shows an observed (expected) significances of 2.6(2.2) standard deviations above the background-only prediction for the $(W/Z)Z(\rightarrow c\bar{c})$ process and 3.8(4.6) standard deviations for the $(W/Z)W(\rightarrow cq)$ process. The $(W/Z)H(\rightarrow c\bar{c})$ search yields an observed (expected) upper limit of 26(31) times the predicted SM cross-section times branching fraction for a Higgs boson with a mass of 125 GeV, corresponding to an observed (expected) constraint on the charm Yukawa coupling modifier $|\kappa_c| < 8.5(12.4)$, at the 95% confidence level.

A combination with the ATLAS $(W/Z)H, H \rightarrow b\bar{b}$ analysis is performed, allowing the ratio κ_c/κ_b to be constrained to less than 4.5 at the 95% confidence level, smaller than the ratio of the b - and c -quark masses, and therefore determines the Higgs–charm coupling to be weaker than the Higgs–bottom coupling at the 95% confidence level.

The result is shown in Fig. 1. The vertical green lines correspond to the values of $|\kappa_c/\kappa_b|$ for which the Higgs–charm and Higgs–bottom couplings are equal, where each coupling strength $|\kappa_i y_i|$ is the product of the κ_i modifier and the Yukawa coupling, y_i , for $i = b, c$, and is equal to $m_b/m_c = 4.578 \pm 0.008$.

2.3. Combined measurement with the ATLAS Run-2 data

The Higgs boson production rates are probed by the likelihood fit to the observed signal yields of all previous analyses [6]. Because the production cross-section σ_i and the branching fraction B_f for a specific production process i and decay mode f cannot be measured separately without further assumptions,

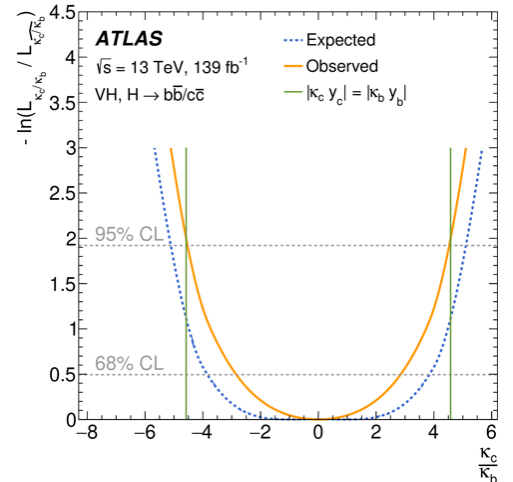


Fig. 1. Expected and observed values of the combined $VH, H \rightarrow c\bar{c}$ and $VH, H \rightarrow b\bar{b}$ negative profile log-likelihood ratio as a function of κ_c/κ_b , where κ_b is a free parameter

the observed signal yield for a given process is expressed in terms of a single signal strength modifier $\mu = (\sigma_i/\sigma_i^{\text{SM}})(B_f/B_f^{\text{SM}})$, where the superscript ‘‘SM’’ denotes the corresponding standard model prediction.

Assuming that all production and decay processes scale with the same global signal strength $\mu = \mu_{if}$, the inclusive Higgs boson production rate relative to the standard model prediction is measured to be $\mu = 1.05 \pm 0.06 = 1.05 \pm 0.03(\text{stat}) \pm 0.03(\text{exp}) \pm 0.04(\text{sig. th}) \pm 0.02(\text{bkg. th})$. The total measurement uncertainty is decomposed into components for statistical uncertainties, experimental systematic uncertainties, and theory uncertainties in both signal and background modelling. Both the experimental and the theoretical uncertainties are almost a factor of two lower than for the Run-1 result. The presented measurement supersedes the previous ATLAS combination with a partial Run-2 dataset decreasing the latest total measurement uncertainty by about 30%.

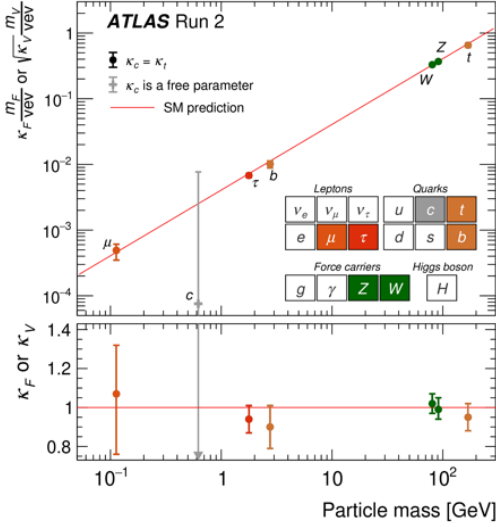


Fig. 2. Reduced Higgs boson coupling strength modifiers and their uncertainties

$\kappa_F m_F / \text{vev}$ for fermions ($F = t, b, \tau, \mu$) and $\sqrt{\kappa_V} m_V / \text{vev}$ for vector bosons as a function of their masses m_F and m_V . The ‘‘vev’’ is vacuum expectation value of the Higgs field. Two fit scenarios with $\kappa_c = \kappa_t$ (coloured circle markers), or κ_c left free-floating in the fit (grey cross markers) are shown. Loop-induced processes are assumed to have the SM structure, and Higgs boson decays into non-SM particles are not allowed. The vertical bar at each point denotes the 68% confidence interval. The p -values for compatibility of the combined measurement and the SM prediction are 56 and 65% for the respective scenarios. The lower panel shows the ratios of the coupling strength modifiers to the SM prediction. The grey arrow points in the direction of the best-fit value and the corresponding grey uncertainty bar extends beyond the lower panel range.

2.4. $H \rightarrow \ell\ell\gamma$ decay

The investigation of rare Higgs boson decay modes, such as the decay to pair of leptons and a photon ($H \rightarrow \ell\ell\gamma$), gives a way to probe a possible extension of the SM. There are many processes contributing to that decay: Dalitz decays involving a Z boson or a virtual photon (γ^*), as well as the decay of the Higgs boson to two leptons and a photon from final-state radiation. Their respective contribution depends on the invariant mass of the dilepton pair, $m_{\ell\ell}$. Higgs boson decay through virtual photon γ^* is completely dominated in the region with $m_{\ell\ell} < 30$ GeV, and contributions of other processes and interferences are negligible.

ATLAS has performed a search for $H \rightarrow \ell\ell\gamma$ decay with $m_{\ell\ell} < 30$ GeV [9]. One particularly challenging aspect of this analysis is that for the low invariant mass of the two electrons the transverse momentum of the dielectron system is high and therefore their electromagnetic showers can overlap in the calorimeter with high probability. It leads to a drop in efficiency when using the conventional electron reconstruction algorithms. Therefore, the search for $ee\gamma$ final states requires the development of dedicated electron trigger and identification algorithms.

The selected events are classified into mutually exclusive categories, depending on the lepton types and event topologies: VBF -enriched, high p_{Tt} or low p_{Tt} . The p_{Tt} is defined as the component of p_T of the $\ell\ell\gamma$ system

that is perpendicular to the difference of the three-momenta of the dilepton system and the photon candidate, *i. e.* $p_{Tt} = |\vec{p}_T^{\ell\ell\gamma} \times \hat{t}|$, with $\hat{t} = (\vec{p}_T^{\ell\ell} - \vec{p}_T^\gamma) / |\vec{p}_T^{\ell\ell} - \vec{p}_T^\gamma|$. The p_{Tt} shows better experimental resolution by being less sensitive to p_T systematic uncertainties [10]. The final signal strength is determined from a simultaneous fit to all of the categories. In these fits, the signal is parameterised by the double-sided Crystal Ball function, and the background distribution is parameterised by either an exponential function, or by a polynomial one. The particular functions in categories are summed being weighted by their sensitivity, and the result is shown in Fig. 3. The red curve shows the combined signal-plus-background model when fitting all analysis categories simultaneously, the dashed black line shows the model of the non-resonant background component, and the dotted blue line denotes the sum of the non-resonant background $\ell\ell\gamma$ and the resonant $H \rightarrow \gamma\gamma$ background. The bottom panel shows the residuals of the data with respect to the non-resonant background component of the signal-plus-background fit. The final fit provides a signal strength parameter of $\mu = 1.5 \pm 0.5$ relative to the SM expectation. This corresponds to a significance of 3.2σ over the background only hypothesis (2.1σ expected) and can be considered as the first evidence of Higgs boson decays to this final state.

3. Top quark physics

Being the heaviest known elementary particle of the SM, the top quark has a large coupling to the SM Higgs boson and is predicted to have large couplings to hypothetical new particles in many models of physics beyond the SM. Over 100 million top-antitop events have been recorded by the ATLAS detector in Run-2. This has allowed measurements of top pair and single-top production in much more detail than before, and studies of top-quark properties with unprecedented precision. Measurements of top-quark properties provide important input to test theoretical calculations and have the potential to reveal deviations from the SM predictions. The study of top quark-antiquark ($t\bar{t}$) production is a key part of the physics program of the ATLAS experiment. It includes a wide range of studies, *e. g.* cross-section measurement, spin correlation and charge asymmetry study, *etc.*

3.1. $t\bar{t}$ cross-section measurements

As the top quarks form an important background in any searches for physics beyond the SM, a precise measurement of the $\sigma_{t\bar{t}}$ and its comparison with theoretical prediction of high precision are a very important part of the ATLAS physics program. Indeed, theoretical calculation of the $t\bar{t}$ production cross-section, $\sigma_{t\bar{t}}$, is now made at the next-to-next-to-leading order (NNLO) in QCD. It includes the resummation of the next-to-next-to-leading logarithmic (NNLL) soft-gluon terms.

The ATLAS experiment has measured the $t\bar{t}$ cross-section at $\sqrt{s} = 13$ TeV using the data collected in 2015–2016 years with the luminosity 36.1 fb^{-1} . This analysis has used the so-called “gold channel”, *i. e.* channel with an $e\mu$ opposite charged pair and exactly one or two b jets in the final state [11]. The selected events sample has a purity of about 88% for the events with one b -jet and 96% for two b -jets, with most of the background coming from associated production of a W boson and single top quark. This events selection allowed to minimize the systematic errors by measuring b -tagging and jet reconstruction efficiencies from the data. The inclusive cross-section was obtained to be $\sigma_{t\bar{t}} = 826.4 \pm 3.6(\text{stat}) \pm 11.5(\text{syst}) \pm 15.7(\text{lumi}) \pm 1.9(\text{beam}) \text{ pb}$, and to be consistent with NNLO + NNLL QCD calculations.

ATLAS has also measured the $t\bar{t}$ cross-section in the lepton + jets channel, with a single lepton, missing transverse momentum and at least four jets in the final state with full statistics of Run-2 (139 fb^{-1}) [12]. Three

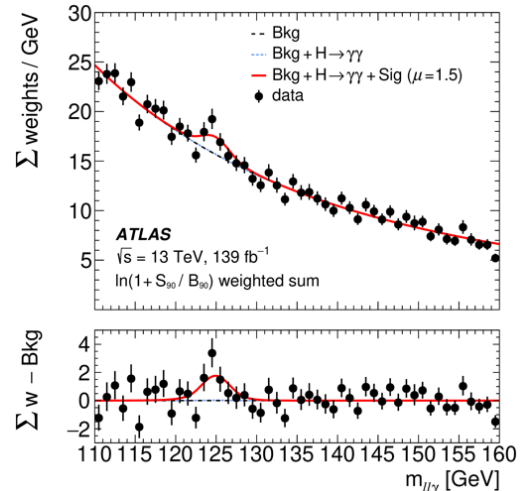


Fig. 3. The results for evidence of the non-resonant $H \rightarrow \ell\ell\gamma$

signal regions were selected, with different jet and b -tagged jet multiplicity requirements, and $t\bar{t}$ purities in the range 80–92%. The measurement was performed using a profile likelihood fit to a different discriminating variable in each signal region, *e. g.* the minimum lepton-jet invariant mass was used in the region with exactly four jets with two being b -tagged. The inclusive cross-section is obtained to be $\sigma_{t\bar{t}} = 830 \pm 0.4(\text{stat}) \pm 36(\text{syst}) \pm 14(\text{lumi})$ pb. It is in good agreement with the theoretical NNLO + NNLL QCD calculation as well as with the ATLAS measurement in the electron–muon channel.

In a special LHC Run at low energy of proton–proton interactions $\sqrt{s} = 5.02$ TeV performed in 2017, ATLAS measured the $t\bar{t}$ production cross-section in two channels: dilepton and lepton + jet [13]. The obtained combined result is $\sigma_{t\bar{t}} = 67.5 \pm 0.9(\text{stat}) \pm 2.3(\text{syst}) \pm 1.1(\text{lumi}) \pm 0.2(\text{beam})$ pb, and this is the best result to date. Figure 4 (*left*) shows all ATLAS measurements of the $t\bar{t}$ production cross-section at different centre-of-mass energies \sqrt{s} from 5 to 13 TeV, which are in excellent agreement with QCD NNLO + NNLL predictions over the full energy range.

The ATLAS experiment also made a constraint on the gluon distribution of the proton parton distribution functions (PDFs) at large value of Bjorken x -value > 0.05 (the fraction of the proton momentum carried by the parton participating in the initial interaction). Figure 4 (*right*) shows the change in the gluon PDF at a squared-momentum-transfer value of $Q^2 = 10^4$ GeV² when the $\sqrt{s} = 5.02$ TeV $\sigma_{t\bar{t}}$ result is added. The *red hatched band* presents the ratio of the gluon PDF determined using the data which include a diverse set of ATLAS Collaboration measurements at $\sqrt{s} = 7, 8$ and 13 TeV (including $t\bar{t}$ differential cross-section measurements at $\sqrt{s} = 8$ and 13 TeV), together with deep-inelastic scattering data from ep collisions at the HERA collider (ATLASpdf21) to the reference gluon PDF (*red*) as a function of Bjorken x -value and the *blue line* shows the shift in the central value when adding the $\sqrt{s} = 5$ TeV cross-section measurements. At a squared-momentum-transfer value of $Q^2 = 10^4$ GeV², the addition of the new data reduces the gluon PDF uncertainty in the region of Bjorken x above $x \approx 0.05$, and gives *e. g.* a 5% reduction at $x = 0.1$.

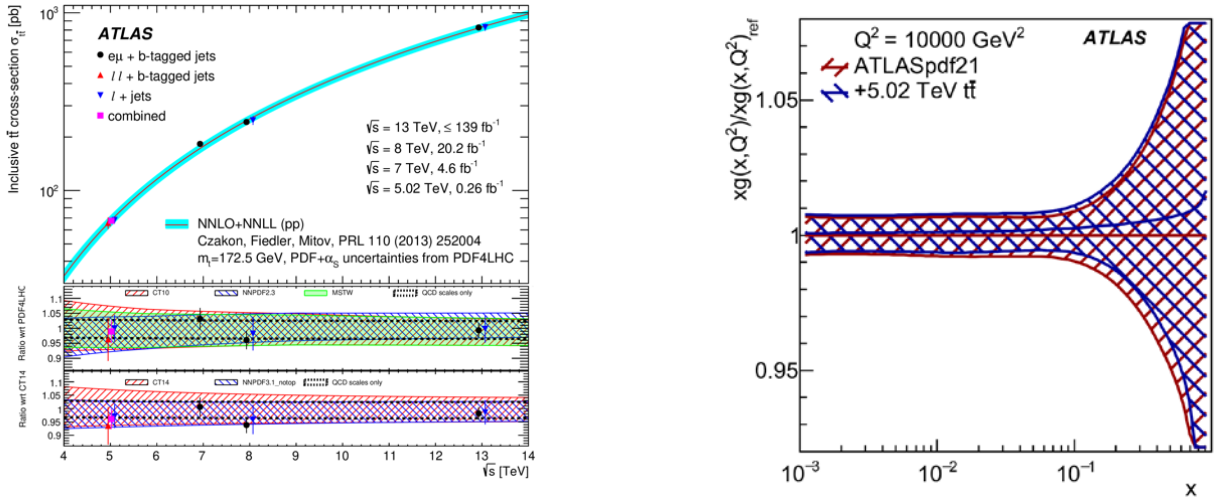


Fig. 4. The *left plot* shows the inclusive $t\bar{t}$ cross-section as a function of the centre-of-mass energies \sqrt{s} , comparing ATLAS results from the dilepton and lepton + jets final states with QCD NNLO + NNLL predictions using various PDF sets. The *right plot* shows the ratio of the gluon PDF determined using the data which include a diverse set of ATLAS Collaboration measurements at $\sqrt{s} = 7, 8$ and 13 TeV, together with deep-inelastic scattering data from ep collisions at the HERA collider, (the so called ATLASpdf21 PDFs set) to the reference gluon PDF (*red*) as a function of Bjorken- x and the *blue line* shows the shift in the central value when adding the $\sqrt{s} = 5$ TeV cross-section measurements

3.2. $t\bar{t}t\bar{t}$ production in proton–proton collision

The cross-section for the four-top-quark production is predicted by the SM to be $\sigma_{t\bar{t}t\bar{t}} = 12.0$ fb at the next-to-leading order (NLO) calculation, but this process has not been observed yet. In 2020, the ATLAS experiment reported the evidence of four-top-quark production [14] using the full Run-2 dataset at

$\sqrt{s} = 13$ TeV. That analysis was made using events with a same-sign charged lepton pair (2LSS) or at least three leptons (3L, where lepton is electron or muon) in the final state. The measured cross-section is found to be 24_{-6}^{+7} fb. This corresponds to an observed (expected) significance with respect to the background-only hypothesis of 4.3(2.4) standard deviations.

In the next step, ATLAS measured $\sigma_{t\bar{t}t\bar{t}}$ in the same data sample but making use of events containing a single lepton (electron or muon) (1L) or an opposite-sign charged lepton pair (2LOS), in association with multiple jets [15]. A multivariate technique is then used to discriminate between signal and background events in the defined event categories depending on the number of jets in event and how likely these are b -jets. The measured four-top-quark production cross section is found to be 26_{-15}^{+17} fb, with a corresponding observed (expected) significance of 1.9(1.0) standard deviations over the background-only hypothesis. The result is combined with the previous measurement obtained making use the multilepton final state. The combined four-top-quark production cross section is measured to be 24_{-6}^{+7} fb, with a corresponding observed (expected) signal significance of 4.7(2.6) standard deviations over the background-only predictions. It is consistent within 2.0 standard deviations with the SM expectation of production cross section 12.0 ± 2.4 fb. The signal strength, which is a ratio of the measured to predicted by SM $\sigma_{t\bar{t}t\bar{t}}$, is shown in Fig. 5.

Despite small significance of the observed deviation, four top quark production may be enhanced in some BSM, for instance, by gluino pair production in supersymmetric theories [16], by pair production of scalar gluons [17], or by the production of a heavy scalar or pseudoscalar boson in association with a top-quark pair in type II two-Higgs-doublet models [18].

4. Searches beyond the Standard Model

4.1. Test of the lepton flavour universality

Lepton flavour universality (LFU) is one of the fundamental axioms of the SM. It states that the couplings of the electroweak gauge bosons (W, Z) to charged leptons are independent of the different generations of leptons. This statement can be tested, for instance, by measuring the ratio of fractions of W -boson decays to τ -leptons and muons, $R(\tau/\mu) = \mathcal{B}(W \rightarrow \tau\nu_\tau)/\mathcal{B}(W \rightarrow \mu\nu_\mu)$. Last measurement of this ratio was performed at LEP and the combined result of all four LEP experiments has shown the 2.7σ deviation from the SM prediction, *i. e.* $R(\tau/\mu) = 1.070 \pm 0.026$ [19], thus motivating a precise measurement of this ratio at the LHC.

It was performed at ATLAS using a novel technique for selection of di-leptonic decays in $t\bar{t}$ events and the full Run-2 dataset [20]. The $t\bar{t}$ production is utilized because the $\sigma_{t\bar{t}}$ is significantly larger than the WW production cross-section (826 pb instead of 130 pb). One lepton, electron or muon, was used to tag the event, while the other probe lepton, which was required to be the opposite charged muon, was used to measure $R(\tau/\mu)$. Muons originated from the τ -lepton decays ($W \rightarrow \tau\nu_\tau \rightarrow \mu\nu_\mu\nu_\tau\nu_\tau$) were distinguished from prompt muons, $W \rightarrow \mu\nu_\mu$, through their softer p_T spectrum and the displacement of the decay point from the primary vertex, which can be determined from the track transverse impact parameter, $|d_0^\mu|$. So, the transverse impact parameter distribution is crucial for this analysis. The shape of the $|d_0^\mu|$ distribution for prompt muons was determined using a $Z \rightarrow \mu\mu$ calibration region.

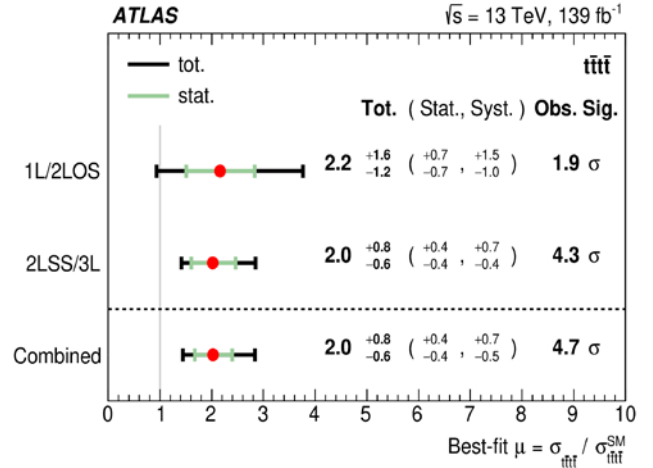


Fig. 5. Fitted signal strengths in the signal-plus-background fits to the same data set for the individual final states (1L/2LOS and 2LSS/3L) and the combined signal strength from all $t\bar{t}t\bar{t}$ analysis regions

The $R(\tau/\mu)$ value is found to be $R(\tau/\mu) = 0.992 \pm 0.007(\text{stat}) \pm 0.011(\text{syst})$ which is the most precise measurement to date. The result is shown in Fig. 6 and compared with the combination of LEP measurements. In contrast to the LEP result, the ATLAS result agrees with the SM expectation of equal couplings for charged lepton of different flavours and supports the LFU hypothesis.

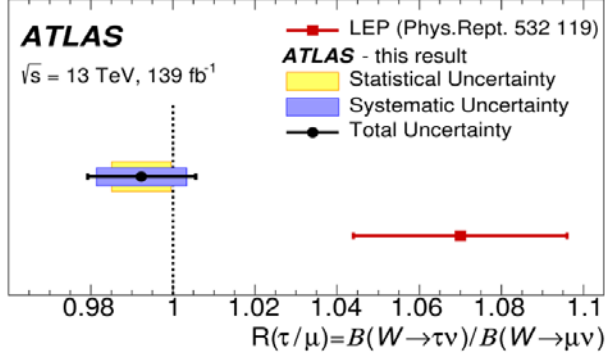


Fig. 6. The measurement of $R(\tau/\mu)$ is shown (black circular marker) and compared with the previous LEP result (red square marker). The statistical and systematic errors are shown separately and also the total error of the measurement. The vertical dashed line indicates the Standard Model prediction of the lepton-flavour universality, with equal W boson branching ratios to different lepton flavours

4.2. Lepton flavour violation searches

Three lepton generations (flavours) are established to exist in the SM, and the lepton flavour is conserved in particle interactions. However, there is no fundamental principle in theory which prohibits a lepton flavour changing. Moreover, neutrino oscillations [21, 22] indicate that there are some processes violating the lepton flavour conservation, while in the case of charged leptons no lepton-flavour-violating (LFV) processes have been observed so far. In the framework of the SM, the violation of charged lepton flavour gets, in principle, possible due to neutrino mixing, but it is strongly suppressed to be detected in current experiments [23], giving, for example, $\mathcal{B}(Z \rightarrow e\mu) < 4 \cdot 10^{-60}$. Thus, an observation of such process would point out the existence of physics BSM. A number of models extending the SM, for example, models including heavy neutrinos, predict LFV decays of the Z boson with a measurable branching of about 10^{-5} – 10^{-10} .

The search for $Z \rightarrow e\tau$ and $Z \rightarrow \mu\tau$ LFV decays has been performed at ATLAS using the full set of proton–proton collision data corresponding to the integrated luminosity of 139 fb^{-1} at a centre-of-mass energy $\sqrt{s} = 13 \text{ TeV}$ collected in the LHC Run-2. The τ -leptons have been identified using both the hadronic and the leptonic decay modes [24]. There was no excess above the predicted SM background observed in neither of these analyses. The combination of these two results sets the strongest constraints to date $\mathcal{B}(Z \rightarrow e\tau) < 5.0 \cdot 10^{-6}$ and $\mathcal{B}(Z \rightarrow \mu\tau) < 6.5 \cdot 10^{-6}$ at 95% confidence level which supersede previous best limits obtained by the OPAL $\mathcal{B}(Z \rightarrow e\tau) < 9.8 \cdot 10^{-6}$ [25] and by the DELPHI $\mathcal{B}(Z \rightarrow \mu\tau) < 12 \cdot 10^{-6}$ [26] collaborations at LEP.

In addition, the ATLAS experiment has performed the search for Z boson LFV decay to light charged leptons ($e\mu$) [27]. It was done by examining the invariant mass distribution of opposite-charge $e\mu$ candidates for evidence of a narrow peak consistent with direct Z boson decay. The event selection requires two isolated energetic, oppositely charged leptons of different flavour: $e^{\pm}\mu^{\mp}$. The primary backgrounds consist of Z boson decays into τ -lepton pairs ($Z \rightarrow \tau\tau \rightarrow e\mu\nu\bar{\nu}\bar{\nu}$), decays into muon pairs $Z \rightarrow \mu\mu$ when one muon is misidentified as an electron, dileptonic final states from decays of top quark pairs ($t\bar{t} \rightarrow e\mu\nu\bar{b}\bar{b}$), and decays of weak boson pairs ($WW \rightarrow e\mu\nu\bar{\nu}$). To suppress the contribution from the top quark and boson pairs, events were required to have little jet activity and only a small amount of missing transverse momentum. To further reduce the background, a multivariate boosted decision tree (BDT) was used to optimize the ratio of the expected signal to the square root of the expected background yield. Events from background processes which passed the selection were expected to form a smooth spectrum in the electron–muon invariant mass ($m_{e\mu}$) within the window $70 < m_{e\mu} < 110 \text{ GeV}$. A binned likelihood fit, in which the signal was unconstrained, was performed. While a signal was not observed, the observed (expected) upper limit on the branching fraction $\mathcal{B}(Z \rightarrow e\mu)$ is 2.62 (2.37) $\cdot 10^{-7}$ at 95% confidence level. This result supersedes former limits set by searches

at LEP giving $\mathcal{B}(Z \rightarrow e\mu) < 1.7 \cdot 10^{-6}$ at 95% confidence level [25, 26, 28, 29] and a previous search at the LHC which yielded $\mathcal{B}(Z \rightarrow e\mu) < 7.5 \cdot 10^{-7}$ at 95% confidence level [30] in 20.3 fb^{-1} of 8 TeV proton–proton collision data collected by the ATLAS experiment. The distribution of the invariant mass of the $e\mu$ pair in the selected events is shown in Fig. 7. The goodness-of-fit, as measured by the χ^2 divided by the number of degrees of freedom is 1.2, with probability 0.24. The final total fit is shown with a *blue solid line*, the $Z \rightarrow \tau\tau$ component with a *green dashed line*, the $Z \rightarrow \mu\mu$ component with a *brown dotted line*, and the pink *dash-dotted curve* represents all non-resonant background contributions. The statistical uncertainty is shown with the *light blue band*. A hypothetical $Z \rightarrow e\mu$ signal scaled by 20 times as compared with the observed upper limit is shown as the *dark red solid line* for illustration purposes. The *lower panel* shows the ratio of the observed data to expected background yields.

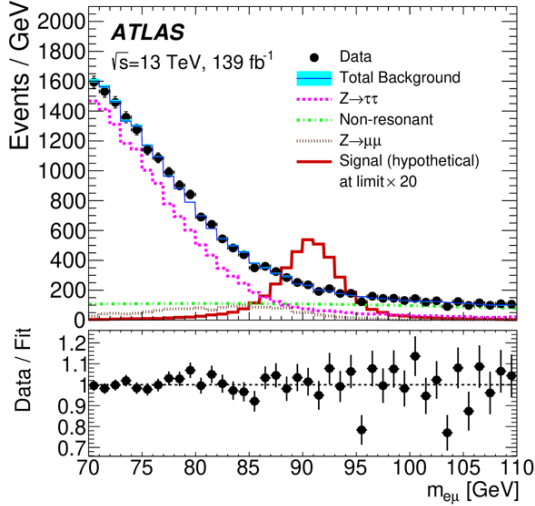


Fig. 7. Distribution of the invariant mass $m_{e\mu}$ of the $Z \rightarrow e\mu$ candidates, for data (*points*) expected backgrounds (*lines*) after the background-only likelihood fit

4.3. Dark matter searches

One of the major subjects of the ATLAS physics program is a search of DM particles. A number of evidences for the existence of DM have been found from astronomical observations for over eight decades, but its nature is still unknown. There are different candidates for DM particle(s) suggested by various BSM models. Weakly interacting massive particles (WIMP) are considered as the most promising ones. They may be pair-produced in pp collisions at the LHC. As DM particles can't be directly detected, additional particle(s) ($X = \text{jet}, \gamma, W, Z, h, (t)\bar{t}, (b)\bar{b}$) have to be produced in association with a DM particle in order to tag the event and to detect the recoiling WIMPs as a missing transverse energy E_T^{miss} . DM particles may be also produced at the LHC *via* an s -channel exchange of a new particle (mediator), which would decay into SM particles. Thus, resonance searches could also be used to constrain DM models.

There are two large groups of BSM models commonly used for the interpretations of the LHC data. One of the groups includes simplified models mediated by a vector, axial-vector, scalar or pseudoscalar mediator. Another one consists of less simplified models involving an extended Higgs sector plus an additional mediator, either a vector or a pseudoscalar particle, *e. g.* the simplest gauge-invariant and renormalizable extension of a simplified pseudoscalar model 2HDM + a, where “a” is a pseudoscalar mediator.

A lot of possible channels of the DM production have been analysed in the ATLAS experiment based on the data collected in Run-2 of proton–proton interactions with the $\sqrt{s} = 13 \text{ TeV}$ and integrated luminosity 139 fb^{-1} . A wide range of DM masses, mediator masses and couples were scanned. No deviation from the SM prediction was found, and upper limits on the DM mass vs mediator masses were obtained. One of the summary plots of the exclusion limits for $m_{Z'_A}$ vs m_χ , obtained within simplified models for different channel is presented in Fig. 8, where $m_{Z'_A}$ is the mass of a leptophobic axial-vector Z'_A mediator, and m_χ is the mass of a DM particle [31]. The $m_{Z'_A}$ values below $\sim 3.7 \text{ TeV}$ are now excluded. There were also set limits on the 2HDM + a model parameters.

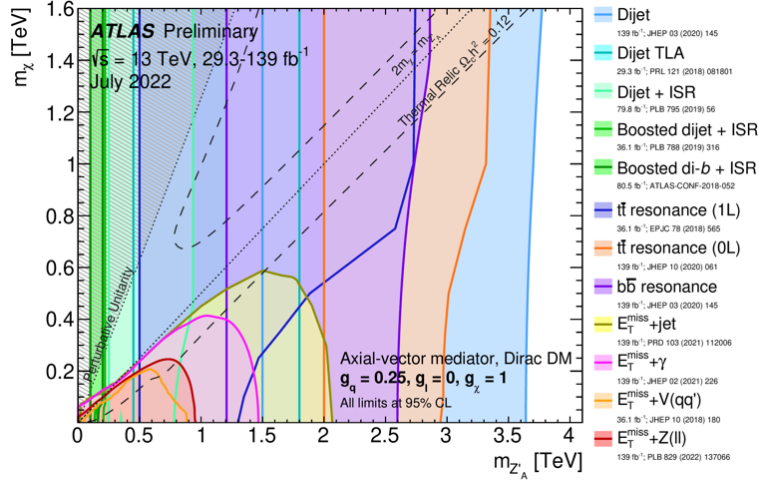


Fig. 8. Regions in the (mediator-mass, DM-mass) plane excluded at 95% confidence level by visible and invisible searches, for leptophobic ($g_l = 0$) axial-vector mediator simplified models. The exclusions are computed for a DM coupling $g_\chi = 1$, quark coupling $g_q = 0.25$, universal to all flavours, and no coupling to leptons. A dotted line indicates the kinematic threshold where the mediator can decay on-shell into DM

5. Summary

Selected results of the ATLAS Collaboration are presented. In recent years, as the complexity of the studied processes increased, the use of multivariate data analyses like neural networks became more relevant. These methods provide improvements in multiple applications, *e. g.* for signal-to-background discrimination or event reconstruction. Rare processes like the $t\bar{t}t\bar{t}$ production or $H \rightarrow l\bar{l}\gamma$ decay were observed for the first time using the LHC Run-2 dataset. In spite of the much more complex environment (multiple scattering, background conditions, *etc.*) of proton–proton collisions at the LHC, the accuracy of some results is superior to the results of the LEP collaborations. So far, despite all the efforts no significant deviations from the SM predictions have been found.

References

1. ATLAS Collab., JINST **3**, S08003 (2008).
2. ATLAS Collab., Phys. Lett. B **716**, 1 (2012), arXiv:1207.7214 [hep-ex].
3. CMS Collab., Phys. Lett. B **716**, 30 (2012), arXiv:1207.7235 [hep-ex].
4. ATLAS Collab., Phys. Lett. B **812**, 135980 (2021), arXiv:2007.07830.
5. ATLAS Collab., Eur. Phys. J. C **82**, 717 (2022), arXiv:2201.11428.
6. ATLAS Collab., Nature **607**, 52 (2022), arXiv:2207.00092.
7. ATLAS Collab., Eur. Phys. J. C **81**, 178 (2021), arXiv:2007.02873.
8. ATLAS Collab., Eur. Phys. J. C **81**, 537 (2021), arXiv:2011.08280.
9. ATLAS Collab., Phys. Lett. B **819**, 136412 (2021), arXiv:2103.10322.
10. M. Vesterinen, T.R. Wyatt. Nucl. Instrum. Meth. A **602**, 432 (2009).
11. ATLAS Collab., Eur. Phys. J. C **80**, 528 (2020), arXiv:1910.08819.
12. ATLAS Collab., Phys. Lett. B **810**, 135797 (2020), arXiv:2006.13076.
13. ATLAS Collab., Submitted to JHEP, arXiv:2207.01354.
14. ATLAS Collab., JHEP **11**, 118 (2021), arXiv:2106.11683.
15. ATLAS Collab., Eur. Phys. J. C **80**, 1085 (2020), arXiv:2007.14858.
16. H.P. Nilles, Phys. Rept. **110**, 1 (1984).
17. T. Plehn, T.M.P. Tait, J. Phys. G **36**, 075001 (2009), arXiv:0810.3919.
18. D. Dicus, A. Stange, S. Willenbrock, Phys. Lett. B **333**, 126 (1994), arXiv:hep-ph/9404359.
19. ALEPH, DELPHI, L3, OPAL, LEP Electroweak Collab., Phys. Rept. **532**, 119 (2013), arXiv:1302.3415.
20. ATLAS Collab., Nat. Phys. **17**, 813 (2021), arXiv:2007.14040.
21. Super-Kamiokande Collab., Phys. Rev. Lett. **81**, 1562 (1998).

22. SNO Collab., Phys. Rev. Lett. **89**, 011301 (2002).
23. J.I. Illana, M. Jack, T. Riemann, in *Proc. of the 2nd Workshop of the 2nd Joint ECFA/DESY Study on Physics and Detectors for a Linear Electron Positron Collider*, 490 (1999), arXiv:hep-ph/0001273.
24. ATLAS Collab., Phys. Rev. Lett. **127**, 271801 (2021).
25. OPAL Collab., Z. Phys. C **67**, 555 (1995).
26. DELPHI Collab., Z. Phys. C **73**, 243 (1997).
27. ATLAS Collab., Accepted by Phys. Rev. D, arXiv:2204.10783 [hep-ex].
28. L3 Collab., Phys. Lett. B **316**, 427 (1993).
29. ALEPH Collab., Phys. Rept. **216**, 253 (1992).
30. ATLAS Collab., Phys. Rev. D **90**, 072010 (2014), arXiv:1408.5774.
31. ATLAS Collab., JHEP **1905**, 142 (2019), arXiv:1903.01400.

EXPERIMENT LHCb AT THE LARGE HADRON COLLIDER

PNPI participants of the LHCb Collaboration: G.D. Alkhazov, A.V. Andreyanov, N.F. Bondar, A.D. Chubykin, A.A. Dzyuba, P.V. Kravchenko, O.E. Maev, D.A. Maisuzenko, N.R. Sagidova, A.N. Solovyev, I.N. Solovyev, A.A. Vorobyev, N.I. Voropaev

1. Introduction

LHCb is an international collaboration of about 1 400 scientists, engineers and technicians representing 86 different universities and laboratories from 18 countries, who have designed, built and operated a collider detector at the CERN Large Hadron Collider (LHC).

Main physics goals of the LHCb experiment are the following:

- Precision tests of the Standard Model (SM) and searches for effects beyond it (so-called new physics – NP) in the heavy quark sector *via* measurements of the parameters of the rare decays of heavy hadrons;
- Overconstraining measurements of the parameters of the quark mixing matrix (Cabibbo–Kobayashi–Maskawa – CKM-matrix);
- Investigation of the CKM-induced and searches of new sources of the *CP* violation;
- Precision spectroscopy of heavy hadrons to understand quantum chromodynamics (QCD), the theory of the strong interaction.

Besides this, LHCb experiment has a large program of studying proton–ion collisions in both collider and fixed target modes, as well as general QCD and electroweak (EW) measurements, and searches for exotic particles in forward spectrometer regime. Among main LHCb physics results are the discovery of new heavy particles including those, which have an exotic nature (the so-called pentaquarks and tetraquarks), the precise measurements of the parameters of the elements of the CKM-matrix, search and study for the rare decays of the heavy hadrons, lepton universality tests, as well as QCD production and spectroscopy studies. This report presents several main LHCb results obtained in 2019–2022. Results on the spectroscopy of heavy baryons and on searches and properties of the rare decays of *b*-hadrons are covered by dedicated articles in this collection of the main results of PNPI HEPD.

During Run-1, the LHC was operated at an *pp* centre-of-mass energy of 7 and 8 TeV, and the LHCb experiment has collected experimental data samples corresponding to 1 and 2 fb⁻¹ of an integrated luminosity, respectively. The second LHC Run was finished at the end of 2018. During Run-2, the LHC was operated at an *pp* centre-of-mass energy of 13 TeV. LHCb has collected the data sample corresponding to more than 6 fb⁻¹ of an integrated luminosity. PNPI was involved in the LHCb project through the design, production, commissioning and operation of the LHCb muon system. PNPI physicists took part in the data analysis, including QCD, charm and *B*-physics studies.

2. LHCb detector

The LHCb detector is a forward spectrometer [1, 2]. The angular distribution for the charm and beauty hadrons, produced in collisions of high energy protons, is boosted into the forward direction, where the products of their decays are registered in the 10 to 250 mrad range of the polar angle. A schematic view of the LHCb experiment is presented in Fig. 1.

The LHCb detector is a single-arm forward spectrometer covering the pseudorapidity range $2 < \eta < 5$. The detector includes a high-precision tracking system comprising a silicon-strip vertex detector (vertex locator) surrounding the *pp* interaction region, a large-area silicon-strip detector (TT) located upstream of a dipole magnet with a bending power of about 4 Tm, and three stations of silicon-strip detectors and straw drift tubes placed downstream of the magnet (T1–T3). The tracking system provides a measurement of the momentum, p_{tot} of charged particles with a relative uncertainty that varies from 0.5% at low momentum to 1.0% at 200 GeV/*c*. The minimum distance of a track to a primary vertex, the impact parameter, is measured with a resolution of $15 \mu\text{m} + 29 p_{\text{T}} \mu\text{m} c/\text{GeV}$, where p_{T} is the component of the momentum transverse to the beam.

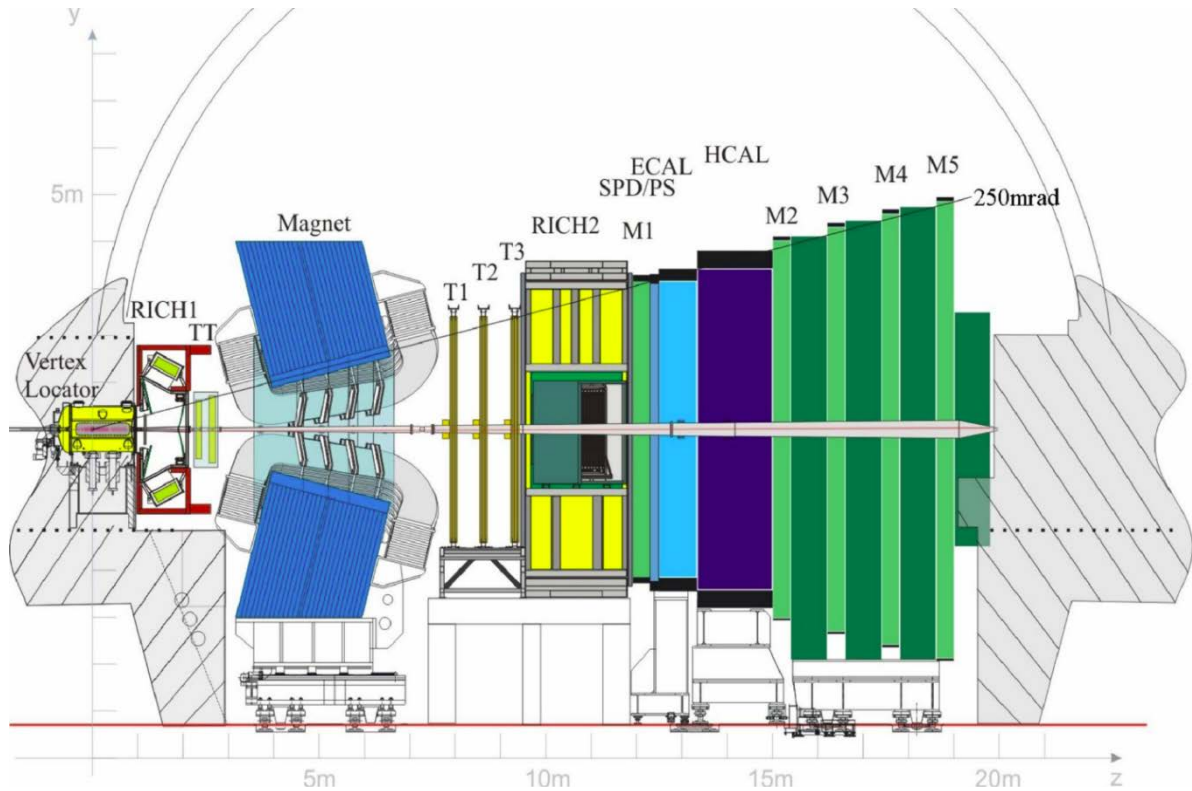


Fig. 1. Schematic view of the LHCb experiment

Different types of charged hadrons are distinguished using information from two ring-imaging Cherenkov detectors (RICH). Photons, electrons and hadrons are identified by a calorimeter system consisting of scintillating-pad and preshower detectors (SPD/PS), an electromagnetic calorimeter (ECAL), and a hadronic calorimeter (HCAL). Muons are identified with a system composed of alternating layers of iron and multiwire proportional chambers (M1–M5). The online event selection is performed by a trigger, which consists of a hardware stage, based on information from the calorimeter and muon systems, followed by a software stage, which applies a full event reconstruction.

In the Run-2 data taking campaign, LHCb implemented, tested and used a new real-time data processing strategy based on a reduced event model which allows to save not only the candidate signal firing the trigger, as previously was available, but also an arbitrary set of other reconstructed or raw objects from the event. This allowed for higher trigger rates for a given output data bandwidth, when compared to the traditional model of saving the full raw detector data for each trigger, whilst accommodating inclusive triggers and preserving data mining capabilities. The gain of almost a factor of two was achieved, which allowed to increase the statistical precision for the measurements in the charm sector of the SM.

3. *CP* violation and mixing in the charm sector of the Standard Model

Searches for new sources of charge-parity (*CP*) violation are very important for understanding of the Universe evolution during the first seconds after the Big Bang. A difference between particles and antiparticles, which manifests itself in non-invariance of the fundamental interactions under the combined action of the charge conjugation (*C*) and parity (*P*) transformation, is one of the necessary conditions proposed by A. Sakharov for the dynamical generation of the baryon asymmetry of the Universe. *CP* violation occurs in the quark sector of the SM. This effect relates to an irreducible complex phase in the CKM-matrix. Before 2019, only the processes connected with the transformation of the down-type quarks (*d*, *s*, *b*) were known as *CP* violating. The charm quark belongs to the up-type quark family. The SM predicts very tiny (typically order of 10^{-3} – 10^{-4}) effects of the *CP* violation for charm hadrons.

Three types of CP -violating effects can occur in the quark sector: CP violation in decay (measured *via* CP -asymmetries), CP violation in mixing, and CP violation in interference between a decay without mixing and a decay with mixing.

In 2019, the LHCb Collaboration announced an observation of the CP violation in D^0 meson decays [3]. In order to establish the effect, one has to find a different probability of the decay of D^0 mesons and their antiparticles for a particular decay channel. An accounting of the initial numbers of particles and antiparticles is done *via* the so-called tagging procedures. In the LHCb analysis, two tagging methods have been used. The first method uses a strong decay of D^* mesons, where a charge of the π -meson fixes the flavour of D^0 . The second method uses the so-called semimuonic decays of b -hadrons, where the electric charge of a muon determines the tag-decision. The CP -even decays $D^0 \rightarrow K^-K^+$ and $D^0 \rightarrow \pi^-\pi^+$ are used to cancel out detection asymmetry effects. A difference between these rates eliminates an influence of the D^0 production asymmetry, as well as asymmetries of a tagger-particles detection. A non-zero value of the ΔA_{CP} observable is an indication that the CP symmetry is broken. LHCb measured ΔA_{CP} to be $(-15.4 \pm 2.9) \cdot 10^{-4}$, where statistical and systematic uncertainties are combined. Thus, the effect of CP violation is observed with a significance above 5.3 standard deviation. This is the first observation of CP violation in the decays of charm hadrons.

In 2022, these studies were supplemented by the measurement of the time-integrated CP asymmetry in $D^0 \rightarrow K^-K^+$ decays using Run-2 data [4]. Prompt tagging technique was used. The time-integrated CP asymmetry is measured to be $A_{CP}(K^-K^+) = (6.8 \pm 5.4_{\text{stat}} \pm 1.6_{\text{syst}}) \cdot 10^{-4}$. The direct CP asymmetries in $D^0 \rightarrow K^-K^+$ and $D^0 \rightarrow \pi^-\pi^+$ decays were derived by combining $A_{CP}(K^-K^+)$ and ΔA_{CP} , giving

$$a^d(K^-K^+) = (7.7 \pm 5.7) \cdot 10^{-4} \quad \text{and} \quad a^d(\pi^-\pi^+) = (23.2 \pm 6.1) \cdot 10^{-4}.$$

A correlation coefficient between $a^d(K^-K^+)$ and $a^d(\pi^-\pi^+)$ was 0.88, and the compatibility of these values with the CP symmetry is 1.4 and 3.8 standard deviation, respectively. This is the first evidence for direct CP violation in a specific D^0 decay.

Direct CP -violating effects were also searched in two body decays of D^0 into $K_S^0 K_S^0$ final state [5], $D_{(s)}^+$ into $\pi^+\pi^0$, $K^+\pi^0$, $\pi^+\eta$, and $K^+\eta$ [6]. Corresponding CP asymmetries were found consistent with zero for all of the investigated decay channels. LHCb also performed model-independent searches for CP violation in a three-body $\Xi_c^+ \rightarrow pK^-\pi^+$ decays [7]. The obtained results are consistent with the absence of CP violation.

For electrically neutral mesons as the mass eigenstates are linear combinations of the flavour eigenstates, *i. e.* $|D_{1,2}\rangle \equiv p|D^0\rangle \pm q|\underline{D}^0\rangle$, where p and q are complex parameters and, in the limit of CP symmetry, $|D_{1,2}\rangle$ is defined as the CP even and odd eigenstate. Mixing of flavour eigenstates is described by the dimensionless mixing parameters $x \equiv (m_1 - m_2)/\Gamma$ and $y \equiv (\Gamma_1 - \Gamma_2)/(2\Gamma)$, where $m_{1,2}$ and $\Gamma_{1,2}$ are the mass and decay width of the $D_{1,2}$ states 1,2, respectively, and Γ is the average decay width. If meson and antimeson decays into the same final state (f), CP violation in mixing manifests itself if $|q/p| \neq 1$ or in the interference between mixing and decay if $\varphi_f \equiv \arg(qA_f/pA_f) \neq 0$, where A – amplitudes of decay processes.

In 2019–2022, LHCb performed several analyses to improve knowledge about, x , y , $|q/p|$ and φ . The most important was the measurement of mixing and CP violation in $D^0 \rightarrow K_S^0 \pi^+ \pi^-$ decays performed with the so-called bin-flip method, using pp collision data collected by the LHCb experiment and corresponding to an integrated luminosity of 5.4 fb^{-1} [8]. This resulted in the first observation of a nonzero value of the mass difference x of neutral charm meson mass eigenstates with a significance of more than 7σ , and significantly improves limits on mixing-induced CP violation in the charm sector. The mixing parameters were found to be $x = (3.98_{-0.54}^{+0.56}) \cdot 10^{-3}$ and $y = (4.6_{-1.4}^{+1.5}) \cdot 10^{-3}$. This analysis and the other one on the topic [9] didn't find time-dependent CP violation effects.

4. Cabibbo–Kobayashi–Maskawa parameters and CP violation in the beauty sector of the Standard Model

The quark-mixing matrix (CKM) is a unitary 3×3 matrix, which contains information on the strength of the flavour-changing weak interaction in the SM. The constraints of unitarity of the CKM-matrix on the diagonal terms can be written as $\sum_i |V_{ik}|^2 = 1$, while for non-diagonal elements the relations of the type $\sum_k V_{ik} V_{jk}^* = 0$ must be met. The strategy of searches for NP in the CKM sector is based on precise measurements of the elements (or the combinations) of the quark mixing matrix and checking the conditions of unitarity,

as well as consistency between measurements of different types for the same quantity. LHCb performed a number of such measurements in 2018–2022 for the b -hadrons.

One of the parameters, which can be predicted with high accuracy in the framework of the SM is the γ angle of the unitarity triangle (relation for the off-diagonal CKM elements). This angle is related to the elements of the quark mixing matrix as $\gamma = \arg[-V_{ud}V_{ub}^*/V_{cd}V_{cb}^*]$. The uncertainty of the theoretical predictions for γ is less than 10^{-7} in tree level processes. The angle γ can be determined in the measurement of the ratio between the favoured ($b \rightarrow cW$) and suppressed ($b \rightarrow uW$) amplitudes in weak decays of the charged and neutral B mesons. Since 2018, several new measurements of γ were presented by the LHCb Collaboration [10–13]. The most powerful method to measure the angle γ is provided by $B^\pm \rightarrow DK^\pm$ decays followed by different decays of the D meson. Here D is an admixture of the meson and antimeson states (due to mixing). This allows one to get rid of a nuisance strong phase and extract the weak one. The LHCb Collaboration has performed such measurements in a wide ensemble of B and D decay modes and arrived at an overall result of $\gamma = (65.4_{-4.2}^{+3.8})^\circ$, see combination plot in the *left panel* of Fig. 2. This result is already more precise than the original goal for the LHCb experiment. Recent experimental constraints on the unitarity triangle provided by the CKMfitter group are presented in the *right panel* of Fig. 2. The overall picture is self-consistent and is in good agreement with the SM expectations.

In Ref. [13], charmed D meson decays into four charged mesons $K^\mp\pi^\pm\pi^\pm\pi^\mp$ were used. The sensitivity to the angle γ has been significantly improved by studying the $B^\pm \rightarrow DK^\pm$ and $B^\pm \rightarrow D\pi^\pm$ decay rates in separate regions (bins) of the $D \rightarrow K^\mp\pi^\pm\pi^\pm\pi^\mp$ phase space. A typical invariant mass distribution in one of the bins separately for B^- and B^+ decays is presented in Fig. 3. A large difference between the heights of the mass peaks for B^- and B^+ decays indicates CP violation of 85%. This is the largest CP violation ever observed.

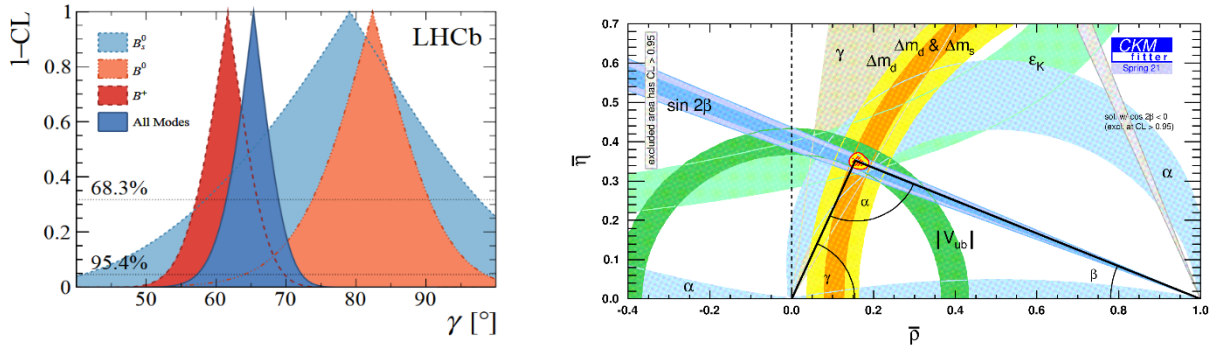


Fig. 2. The combination of γ angle measurements performed by the LHCb Collaboration (*left panel*); recent experimental constraints on the unitarity triangle (*right panels*)

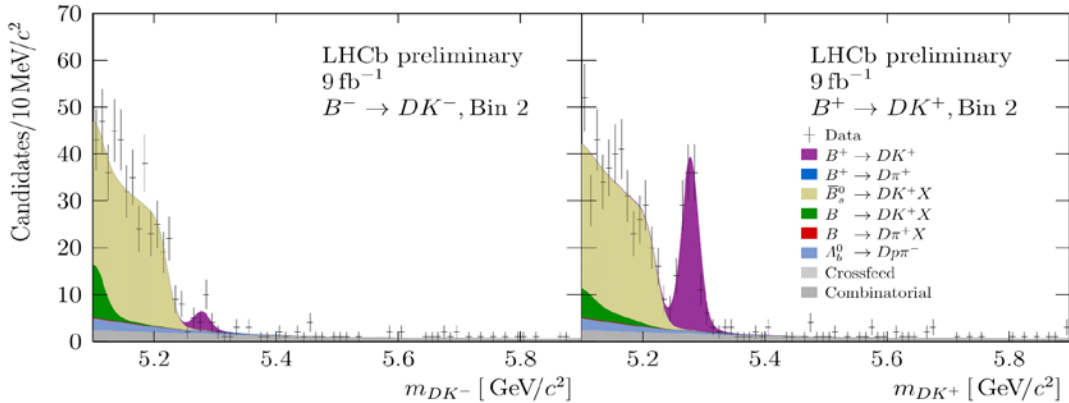


Fig. 3. Mass of the BD system for B^+ decays (*left*) and for B^- (*right*). The distribution is done for one of the bins of the $D \rightarrow K^\mp\pi^\pm\pi^\pm\pi^\mp$ phase space

Another interesting topic is the experimental puzzle related to the measurement of the CKM matrix elements $|V_{cb}|$ and $|V_{ub}|$. These quantities can be measured in two ways: “exclusive”, when one of the numerous decays of b hadrons is used, and “inclusive”, in which all $b \rightarrow c\mu\nu_\mu$ transitions are measured “in bulk”. The results of these two classes of measurements are suspiciously different, with the “exclusive” method yielding a lower result than the “inclusive” one for both $|V_{cb}|$ and $|V_{ub}|$. The measurements made for the decays $\Lambda_b^0 \rightarrow p\mu\nu_\mu$ are sensitive to the ratio $|V_{ub}|/|V_{cb}|$. However, they do not clarify which type of measurements (“exclusive” or “inclusive”) is correct.

Meanwhile, two new methods to determine $|V_{cb}|$ and $|V_{ub}|$ was developed by LHCb. The first one applied for the $|V_{cb}|$ measurements uses semimuonic decays of B_s^0 mesons: $B_s^0 \rightarrow D_s^- \mu^+ \nu_\mu$ and $B_s^0 \rightarrow D_s^{*-} \mu^+ \nu_\mu$ [14], and the second one (sensitive to the ratio $|V_{ub}|/|V_{cb}|$) rely on detection of $B_s^0 \rightarrow K^- \mu^+ \nu_\mu$ [15]. The difficulty in both cases is that in isolation the signal arises from the fact that neutrinos are not detected by the experimental set-up, and when determining the kinematic characteristics of decays, uncertainties arise, the procedures for eliminating which are rather complicated. To emphasize this, a spectrum of the so-called corrected mass for $B_s^0 \rightarrow K^- \mu^+ \nu_\mu$ decays is presented in the *left panel* of Fig. 4. Theory also plays an important role in the measurements. Two schemes of theoretical calculations were used. This allowed one to take into account the influence of the quark–gluon environment of the decay process occurring under the influence of the weak interaction. The final result, as it turns out, slightly (at the level of one standard deviation) depends on the choice of the theoretical model.

Two new measurements have not clarified the situation with a puzzle, which can be demonstrated by placing different experimental results into the plane formed by the hypothetically possible values of $|V_{cb}|$ and $|V_{ub}|$. Stripes in Fig. 4 (*right*) represent different measurements of $|V_{cb}|$, $|V_{ub}|$ and their ratios. If all measurements, as well as the theoretical calculations underlying them, are correct, then the lines should overlap around one single point, which corresponds to the true parameters of the SM. However, it is seen that it is impossible to find such a point that satisfies all observations. This means that further work needs to be done to solve this puzzle. Its solution will mean that the present knowledge of the fundamental parameters of the SM will be refined and, perhaps, better understanding on how to describe the strong interaction will be achieved. It is also possible that this discrepancy in the measurement results is a manifestation of some still unknown fundamental interactions.

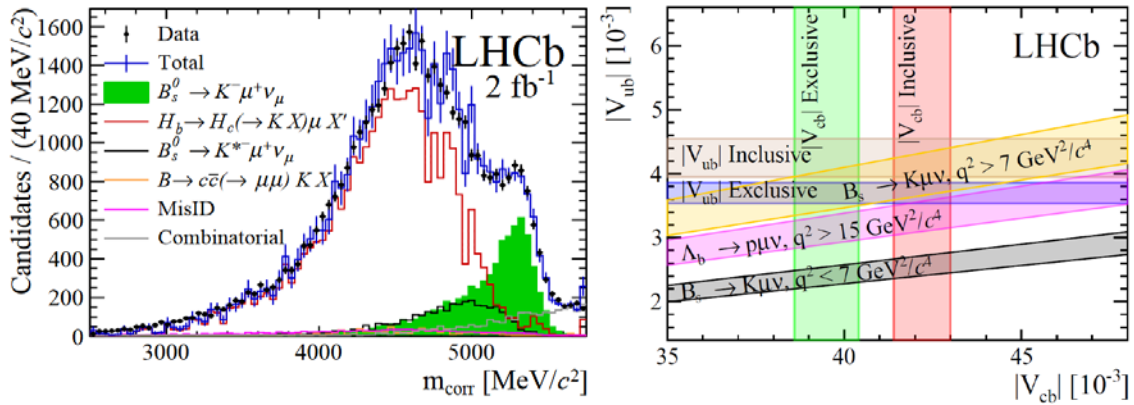


Fig. 4. Distribution of corrected mass for the signal $B_s^0 \rightarrow K^- \mu^+ \nu_\mu$, for di-lepton invariant mass squared less than 7 GeV^2 . *Green histogram* indicates signal contribution (*left panel*). Different measurements of $|V_{cb}|$, $|V_{ub}|$ and measured relations between them (*right panel*)

5. Electroweak measurements

Besides the charm and beauty quark physics, the LHCb experiment carries an experimental program on direct searches for NP particles, as well as the part devoted to measurements in the EW and top quark sectors of the SM.

The W boson mass (m_W) is directly related to EW symmetry breaking in the SM. The value of m_W is related to the precisely measured fine-structure constant, the mass of the Z boson and the Fermi constant. A global fit

of EW observables, excluding direct measurements of m_W , yields a prediction of $m_W = 80\,354 \pm 7$ MeV. This can be compared with direct measurements to test for possible beyond the SM contribution. The sensitivity of the global EW fit to NP is primarily limited by the precision of the direct measurements of m_W .

In 2021, LHCb presented its first measurement of m_W using $W \rightarrow \mu\nu$ decays [16]. The measurement is based on the shape of the transverse momentum (p_T) distribution of muons from W boson decays. A simultaneous fit of the q/p_T distribution of W boson decay candidates (where q is the muon charge) and of the parameters of distribution for Z boson decay candidates is verified to reliably determine m_W . This method has a reduced sensitivity to the uncertainties related to a model of the W boson transverse momentum distribution compared to previous determinations of m_W at hadron colliders. The following result was obtained:

$$m_W = 80\,354 \pm 23_{\text{stat}} \pm 10_{\text{exp}} \pm 17_{\text{th}} \pm 9_{\text{PDF}} \text{ MeV}.$$

This result is in agreement with the expectation from the global fit of EW observables. A comparison of this result with m_W reported by other experiments, as well as with the SM expectation is presented in the *left panel* of Fig. 5. Future analysis of the rest part of Run-2 data will reduce statistical uncertainty. This is particularly interesting, as the m_W measurement performed by the CDF Collaboration is in significant disagreement with the SM predictions (see Fig. 5).

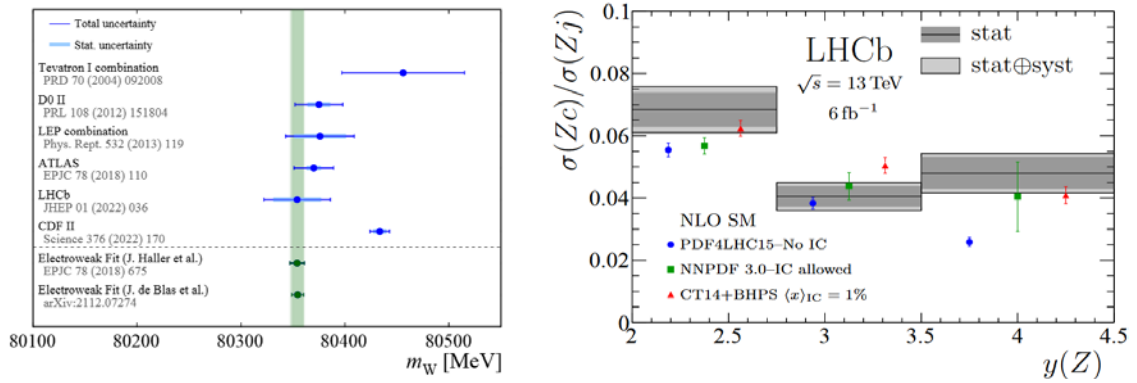


Fig. 5. Summary of W boson mass measurements (*blue markers*) in comparison with SM expectations (*green*) – *left panel*. Distribution (*gray bands*) for three intervals of forward Z rapidity, compared to NLO SM predictions without (*blue markers*), with the charm PDF shape allowed to vary (hence, permitting IC (*red and green*)) – *right panel*

Another important LHCb result at the EW sector was the measurement of the Z boson production accompanied by a charm jet [17]. Events of this type provide constraints on the so-called intrinsic charm (IC) of proton – a possible admixture of the charm contribution into the proton wave function. The possible existence of IC would have many phenomenological consequences. For example, IC would alter both the rate and kinematics of charm hadrons produced by cosmic-ray proton interactions in the atmosphere, which are an important source of background in studies of astrophysical neutrinos. The cross sections of many processes at the LHC and other accelerators would also be affected. The key observable sensitive to IC is the ratio of production cross sections $R_j^c = \sigma(Zc)/\sigma(Zj)$, where Zj refers to events containing a Z boson and charm (c) or any type of jet (j). This ratio is less sensitive than $\sigma(Zc)$ to experimental and theoretical uncertainties.

The data sample used corresponds to an integrated luminosity of 6 fb^{-1} collected at a centre-of-mass energy of 13 TeV. The Z boson rapidity was in the range $2.0 < y_Z < 4.5$. The ratio of interest was determined in three intervals of y_Z . This result together with predictions are presented on the right panel of Fig. 5. The observed R_j^c values are consistent with both the no-IC and IC hypotheses in the first two y_Z intervals; however, this is not the case in the forward-most interval where the ratio of the observed to no-IC-expected values is 1.85 ± 0.25 . Figure 5 shows that, after including the IC shape into the parton distribution function with a mean momentum fraction of 1%, the theory predictions are consistent with the experimentally measured R_j^c . However, conclusions about whether the proton contains valence-like intrinsic charm can only be drawn after incorporating these results into global analyses of the parton distribution functions.

The LHCb experiment also performed several important measurements for Z boson production and properties. They were done in pp collisions at $\sqrt{s} = 13$ TeV. Among them a precision measurement of forward

Z boson production [18] and the first measurement of $Z \rightarrow \mu^+\mu^-$ angular coefficients in the forward region of pp collisions [19] should be mentioned.

The direct search for the NP particles is also an essential part of the LHCb physics program. During 2019–2022, the LHCb experiment performed a search for massive long-lived particles decaying semileptonically at $\sqrt{s} = 13$ TeV [20], a search for heavy neutral leptons in W decays into $\mu^+\mu^\pm$ and jet [21], searches for low-mass dimuon resonances [22], as well as a study of $A' \rightarrow \mu^+\mu^-$ decays in a wider mass range [23]. Note that all measurements, which are presented in this section, relied on the excellent performance of the LHCb muon system.

6. Summary

The LHCb detector was performing well with a high data taking efficiency during Run-1 and Run-2. A lot of new physics results on different topics have been obtained in recent years. Many physics data analyses already used full available statistics. The data taking will be continued in 2023 after the upgrade of the experiment.

Alexey A. Vorobyev

Former head of the HEPD Prof. Alexey A. Vorobyev passed away in November 2021. Besides many of his outstanding scientific achievements, he was one of the co-founders of the LHCb Collaboration. Colleagues from the experiment recognized his role especially in early days of the experiment. So, in the very beginning of the collaboration Prof. Vorobyev insisted on switching to the geometry that LHCb has now, rather than a complex of two magnets that was originally proposed. The design of the muon chambers was also done according to the proposal of Prof. Vorobyev and turned out to be extremely successful. In their condolence letters the members of the LHCb Collaboration emphasized the remarkable ability of Prof. Vorobyev to propose elegant solutions for complex problems.

References

1. LHCb Collab., JINST **3**, S08005 (2008).
2. LHCb Collab., JINST **14**, P04006 (2019).
3. LHCb Collab., Phys. Rev. Lett. **122**, 211803 (2019).
4. LHCb Collab., arXiv:2209.03179.
5. LHCb Collab., Phys. Rev. D **104**, 031102 (2021).
6. LHCb Collab., JHEP **06**, 019 (2021).
7. LHCb Collab., Eur. Phys. J. C **80**, 986 (2020).
8. LHCb Collab., Phys. Rev. Lett. **127**, 111801 (2021).
9. LHCb Collab., Phys. Rev. D **104**, 072010 (2021).
10. LHCb Collab., JHEP **12**, 141 (2021).
11. LHCb Collab., JHEP **02**, 169 (2021).
12. LHCb Collab., JHEP **04**, 081 (2021).
13. LHCb Collab., arXiv:2209.03692.
14. LHCb Collab., Phys. Rev. D **101**, 072004 (2020).
15. LHCb Collab., Phys. Rev. Lett. **126**, 081804 (2021).
16. LHCb Collab., JHEP **01**, 036 (2022).
17. LHCb Collab., Phys. Rev. Lett. **128**, 082001 (2022).
18. LHCb Collab., JHEP **07**, 26 (2022).
19. LHCb Collab., Phys. Rev. Lett. **129**, 091801 (2022).
20. LHCb Collab., Eur. Phys. J. C **82**, 373 (2022).
21. LHCb Collab., Eur. Phys. J. C **81**, 248 (2021).
22. LHCb Collab., JHEP **10**, 156 (2020).
23. LHCb Collab., Phys. Rev. Lett. **124**, 041801 (2020).

BRIEF OVERVIEW OF SOME ALICE RESULTS IN 2019–2022

PNPI participants of the ALICE Collaboration: V.V. Ivanov, A.V. Khanzadeev, E.L. Kryshen, M.V. Malaev, V.N. Nikulin, A.Yu. Ryabov, V.G. Ryabov, Yu.G. Ryabov, V.M. Samsonov, M.B. Zhalov

1. Introduction

One of the priority fundamental problems of relativistic nuclear physics and the physics of strong interactions in general is the study of a new extreme state of matter, the high-temperature quark–gluon plasma (QGP), arising in collisions of ultrarelativistic ions at hadron and ion colliders. For a decade, the ALICE Collaboration including a team of scientists from PNPI, is deeply involved in studies of the QGP, as well as of other numerous phenomena revealing in the high-energy proton–proton, proton–nucleus and nucleus–nucleus collisions. Some of these exciting results published by ALICE in 2019–2022 are presented below.

2. Femtoscopy in proton–proton interactions at the Large Hadron Collider: a new method to study the interaction potentials of unstable baryons

In 2020, the ALICE Collaboration published in *Nature* the results of studies of low-energy interactions of $\Xi^- (dss)$ и $\Omega^- (sss)$ hyperons with protons [1]. The knowledge of baryon–baryon potentials is one of the key problems of nuclear physics, physics of neutron stars, and a more global challenge to construct the fundamental theory of strong interactions, quantum chromodynamics (QCD), in the non-perturbative region. In terms of quarks and gluons, the fundamental degrees of freedom of QCD, a significant progress in this area has been achieved in the determination of baryon–baryon potentials on the lattice with their subsequent verification using a comparison to experimental data.

The traditional method of experimental studies of the interaction potential of low-energy protons and neutrons using their elastic scattering is not applicable in the case of unstable baryons because of their short lifetime. In the ALICE experiment, there has been proposed a new approach to this problem based on the method of femtoscopy. Formulated by analogy with the Hanbury Brown and Twiss (HBT) effect of interferometry in astrophysics, in high-energy nuclear physics this method is actively used to determine the size of proton–proton and nucleus–nucleus interaction zones in events with high multiplicity of the produced particles. The method is based on a comparison of the experimental correlation function $C^{\text{exp}}(\mathbf{k}^*)$ of pairs of particles with the theoretically modelled correlation function $C^{\text{theor}}(\mathbf{k}^*) = \int S(\mathbf{r}) |\Psi(\mathbf{k}^*, \mathbf{r})|^2 d\mathbf{r}$, where $|\mathbf{k}^*|$ is the relative momentum. From the comparison one determines the source function $S(\mathbf{r})$, which describes the spatial distribution of the particle emission region in a parametric form provided that the wave function $\Psi(\mathbf{k}^*, \mathbf{r})$ of the pair of the correlated particles is known. In ultrarelativistic proton–proton collisions with high multiplicity of produced particles, correlations between protons and hyperons at relatively low energies originate due to their final-state interactions. In the ALICE experiment, using a large amount of data on proton–proton collisions at $\sqrt{s_{NN}} = 13$ TeV, it is possible to select events with pp , $p\Xi^-$ and $p\Omega^-$ pairs with the relative momenta $|\mathbf{k}^*|$ in the $20 \text{ MeV}/c < |\mathbf{k}^*| < 300 \text{ MeV}/c$ interval and determine the experimental correlation functions $C_{pp}^{\text{exp}}(\mathbf{k}^*)$, $C_{p\Xi}^{\text{exp}}(\mathbf{k}^*)$ and $C_{p\Omega}^{\text{exp}}(\mathbf{k}^*)$. Knowledge of the potential of the proton–proton interaction allows one to find $\Psi(\mathbf{k}^*, \mathbf{r})$ by solving the Schrödinger equation and to extract the source function $S_{pp}(\mathbf{r})$ from the femtoscopy analysis of $C_{pp}^{\text{exp}}(\mathbf{k}^*)$.

Figure 1 shows a comparison of the measured $C_{p\Xi}^{\text{exp}}(\mathbf{k}^*)$ and $C_{p\Omega}^{\text{exp}}(\mathbf{k}^*)$ with the theoretical correlation functions for $p\Xi^-$ and $p\Omega^-$ pairs, which were obtained using this $S_{pp}(\mathbf{r})$ source function and the wave functions of the correlated $p\Xi^-$ and $p\Omega^-$ pairs obtained by solving the Schrödinger equation with the Coulomb interaction and the hyperon–proton potentials from the hadrons lattice quantum chromodynamics calculations by HAL QCD Collaboration. These calculations predict strong attraction for the $p\Omega^-$ interaction, which may lead to formation of a bound state with the binding energy of 2.5 MeV. Similarly, a strong attraction is predicted for $p\Xi^-$ in the $0.5 \text{ fm} < r < 2 \text{ fm}$ region; however, for $r < 0.2 \text{ fm}$, the attraction changes to repulsion. This behaviour of the potentials is reflected in the behaviour of the calculated correlation functions presented in Fig. 1.

The *green line* shows the correlations due to Coulomb attraction only, while the *magenta* and *orange lines* also include correlations due to the strong interaction. Besides the $p\Xi^-$ and $p\Omega^-$ potential interaction, inelastic channels ($p\Xi \rightarrow \Lambda\Lambda$, $p\Omega \rightarrow \Xi\Lambda\dots$) were also considered. Their effect has turned out to be negligible for $p\Xi^-$, while leading to deviations from the data for $p\Omega^-$ (compare the *blue* and *orange lines*). This behaviour of the experimental correlation functions confirms the attraction in the strong interaction of Ξ^- and Ω^- hyperons with protons predicted by HAL QCD, but does not agree with the existence of a bound state in the $p\Omega^-$ system, which is realized as a local minimum of $C(\mathbf{k}^*)$ at $100 \text{ MeV}/c < |\mathbf{k}^*| < 300 \text{ MeV}/c$.

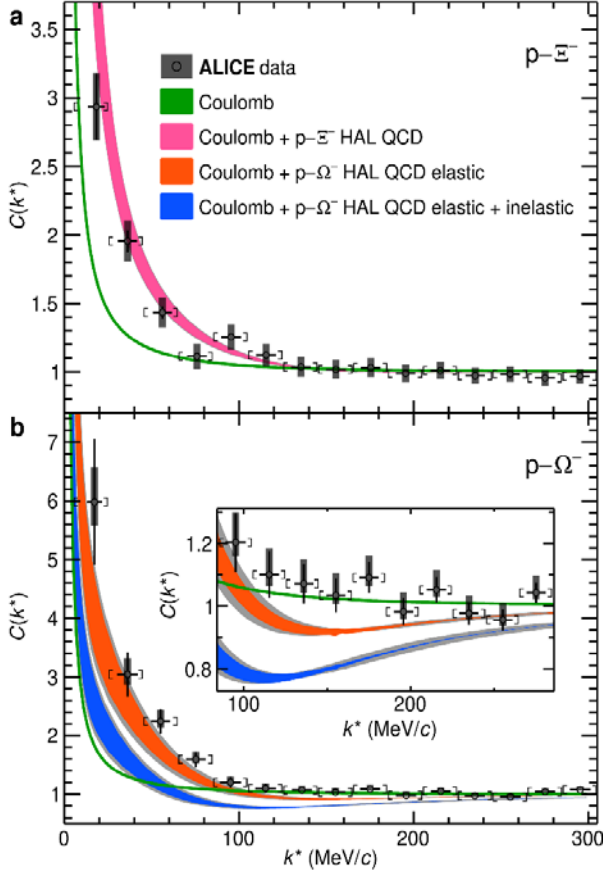


Fig. 1. Comparison of the correlation function measured by ALICE with that theoretically modelled using the HAL QCD lattice calculations of the hyperon-proton potentials

Such a minimum is absent in the measured correlation function $C_{p\Omega}^{\text{exp}}(\mathbf{k}^*)$ in the entire momentum range $|\mathbf{k}^*| < 300 \text{ MeV}/c$. These results demonstrate the potential of the femtoscopia method to study strong baryon-baryon interactions at low energies and to reconstruct baryon-baryon potentials down to distances of the order of 10^{-14} cm using data on ultrarelativistic proton-proton collisions at the Large Hadron Collider (LHC).

3. First observation of spin-orbit effects in quark-gluon plasma at the Large Hadron Collider

The main goal of the ALICE experiment is to study properties of the strongly interacting QGP formed in the interaction region of colliding ultrarelativistic heavy nuclei. The semicentral high energy collisions of nuclei with large Z , schematically shown in Fig. 2, create the QGP in the interaction zone (*red ellipse*) and the very strong electromagnetic field during the interaction time. The non-uniform distribution of nucleons in the nuclei and the non-zero impact parameter in such collisions may result in the high rotation speed of the created QGP and, correspondingly, in the perpendicular to the reaction plane (x - z plane) large orbital angular momentum L of quarks in this region. The spin-orbit interaction of quarks in the QGP may lead to their polarization along L and, in the transition of the QGP into the hadron gas, to polarization of hadrons in the processes of recombination or fragmentation of the polarized quarks. The ALICE Collaboration has analysed

the data on the yield of short-lived $K^*(892)^0$ vector mesons in hadronization of the QGP to measure the orientation of the spin of $K^*(892)^0$ with respect to the reaction plane in semicentral Pb–Pb collisions at $\sqrt{s_{NN}} = 2.76$ TeV and pp collisions at $\sqrt{s_{NN}} = 13$ TeV [2].

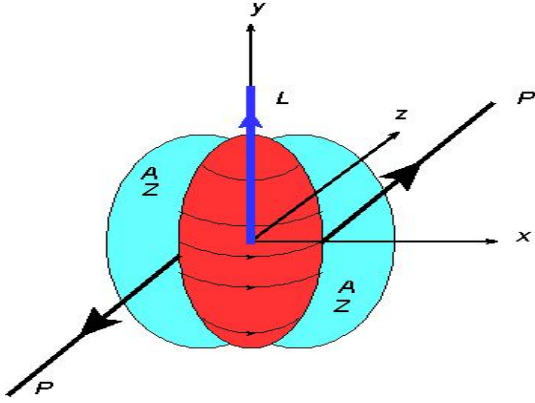


Fig. 2. Schematic representation of a semicentral collision of ultrarelativistic nuclei (*blue disks* due to Lorentz compression) with large momenta P , mass number A and charge Z

For an unpolarized vector meson, the probabilities of the spin projections of 1, 0 and -1 are the same and equal to $1/3$, and the angular distribution of $K^*(892)^0$ decay products should be isotropic with respect to the quantization axis. The angular distribution asymmetry allows one to measure the value of the ρ_{00} spin density matrix element, which determines the probability for $K^*(892)^0$ to be in the state with the spin-zero projection. The deviation of ρ_{00} from $1/3$ indicates polarization of $K^*(892)^0$.

The results of the analysis are presented in Fig. 3. In Pb–Pb collisions, the magnitude of ρ_{00} is noticeably smaller than $1/3$ for small transverse momenta $p_T \approx 1$ GeV/c.

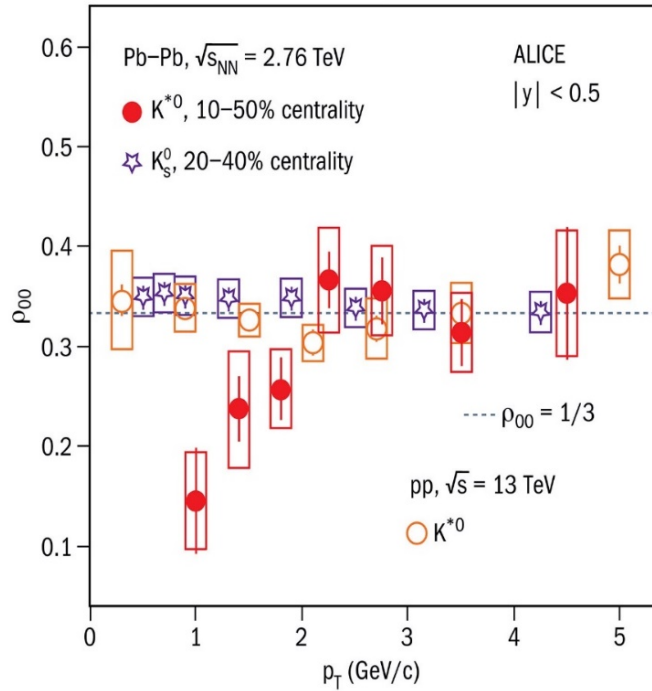


Fig. 3. Dependence of ρ_{00} on the transverse momentum of K mesons

In pp scattering, where the probability to have a large angular momentum is small, the measured values of ρ_{00} agree with $1/3$ in the entire range of the transverse momentum. The polarization of Λ hyperons produced in Pb–Pb interactions, which was measured earlier in similar conditions, has turned out to be close to zero

within 1σ . Taking this into account, the effect of vector meson polarization observed at a 3σ level can be considered not only as evidence of noticeable spin-orbit interactions in the evolution of the QGP formed in semicentral heavy-ion interactions at the LHC energies, but also as an indication of the possibility of different hadronization mechanisms in formation of vector mesons and baryons in the process of the QGP transition into the hadron phase.

4. First direct observation of the quark–gluon plasma dead cone effect in hard proton–proton interactions at the Large Hadron Collider

One of the main methods of diagnostics of QGP created in the ultrarelativistic heavy ion collisions is an analysis of energy losses of relativistic quarks, which are created in hard parton–parton interactions in the collision zone and traverse the region of the formed QGP. To estimate the magnitude of radiative energy losses and transport coefficients characterizing the viscosity of the QGP matter, it is essential to account for the “dead cone” effect, which consists in the suppression of gluon radiation by relativistic heavy quarks in a narrow cone around the direction of the quark motion, whose aperture depends on the ratio of the quark mass M to its energy E . While in perturbative QCD the “dead cone” effect was predicted back in 1991 by PNPI theorists [3], its observation has been challenging in many experiments. Primarily, it was hindered by difficulties in reconstructing the true direction of the quark motion and the precise determination of the cone size as well as the identification and removal from the cone region the particles that are not related to gluon emission. At ALICE, there has been carried out a detailed investigation of hadron multiplicity in events of proton–proton interactions with a production of hadron jets initiated by massive charm quarks [4].

Precision particle detectors at ALICE, the development of methods of experimental data analysis, and detailed modeling of proton interactions at the LHC energies combined with the existing computer capabilities have allowed one to reconstruct the process of gluon emission by charm quarks. Figure 4 shows schematically such a reconstruction: the solid line is the trajectory of a c -quark motion from the proton–proton interaction vertex; the wavy lines denote emitted gluons. Extracted from the data the ratio $R(\theta)$ of the angular distributions of emitted gluons in jets initiated by a charm quark with the energy E to that in inclusive jets is shown in Fig. 5. In the latter case, the “dead cone” effect is essentially absent because light quarks characterized by a very small ratio $M/E \ll 1$ and massless gluons emit forward gluons with a logarithmically increasing probability. The *red solid squares with pink strips* show the values of $R(\theta)$ extracted from the data of the ALICE experiment [4]; the *blue and green solid curves* present the results of calculations using event generators SHERPA and PYTHIA including the “dead cone” effect, while the *dashed lines* give the results without its account. The *three panels from left to right* in Fig. 5 show the narrowing of the dead cone with an increase of the charm quark energy E and a corresponding decrease of the ratio M/E .

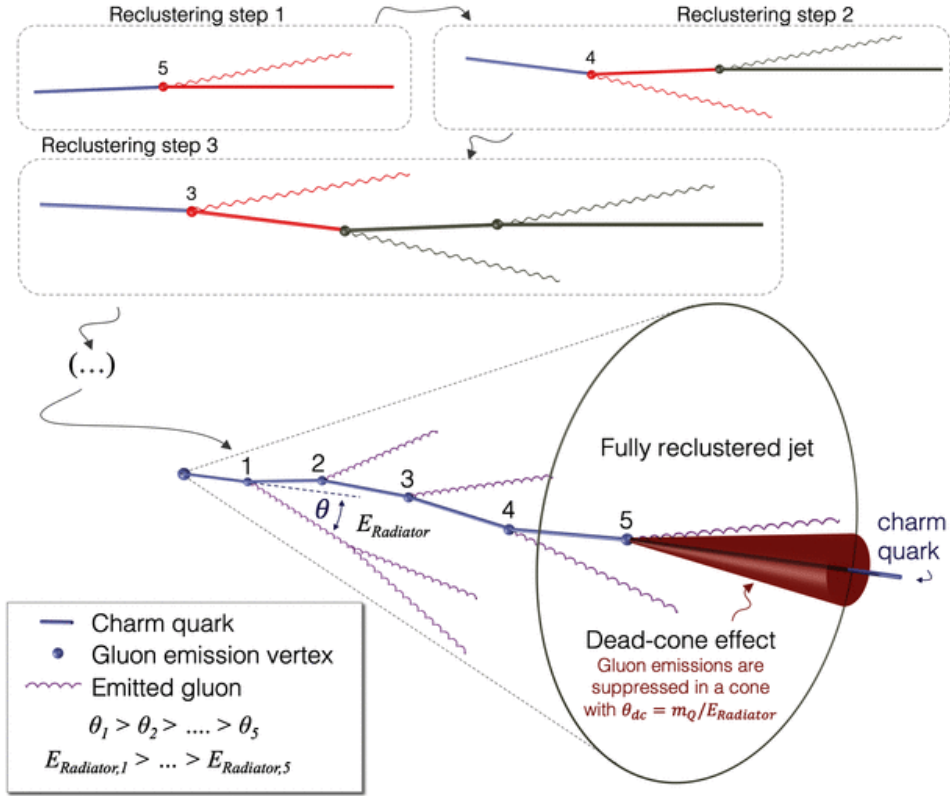


Fig. 4. Schematic picture of the reconstruction of the process of gluon emission by a charm quark in the event of a jet initiated by a charm quark [4]

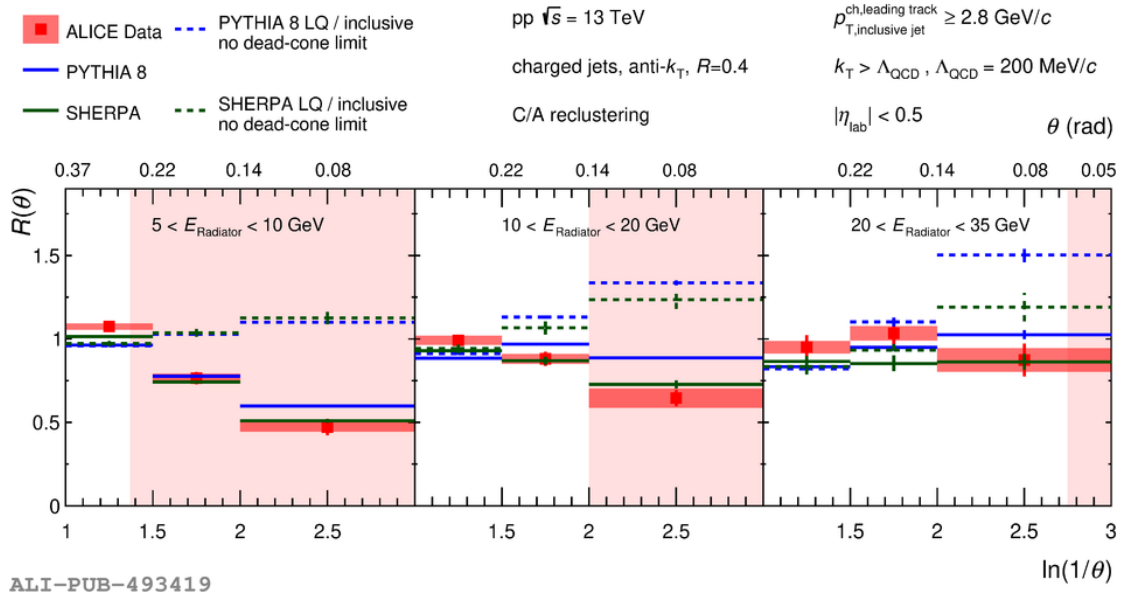


Fig. 5. The ratios of the splitting-angle probability distributions for D^0 -meson tagged jets to inclusive jets, $R(\theta)$, measured in pp collisions at $\sqrt{s} = 13$ TeV at ALICE

These results convincingly demonstrate a two-fold suppression of the gluon emission in the region of small angles by heavy charm quarks compared to the emission in the same region by light quarks. Thus, for the first time, the ALICE experiment not only confirmed the theoretically predicted “dead cone” effect but also clearly demonstrated that the kinematics of produced hadrons reproduces the kinematics of emitted QCD partons even

at so narrow angles, hence, justifying a hypothesis of the local parton–hadron duality formulated by PNPI theorists nearly forty years ago. A comparison of the experimental result with the results of modeling also confirms the adequate account of this effect in event generators SHERPA and PYTHIA, which are used in modeling of processes of hard proton–proton interactions and formation and evolution of the QGP created in collisions of ultrarelativistic ions.

5. Measurement of the ${}^3\text{H}_\Lambda$ lifetime and the separation energy of Λ in hypertriton in Pb–Pb collisions with ALICE detector at 5.02 TeV

The ALICE Collaboration made a significant contribution to the measurement of the hypertriton ${}^3\text{H}_\Lambda$ lifetime and the Λ separation energy [5, 6]. These measurements are undoubtedly useful since hypertriton can be used to study the hyperon–nucleon interaction, which is important for understanding of the main properties and structure of the neutron stars. Due to estimates of the separation energy of Λ in the hypertriton about 100–200 KeV, the average distance of Λ to the remaining proton–neutron pair in ${}^3\text{H}_\Lambda$ should be large, of the order of 10 fm, and one can expect that the Λ lifetime in hypertriton should be close to that of a free Λ , which is experimentally known to be $\tau(\text{free } \Lambda) = (263.2 \pm 2.0)$ ps. Earlier, many estimates of the ${}^3\text{H}_\Lambda$ lifetime have been obtained from measurements with emulsions and the bubble chambers and those values were in average more than 3σ lower than (263.2 ± 2.0) ps. Recent studies of the hypertriton production in Au–Au collisions at Relativistic Heavy Ion Collider resulted in the value more close to $\tau(\text{free } \Lambda)$, though the experimental errors were large due to low statistics. In the ALICE experiment the hypertritons produced in Pb–Pb collisions at energies of colliding beams 2.51 and 5.02 TeV were identified *via* their charged pion decay ${}^3\text{H}_\Lambda \rightarrow \pi + {}^3\text{He}$. The same approach was used to detect antihypertriton. High performance of the ALICE detector allowed one to accumulate statistics much higher than that of all previous experiments. The ${}^3\text{H}_\Lambda$ lifetime was determined with an exponential fit of the measured yield as a function of the decay length. The slope of the fit line resulted in a proper decay length, corresponding to a lifetime $\tau = 253 \pm 11(\text{stat}) \pm 6(\text{syst})$ ps. Figure 6 shows the lifetime of a free Λ (*black vertical line*), the ${}^3\text{H}_\Lambda$ lifetime predicted theoretically and all existing experimental estimates of this quantity including two results of the ALICE [5, 6] (the last result from Ref. [6] is shown by the *red point*).

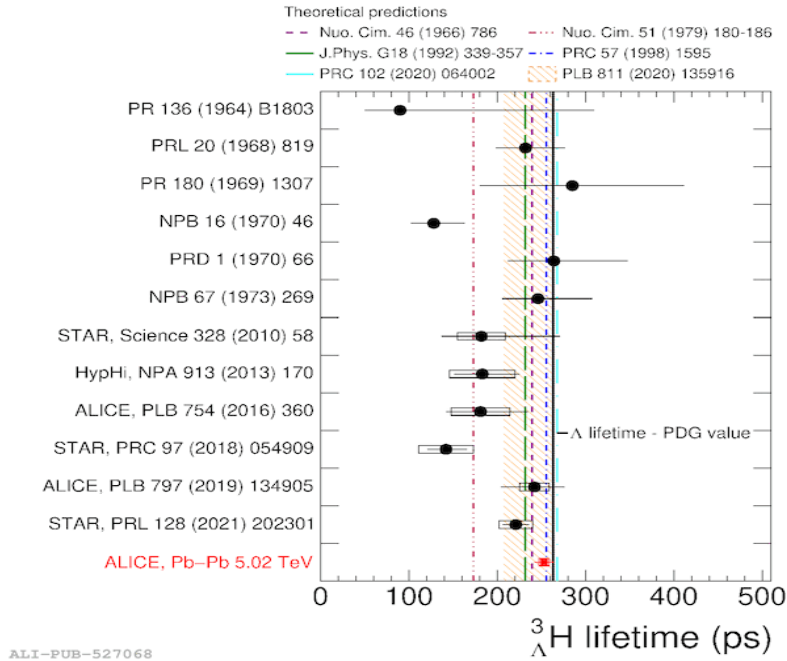


Fig. 6. Comparison of the ALICE result for the ${}^3\text{H}_\Lambda$ lifetime with the world data and theoretical predictions

Accumulated data also allowed one to estimate the separation energy of Λ in the hypertriton from the measured mass of ${}^3\text{H}_\Lambda$, the deuteron mass from CODATA and the mass of Λ from Particle Data Group review. This resulted in the value $B_\Lambda = [72 \pm 63(\text{stat}) \pm 36(\text{syst})]$ keV shown in Fig. 7. Also, from the data analysis it has been found that the difference δ between the lifetimes of hypertriton and antihypertriton is $\delta = [2 \pm 19(\text{stat}) \pm 11(\text{syst})]$ ps, which is consistent with zero within experimental uncertainties. This can be considered as one more experimental evidence of CPT -symmetry in nuclei.

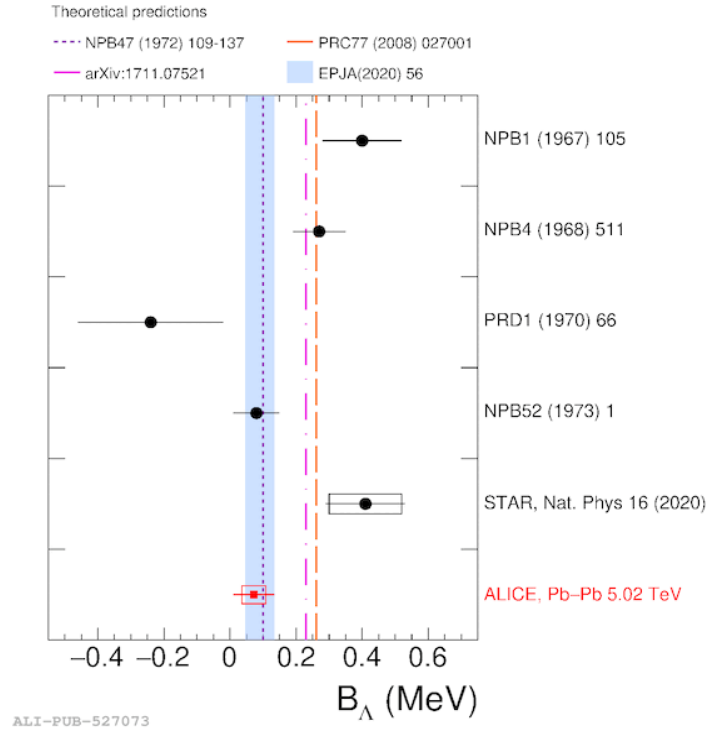


Fig. 7. Comparison of the ALICE result for the Λ separation energy in hypertriton [6] with the world data and theoretical predictions

6. Conclusion

Most of the results overviewed in this note need to be obtained with higher precision. During the LHC Run-3 and Run-4 with an increased luminosity and upgraded detector systems, the ALICE will be able to perform such studies thus contributing to deeper understanding of physics of all these phenomena revealed in ultrarelativistic ion collisions at the LHC.

References

1. ALICE Collab., S. Acharya *et al.*, Nature **588**, 232 (2020); **590**, E13 (2021) (erratum).
2. ALICE Collab., S. Acharya *et al.*, Phys. Rev. Lett. **125**, 012301 (2020).
3. Yu.L. Dokshitzer, V.A. Khoze, S.I. Troyan, J. Phys. G **17**, 1602 (1991).
4. ALICE Collab., S. Acharya *et al.*, Nature **605**, 440 (2022).
5. ALICE Collab., S. Acharya *et al.*, Phys. Lett. B **797**, 134905 (2019).
6. ALICE Collab., S. Acharya *et al.*, arXiv:2209.07360 [nucl-ex].

SEARCH FOR HEAVY RESONANCES DECAYING INTO A PAIR OF Z-BOZONS

PNPI participants of the ATLAS Collaboration: S.G. Barsov, A.E. Ezhilov, O.L. Fedin, M.P. Levchenko, V.P. Maleev, Yu.G. Naryshkin, V.A. Schegelsky, V.M. Solovyev, D. Pudza

1. Introduction

After the discovery of Higgs boson in the ATLAS [1] and CMS [2] experiments, one of the main tasks of the experiments conducted at the Large Hadron Collider (LHC) is the search for new physics, *i. e.* physics beyond the Standard Model (SM). This gave rise to the development of new theories that extend the SM – beyond the Standard Models (BSM), in particular, its Higgs sector. The two Higgs doublet model 2HDM [3] is the simplest extension of the SM with two doublets of the Higgs fields. There are several types of the 2HDM depending on which type of fermions couples to which doublet [4]. Two Higgs doublets Φ_1 and Φ_2 can couple to leptons and up- and down-type quarks in different ways. In the 2HDM Type I, Φ_2 couples to all quarks and charged leptons, whereas for Type II, Φ_1 couples to down-type quarks and leptons and Φ_2 couples to up-type quarks. In all these types of the 2HDM models, the coupling of the heavier CP (charge parity)-even Higgs boson to vector bosons is proportional to $\cos(\beta - \alpha)$ where β is the ratio of vacuum expectation values of the two Higgs doublets $v_{1,2}$: $\tan\beta = \frac{v_1}{v_2}$ and the mixing angle α , which diagonalizes the mass matrix of the CP -even Higgs bosons. In the limit $\cos(\beta - \alpha) \rightarrow 0$, the light CP -even Higgs boson is indistinguishable from the SM Higgs boson and has the same mass. In this model, the electroweak (EW) symmetry breaking leads to five physical Higgs particles: two neutral Higgs bosons that are CP -even (scalar) h , H , one neutral CP -odd (pseudoscalar) A , and charged Higgs boson. The model is parameterized by the following parameters: Higgs masses m_h , m_H , m_A , m_{H^\pm} , ratio of vacuum expectation values of the two Higgs doublets: $\tan\beta = \frac{v_1}{v_2}$ and the mixing angle α , which diagonalizes the mass matrix of the CP -even Higgs bosons. At certain conditions, it could be described with two parameters: $\tan\beta$ and m_A .

Another interesting topic in BSM physics is the search for the extra dimensions. If there were two or more extra space-time dimensions, then the gravity might, in fact, be just as strong as all other forces. Models with extra dimensions also predict a massive graviton – the particle which mediates gravity [5].

In the ATLAS experiment, a search for additional heavy neutral Higgs bosons H and a spin-2 Kaluza–Klein (KK) excitation of the graviton G_{KK} was performed [6]. The heavy Higgs boson H (spin-0 resonance) was assumed to be produced mainly *via* gluon–gluon fusion (ggF) and vector-boson fusion (VBF) processes. The search was performed for $H \rightarrow ZZ \rightarrow 4\ell$ ($2\ell 2\nu$) decay and covered a wide mass range from 200 GeV up to 2 000 GeV to look for an excess in the distribution of the four-lepton invariant mass, $m_{4\ell}$, for the ℓ^+ , ℓ^- , ℓ^+ , ℓ^- final state, and the transverse mass, m_T , for the ℓ^+ , ℓ^- , ν , $\bar{\nu}$ final state, as the escaping neutrinos do not allow the full reconstruction of the final state. This mass range was chosen based on the sensitivity of the analysis as determined by the selection criteria and the size of the data sample. Two hypotheses of the width of heavy Higgs boson were studied: narrow-width approximation (NWA) and large-width assumption (LWA), assuming widths of 1, 5, 10 and 15% of the resonance mass.

2. Data analysis

The analysis was based on collision data collected for the full LHC Run-2 in the ATLAS experiment with proton–proton interactions at the centre-of-mass energy of 13 TeV recorded from 2015 to 2018 with the corresponding integrated luminosity of 139 fb^{-1} . The Monte Carlo (MC) simulation with the ATLAS detector simulation [7] within the GEANT4 framework [8] was used to determine the signal acceptance and some of the background contributions.

The analysis was performed separately for $H \rightarrow ZZ \rightarrow 4\ell$ and $H \rightarrow ZZ \rightarrow 2\ell 2\nu$ channels, where ℓ is electron or muon. Data and MC simulation results were compared in the signal region (SR, the region with the maximum sensitivity to the searched signal) for the corresponding observable to find the excess of data over the SM prediction.

In the four-lepton channel, events were selected and classified according to the lepton flavours: 4μ , $4e$ and $2e2\mu$. They were selected using a combination of single-lepton, dilepton and trilepton triggers with different transverse momentum thresholds. Two types of analysis were carried out for this channel: multivariate analysis (MVA) and cut based analysis. In order to improve the sensitivity in the search for an NWA Higgs boson signal produced either in the VBF or the ggF production mode, two multivariate classifiers were used. These classifiers are built with deep neural networks (DNN), combining a multilayer perceptron (MLP) and one or two recurrent neural networks (rNN) [9]. A cut-based analysis is performed to probe the sensitivity in the VBF production mode. In each channel, four-lepton candidates are formed by selecting a lepton-quadruplet made out of two same-flavour, opposite-sign lepton pairs. Each electron (muon) must satisfy $p_T > 7$ (5) GeV and be measured in the pseudorapidity range of $|\eta| < 2.47$ (2.7). The highest- p_T lepton in the quadruplet must satisfy $p_T > 20$ GeV, and the second (third) lepton in p_T order must satisfy $p_T > 15$ GeV (10 GeV). In the case of muons, at most one calorimeter-tagged, segment-tagged or stand-alone ($2.5 < |\eta| < 2.7$) muon was allowed per quadruplet.

The main background source in the four lepton channel is non-resonant ZZ production, accounting for 97% of the total background events in the inclusive category. It arises from quark–antiquark annihilation $qq \rightarrow ZZ$ (86%), gluon-initiated production $gg \rightarrow ZZ$ (10%), and a small contribution from EW vector-boson scattering (1%). The ZZ background was estimated from simulation for both the shape and the normalization. In this analysis its normalization is derived from the data in the likelihood fit used in the statistical treatment of the data. Additional background comes from the $Z + \text{jets}$ and $t\bar{t}$ processes. These contribute to the total background yields at the percent level and decrease more rapidly than the non-resonant ZZ contribution as a function of $m_{4\ell}$. These backgrounds are estimated using data-driven methods [10, 11].

The WZ production process was estimated with the data-driven method for the $\ell\ell$, ee final states, while for the $\ell\ell$, $\mu\mu$ final states it was estimated with the simulation, even though its contribution to the total background is very small. The contributions from $t\bar{t}V$ (where V is W or Z boson) and triboson processes are minor and taken from simulated samples.

The ggF production of a heavy scalar H , the SM Higgs h and the $gg \rightarrow ZZ$ continuum background all have the same initial and final state, and thus lead to interference terms in the total amplitude. Theoretical calculations described in Ref. [12] have shown that the effect of interference could modify the integrated cross section by up to $\mathcal{O}(10\%)$, and this effect is enhanced as the width of the heavy scalar increases. Therefore, a search for a heavy scalar Higgs boson in the LWA case must properly account for two interference effects: the interference between the heavy scalar and the SM Higgs boson (denoted by $H - h$) and between the heavy scalar and the $gg \rightarrow ZZ$ continuum (denoted by $H - B$). The interference effect for KK excitation resonance is assumed to be negligible due to its small width.

The reconstructed four-lepton invariant mass $m_{4\ell}$ distribution was used as the discriminating variable for the $\ell^+, \ell^-, \ell^+, \ell^-$ final state. Data to MC comparisons are presented in Fig. 1 (*left*).

The $\ell^+, \ell^-, \nu, \bar{\nu}$ final state consists of a pair of high- p_T isolated leptons (electrons or muons) and large E_T^{miss} , and has a larger background contamination than the $\ell^+, \ell^-, \ell^+, \ell^-$ channel. Candidate events are recorded with a combination of multiple single-lepton triggers, which gives a high efficiency of about 98% for typical signal processes in the signal region defined in the following. Events were preselected by requiring exactly two electrons or muons with opposite charges and $p_T > 20$ GeV, where the electrons (muons) must have $|\eta| < 2.47$ (2.5). The leading lepton is required to have $p_T > 30$ GeV, which is well above the threshold of the single-lepton triggers. The data sample after the preselection is dominated by the $Z + \text{jets}$ and non-resonant- $\ell\ell$ backgrounds. To suppress these backgrounds, a further selection based on E_T^{miss} and event topology was applied. Candidate events are required to have $E_T^{\text{miss}} > 120$ GeV, which suppresses the $Z + \text{jets}$ contamination by several orders of magnitude. The number of residual $Z + \text{jets}$ events, which have large fake E_T^{miss} , is further reduced by requiring $S(E_T^{\text{miss}}) > 10$, where $S(E_T^{\text{miss}})$ is the statistical significance of the E_T^{miss} value against the null hypothesis of zero- E_T^{miss} [13].

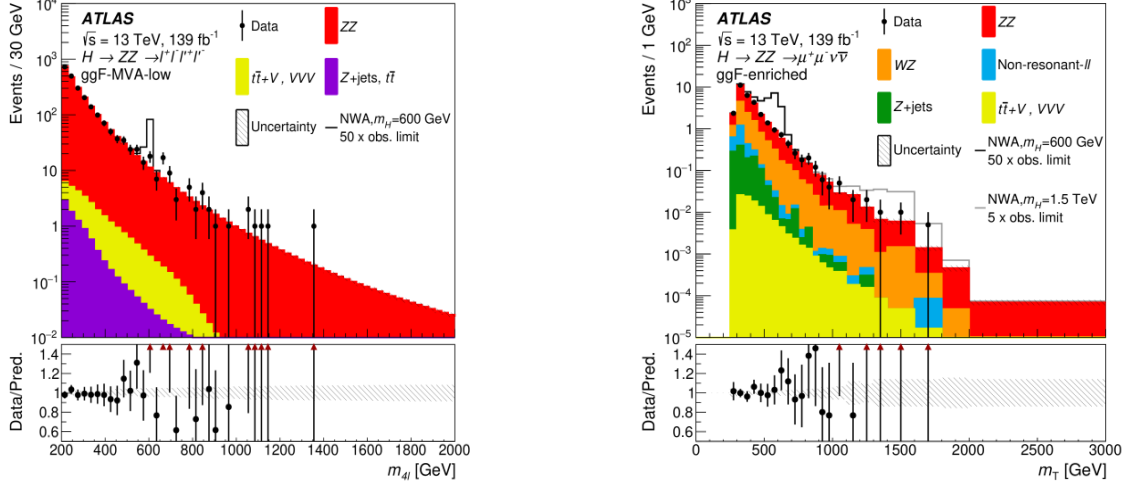


Fig. 1. Distributions of the four-lepton invariant mass $m_{4\ell}$ in the $\ell^+, \ell^-, \ell^+, \ell^-$ channel for the ggF -MVA-low [6] category (*left*) and the m_T distribution in the $\ell^+, \ell^-, \nu, \bar{\nu}$ channel for the ggF category (*right*). The simulated $m_H = 600$ GeV (1.5 TeV) signals are normalized to a cross section corresponding to 50(5) times the observed limit. The error bars on the data points indicate the statistical uncertainty and markers are drawn at the bin centre. The systematic uncertainty is shown by the *hatched band*. The *lower panels* show the ratio of data to prediction. The *red arrows* indicate data points that are outside the displayed range

Additional selection criteria based on angular variables are imposed to further reject the $Z + \text{jets}$ and non-resonant- $\ell\ell$ background events. The selection on angular variables is motivated by the desired detector signature, where the \vec{E}_T^{miss} is back-to-back with the transverse momentum of the dilepton system. The azimuthal angle difference between the dilepton system and \vec{E}_T^{miss} , $\Delta\phi(\vec{p}_T^{\ell\ell}, \vec{E}_T^{\text{miss}})$, must be larger than 2.5 rad, and the selected leptons must be close to each other, with the distance

$\Delta R_{\ell\ell} = \sqrt{(\Delta\phi_{\ell\ell})^2 + (\Delta\eta_{\ell\ell})^2} < 1.8$. In addition to that, the azimuthal angle difference between any of the selected jets with $p_T > 100$ GeV and \vec{E}_T^{miss} must be larger than 0.4 rad. As a consequence of all applied requirements, the $Z + \text{jets}$ process contributes only a small fraction of the total background (about 4%) after the full selection. Finally, events containing one or more b -jets are vetoed to further suppress the contribution from $t\bar{t}$ and Wt backgrounds.

The signal region for the VBF production mode is defined for events containing at least two selected jets with $p_T > 30$ GeV, where the two leading jets must have $m_{jj} > 550$ GeV and $\Delta\eta_{jj} > 4.4$. The remaining events, failing the requirements for the VBF -enriched signal region, are assumed to be produced by ggF -process.

In the ggF -enriched signal region, the major backgrounds originate from the ZZ and WZ processes, which account for 60 and 30% of the total background contribution, respectively. The non-resonant- $\ell\ell$ background yields a relative contribution of about 5% to the total background, while the largely suppressed $Z + \text{jets}$ background only constitutes a small fraction (4%). Finally, the remaining contributions from other processes (VVV and $t\bar{t}V$), amount in total to less than 1% of the total background. A similar composition of background processes is found in the VBF -enriched signal region, where the total background yield is expected to be smaller than 1% of that in the ggF -enriched signal region, due to the event selection for the VBF phase space.

The main background contribution from ZZ production is estimated using a semidata-driven method. Similarly, to the $\ell^+, \ell^-, \ell^+, \ell^-$ analysis, the predicted ZZ yield is scaled by a floating normalization factor, which is determined in the statistical fit to the signal-region data. To estimate the background from WZ production in the ggF -enriched signal region, a control region enriched in WZ events, with a purity of over 90%, is defined using the preselection criteria, except that a third lepton with $p_T > 20$ GeV is required. A normalization factor is calculated in the control region as the number of observed events in data, after subtracting the non- WZ contributions estimated from simulation, divided by the predicted WZ yield. The main systematic uncertainty is evaluated for the ratio of the WZ predictions in the signal and control regions, and covers the experimental uncertainties and the theoretical ones related to the parton distribution functions (PDFs) and the quantum

chromodynamics (QCD) scales. A similar method is adopted to estimate the WZ contribution in the VBF -enriched signal region, except that the control region additionally selects two jets with $p_T > 30$ GeV. The total uncertainty in the WZ estimate for the VBF -enriched signal region is about 30%.

To estimate the non-resonant- $\ell\ell$ background in ggF signal region, a control region dominated by the non-resonant- $\ell\ell$ processes (with a purity of about 95%) is defined with all the event selection criteria except that the final state is required to contain an opposite-sign $e\mu$ pair. The non-resonant- $\ell\ell$ contribution in the ee ($\mu\mu$) channel is calculated as one half of the observed data yield after subtracting the contribution from the other background processes in the control region, and then corrected for the difference in the lepton reconstruction and identification efficiencies between selecting an $e\mu$ pair and an ee ($\mu\mu$) pair. The lepton efficiency correction is derived as the square root of the ratio of the numbers of $\mu\mu$ and ee events in data after the preselection. The choice of deriving the correction after preselection minimizes the resulting statistical uncertainty. The total uncertainty in the non-resonant- $\ell\ell$ estimate in the ggF -enriched signal region is on the level of 9%. The estimation of the non-resonant- $\ell\ell$ background in the VBF -enriched signal region relies on a similar methodology, except that the control region is defined with a jet selection that is looser than in the signal region. The kinematic distributions for the non-resonant- $\ell\ell$ background in the signal region are predicted with MC simulation, and the assigned systematic uncertainty covers the experimental uncertainty in the simulated shape as well as the difference between data and simulation in the control region.

The contribution of Z + jets background is estimated from simulation and scaled by a normalization factor derived in a control region enriched in Z + jets events. The total uncertainty in the Z + jets estimate is about 40%. The backgrounds from the VVV and $t\bar{t}V$ processes, which contribute less than 1% of the total background, are estimated from the MC simulation.

In this channel the transvers mass is the discriminating variable, which is defined as

$$m_T = \sqrt{\left[\sqrt{m_Z^2 + (p_T^{\ell\ell})^2} + \sqrt{m_Z^2 + (E_T^{\text{miss}})^2} \right]^2 - |\vec{p}_T^{\ell\ell} - \vec{E}_T^{\text{miss}}|^2},$$

where m_Z is the mass of the Z boson [14], $\vec{p}_T^{\ell\ell}$ and \vec{E}_T^{miss} are the transverse momentum of the lepton pair and the missing transverse momentum with magnitudes of $p_T^{\ell\ell}$ and E_T^{miss} , respectively. Data comparisons with SM backgrounds for ℓ^+ , ℓ^- , ν , $\bar{\nu}$ channels are presented in Fig. 1 (*right*). No deviations from the SM prediction were found both for the ℓ^+ , ℓ^- , ℓ^+ , ℓ^- and ℓ^+ , ℓ^- , ν , $\bar{\nu}$ channels.

3. Systematic uncertainties

Experimental uncertainties include the uncertainties resulting from the integrated luminosity, the trigger efficiencies, the momentum scale and resolution of tracks, the reconstruction and identification of leptons and jets, and their energy scale and resolution calibrations. These systematic uncertainties evaluated separately for signal and background in each category affect signal acceptances and background yields as well as the probability density distributions of the discriminating variables. Theoretical uncertainties include the uncertainties in the theoretical descriptions of the signal and background simulations. In total, the theoretical uncertainty in the signal acceptance varies from less than 1% in the low mass region to 12% in the high mass region of the ℓ^+ , ℓ^- , ν , $\bar{\nu}$ final state, and from less than 1% in the low mass region to up to 20% in the high mass region of the ℓ^+ , ℓ^- , ℓ^+ , ℓ^- final state.

4. Results and interpretations: spin-0 resonances

Upper limits on the cross-section times branching ratio $\sigma \cdot B(H \rightarrow ZZ)$ for a heavy resonance are obtained from the combination of the two final states, as a function of m_H with the CLs procedure [15]. It is assumed that an additional heavy scalar would be produced mainly *via* the ggF and VBF processes but that the ratio of the two production mechanisms might depend on the model considered. For this reason, fits for the ggF and VBF processes are done separately, and in each case the other process is allowed to float in the fit as an additional free parameter. Figure 2 presents the observed and expected limits at 95% CL on the $\sigma \cdot B(H \rightarrow ZZ)$

for two particular cases: NWA for the ggF (left) and for LWA VBF assuming a width of 15%, of m_H (right) production modes, as well as the expected limits from the $\ell^+, \ell^-, \ell^+, \ell^-$ and $\ell^+, \ell^-, \nu, \bar{\nu}$ searches. When combining the two final states, the 95% CL upper limits range from 215 fb at $m_H = 240$ GeV to 2.0 fb at $m_H = 1900$ GeV for the ggF production mode and from 87 fb at $m_H = 255$ GeV to 1.5 fb at $m_H = 1800$ GeV for the VBF production mode. In the case of the LWA, upper limits on the cross section for the ggF process times branching ratio ($\sigma_{ggF} \cdot B(H \rightarrow ZZ)$) were set for different widths (1, 5, 10, 15%) of the heavy scalar mass [6].

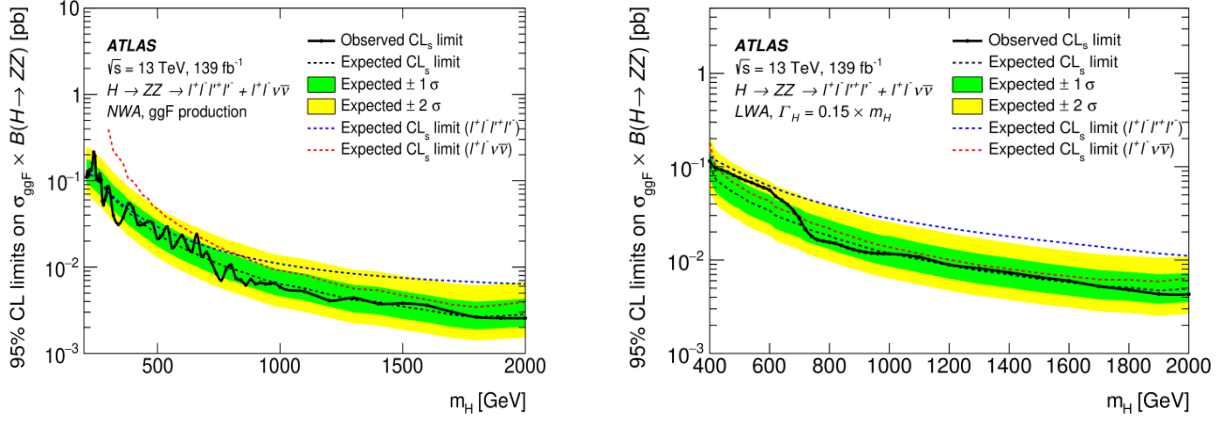


Fig. 2. The upper limits at 95% CL on the cross-section times branching ratio as a function of the heavy resonance mass m_H for the ggF production mode ($\sigma_{ggF} \cdot B(H \rightarrow ZZ)$) in the case of the NWA (left) and for LWA assuming a width of 15%, of m_H (right). The black line indicates the observed limit. The green and yellow bands represent the $\pm 1\sigma$ and $\pm 2\sigma$ uncertainties in the expected limits. The dashed coloured lines indicate the expected limits obtained from the individual decay channel

The interpretation has been carried out within 2HDM Type I and Type II. Figure 3 shows exclusion limits in the $\tan\beta$ versus $\cos(\beta - \alpha)$ plane, for a heavy Higgs boson with the mass $m_H = 220$ GeV. This m_H value is chosen so that the assumption of a narrow Higgs boson is valid over most of the parameter space, and the experimental sensitivity is maximal. At this low mass, only the $\ell^+, \ell^-, \ell^+, \ell^-$ final state contributes to this result. The range of $\cos(\beta - \alpha)$ and $\tan\beta$ is limited to the region where the assumption of a heavy narrow Higgs boson with negligible interference is valid. Figure 4 shows exclusion limits as a function of the heavy Higgs boson mass m_H and the parameter $\tan\beta$ for the fixed value of $\cos(\beta - \alpha) = -0.1$, which is chosen so that the light Higgs boson properties are still compatible with the recent measurements of the SM Higgs boson properties [16]. The white regions in the exclusion plots indicate regions of the parameter space which are not excluded by this analysis. In these regions the cross section predicted by the 2HDM is below the observed cross-section limit.

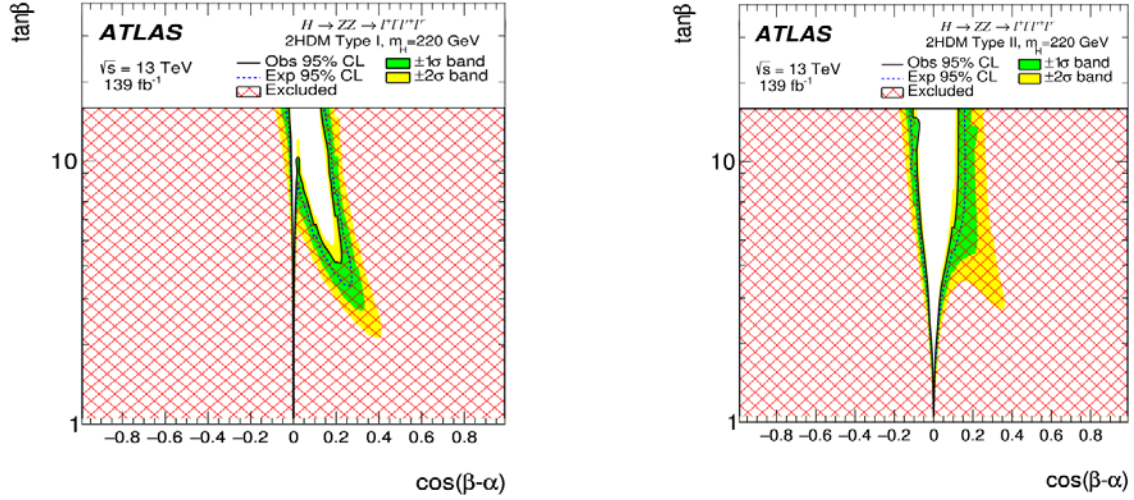


Fig. 3. The exclusion contour in the 2HDM Type I (a) and Type II (b) models for $m_H = 220$ GeV shown as a function of the parameters $\cos(\beta - \alpha)$ and $\tan\beta$. The *green* and *yellow bands* represent the $\pm 1\sigma$ and $\pm 2\sigma$ uncertainties in the expected limits. The *hatched area* shows the observed exclusion

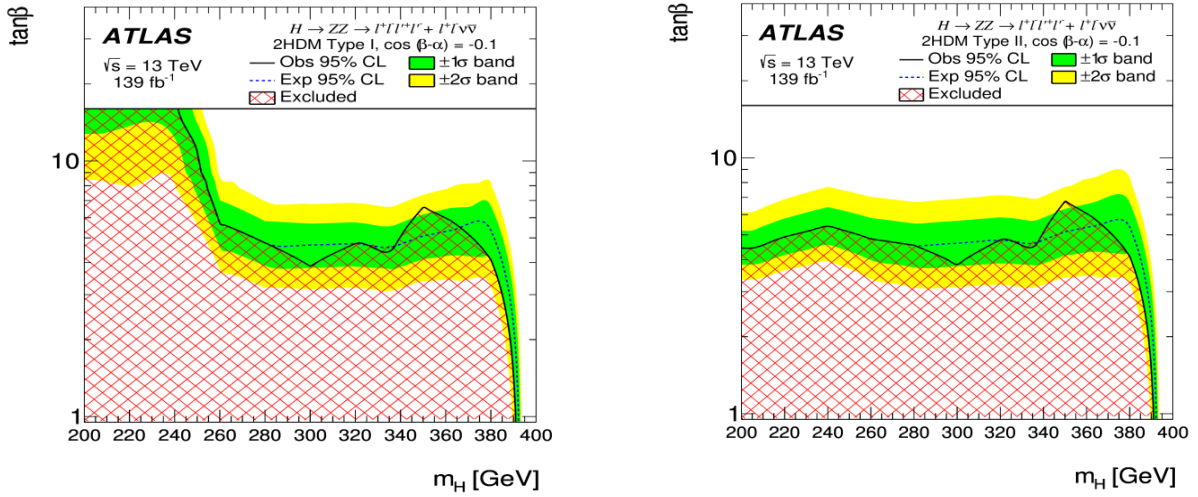


Fig. 4. The exclusion contour in the 2HDM Type I (a) and Type II (b) models for $\cos(\beta - \alpha) = -0.1$, shown as a function of the heavy scalar mass m_H and the parameter $\tan\beta$. The *green* and *yellow bands* represent the $\pm 1\sigma$ and $\pm 2\sigma$ uncertainties in the expected limits. The *hatched area* shows the observed exclusion

5. Results and interpretation: spin-2 resonances

The results were also interpreted as a search for a KK graviton excitation, G_{KK} , in the context of the bulk Randall–Sundrum model with dimensionless coupling $k/\overline{M}_{Pl} = 1$, where $\overline{M}_{Pl} = M_{Pl}/\sqrt{8\pi}$ is the reduced Planck scale and k is the curvature scale of the extra dimension. The limits on $\sigma \cdot B(G_{KK} \rightarrow ZZ)$ at 95% CL as a function of the KK graviton mass, $m(G_{KK})$, are shown in Fig. 5 together with the predicted G_{KK} cross section. A spin-2 graviton is excluded up to a mass of 1 830 GeV.

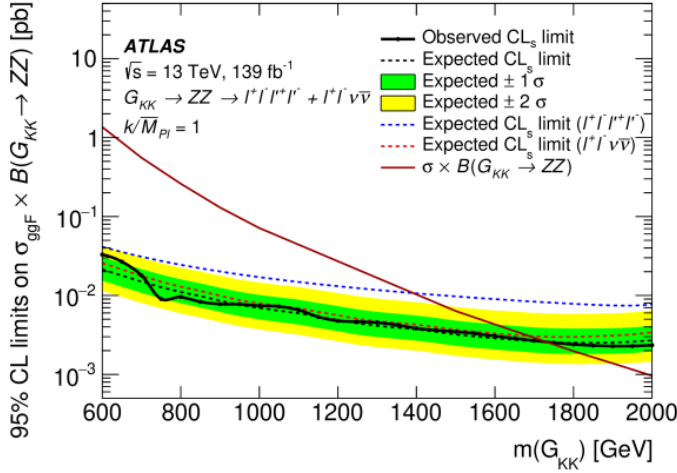


Fig. 5. The upper limits at 95% CL on cross section times branching ratio $\sigma \cdot B(G_{\text{KK}}) \rightarrow ZZ$ for a KK graviton produced with $k/\overline{M}_{\text{Pl}} = 1$. The *black line* indicates the observed limit. The *green and yellow bands* give the 1σ and 2σ uncertainties in the expected limits. The predicted production cross section times branching ratio as a function of the G_{KK} mass (G_{KK}) is shown by the *red solid line*

6. Summary

A search for new heavy resonances decaying into a pair of Z bosons with four leptons (muons or electrons) or two charged leptons and two neutrinos in final states was performed in the ATLAS experiment. The search used proton–proton collision data collected with the ATLAS detector for LHC Run-2 (2015–2018) at a centre-of-mass energy of 13 TeV corresponding to the full Run-2 integrated luminosity of 139 fb^{-1} . The upper limits on the production cross section of spin-0 resonances or a spin-2 resonance were obtained. The mass range of the hypothetical resonances is assumed to be between 200 and 2 000 GeV depending on the final state and the model. In the case of the narrow-width approximation, upper limits on the production rate of a heavy scalar are set separately for ggF and VBF production modes. Based on the combination of two final states, 95% CL upper limits range from 215 fb at $m_H = 240$ GeV to 2.0 fb at $m_H = 1\,900$ GeV for the ggF production mode and from 87 fb at $m_H = 255$ GeV to 1.5 fb at $m_H = 1\,800$ GeV for the VBF production mode. The limits on the production rate of a large-width scalar were obtained for widths of 1, 5, 10 and 15% of the mass of the resonance. The interference between the heavy scalar and the SM Higgs boson as well as between the heavy scalar and the $gg \rightarrow ZZ$ continuum was taken into account. The results were interpreted in the context of Type I and Type II 2HDM, and exclusions of 2HDM parameters were obtained in the $\tan\beta$ versus $\cos(\beta - \alpha)$ (for $m_H = 220$ GeV) and the $\tan\beta$ versus m_H planes. Within the framework of the Randall–Sundrum Type I model with one warped extra dimension, a spin-2 KK graviton with $m(G_{\text{KK}}) < 1\,830$ GeV is excluded at 95% CL.

References

1. ATLAS Collab., G. Aad, T. Abajyan, B. Abbott *et al.*, Phys. Lett. B **716**, 1 (2012).
2. CMS Collab., S. Chatrchyan, V. Khachatryan, A.M. Sirunyan *et al.*, Phys. Lett. B **716**, 30 (2012), arXiv:1207.7235.3.
3. N. Craig, J. Galloway, S. Thomas, arXiv:1305.2424.
4. G.C. Branco, P.M. Ferreira, L. Lavoura *et al.*, Phys. Rep. **516**, 1 (2012), arXiv:1106.0034.
5. L. Randall, R. Sundrum, Phys. Rev. Lett. **83**, 3370 (1999), arXiv:9905221.
6. ATLAS Collab., G. Aad, T. Abajyan, B. Abbott, *et al.*, Eur. Phys. J. C **81** (4), 332 (2021), arXiv:hep-ph/2009.14791.
7. ATLAS Collab., Eur. Phys. J. C **70**, 823 (2010), arXiv:1005.4568.
8. S. Agostinelli *et al.*, GEANT4: Nucl. Instrum. Meth. A **506**, 250 (2003).
9. M. Abadi *et al.*, TensorFlow: Large-Scale Machine Learning on Heterogeneous Systems (2015).
10. ATLAS Collab., JHEP **10**,132 (2017), arXiv:1708.02810.
11. ATLAS Collab., JHEP **03**, 095 (2018), arXiv:1712.02304 [hep-ex].
12. N. Kauer, C.O’Brien, Eur. Phys. J. C **75**, 374 (2015), arXiv:1502.04113.

13. ATLAS Collab., ATLAS-CONF-2018-038 (2018).
14. M. Tanabashi *et al.*, Phys. Rev. D **98**, 030001 (2018).
15. A.L. Read, J. Phys. G **28**, 2693 (2002).
16. ATLAS Collab., Phys. Rev. D **101**, 012002 (2020), arXiv:1909.02845.

MEASUREMENT OF TOP-QUARK PAIR SPIN CORRELATIONS

PNPI participants of the ATLAS Collaboration: S.G. Barsov, A.E. Ezhilov, O.L. Fedin, M.P. Levchenko, V.P. Maleev, Yu.G. Naryshkin, V.A. Schegelsky, V.M. Solovyev

1. Introduction

The lifetime of the top quark is shorter than the timescale for hadronisation ($\sim 10^{-23}$ s) and is much shorter than the spin decorrelation time ($\sim 10^{-21}$ s) [1]. As a result, the spin information of the top quark is transferred directly to its decay products. Top quark pair production ($t\bar{t}$) in quantum chromodynamics (QCD) is parity invariant and hence the top quarks are not expected to be polarized in the Standard Model (SM); however, the spins of the top and antitop quarks are predicted to be correlated. This correlation has been observed experimentally by the ATLAS and CMS Collaborations in proton–proton (pp) collision data at the Large Hadron Collider (LHC) at centre-of-mass energies of $\sqrt{s} = 7$ TeV [2–5] and $\sqrt{s} = 8$ TeV [6–9]. It was also studied in proton–antiproton collisions at the Tevatron Collider [10–14]. This article presents measurements of spin correlation at a centre-of-mass energy of $\sqrt{s} = 13$ TeV in pp collisions using the ATLAS detector and data collected in 2015 and 2016 [15].

Charged leptons arising from leptonically decaying W bosons carry almost the full spin information of the parent top quark [16–19]. This feature, along with the fact that charged leptons are readily identified and reconstructed by collider experiments, means that observables to study spin correlation in $t\bar{t}$ events are often based on the angular distributions of the charged leptons in events where both W bosons decay leptonically (referred to as the dilepton channel). The simplest observable is the absolute azimuthal opening angle between the two charged leptons [20], measured in the laboratory frame in the plane transverse to the beam line. This opening angle is denoted by $\Delta\phi$ and is used to measure spin correlation in this analysis.

Charged-lepton observables can be used to search for the production of supersymmetric (SUSY) top squarks with masses close to that of the SM top quark. Such a scenario is difficult to constrain with conventional searches; however, observables such as $\Delta\phi$ and the absolute difference between the pseudorapidities of the two charged leptons, $\Delta\eta$, are highly sensitive in this regard. The two observables are used together in this article to set limits on the SUSY top squark production.

2. Analysis strategy and details

The pp collision data used in this analysis were collected during 2015 and 2016 by the ATLAS experiment at a centre-of-mass energy of $\sqrt{s} = 13$ TeV and correspond to an integrated luminosity of 36.1 fb^{-1} . The data considered in this analysis were recorded under stable beam conditions and required all sub-detectors to be operational. Events were required to pass either a single-electron or single-muon trigger. Multiple triggers were used to select events: the lowest-threshold triggers utilized isolation requirements to reduce the trigger rate and had transverse momentum (p_T) thresholds of 24 GeV for electrons and 20 GeV for muons in 2015 data, or 26 GeV for both lepton types in 2016 data. These triggers were complemented by others with higher p_T thresholds and no isolation requirements to increase event acceptance.

Monte Carlo (MC) simulations were used to model signal and background processes and to correct the data for detector acceptance and resolution effects. The primary $t\bar{t}$ sample used in this result (hereafter referred to as nominal) was simulated using the next-to-leading order (NLO) Powheg-Box matrix-element event generator [21–23] interfaced to PYTHIA8 [24] for the parton shower and fragmentation. An alternative $t\bar{t}$ sample was simulated with the same settings but with the top quarks decayed using MadSpin [25] and with spin correlations between the t and \bar{t} disabled. This sample was used, along with the nominal sample, as a template in the extraction of spin correlation.

Background processes were simulated using a variety of MC event generators, which are not described here for brevity, for more details see Ref. [15]. The main background process is the single top quark production in association with a W boson. Smaller background contributions arise from the $t\bar{t}$ production in association with a vector boson or a Higgs boson, electroweak diboson production, Drell–Yan processes and

events containing one prompt lepton from the decay of a W or Z boson and either a non-prompt lepton or a particle misidentified as a lepton.

This analysis utilizes reconstructed electrons, muons, jets, and missing transverse momentum. The missing transverse momentum (with the magnitude E_T^{miss}) is defined as the negative vector sum of the transverse momenta of reconstructed, calibrated objects in the event. Jets are identified as containing b -hadrons (b -jets) using a multivariate discriminant [26]. Events are selected by requiring exactly one electron and one muon of opposite electric charge ($e\mu$ decay channel), where at least one of them has $p_T > 27$ GeV, and at least two jets, at least one of which must be a b -jet.

In order to measure spin correlations as a function of the $t\bar{t}$ invariant mass at the detector level, the kinematic properties of the event must be reconstructed from the identified leptons, jets, and missing transverse momentum. The top quark, top antiquark, and reconstructed $t\bar{t}$ system are built using the neutrino weighting (NW) method [27].

In the measurements presented in this article, events are corrected for detector effects using parton level definition of particles in the generator-level record of the simulation. Parton-level objects are taken from the MC simulation history. Top quarks are taken after radiation but before decay whereas leptons are taken before radiation. The measurement corrected to the parton level is extrapolated to the full phase-space, where all generated dilepton events are considered. However, events with leptons originating from an intermediate τ -lepton in the $t \rightarrow bW \rightarrow bl\nu$ decay chain are not considered as their subsequent decays do not carry the full spin information of their parent top quark.

The data are corrected for detector resolution and acceptance effects using an iterative Bayesian unfolding procedure [28] in order to create distributions at parton level in a full phase-space. The unfolding itself is performed using the RooUnfold package [29].

The measured differential cross-sections are affected by systematic uncertainties arising from detector response, signal modelling, and background modelling. The contributions from various sources of uncertainty are summed in quadrature to obtain the total systematic uncertainty, and the overall uncertainty is calculated by summing the systematic and statistical uncertainties in quadrature.

3. Differential cross-section results

The absolute and normalised parton-level cross-sections for $\Delta\phi$ and $\Delta\eta$ are measured in this analysis. Figure 1 shows cross-sections compared to several NLO MC generators interfaced to parton showers. Overall, a reasonable agreement is observed in the cross-section between the data and MC predictions, but significant shape effects are apparent. The shapes predicted by different generators are fairly consistent. In the $\Delta\phi$ observable, an obvious trend is observed, with the data tending to be higher than the expectation at low $\Delta\phi$ and lower than the expectation at high $\Delta\phi$. For $\Delta\eta$, the data and expectation agree well at low values but there is a slight tension at higher values.

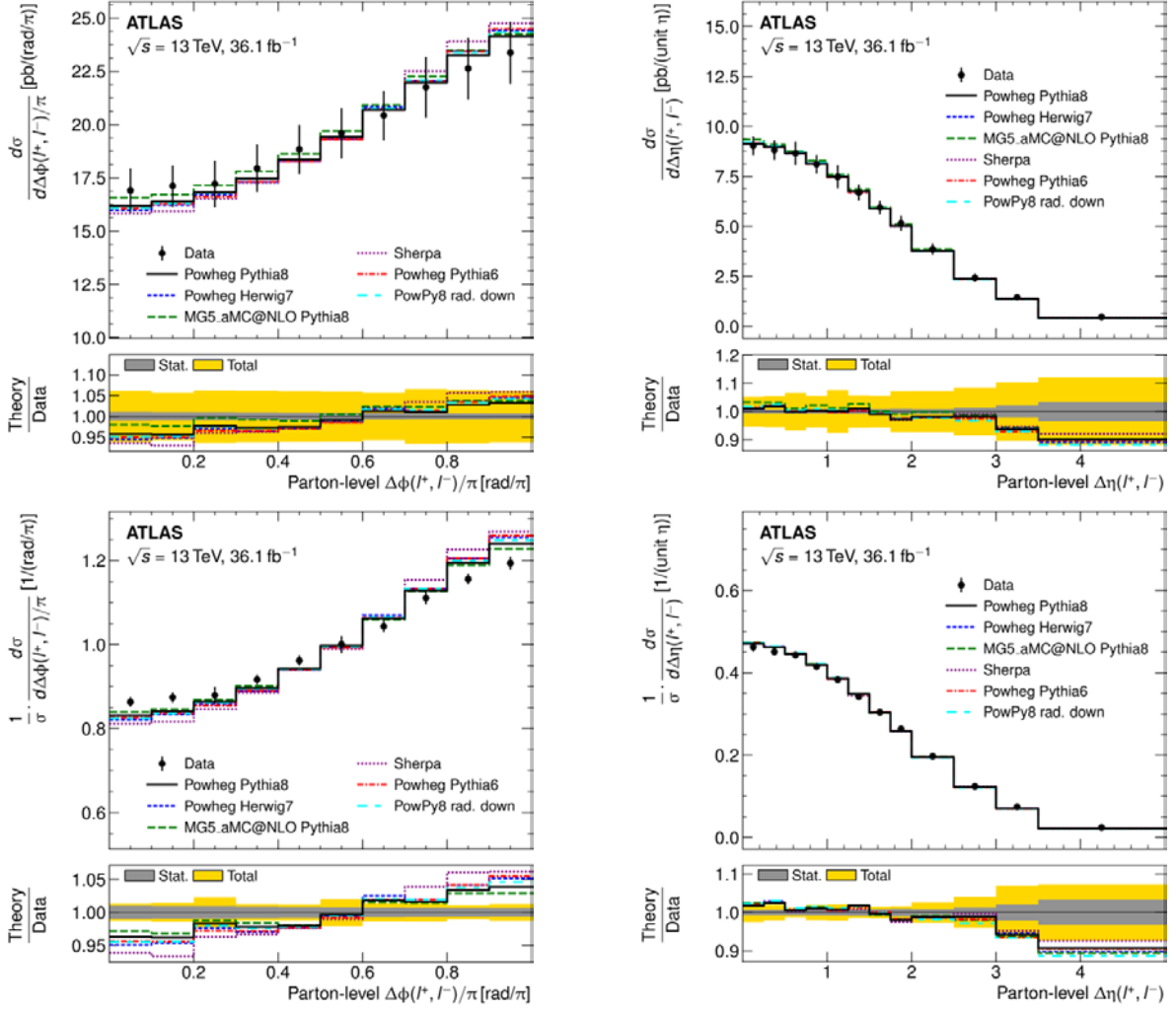


Fig. 1. The parton-level differential cross-sections compared to predictions from POWHEG, MadGraph5_aMC@NLO and SHERPA: absolute $\Delta\phi$ (top left) and $\Delta\eta$ (top right) and normalised $\Delta\phi$ (bottom left) and $\Delta\eta$ (bottom right)

4. Spin correlation results

The level of spin correlation observed in data is assessed by quantifying it in relation to the amount of correlation expected in the SM [2–9]. This fraction of SM-like spin correlation (f_{SM}) is extracted using hypothesis templates that are fitted to the parton-level, unfolded normalised cross-sections from data. Two hypotheses are used: dileptonic $t\bar{t}$ events with SM spin correlation (the nominal $t\bar{t}$ sample) and dileptonic events where the effect of spin correlation has been removed (the nominal $t\bar{t}$ sample where the top quarks are decayed using MadSpin with spin correlations disabled). In each observable, a binned maximum-likelihood fit is performed using MINUIT [30]. The predicted normalised cross-section in bin i , x_i , is determined as a function of f_{SM} using the expression:

$$x_i = f_{\text{SM}} \cdot x_{\text{spin}, i} + (1 - f_{\text{SM}}) \cdot x_{\text{nospin}, i},$$

where x_{spin} and x_{nospin} are the expected normalised cross-sections under the SM spin hypothesis and the uncorrelated hypothesis, respectively. The negative logarithm of a likelihood function is minimised in order to determine f_{SM} . The extraction of f_{SM} is performed in the $\Delta\phi$ observable.

The hypothesis templates for the $\Delta\phi$ observable, the unfolded data, and the resulting fit are presented in Fig. 2. The fraction of SM-like spin correlation was found to be $f_{\text{SM}} = 1.249 \pm 0.024(\text{stat}) \pm$

$\pm 0.061(\text{syst})^{+0.067}_{-0.090}(\text{th})$. This value is higher than the SM expectation with a significance of 2.2 standard deviations. Previous measurements from ATLAS and CMS also observed $f_{\text{SM}} > 1$, but the uncertainties were such that the results were consistent with the prediction [2–9].

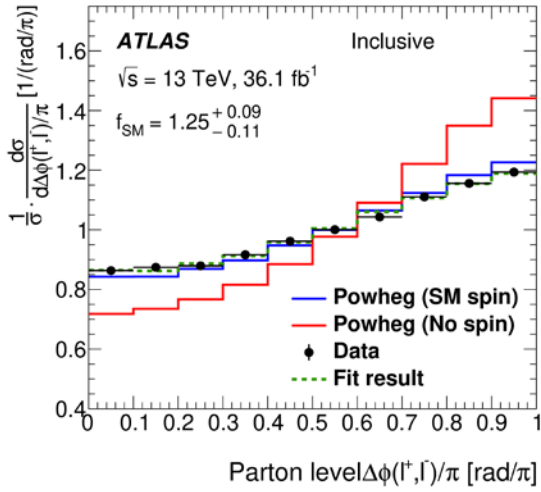


Fig. 2. Results of the fit of hypothesis templates to the unfolded data showing the $\Delta\phi$ distribution

A few cross-checks were performed to attempt to understand the results in terms of either the limitations of the modelling of the $t\bar{t}$ system or by experimental effects not covered by the systematic uncertainties. For this purpose, different alternative SM predictions (MC generators and calculations) for $t\bar{t}$ production were considered. For more details see Ref. [15]. A comparison between data and various SM predictions is illustrated in Fig. 3 and Fig. 4. A disagreement between the data and the NLO predictions from MCFM and POWHEG + PYTHIA8 can be clearly observed in Fig. 4 (*left*). The next-to-next-to-leading order (NNLO) fixed-order prediction agrees better with the data but still differs significantly. Finally, the expanded NLO predictions agree with the data within their large scale uncertainties, as shown in Fig. 4 (*right*), but the NNLO prediction using the same expansion does not.

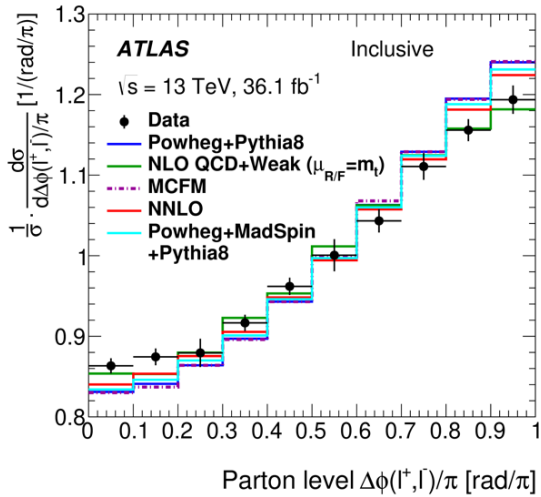


Fig. 3. Comparison of the unfolded $\Delta\phi$ distribution with theoretical predictions for the normalised cross-section. Each prediction is discussed in Ref. [15]

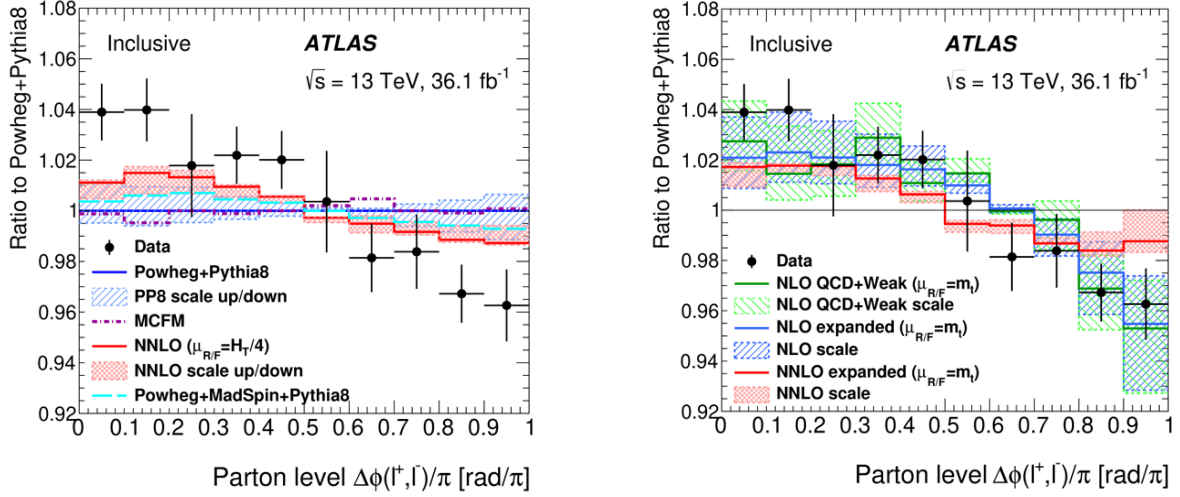


Fig. 4. Comparison of the unfolded $\Delta\phi$ distribution with theoretical predictions: ratio as compared with POWHEG + PYTHIA8 for NLO generators and NNLO fixed-order predictions (*left*), NLO and NNLO theoretical predictions expanded in the normalised cross-section ratio (*right*). Each prediction is discussed in Ref. [15]

5. SUSY interpretation

The detector-level $\Delta\phi$ and $\Delta\eta$ observables are used to search for SUSY top squark pair production ($\tilde{t}_1\tilde{\bar{t}}_1$) with $\tilde{t}_1 \rightarrow t\tilde{\chi}_1^0$ decays. Double-differential distributions of $\Delta\phi$ in ranges of $\Delta\eta$ of $|\Delta\eta| < 1.5$, $1.5 < |\Delta\eta| < 2.5$ and $2.5 < |\Delta\eta| < 4.5$ are constructed. In the absence of signal from $\tilde{t}_1\tilde{\bar{t}}_1$, the observed and expected limits are set on the $\tilde{t}_1\tilde{\bar{t}}_1$ production cross-section by simultaneously fitting the SM prediction to the observed data in the three double-differential distributions and varying the supersymmetric signal strength parameter μ . Limits are determined using a profile likelihood ratio, using nuisance parameters to account for sources of systematic uncertainties. The limits are extracted at the 95% confidence level (CL) using the CL_s prescription [31].

SUSY production for a given $m_{\tilde{t}_1}$, $m_{\tilde{\chi}_1^0}$ is considered to be excluded when the observed limit is below the expected SUSY cross-section. For a neutralino mass $m_{\tilde{\chi}_1^0} = 0.5$ GeV, Fig. 5 shows the observed (expected) limit, where top squarks with a mass between 170(170) GeV and 230(213) GeV are excluded with respect to the background generator prediction. Figure 6 shows the observed (expected) limit as functions of both $m_{\tilde{\chi}_1^0}$ and $m_{\tilde{t}_1}$ assuming the expected SUSY cross-sections. Observed (expected) limits are set on top squarks with masses between 170(170) GeV and 230(217) GeV for different values of $m_{\tilde{\chi}_1^0}$, and top squark production with neutralinos with masses below 62(42) GeV is excluded for different values of $m_{\tilde{t}_1}$. Figure 5 also shows the expected limits derived using only the single-differential distributions of $\Delta\phi$ and $\Delta\eta$. The limits on top squark production are dominated by the $\Delta\eta$ observable, and are relatively insensitive to the contribution of the $\Delta\phi$ distribution and its modelling at NLO.

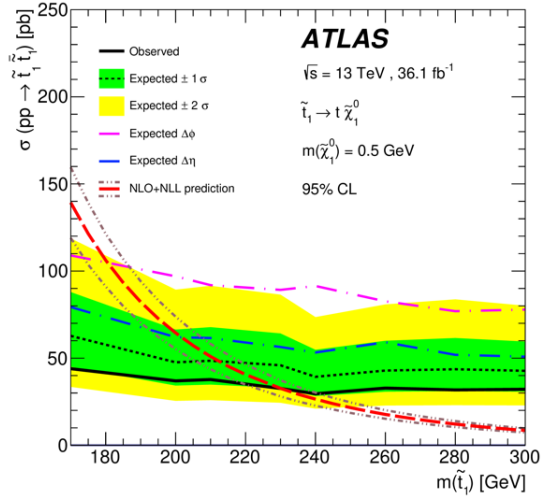


Fig. 5. Expected and observed limits at 95% CL on the top squark pair production cross-section as a function of $m_{\tilde{t}_1}$ assuming a 100% branching ratio for $\tilde{t}_1 \rightarrow t\tilde{\chi}_1^0$ decays with $m_{\tilde{\chi}_1^0} = 0.5$ GeV. The *dashed line* shows the expected limit with ± 1 and ± 2 standard deviation bands. The *dashed line* shows the theoretical cross-section with uncertainties. The *solid line* gives the observed limit. Also shown are the expected limits using the $\Delta\phi$ and $\Delta\eta$ distributions separately

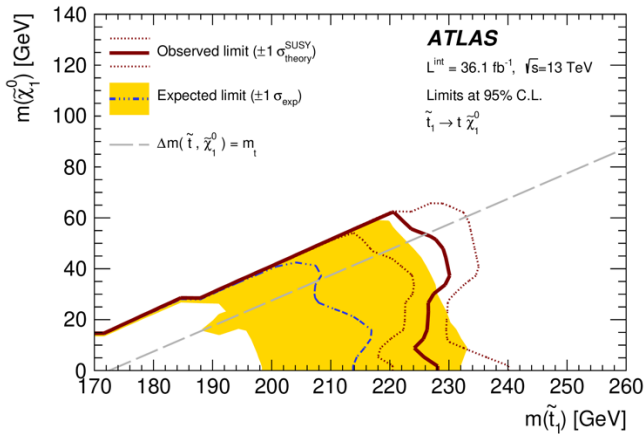


Fig. 6. Expected and observed limits at 95% CL on the top squark pair production cross-section as a function of $m_{\tilde{\chi}_1^0}$ and $m_{\tilde{t}_1}$ assuming a 100% branching ratio for $\tilde{t}_1 \rightarrow t\tilde{\chi}_1^0$ decays. The *dashed line* shows the expected limit with ± 1 standard deviation band. The *solid line* shows the observed limit with the $\pm 1\sigma$ (*dotted*) SUSY cross-section theoretical uncertainties

6. Conclusion

Absolute and normalised differential cross-sections have been measured as a function of the azimuthal angle difference, $\Delta\phi$, and the pseudorapidity difference, $\Delta\eta$, between the two charged leptons in the $e\mu$ decay channel of top quark pairs using 36.1 fb^{-1} of data recorded by the ATLAS detector in proton–proton collisions at $\sqrt{s} = 13 \text{ TeV}$ during 2015 and 2016 at the LHC. None of the studied generators are able to reproduce the normalised $\Delta\phi$ distribution within the experimental errors.

An extraction of spin correlation was performed using the normalised parton-level $\Delta\phi$ observable. The spin correlation was found to be higher than that predicted by the SM as implemented in NLO MC generators with a significance of 2.2 standard deviations. The measured value of spin correlation agrees well with the prediction by the expansion at NLO in QCD and weak couplings, but is less consistent with NNLO predictions, with or without expansion in the normalised cross-section.

A search for $\tilde{t}_1\tilde{\bar{t}}_1$ production was also performed using double-differential distributions of $\Delta\phi$ in ranges of $\Delta\eta$. In the absence of a SUSY signal in data, limits were set on top squark and neutralino production, taking into account the current limitations of the signal and background modelling. Top squarks with masses between 170 and 230 GeV are excluded for most kinematically allowed values of the neutralino mass, compared to expected limits of 170 and 217 GeV.

References

1. M. Tanabashi *et al.*, Phys. Rev. D **98**, 030001 (2018).
2. ATLAS Collab., Phys. Rev. Lett. **108**, 212001 (2012).
3. ATLAS Collab., Phys. Rev. D **90**, 112016 (2014).
4. ATLAS Collab., Phys. Rev. D **93**, 012002 (2016).
5. CMS Collab., Phys. Rev. Lett. **112**, 182001 (2014).
6. ATLAS Collab., Phys. Rev. Lett. **114**, 142001 (2015).
7. CMS Collab., Phys. Lett. B **758**, 321 (2016).
8. CMS Collab., Phys. Rev. D **93**, 052007 (2016).
9. ATLAS Collab., JHEP **03**, 113 (2017).
10. DØ Collab., Phys. Rev. Lett. **107**, 032001 (2011).
11. DØ Collab., Phys. Lett. B **702**, 16 (2011).
12. DØ Collab., Phys. Rev. Lett. **108**, 032004 (2012).
13. DØ Collab., Phys. Lett. B **757**, 199 (2016).
14. CDF Collab., Phys. Rev. D **83**, 031104 (2011).
15. ATLAS Collab., Eur. Phys. J. C **80**, 754 (2020).
16. W. Bernreuther, A. Brandenburg, Z.G. Si, P. Uwer, Phys. Rev. Lett. **87**, 242002 (2001).
17. M. Jezabek, J.H. Kühn, Nucl. Phys. B **320**, 20 (1989).
18. A. Czarnecki, M. Jezabek, J.H. Kühn, Nucl. Phys. B **351**, 70 (1991).
19. S.J. Parke, Nuovo Cim. C **035** (3), 111 (2012).
20. G. Mahlon, S.J. Parke, Phys. Rev. D **81**, 074024 (2010).
21. P. Nason, JHEP **11**, 040 (2004).
22. S. Frixione, P. Nason, C. Oleari, JHEP **11**, 070 (2007).
23. S. Alioli *et al.*, JHEP **06**, 043 (2010).
24. T. Sjöstrand, S. Mrenna, P.Z. Skands, Comput. Phys. Commun. **178**, 852 (2008).
25. P. Artoisenet *et al.*, JHEP **03**, 015 (2013).
26. ATLAS Collab., JHEP **08**, 089 (2018).
27. DØ Collab., Phys. Rev. Lett. **80**, 2063 (1998).
28. G. D'Agostini, Nucl. Instrum. Meth. A **362**, 487 (1995).
29. T. Adye, arXiv:1105.1160 (2011).
30. F. James, M. Roos, Comput. Phys. Commun. **10**, 343 (1975).
31. A.L. Read, J. Phys. G **28**, 2693 (2002).

MEASUREMENT OF THE TRANSVERSE MOMENTUM DISTRIBUTION OF DRELL–YAN LEPTON PAIRS IN PROTON–PROTON COLLISIONS AT $\sqrt{s} = 13$ TeV WITH THE ATLAS DETECTOR

PNPI participants of the ATLAS Collaboration: O.L. Fedin, V.P. Maleev, Yu.G. Naryshkin, V.A. Schegelsky, S.G. Barsov, V.M. Solovyeu, A.E. Ezhilov, M.P. Levchenko, D. Pudzha

1. Introduction

The Drell–Yan production of lepton pairs is a benchmark process at hadron colliders like the Large Hadron Collider (LHC). The production of Z -bosons with subsequent leptonic decays has both a clean and readily identifiable signature and a large event rate. A precise measurement of the p_T^{ll} spectrum provides an important input to the background prediction in searches for beyond the Standard Model (SM) processes, *e. g.* in the monojet signature, as well as to SM precision measurements, *e. g.* the measurement of the mass of the W boson, since a direct measurement of the transverse momentum distribution of W bosons is experimentally challenging. Also, it provides stringent tests of perturbative quantum chromodynamics (QCD) and gives important information about the parton distribution functions (PDFs) for quarks within the proton. Phenomenologically, the spectrum at low transverse momentum p_T^{ll} of the Z boson, reconstructed through the decay into a pair of charged leptons, can be described using soft-gluon resummation together with non-perturbative contribution from the intrinsic transverse momentum of partons. At high p_T^{ll} , the spectrum can be calculated by fixed-order perturbative QCD predictions, and next-to-leading order electroweak (NLO EW) effects are expected to be important. Parton-shower models or resummation may be matched to fixed-order calculations to describe the full spectrum.

Measurements of p_T^{ll} require a precise understanding of the transverse momentum calibration and resolution of the final-state leptons. Associated systematic uncertainties affect the resolution in p_T^{ll} and limit the ultimate precision of the measurements, particularly in the low- p_T^{ll} domain. To minimize the impact of these uncertainties, the ϕ_η^* observable was introduced as an alternative probe of p_T^{ll} :

$$\phi_\eta^* = \tan\left(\frac{\pi - \Delta\phi}{2}\right) \sin \theta_\eta^*,$$

where $\Delta\phi$ is the azimuthal angle in radians between the two leptons. The angle θ_η^* is a measure of the scattering angle of the leptons with respect to the proton beam direction in the rest frame of the dilepton system and is defined by $\cos(\theta_\eta^*) = \tanh[(\eta^- - \eta^+)/2]$, where η^- and η^+ are the pseudorapidities of the negatively and positively charged lepton, respectively. Therefore, ϕ_η^* depends exclusively on the directions of the two leptons, which are more precisely measured than their momenta.

PNPI physicists participate in all stages of measurements for the electron channel, as well as to obtain the combined result. These results are based on 36.1 fb^{-1} of pp collision data collected at $\sqrt{s} = 13$ TeV by the ATLAS experiment at the LHC in 2015–2016. A detailed description of the ATLAS detector is available in Ref. [1]. Both the dielectron and dimuon final states $Z/\gamma^* \rightarrow ll$ ($l = e$ or μ) are analysed in a dilepton mass window of $m_{ll} = 66\text{--}116$ GeV. The measurement is performed in a fiducial phase space that is close to the detector acceptance for leptons in transverse momentum p_T^l and pseudorapidity η_l .

2. Data analysis

The data recorded with the ATLAS detector in 2015–2016 for proton–proton collisions with a centre of mass energy of 13 TeV corresponding to the total integrated luminosity of 36.1 fb^{-1} was used for precision measurement of the transverse momentum and angular variable ϕ_η^* . The measurements were performed separately for the electron and muon channels. The selected events are required to be in the data-taking period in which the beams were stable, and all subdetectors were functioning without errors. Candidate $Z \rightarrow ee$ events are selected using a single electron trigger with $p_T > 24$ GeV in 2015 and $p_T > 26$ GeV in 2016 data.

Additionally, to the increased p_T threshold, the electron also has to meet the isolation criteria in the 2016 data. Also, two high- p_T single-electron triggers are added using a logical “OR” to avoid inefficiencies in the high- p_T region. Electron candidates are reconstructed from clusters of energy in the electromagnetic calorimeter matched to inner detector (ID) tracks [2]. They are required to have $p_T > 27$ GeV and $|\eta| < 2.47$ (excluding the transition regions between the barrel and the endcap electromagnetic calorimeters, $1.37 < |\eta| < 1.52$). Electron candidates are required to pass the “medium” identification requirement and are also required to be isolated according to the “gradient” isolation criterion [2]. Candidate $Z \rightarrow \mu\mu$ events were selected with triggers that require at least one isolated muon with $p_T > 20$ GeV in 2015 and $p_T > 26$ GeV in 2016 data. The high- p_T single-muon triggers are added using a logical “OR”. Muon candidates are reconstructed by combining tracks reconstructed in the ID with tracks reconstructed in the muon spectrometer (MS) [3]. They are required to have $p_T > 27$ GeV and $|\eta| < 2.5$ and satisfy identification criteria corresponding to the “medium” working point [3]. Track quality requirements are imposed to suppress backgrounds, and the muon candidates are required to be isolated according to the “gradient” isolation criterion [3], which is p_T - and $|\eta|$ -dependent and based on the calorimeter and track information. Electron and muon candidates are required to originate from the primary pp interaction vertex. Thus, the significance of the track’s transverse impact parameter calculated relative to the beam line, $|d_0/\sigma_{d_0}|$, must be smaller than 3.0 for muons and less than 5.0 for electrons. The longitudinal impact parameter, z_0 (the difference between the z -coordinate of the point on the track at which d_0 is defined and the longitudinal position of the primary vertex), is required to satisfy $|z_0 \cdot \sin(\theta)| < 0.5$ mm for both channels. Events are required to contain exactly two leptons satisfying the above criteria. The two leptons must be of opposite electric charge and their invariant mass must satisfy $66 < m_{ll} < 116$ GeV. The backgrounds from lepton pairs are estimated using the simulated Monte Carlo (MC) samples and consist of lepton pairs from electroweak processes (diboson production and $Z \rightarrow \tau\tau$ decays), from top-quark processes and photon-induced processes ($\gamma\gamma \rightarrow ll$). The number and properties of the background events where one or two reconstructed lepton candidates originate from hadrons or hadron decay products, *i. e.* multijet processes, as well as W + jets, are estimated using the data-driven techniques from the obtained data. Figure 1 shows the dilepton invariant mass and the lepton pseudorapidity distribution, for the electron and muon channels separately for the data, for the Z -boson signal (MC) sample, and for the main sources of background. Figure 2 compares the measured p_T^{ll} and ϕ_η^* distributions for both channels with the signal MC predictions.

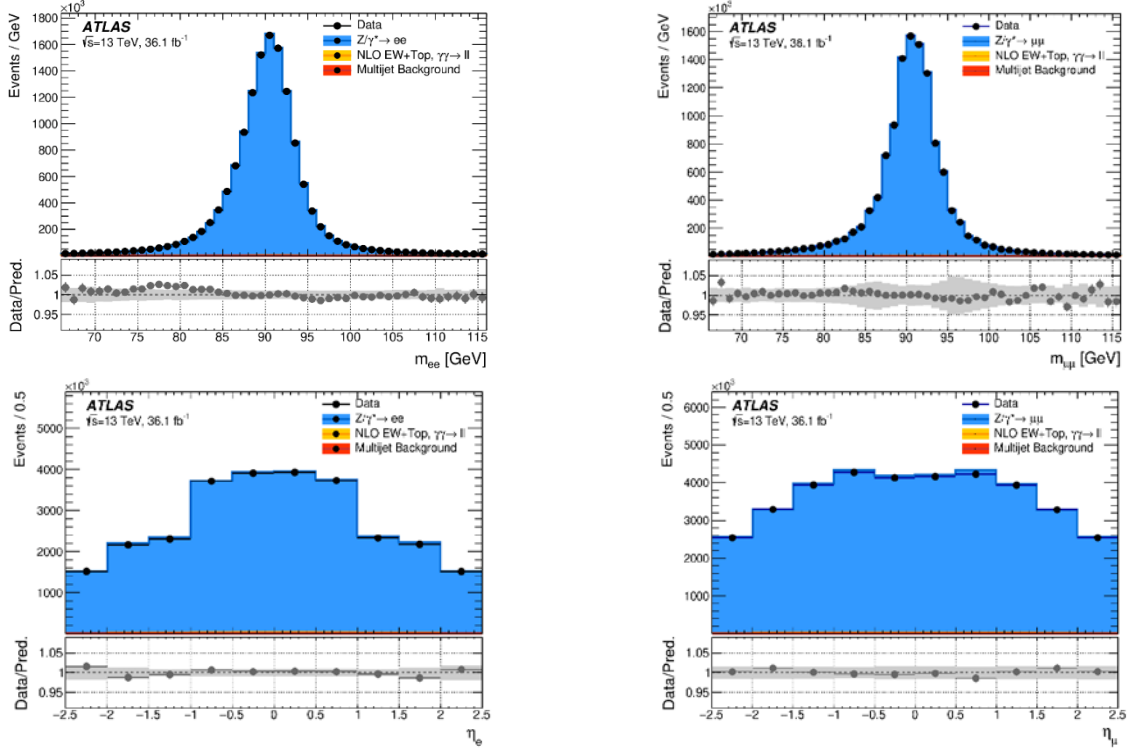


Fig. 1. The distribution of events passing the selection requirements in the electron channel (*left*) and muon channel (*right*) as a function of dilepton invariant mass $m_{\ell\ell}$ (*upper row*) and lepton pseudorapidity η (*lower row*). The statistical uncertainties of the data points are generally smaller than the size of the markers

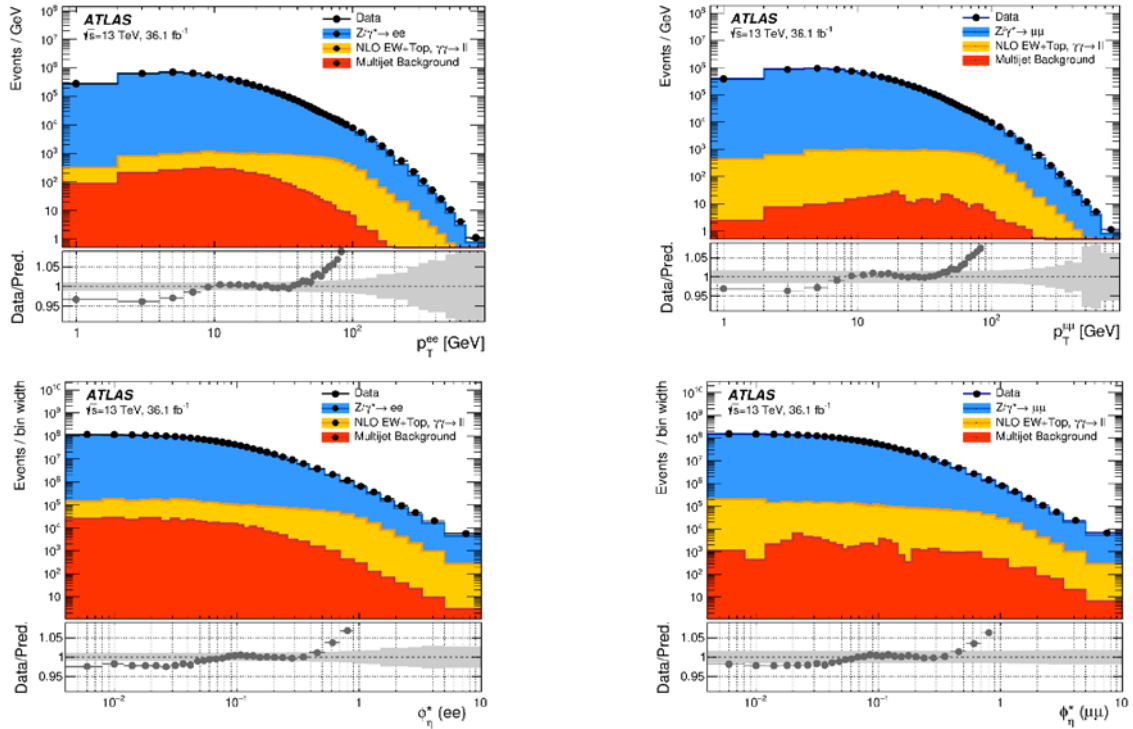


Fig. 2. The distribution of events passing the selection requirements in the electron channel (*left*) and muon channel (*right*) as a function of dilepton transverse momentum (*upper row*) and $\Delta\eta^*$ (*lower row*). The statistical uncertainties of the data points are generally smaller than the size of the markers

3. Results in the individual and combined channels

The production cross-section times the branching ratio for electron and muon channels are measured in fiducial volumes ($p_T > 27$ GeV, $|\eta| < 2.5$ and $66 < m_{ll} < 116$ GeV) and are computed using the following equation:

$$\sigma_{Z/\gamma^* \rightarrow ll}^{\text{fid}} = \frac{N_{\text{Data}} - N_{\text{Bkg}}}{C_Z \cdot L},$$

where N_{Data} is the number of the observed signal events and N_{Bkg} is the number of background events. The integrated luminosity corresponds to pp collision data collected at $\sqrt{s} = 13$ TeV by the ATLAS experiment at the LHC in 2015–2016, $L = 36.1 \text{ fb}^{-1}$. A correction for the event detection efficiency is applied with the factor C_Z , which is defined as the ratio of signal event weights passing the selection at the reconstruction level to the sum of MC satisfying the fiducial requirements. The factor C_Z is affected by experimental uncertainties, while theory and modelling uncertainties are negligible. The results are summarized in the Table below for individual channels and for the combined result including statistical, systematic and luminosity uncertainties.

Table

Measured integrated cross-section in the fiducial volume
in the electron and muon channel and the combined result as well at the Born level

Channel	Measured cross-section $\times B(Z/\gamma^* \rightarrow ll)$, pb
$Z \rightarrow ee$	$738.3 \pm 0.2^{\text{stat}} \pm 7.7^{\text{syst}} \pm 15.5^{\text{lumi}}$
$Z \rightarrow \mu\mu$	$731.7 \pm 0.2^{\text{stat}} \pm 11.3^{\text{syst}} \pm 15.3^{\text{lumi}}$
$Z \rightarrow ll$	$736.2 \pm 0.2^{\text{stat}} \pm 6.4^{\text{syst}} \pm 15.5^{\text{lumi}}$

The differential distributions within the fiducial volume are corrected for detector effects and bin-to-bin migrations using an iterative Bayesian unfolding method. At the first stage, the data events that have passed the event selections (after background subtraction) are corrected for events that pass the detector-level selection and failing the particle-level selection. Then, the iterative Bayesian unfolding technique is used to correct for the detector resolution in events that pass both the detector-level and particle-level selections using the response matrix. These response matrices and the correction factors are derived using the signal MC samples. Finally, the correction is applied to account for events that pass the particle-level but not detector-level selection. The results for separate channels and separate variables are obtained on Born and dressed particle level. The results in the individual channels are combined using χ^2 minimization, following the best linear unbiased estimator prescription. The measurement uncertainties are separated into those from bin-to-bin uncorrelated sources and those from bin-to-bin correlated sources and are largely reduced due to the normalization by the fiducial cross-section. The normalized differential cross-sections $1/\sigma_{\text{fid}} \times d\sigma_{\text{fid}}/dp_T^l$ and $1/\sigma_{\text{fid}} \times d\sigma_{\text{fid}}/d\phi_\eta^*$ measured in the two decay channels as well as their combination are illustrated in Fig. 3.

The measurement results are presented at Born level. The factors k_{dr} , the binwise ratio to transfer to the dressed particle level, are given in Ref. [4].

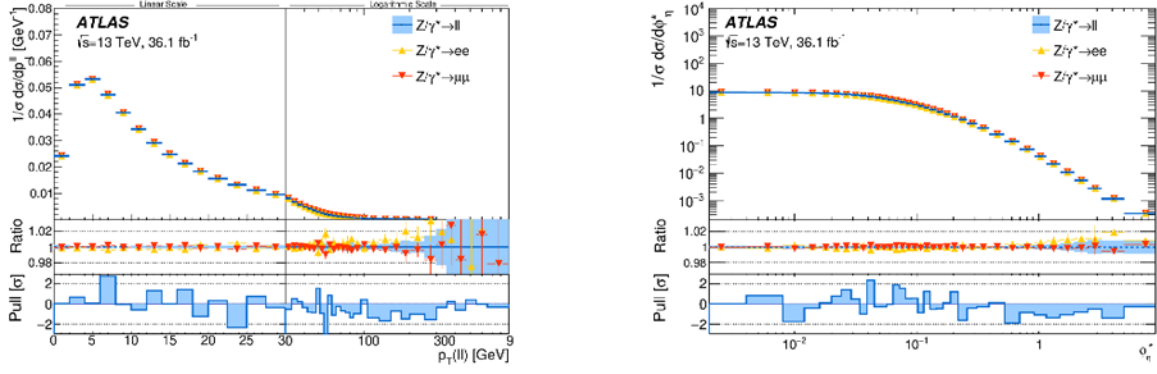


Fig. 3. The measured normalized cross-sections as a function of dilepton transverse momentum (*left*) and ϕ_{η}^* (*right*) for the electron and muon channels and the combined results

4. Comparison with the theory predictions

The differential measurements are compared with different predictions of the p_T^{ll} and ϕ_{η}^* spectra that are based on different theoretical approaches, taking into account both the soft and hard emissions from the initial state radiation. The comparisons between the combined result corrected to quantum electrodynamic Born level and the various predictions are shown in Figs. 4 and 5.

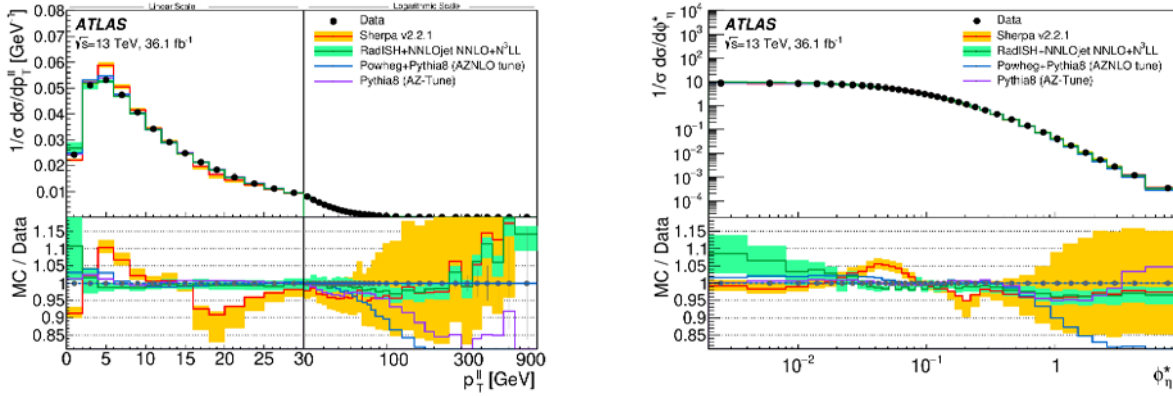


Fig. 4. Comparison of the normalized p_T^{ll} (*left*) and ϕ_{η}^* (*right*) distributions predicted by different computations: PYTHIA8 with the AZ-tune, POWHEG + PYTHIA8 with the AZNLO-tune, SHERPA v2.2.1 and RadISH with the Born level combined measurement

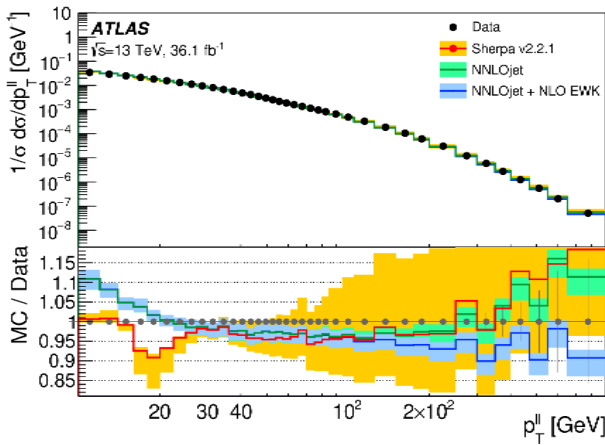


Fig. 5. Comparison of the normalized p_T^{ll} distribution in the range $p_T^{ll} > 10$ GeV. The Born level combined measurement is compared with predictions by SHERPA v2.2.1, fixed-order NNLOjet and NNLOjet supplied with NLO electroweak corrections

The predictions based on the PYTHIA8 parton shower with parameters tuned basing on 7 TeV ATLAS data are found to describe the 13 TeV data well at low p_T^{ll} and ϕ_η^* . The SHERPA prediction based on merging of higher-order, high-multiplicity matrix elements give an excellent description of the data at high p_T^{ll} . Only very accurate RadISH at next-to-next-to-leading order and using next-to-next-to-to-leading logarithmic resummation (NNLO + N³LL) prediction agrees with data for the full spectrum. The fixed-order NNLOjet prediction with and without NLO EW effects describes the data well for high p_T^{ll} .

5. Conclusion

Measurements of the p_T^{ll} and ϕ_η^* distribution of Drell–Yan lepton-pair, using the 36.1 fb⁻¹ of data from proton–proton collisions were carried out in 2015 and 2016 at $\sqrt{s} = 13$ TeV with the ATLAS experiment at the LHC. These measurements of the differential cross-sections have been performed in a fiducial volume defined by $p_T > 27$ GeV, $|\eta| < 2.5$ and $66 < m_{ll} < 116$ GeV. The used data-set allows coverage of a kinematic range up to the TeV-range. The cross-section results obtained in the individual channels were combined and good agreement between the two was observed. The relative precision of the combined result is better than 0.2% for $p_T^{ll} < 30$ GeV, which provides crucial information to validate and tune MC event generators and will constrain models of vector-boson production in future measurements of the W -boson mass.

The integrated fiducial cross-section measurements are compared with fixed-order perturbative QCD predictions. Differential spectra in p_T^{ll} and ϕ_η^* are compared with a selection of calculations implementing resummation and non-perturbative effects through parton showers or analytic calculations.

References

1. ATLAS Collab., JINST **3**, S08003 (2008).
2. ATLAS Collab., Eur. Phys. J. C **79**, 639 (2019).
3. ATLAS Collab., Eur. Phys. J. C **76**, 292 (2016).
4. ATLAS Collab., Eur. Phys. J. C **80**, 616 (2020).

DIJETS WITH LARGE RAPIDITY SEPARATION AT CMS AS A PROBE FOR BFKL EFFECTS

PNPI participants of the CMS Collaboration: A.Iu. Egorov, V.T. Kim, G.E. Gavrillov, V.L. Golovtsov, Yu.M. Ivanov, E.V. Kuznetsova, V.A. Murzin, V.A. Oreshkin, I.B. Smirnov, D.E. Sosnov, V.V. Sulimov, L.N. Uvarov, S.S. Volkov, A.A. Vorobyev

1. Introduction

The search for manifestations of Balitsky–Fadin–Kuraev–Lipatov (BFKL) evolution is of special importance for PNPI because of the key contribution of the institute to the discovery and development of the theory. The BFKL approach describes the high-energy limit of quantum chromodynamics (QCD). Thus, in the light of the development of modern colliders towards high collision energies, the importance of BFKL is growing. The parton processes that are described by BFKL become important when the momentum transfer is kept finite such that $\sqrt{s} \gg Q \gg \Lambda_{\text{QCD}}$, while the collision energy tends to infinity, $\sqrt{s} \rightarrow \infty$. In this kinematic regime, referred to as the (semihard) Gribov–Regge regime or the high-energy limit, a resummation of large logarithms of s is required. The resummation is performed within the BFKL formalism [1–3]. The BFKL evolution in the Gribov–Regge regime can be contrasted with the Dokshitzer–Gribov–Lipatov–Altarelli–Parisi (DGLAP) evolution, which is relevant in the so called hard regime, a kinematic regime where $\sqrt{s} \approx Q \gg \Lambda_{\text{QCD}}$, such that the large logarithms amenable to resummation are of the type $\ln Q^2$ [4–8], rather than the large logarithms of s . Incidentally, the DGLAP formalism is also marked with a seminal contribution from PNPI. While the hard regime is well tested, and calculations based on the DGLAP formalism are widely used in various searches for new physics phenomena, the evidence for the BFKL evolution remains uncertain. Nevertheless, the BFKL effects are expected to become crucial with the increase of the collision energy.

In this contribution, we discuss a new CMS measurement of the dijet production with a large rapidity separation and a jet veto on additional jets [9] in proton–proton collisions at $\sqrt{s} = 2.76$ TeV. An analytic calculation of the influence of the jet veto on the large angle soft gluon resummation with Banfi–Marchesini–Smye (BMS) equation [10], as well as a comparison to the CMS measurement at $\sqrt{s} = 7$ TeV [11] are also discussed.

2. Probes for the BFKL evolution manifestation

One of the difficulties in search for signals of the BFKL evolution is to find proper observables, which can be calculated with the next-to-leading logarithmic (NLL) BFKL accuracy and at least the leading logarithmic (LL) accuracy of DGLAP. Unfortunately, BFKL calculations in the LL accuracy cannot be used for such a search since it provides only qualitative results with a too large pomeron intercept value. Also, when one looks for an observable, one needs to consider such features of both DGLAP and BFKL emissions that would allow one to distinguish one from another.

In the DGLAP evolution, the emitted partons, which are carrying similar values of the longitudinal momentum fraction x of the colliding proton, are ordered in transverse momentum p_{T} . Being ordered in p_{T} , the jets tend to be emitted in a small rapidity region of the detector, where rapidity $y = 0.5 \ln(E + p_z)/(E - p_z)$ is the Lorentz-boost-invariant function of energy E and longitudinal momentum p_z . On the other hand, the BFKL emission happens to be ordered in x (and therefore in y) and diffused in p_{T} . Therefore, the production of jet pairs (dijets) with a wide rapidity separation, $\Delta y = |y_1 - y_2|$ (where y_1 and y_2 are the rapidities of the first and second jet in a dijet) has long been considered to be a good probe for a search for the BFKL signals.

One can distinguish three main types of observables that use jets separated in rapidity as a probe. The first one is the cross sections and the ratios of cross sections of dijet production [12–17]. The ratios can be measured either for the cross sections at different \sqrt{s} , because the s dependence of BFKL and DGLAP evolution is expected to be different, or with various jet veto conditions imposed on the additional emission. The imposition of the veto is justified by the fact that DGLAP emissions are p_{T} -ordered, while BFKL emissions obey diffusion in p_{T} . The second type of observables is the azimuthal decorrelations between jets widely separated

in Δy [18–20]. The azimuthal decorrelation in a dijet is a result of an additional emission with a similar p_T in the BFKL evolution, while, in the DGLAP evolution, additional jets are emitted with much smaller p_T s and, thus cannot produce a large decorrelation. Finally, the third type of observables deals with the jet-gap-jet events production [21–23], where a gap means no hadronic activity in the rapidity interval between the two jets of a dijet. This is achieved *via* the colour singlet state exchange in the parton scattering. Within the BFKL approach, the colour singlet state may be described as a hard pomeron.

Currently, the NLL BFKL calculation is developed for the Mueller–Navelet (MN) dijet cross section production and azimuthal decorrelations between jets in an MN dijet. Here, an MN dijet denotes a pair of jets with the largest Δy among all the jet pairs constructed from jets with transverse momentum above some $p_{T\min}$. The jet-gap-jet events can be calculated within BFKL only using the LL approximation, albeit improved with certain principal contributions of the NLL approximation. The worst situation is for the case of the cross sections with a jet veto, where the BFKL-based Monte Carlo (MC) predictions are available only at the LL accuracy, and are provided by the MC generator HEJ [24]. HEJ provides parton-level predictions based on LL BFKL-based calculations at all-order resummation, with the subsequent parton showering and hadronization (optionally) performed by the BFKL-motivated MC generator ARIADNE [25], distributed along with the HEJ source code.

On the side of DGLAP-based calculations, the predictions are mainly provided by the MC shower generators performing calculations at the fixed QCD order enhanced with a LL DGLAP shower. An essential caveat in using DGLAP-based generators for the BFKL search consists in the fact that they employ improvements beyond the main DGLAP approximation, *e. g.*, the corrections for the colour coherence effects. Colour coherence leads to angular ordering and, eventually, to rapidity ordering reproducing the BFKL-like behaviour. The corrections for colour coherence are small in the domain of the DGLAP evolution at small rapidity, but their implementation can become unstable at large rapidity, where the BFKL evolution is a proper tool. Thus, PYTHIA8 [26] and HERWIG [27] MC generators provide calculations at the leading order (LO) + LL DGLAP accuracy. The next-to-leading order (NLO) matrix elements for parton subprocess are used by the MC generator POWHEG [28]. The LL DGLAP parton shower and hadronization in that case can be done by PYTHIA8 or HERWIG.

3. Previous search in hadron colliders

The measurements of dijet production at large Δy were performed previously at TeV collision energies at both the Tevatron and the Large Hadron Collider (LHC). The D0 experiment at the Tevatron, which performed measurements at $\sqrt{s} = 0.68$ and 1.8 TeV, observed a stronger dependence of the MN dijet production on \sqrt{s} than expected in the LL BFKL approach [29].

On the other hand, no indications of BFKL effects in the MN dijet azimuthal decorrelations were observed by D0 [30]. The jet-gap-jet events measured by D0 [31] are consistent with the LL BFKL-based calculations enhanced with the basic NLL contributions [22]. The measurements of colour singlet exchange by the CDF experiment at the Tevatron agree with BFKL-based calculations [32].

Both the ATLAS and the CMS Collaborations at the LHC provided results of measurements at $\sqrt{s} = 7$ TeV [33–37]. Jet-gap-jet events were additionally measured by CMS at $\sqrt{s} = 13$ TeV [38]. It is worth to note that the CMS experiment explored a much lower reach of $p_{T\min}$ and much wider range of Δy , than it was available at previous (other) experiments. This makes the measurements more sensitive to the BFKL evolution effects. In summary, among all the LHC measurements, none of the DGLAP-based MC model can reproduce all aspects of the data. The difference between the growth rates of the PYTHIA8 and HERWIG predictions, rising with Δy , demonstrates an instability of the colour coherence corrections at large rapidities. The inclusion of NLO corrections with the MC generator POWHEG does not improve the agreement with the data. The MC generator HEJ + ARIADNE overestimates the possible signal in the data, which is an expected behaviour for the LL BFKL-based predictions. Analytical NLL BFKL-based predictions available for azimuthal decorrelations agree with the data, as well as LL BFKL calculations, enhanced with principal NLL contributions, agree with jet-gap-jet measurements.

In summary, the development of NLL BFKL-based calculations for veto observables is of utmost importance.

4. New measurement of cross sections and ratios with veto of dijet production with large Δy at $\sqrt{s} = 2.76$ TeV with the CMS detector

The following differential dijet production cross sections are measured as a function of Δy in proton–proton collisions at $\sqrt{s} = 2.76$ TeV by the CMS collaboration [9]:

$$\begin{aligned} d\sigma^{\text{incl}}/d\Delta y, \\ d\sigma^{\text{MN}}/d\Delta y, \end{aligned} \tag{1}$$

where σ^{incl} is the inclusive dijet production cross section. Each pairwise combination of jets with $p_T > p_{T\text{min}}$ contributes to the cross section. σ^{MN} is the MN dijet cross section. A pair of jets with the maximal Δy among all the jets with $p_T > p_{T\text{min}}$ contributes to the σ^{MN} .

The ratios with veto are also measured:

$$\begin{aligned} R^{\text{incl}} &= (d\sigma^{\text{incl}}/d\Delta y)/(d\sigma^{\text{excl}}/d\Delta y), \\ R^{\text{MN}} &= (d\sigma^{\text{MN}}/d\Delta y)/(d\sigma^{\text{excl}}/d\Delta y), \\ R_{\text{veto}}^{\text{incl}} &= (d\sigma^{\text{incl}}/d\Delta y)/(d\sigma_{\text{veto}}^{\text{excl}}/d\Delta y), \\ R_{\text{veto}}^{\text{MN}} &= (d\sigma^{\text{MN}}/d\Delta y)/(d\sigma_{\text{veto}}^{\text{excl}}/d\Delta y), \end{aligned} \tag{2}$$

where σ^{excl} is the “exclusive” dijet cross section. The events with exactly two jets with $p_T > p_{T\text{min}}$ contribute to the “exclusive” cross section. $\sigma_{\text{veto}}^{\text{excl}}$ is the “exclusive” with veto dijet cross section. “Exclusive” events with no additional jet activity above $p_{T\text{veto}}$ contribute to this cross section.

The kinematic constraints in the current measurement are chosen to match them in the CMS measurements at $\sqrt{s} = 7$ TeV [35]. Namely, $p_{T\text{min}}$ is set at 35 GeV. Jets are clustered with the anti-kt algorithm [39] with the jet size parameter 0.5 and required to have rapidity in $|y| < 4.7$. Therefore the \sqrt{s} dependence of ratios R^{incl} and R^{MN} can be observed. The cross sections σ^{incl} and σ^{MN} are measured for the first time, which makes it possible to better test phenomenological models, because the fixed order calculations are expected to better reproduce the ratios of cross sections than their absolute values. The ratios $R_{\text{veto}}^{\text{incl}}$ and $R_{\text{veto}}^{\text{MN}}$ are also measured for the first time. The $p_{T\text{veto}}$ is set at 20 GeV.

It is worth noting that not only $R_{\text{veto}}^{\text{incl}}$ and $R_{\text{veto}}^{\text{MN}}$, but R^{incl} and R^{MN} are essentially the ratios with a veto, because in σ^{excl} the veto threshold is just equal to $p_{T\text{min}}$. The influence of the veto threshold is difficult to calculate. This is the main reason why the calculations are still at LL BFKL accuracy for this type of observable. An attempt to approach this problem is described in the next section.

All the measured observables are presented in comparison to the predictions of LO + LL DGLAP-based models of PYTHIA8 and HERWIG++, NLO + DGLAP-based models of POWHEG + PYTHIA8, POWHEG + HERWIG++ and POWHEG + HERWIG7 as well as LL BFKL-based model of HEJ + ARIADNE.

Figure 1 shows σ^{incl} and σ^{MN} . As one can see, none of the inspected theoretical models describes the data. The LO + LL DGLAP-based PYTHIA8 simulation overestimates the data, whereas HERWIG, performing calculations with a similar accuracy, underestimates them for $\Delta y < 4$ and overestimates them for $\Delta y > 6$. The inclusion of NLO corrections to the DGLAP-based calculations by the MC generator POWHEG improves agreement only in the central region for $\Delta y < 4$, but the data are overestimated at large Δy . The predictions of the LL BFKL-based MC generator HEJ + ARIADNE systematically underestimate the data for $\Delta y < 7$ and overestimate them in the largest Δy bin. It is important not to overlook that the measured cross sections decrease with Δy faster than the DGLAP-based MC predictions.

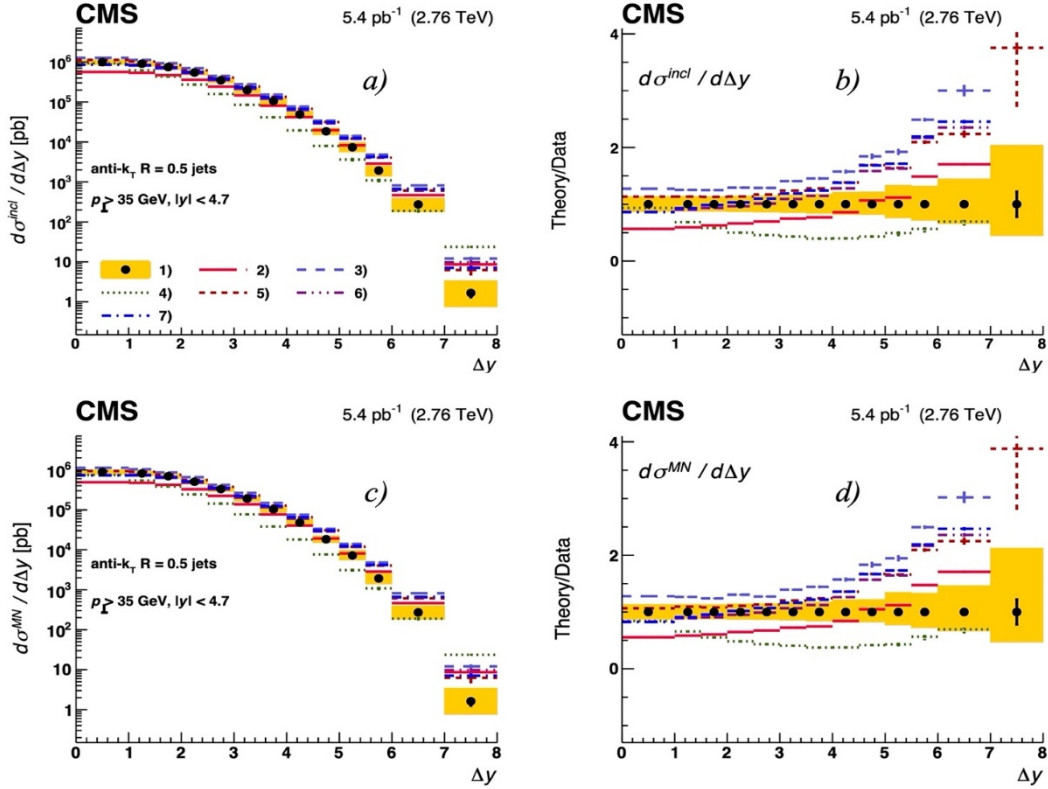


Fig. 1. Differential cross sections (*a, b*) $d\sigma^{\text{incl}}/d\Delta y$, as well as (*c, d*) $d\sigma^{\text{MN}}/d\Delta y$ of dijet production in comparison with predictions of different MC models: 1) DATA; 2) HERWIG++; 3) PYTHIA8; 4) HEJ + ARIADNE; 5) POWHEG + PYTHIA8; 6) POWHEG + HERWIG++; 7) POWHEG + HERWIG7. *Panels a, b* are the measured cross sections. *Panels b, d* are the ratios of theoretical predictions to data. For DATA the *points* depict the measured values, the *vertical bars* are the statistical uncertainty, and the *yellow band* is the systematic uncertainty. For MC models the *vertical bars* are the statistical uncertainty, the *horizontal bars* are the bin widths

The ratios R^{incl} and R^{MN} are presented in Fig. 2*a* and 2*c*. The prediction of PYTHIA8 agrees with the data. It should be noted that the HERWIG prediction deviates significantly from the PYTHIA8 prediction with the deviation steadily increasing with Δy , which indicates that the colour coherence implementation is instable at large rapidity separation, and further suggests that the DGLAP-based models improved with colour coherence can accidentally coincide with the data. The inclusion of NLO corrections to POWHEG does not improve the agreement and even worsen it at small Δy . The HEJ + ARIADNE predictions significantly overestimate the data; this points out to the necessity of NLL BFKL corrections.

The ratios $R_{\text{veto}}^{\text{incl}}$ and $R_{\text{veto}}^{\text{MN}}$ are presented in Figs. 2*b* and 2*d*. The rise of the ratios both with veto and with increase of Δy becomes even more pronounced. The prediction of PYTHIA8 gives the best agreement with the data. However, a local deviation of the PYTHIA8 prediction from the data is observed in the $1 < \Delta y < 4$ region. The difference between PYTHIA8 and HERWIG is even more prominent than the analogous difference for the ratios R^{incl} and R^{MN} . All these facts argue in favour of the BFKL approach to be considered as a proper tool at large Δy . Therefore, the development of NLL BFKL-based calculations is a better strategy than an attempt to save the DGLAP-based models by inclusion of colour coherence corrections. A stronger rise of LL BFKL-based predictions HEJ + ARIADNE for $R_{\text{veto}}^{\text{incl}}$ and $R_{\text{veto}}^{\text{MN}}$ than for R^{incl} and R^{MN} evidences for the increase in sensitivity of $R_{\text{veto}}^{\text{incl}}$ and $R_{\text{veto}}^{\text{MN}}$ to the BFKL effects in comparison with the ratios R^{incl} and R^{MN} .

A comparison of R^{incl} and R^{MN} measured at different energies, namely $\sqrt{s} = 2.76$ [9] and 7 TeV [35], is presented at Fig. 3. The qualitative features of the ratios can be understood as follows. The ratios rise with Δy because of increasing the phase space volume for a hard parton radiation. At very large Δy , the ratios decrease because of kinematic limitations on the productions of events with more than two jets, each with $p_T > p_{T\text{min}}$.

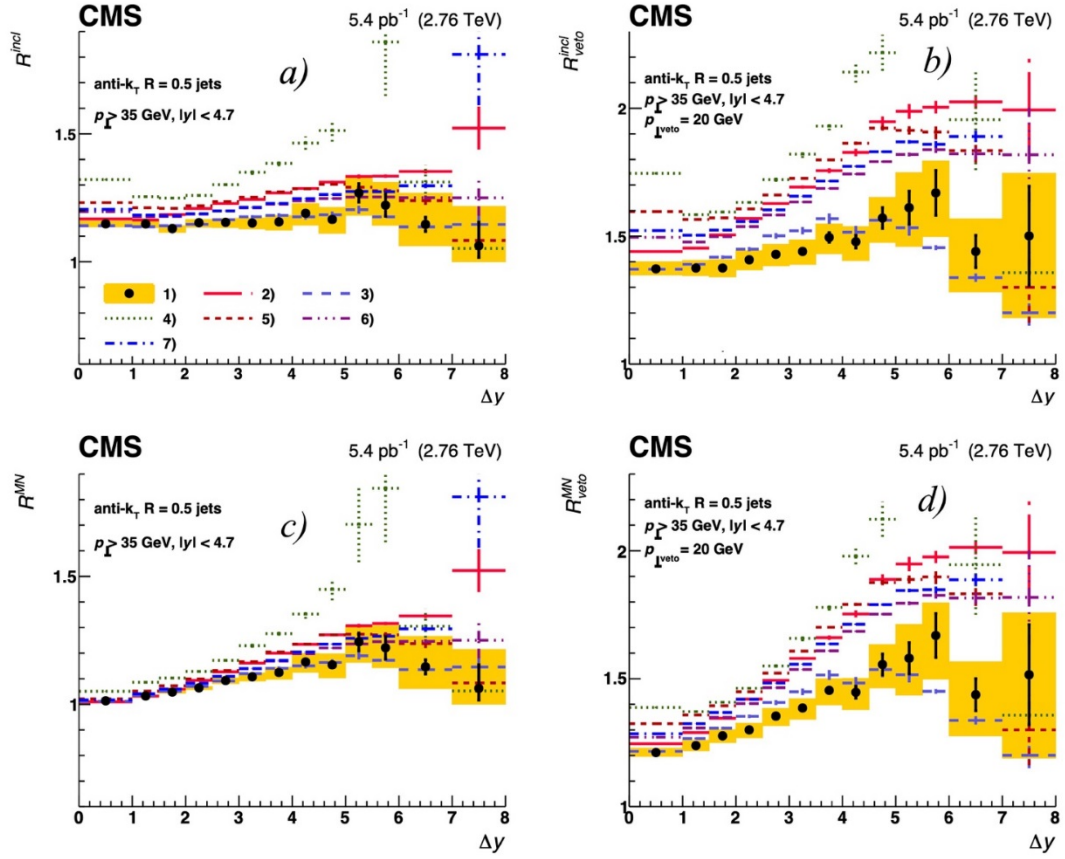


Fig. 2. Ratios of differential cross sections R^{incl} (a), $R^{\text{incl}}_{\text{veto}}$ (b), R^{MN} (c) and $R^{\text{MN}}_{\text{veto}}$ (d) of dijet production in comparison with predictions of different MC models 1) DATA; 2) HERWIG++; 3) PYTHIA8; 4) HEJ + ARIADNE; 5) POWHEG + PYTHIA8; 6) POWHEG + HERWIG++; 7) POWHEG + HERWIG7. For DATA the *points* depict the measured values, the *vertical bars* are the statistical uncertainty, and the *yellow band* is the systematic uncertainty. For MC models the *vertical bars* are the statistical uncertainty, the *horizontal bars* are the bin widths

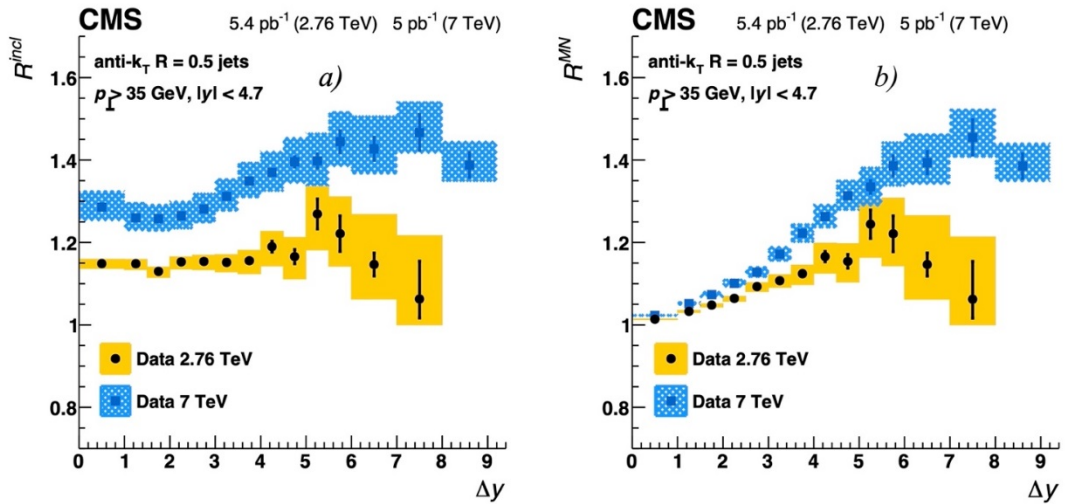


Fig. 3. Ratios of differential cross sections R^{incl} (a) and R^{MN} (b) of dijet production measured at $\sqrt{s} = 2.76$ [34] and 7 TeV [30]. The *points* depict the measured value, the *vertical bars* are the statistical uncertainty, and the *shaded band* is the systematic uncertainty

The comparison at different energies shows that the ratios rise faster with Δy at higher energy, which may reflect both the increasing of the available phase space and BFKL dynamics. Large Δy can be more easily reached at higher energy. According to the present results (see Fig. 2) and the results of Ref. [35], the predictions made by Pythia8 agree with the data best for these observables. Therefore, different observables at different collision energies are needed to find the deviations from DGLAP-based models.

5. BMS approach to veto

As already mentioned, one of the difficulties in drawing a firm conclusion about manifestation of BFKL effects in ratios of cross sections with veto is the absence of a method of calculation for the veto influence. A veto condition, *i. e.*, a prohibition of radiation of additional (besides our dijet) jets with $p_T > p_{T\text{veto}}$, can be imposed between jets of our dijet, which is known as the inter-jet veto, or in the whole rapidity interval, which can be called jet veto. In Ref. [10], it was demonstrated by BMS how the Sudakov and non-global logarithms can be used to account for the veto. Whereas the Sudakov logarithms arise from the gluons primarily emitted to the veto region C_{out} away from jets (the region of rapidity where the veto is imposed), the non-global logarithms come from a secondary emission by gluons emitted in the jet region C_{in} (C_{in} is the region complementary to C_{out}). In the original BMS equation, the soft gluon splitting function was used to describe emission by colour dipoles, therefore it performs a resummation of large logarithms of gluon energy E . By the soft gluon splitting function we mean

$$\omega_{\alpha\beta\gamma} = \frac{1 - \cos \theta_{\alpha\beta}}{(1 - \cos \theta_{\alpha\gamma})(1 - \cos \theta_{\gamma\beta})}, \quad (3)$$

where $\theta_{\alpha\beta}$ is the angle between the ends of the dipole, $\theta_{\alpha\gamma}$ is the angle between the end of dipole α and the direction of the emitted gluon γ , and $\theta_{\gamma\beta}$ is the angle between the end of dipole β and the direction of emitted gluon γ . The BMS equation accounts for colour coherence because the radiation by dipoles is employed.

The BMS equation can be written for an arbitrary complicated region C_{out} , but most easily it can be solved numerically for the inter-jet veto. In Ref. [40], the BMS equation was tested for the inter-jet veto observable measured by ATLAS [33]. Some level of agreement was achieved with data with “forward-backward” selection, whereas the authors of Ref. [40] expected that their calculations would be consistent with “two-leading” selection of the ATLAS measurement.

Ref. [11] presents various ways of employing the BMS equation to approach the jet veto measurement by CMS [35]. The comparison of different approaches to solution of BMS equations for jet veto (*solid lines*) and inter-jet veto (*non-solid lines*) with the CMS data is presented in Fig. 4. The approach which involves naive multiplication model for jet veto and numerical solution of the BMS equation with single veto region is denoted in Fig. 4a by “BMS”. The approach simplifying the BMS equation to Sudakov part is denoted by “Sudakov” (Fig. 4a). The approach based on the MC algorithm described in Ref. [41] with various adjustment parameter values $Q_0 = 2$ and 5 GeV is denoted by “MC qabt ON” (Fig. 4b). The modification of the MC algorithm to be more consistent with the original BMS equation with different cuts for singular region is denoted by “MC qabt OFF” (Fig. 4c). We address the reader to Ref. [11] for more detailed description of the calculation.

As can be seen in Fig. 4a, b, c, the jet veto calculations significantly overestimate the data at small Δy . This can be explained by jet veto aggravating the situation with the non-conservation of energy. The non-conservation of energy is already present in the original BMS approach, but when the angles of emission are large, the emitted gluons are soft, then a small non-conservation is tolerable. However, when the jet veto is applied, its region stretches up to rapidity $|y| = 4.7$. This is close in angle to the proton residues and, thereby, leads to intensive emission, described by singularities in the soft gluon splitting function (Eq. (3)), and, eventually, to a non-conservation of energy that cannot be ignored. To overcome this difficulty, a simple recoil model of energy conservation was added to the MC BMS calculation. The results of comparison of calculations with and without the recoil model are presented in Fig. 4d. As one can see, the inclusion of the recoil leads to a decrease of the emission excess at small Δy , but a more accurate implementation of the energy-momentum conservation is needed.

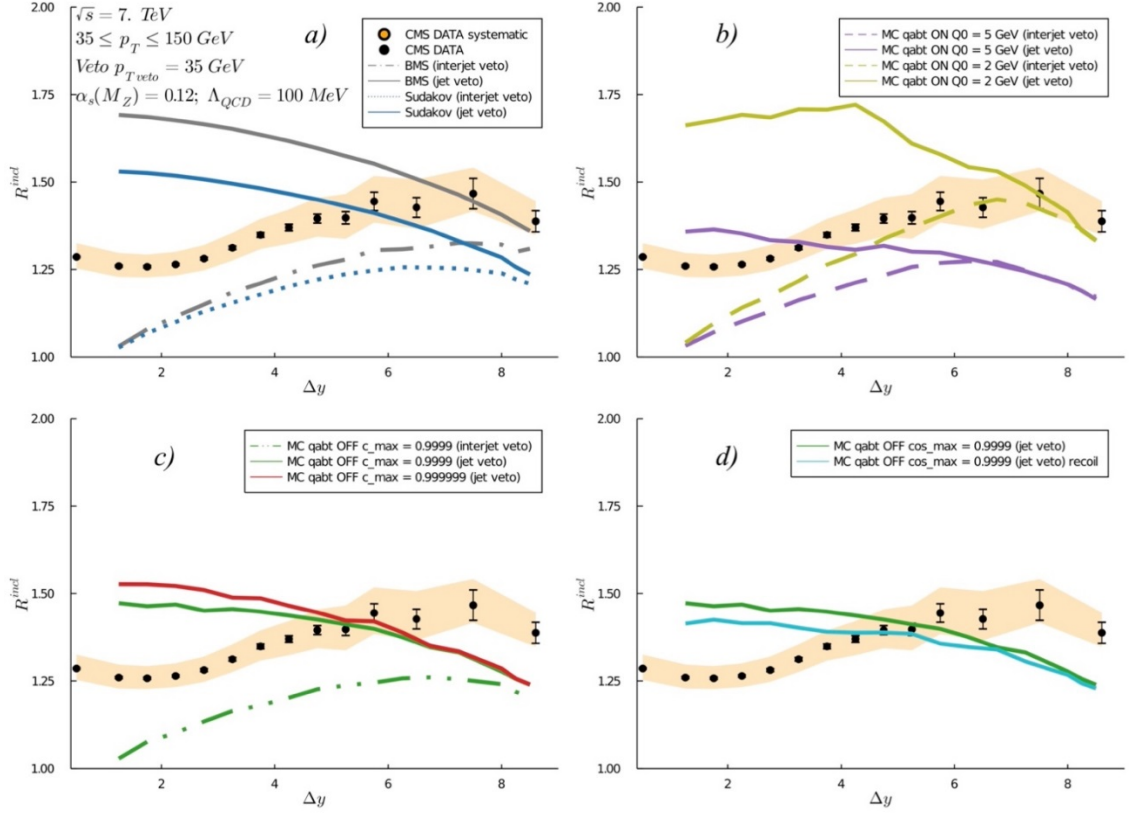


Fig. 4. Calculations of the ratio R^{incl} of dijet cross sections in comparison with measurements by the CMS Collaboration [30] in proton–proton collisions at $\sqrt{s} = 7$ TeV. The results of calculations are depicted by *lines*, the data are presented by *black dots with bars* representing statistical uncertainty and a *shaded band* representing the systematic uncertainty

It should be mentioned that the BMS equation has some resemblance to the BFKL equation, which is due to the resummation of the multisoft gluon states. However, the dominant contributions in the BMS equation come from a different kinematic configuration. In the BMS approach, all angles of emitted gluons are of the same order, because all the collinear singularities are excluded. Moreover, in the leading infrared limit, the energies of gluons are ordered in the BMS evolution. This contrasts to the p_T diffusion of the BFKL evolution. However, a detailed study of the BMS approach can help to develop a method, accounting for the veto, based purely on BFKL calculations.

6. Summary

The first measurement of differential inclusive σ^{incl} and MN σ^{MN} dijet cross sections as functions of rapidity separation Δy in proton–proton collisions at $\sqrt{s} = 2.76$ TeV is performed with the CMS detector. Their ratios to the “exclusive” and the “exclusive” with a veto cross sections, namely R^{incl} , R^{MN} and $R_{\text{veto}}^{\text{incl}}$, $R_{\text{veto}}^{\text{MN}}$, are also measured. The ratios R^{incl} , R^{MN} were measured previously by CMS at $\sqrt{s} = 7$ TeV, while the ratios $R_{\text{veto}}^{\text{incl}}$, $R_{\text{veto}}^{\text{MN}}$ are measured for the first time.

The measured set of observables cannot be described by the MC generators based on the DGLAP evolution and equipped with the leading order or NLO matrix elements. The predictions based on the leading logarithmic approximation of the BFKL equation overestimates the rise of the ratios with Δy , pointing out to a necessity of the development of a NLL BFKL approximation.

The method of calculation of the jet veto influence on the ratios R^{incl} and R^{MN} based on the BMS evolution is tested against the data measured by CMS at $\sqrt{s} = 7$ TeV. The results show that the jet veto is overestimated by this approach at small Δy , and some level of agreement is achieved at large Δy . A detailed investigation of

the BMS approach can help in the development of a method for a jet veto calculation based solely on the BFKL evolution.

The current study may serve as an indication of the BFKL evolution and, extended to other energies, it may help to reveal possible effects beyond the DGLAP approach.

References

1. E.A. Kuraev, L.N. Lipatov, V.S. Fadin, Sov. Phys. JETP **44**, 443 (1976); Zh. Eksp. Teor. Fiz. **71**, 840 (1976).
2. E.A. Kuraev, L.N. Lipatov, V.S. Fadin, Sov. Phys. JETP **45**, 199 (1977); Zh. Eksp. Teor. Fiz. **72**, 377 (1977).
3. I.I. Balitsky, L.N. Lipatov, Sov. J. Nucl. Phys. **28**, 822 (1978); Yad. Fiz. **28**, 1597 (1978).
4. V.N. Gribov, L.N. Lipatov, Sov. J. Nucl. Phys. **15**, 438 (1972); Yad. Fiz. **15**, 781 (1972).
5. V.N. Gribov, L.N. Lipatov, Sov. J. Nucl. Phys. **15**, 675 (1972); Yad. Fiz. **15**, 1218 (1972).
6. L.N. Lipatov, Sov. J. Nucl. Phys. **20**, 94 (1975); Yad. Fiz. **20**, 181 (1974).
7. G. Altarelli, G. Parisi, Nucl. Phys. B **126**, 298 (1977).
8. Y.L. Dokshitzer, Sov. Phys. JETP **46**, 641 (1977); Zh. Eksp. Teor. Fiz. **73**, 1216 (1977).
9. CMS Collab., A. Tumasyan *et al.*, JHEP **03**, 189 (2022).
10. A. Banfi, G. Marchesini, G. Smye, JHEP **08**, 006 (2002).
11. A.Iu. Egorov, V.T. Kim, J. Phys.: Conf. Ser. **1690**, 012158 (2020).
12. A.H. Mueller, H. Navelet, Nucl. Phys. B **282**, 727 (1987).
13. V.T. Kim, G.B. Pivovarov, Phys. Rev. D **53**, 6 (1996).
14. V.T. Kim, Int. J. Mod. Phys. Conf. Ser. **39**, 1560106 (2015).
15. V.T. Kim, Phys. Part. Nucl. Lett. **16** (5), 414 (2019).
16. V.B. Gavrilov, V.T. Kim, V.A. Murzin *et al.*, Nucl. Phys. B **245**, 153 (2013).
17. A.Iu. Egorov, Ya.A. Berdnikov, St. Petersburg Polytechnical State University Journal. Phys. Math. **12**, 121 (2019).
18. V. Del Duca, C.R. Schmidt, Phys. Rev. D **49**, 177 (1994).
19. W.J. Stirling, Nucl. Phys. B **423**, 56 (1994).
20. A. Sabio Vera, F. Schwennsen, Nucl. Phys. B **776**, 170 (2007).
21. A.H. Mueller, W.K. Tang, Phys. Lett. B **284**, 123 (1992).
22. R. Engerg, G. Ingelman, L. Motyka, Phys. Lett. B **524**, 273 (2002).
23. O. Kepka, C. Marquet, C. Royon, Phys. Rev. D **83**, 034036 (2011).
24. J.R. Andersen, J.M. Smillie, JHEP **06**, 010 (2011).
25. L. Lönnblad, Comput. Phys. Commun. **71**, 15 (1992).
26. T. Sjöstrand, S. Mrenna, P.Z. Skands, Comput. Phys. Commun. **178**, 852 (2008).
27. M. Bähr, S. Gieseke, M.A. Gigg *et al.*, Eur. Phys. J. C **58**, 639 (2008).
28. S. Alioli, K. Hamilton, P. Nason, C. Oleari, E. Re, JHEP **04**, 081 (2011).
29. D0 Collab., B. Abbot *et al.*, Phys. Rev. Lett. **84**, 5722 (2000).
30. D0 Collab., B. Abbot *et al.*, Phys. Rev. Lett. **77**, 595 (1996).
31. D0 Collab., B. Abbot *et al.*, Phys. Lett. B **440**, 189 (1998).
32. CDF Collab., F. Abe *et al.*, Phys. Rev. Lett. **80**, 1156 (1998).
33. ATLAS Collab., G. Aad *et al.*, JHEP **09**, 053 (2011).
34. ATLAS Collab., G. Aad *et al.*, Eur. Phys. J. C **74**, 3117 (2014).
35. CMS Collab., S. Chatrchyan *et al.*, Eur. Phys. J. C **72**, 2216 (2012).
36. CMS Collab., V. Khachatryan *et al.*, JHEP **08**, 139 (2016).
37. CMS Collab., A.M. Sirunyan *et al.*, Eur. Phys. J. C **78**, 242 (2018).
38. CMS Collab., A.M. Sirunyan *et al.*, Phys. Rev. D **104**, 032009 (2021).
39. M. Cacciari, G.P. Salam, G. Soyez, JHEP **04**, 063 (2008).
40. Y. Hatta, C. Marquet, C. Royon *et al.*, Phys. Rev. D **87**, 054016 (2013).
41. G. Marchesini, Gribov-75: Memorial Workshop on Quarks, Hadrons, and Strong Interactions 91 (2005).

PNPI STUDY OF RARE DECAYS OF B^0 AND B_s^0 MESONS IN THE LHCb EXPERIMENT

Participants of the LHCb Collaboration: G.D. Alkhazov, A.V. Andreyanov, N.F. Bondar, A.D. Chubykin, A.A. Dzyuba, P.V. Kravchenko, O.E. Maev, D.A. Maisuzenko, N.R. Sagidova, A.N. Solovyev, I.N. Solovyev, A.A. Vorobyev, N.I. Voropaev

1. Introduction

In the Standard Model (SM) of particle physics, decays of neutral beauty mesons B^0 into lepton pairs (with or without additional hadrons) in the final states proceed *via* $b \rightarrow s$ or $b \rightarrow d$ flavour-changing neutral current (FCNC) transition. Such processes are suppressed as they are forbidden at the tree-level and can proceed *via* loop diagrams of the electroweak penguin or box types diagrams. In extensions of the SM, new particles may enter in competing processes and can significantly change the decay branching fraction and the angular distribution of the final-state particles. Thus, precision studies of such decays provide a natural test of SM predictions and could provide evidence of new physics (NP).

LHCb strategy in this field relies on choosing observables, for which SM predictions have small or moderate corrections on quantum chromodynamics (QCD) effects. Recently, the LHCb experiment has released a series of results on the test of the principle of lepton universality (LU) in FCNC-driven decays. Several of them demonstrate deviations from LU predictions at the 2–4 σ level, which might be an indication of NP. These results are often named as flavour anomalies.

The PNPI group is involved in the LHCb project mainly through the design, construction, and operation of the LHCb muon system. Also, PNPI physicists took part in analyses of the experimental data related to studies of rare B meson decays. This report presents several LHCb results obtained in 2015–2017.

2. $B_{(s)}^0$ decays into muons

The leptonic decays $B^0 \rightarrow \mu^+\mu^-$ and $B_s^0 \rightarrow \mu^+\mu^-$ are very rare in the SM of particle physics because they only proceed *via* quantum-loop transitions and are helicity and Cabibbo–Kobayashi–Maskawa (CKM) suppressed. The SM predictions of their time-integrated branching fractions are $\mathcal{B}(B_s^0 \rightarrow \mu^+\mu^-) = (3.66 \pm \pm 0.14) \cdot 10^{-9}$ and $\mathcal{B}(B^0 \rightarrow \mu^+\mu^-) = (1.03 \pm 0.05) \cdot 10^{-10}$. Such small relative uncertainties are due to the leptonic final state and to the progress in lattice QCD calculations. Precise measurements of these observables may reveal discrepancies with the expected values due to the existence of new particles contributing to the decay amplitudes, such as heavy Z' gauge bosons, leptoquarks or non-SM Higgs bosons. The ratio of branching fractions for the $B^0 \rightarrow \mu^+\mu^-$ and $B_s^0 \rightarrow \mu^+\mu^-$ decays also provides powerful discrimination between NP theories. This quantity is theoretically more precise than the two individual branching fractions due to the cancellation of common theoretical uncertainties. In the SM this ratio is predicted to be $2.81 \pm 0.16\%$.

Another possible tool for indirect searches of NP effects is a measurement of the effective lifetime of the $B_s^0 \rightarrow \mu^+\mu^-$ decay ($\tau_{\mu\mu}$). The mass eigenstates for the system of the B_s^0 meson and the corresponding antiparticle are characterized by the difference between their decay width $\Delta\Gamma = 0.085 \pm 0.004 \text{ ps}^{-1}$. Only the heavy state can decay into the $\mu^+\mu^-$ -pair in the SM, but NP could violate this scenario. The dependency of $\tau_{\mu\mu}$ on the B_s^0 meson mean lifetime and $\Delta\Gamma$ includes the $A_{\Delta\Gamma}$ parameter, which is equal to unity for the SM, but could vary in the range $[-1, 1]$ for its extensions.

In the new LHCb analysis, all available statistics collected in Run-1 and Run-2 was analysed [1, 2]. The proton–proton collision dataset corresponds to the integral luminosity of 9 fb^{-1} . After loose trigger and selection requirements, $B_{(s)}^0 \rightarrow \mu^+\mu^-$ candidates are classified based on the dimuon mass and the output variable, a boosted decision tree (BDT) classifier designed to distinguish signal from combinatorial background. The BDT variable is constructed to be distributed uniformly in the range $[0, 1]$ for the signal, and to peak strongly at zero for the background. It has less than 5% residual correlation with the di-muon mass. The multivariate classifier makes a decision on the base of the kinematical parameters of the decay, as well as on the isolation variables. The signal for the BDT > 0.5 requirement presented in the *left panel* of Fig. 1 demonstrates a clear excess of the candidates in the B_s^0 mass range. An excess of $B_s^0 \rightarrow \mu^+\mu^-$ decays with

respect to the expectation from background is observed with a significance of about 10 standard deviations, while the significance of the $B^0 \rightarrow \mu^+\mu^-$ signal is at the 1.7σ level. The two-dimensional profile likelihood of the branching fractions is presented in the right panel of Fig. 1. Individual branching fractions were determined to be

- $\mathcal{B}(B_s^0 \rightarrow \mu^+\mu^-) = (3.09_{-0.43-0.11}^{+0.46+0.15}) \cdot 10^{-9}$,
- $\mathcal{B}(B^0 \rightarrow \mu^+\mu^-) = (1.2_{-0.7}^{+0.8} \pm 0.1) \cdot 10^{-10}$,

where the first uncertainties are statistical and the second are of systematic nature. They, as well as their ratio, are in agreement with the SM predictions.

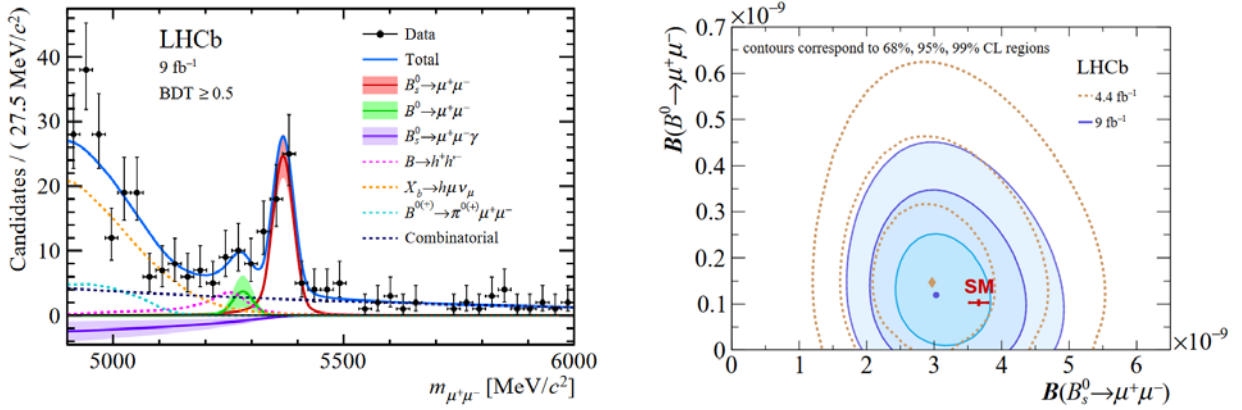


Fig. 1. Mass distribution of the selected $B_{(s)}^0 \rightarrow \mu^+\mu^-$ candidates (black dots) with $\text{BDT} > 0.5$ (left panel). Two dimensional profile likelihood of the branching fractions for the decays $B^0 \rightarrow \mu^+\mu^-$ and $B_s^0 \rightarrow \mu^+\mu^-$ (right panel)

The background-subtracted decay-time distributions with the fit model used to determine the $B_{(s)}^0 \rightarrow \mu^+\mu^-$ effective lifetime are presented in Fig. 2. Two intervals of the BDT variable were investigated. They were approximated by the model, which consists of a single exponential multiplied by an acceptance function that describes the decay time dependence of the reconstruction and selection efficiency. The effective lifetime is found to be $\tau_{\mu\mu} = 2.07 \pm 0.29 \pm 0.03$ ps, where the first uncertainty is statistical and the second systematic. This value lies outside the range between the lifetimes of the light ($A_{\Delta\Gamma} = -1$) and heavy ($A_{\Delta\Gamma} = +1$) mass eigenstates, but is consistent with these values at 2.2 and 1.5 standard deviations, respectively.

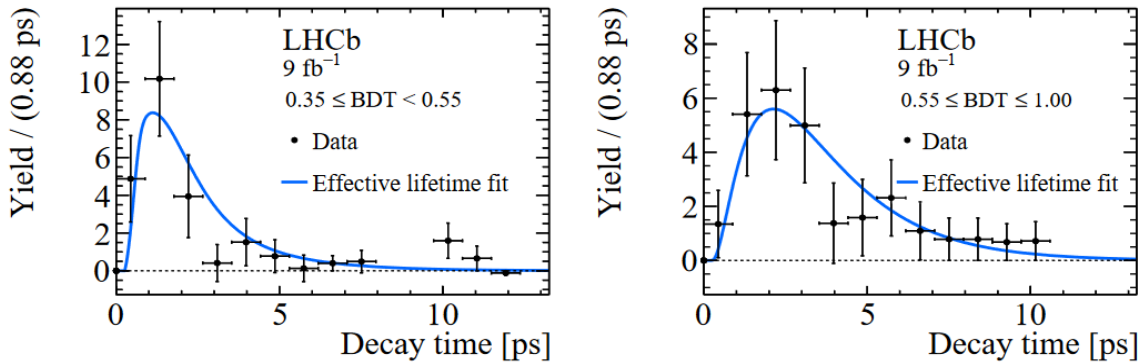


Fig. 2. The background-subtracted decay-time distributions with the fit model used to determine $\tau_{\mu\mu}$. The distributions in the low and high BDT regions are shown in the left and right columns, respectively

Another important measurement of decays of B mesons into fully muonic final state is the LHCb measurements of the branching fractions of the $B_{(s)}^0 \rightarrow \mu^+\mu^-\mu^+\mu^-$ decays [3]. The SM predicts them to be on a level of $(0.9-1.0) \cdot 10^{-10}$ for B_s^0 and $(0.4-4.0) \cdot 10^{-12}$ for B^0 . The BDT-based technique similar to what was done for the di-muon final state was used. The resonant decay channel $B_s^0 \rightarrow J/\psi(\rightarrow \mu^+\mu^-) \phi(\rightarrow \mu^+\mu^-)$ was used

for calibration and normalisation purposes. The limits at 95% confidence level (CL) are determined to be $\mathcal{B}(B_s^0) < 8.6 \cdot 10^{-10}$ and $\mathcal{B}(B^0) < 1.8 \cdot 10^{-10}$, which are in agreement with the SM expectation.

3. Analysis of the $H_b \rightarrow H\mu^+\mu^-$ decays

Decays of beauty hadrons into hadron(s) and emission of $\mu^+\mu^-$ pairs in the final state ($H_b \rightarrow H\mu^+\mu^-$) are also described with the loop FCNC-diagrams and belong to the rare decay type. The differential characteristics of such suppressed processes are a slightly less clearly observable due to a sizeable QCD-induced correction. Nevertheless, they can be theoretically predicted with sufficiently good accuracy. The deviation of experimentally obtained values from theoretical predictions will be evidence of the existence of new fundamental particles and interactions that go beyond the scope of modern theory.

The largest deviation with respect to SM predictions was observed by LHCb for the rare decay of B_s^0 meson into $\phi\mu^+\mu^-$ [4, 5]. Another goal of this analysis was a search for previously unobserved decays of this type.

Measurements of angular distributions and mass dependence for the decay $B_s^0 \rightarrow \phi(\rightarrow K^+K^-)\mu^+\mu^-$ were done for the data-sample collected by LHCb experiments during the first and the second runs of the Large Hadron Collider in 2011–2018. Energies in the centre-of-mass system of interacting protons were 7, 8 and 13 TeV. The so-called. multivariate analysis methods were used to identify $1\,530 \pm 52$ candidates for this decay. The analysis of mass and angular distributions was performed for selected events. In particular, the differential branching fraction for the decay $B_s^0 \rightarrow \phi\mu^+\mu^-$ was obtained as a function of q^2 – squared mass of the di-muon pair (Fig. 3). The mass range of the K^+K^- system above the mass of ϕ resonance was also investigated.

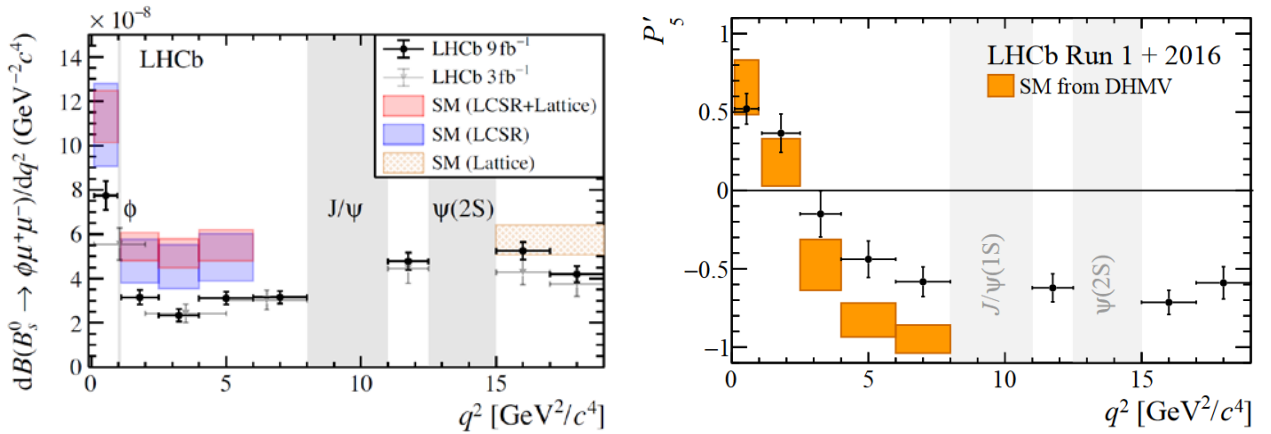


Fig. 3. Differential branching fraction for the $B_s^0 \rightarrow \phi\mu^+\mu^-$ decay as a function of the squared mass of the di-muon pair overlaid with SM predictions using light cone sum rules (LCSR) and lattice quantum-chromodynamics calculations (lattice); the results from the previous LHCb analysis are shown with gray markers – *left panel*. Results for the CP -averaged angular observable P'_5 for the $B^0 \rightarrow K^{*0}\mu^+\mu^-$ decay in bins of q^2 compared with SM predictions (yellow boxes) – *right panel*

A comparison of the experimentally obtained $\frac{d\mathcal{B}(B_s^0 \rightarrow \phi\mu^+\mu^-)}{dq^2}$ distributions with a set of theory predictions shows a discrepancy between them at the low- q^2 region. The statistical significance of the evidence is at the level of 3.6 standard deviations. In addition, in this analysis a new rare decay of the B_s^0 meson into $f_2'(1525)\mu^+\mu^-$ final state was observed for the first time. This decay channel can be in future used for indirect searches for NP.

A search for the decay of B^0 meson into the $\phi\mu^+\mu^-$ decay channel was performed as a separate analysis [6]. As the ϕ meson is almost pure strange–antistrange state such decays proceed in the SM mainly *via* the colour-suppressed penguin annihilation diagram. Their branching fraction is estimated to be approximately of the order of 10^{-12} in the SM calculation made under the QCD factorization approach. NP contributions (for

example from a Z' boson) in the annihilation diagrams could be of the order of 10^{-9} – 10^{-8} . The analysis of all available LHCb data collected in Run-1 and Run-2 allows one to set an upper limit on $\mathcal{B}(B^0 \rightarrow \phi\mu^+\mu^-)$ in the full q^2 range to the value of $3.2 \cdot 10^{-9}$ at a 90% CL, which is compatible with the SM prediction.

Another interesting three-body FCNC-driven decay with di-muons in the final state is $B^{0,+} \rightarrow K^{*0,+}\mu^+\mu^-$. The angular distributions of this decay can be used to determine the CP -averaged observables. A global fit of the complete set of the CP -averaged observables is a powerful tool to search for NP. Six complex decay amplitudes that describe the decay can be extracted in the bins of q^2 , and the optimised angular observables can be produced on their basis. For such observables (named as P_{1-3} and $P'_{4,5,6,8}$), their theoretical prediction is much less dependent on understanding of the hadronic form-factors involved in turning a B meson into a K^* . This fit performed for the Run-1 data indicated differences with predictions based on the SM at the level of 3.4 standard deviations. Mainly this deviation comes from the $4 < q^2 < 8 \text{ GeV}^2/c^4$ region for the P_5' observable.

The angular analysis for the $B^0 \rightarrow K^{*0}\mu^+\mu^-$ decay was recently updated using the data sample collected in 2016 during Run-2 [7]. The CP -averaged observables were extracted using the maximum likelihood fit. For example, the P_5' observable is presented on the *right panel* of Fig. 3. Considering the observables individually, the results are largely in agreement with the SM predictions. The local discrepancy in the P_5' observable in the $4.0 < q^2 < 6.0 \text{ GeV}^2/c^4$ and $6.0 < q^2 < 8.0 \text{ GeV}^2/c^4$ bins reduces from the 2.8σ and 3.0σ observed in the past to 2.5σ and 2.9σ . However, the overall tension with the SM is observed to increase mildly. It should be stressed that the precise value of the significance of this tension depends on the choice of theory nuisance parameters.

The same angular analysis was performed for the first time using the complete pp data set collected with the LHCb experiment in Run-1 and Run-2 for the decay $B^+ \rightarrow K^{*+}\mu^+\mu^-$ [8]. The majority of observables show good agreement with the SM predictions. The largest local discrepancy is in the measurement of P_2 in the interval $6.0 < q^2 < 8.0 \text{ GeV}^2/c^4$, where a deviation of 3.0σ with respect to the SM prediction is observed (Fig. 4). The pattern of deviations from the SM predictions in the observable P_5' broadly agrees with the deviations observed in the $B^0 \rightarrow K^{*0}\mu^+\mu^-$ channel.

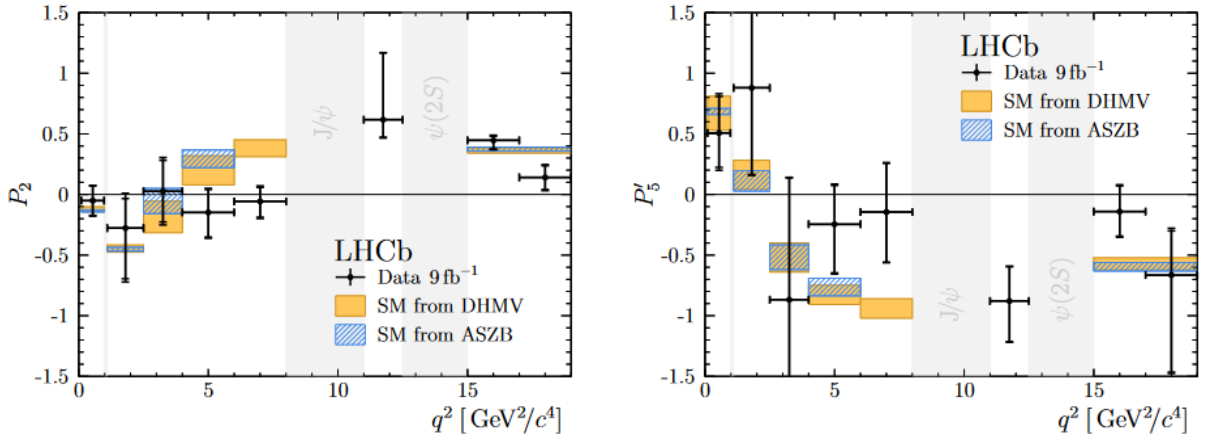


Fig. 4. The CP -averaged angular observable P_2 (left) and P_5' (right) for the $B^+ \rightarrow K^{*+}\mu^+\mu^-$ decay in bins of q^2 compared with SM predictions (yellow and blue boxes)

4. Lepton universality tests

The calculation of the SM predictions for the branching fractions of $B \rightarrow H\ell^+\ell^-$ decays, where B corresponds to a beauty hadron and H is a hadron (or system of hadrons), and ℓ corresponds to μ or e , is complicated due to the strong nuclear force that binds together the quarks into hadrons, as described by the QCD. However, the strong force does not couple directly to leptons and hence its effect on the decays with muons or electrons is identical. This is named the LU principle. As a consequence of the small masses of both electrons and muons with respect to the mass of the b quark, ratios of branching fractions of di-muon and di-electron decays are predicted to be close to unity, except where the value of the dilepton invariant mass-squared (q^2) significantly restricts the phase space available to form the two leptons. The ratio of branching

fractions for $B \rightarrow H\mu^+\mu^-$ and $B \rightarrow He^+e^-$ decays, integrated in an appropriately chosen range of the dilepton mass squared is a theoretically clean observable, which allows one to precisely test SM predictions and therefore perform indirect searches for NP. Such ratios are defined as

$$R_H = \int (dB/dq^2) (B \rightarrow H\mu^+\mu^-) dq^2 / \int (dB/dq^2) (B \rightarrow He^+e^-) dq^2.$$

Measurements performed by the LHCb experiment in previous periods demonstrated evidence of the LU violation. In the period between 2019 and 2022, LHCb released several experimental results, which support previous evidence. These are LU tests with H corresponding to K^+ [9, 10], K_S^0 or K^{*+} [11], and pK^- [12]. Similar experimental strategies were used in these studies. To overcome the challenge of modelling precisely the different electron and muon reconstruction efficiencies, the branching fractions of di-lepton decays were measured relative to those of $B \rightarrow H J/\psi(\rightarrow \ell^+\ell^-)$ decays. As the detector signatures of each resonant ($J/\psi \rightarrow \ell^+\ell^-$) decay are similar to those of the corresponding nonresonant decay, systematic effects are reduced and the precision on R_H is dominated by the statistical uncertainty. As an example, individual mass spectra for both signal and calibration channels for $B^+ \rightarrow K^+\ell^+\ell^-$ decays are presented in Fig. 5. In all cases the largest fraction of the uncertainties (both statistical and systematic) arises from the signal distribution in the $B \rightarrow He^+e^-$ decay.

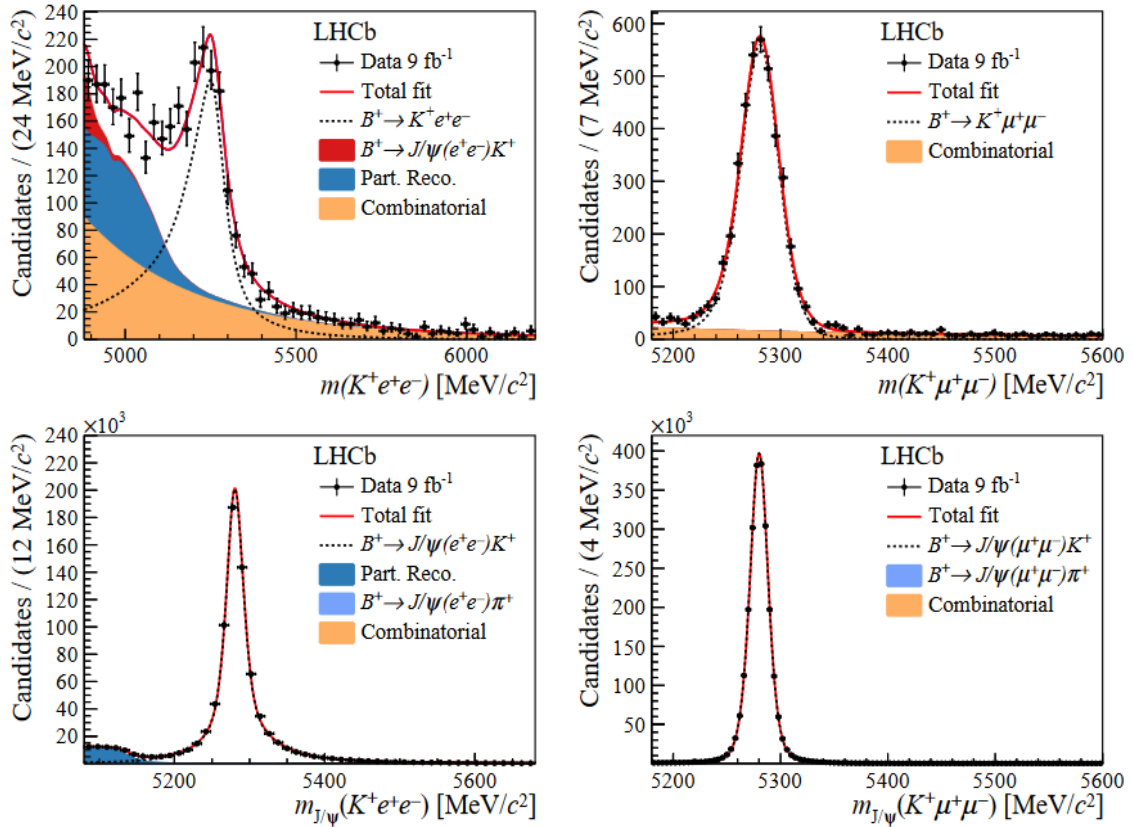


Fig. 5. Candidate invariant mass distributions for $B^+ \rightarrow K^+\ell^+\ell^-$ (top) and $B \rightarrow H J/\psi(\rightarrow \ell^+\ell^-)$ (bottom) decays. Distributions with di-electron in final states are presented at left panels and with di-muon at right panels

A summary of LHCb results on LU tests is presented in the Table. All performed measurements demonstrate the same pattern of deviation from the SM prediction as were observed before. R_H are found to be less than the SM predicts. A comparison of LHCb results for the $B^+ \rightarrow K^+\ell^+\ell^-$ and $B^{*+0} \rightarrow K^{*+0}\ell^+\ell^-$ decays with the SM predictions is also presented in Fig. 6. The statistical significance doesn't exceed 5 standard deviations for each of individual R_H measured. However, an overall significance of the LU violation in all measured decays is approaching the discovery level. Analyses of the rest of the Run-2 data samples will have a decisive role in this regard.

Table

Summary of LHCb results on lepton universality tests

R_H	Decay	q^2 range, GeV^2	Measured value	Significance	Ref.
R_{K^+}	$B^+ \rightarrow K^+ \ell^+ \ell^-$	[1.1; 6.0]	$0.846^{+0.044}_{-0.041}$	3.1σ	[9, 10]
$R_{K_S^0}$	$B^0 \rightarrow K_S^0 \ell^+ \ell^-$	[1.1; 6.0]	$0.66^{0.20}_{-0.14} \text{ (stat)}^{0.02}_{-0.04} \text{ (syst)}$	1.5σ	[11]
$R_{K^{*+}}$	$B^+ \rightarrow K^{*+} \ell^+ \ell^-$	[0.045; 6.0]	$0.70^{0.18}_{-0.13} \text{ (stat)}^{0.03}_{-0.04} \text{ (syst)}$	1.4σ	[11]
R_{pK}	$\Lambda_b \rightarrow p K^- \ell^+ \ell^-$	[0.1; 6.0]	$0.86^{+0.14}_{-0.11} \pm 0.05$	$\approx 1\sigma$	[12]

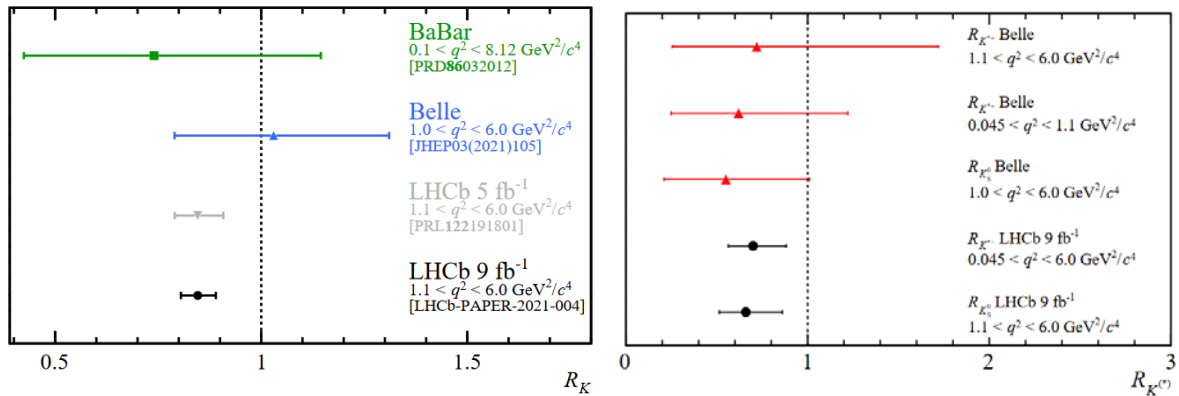


Fig. 6. The ratio of the branching fractions for $B^+ \rightarrow K^+ \ell^+ \ell^-$ (left) and $B^{+,0} \rightarrow K^{*+,0} \ell^+ \ell^-$ (right) decays. Recent LHCb results are presented by *black markers*, while Belle and BaBar measurements are presented by *colour markers*. *Dotted line* corresponds to SM predictions

5. Search for the lepton-flavour violating decays

Lepton-flavour violating (LFV) decays are forbidden in the SM, but the observation of neutrino oscillations shows the existence of LFV in the neutral lepton sector. An observation of LFV decays involving charged leptons would constitute a clear and unambiguous sign of NP. The tensions with SM predictions seen in the lepton flavour universality tests discussed in Section 4, in particular, motivate searches for LFV b -hadron decays, as lepton flavour non-universality is closely connected with LFV. For example, in theoretical models with scalar or vector leptoquarks, or in models with additional Z' bosons used to address LU-related tensions between experimental observations and SM predictions, the predicted values for the $b \rightarrow s \mu^\pm e^\mp$ driven decays could be as large as 10^{-8} level, which is reachable at LHCb. During 2019–2022, the LHCb Collaboration presented several results on the topic. A summary of the obtained upper limits at 95% CL is presented in the list below:

- $\mathcal{B}(B_s^0 \rightarrow \tau^\pm \mu^\mp) < 4.2 \cdot 10^{-5}$ [13],
- $\mathcal{B}(B^0 \rightarrow \tau^\pm \mu^\mp) < 1.4 \cdot 10^{-5}$ [13],
- $\mathcal{B}(B^+ \rightarrow K^+ \mu^- e^+) < 9.5 \cdot 10^{-9}$ [14],
- $\mathcal{B}(B^+ \rightarrow K^+ \mu^+ e^-) < 8.8 \cdot 10^{-9}$ [14],
- $\mathcal{B}(B^+ \rightarrow K^+ \mu^- \tau^+) < 3.9 \cdot 10^{-5}$ [15],

- $\mathcal{B}(B^0 \rightarrow K^{*0}\mu^+e^-) < 5.7 \cdot 10^{-9}$ [16],
- $\mathcal{B}(B^0 \rightarrow K^{*0}\mu^-e^+) < 6.8 \cdot 10^{-9}$ [16],
- $\mathcal{B}(B^0 \rightarrow K^{*0}\mu^\pm e^\mp) < 11.7 \cdot 10^{-9}$ [16],
- $\mathcal{B}(B_s^0 \rightarrow \phi\mu^\pm e^\mp) < 16.0 \cdot 10^{-9}$ [16].

The same type of studies was also performed in the charm sector. Decays of the form $D_{(s)}^+ \rightarrow h^\pm \ell'^+ \ell'^\mp$, where h^\pm is a charged pion or kaon and ℓ'^{\pm} is an electron or muon were considered. The upper limits for the corresponding branching fractions are reported in Ref. [17].

6. Summary

The LHCb experiment plays the world leading role in studies of the di-lepton rare decays of beauty hadrons. Suppressed in the SM, such processes offer an attractive area for search of NP effects. In the present report, results on the branching fractions of the $B_{(s)}^0 \rightarrow \mu^+\mu^-$ decays impose a strong constraint on the Minimal Supersymmetry Model, which is a benchmark model for searches for effects beyond the SM. The current results are in agreement with the SM predictions. On the other hand, the studies of the angular distributions for the $B^{0,+} \rightarrow K^{*0,+}\mu^+\mu^-$ decays provide some hints (3.4σ) on possible deviation from the SM predictions. LU tests performed by LHCb for the $H_b \rightarrow H\mu^+\mu^-$ decays also provide evidence of noticeable disagreements of the experimental results and expectations on the basis of the SM. In Run-3 LHCb plans to increase the statistics and thus the sensitivity in the corresponding analyses.

The LHCb muon system is a crucial ingredient for studies of these decay channels. It was designed and constructed with active participation of PNPI. During Run-1 and Run-2, the PNPI group shared responsibility for operation of the muon system.

The LHCb Collaboration recognized the leading role of Prof. Alexey A. Vorobyev in the success of the experiment. The scientific paper on searches for rare B_s^0 and B^0 decays into four muons [18] was dedicated to the memory of former director of PNPI HEPD.

References

1. LHCb Collab., Phys. Rev. D **105**, 012010 (2022).
2. LHCb Collab., Phys. Rev. Lett. **128**, 041801 (2022).
3. LHCb Collab., JHEP **03**, 109 (2022).
4. LHCb Collab., Phys. Rev. Lett. **127**, 151801 (2021).
5. LHCb Collab., JHEP **11**, 043 (2021).
6. LHCb Collab., JHEP **05**, 67 (2022).
7. LHCb Collab., Phys. Rev. Lett. **125**, 011802 (2020).
8. LHCb Collab., Phys. Rev. Lett. **126**, 161802 (2021).
9. LHCb Collab., Phys. Rev. Lett. **122**, 191801 (2019).
10. LHCb Collab., Nature Phys. **18**, 277 (2022).
11. LHCb Collab., Phys. Rev. Lett. **128**, 191802 (2022).
12. LHCb Collab., JHEP **05**, 040 (2020).
13. LHCb Collab., Phys. Rev. Lett. **123**, 211801 (2019).
14. LHCb Collab., Phys. Rev. Lett. **123**, 241802 (2019).
15. LHCb Collab., JHEP **06**, 129 (2020).
16. LHCb Collab., arXiv:2207.04005.
17. LHCb Collab., JHEP **06**, 044 (2021).
18. LHCb Collab., JHEP **03**, 109 (2022).

HEAVY BARYONS AT LHCb

PNPI participants of the LHCb Collaboration: G.D. Alkhazov, A.V. Andreyanov, N.F. Bondar, A.D. Chubykin, A.A. Dzyuba, P.V. Kravchenko, O.E. Maev, D.A. Maisuzenko, N.R. Sagidova, A.N. Solovyev, I.N. Solovyev, A.A. Vorobyev, N.I. Voropaev

1. Introduction

The LHCb experiment is operating in conditions which allow to record huge data samples of charm and beauty hadrons produced in the forward direction ($2 < \eta < 5$). The large cross sections of the charm–anticharm and beauty–antibeauty quark pair production allow searching for new baryons predicted by the quantum chromodynamics (QCD) part of the Standard Model (SM). New excited states of already discovered c - and b -baryons, ground states containing a pair of heavy quarks, as well as exotic (pentaquark) states are the natural part of the LHCb physics program.

During the last ten years, the LHCb experiment discovered 59 new hadronic states. Their masses, the assigned quark content, and the date of the public release of a corresponding publication are presented in Fig. 1. Since 2018, major discoveries have been done in three sectors: conventional baryons, tetraquarks and pentaquarks. This article contains an overview of the LHCb results for heavy baryons, *e. g.* those which contain charm or beauty quarks.

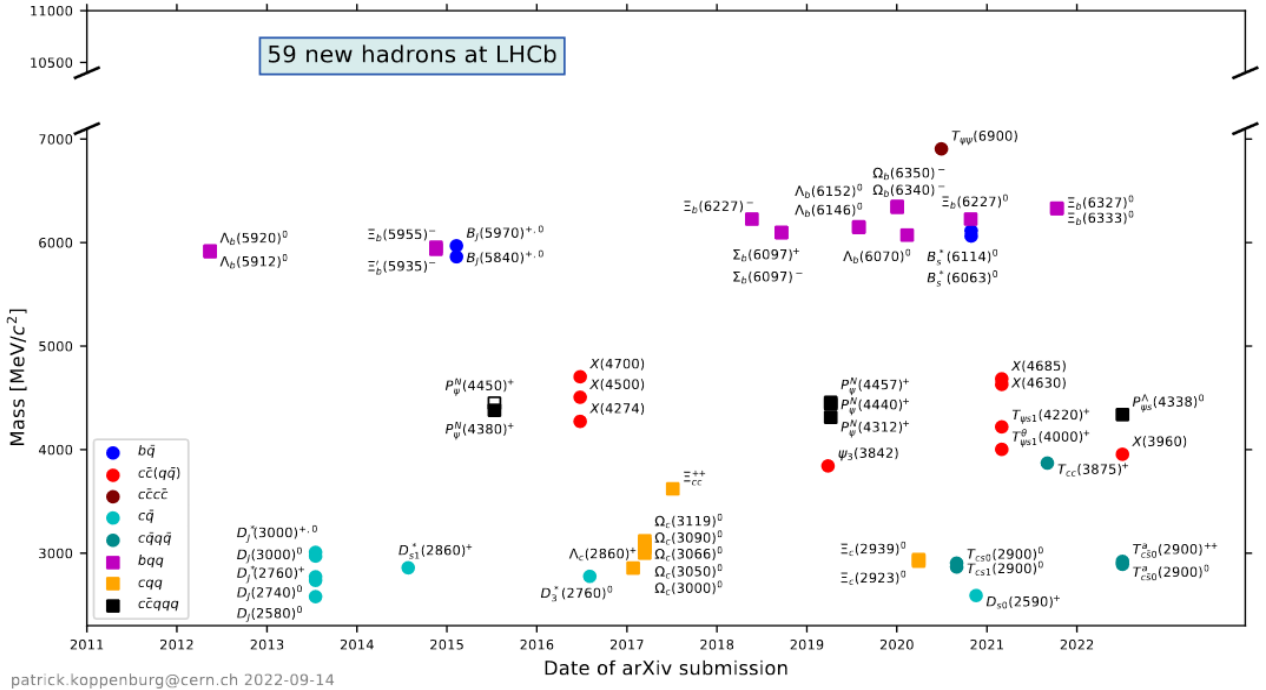


Fig. 1. Masses and discovery dates for the states observed at LHCb. *Hollow markers* indicate superseded states. The figure source: <https://www.nikhef.nl/~pkoppenb/particles.html>

2. Spectroscopy of conventional heavy baryons

In the period 2019–2022, LHCb reported more than ten new baryonic states which can be interpreted as conventional baryons, *i. e.* states with minimal valence quarks content of three. Their properties (masses, widths, decay channels) are presented in Table 1.

Table 1

Properties of conventional baryonic states discovered by the LHCb experiment

Baryon	Decay	Mass, MeV	Width, MeV	Ref.
$\Xi_b(6627)^0$	$\Xi_b(6627)^0 \rightarrow \Xi_b^- \pi^+$	$6\,227.1_{-1.5}^{+1.4} \pm 0.5$	$18.6_{-4.1}^{+5.0} \pm 1.4$	[1]
$\Omega_c(3000)^0$	$\Omega_c(3000)^0 \rightarrow \Xi_c^- K^+$	$2\,999.2 \pm 0.9 \pm 0.9_{-0.22}^{+0.19}$	$4.8 \pm 2.1 \pm 2.5$	[2]
$\Omega_c(3050)^0$	$\Omega_c(3050)^0 \rightarrow \Xi_c^- K^+$	$3\,050.1 \pm 0.3 \pm 0.2_{-0.22}^{+0.19}$	$< 1.6, \text{CL } 95\%$	[2]
$\Omega_c(3065)^0$	$\Omega_c(3065)^0 \rightarrow \Xi_c^- K^+$	$3\,065.9 \pm 0.4 \pm 0.4_{-0.22}^{+0.19}$	$1.7 \pm 1.0 \pm 0.5$	[2]
$\Omega_c(3090)^0$	$\Omega_c(3090)^0 \rightarrow \Xi_c^- K^+$	$3\,091.0 \pm 1.1 \pm 1.0_{-0.22}^{+0.19}$	$7.4 \pm 3.1 \pm 2.8$	[2]
$\Xi_b(6327)^0$	$\Xi_b(6327)^0 \rightarrow \Lambda_b^0 K^- \pi^+$	$6\,327.28_{-0.21}^{+0.23} \pm 0.12 \pm 0.24$	$< 2.56, \text{CL } 95\%$	[3]
$\Xi_b(6333)^0$	$\Xi_b(6333)^0 \rightarrow \Lambda_b^0 K^- \pi^+$	$6\,332.69_{-0.18}^{+0.17} \pm 0.03 \pm 0.22$	$< 1.92, \text{CL } 95\%$	[3]
$\Lambda_b(6146)^0$	$\Lambda_b(6146)^0 \rightarrow \Lambda_b^0 \pi^+ \pi^-$	$6\,146.17 \pm 0.33 \pm 0.22 \pm 0.16$	$2.9 \pm 1.3 \pm 0.3$	[4]
$\Lambda_b(6152)^0$	$\Lambda_b(6152)^0 \rightarrow \Lambda_b^0 \pi^+ \pi^-$	$6\,152.51 \pm 0.26 \pm 0.22 \pm 0.16$	$2.1 \pm 0.8 \pm 0.3$	[4]
$\Lambda_b(6072)^0$	$\Lambda_b(6072)^0 \rightarrow \Lambda_b^0 \pi^+ \pi^-$	$6\,072.3 \pm 2.9 \pm 0.6 \pm 0.2$	$72 \pm 11 \pm 2$	[5]
$\Omega_b(6316)^-$	$\Omega_b(6316)^- \rightarrow \Xi_b^0 K^-$	$6\,315.64 \pm 0.31 \pm 0.07 \pm 0.50$	$< 2.8, \text{CL } 90\%$	[6]
$\Omega_b(6330)^-$	$\Omega_b(6330)^- \rightarrow \Xi_b^0 K^-$	$6\,330.30 \pm 0.28 \pm 0.07 \pm 0.50$	$< 3.1, \text{CL } 90\%$	[6]
$\Omega_b(6340)^-$	$\Omega_b(6340)^- \rightarrow \Xi_b^0 K^-$	$6\,339.71 \pm 0.26 \pm 0.05 \pm 0.50$	$< 1.5, \text{CL } 90\%$	[6]
$\Omega_b(6350)^-$	$\Omega_b(6350)^- \rightarrow \Xi_b^0 K^-$	$6\,349.88 \pm 0.35 \pm 0.05 \pm 0.50$	$1.4_{-0.8}^{+1.0} \pm 0.1$	[6]
$\Xi_c(2923)^0$	$\Xi_c(2923)^0 \rightarrow \Lambda_c^+ K^-$	$2\,923.04 \pm 0.25 \pm 0.20 \pm 0.14$	$7.1 \pm 0.8 \pm 1.8$	[7]
$\Xi_c(2939)^0$	$\Xi_c(2939)^0 \rightarrow \Lambda_c^+ K^-$	$2\,938.55 \pm 0.21 \pm 0.17 \pm 0.14$	$10.2 \pm 0.8 \pm 1.1$	[7]
$\Xi_c(2965)^0$	$\Xi_c(2965)^0 \rightarrow \Lambda_c^+ K^-$	$2\,964.88 \pm 0.26 \pm 0.14 \pm 0.14$	$14.1 \pm 0.9 \pm 1.3$	[7]

Among these discoveries, the first observation of excited Ω_b^- states is particularly interesting. In 2017, the LHCb experiment observed five narrow states, assumed to be excited Ω_c^0 baryons, which decay into $\Xi_c^+ K^-$ pairs. Five narrow states were observed in a mass interval of less than 120 MeV width in the $\Xi_c^+ K^-$ mass distribution. This inspired searches of the same kind in the beauty sector.

Samples of Ξ_b^0 candidates are formed by pairing Ξ_c^+ and π^- candidates, where the Ξ_c^+ decays are reconstructed in the $pK^- \pi^+$ final state [6]. The particle-identification information and decay chain topology and a power of boosted decision tree (BDT) discriminant technique allowed to obtain a clean sample of Ξ_b^0 , which was later on combined with the charged kaons originating from the point where two Large Hadron Collider (LHC) protons collided. To search for peaking structures in the $\Xi_b^0 K^-$ mass spectrum, a requirement that the absolute value of the difference between the mass of the reconstructed $\Xi_c^+ \pi^-$ system and the known mass of Ξ_b^0 should be less than 40 MeV is imposed. Note, that the charges of the charged particles in the final state define a flavour of the reconstructed neutral beauty-strange baryon. A mass distribution for pairs, which can

form excited Ω_b^- states is presented in Fig. 2. Four peaks were observed in this spectrum. In contrast, $\Xi_b^0 K^+$ mass spectrum didn't contain structures which can be interpreted as a signal. Two of four peaks had a global significance of more than 5 standard deviations, which is commonly used as a discovery level in particle physics. The masses and widths obtained with a lineshape parameterization by S -wave relativistic Breit–Wigner function with a Blatt–Weisskopf barrier factor were reported in Ref. [6]. The observed states have the natural widths of the same order or less than the LHCb mass resolution. The upper limits for all of them are below 3.1 MeV at 90% CL.

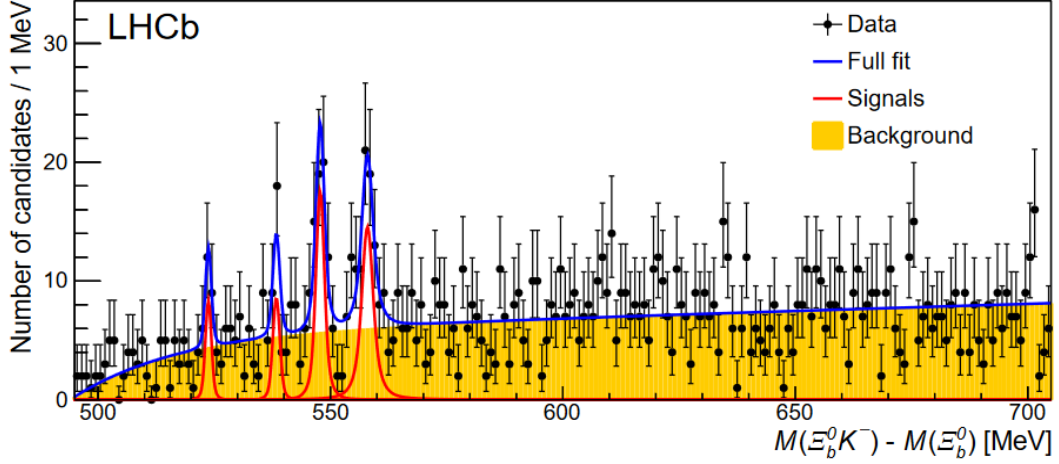


Fig. 2. Distribution of the mass difference for $\Xi_b^0 K^-$ candidates. *Red lines* demonstrate contributions from the excited Ω_b^- states, while the background is shown by the *gold area*

Due to the Lorentz boost for the relativistic particles, which are produced in pp collisions and due to the excellent tracking in the vertex region available at LHCb, the lifetime of the hadrons can be measured with high precision. In 2017, LHCb presented a new result of a measurement of the lifetime of the Ω_c^0 , which suggested that the lifetime hierarchy known by that time was wrong. These studies were continued in 2019–2022. Precision measurements of the Λ_c^+ , Ξ_c^+ and Ξ_c^0 baryon lifetimes were performed with the same technique as for Ω_c^0 [8]. Namely, these baryons were identified *via* measurements of semimuonic decays of the corresponding beauty baryons Λ_b and Ξ_b . The intercept region for the muon track and the reconstructed track of the charm baryon candidate fixes the production point, and the intercept of the tracks from the charm baryon decay fixes the decay point. The lifetime was evaluated from this information and the momentum of the Λ_c^+ , Ξ_c^+ or Ξ_c^0 candidate. The decay-time distribution of the charm baryons reconstructed in the analysed sample was measured relative to that of D^+ meson decays. The lifetime of the D^+ meson is known with better than 1% precision. This approach allowed for significant reductions in the systematic uncertainty.

Later, the lifetime measurements for the neutral charm baryons was supplemented with a measurement done with promptly produced Ω_c^0 and Ξ_c^0 baryons [9]. The primary vertex of proton–proton collision fixes the production point of the charm baryon and the intercept of the tracks from its child particles fixes the decay point. This allows to measure lifetime. The obtained result is consistent with the previous LHCb measurements of the Ω_c^0 and Ξ_c^0 lifetimes, obtained from semileptonic beauty-hadron decays [8], and confirms the charmed-hadron lifetime hierarchy of $\tau(\Xi_c^+) > \tau(\Omega_c^0) > \tau(\Lambda_c^+) > \tau(\Xi_c^0)$.

Other noticeable results of the spectroscopy of conventional heavy baryons are presented briefly in the list below. These are:

- Measurement of the mass and production rate of Ξ_b^- baryons [10];
- Measurement of the ratio of branching fractions of the decays $\Lambda_b^0 \rightarrow \psi(2S)\Lambda$ and $\Lambda_b^0 \rightarrow J/\psi\Lambda$ [11];
- Determination of isospin amplitudes in $\Lambda_b^0 \rightarrow J/\psi\Lambda(\Sigma^0)$ and $\Xi_b^0 \rightarrow J/\psi\Xi^0(\Lambda)$ decays [12];
- Amplitude analysis of the $\Lambda_c^+ \rightarrow pK^-\pi^+$ decay and Λ_c^+ baryon polarization measurement in semileptonic beauty hadron decays [13];
- Measurement of the $\Lambda_b^0 \rightarrow J/\psi\Lambda$ angular distribution and the Λ_b^0 polarisation in pp collisions [14].

3. Decays of heavy baryons

Hierarchy of the Cabibbo–Kobayashi–Maskawa (CKM) matrix elements defines in a first approximation branching fractions for tree-level decays of charm hadrons. Decays depending on both V_{us} and V_{cd} matrix elements are known as doubly Cabibbo-suppressed (DCS) decays. They have small branching fractions compared to the Cabibbo-favoured (CF) and the singly Cabibbo-suppressed (SCS) decays. A systematic study of the relative contributions of DCS and CF diagrams to decays of charm baryons could shed light on the role of the non-spectator quark, and in particular the Pauli interference.

In 2019, LHCb Collaboration reported the first observation of the DCS decay $\Xi_c^+ \rightarrow p\phi$ with $\phi \rightarrow K^+K^-$ [15]. The leading-order diagram for the $\Xi_c^+ \rightarrow p\phi$ decay is presented in the left panel of Fig. 3. The measurement is based on a data sample of pp collisions collected in 2012 at the centre-of-mass energy of 8 TeV, corresponding to an integrated luminosity of 2 fb^{-1} . The signal from the DCS $\Xi_c^+ \rightarrow pK^-K^+$ decay is clearly visible in the corresponding mass spectrum for the events with the mass requirement of $M_{K^-K^+} < 1.07 \text{ GeV}/c^2$ (see Fig. 3), where the contribution from the ϕ meson dominates. An evidence of the 3.5σ , including systematic uncertainties, for a non- ϕ contribution to the DCS $\Xi_c^+ \rightarrow pK^-K^+$ decay is also found. For the $\Xi_c^+ \rightarrow p\phi$ decay channel, the ratio of the branching fractions with respect to the SCS $\Xi_c^+ \rightarrow pK^-\pi^+$ decay channel is measured to be $(19.8 \pm 0.7_{\text{stat}} \pm 0.9_{\text{syst}} \pm 0.2_{\text{norm}}) \cdot 10^{-3}$. This analysis was performed by the PNPI–LHCb group.

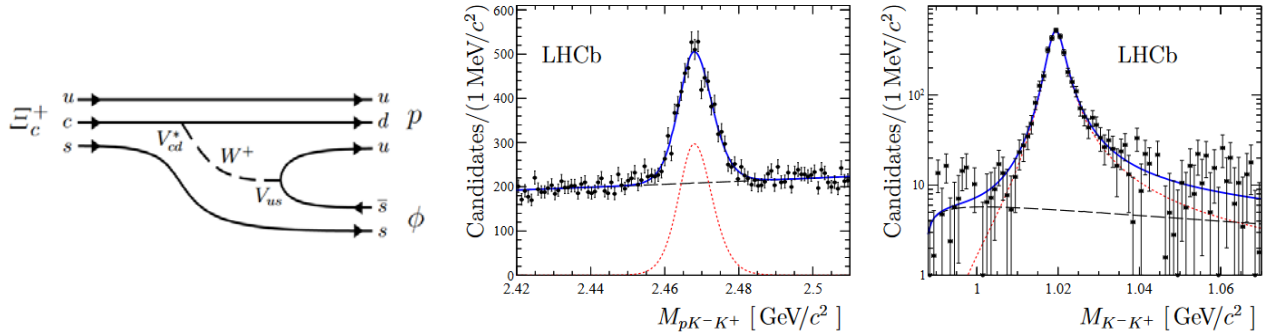


Fig. 3. Tree quark diagram for the $\Xi_c^+ \rightarrow p\phi$ decay (left panel). Fit results for the $\Xi_c^+ \rightarrow pK^-K^+$ decay. The candidates are selected in the ϕ meson region, *i. e.* with the requirement of $M_{K^-K^+} < 1.07 \text{ GeV}/c^2$ (central panel). Background subtracted K^-K^+ mass distribution for the $\Xi_c^+ \rightarrow pK^-K^+$ decay (right panel)

Weak decays of the ground states of Ξ_c baryons usually go *via* the channels which do not contain charm quarks in their final states. However, a heavy quark baryon decay which conserves charm quantum number is possible. An example is $\Xi_c^0 \rightarrow \pi^-\Lambda_c^+$. This transition can be described by s -quark decay or by weak scattering process. The corresponding quark diagrams are presented in the right panel of Fig. 4. For the Ξ_b^- baryons a decay of similar type with a conservation of beauty quantum number is also possible. However, due to the structure of weak interaction at the quark sector of the SM (absence of the flavour changing neutral currents at the tree level of theory) only the s -quark decay amplitude plays a role for the $\Xi_b^- \rightarrow \pi^-\Lambda_b^0$ decay. A comparison of branching fractions for the $\Xi_c^0 \rightarrow \pi^-\Lambda_c^+$ and $\Xi_b^- \rightarrow \pi^-\Lambda_b^0$ decays will help to establish the role of the exchange diagram.

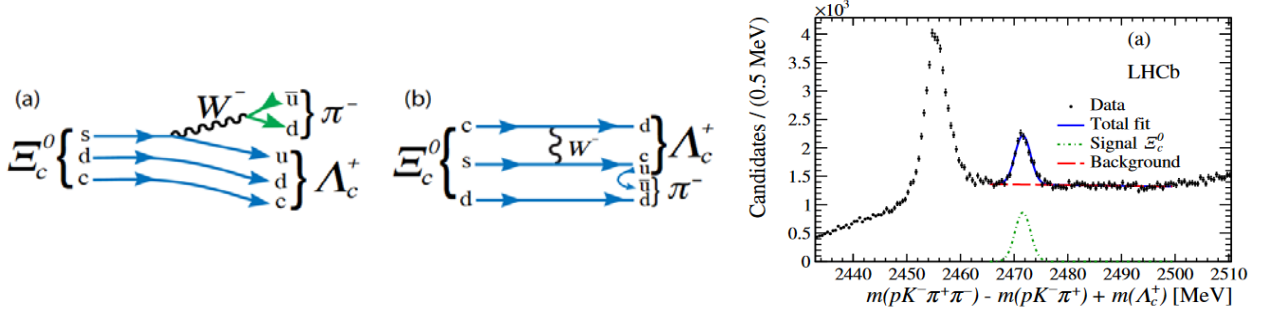


Fig. 4. Tree quark diagram for the $\Xi_c^0 \rightarrow \pi^- \Lambda_c^+$ decay (*left and central panels*). Reconstructed $\pi^- \Lambda_c^+$ -mass distribution for the selected candidates; lines demonstrate a spectrum description in the region which corresponds to the $\Xi_c^0 \rightarrow \pi^- \Lambda_c^+$ decay (*right panel*)

In 2020, LHCb Collaboration published an analysis devoted to the measurements of the $\Xi_c^0 \rightarrow \pi^- \Lambda_c^+$ decay branching fraction [16]. This decay was observed for the first time in the LHC data by the analysis group of the PNPI. The data from the first run of the LHC collected at the centre-of-mass energies of 7 and 8 TeV for colliding protons were used. The branching fraction measurement was done at 13 TeV using the Run-2 data. An event selection procedure using multivariate machine learning techniques allowed to obtain 6320 ± 230 candidates for this decay (see Fig. 4, *right panel*). Decays of Λ_c^+ and Ξ_c^+ baryons with the known absolute branching fractions were used as normalization channels. In addition, an assumption about symmetries of heavy quark baryon production processes was used. The first measurement of the branching fraction of the suppressed $\Xi_c^0 \rightarrow \pi^- \Lambda_c^+$ decay was performed, giving $B = (0.55 \pm 0.02_{\text{stat}} \pm \pm 0.18_{\text{syst}}) \cdot 10^{-2}$. This result can be theoretically explained assuming constructive interference between the s -quark decay and the weak scattering amplitudes.

Besides measurements of the suppressed decays of Ξ_c baryons, the LHCb experiment presented several observations of and searches for new decay channels for conventional beauty baryons. Several decay channels were observed for the first time:

- $\Lambda_b^0 \rightarrow \Lambda_c^+ K^+ K^- \pi^-$ decay [17],
- $\Lambda_b^0 \rightarrow D p K^-$ decay [18],
- $\Lambda_b^0 \rightarrow D^+ p \pi^- \pi^-$ and $\Lambda_b^0 \rightarrow D^{*+} p \pi^- \pi^-$ decays [19],
- Semileptonic decay $\Lambda_b^0 \rightarrow \Lambda_c^+ \tau \nu_\tau$ [20],
- $\Lambda_b^0 \rightarrow \eta_c(1S) p K^-$ decay [21],
- $\Lambda_b^0 \rightarrow \chi_{c1} p \pi^-$ decay [22],
- Radiative decay $\Lambda_b^0 \rightarrow \Lambda \gamma$ [23].

In future, these decay modes will be used to study CP violation effects in the baryon sector, determination of the CKM-matrix elements and searches for the resonances with exotic nature in the intermediate states.

A search for the radiative $\Xi_b^- \rightarrow \Xi^- \gamma$ decay was also performed [24] resulting with an upper limit of $B(\Xi_b^- \rightarrow \Xi^- \gamma) < 1.3 \cdot 10^{-4}$ at 95% CL.

4. Studies of doubly-heavy baryons

In the quark model, conventional baryonic states are formed by three valence quarks belonging to a set of quarks (u, d, s, c, b). First four of them form the $SU(4)$ multiplets. All expected ground states with the charm quantum number equal to 0 or 1 were observed before LHCb started data taking, while baryons containing two c -quarks which form isospin doublet ($\Xi_{cc}^{++} = ccu$ and $\Xi_{cc}^+ = ccd$) and isospin singlet ($\Omega_{cc}^+ = ccs$) with the $J^P = 1/2^+$ were not reliably measured.

The Ξ_{cc}^{++} baryon was observed by the LHCb experiment in $\Lambda_c^+ K^- \pi^+ \pi^+$ and $\Xi_c^+ \pi^+$ decay modes. The mass and lifetime of this particle was measured. In 2019–22, LHCb performed the most precision measurement of the Ξ_{cc}^{++} mass [25] and observed a new decay channel: $\Xi_{cc}^{++} \rightarrow \Xi_c^+ \pi^+$ [26].

For the mass measurements all available LHCb statistics collected in 2016–2018 for the $\Lambda_c^+ K^- \pi^+ \pi^+$ and $\Xi_c^+ \pi^+$ decay channels were used. The mass distributions are presented in Fig. 5. The Ξ_{cc}^{++} mass is determined to be $3621.55 \pm 0.23_{\text{stat}} \pm 0.30_{\text{syst}}$ MeV. The $\Xi_{cc}^{++} \rightarrow \Xi_c^+ \pi^+$ decay manifests itself as a broad feed-down structure below Ξ_{cc}^{++} peak in the $\Xi_c^+ \pi^+$ mass distribution, as the photon from the radiative decay of the Ξ_c^+ wasn't detected. The branching fraction of this new decay channel relative to that of the $\Xi_{cc}^{++} \rightarrow \Xi_c^+ \pi^+$ decay is measured to be $1.41 \pm 0.17 \pm 0.10$, where the first uncertainty is statistical and the second systematic.

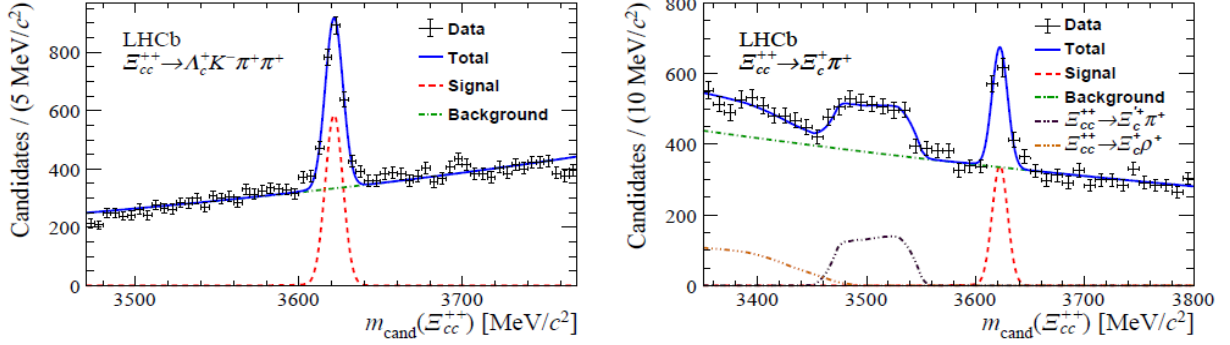


Fig. 5. Mass distributions for $\Lambda_c^+ K^- \pi^+ \pi^+$ (left) and $\Xi_c^+ \pi^+$ decay modes (right). The results of unbinned extended maximum-likelihood fits to the mass distributions are indicated by the blue solid lines

Besides measurements of Ξ_{cc}^{++} properties, the LHCb experiment performed a bunch of searches for other doubly-heavy baryonic states: Ξ_{cc}^+ , $\Xi_{bc}^{0,+}$ and Ω_{bc}^0 . The results of these searches as well as the results of searches for new Ξ_{cc}^{++} decay channels are presented in Table 2.

Table 2

Summary of the LHCb searches for the doubly-heavy baryons

Baryons	Decay channels	Ref.
Ξ_{cc}^{++}	$\Xi_{cc}^+ \rightarrow \Xi_c^+ (\rightarrow pK^- \pi^+) \pi^+ \pi^-$	[27]
Ξ_{cc}^{++}	$\Xi_{cc}^{++} \rightarrow D^+ (\rightarrow K^- \pi^+ \pi^-) pK^- \pi^+$	[28]
Ξ_{cc}^+	$\Xi_{cc}^+ \rightarrow \Lambda_c^+ (\rightarrow pK^- \pi^+) K^- \pi^+$	[29]
Ξ_{bc}^0	$\Xi_{bc}^0 \rightarrow D^0 (\rightarrow K^- \pi^+) pK^-$	[30]
Ξ_{bc}^+	$\Xi_{bc}^+ \rightarrow J/\psi (\rightarrow \mu^+ \mu^-) \Xi_c^+ (\rightarrow pK^- \pi^+)$	[31]
$\Xi_{bc}^0, \Omega_{bc}^0$	$\Xi_{bc}^0 \rightarrow \Lambda_c^+ (\rightarrow pK^- \pi^+) \pi^-, \Xi_{bc}^0 \rightarrow \Xi_c^+ (\rightarrow pK^- \pi^+) \pi^-, \Omega_{bc}^0 \rightarrow \Lambda_c^+ (\rightarrow pK^- \pi^+) \pi^-, \Omega_{bc}^0 \rightarrow \Xi_c^+ (\rightarrow pK^- \pi^+) \pi^-$	[32]
Ω_{cc}^+	$\Omega_{cc}^+ \rightarrow \Xi_c^+ (\rightarrow pK^- \pi^+) K^- \pi^+$	[33]

5. Pentaquarks with hidden charm

Due to the confinement, quarks and antiquarks can form only colour-singlet hadron states. Two widespread types of hadrons are baryons (three valence quarks) and mesons (quark–antiquark state). Some other combinations are also not theoretically forbidden, for example, pentaquarks (four quarks and one antiquark). A great success of the LHCb Collaboration was a discovery of heavy pentaquarks in 2015 [34]. These particles contain a pair of heavy quarks (charm and anticharm). They were discovered using Λ_b^0 decays into the $pK^- J/\psi$

final state. Results of both model-dependent and model-independent data analyses indicated an intermediate resonance $P_c^+ \rightarrow pJ/\psi$.

In 2019, LHCb released a new data analysis on a search of pentaquark states with hidden charm for Λ_b^0 decays into pK^-J/ψ [35]. A Run-2 dataset collected between 2015 and 2019 was used. The available statistics was increased by a factor of ten due to the higher integrated luminosity, higher Λ_b^0 production cross section at 13 TeV and also due to the improved selection algorithms.

Three narrow peaks were observed in the pJ/ψ mass spectrum (Fig. 6, *left panel*). They correspond to three new narrow resonances named: $P_c(4312)^+$, $P_c(4440)^+$ and $P_c(4457)^+$. Masses, widths as well as partial contributions of these resonances into the Λ_b^0 decay were determined from using a one-dimensional approximation of the pJ/ψ mass spectrum. The discovered particles have masses right below thresholds for the open charm decay channels: $\Sigma_c D$ and $\Sigma_c D^*$. This allows to interpret these resonances as weakly bounded broad meson-baryonic states. Though they can be also interpreted as strongly bounded compact hadronic clusters (so-called hadrocharmonium).

In the summer of 2022, the LHCb experiment presented preliminary results on studies of the B^- decays into the $\bar{p}\Lambda J/\psi$ final state [36]. About 4 600 candidates for this decay (93% of purity) were identified in the analysis of the full dataset collected during Run-1 and Run-2 data taking campaigns. An amplitude analysis was performed. A new pentaquark state $P_{\psi s}^\Lambda(4338)^0$ was observed. It manifests itself as a peak in the $J/\psi\Lambda$ mass spectrum (Fig. 6, *right panel*). The mass and the width of the new pentaquark is measured to be $4338.2 \pm 0.7 \pm 0.4$ MeV and $7.0 \pm 1.2 \pm 1.3$ MeV, respectively. The preferred quantum numbers are $J^P = 1/2^-$. The observed state has the mass near $\Xi_c^+ D^-$ threshold, which opens a possibility for a molecular interpretation.

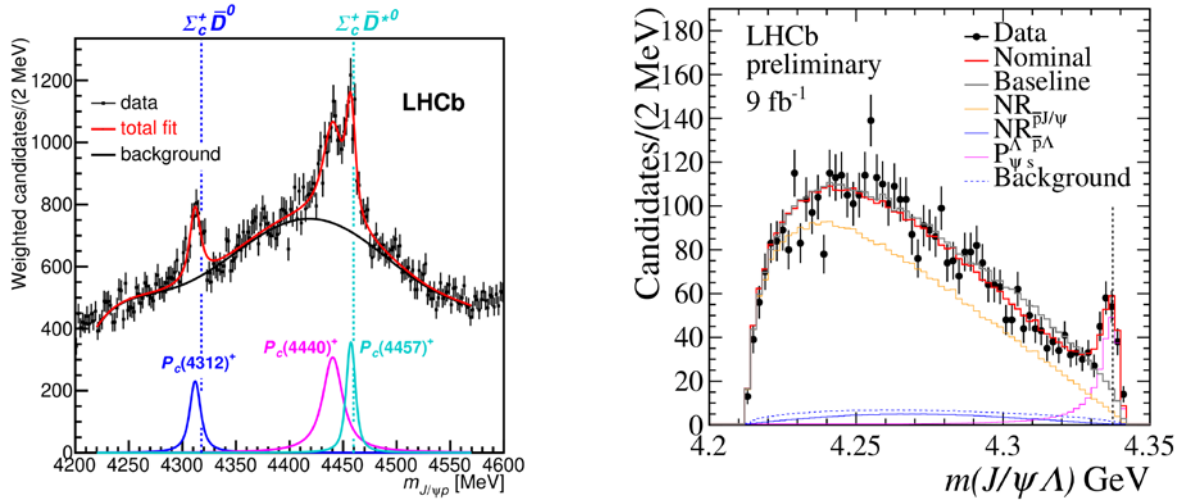


Fig. 6. Mass spectrum for the pJ/ψ system in $\Lambda_b^0 \rightarrow pK^-J/\psi$ decays; *blue, magenta and cyan lines* show contributions from new pentaquark states; *vertical dotted lines* show thresholds for other possible open charm decay channels (*left panel*). $J/\psi\Lambda$ mass spectrum for the B^- decays into antiproton, J/ψ and Λ ; *magenta line* shows contributions from $P_{\psi s}^\Lambda(4338)^0$; the $\Xi_c^+ D^-$ threshold is indicated by a *vertical dotted line* (*right panel*)

Besides discoveries discussed above, two more evidences for the pentaquark states were reported by LHCb in the period between 2019 and 2022. These are:

- Evidence for $P_{\psi s}(4459)$ in $\Xi_b^- \rightarrow J/\psi\Lambda K^-$ with the statistical significance of 3.1σ [37],
- Evidence for $P_{\psi}(4337)$ in $B_s^0 \rightarrow J/\psi p\bar{p}$ with the statistical significance also of 3.1σ [38].

6. Conclusion

The LHCb experimental program is very successful in the discovery of new particles containing one or a pair of charm quarks, including pentaquarks with hidden charm, as well as in research devoted to the conventional beauty baryons. The PNPI analysis group participates in these investigations as a part of the Charm Physics Group.

References

1. LHCb Collab., Phys. Rev. D **103**, 012004 (2021).
2. LHCb Collab., Phys. Rev. D **104**, L091102 (2021).
3. LHCb Collab., Phys. Rev. Lett. **128**, 162001 (2022).
4. LHCb Collab., Phys. Rev. Lett. **123**, 152001 (2019).
5. LHCb Collab., JHEP **06**, **136** (2020).
6. LHCb Collab., Phys. Rev. Lett. **124**, 082002 (2020).
7. LHCb Collab., Phys. Rev. Lett. **124**, 222001 (2020).
8. LHCb Collab., Phys. Rev. D **100**, 032001 (2019).
9. LHCb Collab., Sci. Bull. **67** (5), 479 (2022).
10. LHCb Collab., Phys. Rev. D **99**, 052006 (2019).
11. LHCb Collab., JHEP **03**, 126 (2019).
12. LHCb Collab., arXiv:2208.03262.
13. LHCb Collab., Phys. Rev. Lett. **124**, 111802 (2020).
14. LHCb Collab., JHEP **06**, 110 (2020).
15. LHCb Collab., JHEP **04**, 084 (2019).
16. LHCb Collab., Phys. Rev. D **102**, 071101(R) (2020).
17. LHCb Collab., Phys. Lett. B **815**, 136172 (2021).
18. LHCb Collab., Phys. Rev. D **104**, 112008 (2021).
19. LHCb Collab., JHEP **03**, 153 (2022).
20. LHCb Collab., Phys. Rev. Lett. **128**, 191803 (2022).
21. LHCb Collab., Phys. Rev. D **102**, 112012 (2020).
22. LHCb Collab., JHEP **05**, 95 (2021).
23. LHCb Collab., Phys. Rev. Lett. **123**, 031801 (2019).
24. LHCb Collab., JHEP **01**, 069 (2022).
25. LHCb Collab., JHEP **02**, 049 (2020).
26. LHCb Collab., JHEP **05**, 038 (2022).
27. LHCb Collab., JHEP **11**, 095 (2020).
28. LHCb Collab., Chin. Phys. C **45**, 093002 (2021).
29. LHCb Collab., Sci. China-Phys. Mech. Astron. **64**,101062 (2021).
30. LHCb Collab., JHEP **12**, 107 (2021).
31. LHCb Collab., arXiv:2204.09541.
32. LHCb Collab., JHEP **10**, 124 (2019).
33. LHCb Collab., Sci. China-Phys. Mech. Astron. **63**, 221062 (2020).
34. LHCb Collab., Phys. Rev. Lett. **115**, 072001 (2015).
35. LHCb Collab., Phys. Rev. Lett. **122**, 222001 (2019).
36. LHCb Collab., <https://indico.cern.ch/event/1176505/>
37. LHCb Collab., Sci. Bull. **66**, 1278 (2021).
38. LHCb Collab., Phys. Rev. Lett. **128**, 062001 (2022).

FIRST MEASUREMENT OF DIFFRACTIVE PROTON–NUCLEUS COLLISIONS WITH CMS AT THE LARGE HADRON COLLIDER

PNPI participants of the CMS Collaboration: E.V. Kuznetsova, D.E. Sosnov, V.T. Kim, S.A. Nasybulin, G.E. Gavrilov, V.L. Golovtsov, Yu.M. Ivanov, V.A. Murzin, V.A. Oreshkin, I.B. Smirnov, V.V. Sulimov, L.N. Uvarov, S.S. Volkov, [A.A. Vorobyev](#)

1. Introduction

The pomeron (\mathbb{P}), an object with the quantum numbers of the vacuum [1, 2], is deeply connected to the fundamental nature of the quantum chromodynamics (QCD) [3–8] and responsible for elastic and diffractive scattering [9–13]. Those processes significantly contribute to the high energy hadron–hadron and hadron–nucleus interactions and are accessible at the Large Hadron Collider (LHC). Diffractive scattering in proton–nucleus collisions can also serve as a probe for collective effects inside a nucleus exploiting the dependence of the diffractive cross section on the nuclear mass [14, 15]. Besides of the fundamental studies, the diffractive proton–nucleus scattering is also of particular interest in modeling of extensive air showers from cosmic rays [16].

As a consequence of the pomeron exchange, the final state particles originating from a diffractive scattering event demonstrate a significantly large gap in their rapidity distribution, in contrast to non-diffractive processes. This signature is often used to tag diffractive production events in experimental measurements, although it may cause ambiguity in the presence of the ultraperipheral photoproduction [17].

Measurements of events with forward rapidity gaps (FRG) produced in proton–lead collisions at centre-of-mass energy per nucleon pair of 8.16 TeV were performed in the CMS experiment. This energy is about 300 times larger than the one of the previous measurements done by the HELIOS Collaboration [18] at proton–nucleon centre-of-mass energy of 29.1 GeV.

2. Data analysis

The measurement of the differential cross-section for events with FRG in the proton–lead (p –Pb) collisions was performed with the CMS detector [19] using $6.4 \mu\text{b}^{-1}$ of collision data collected in 2016 [20–23]. The FRG was searched in the CMS detector using particle flow objects [24] in the pseudorapidity region of $|\eta| < 3.0$, starting from $+3.0$ or -3.0 depending on the process of interest. Events with large FRG are expected to be significantly contributed by the single diffractive scattering. The topologies of the considered pomeron–lead and pomeron–proton scattering are shown in Fig. 1, *left* and *right*, respectively, together with the corresponding Feynman diagrams. It should be noted that, due to the high electric charge, the probability for emission of a coherent quasireal photon by the lead ion is significantly high [17, 25–28], and the contribution of ultraperipheral photoproduction (γp) to the events with large FRG is significant. The topology of the photoproduction is identical to the one of the pomeron–proton scattering and these kinds of events cannot be disentangled in the analysis.

The distribution of the FRG sizes is done in bins of half-unit of pseudorapidity for both event topologies. To enhance the sensitivity to the events with large rapidity gaps, the distributions are re-weighted with the probability to have no final state particles in the acceptance of the hadron forward calorimeter [19] covering the pseudorapidity regions $3.0 < |\eta| < 5.2$.

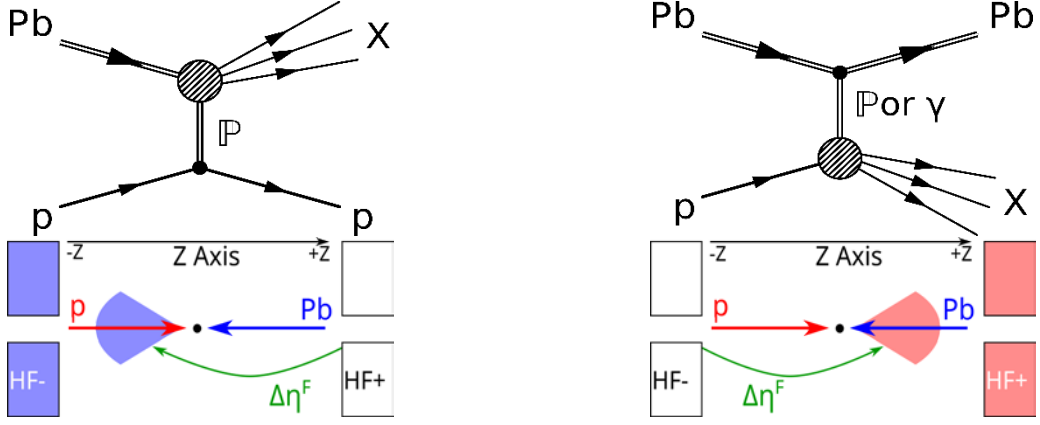


Fig. 1. Diagrams of p -Pb events with large rapidity gaps for pomeron-lead (*left*) and pomeron-proton (*right*) topologies (*top*). Topologies of such events; the *blue (red) cones* indicate the products of diffractive dissociation for the lead ion (proton); the rapidity gaps are marked with *green arrows (bottom)*

3. Results

Figure 2 shows the resulting differential cross-sections corrected for the detector effects and compared to the corresponding predictions of EPOS-LHC [29], HIJING [30] and QGSJET II [31] Monte Carlo event generators. None of them adequately describes the data. The discrepancy between the generator predictions and the data in the case of $\mathbb{P}p$ topology in the range $\Delta\eta^F > 3$ may be explained by a significant contribution of photoproduction events, not accounted for in those generators [32].

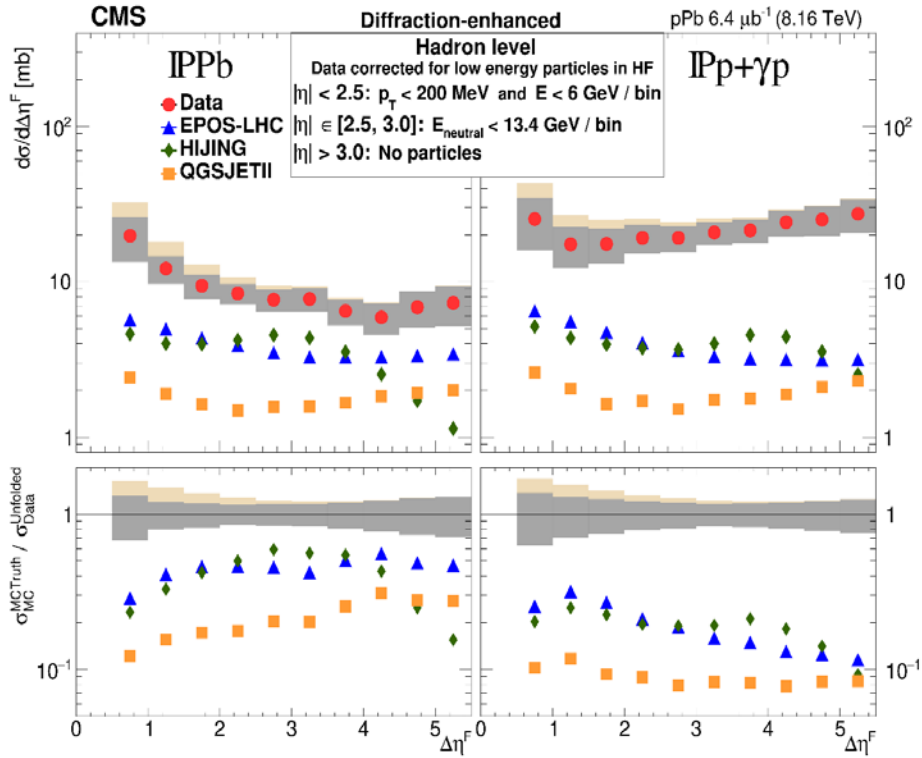


Fig. 2. The hadron level distribution with no energy deposition in the region adjacent to FRG for the CMS data, and the predictions of the EPOS-LHC, QGSJET II and HIJING event generators; the distributions are shown for the pomeron-lead (*left*) and pomeron-proton (*right*) topologies (*top*). Ratios between generator predictions and CMS data (*bottom*)

The cross-section for the pomeron–lead topology, where the photoproduction contribution is negligible, is described by the event generators much better. EPOS–LHC and QGSJET II predictions have the FRG distribution shape similar to the data. In contrast, HIJING distributions falls rapidly at the high FRG size.

Figure 3 shows the EPOS–LHC and QGSJET II distributions split into non-diffractive (ND), single (SD), central (CD) and double (DD) diffractive scattering contributions. It is seen that the non-diffractive contribution is significantly suppressed (EPOS) or negligible (QGSJET) for large FRG of $\Delta\eta^F > 3$.

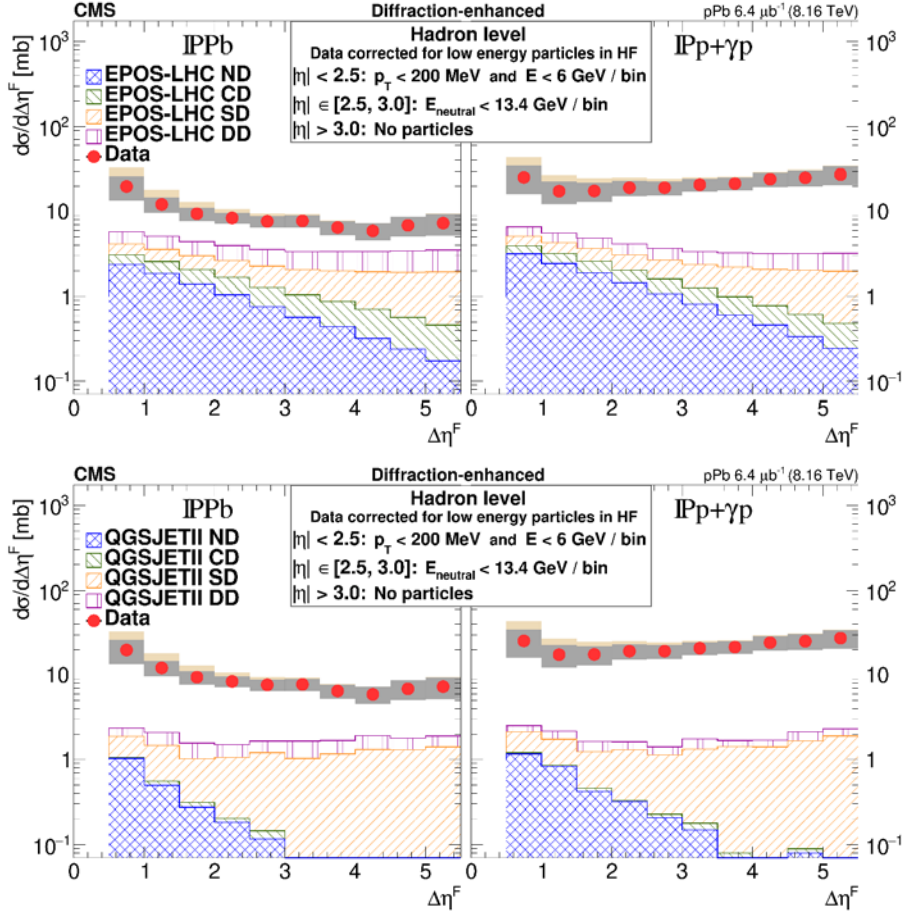


Fig. 3. The hadron-level prediction for the $\Delta\eta^F$ cross section distribution with no energy deposition in the region adjacent to FRG of the EPOS–LHC (*top*) and QGSJET II (*bottom*) event generator for pomeron–lead (*left*) and pomeron–proton (*right*) topologies, splitted down to nondiffractive, single, central and double diffractive components compared with CMS data

In this region, a rough comparison of the measured pomeron–lead cross-section to the pomeron–proton one measured in the CMS proton–proton collisions at 7 TeV centre-of-mass energy [10] can be done to probe its dependence on the nuclear mass A . The ratio has been found to be around $A^{1/3}$, which is compatible with Gribov–Glauber prediction [14, 33] and the HELIOS results.

4. Conclusion

The FRG cross section is measured at 8.16 TeV of the centre-of-mass energy per nucleon pair, what is about 300 times larger than the energy for which such measurements were done in the past. The measurements are performed for both pomeron–lead ($\mathbb{P}Pb$) and pomeron–proton ($\mathbb{P}p + \gamma p$) topologies and compared to the predictions of the EPOS–LHC, QGSJET II, and HIJING event generators. Contribution of γp interactions are not accounted for in those Monte Carlo generators and may be responsible for a large discrepancy between the generator predictions and data observed for the $\mathbb{P}p + \gamma p$ case. For the \mathbb{P} –Pb topology, where the photon-

exchange contribution is expected to be negligible, the EPOS–LHC and QGSJET II predictions are about a factor of 2 to 4 below the data, however describe well the shape of the data distribution.

At large FRG sizes the ratio of the \mathbb{P} –Pb differential cross section compared to that measured for pp collisions at 7 TeV is found to be A^α , where $\alpha \approx 1/3$, as expected in the Glauber–Gribov approach. These results will be helpful to understand the high energy limit of quantum chromodynamics and in modeling cosmic ray air showers.

References

1. V.N. Gribov, JETP Lett. **41**, 667 (1961).
2. G.F. Chew, S.C. Frautschi, Phys. Rev. Lett. **7**, 394 (1961).
3. F.E. Low, Phys. Rev. D **12**, 163 (1975).
4. S. Nussinov, Phys. Rev. Lett. **34**, 1286 (1975).
5. V.S. Fadin, E.A. Kuraev, L.N. Lipatov, Phys. Lett. B **60**, 50 (1975).
6. A.B. Kaidalov, Phys. Rept. **50**, 157 (1979).
7. A. Donnachie, P.V. Landshoff, Nucl. Phys. B **244**, 322 (1984).
8. LHC Forward Physics Working Group Collab., J. Phys. G **43**, 110201 (2016).
9. ATLAS Collab., Eur. Phys. J. C **72**, 1926 (2012).
10. CMS Collab., Phys. Rev. D **92**, 012003 (2015).
11. TOTEM Collab., Eur. Phys. Lett. **96**, 21002 (2011).
12. TOTEM Collab., Eur. Phys. Lett. **101**, 21002 (2013).
13. TOTEM Collab., Eur. Phys. J. C **79**, 103 (2019).
14. V.N. Gribov, Sov. Phys. JETP **29**, 483 (1969).
15. B.Z. Kopeliovich, I.K. Potashnikova, I. Schmidt, Phys. Rev. C **73**, 034901 (2006).
16. R. Luna, A. Zepeda, C.A. Garcia Canal, S.J. Sciutto, Phys. Rev. D **70**, 114034 (2004).
17. A.J. Baltz, Phys. Rept. **458**, 1 (2008).
18. T. Akesson *et al.*, Z. Phys. C **49**, 355 (1991).
19. CMS Collab., JINST **3**, S08004 (2008).
20. CMS Collab., arXiv:2301.07630.
21. D. Sosnov, J. Phys.: Conf. Ser. **1690**, 012105 (2020).
22. D. Sosnov, Phys. Part. Nucl. **53** (2), 393 (2022).
23. D. Sosnov, SciPost Phys. Proc. **8**, 65 (2022).
24. CMS Collab., JINST **12**, P10003 (2017).
25. CMS Collab., Phys. Lett. B **772**, 489 (2017).
26. CMS Collab., Eur. Phys. J. C **79**, 702 (2019).
27. CMS Collab., Eur. Phys. J. C **79**, 277 (2019).
28. CMS Collab., Phys. Lett. B **797**, 134826 (2019).
29. T. Pierog, I. Karpenko, J. M. Katzy *et al.*, Phys. Rev. C **92**, 034906 (2015).
30. X.-N. Wang, M. Gyulassy, Phys. Rev. D **44**, 3501 (1991).
31. S. Ostapchenko, Phys. Rev. D **83**, 014018 (2011).
32. V. Guzey, M. Strikman, M. Zhalov, Phys. Rev. C **106**, 2 (2022).
33. R.J. Glauber, High-Energy Collision Theory in *Lectures in Theoretical Physics* **1**, 3151959 (1959).

ULTRAPERIPHERAL NUCLEAR COLLISIONS IN ALICE AT THE LARGE HADRON COLLIDER

PNPI participants of the ALICE Collaboration: V.A. Guzey, V.V. Ivanov, A.V. Khanzadeev, E.L. Kryshen, M.V. Malaev, V.N. Nikulin, A.Yu. Ryabov, V.G. Ryabov, Yu.G. Ryabov, V.M. Samsonov, M.B. Zhalov

1. Introduction

An important part of the heavy-ion program at the Large Hadron Collider (LHC) is studies of ultraperipheral collisions (UPCs), when colliding beams intersect at large impact parameters $b \gg R_A + R_B$ (R_A, R_B denote the radii of the involved nuclei). In this case, the short-range strong interaction is suppressed and the reaction proceeds through emission of quasireal photons, which is usually treated in the Waizsäcker–Williams equivalent photon approximation. The high intensity and energy of the photon fluxes result in photon–photon and photon–nucleus (photon–proton) interactions at unprecedentedly high energies allowing one to address open questions of the proton and nucleus structure in quantum chromodynamics (QCD) and to search for signals of new physics. The most interesting results in this field obtained in ALICE with significant contributions of the PNPI scientists during the 2019–2021 period are presented below.

2. Photoproduction of ρ mesons in ultraperipheral collisions of nuclei at the Large Hadron Collider and the effect of Glauber–Gribov nuclear shadowing

The cross section for coherent photoproduction of ρ mesons in ultraperipheral collisions of lead nuclei at $\sqrt{s_{NN}} = 5.02$ TeV has been measured by the ALICE Collaboration in the $y < 0.8$ rapidity interval [1]. Since the large value of the electric charge of the nucleus ($Z = 82$) largely compensates the smallness of the α_{em} fine-structure constant, the process of coherent photoproduction can be accompanied by excitation of the nuclei due to an additional exchange of one or several photons of relatively low energies with the subsequent decay of the nuclei *via* neutron emission. It allows one to measure the photoproduction cross section in the channels with different numbers of neutrons. As an example, the results of the measurement for the cases of 0n0n channel without additional photon exchanges and the XnXn channel which corresponds to the situation when both colliding nuclei become additionally excited are presented in Fig. 1 along with theoretical predictions for these cross sections obtained in different models for the description of coherent photoproduction of light vector mesons on nuclei. A comparison of the theoretical models with the data shows that the approach developed at PNPI [2], which is based on the use of the Gribov–Glauber model for photon nucleus scattering and a modified model of vector meson dominance for the hadron structure of the photon, describes (the *red lines* labeled GKZ [3]) these experimental data with reasonable accuracy.

This model has also been used to describe energy dependence of the coherent photoproduction of ρ mesons in ultraperipheral collisions of nuclei at the LHC, see the upper panel of Fig. 2. Then it is reasonable to use an analogous approach for predictions of the cross section for incoherent photoproduction of ρ mesons in Pb–Pb UPCs in the LHC kinematics [4].

The *lower panel* of Fig. 2 demonstrates that the effect of nuclear shadowing in this process is significant and leads to a factor of 10 suppression of the cross section $\sigma_{\gamma A \rightarrow \rho A'}$ for incoherent photoproduction of ρ mesons on nuclei compared to its estimate in the impulse approximation giving $\sigma_{\gamma A \rightarrow \rho A'} = A\sigma_{\gamma N \rightarrow \rho N}$. In particular, while approximately 70% of the suppression effect comes from the elastic Glauber rescattering, the remaining 30% of the effect originates from the Gribov inelastic shadowing. A comparison of the cross sections predicted in Ref. [4] with those calculated within the STARlight framework, which is commonly used in the data analysis, shows that the approximations used in STARlight overestimate the cross section for incoherent photoproduction of ρ on nuclei by a factor of four compared to the Glauber model calculations.

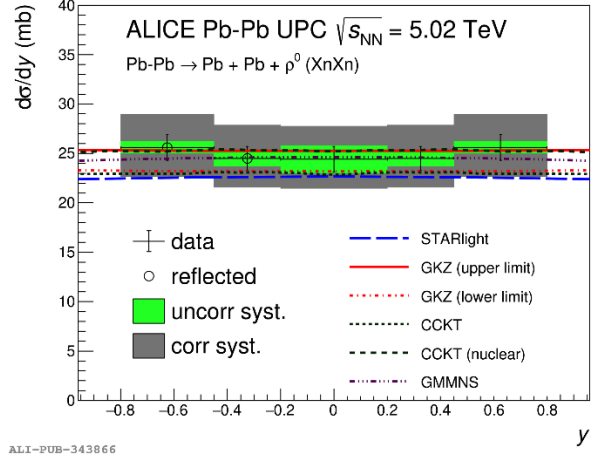
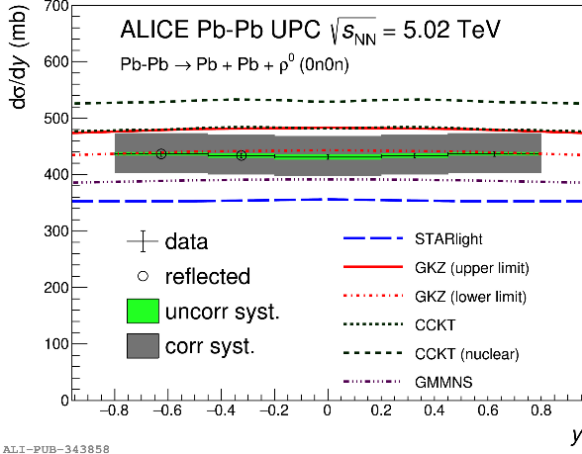


Fig. 1. Comparison of the ALICE measurements of the coherent ρ mesons photoproduction in ultraperipheral collisions of lead nuclei at $\sqrt{s_{NN}} = 5.02$ TeV with theoretical predictions

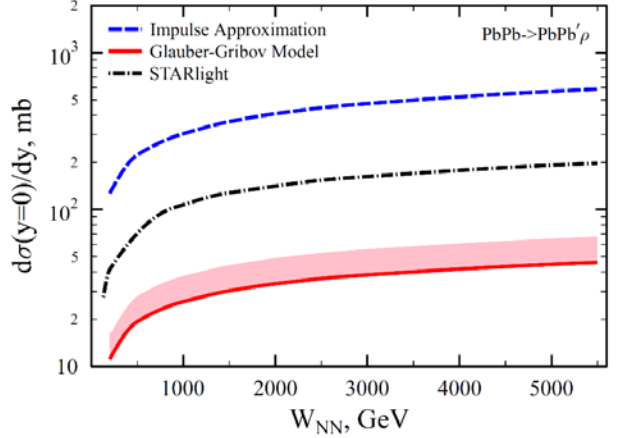
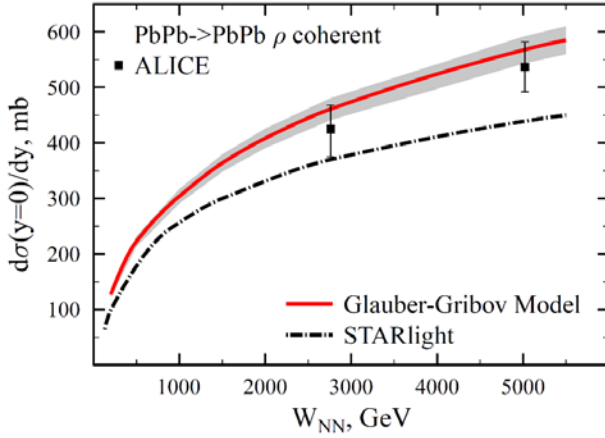


Fig. 2. Comparison of the calculation results of the cross sections for ρ meson photoproduction in Pb–Pb UPCs in the Glauber–Gribov model with those of STARlight, the impulse approximation, and the ALICE data

The ALICE Collaboration has also measured photoproduction of ρ -meson in ultraperipheral Xe–Xe collisions at midrapidity [5]. Since the energy dependence of the γ –Pb cross section is quite mild, a small difference in the centre-of-mass energy in the Pb–Pb and Xe–Xe system can be neglected and the measurements can be used to extract from the ultraperipheral data the A -dependence of the $\gamma A \rightarrow \rho A$ cross section shown in Fig. 3. The trend in the data is quite different from that expected for coherent ρ -photoproduction in the impulse approximation, represented in the figure by the cross section scaling as $A^{4/3}$. The data are compatible with a power-law behaviour A^α with the exponent $\alpha = 0.963 \pm 0.019$, demonstrating clear nuclear shadowing close to that predicted in Refs. [3, 6] in the framework of the Glauber–Gribov model, but still far from the black-disk limit that predicts $A^{2/3}$.

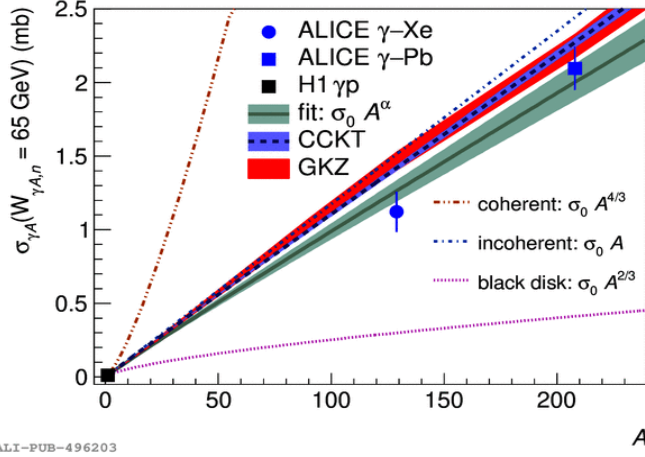


Fig. 3. A -dependence of the coherent $\gamma A \rightarrow \rho A$ cross section and the corresponding power-law fit shown as a band. The general expectations for three extreme cases are represented by the *dashed*, *dotted-dashed* and *dotted* lines, respectively. The *red band* corresponds to the GKZ predictions [3, 6] when varying the parameters of the model

3. Exclusive photoproduction of J/Ψ on nuclei in ultraperipheral collisions at $\sqrt{s_{NN}} = 5.02$ TeV

The soft gluon density in nuclei $G_A(x, \mu^2)$ is a key parameter characterizing properties of high-temperature quark–gluon matter formed in central collisions of ultrarelativistic nuclei. However, the calculation of this distribution from the first principles is hindered due to a significant role of non-perturbative effects. The sizeable effect of nuclear shadowing makes $G_A(x, \mu^2) \neq A G_N(x, \mu^2)$, and the global QCD analyses of nuclear parton distributions are sensitive to the gluon density only through the evolution equations. A promising way to study the small- x gluon distributions in nuclei is offered by the measurement and analysis of quarkonium photoproduction in ultraperipheral collisions of heavy ions at the LHC. The UPC measurements at the LHC were focused on exclusive photoproduction of charmonia (J/ψ , ψ') called to provide new constraints on the nuclear gluon distribution $g_A(x, Q^2)$ at small x (x is the momentum fraction of the nucleus carried by gluons) down to $x \approx 6 \cdot 10^{-4}$. These ALICE measurements [7, 8] of exclusive photoproduction of J/Ψ and $\Psi(2S)$ vector mesons in Pb–Pb UPCs at $\sqrt{s_{NN}} = 5.02$ TeV in the central and forward rapidity interval, which are presented in the form of the UPC cross section integrated over the momentum transfer t for various values of the J/ψ rapidity y , helped to establish a significant suppression of $g_A(x, Q^2)$ at small x compared to its free proton counterpart because of the gluon nuclear shadowing [9]. The measured values agree within reasonable accuracy with the theoretical predictions [3] of the PNPI group (Fig. 4, the *curves* labeled GKZ in the figure).

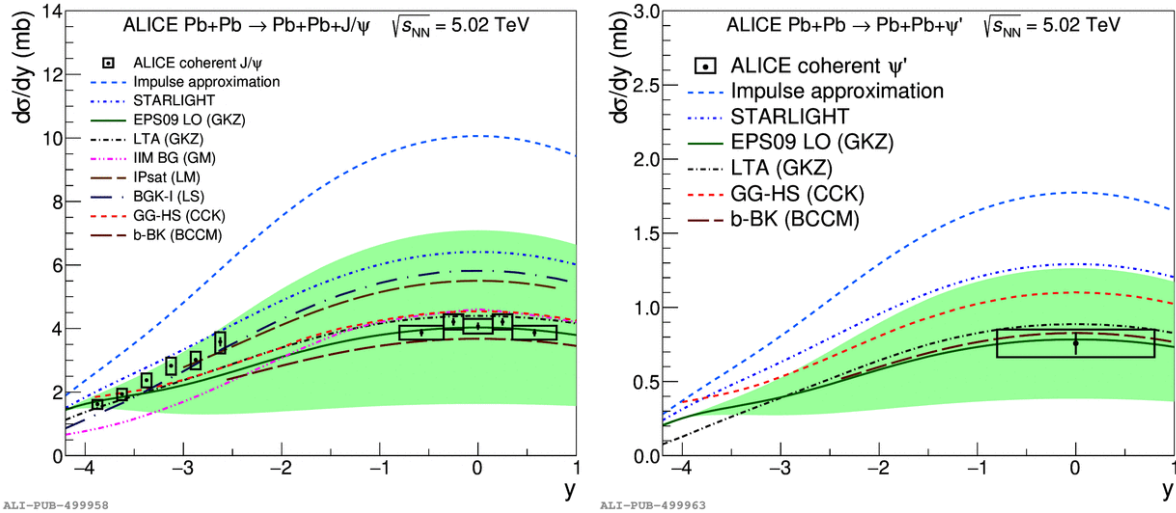


Fig. 4. Comparison of the charmonium photoproduction cross section on Pb measured by ALICE in ultraperipheral Pb–Pb collisions with theoretical predictions. The *shadowed green region* presents uncertainties of the EPS09 nuclear gluon distribution used in the calculations EPS09 LO (GKZ) [3]

Using the ratio of the nucleus and nucleon cross sections, the analysis of these data allowed one practically model-independently to determine the factor of nuclear shadowing $R_g \approx (0.8\text{--}0.9)$ at $0.03 < x < 0.07$ and $R_g \approx 0.6$ at $x \approx 0.001$. Besides, the measured ratio of the $\Psi(2S)$ and J/Ψ photoproduction cross sections in these regions of x is approximately equal to $R = 0.150 \pm 0.018(\text{stat}) \pm 0.021(\text{syst})$, which is close to the predictions of Ref. [3] and practically coincides with the respective cross section ratio for the proton target measured at HERA. Hence, one can conclude that the magnitudes of nuclear shadowing do not significantly differ in these two cases.

4. First measurement of the momentum transfer dependence of coherent J/ψ photoproduction in Pb–Pb UPCs at the Large Hadron Collider and 3D imaging of nuclear gluons

The ALICE Collaboration has for the first time measured the t dependence of coherent J/ψ photoproduction in Pb–Pb UPCs in the central rapidity region $|y| < 0.8$ at 5.02 TeV [10], which corresponds to the small- x range $x \approx (0.3\text{--}1.4) \cdot 10^{-3}$. It extended the previous UPC results at the LHC by providing information on the spatial distribution of nuclear gluons as a function of the impact parameter, which can be readily obtained by a two-dimensional Fourier transform of the measured t dependence. Thus, this measurement gives insight into the three-dimensional structure of the nuclear gluon distribution. Figure 5 shows the ALICE results for the t dependence of the photonuclear cross section in six bins of t . The data clearly deviate from the t dependence given by the nuclear form factor squared $|F_A(t)|^2$ (shown by the *blue solid curve*), which is implemented in the commonly used Monte Carlo generator STARlight.

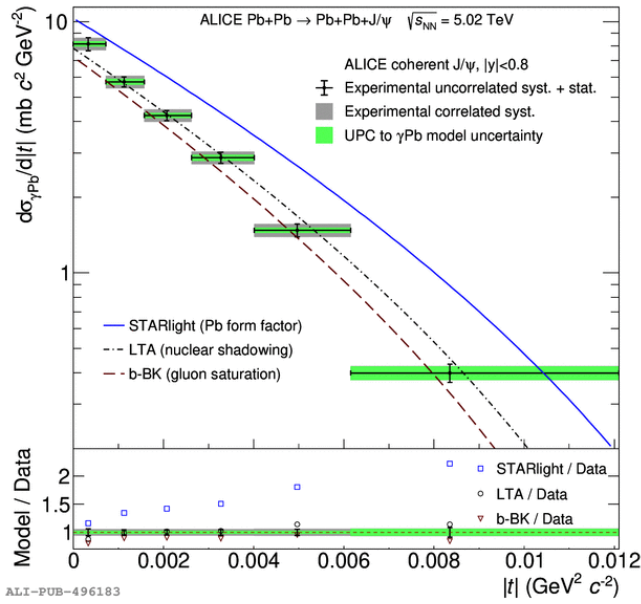


Fig. 5. Comparison of the momentum transfer dependence of coherent J/ψ photoproduction in Pb–Pb UPCs measured by ALICE with theoretical predictions

At the same time, the ALICE data agree well with predictions of two theoretical approaches, where the effect of nuclear shadowing is correlated with the t dependence. In the approach developed at PNPI [11], which is based on the leading twist approximation (the *dot-dashed curve* labeled “LTA”), the nuclear shadowing is stronger at small impact parameters closer to the centre of the nucleus because of the stronger nucleon overlap (higher nuclear density) there. This leads to broadening of the gluon distribution in the impact parameter space, which translates into a modified, narrower t dependence [11] compared to that given by $|F_A(t)|^2$. A similar trend is predicted in the approach based on the colour dipole model, where the scattering amplitude is obtained from the impact-parameter dependent solution of the Balitsky–Kovchegov equation, which incorporates gluon saturation effects (the *red dashed curve* labeled “b–BK”). The *lower panel* of the figure presents the ratio of the model predictions to the data.

These results indicate that the nuclear gluon distribution is different from that in the free proton both in the space of x and the impact parameter and, hence, pave the way to a 3D imaging of nuclear gluons using coherent photoproduction of charmonia at the LHC.

5. Photoproduction of J/Ψ mesons in ultraperipheral proton–nucleus scattering at the Large Hadron Collider

Ultraperipheral collisions in proton–nucleus scattering, where the nucleus serves as an intensive source of quasireal photons and the proton plays the role of the target, give an opportunity to study photon–proton interactions at unprecedentedly high energies at the LHC. Taking advantage of unique capabilities of the ALICE detector, the cross section for J/Ψ photoproduction on the proton in the interval of photon–proton energies from 50 to 500 GeV has been determined using the analysis of the data collected in 2019 [12]. In the framework of the perturbative QCD, the cross section for this process is determined by the gluon density in the proton.

Figure 6 presents a comparison of the obtained cross section with the results of theoretical calculations employing the next-to-leading order (NLO) of the Balitsky–Fadin–Kuraev–Lipatov (BFKL) approximation and the approach of the colour glass condensate (CGC) with the gluon density saturation. An analysis of these data allows one to significantly reduce the uncertainty in the small- x gluon density in the nucleon.

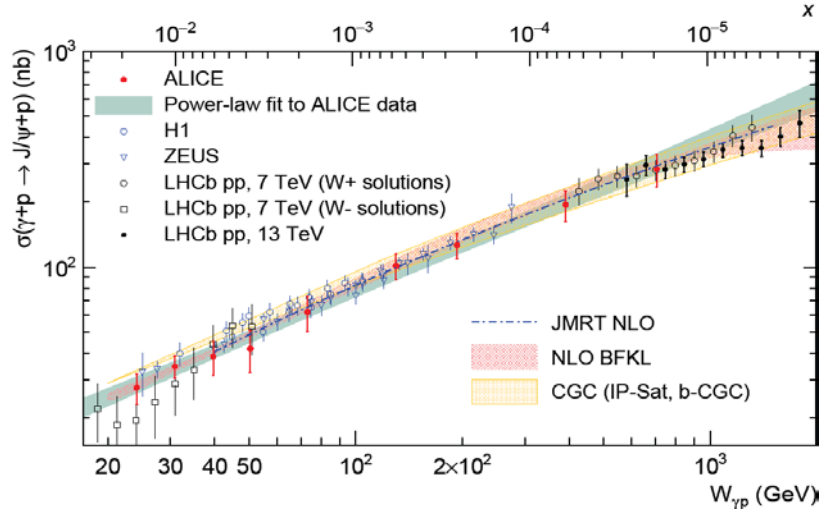


Fig. 6. Comparison of the world data on the energy dependence of coherent photoproduction of charmonium on proton with theoretical predictions. The ALICE cross sections extracted from the ultraperipheral Pb– p collisions are shown by *red circles*

6. Conclusion

The measurements described in the preceding sections can still be improved substantially with the data samples expected from the LHC Run-3 and Run-4, which are expected to be at least three orders of magnitude larger than those from Run-2. This huge increase in the available number of events will not only reduce the statistical errors but will also allow for a series of studies to reduce systematic uncertainties. The expected data samples will also permit one to explore multidimensional versions of the current observables, as well as to study new signatures beyond the reach of the current data that will advance our understanding of fundamental properties of physics of strong interactions.

References

1. ALICE Collab., S. Acharya *et al.*, JHEP **06**, 035 (2020).
2. L. Frankfurt, V. Guzey, M. Strikman, M. Zhalov, Phys. Lett. B **752**, 51 (2016).
3. V. Guzey, E. Kryshen, M. Zhalov, Phys. Rev. C **83**, 055206 (2019).
4. V. Guzey, E. Kryshen, M. Zhalov, Phys. Rev. C **102** (1), 015208 (2020).
5. ALICE Collab., S. Acharya *et al.*, Phys. Lett. B **820**, 136481 (2021).
6. V. Guzey, E. Kryshen, M. Zhalov, Phys. Lett. B **782**, 251 (2018).
7. ALICE Collab., S. Acharya *et al.*, Phys. Lett. B **758**, 134926 (2019).
8. ALICE Collab., S. Acharya *et al.*, Eur. Phys. J. C **81** (8), 712 (2021).
9. V. Guzey, E. Kryshen, M. Strikman, M. Zhalov, Phys. Lett. B **816**, 136202 (2021).
10. ALICE Collab., S. Acharya *et al.*, Phys. Lett. B **817**, 136280 (2021).
11. V. Guzey, M. Strikman, M. Zhalov, Phys. Rev. C **95** (2), 025204 (2017).
12. ALICE Collab., S. Acharya *et al.*, Eur. Phys. J. C **79** (5), 402 (2019).

THE HADRONIC PHASE LIFETIME DURING THE EVOLUTION OF EXTREME STATES OF MATTER IN COLLISIONS OF ULTRARELATIVISTIC NUCLEI AT THE LARGE HADRON COLLIDER

PNPI participants of the ALICE Collaboration: V.V. Ivanov, A.V. Khanzadeev, E.L. Kryshen, M.V. Malaev, V.N. Nikulin, A.Yu. Ryabov, V.G. Ryabov, Yu.G. Ryabov, V.M. Samsonov, M.B. Zhalov

Heavy-ion collisions are used to study properties of the strongly interacting matter at high temperatures and baryon densities where the focus is on formation of a new state of matter – the quark–gluon plasma (QGP). This is a state of the strongly interacting matter in which the dominant degrees of freedom are quarks and gluons in a relatively large volume exceeding the size of a nucleon. The QGP leaves and evolves for some time and then hadronize. Properties of the QGP cannot be measured directly, since it is produced for a tiny period of time. Instead, they are inferred from the measurements of the final state particles, such as their yields, angular distributions and correlations. Properties of the final state particles are affected in the late hadronic phase; the particles can rescatter, be absorbed there or newly produced. Unambiguous interpretation of the measured signatures of the phase transition requires a full understanding of the hadronic phase.

Resonances come at help because they provide the means to directly probe the hadronic phase properties. Abundancies of the long-lived particles are fixed at chemical freeze-out. However, interactions between hadrons continue between the chemical and kinetic freeze-out. In contrast to stable particles, a part of the short-lived resonances decays right after the chemical freeze-out or even earlier. The fraction of the decayed resonances depends on their lifetime, the smaller the lifetime the larger the fraction of the decayed resonances. The daughter particles continue to interact with the surrounding hadrons between the chemical and kinetic freeze-out. For example, one of the daughter particles can rescatter elastically. As a result, the angular correlation between the daughter particles gets broken and the parent resonance cannot be reconstructed because the invariant mass of the daughter particles will not be consistent with the resonance mass in vacuum. Another case is when one of the daughter particles is absorbed in pseudoeelastic scattering. The consequence is the same, the parent resonance is not reconstructed because the reconstruction would require both daughter particles in the final state. However, there is an opposite process of regeneration that occurs when two background hadrons regenerate and form a new resonance. This process increases the number of reconstructed resonances. As a result, the resonance yields measured in heavy-ion collisions are defined by their yields at chemical freeze-out as well as by hadronic processes occurring between chemical and kinetic freeze-out which are often referred to as rescattering and regenerations.

The cumulative effect of the hadronic phase for resonances depends on the lifetime and density of the hadronic phase, the resonance lifetime and scattering cross-sections (on the type of daughter particles and density). The hadronic phase lifetime and density do not depend on the resonance type. Hence, these parameters can be probed with resonances, which have comparable but yet different lifetimes. Properties of the resonances that are most often measured in heavy-ion collisions are shown in Table [1]. The resonance lifetimes vary in a wide range from ~ 1 fm/c for $\rho(770)^0$ up to ~ 45 fm/c for $\phi(1020)$ and hence each of the resonances should have different sensitivity to the hadronic phase. The shorter the lifetime, the larger the fraction of resonances decays, and to a greater extent it is affected by rescattering of daughter particles in the hadronic phase. The longer the lifetime, the smaller the fraction of decayed resonances and the smaller the effect of the hadronic phase.

In practice, properties of the hadronic phase are studied by measuring the ratios of the resonance yields (p_T -integrated) to the yields of long-lived particles with similar quark contents: $\rho(770)^0/\pi$, $K^*(892)/K$, $\phi(1020)/K$, $\Lambda(1520)/\Lambda$, $\Sigma(1385)^{\pm}/\Lambda$ and $\Xi(1530)^0/\Xi$. The ratios are measured as a function of the final state charged-particle multiplicity in pp (reference system), p - A (intermediate) and $A + A$ (heavy-ion) collisions. The variation of the ratios with multiplicity probes the interplay between the rescattering and regeneration effects in the hadronic phase, which changes the reconstructed yields of resonances in the opposite way. The modifications of the resonance properties in the hadronic phase have been studied experimentally. The most advanced measurements for resonances in heavy-ion collisions have been carried out by the STAR

experiment at Relativistic Heavy Ion Collider at the collision energy of $\sqrt{s_{NN}} = 200$ GeV [2–10] and by the ALICE experiment at the Large Hadron Collider (LHC) at an order of magnitude higher collision energies of $\sqrt{s_{NN}} = 2.76$ and 5 TeV [11–21] as shown in Fig. 1.

Table

Properties of hadronic resonances

Particle	Mass, MeV/c ²	Width, MeV/c ²	Quarks	Decay	BR, %
$\rho(770)^0$	770	150	$\frac{u\bar{u} + d\bar{d}}{\sqrt{2}}$	$\pi^+\pi^-$	100
$K^*(892)^\pm$	892	50.3	$u\bar{u}, \bar{u}s$	$\pi^\pm K_s^0$	33.3
$K^*(892)^0$	896	47.3	$d\bar{s}$	$\pi^\pm K^\pm$	66.7
$\phi(1020)$	1 019	4.3	$s\bar{s}$	K^+K^-	48.9
$\Delta(1232)^{++}$	1 232	117	uuu	$p\pi^+$	99.4
$\Sigma(1385)^+$	1 383	36	uus	$\pi^+\Lambda$	87
$\Sigma(1385)^-$	1 387	39.4	dds	$\pi^-\Lambda$	87
$\Lambda(1520)$	1 520	15.7	uds	K^-p	22.5
$\Xi(1530)^0$	1 532	9.1	uss	$\pi^+\Xi^-$	66.7

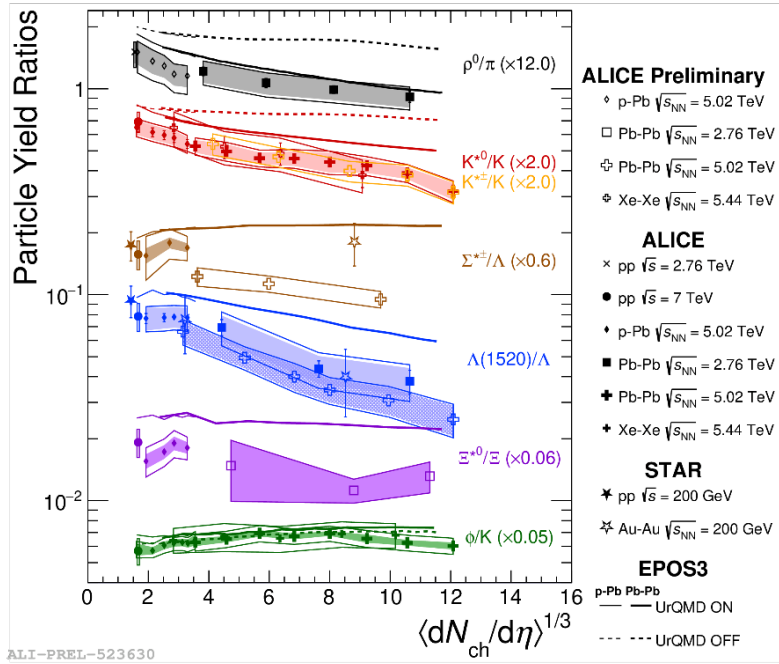


Fig. 1. Summary of particle yield ratios, $\rho(770)^0/\pi$, $K^*(892)^0/K$, $\Sigma(1385)^\pm/\Lambda$, $\Lambda(1520)/\Lambda$, $\Xi(1530)^0/\Xi^-$ and $\phi(1020)/K$ as a function of multiplicity in pp , p -Pb, Xe-Xe and Pb-Pb collisions at $\sqrt{s_{NN}} = 2.76$ –7 TeV and in pp and Au-Au collisions at $\sqrt{s_{NN}} = 200$ GeV, with comparison to EPOS3

Regardless of the huge difference in the collision energies, the results obtained for the resonances are quite similar, although not identical. The production of the three shortest-lived resonances, such as $\rho(770)^0$,

$K^*(892)^0$ and $\Lambda(1520)$ is suppressed in central heavy-ion collisions. For $\rho(770)^0$ and $K^*(892)^0$ the suppression gradually increases with multiplicity. These are two particles with lifetimes smaller than 5 fm/c. The production of $\Lambda(1520)$ is not suppressed in pp and p -Pb collisions, the suppression emerges only in central heavy-ion collisions. Measurements for $\Xi(1530)^0$ are not conclusive because of large uncertainties but hint a suppression in central collisions. And finally, the production of the longest-lived $\phi(1020)$ resonance is not affected by multiplicity, it behaves like a pseudo stable particle, which mostly decays after kinetic freeze-out. The suppression observed at high final state multiplicities for $\rho(770)^0$, $K^*(892)^0$, $\Lambda(1520)$ and probably for $\Xi(1530)^0$ is explained by rescattering processes in the hadronic phase taking over regeneration. The measurements have been compared to model calculations, which take into account the late hadronic phase. The EPOS3 with the UrQMD-based hadronic phase afterburner [22] qualitatively and numerically reproduces the observed effects for resonances and fails if the hadronic phase is switched off. Results obtained for different resonances at the LHC support the existence of a long-lived hadronic phase that causes a noticeable reduction of the reconstructed yields of the resonances.

Figure 2 shows the obtained lifetime of the hadronic medium in nucleus–nucleus and proton–nucleus collisions at $\sqrt{s_{NN}} = 5.02$ TeV as a function of the multiplicity of produced charged hadrons. One can see that at high multiplicities, which are characteristic of events with formation of the QGP, the lifetime of the hadronic phase in central heavy-ion collisions at the LHC was estimated to be (4–7) fm/c [23], which is about four times longer than the lifetime of $\rho(770)^0$ (1.3 fm/c), comparable or slightly longer than the lifetime of $K^*(892)^0$ (4.16 fm/c), much shorter than the lifetime of $\phi(1020)$ which is about 45 fm/c and reaches the values comparable to that of the QGP estimated from the data analysis at the same energy of Pb–Pb collisions at the LHC.

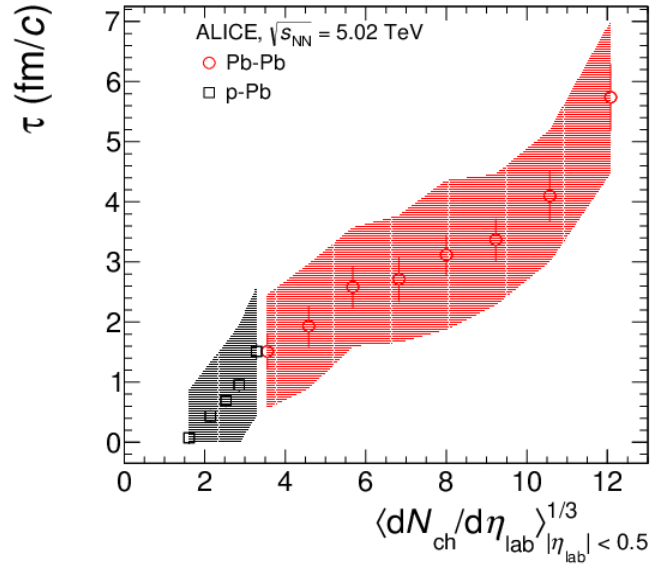


Fig. 2. Lower limit on the hadronic phase lifetime between chemical and kinetic freeze-out as a function of charge particle multiplicity in p -Pb and Pb-Pb collisions at $\sqrt{s_{NN}} = 5.02$ TeV [23]. The bars and bands represent the statistical and systematic uncertainties, respectively, propagated to the lifetime from the uncertainties associated with the measured yields

References

1. P.A. Zyla *et al.*, Prog. Theor. Exp. Phys. **2020** (8), 083C01 (2020).
2. J. Adams *et al.*, Phys. Rev. C **71**, 064902 (2005).
3. M.M. Aggarwal *et al.*, Phys. Rev. C **84**, 034909 (2011).
4. B.I. Abelev *et al.*, Phys. Rev. C **78**, 044906 (2008).
5. M.M. Aggarwal *et al.*, Phys. Rev. C **83**, 034910 (2011).
6. C. Adler *et al.*, Phys. Rev. C **65**, 041901(R) (2002).
7. B.I. Abelev *et al.*, Phys. Rev. C **79**, 064903 (2009).
8. J. Adams *et al.*, Phys. Lett. B **612**, 181 (2005).
9. B.I. Abelev *et al.*, Phys. Rev. C **79**, 064903 (2009).
10. B.I. Abelev *et al.*, Phys. Rev. Lett. **97**, 132301 (2006).
11. B. Abelev *et al.*, Phys. Rev. C **91**, 024609 (2015).
12. J. Adams *et al.*, Eur. Phys. J. C **76**, 245 (2016).
13. J. Adams *et al.*, Phys. Rev. C **95**, 6, 064606 (2017).
14. D. Adamova *et al.*, Eur. Phys. J. C **77**, 6 389 (2017).
15. S. Acharya *et al.*, Eur. Phys. J. C **80**, 2 160 (2020).
16. S. Acharya *et al.*, Phys. Rev. C **99**, 024905 (2019).
17. S. Acharya *et al.*, Phys. Rev. C **99**, 6, 064901 (2019).
18. S. Acharya *et al.*, Phys. Rev. C **106**, 034907 (2022).
19. S. Acharya *et al.*, Phys. Lett. B **828**, 137013 (2022).
20. S. Acharya *et al.*, Phys. Rev. C **102**, 024912 (2020).
21. S. Acharya *et al.*, Phys. Lett. B **807**, 135501 (2020).
22. A.G. Knospe *et al.*, Phys. Rev. C **93**, 014911 (2016).
23. S. Acharya *et al.*, Phys. Lett. B **802**, 135225 (2020).

GENERALIZATION OF SUDAKOV FORM FACTOR FOR SKEWED KINEMATIC REGIME

V.T. Kim

It is impossible in quantum field theory to overestimate the role of Sudakov's pioneer method [1] for summing leading logarithmic corrections in all orders of perturbative theory. Let us start with recalling the classical result of Ref. [1] for photon–electron vertex Γ_μ , the so-called double logarithmic Sudakov form factor, introducing our notations along the way. One can set the sum of all three momenta to zero without loss of generality, so the three-point amplitude has only two independent variables. Let also $\Gamma_\mu(p, p')$ be a connected three-point amplitude of massless quantum electrodynamics (QED) renormalized with minimal subtractions. Here p and p' are the momenta of the incoming and outgoing electrons, respectively. The use of the connected amplitude will be technically important for our consideration to include self-energy corrections to one of the external electron legs of $\Gamma_\mu(p, p')$. The overall factor with electron charge, *i. e.*, is also excluded from the definition of $\Gamma_\mu(p, p')$. Due to this, the expansion of $\Gamma_\mu(p, p')$ in the coupling starts with Dirac γ -matrix, $\Gamma_\mu(p, p') = \gamma_\mu + \dots$.

To avoid infrared problems, one considers $\Gamma_\mu(p, p')$ at negative virtualities of the external electrons, $p^2 < 0$, $p'^2 < 0$, and of the external photon, $(p' - p)^2 < 0$. The results of Ref. [1] are for the kinematics when, on top of the above restrictions, the Minkowski product of the electron momenta satisfies the inequality preventing Wick rotation, $(pp')^2 > p^2 p'^2$. These combined conditions imply that if $|p^2|$ and $|p'^2|$ are small with respect to $|(p - p')^2|$, then $pp' > 0$. Hereafter, two positive variables will be used to describe this kinematics:

$$x = \frac{-p^2}{2pp'} > 0 \quad \text{and} \quad y = \frac{-p'^2}{2pp'} > 0. \quad (1)$$

With the notations introduced, the celebrated Sudakov's result [1] reads

$$\Gamma_\mu(p, p') \approx \gamma_\mu \exp\left(-\frac{\alpha}{2\pi} \log(x) \log(y)\right), \quad (2)$$

where the approximate equality holds when both $|p^2|$ and $|p'^2|$ are small with respect to $|(p' - p)^2|$, and their ratio is of the order of unity. Also, α is the fine structure constant normalized at any of the small virtualities.

In Ref. [2], a generalization of approximate Eq. (2) was derived valid in a wider region where the magnitude of only one of the two electron virtualities is small with respect to the magnitude of the virtuality of the photon. Since the symmetry between the two electron virtualities present in the Sudakov regime is lost in this generalization, one can call this generalized regime as the skewed Sudakov regime. For definiteness, one considers the kinematics with $|p^2|$ small with respect to the magnitude of the photon virtuality, and no restrictions on $|p'^2|$ are present. All the considerations can be repeated with the obvious changes for the case when $|p'^2|$ is small instead of $|p^2|$.

After the external electron with small virtuality magnitude is specified, one can also specify the external electron leg of $\Gamma_\mu(p, p')$ with self-energy corrections included – it is the leg of small virtuality. Also, as before, the fine structure constant in the subsequent formulas is normalized at the small virtuality.

To write down a generalization of approximation (2), one can introduce the following variables:

$$t = -\frac{\alpha \log(x)}{2\pi} \quad \text{and} \quad z = \frac{1}{1+y}. \quad (3)$$

Note that $0 < z < 1$, and in the Sudakov regime $z \rightarrow 1$. With these variables the approximation valid in the skewed Sudakov regime reads

$$\Gamma_\mu(p, p') \approx \gamma_\mu F(t, z) + \frac{p_\mu \hat{p}'}{pp'} \left[e^{t/2} - F(t, z) \right], \quad (4)$$

where the form factor $F(t, z)$ is as follows:

$$F(t, z) = e^{3t/2} \sum_{n=0}^{\infty} e^{-tH_{n+1}} z^n (1-z). \quad (5)$$

Here H_{n+1} are the harmonic numbers,

$$H_k = \sum_{i=1}^k \frac{1}{i}. \quad (6)$$

It has been pointed out in Ref. [2] that the series in the right hand side of Eq. (5) converges at $|z| < 1$, and to recover approximation (2), one has to send $z \rightarrow 1$, where the convergence fails.

To overcome this difficulty, one can derive from Eq. (5) the following representation:

$$F(t, z) = e^{3t/2} \left[1 + \frac{1}{z} \sum_{\underline{s}} \frac{(-t)^{|\underline{s}|}}{\underline{s}!} Li_{\underline{s}}(z) \right], \quad (7)$$

where the sum runs over strings of positive integers of arbitrary depth d , $\underline{s} = (s_1, s_2, \dots, s_d)$; $|\underline{s}|$ denotes the weight of the string,

$$|\underline{s}| = \sum_{i=1}^d s_i,$$

and the factorial of the string is the product of the factorials,

$$\underline{s}! = \prod_{i=1}^d s_i!.$$

The key ingredient of representation (7) is the so called multiple polylogarithm $Li_{\underline{s}}(z)$. See, *e. g.*, Ref. [3] for an introductory exposition of these functions, and Refs. [4, 5] for their recent applications to Feynman integrals.

Using the properties of multiple polylogarithms discussed in Ref. [3], one can single out the terms of the sum of Eq. (7) most singular in the limit $z \rightarrow 1$. ‘‘Most singular’’ means that each power of t is compensated by a power of $\log(1 - z)$. These are the terms with the strings \underline{s} consisting of units, $\underline{s}_d = (1, \dots, 1)$, with the unit repeated $d = |\underline{s}|$ times. Explicitly,

$$Li_{\underline{s}_d}(z) = (-\log(1 - z))^d / d! \approx \frac{(-\log(y))^d}{d!}. \quad (8)$$

Using this and taking into account that \hat{p}' is small in the Sudakov regime, one reproduces approximation (2) from approximation (4).

On the other hand, at fixed $z < 1$ and large t one picks up the infinitely growing term in Eq. (5) and obtains the following approximation valid at $x \rightarrow +0$ and $y > 0$ fixed:

$$\Gamma_{\mu}(p, p') \approx \frac{y}{(1+y)x^{\frac{\alpha}{4\pi}}} \left[\gamma_{\mu} + 2 \frac{p_{\mu} \hat{p}'}{-p'^2} \right]. \quad (9)$$

Therefore, one concludes that Eqs. (4) and (5) give a unified description for qualitatively different asymptotic of the vertex, one of which coincides with the known Sudakov asymptotic.

The validity of approximations (4, 5), and representation (7) are the main results of paper [2]. The one-loop approximation [7] of the Sudakov form factor in the skewed regime agrees with the result of Ref. [2]. In papers [2, 7] one can find details of the way these results were derived. The introduction of the inclination variable in Refs. [2, 7] was one of the essential technical points in the derivation of the Sudakov form factor in the skewed kinematic regime.

In conclusion, a generalizing Eq. (4) has been derived from the Sudakov approximate Eq. (2) in QED for a wider kinematic range. The generalization of Eq. (2) is valid in an extended region, where the magnitude of only one of the two electron virtualities is small with respect to the magnitude of the virtuality of the photon (skewed Sudakov regime). Considering the abundant literature (see, *e. g.*, [8–10]) derived in various ways from Ref. [1], one may envisage a scientific program trying to give a skewed version to any result descending from the original paper [1].

Our subjective choice for the sequence of these possible generalizations is as follows: first, one may try to study the skewed asymptotic for non-abelian gauge theories [8], second, the subleading corrections [9], third, the phenomenology [10].

The idea of papers [2, 7] belongs to Lev N. Lipatov and Grigorii B. Pivovarov, who passed away in 2017 and 2020, respectively.

References

1. V.V. Sudakov, Sov. Phys. JETP **3**, 65 (1956); Zh. Eksp. Teor. Fiz. **30**, 87 (1956).
2. V.T. Kim, V.A. Matveev, G.B. Pivovarov, Phys. Rev. D **99**, 025016 (2019), arXiv:1812.07269 [hep-th].
3. M. Waldschmidt, Multiple Polylogarithms: An Introduction, in *Number Theory and Discrete Mathematics* (2002).
4. S. Weinzierl, IRMA Lect. Math. Theor. Phys. **15**, 247 (2009), arXiv:075.0900 [hep-ph].
5. C. Brogner, F. Brown, PoS LL **2012**, 053 (2012), arXiv:1209.6524 [hep-ph].
6. C. Brogner, S. Weinzierl, Int. J. Mod. Phys. A **25**, 2585 (2010), arXiv:1002.3458 [hep-ph].
7. V.T. Kim, G.B. Pivovarov, Phys. Part. Nucl. Lett. **16**, 530 (2019).
8. A. Sen, Phys. Rev. D **24**, 3281 (1981).
9. G.P. Korchemsky, Phys. Lett. B **220**, 629 (1989).
10. A.J. Larkoski, S. Marzani, J. Thaler, Phys. Rev. D **91** (11), 111501 (2015), arXiv:1502.01719 [hep-ph].

BENT CRYSTALS FOR SPS AND LARGE HADRON COLLIDER BEAMS

Yu.M. Ivanov, A.S. Denisov, Yu.A. Gavrikov, B.L. Gorshkov, M.A. Koznov, L.P. Lapina, L.G. Malyarenko, V.I. Murzin, L.F. Pavlova, V.V. Skorobogatov, L.A. Vaishnene

1. Introduction

For more than a decade, the UA9 Collaboration in cooperation with the CERN Accelerator and Technology Sector (ATS) extensively studied channeling in bent silicon crystals at the CERN super proton synchrotron (SPS) and Large Hadron Collider (LHC) to adopt bent crystals for high-energy beam collimation. Successful construction and operational tests of the crystal-assisted collimation prototype set-ups in the SPS and LHC have fully demonstrated the feasibility of crystal assisted collimation in hadron colliders [1]. Now this approach becomes a base line to increase luminosity of the LHC. As an important achievement on this way, Fig. 1 shows crystal collimators designed and produced at PNPI for the LHC collimation system.



Fig. 1. The LHC crystal collimators designed and produced at PNPI

The crystal studies performed by the UA9 Collaboration cover main effects of high-energy beam-crystal interactions: channeling, volume reflection, volume capture, dechanneling, inelastic nuclear interaction, multiple scattering, degradation of crystalline lattice, that are crucial for deep understanding of processes inside bent crystals to develop bent crystal applications to high-energy beam steering, focusing and extraction. Here we present some recent results of these studies obtained with participation of PNPI researchers.

2. Electrostatic septum shadowing by means of a bent crystal to reduce slow extraction beam losses

The beam extraction based on electrostatic septum is a well proved technology widely implemented in circulating beam accelerators including the CERN SPS. With the present extraction method and efficiency, the annually achievable extracted flux will soon be limited to well below the total flux that the SPS could potentially deliver because of the increased radiation levels in the slow extraction segment. It is a key for the future increase of proton extraction fluxes by a factor of four requested in the framework of the SPS beam dump facility and search for hidden particles (SHiP) prototype target tests. Increases in the residual activation would impose significantly longer cool-down duration before any intervention, which has the impact on operational beam availability and delays in experiments requiring test beams. One of the most promising technological fields to substantially reduce the beam losses and equipment activation during slow extraction is the use of bent silicon crystals for assisting the beam extraction or directly for beam extraction.

Before implementation of crystals for beam extraction, a set of simulations were performed at CERN to determine the optimal crystal parameters and the location of the crystal in the slow extraction region. Two configurations were considered for prototyping of the crystal shadowing concept at the SPS: local shadowing – with a crystal located directly upstream of the extraction septum and essentially aligned with it inside the same

extraction bump, and non-local shadowing – with a crystal located some betatron wavelengths upstream of the extraction septum and inside a separate closed-orbit bump. The non-local scheme simplifies optics requirements for the beam extraction to fixed target CERN experimental North Area but requires additional hardware upgrades and developments.

An experiment demonstrating the feasibility of using a bent crystal aligned upstream of an extraction electrostatic septum (ES) located at the long straight section 2 (LSS2) to increase the efficiency of the third-integer resonant slow extraction process was carried out at the SPS. In the local shadowing scheme, the electrostatic septum deflects large amplitude particles out of the circulating beam aperture and into the external transfer line. The beam envelope during slow extraction in the LSS2 is shown in Fig. 2, where the largest amplitude particles can be seen leaving the SPS ring toward the electrostatic septum and further toward the magnetic septum. The crystal can shadow the anode wires of the septum by deviating into the extraction channel the particles that would otherwise impinge on the anode wires and effectively reduce losses at the ES.

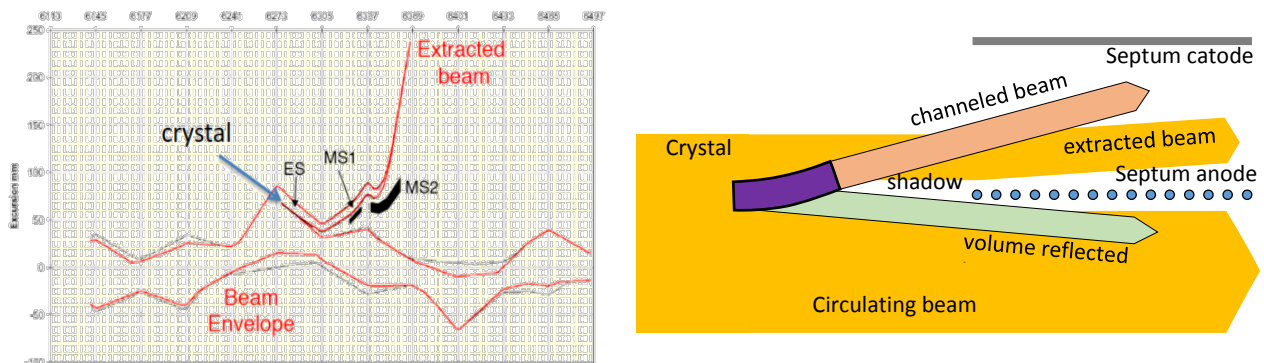


Fig. 2. A working principle of the crystal assisted local shadowing of the slow extraction system: *left* – the layout of beams in the extraction region; *right* – schematic principle of septum anode wires shadowing; ES – lectrostatic septum; MS – magnetic septum

The optimal parameters of a bent silicon crystal required for local shadowing are the following: 2 mm length in beam direction, 0.78 mm thickness across the beam, bending angle near $175 \mu\text{rad}$, and torsion less than $1 \mu\text{rad}/\text{mm}$. The bending device should provide a 35 mm vertical opening and at least 35 mm horizontal clearance from the crystal to the holder. Figure 3 shows a new set of crystal devices for the SPS [2] developed at PNPI on the base of the design successfully implemented earlier in the LHC collimation system.

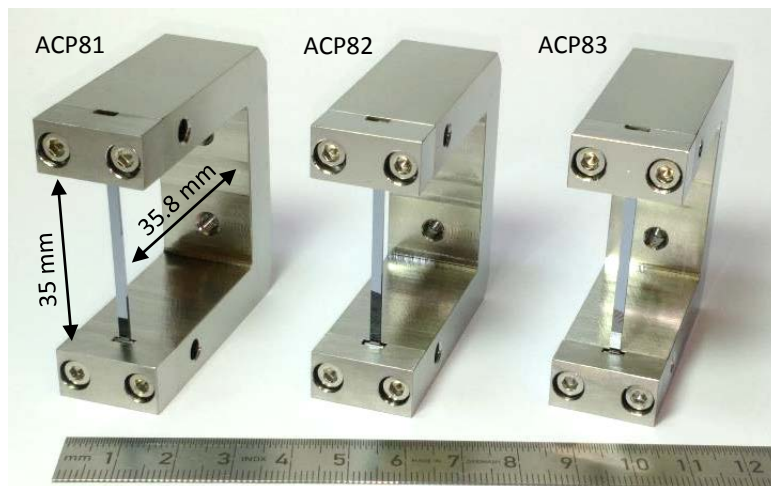


Fig. 3. Crystal devices developed and assembled by PNPI for the electrostatic septum local shadowing experiment in the SPS. Crystal bending of (110) planes are based on the anticlastic effect

The UA9 Collaboration equipped a test facility in the SPS H8 test beam line at the North Area with an experimental apparatus to measure the crystal bending angle, the channeling efficiency and the torsion. All devices fulfilled requirements and demonstrated high stiffness, high long-term stability and robustness in extensive tests prior of installation.

Since particle deflection with good efficiency is achieved only when the crystal lattice is aligned within $10 \mu\text{rad}$ to the trajectory of the incoming particles at $p = 400 \text{ GeV}/c$, a compact goniometer was built to allow the correct angular alignment of the crystal with a precision of a few μrad . The motion system consists of two precise linear shift mechanisms: one is used to position the crystal transversely and the second one to rotate the crystal at a certain position. The suitable location for the crystal in the LSS2 with a very limited longitudinal space available was identified $\sim 5 \text{ m}$ upstream of the ES separated by a wide-aperture focusing quadrupole with 4° of betatron phase advance from the crystal to the ES. The design, production and integration of precise goniometer for the SPS resonant extraction system were carried out in cooperation by PNPI, IHEP and CERN. The crystal, goniometer and a moment of their installation to the SPS ring are shown in Fig. 4.

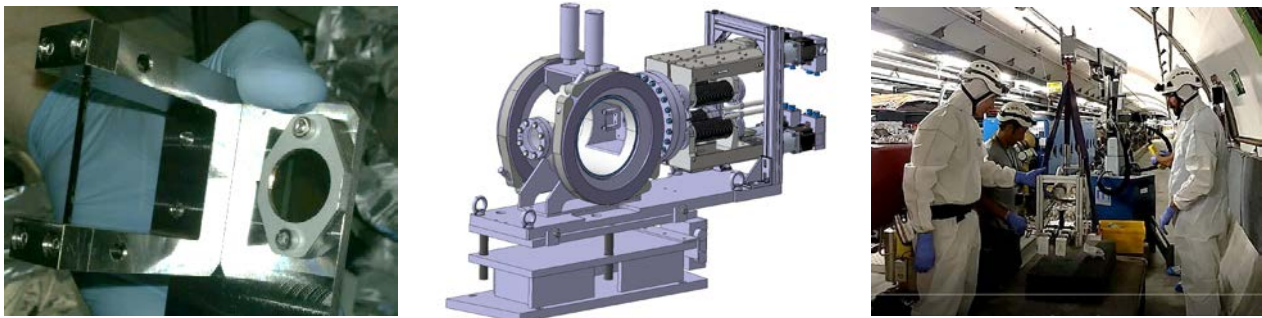


Fig. 4. The compact SPS crystal goniometer for electrostatic septum shadowing: *left* – crystal; *middle* – 3D model of the SPS crystal goniometer; *right* – installation of the crystal in the SPS tunnel at the LSS2

If the channeling angle and the phase advance between the crystal and septum are adequate, the coherently deflected protons all miss the septum and can be dumped at a dedicated absorber along the transfer line or directed towards an experimental target. A key requirement is that the extraction separatrix angle of the beam stays within the crystal's channeling acceptance of about $\pm 10 \mu\text{rad}$ throughout the spill and from spill-to-spill, which requires a narrow angular spread, excellent control and motion reproducibility, long term stability of the crystal and goniometer, as well as radiation hardness solutions to build all crystal assisted extraction components.

In the studies, a shadowing effect was most clearly revealed when setting the crystal position at 70 mm and scanning the crystal angle [3], as shown in Fig. 5. The two regimes that provide loss reduction at the ES *via* shadowing are visible in the angular scan: the channeling regime, with a loss reduction recorded of 40 to 44% (depending on the angular step), and the volume reflection regime, with a loss reduction in the order of 20% across a much wider angular acceptance of $\sim 170 \mu\text{rad}$.

One of the main concerns for the feasibility of the crystal shadowing concept with a resonantly extracted beam was the machine stability required to hold the separatrix angle at the crystal inside a very limited channeling angular acceptance of the crystal. The stability was tested by holding the crystal fixed for a large number of cycles in channeling and volume reflection, with an root mean square (RMS) stability of 1.1 and 0.4%, respectively. The crystal was also deployed for a 13 h period on the operational beam to the North Area experiments, with a high intensity of $2.8 \cdot 10^{13}$ protons per spill. A total of $\sim 6 \cdot 10^{16}$ protons were extracted during this time, and it was estimated that about 5% of this intensity directly hit the crystal.

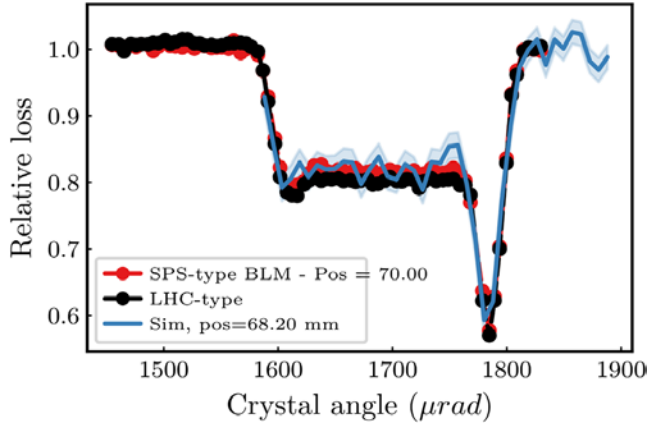


Fig. 5. Relative beam loss measured on the beam loss monitors next to the electrostatic septum during an angular scan of the crystal positioned to shadow

To further reduce losses at the ES in the local mode, an array of precisely aligned crystals set to the volume reflection (VR) mode to optimize the efficiency could be envisaged. In this configuration, the sensitivity to separatrix angle variations would be reduced due to the large available angular acceptance of the VR in crystals.

The performed experiments [4] allowed establishing the local crystal shadowing scheme as an operational instrument of slow extraction in the SPS for the next years and to focus further studies on a non-local crystal shadowing scheme.

3. Studies of beam focusing with bent strip crystals

In the first focusing crystals, an A.I. Smirnov's idea was realized to obtain focusing by giving the input/output facet of a curved crystal an exact cylindrical shape [5]. He showed that the bending radius R , the facet radius r and the focal length L are related by a simple formula $L = \sqrt{4r^2 - R^2}$, if the facet cylinder passes through the curvature axis of the bend, as shown in Fig. 6.

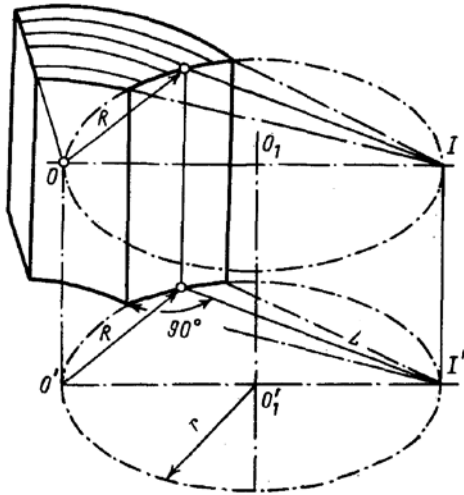


Fig. 6. The principle for focusing a beam by means of a bent crystal: OO' – the axis of cylindrically bent atomic planes; O_1O_1' – the axis of the facet cylinder; II' – the focus line

The development of crystal optics of high-energy charged particle beams has led to the use of the anticlastic bending method, which makes it possible to remove the crystal holder outside the beam and ensure high bending uniformity. The processing of the end facets of a crystal bent in this way is difficult to perform; therefore, obtaining a focusing effect requires a different approach. It consists in giving the strip a trapezoidal cross section before bending. The focusing effect that occurs when such a strip is bent becomes approximate, but the introduced aberration is small due to the small size of the crystal compared to the bending radius and focal length. Assuming the acute angle of the trapezoid is equal to α , we can rewrite the exact formula for the focal length as $L \approx R \tan \alpha$.

Several strip crystals with skew-cut facets were prepared at IHEP to study focusing and defocusing effects. The UA9 Collaboration investigated them with 400 GeV/c proton and 180 GeV/c π^+ beams at the CERN SPS [6]. One of the used crystals and its focusing effect are shown in Fig. 7.

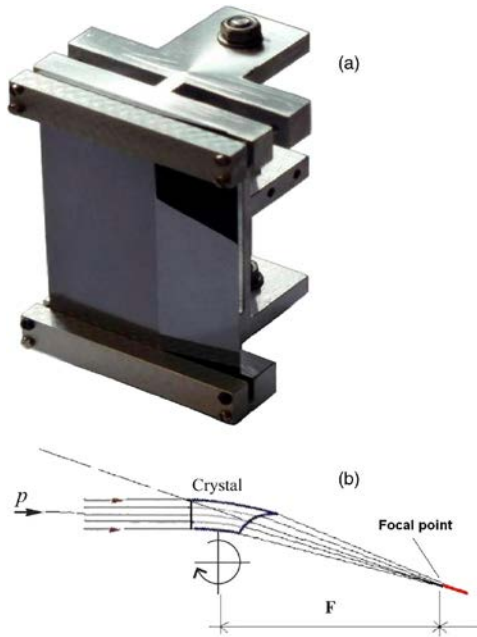


Fig. 7. The bent strip crystal with a skew-cut facet (a); focusing of a parallel proton beam with such a crystal (b)

The measured beam profiles are shown in Fig. 8. Typically, the size of the channeled beam at the focus was 5–8 times smaller than at the exit of the crystals, the measured focal lengths were found to be in the range from 4 to 21 m. The measurement results are in agreement with estimations and give a practical solution for possible applications in high-energy accelerators.

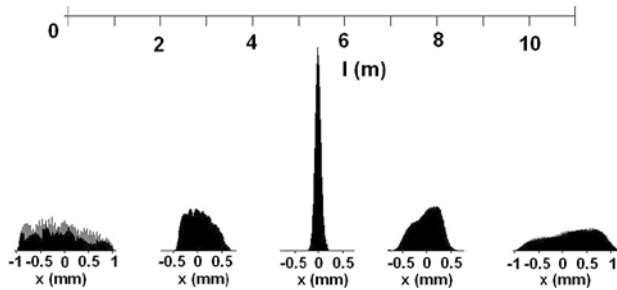


Fig. 8. The profiles of the 400 GeV/c proton beam at different distances from the crystal. The distance from the crystal is shown above the plots

However, it is difficult to use a crystal with a skew-cut facet to reach the focal lengths much less than a metre, because the required angle α becomes too small for strip crystal production. The UA9 Collaboration investigated another new approach based on the bending of a strip crystal with channeling planes parallel to the strip cross section diagonal [7].

The trajectories of 180 GeV/c π^+ mesons passing through such a crystal with a thickness of 500 μm were reconstructed using silicon microstrip detectors. A cross section of the strip crystal and its focusing effect are shown in Fig. 9.

The measured dependence of the channeled beam size on the distance to the crystal is given in Fig. 10. From this dependence it is found that the channeled beam has a focus at a distance of 15.5 cm from the crystal and its size is of the order of 10 μm . This result contributes to the development of microbeam manipulation tools.

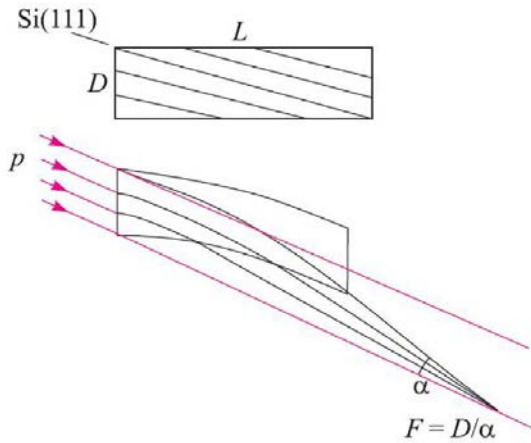


Fig. 9. Focusing of the channeled beam by a bent silicon strip with atomic planes parallel to the diagonal of the strip cross section; α is the bending angle of the channeling plane coinciding with the strip cross section diagonal; F is the focal length; D is the strip thickness

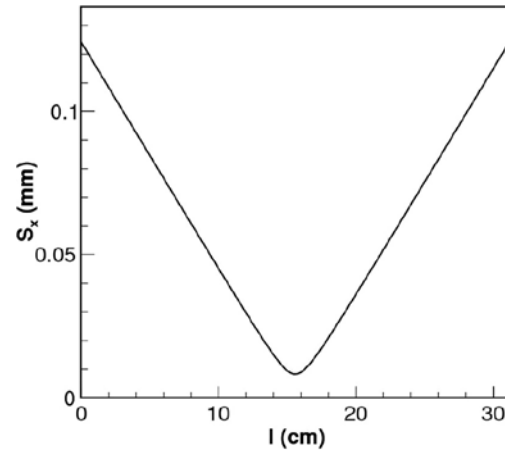


Fig. 10. The measured size of the channeled beam versus the distance from the crystal

4. Studies of channeling efficiency in crystals after heavy irradiation with protons and neutrons

The beam steering performance of bent silicon crystals irradiated with high-intensity high-energy protons was studied in Ref. [8], where the crystals of the types used for collimation and extraction in the LHC and the SPS at CERN were irradiated at the HiRadMat CERN facility. HiRadMat is a CERN facility able to provide high-intensity high-energy pulsed beams to test accelerator components and material samples. The facility can use an SPS beam made of up to 288 bunches of 10^{11} protons at 440 GeV/c, with a pulse length of 7.2 μ s, for a maximum pulse energy of 3.4 MJ. Two crystals, the QMP33 and STF103, were irradiated at the same time with four-batch injections: three with 216 bunches and one with 288 bunches of $\sim 10^{11}$ protons. The QMP33 is a quasimosaic silicon crystal of the same kind already installed and tested in the LHC between 2014 and 2018 for collimation purposes. The STF103 is a strip silicon crystal that has the same bending angle of a typical LHC strip crystal.

The first visual inspection of the two crystal samples after the HiRadMat test did not demonstrate any macroscopic damage, such as cracks, deformations or surface vitrification. Both crystals were characterized at the H8 SPS extraction line before and after the irradiation, in the same experimental conditions, and the results obtained were analysed.

For the QMP33, it was possible to perform both measurements with 180 GeV/c positive hadron beam ($\sim 70\%$ of protons and $\sim 30\%$ of pions) and the crystal did not show any variation of the channeling angle and total efficiency within the error bars. To further prove the integrity of the crystals, the efficiency of the two crystals after irradiation was studied by dividing the surface into small bins of 0.2×0.2 mm². In Figures 11 and 12, the channeling efficiency maps of the QMP33 and STF103 surfaces, perpendicular to the beam direction, are shown. The efficiency is calculated individually for each interval with respect to the optimal impact angle required for channeling within the bin itself. *Left* and *right sides* of the plot are aligned with edges of the crystal and the area of the HiRadMat beam impacts is delimited by a green dashed rectangle. 2D plots validate that the crystal surfaces have a very homogeneous efficiency within the impact area, proving that the HiRadMat irradiations affected the quality of the crystal atomic structure, and consequently its channeling efficiency, in a negligible way (within an error bar of $\pm 2\%$).

A comparison between the efficiency measurements performed before and after the irradiation did not reveal any appreciable performance reduction in any crystal. The result demonstrated that the crystal technology is reliable in the case of a rapid irradiation of the crystal.

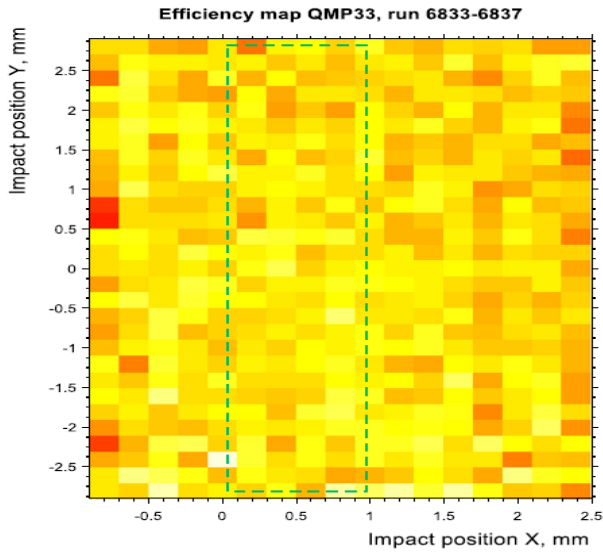


Fig. 11. Channeling efficiency map of the quasimosaic crystal surface perpendicular to the beam axis

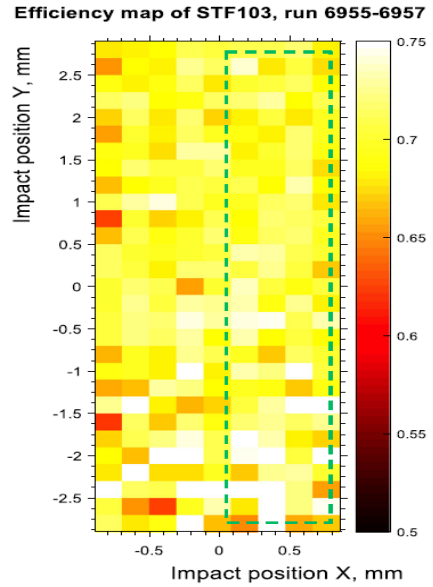


Fig. 12. Channeling efficiency map of the strip crystal surface perpendicular to the beam axis

The crystals preserve their beam steering performance in terms of channeling angle and efficiency, ensuring their operational stability. It is also indirectly confirmed that the number of dislocations produced by $\sim 10^{14}/\text{cm}^2$ 400 GeV/c protons is not enough to change appreciably the channeling performance. Earlier, in 1992, a first study was performed at the U-70 IHEP accelerator, where a crystal was irradiated with 10^{19} protons/cm² at 70 GeV/c without showing a measurable efficiency degradation.

Another important irradiation experiment was performed to estimate crystal degradation in high fluxes of hadrons [9]. A series of silicon strip crystals were exposed to $2.5 \cdot 10^{21}$ neutrons/cm² in the SCK-CEN BR2 reactor in Belgium. The channeling efficiency of each crystal was measured with SPS beams before and after neutron irradiation. A plot with the results is shown in Fig. 13, where the mean efficiency reduction is found to be about 8%.

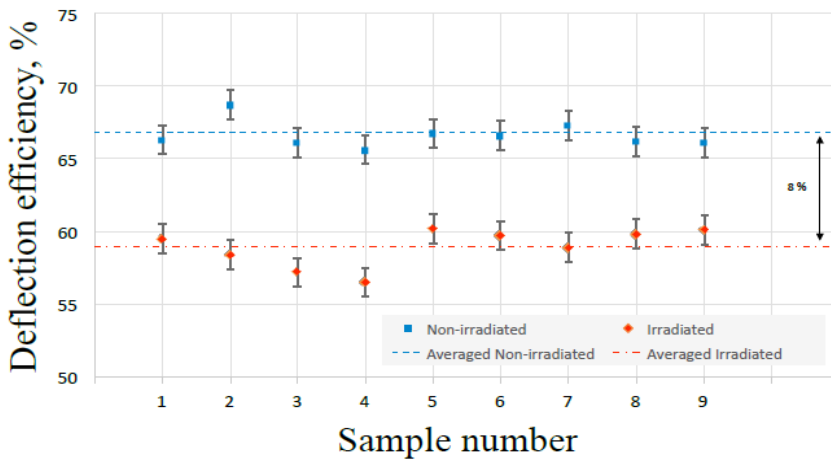


Fig. 13. Channeling efficiencies of nine crystal samples measured using the 180 GeV/c positive hadron beam before (blue squares) and after (red diamonds) neutron irradiation. The mean efficiency reduction is about 8%

To estimate the crystal robustness in a high-energy proton accelerator, it is needed to rescale the effect produced on the crystal by neutrons of the SCK-CEN reactor to the case of protons and heavy ions at the SPS and LHC. Skipping details, the rescaling gives a crystal lifetime more than five years for the SPS and LHC conditions.

5. Study of inelastic nuclear interactions of high energy hadrons in bent silicon crystals

The probability of inelastic nuclear interaction (INI) of 400 GeV/c protons with both types of crystals installed at the CERN LHC was investigated in Ref. [10]. The detection of INI is clarified in Fig. 14, the full experimental set-up is shown in Fig. 15.

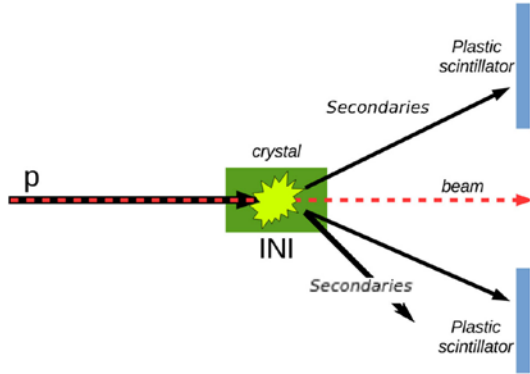


Fig. 14. INI produces secondary particles detected with plastic scintillators in the coincidence mode

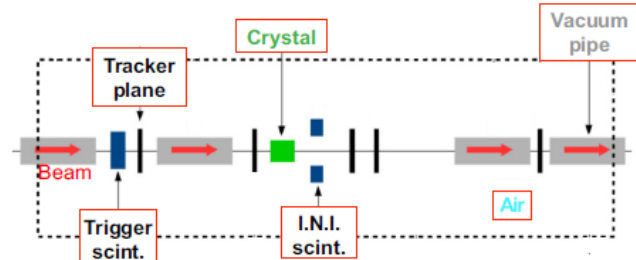


Fig. 15. Experimental set-up layout including INI detectors and multistrip silicon tracker

It was found in the experiment that with respect to the amorphous orientation, in the planar channeling orientation the INI probability is $\sim 36\%$ for the quasimosaic type (atomic planes (111)), and $\sim 27\%$ for the strip type (atomic planes (110)). For the first time, the absolute inelastic nuclear interaction probability at the axial channeling orientation along the $\langle 110 \rangle$ axis was estimated, finding a value of 0.6% for a 2 mm long crystal along the beam direction, with a bending angle of $55 \mu\text{rad}$. This value is more than two times lower with respect to the planar channeling orientation of the same crystal.

An angular asymmetry of the INI rate dependence on the crystal orientation in the vicinity of the planar channeling minimum was observed in Ref. [11]. The obtained result is shown in the Fig. 16.

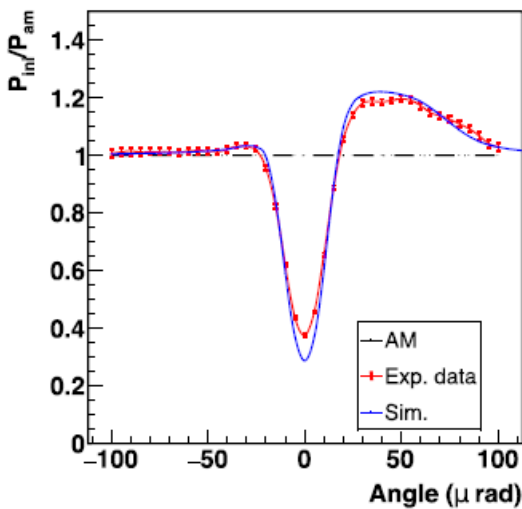


Fig. 16. In red, the observed dependence of the INI rate for 180 GeV/c positive hadrons on the orientation angle of the crystal. The blue curve shows the analytical simulation results. Both are normalized to the amorphous level (black dashed line)

For an LHC collimation crystal, the INI probability in planar channeling orientation is reduced by $\sim 64\%$ with respect to the amorphous orientation, in agreement with [10]. An excess of $\sim 20\%$ in the volume reflection region and a small increment of only $\sim 4\%$ in the angular direction opposite to the volume reflection are precisely found, showing for the first time the INI asymmetry due to the crystal bending.

The studies of the INI rate are essential for a better understanding of the behaviour of bent silicon crystals used as LHC collimators.

6. Studies of multiple scattering in bent silicon crystals and channeling efficiencies in target–crystal and crystal–crystal experiments

The studies of multiple scattering in bent silicon crystals are performed in Refs. [12–15], the studies of different target–crystal and crystal–crystal schemes are carried out in Refs. [16, 17]. The most interesting result is reported in Ref. [14], where a strong reduction of multiple scattering for channeled particles was observed in the experiment on the deflection of a 180 GeV/c π^+ -meson beam by bent silicon crystals. The RMS vertical deflection due to multiple scattering for the channeled particles is about six times smaller than that for non-channeled ones, as shown in Fig. 17.

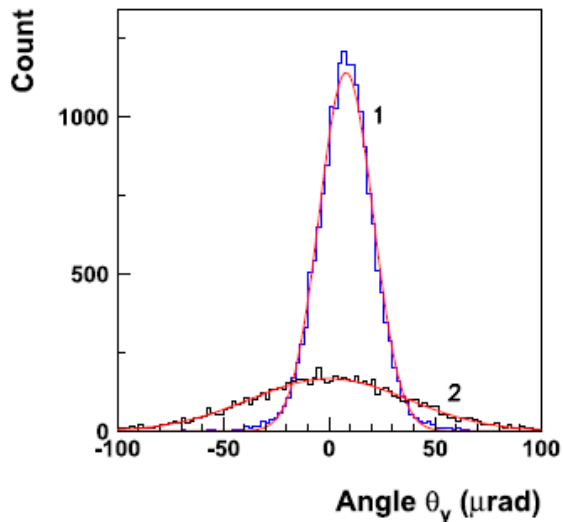


Fig. 17. The vertical deflection angle distributions for the channeled (1) and non-channeled (2) beam fractions. The curves are Gaussian fits to the measured distributions

8. Conclusion

During 2018–2022, the UA9 Collaboration and CERN ATS investigated in details interaction effects, behaviour of bent crystals, different crystal schemes in a series of experiments at the SPS and LHC. The obtained results provide a reliable base to develop crystal-assisted applications at high-energy accelerators.

References

1. The UA9 Collab., *Int. J. Mod. Phys. A* **37** (13), 2230004 (2022).
2. L.S. Esposito *et al.*, in *10th Int. Part. Accel. Conf.* (2019). DOI: 10.18429/JACoW-IPAC2019-WEPMP028.
3. F.M. Velotti *et al.*, in *10th Int. Part. Accel. Conf.* (2019). DOI: 10.18429/JACoW-IPAC2019-THXXPLML.
4. F.M. Velotti *et al.*, *Phys. Rev. Accelerators and Beams* **22**, 093502 (2019).
5. M.A. Gordeeva *et al.*, *JETP Lett.* **54**, 487 (1991); V.M. Biryukov, Y.A. Chesnokov, V.I. Kotov, *Crystal Channeling and Its Application at High-Energy Accelerators*, Springer-Verlag Berlin Heidelberg, 178 (1997).
6. The UA9 Collab., *Phys. Rev. Accelerators and Beams* **21**, 014702 (2018).
7. The UA9 Collab., *Nucl. Inst. Meth. Phys. Res. B* **414**, 104 (2018).
8. W. Scandale *et al.*, *Eur. Phys. J. C* **79** (11), 933 (2019).
9. W. Scandale *et al.*, *JINST* **16**, P08015 (2021).
10. The UA9 Collab., *Eur. Phys. J. C* **78** (6), 505 (2018).
11. W. Scandale *et al.*, *Eur. Phys. J. C* **80** (1), 27 (2020).
12. The UA9 Collab., *Nucl. Inst. Meth. Phys. Res. B* **438**, 38 (2019).
13. W. Scandale *et al.*, *Eur. Phys. J. C* **79** (12), 993 (2019).

14. The UA9 Collab., Phys. Lett. B **804**, 135396 (2020).
15. The UA9 Collab., Eur. Phys. J. Plus **137** (7), 811 (2022).
16. W. Scandale *et al.*, Nucl. Inst. Meth. Phys. Res. B **467**, 118 (2020).
17. W. Scandale *et al.*, Nucl. Inst. Meth. Phys. Res. A **1015**, 165747 (2021).

PRECISION MEASUREMENT OF THE MUON CAPTURE RATE ON DEUTERON, PRELIMINARY RESULT OF THE MUSUN EXPERIMENT

PNPI participants of the MUSUN Collaboration: V.A. Ganzha, K.A. Ivshin, P.V. Kravchenko, P.A. Kravtsov, A.N. Solovyev, I.N. Solovyev, A.A. Vasilyev, A.A. Vorobyov, N.I. Voropaev, M.E. Vznuzdaev

1. Introduction

The MuSun is the third from a series of muon capture experiments on the simplest nuclear ${}^3\text{He}$ [1], ${}^1\text{H}$ [2], and ${}^2\text{H}$ which have been done by this collaboration. As a result of the previous μp and $\mu {}^3\text{He}$ capture experiments, fundamental parameters of the recent effective field theory were obtained, such as the pseudoscalar form factors g_P and F_P . The aim of the MuSun experiment is a 1% precision measurement of the rate Λ_d for the nuclear muon capture on a deuteron $\mu d(F = 1/2) \rightarrow \nu_\mu + n + n$ from the doublet spin state of the $d\mu$ atom. This process is the simplest weak interaction process on a nucleus and it can be calculated with a precision even better than 1%. The measurement provides a benchmark result, far more precise than any current experimental information on weak interaction processes in a two-nucleon system. The result of the experiment contributes to our understanding of fundamental reactions in astrophysics, like the solar pp fusion $p + p \rightarrow \nu_e + e^+ + d$ and neutrino scattering on a deuteron $\nu_e + d \rightarrow e + p + p$, $\nu + d \rightarrow \nu + n + p$. Recent calculations of effective field theory show that all these reactions are related by one axial two-body current term and parameterized by a single low-energy constant L_{1A} . The MuSun measurement provides an unambiguous and accurate way to determine this constant. Once it is known, the mentioned astrophysical and other important two-nucleon reactions will be determined in a model-independent way at 1% precision. Previous measurements performed in different H + D mixtures are far from the above mentioned accuracy, see the Table.

Table

Main parameters of μd capture experiments*

ϕ , %	C_D	T , K	Detection	Statistics	Λ_d , Hz	Reference
100	0.32	20	Neutrons	615	365 ± 96	[3]
0.76	5	300	Neutrons	6 295	–	[4]
100	100	20	Neutrons	$5 \cdot 10^8$	470 ± 29	[5]
4	100	45	Neutrons	10^4	409 ± 40	[6]
6	100	31	Electrons	$1.2 \cdot 10^{10}$	365 ± 5	MuSun

* The density ϕ is normalized to liquid hydrogen $4.25 \cdot 10^{22}$ nuclei/cm³. C_D – deuterium concentration. The result of the experiment [4] is uncertain because the gas condition corresponds to the statistical $d\mu$ spin state population.

The MuSun experiment is based on the “lifetime method” – extracting the capture rate *via* a comparison between the muon disappearance rate in deuterium and the free muon decay rate $\mu^- \rightarrow e^- + \nu_e + \nu_\mu$. The “lifetime method” in combination with a novel cryogenic time-projection chamber (TPC) gives a unique possibility to measure the capture rate with unprecedented precision. The TPC was designed and constructed at PNPI as an active target of the experiment and was filled with ultrapure deuterium. The TPC data were intended to reconstruct the three-dimensional stop positions of muons in the gas. In order to keep deuterium clean, we used two set-ups of purification: an isotopic separation column [7] and a circulation system (CHUPS) [8]. The MuSun experiment was carried out on a muon beam of the Paul Sherrer Institute meson factory. The beam was equipped with the muon-on-request (MORE) system, also referred to as the kicker. Eventually, the experiment collected $1.2 \cdot 10^{10}$ events with the registration of decay electrons when a muon stopped in the deuterium gas of the TPC. Such an amount of data is quite enough to obtain the value of Λ_d with the announced precision. The systematic uncertainties in the experiment were minimized to a level of 1.4 Hz. For a cross-check of quality of the experimental data, an additional run with a μ^+ beam was carried out and analysed.

2. Experimental set-up and data taking

A scheme of the experimental set-up is presented in Fig. 1. A muon is registered first in the scintillator counter μ SC, which gives a primary timing signal for the lifetime measurement. Additionally, the μ SC impulse triggers the MORE system, to kick the beam for 25 μ s when a muon has arrived in the TPC. Afterward μ SC, a muon comes to the multiwire proportional chamber μ PC, which gives a spatial location of each muon entrance in X and Y coordinates with a 2 mm resolution in both directions. The muon then passes through a 0.4 mm thick beryllium window and stops inside the TPC. After the muon decay, a Michel electron is registered with two cylindrical proportional chambers ePC1 and ePC2. The data from the ePCs make it possible to reconstruct the e^- track in the 3D dimensions. Finally, the electron is detected in the eSC, which is a plastic scintillator counter consisting of 32 double-layer segments. The eSC signal is used as the end of the lifetime interval. All electron detectors ePC1, ePC2 and eSC have 70% geometrical acceptance. In order to trigger a “background event”, a muon entrance in the μ SC was simulated by a 2.5 kHz generator signal (μ CL). The μ CL was placed in an OR with a real muon signal and set up throughout the run. 100 MHz waveform digitizers (WFDs) were used to record outputs from the μ SC, eSC and TPC. Additionally, in parallel with WFDs, CAEN time-to-digital converters measured hit times from the μ SC and eSC.

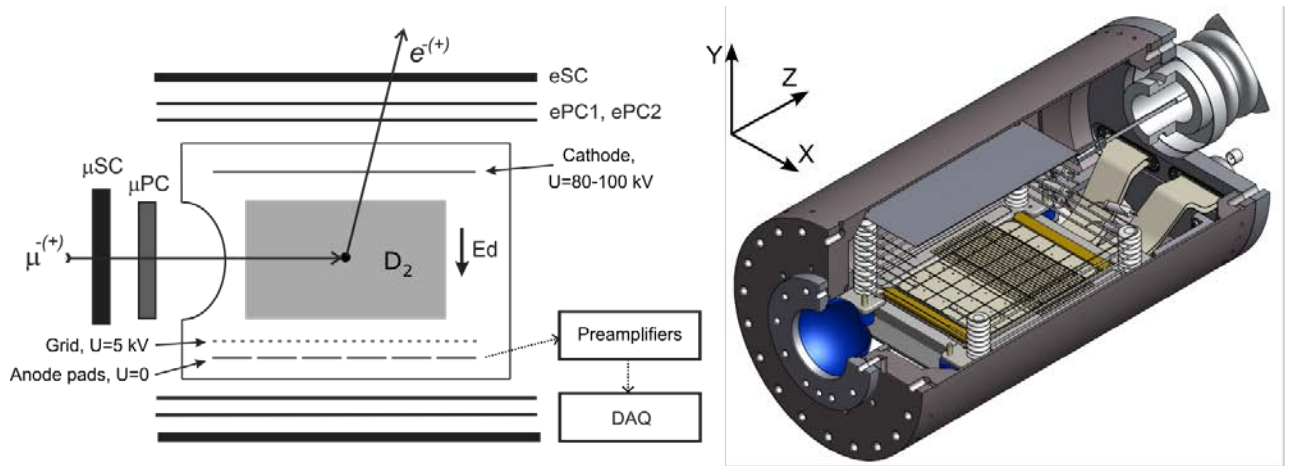


Fig. 1. *Left* – a scheme of the experimental set-up. *Right* – 3D view of the TPC; right handed coordinate system, Z – the beam direction, X/Y – horizontal/vertical directions; the sensitive volume – space between the cathode and the grid with 72 mm distance between them; the electric field – 11 kV/cm; the anode consists of 48 pads 6×8 in $X \times Z$ directions; the pad sizes – 17.5 mm (X) \times 15.25 mm (Z); the pads at the boundaries of the anode are veto pads; the materials around the TPC sensitive volume are made of high Z elements, like silver, tungsten, cuprum, etc. A 50 G magnetic field was applied to the TPC, transverse to the beam axis

The central part of the experiment is the TPC (Fig. 1) with ultrapure deuterium gas at $T = 31$ K and $P = 5$ bar. The TPC operated as an active target in the ionization mode and measured three spatial coordinates of a muon stop point. Due to the pad structure of the TPC anode, we can figure out X and Z coordinates. In addition, we can obtain the Y coordinate due to the drift time of the ionization electrons from the muon track. The anode pads of the TPC had independent readout channels with the WFDs giving the possibility to measure the energy and the time of the signals. The energy was measured with 20 keV resolution (σ) and 80 keV threshold. The TPC time resolution was 100 ns. Before TPC filling, the commercially obtained deuterium was depleted isotopically using a cryogenic distillation procedure with a separation column. In order to clean deuterium from nitrogen, a cryogenic ultra purification system (CHUPS) was used during the entire time of data collection. Additionally, throughout the run, gas samples were periodically extracted from the TPC for chromatography measurements of nitrogen and protium contamination. In order to calibrate the chromatography method, a special doping system [9] was designed, which was able to add a small (~ 0.3 ppb) and known fraction of nitrogen to the gas. As a result, during all data collecting, the gas purity was at a level of 1.2 ± 0.5 ppb for nitrogen and 10 ppm for protium. The MuSun experiment collected: $1.2 \cdot 10^{10}$, $2.3 \cdot 10^9$,

and $2.1 \cdot 10^7$ events with the μ^- , μ^+ beams, and the μ CL background events, respectively. In order to gauge muon losses on the nitrogen nucleus, an additional μ^- run was done at a nitrogen concentration of 2 ppm, where $7.4 \cdot 10^8$ muon decay events were collected.

3. Analysis of the experimental data

The *left side* of Fig. 2 presents the kinetic processes of $d\mu(1S)$ atoms in deuterium. Before the shown kinetics, a negative muon forms a $d\mu$ atom in an excited state, and after the fast cascade of the de-excitation processes it totally loses the initial polarization. On the contrary, a positive muon keeps the polarization and that is why we need to apply a magnetic field of 50 G, which rotates the spin direction of muons with 0.7 MHz frequency.

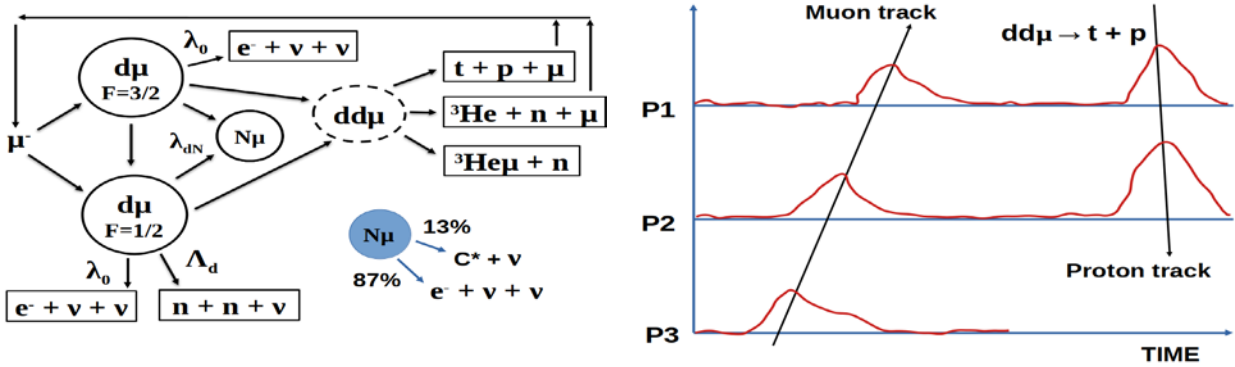


Fig. 2. *Left* – muon kinetics in deuterium; muon decay is going from all states of the scheme; the values of the muon catalyzed fusion parameters were taken from Ref. [10], the muon decay rate $\lambda_0 = 0.4551702(5) \mu\text{s}^{-1}$ from Ref. [11]; the muon capture rate from the quartet state of $d\mu$ atom is highly suppressed and calculated as 12 Hz; not shown the muon catalyzed pd fusion $\mu pd \rightarrow {}^3\text{He} + \mu$ (5.6 MeV) gives the upper limit of 10^{-4} to protium contamination. *Right* – a scheme of a TPC event with a muon and fusion $dd \rightarrow t(1 \text{ MeV}) + p(3 \text{ MeV})$ impulses divided in time; P1 – the muon stop pad; P2 – the previous to P1 pad; P3 – the third pad upstream to the muon stop pad

Experimental data analysis consists of event selection (see the next section) and Λ_d determination from the lifetime distribution (LTD). Figure 3 (*left*) presents a histogram of the time differences between the electron and muon hits in the eSC and μ SC, respectively. In order to find the value of Λ_d from this interval distribution, we built the LTD according to the scheme of Fig. 2 with some value of Λ_d , compared it with the experimental one and tuned the Λ_d value on the scheme until both LTDs were identical.

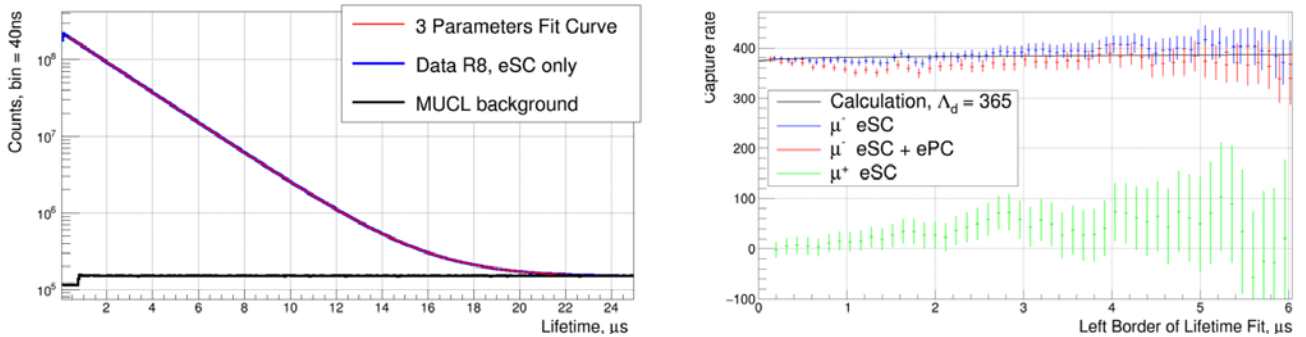


Fig. 3. *Left* – the μ^- lifetime distribution in the MuSun experiment (*blue curve*); the background obtained by the random μ CL generator (*black*); one exponential fit (*red*). *Right* – the obtained capture rates Λ_d vs a left border scan of the lifetime histogram fit; *blue points* – the analyses of the eSC hits only, *red points* – the analyses of the eSC and ePC hits in coincidence, *green points* – the μ^+ data, eSC only

The identical means that one exponential fit gives the same results. This interpolation procedure automatically includes corrections to Λ_d due to the muon catalyzed dd fusion $\mu dd \rightarrow {}^3\text{He}\mu + n$ and muon transfer to nitrogen, which are $\Lambda_{\text{corr}}(\mu dd) = 9.8 \pm 0.2$ Hz and $\Lambda_{\text{corr}}(N_2) = 3.2 \pm 1.4$ Hz, respectively. The factor $\Lambda_{\text{corr}}(N_2)$ was estimated in an additional experiment [12], where as a by product the transfer rate $d\mu + N \rightarrow N\mu + d$ was measured for the first time at low temperature: $\Lambda_{dN}(37\text{ K}) = 2.2(1) \cdot 10^{11}$ Hz. The error of $\Lambda_{\text{corr}}(N_2)$ is the main systematic error of the Λ_d measurement, which roots in uncertainties of nitrogen concentration measurements. Finally, we found $\Lambda_d = [365 \pm 4(\text{stat}) \pm 1.4(\text{syst})]$ Hz. The right part of Fig. 3 demonstrates the stability of the Λ_d value obtained from the scan of the left border of the fit. The lifetime analysis of the μ^+ data (*green points* of Fig. 3) is different in comparison with the μ^- one because positive muons are strongly polarized at the moment of the decay. The treatment procedure of the μ^+ data is explicitly described in Ref. [13].

4. Selection of events

At first, we select the events only by hits of the external counters μSC , μPC and $e\text{SC}$. All these counters should have hits only from a single muon in a time window of ± 25 μs . Additionally for $e\text{SC}$, we demand coincidence of electron hits in both layers of the scintillator segments. The most complicated task of the data analyses was the selection of events by parameters of the TPC pulses, see the *right side* of Fig. 2, which demonstrates a TPC event with dd fusion. The proton of dd fusion could escape to a neighbour pad, and in the case of muon-fusion pile-up a stop pad is disguised. In that case, the selection efficiency of the events with the fusions and without it could not be the same. That is why we cannot locate muon stop points in X and Z directions. It means that a muon stop point could be outside the boundaries of the TPC anode and even inside the materials of the TPC. The selection of the events by a muon stop point is possible only along the vertical Y coordinate using the drift time cut on a muon impulse of the P3 pad. The proton with a range of 13.8 mm cannot reach the P3 pad. In order to check whether the muon stops in high Z materials, we are looking at the presence of a bump at the beginning of the lifetime distribution as an indicator. It can be seen in Fig. 3 (*left part*) that the bump is absent. There is also a way to show quantitatively that muons do not reach the TPC walls. The method relies on a low-energy cut (< 400 keV) for muon signals from pads on the third line upstream to the Z axis. The cut excludes more than 90% of muon stops outside of the anode and only 0.8% inside it. This low-energy cut decreases the Λ_d value only by 0.8 Hz, which means that the number of the muons which stop in the TPC materials is insignificant.

5. Conclusion

As a result of the study of the negative muon capture reaction by the deuteron $\mu d(F = 1/2) \rightarrow \nu_\mu + n + n$, the rate of this process has been measured with an unprecedented accuracy of $\sim 1\%$. In order to obtain such a level of precision, the tasks below were solved:

- A time projection chamber in the cryogenic version was created and used as an active target;
- The low gas temperature (31 K) in the TPC reduced the impact of muon catalyzed dd fusion by an order of magnitude and completely eliminated the influence of electronegative impurities (oxygen and water) on the result of the measurement;
- The constructed circulation system decreased the amount of nitrogen in deuterium to the level of 1 ppb;
- As for the Λ_d correction caused by transfer of muons from deuteron to nitrogen, an independent calibration run with a high concentration of nitrogen was carried out;
- Applying a separation column, the amount of protium in deuterium was decreased to a negligibly small level of 10^{-5} .

Finally, Λ_d has been measured as $\Lambda_d = [365 \pm 4(\text{stat}) \pm 1.4(\text{syst})]$ Hz. A systematic negative correction of 13 Hz was applied to the measured value. The correction is caused by the muon sticking in the dd fusion reaction $-9.8(0.2)$ Hz, and muon transfer to nitrogen $-3.2(1.4)$ Hz.

To date, this is the only measurement that allows to reliably fix the axial low-energy constant L_{1A} of the chiral perturbation theory within the framework of the recent effective field theory. This helps to calculate

precisely the weak interaction cross sections of the pp fusion, the neutrino scattering, and other two-nucleon reactions with such a hadron vertex.

References

1. P. Ackerbauer *et al.*, Phys. Lett. B **417**, 224 (1998).
2. V.A. Andreev *et al.*, Phys. Rev. Lett. **99**, 032002 (2007).
3. I.-T. Wang *et al.*, Phys. Rev. **139**, 0B1539 (1965).
4. A. Bertin, A. Vitale, A. Placci, E. Zavattini, Phys. Rev. D **8**, 3774 (1973).
5. G. Bardin *et al.*, Nucl. Phys. **453**, 591 (1986).
6. M. Cargnelli *et al.*, in *Proc. of the XXIII Yamada Conf.* (1989).
7. I. Alekseev *et al.*, Rev. Sci. Instrum. **86**, 125102 (2015).
8. V.A. Ganzha *et al.*, Nucl. Instrum. Meth. A **578**, 485 (2007).
9. V. Ganzha *et al.*, Nucl. Instrum. Meth. A **880**, 181 (2018).
10. D.V. Balin *et al.*, Part. Nucl. **42**, 361 (2011).
11. D.M. Webber *et al.*, Phys. Rev. Lett. **106**, 041803 (2011).
12. Xiao Luo, A Precision Measurement of the Rate of Muon Capture on the Deuteron, M.A., Boston University (2016).
13. T.I. Banks, The MuCap Experiment: A High-Precision Measurement of Muon Capture by the Proton, M.A., University of California, Berkeley (2001).

HIGH-PRECISION DECAY ENERGY OF ^{187}Re FOR RESEARCH IN FUNDAMENTAL PHYSICS

PNPI participants of the PENTATRAP Collaboration: S.A. Eliseev, P.E. Filianin, Yu.N. Novikov

The nucleus ^{187}Re is a unique representative of the nuclear world. It is a good nuclear cosmochronometer providing our knowledge on the Universe age. Due to the smallest decay energy Q multipole fundamental aspects can be studied [1], including the weak interaction symmetry test, and the test of low-energy electron–electron interactions. This nuclide is an invaluable candidate for research in neutrino physics, namely in determination of the antineutrino effective rest mass, and the search for hypothetical sterile neutrinos.

The value of the decay energy Q is the key parameter for the description of the β -spectrum. It can be deduced from the spectrum itself *via* the Kurie plot. However, if the experimentally measured spectrum is affected by systematic effects, and/or if the shape of the spectrum is not accurately known, the extracted Q value may significantly deviate from the “true” one. High-precision Penning-trap mass spectrometry (PTMS) provides a direct and independent way for determination of the Q value by measuring the mass difference ΔM between the parent and daughter nuclides. In our case between ^{187}Re and ^{187}Os , which has been performed in this work.

A direct determination of ΔM by PTMS will probe the validity of the theoretical model employed to describe the β -decay spectrum, and might point at possible systematic effects inherent in the measurement of the spectrum with cryogenic microcalorimetry (CM) technique. The endpoint energy recommended by the atomic mass evaluation (AME) is 2 466.7(16) eV. The only direct measurement of ΔM was carried out by our group with SHIPTRAP, yielding $\Delta M = 2\,492(33)$ eV [2]. A necessary improvement toward an eV level in the precision of the ΔM determination was required. It has become possible with the development of the experiment PENTATRAP [3] at the Max-Planck Institute for Nuclear Physics in Heidelberg (Germany).

The measurement of the cyclotron frequency ratio R of $^{187}\text{Os}^{29+}$ to $^{187}\text{Re}^{29+}$ ions and the theoretical calculation of the binding energy difference of missing electrons $\Delta E = E^{29+}_{\text{Re}} - E^{29+}_{\text{Os}}$ are combined. In PTMS, the cyclotron frequencies $\nu_c = (1/2\pi)(q/m)B$ of ions with charge q and mass m in a uniform magnetic field B are compared. The ion’s cyclotron frequency is determined by measuring the eigenfrequencies ν_+ , ν_- and ν_z of the ion in a Penning trap. The value of ΔM is determined as

$$\Delta M = [m(^{187}\text{Os}) - 29m_e - E^{29+}_{\text{Os}}][R - 1] + \Delta E,$$

where m_e is the electron mass and $m(^{187}\text{Os})$ is the mass of the neutral ^{187}Os atom.

Figure 1 is a schematic of the PENTATRAP set-up used for the measurements [1, 3]. After 200 ms of the charge breeding time a few μs -long bunches of ions are ejected with 6.5 keV/ q kinetic energy, charge-to-mass ratio separated in a 90° magnetic bender, slowed down with two pulsed drift tubes to a few eV energy, and finally captured in the Penning traps situated inside a 7 T superconducting magnet. PENTATRAP has five identical cylindrical Penning traps, which, with the associated detection electronics, are cooled to the temperature of liquid helium. An ultrastable voltage source is used to create the traps’ potential. Various measures are undertaken to stabilize the magnetic field. Presently, trap 2 and trap 3 are used to measure the ions’ frequencies, whereas the remaining three traps serve for the ion storage. Trap 1 and the above mounted pulsed drift tube are used to load ions. In order to load just a single ion into trap 1, the intensity of the ejected ion beam is reduced such that with approximately every tenth loading attempt an ion reaches trap 1. After every loading attempt, the content of trap 1 is transported to trap 2 for its identification and preparation. The preparation consists of the reduction of the ion’s motional amplitudes with the resistive cooling technique. Following this preparation procedure, the ion can be transported to any of traps 3, 4, or 5 with a subsequent loading of the next ion. A set of three ions is loaded into the starting position 1 (Fig. 1b). The first and the last ion is $^{187}\text{Re}^{29+}$; the middle one is $^{187}\text{Os}^{29+}$. The ν_+ and ν_z frequencies of the ions in trap 2 and trap 3 are then measured for approximately 15 min. Afterward, the ions are moved by consecutive adiabatic transport into the neighbouring traps (position 2 in Fig. 1b) with subsequent measurements of their eigenfrequencies for again about 15 min. This procedure is repeated until the measurement is stopped. A measurement with the same set of ions is called a data block. The total measurement campaign consists of 10 such data blocks. The method of the analysis is based on the assumption that the time dependence of the magnetic field drift and, hence the drift of ν_c , can be approximated by a polynomial. Thus, the ν_c frequency drift of Os and Re ions is approximated by

two polynomials that differ only by a coefficient of proportionality R which is then obtained from the simultaneous fit of two polynomials to the chosen dataset.

The final cyclotron frequency ratio is $R = 1.000\,000\,013\,882(5)(1)$, where the values in the parentheses are the statistical and systematic uncertainties, respectively, and are the one-standard-deviation uncertainties in the last digits of the given value.

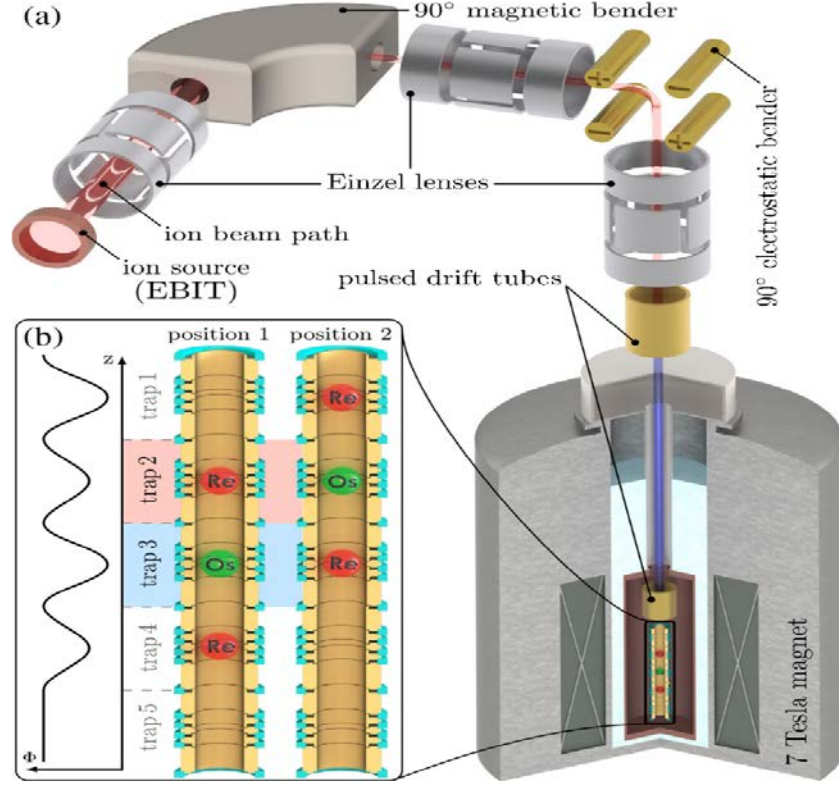


Fig. 1. PENTATRAP experiment: *a* – schematic of the PENTATRAP set-up; the ions are produced in an external ion source, separated by m/q with a magnetic bender, slowed down with two pulsed drift tubes, and finally captured in the Penning traps hosted in a superconducting magnet; *b* – ion positions inside the traps, which are sequentially repeated during the measurement; the electric potential Φ along the trap axis is depicted on the *left side*

In order to determine ΔM from R , the difference of the total binding energy of the 29 outermost electrons E^{29+}_{Re} in the Re atom and E^{29+}_{Os} in the Os atom, is subject to theoretical calculations. For this, two fully relativistic multiconfiguration methods are employed. Details can be extracted from [1]. The first one is the multiconfiguration Dirac–Hartree–Fock method (MCDHF) and its combination with the Brillouin–Wigner many-body perturbation theory. In another set of calculations performed with the QUANTY package, the Hilbert space is spanned by multi-Slater-determinant states constructed from relativistic Kohn–Sham single-electron orbitals. On this basis, the Dirac–Coulomb–Breit Hamiltonian is solved. Note that the correlation terms and errors largely cancel in the binding energy difference $\Delta E = E^{29+}_{\text{Re}} - E^{29+}_{\text{Os}}$ due to the similarities of the two atoms and ions. Thus, the MCDHF method yields a rather accurate value of $\Delta E_{\text{MCDHF}} = 53.4(10)$ eV, whereas the QUANTY package gives $\Delta E_{\text{Quanty}} = 53.4(13)$ eV.

The final value of $\Delta E_{\text{final}} = 53.5(10)$ eV is obtained by averaging the theoretical results for ΔE_{MCDHF} , ΔE_{BMCDHF} and ΔE_{Quanty} , weighted with their inverse uncertainties. Since the employed theoretical methods are not fully independent, the 1.0 eV lowest uncertainty among the three theoretical uncertainties is used for ΔE_{final} . With the measured cyclotron frequency ratio R and the theoretically calculated electron binding energy differences ΔE , the mass difference between the neutral ^{187}Re and ^{187}Os is determined to be 2 470.9(13) eV (Table), which is 25 times more accurate than the previous SHIPTRAP result.

Table

The results achieved in this work*

Mass difference	Value, eV
$m(^{187}\text{Os}^{29+}) - m(^{187}\text{Re}^{29+})$	2 417.4(9)
ΔE_{MCDHF}	53.4(10)
ΔE_{BMCDHF}	53.9(15)
ΔE_{Quanty}	53.4(13)
ΔE_{final}	53.5(10)
ΔM	2 470.9(13)
R_{final}	1.000 000 013 882(5)(1)

* The digits in the parentheses are the one-standard-deviation uncertainties in the last digits of the given value. For R the statistical and systematic errors are shown respectively in the parenthesis.

Figure 2 shows a comparison between the three most precise endpoint energy values obtained by different groups using cryogenic microcalorimetry, the evaluated Q value from AME, and the value of ΔM obtained in the present work.

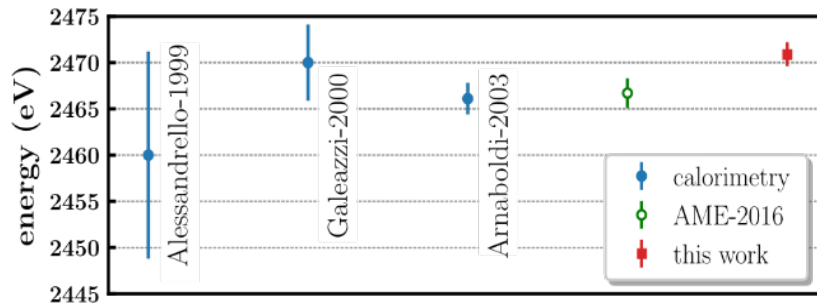


Fig. 2. Various decay energy values for ^{187}Re . The blue filled circles are endpoint energy values obtained from the analysis of the β -decay of ^{187}Re by different authors. The green empty circle is the evaluated Q value from the atomic mass evaluation. The red filled square is the ΔM value (in energy units) determined in this work

The ultraprecise data for the lowest decay energy will work for the benefit of multiple researches in fundamental physics mentioned at the beginning of this article.

References

1. P. Filianin *et al.*, Phys. Rev. Lett. **127**, 072502 (2021).
2. D.A. Nesterenko *et al.*, Phys. Rev. C **90**, 042501(R) (2014).
3. A. Rischka *et al.*, Phys. Rev. Lett. **124**, 113001 (2020).

LONGITUDINAL DOUBLE-SPIN ASYMMETRIES IN SEMI-INCLUSIVE DEEP INELASTIC SCATTERING OF ELECTRONS AND POSITRONS BY PROTONS AND DEUTERONS

PNPI participants of the HERMES Collaboration: **S.L. Belostotski**, G.E. Gavrilo, **A.A. Izotov**,
P.V. Kravchenko, S.I. Manaenkov, Yu.G. Naryshkin, **V.V. Vikhrov**

1. Introduction

The study of deep inelastic scattering (DIS) of unpolarized (longitudinally polarized) leptons off unpolarized (polarized) nucleons provides the unpolarized (polarization-dependent) parton distribution of the nucleon. Semi-inclusive DIS (SIDIS) when one detected hadron is identified gives information not only on parton distributions but also on the fragmentation function and permits to distinguish contributions of various flavours. At the first stage, a collinear approximation was used. Now, the transverse motion of quarks in the nucleon (transverse-momentum dependent, TMD parton distribution) is taken into consideration and also the TMD fragmentation functions are studied. A detailed theoretical picture has been developed, providing a framework for which SIDIS measurements for any combination of the beam and target polarization are related to various combinations of the quark distribution and fragmentation functions [1–3].

The one-photon-exchange approximation is used in the present work and standard variables: lepton and virtual photon energies E_e and ν in the target-rest frame (TRF), $y = \nu/E_e$, Bjorken scaling variable $x = Q^2/(2M\nu)$ with Q^2 being the negative squared photon four-momentum and M the nucleon mass, $\gamma = Q/\nu$, the angle ϕ is the azimuthal angle of the identified hadron three-momentum \vec{P}_h with respect to photon three-momentum \vec{q} in TRF, while E_h is the hadron energy, $z = E_h/\nu$, $\vec{P}_{h\perp}$ denotes the transverse component (with respect to \vec{q}) of \vec{P}_h , $P_{h\perp} = |\vec{P}_{h\perp}|$. The complete model-independent decomposition of the semi-inclusive DIS cross section in the one-photon-exchange approximation can be expressed in terms of moments of azimuthal modulations,

$$\begin{aligned} \frac{d\sigma^h}{dx dy dz dP_{h\perp}^2 d\phi} = & \frac{2\pi\alpha^2}{xyQ^2} \frac{y^2}{2(1-\epsilon)} \left(1 + \frac{\gamma^2}{2x}\right) \{F_{UU,T}^h + \epsilon F_{UU,L}^h + \lambda\Lambda\sqrt{1-\epsilon^2} F_{LL}^h + \\ & + \sqrt{2\epsilon}[\lambda\sqrt{1-\epsilon} F_{LU}^{h,\sin\phi} + \Lambda\sqrt{1+\epsilon} F_{UL}^{h,\sin\phi}]\sin\phi + \sqrt{2\epsilon}[\lambda\Lambda\sqrt{1-\epsilon} F_{LL}^{h,\cos\phi} + \sqrt{1+\epsilon} F_{UU}^{h,\cos\phi}]\cos\phi + \\ & + \Lambda\epsilon F_{UL}^{h,\sin 2\phi} \sin 2\phi + \epsilon F_{UU}^{h,\cos 2\phi} \cos 2\phi\}. \end{aligned} \quad (1)$$

Here λ and Λ are respectively helicity of the beam lepton and target nucleon, ϵ is the ratio of the longitudinal to transverse photon flux. The symbol X of the structure function $F_{X,Y,Z}^{h,\text{mod}}$ denotes unpolarized ($X = U$) or longitudinally polarized ($X = L$) beams, $Y = U$ and $Y = L$ correspond to the unpolarized and longitudinally polarized nucleon, while $Z = T$ ($Z = L$) corresponds to the transverse (longitudinal) photon polarization.

2. HERMES experiment

The data were collected using the HERMES spectrometer at the HERA storage ring during 1996–2000 running period. A longitudinally polarized electron or positron beam with a momentum of 27.6 GeV/c was scattered off a longitudinally polarized atomic hydrogen or deuterium gas target. Typical values for the beam (target) polarization are about 53% (84%). The measured beam-target longitudinal asymmetry $A_{||}^h$ for hadron h is

$$A_{||}^h = \frac{C_\phi^h}{f_D} \left[\frac{N_h^{\leftarrow L^{\rightarrow}} - N_h^{\rightarrow L^{\leftarrow}}}{N_h^{\leftarrow L^{\rightarrow}} + N_h^{\rightarrow L^{\leftarrow}}} \right]_B, \quad (2)$$

where $N_h^{\leftarrow L^{\rightarrow}}$ ($N_h^{\rightarrow L^{\leftarrow}}$) represent the number of observed events with antiparallel (parallel) beam/target polarization that meet kinematic requirements: $Q^2 > 1 \text{ GeV}^2$; $W^2 > 10 \text{ GeV}^2$; $y < 0.85$; $0.2 < z < 0.8$. Here, f_D denotes the delution factor of the nucleon in the target nucleus, the correction factor C_ϕ^h takes into account

ϕ -dependence of the detector efficiency, and the symbol B after the square brackets means that the asymmetry is corrected to the Born level, *i. e.* unfolded for radiative corrections and detector smearing using Monte Carlo (MC) simulations.

The virtual photon–nucleon asymmetry A_1^h is defined as

$$A_1^h = \frac{\sigma_{1/2}^h - \sigma_{3/2}^h}{\sigma_{1/2}^h + \sigma_{3/2}^h}, \quad (3)$$

where $\sigma_{1/2}^h$ ($\sigma_{3/2}^h$) is the photoabsorption cross section with antiparallel (parallel) spins of photons and target nucleons. It is related to $A_{||}^h$ by the equation $A_1^h = A_{||}^h/D[1 + \gamma\eta]$, where $\eta = \epsilon\gamma/[1 - (1 - y)\epsilon]$ with the photon polarization parameter $\epsilon = (1 - y - 1/4\gamma^2 y^2)/[1 - y + 1/4\gamma^2(\gamma^2 + 2)]$. The polarization-transfer coefficient at the electron–photon vertex is $D = [1 - (1 - y)\epsilon]/(1 + \epsilon R)$, where R denotes the longitudinal-to-transverse cross section ratio.

The physical asymmetries were obtained as results of application of many-dimensional unfolding. The x , z and $P_{h\perp}^h$ dependences were parameterized with polynomials which parameters are presented in Ref. [4], where more technical details can be found. The longitudinal double-spin asymmetries as a function of x for the hydrogen and deuterium targets and $h = \pi^\pm, K^\pm$ are presented in Fig. 1. The data are overaged over z and $P_{h\perp}$. As is seen in Fig. 1, the asymmetries are increasing with x in the range [0.03–0.4].

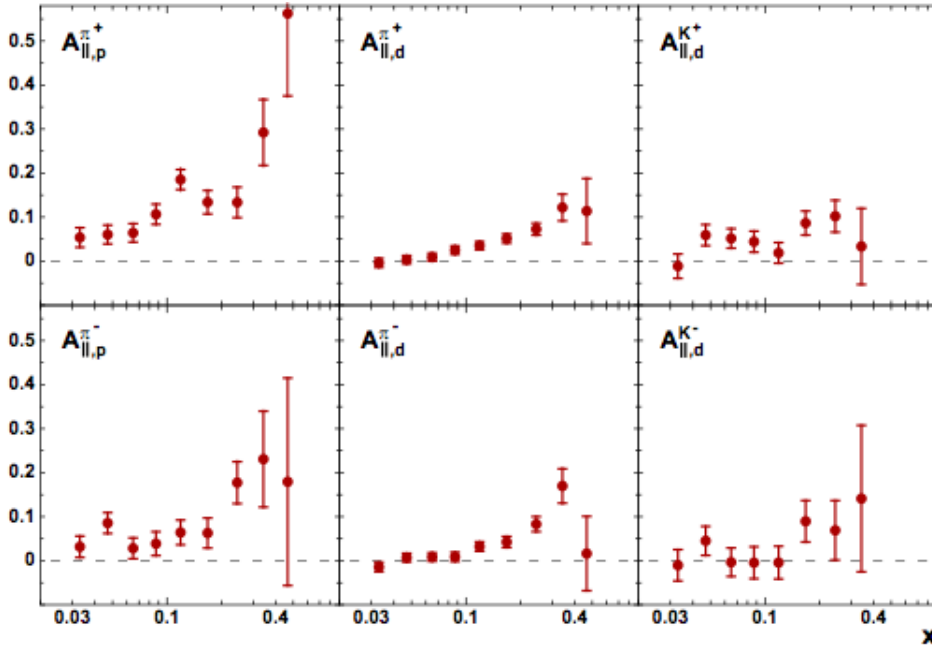


Fig. 1. The longitudinal double-spin asymmetries $A_{||,N}^h$ as a function of x with $N = p, d$ denoting the target nucleus and $h = \pi^\pm, K^\pm$ the final-state hadron detected. The inner error bars represent statistical uncertainties while the outer ones statistical and systematic uncertainties are added in quadrature

3. The measurement of the azimuthal asymmetries

The azimuthal moments of asymmetries are potentially sensitive to unique combinations of the distribution and fragmentation functions. The $P_{h\perp}$ projections of the $\cos\phi$ moments for charged pions for each target, as well as for charged kaons in case of a deuterium target, are presented in Fig. 2.

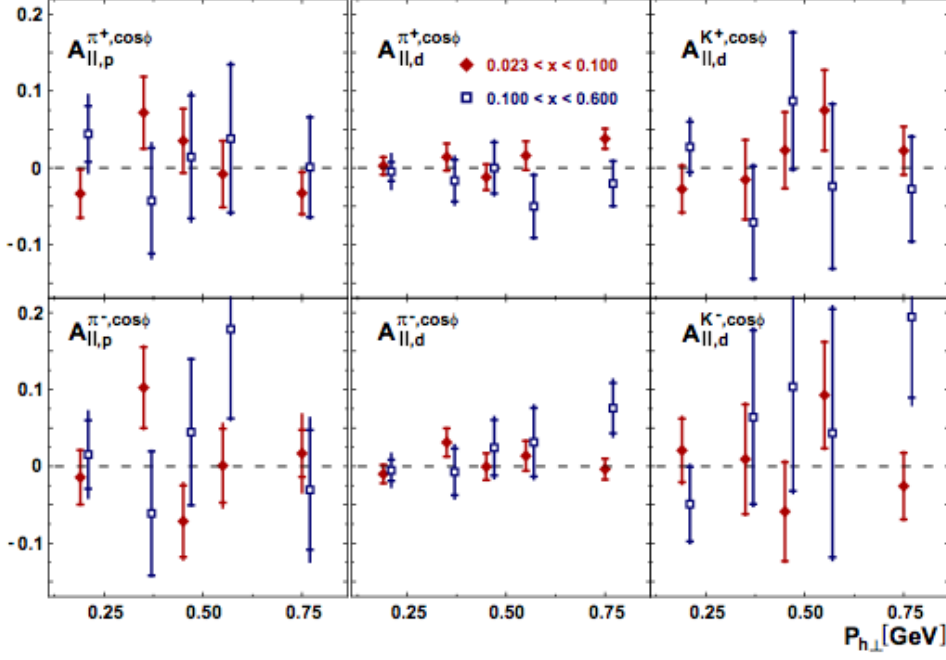


Fig. 2. $A_{||}^{h, \cos\phi}$ vs $P_{h,\perp}$ in two x ranges for charged pions and kaons from protons and deuterons

4. The measurement of the hadron charge-difference asymmetries

The hadron charge-difference asymmetry for hadrons h^+ and h^-

$$A_1^{h^+-h^-} = \frac{(\sigma_{1/2}^{h^+} - \sigma_{1/2}^{h^-}) - (\sigma_{3/2}^{h^+} - \sigma_{3/2}^{h^-})}{(\sigma_{1/2}^{h^+} - \sigma_{1/2}^{h^-}) + (\sigma_{3/2}^{h^+} - \sigma_{3/2}^{h^-})} \quad (4)$$

can provide information on the valence-quark distributions in the leading-order. The validity of isospin invariance of quark distribution and charge-conjugation symmetry of fragmentation functions $D_1^{q \rightarrow h^+} = D_1^{\bar{q} \rightarrow h^-}$ and isospin invariance are assumed in leading twist approximation. The difference asymmetry on the deuteron and hydrogen targets can be equated to a certain combination of parton distributions [5]:

$$A_{1,d}^{h^+-h^-} = \frac{g_1^{uv} + g_1^{dv}}{f_1^{uv} + f_1^{dv}} \equiv \frac{\Delta u_v(x) + \Delta d_v(x)}{u_v(x) + d_v(x)}, \quad A_{1,p}^{h^+-h^-} = \frac{4g_1^{uv} - g_1^{dv}}{4f_1^{uv} - f_1^{dv}} \equiv \frac{4\Delta u_v(x) - \Delta d_v(x)}{4u_v(x) - d_v(x)}. \quad (5)$$

It follows that the charge-difference asymmetries should be independent of the hadron type, a feature consistent with the results shown in Fig. 3. The valence-quark helicity densities computed using Eq. (5) are presented in Fig. 4.

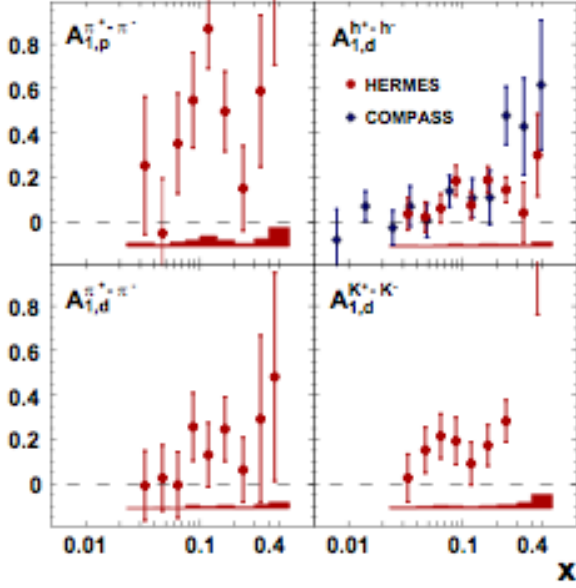


Fig. 3. Hadron charge-difference asymmetries for pions from a hydrogen target and pions, kaons and all hadrons from a deuterium target. Error bars represent statistical uncertainties. Systematic uncertainties are given as bands

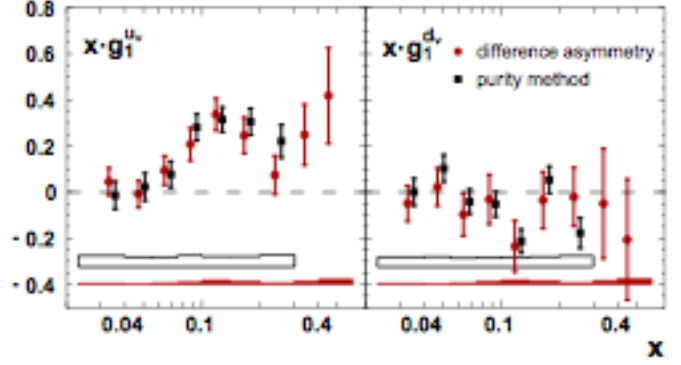


Fig. 4. The helicity distributions for valence quarks computed using pion charge-difference asymmetries and compared with the valence-quark densities computed from HERMES purity extraction [6]

5. Conclusion

Several longitudinal double-spin asymmetries in semi-inclusive deep inelastic scattering have been presented. They extend the analysis of the previous HERMES publications to include also transverse-momentum dependence. Within the precision of the measurements, the virtual photon–nucleon asymmetries $A_1^h(x)$ display no significant dependence on the hadron variables $z, P_{h\perp}$ [4]. Azimuthal moments, $A_{||}^{h, \cos\phi}$ are found to be consistent with zero. The hadron charge-difference asymmetry $A_1^{h^+-h^-}(x)$ yields valence-quark helicity densities consistent with the result of the prior HERMES purity extraction.

References

1. P.J. Mulders *et al.*, Nucl. Phys. B **461**, 197 (1996).
2. A. Bacchetta, *et al.*, JHEP **02**, 093 (2007).
3. A. Bacchetta, *et al.* JHEP **08**, 023 (2008).
4. HERMES Collab., A. Airapetian *et al.*, Phys. Rev. D **99** (11), 112001 (2019).
5. L.I. Frankfurt *et al.*, Phys. Lett. B **230**, 141 (1989).
6. HERMES Collab., A. Airapetian *et al.*, Phys. Rev. Lett. **92**, 012005 (2004).

STUDY OF THE PRODUCTION OF NEGATIVELY CHARGED PIONS IN pn COLLISIONS AT THE BEAM MOMENTA BETWEEN 1 140 AND 1 670 MeV/c

V.V. Sarantsev, S.G. Sherman, V.A. Nikonov, A.V. Sarantsev

1. Introduction

Nucleon–nucleon (NN) collisions are the basic reactions governed by strong interactions, and it is of paramount importance for particle physics to know in detail all properties of these reactions. Elastic collisions have been studied with high precision and over a wide energy range. However, the properties of inelastic processes are known rather poorly. Single pion production in NN collisions is a dominant inelastic process at energies below 1 GeV. It should be noted here that, while the contribution of isovector amplitudes controlling pion production in proton–proton (pp) collisions is known rather well, the contribution of isoscalar ($T = 0$) partial waves to pion production in proton–neutron (pn) collisions has not been studied adequately. The neutron–proton scattering amplitude contains both the isovector ($T = 1$) and the isoscalar ($T = 0$) component. According to currently available estimates, the contribution of the isoscalar cross section is one order of magnitude smaller than the contribution determined by isovector amplitudes. Therefore, it is rather difficult to extract isoscalar amplitudes, which interfere with isovector amplitudes. In addressing this problem, it is of crucial importance to have detailed information about large isovector amplitudes. This provides a motivation for performing a simultaneous analysis of data on pion production both in proton–neutron and in proton–proton collisions.

In the present study, we have performed a partial-wave analysis of data on the reaction $pn \rightarrow pp\pi^-$ that were obtained in proton–deuteron (pd) interactions at nine incident proton energies in the region below 1 GeV. At the first stage, we compared these data with the results of the partial-wave analysis that our group performed earlier for data obtained with a continuous neutron beam [1] and data on π^0 - and π^+ -meson production in pp collisions from our studies reported in Refs. [2, 3] and from Ref. [4] at the momentum of 950 MeV/c. At the second stage, we included data on proton–deuteron collisions in our database and performed a complete simultaneous analysis of all reactions listed above.

2. Description of the experiment and data selection

The experiment being discussed was performed at the synchrocyclotron of PNPI by employing a 35-cm bubble chamber placed in a magnetic field with a strength of 14.8 kG. The 1 GeV energy of the extracted primary proton beam was reduced by employing a copper degrader of the appropriate thickness. After the degrader, the proton beam was formed by three bending magnets and eight quadrupole lenses. The momentum value was established on the basis of the currents in the bending magnets according to the calibration with the aid of a current-carrying filament. In addition, the beam momentum was tested by measuring the curvature of tracks and by subsequently considering the kinematics of events of elastic pd scattering. The uncertainty in determining the momentum of the protons incident into the chamber was ± 2 MeV/c. The root-mean-square spread of the beam momentum was 4–5%. The admixture of heavier particles (d , t and He) in the incident proton beam was determined from time-of-flight measurements and was found to be negligible.

In all, about 400 000 stereoframes were obtained. The irradiation density was on average 12 to 15 tracks per frame. Events involving a negative track and two or three positive tracks were selected in scanning the frames. The double-scan efficiency was 99%. The selected events could belong to the following reactions:

$$\begin{aligned} pd \rightarrow ppp\pi^- & \quad (1), & pd \rightarrow ppp\pi^0 & \quad (2), \\ pd \rightarrow ppn\pi^+ & \quad (3), & pd \rightarrow pd\pi^+\pi^- & \quad (4). \end{aligned}$$

In the reaction of interest to us, three-prong events correspond to the case where the proton is a spectator, has a momentum below 80 MeV/c, and therefore escapes observation in the bubble chamber. Events involving the production of Dalitz pairs were separated on the basis of kinematical and ionization criteria. All events in the fiducial volume of the chamber that were appropriate for measurements were measured

semiautomatically and were geometrically reconstructed. The reaction channels were identified on the basis of the χ^2 values for each specific events at a 1% confidence level.

If the χ^2 values for two hypotheses fell within their confidence intervals, we identified a positive particle by visually estimating the bubble density of tracks, thereby arriving at the ultimate decision on the physics hypothesis for a given track. A procedure that is standard for bubble chambers was used to determine the absolute values of the cross section for the production of negatively charged pions. The accuracy in determining a millibarn-equivalent was $\sim 2\%$. In addition, we introduced corrections for the neutron Fermi momentum in the deuteron and for the Pauli exclusion principle for identical protons [5]. The Table gives the momenta of protons incident into the chamber and the number of events of the reaction $pn \rightarrow pp\pi^-$ at each momentum value.

Table

Momenta of incident protons (in MeV/c units) and number of events of the reaction $pn \rightarrow pp\pi^-$ at each momentum value

Beam momentum	Number of events
1 140	266
1 217	305
1 292	703
1 348	944
1 380	773
1 438	908
1 508	700
1 562	1 139
1 671	1 128

3. Data analysis

The experimental momentum distributions of final particles from the reaction $pn \rightarrow pp\pi^-$ in the laboratory frame are shown in Figs. 1 and 2 at nine momenta of incident protons. For events of this reaction, we took events of reaction (1) where the momentum of the spectator proton is less than 150 MeV/c. The solution for partial waves that was obtained from the data analysis in Ref. [1] predicts fairly well these distributions (see *dotted lines* in Figs. 1 and 2). In either case, however, the predictions exceed substantially the data at the maximum of the distributions. This is likely to be due to overestimating the total neutron-proton cross section, which is hardly controllable in the reaction induced by a continuous neutron beam. In Figure 3, the angular distributions of final state π^- mesons in the reaction centre-of-mass (c. m.) frame are presented along with the respective results of the forementioned partial-wave analysis. The asymmetry of these distributions is defined by the interference between the isoscalar and isovector amplitudes.

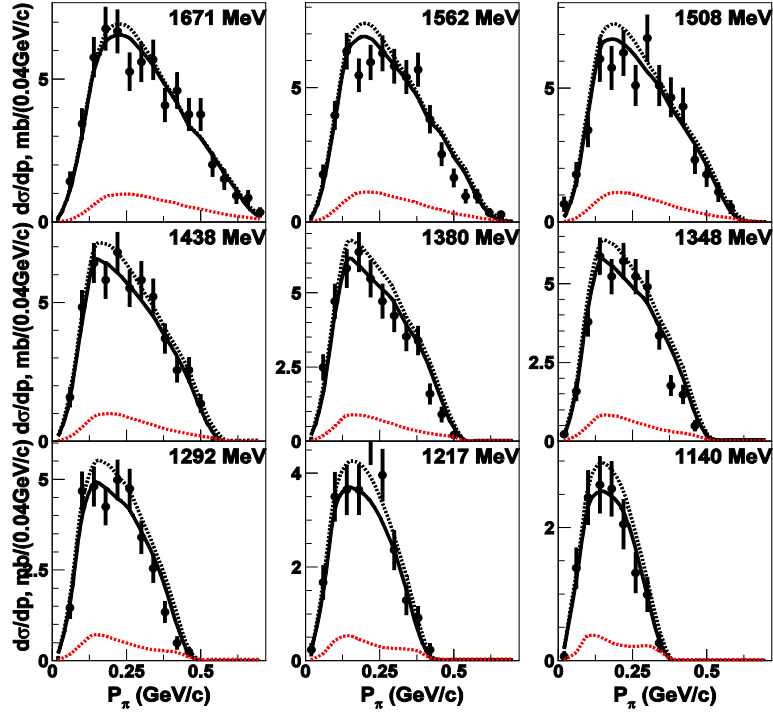


Fig. 1. Momentum distribution of negatively charged pions for events of the reaction $pn \rightarrow pp\pi^-$ in the laboratory frame; *closed circles* – experimental data, *solid curves* – results of our partial-wave analysis, *dotted curves* – results of the partial wave analysis in Ref. [1] and *dashed curves* – contributions of the isoscalar cross section ($T = 0$). The distributions in question are shown for nine values of the primary proton momentum

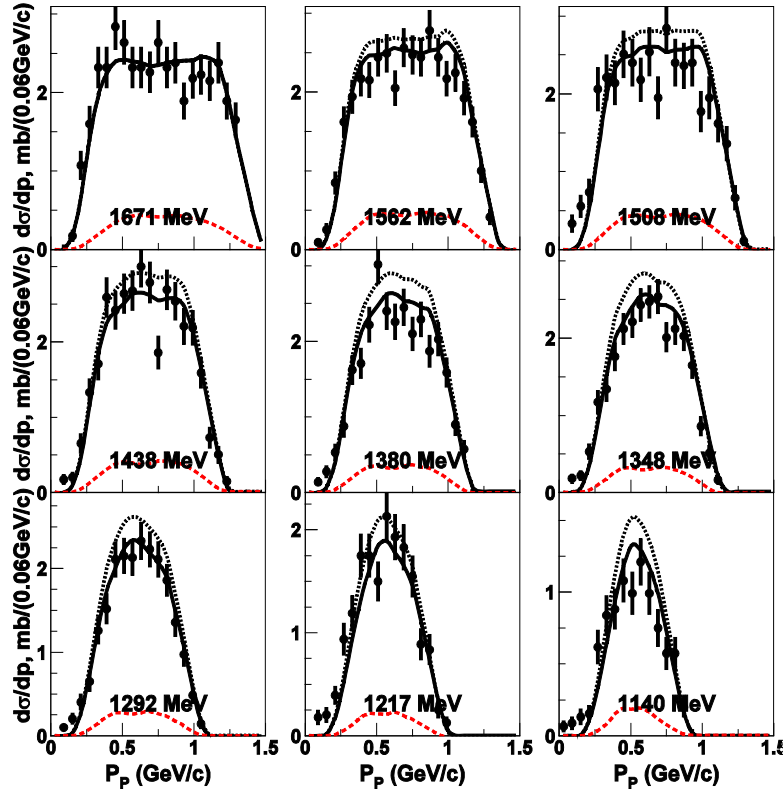


Fig. 2. Momentum distribution of protons for events of the reaction $pn \rightarrow pp\pi^-$ in the laboratory frame. The *closed circles* represent experimental data. The notation for the curves is identical to that in Fig. 1

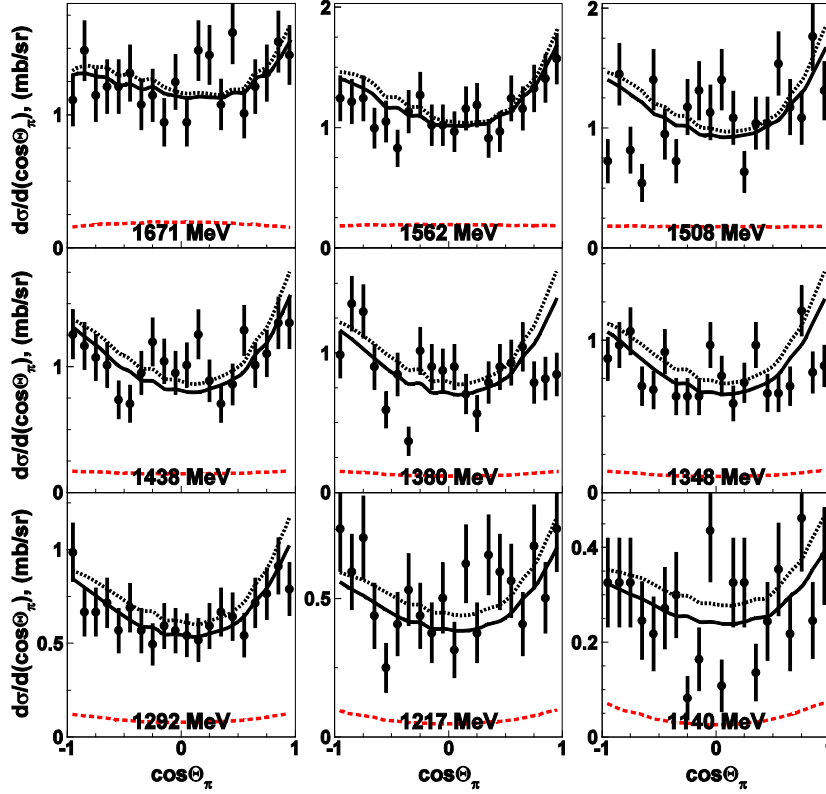


Fig. 3. Angular distribution of negatively charged pions in the reaction centre-of-mass. The *closed circles* represent experimental data. The notation is identical to that in Fig. 1

Although the shape of the distributions, including the asymmetry, is predicted quite accurately, a systematic excess of the predictions above the experimental data is observed here as well. In this article, we do not present the angular distribution of protons, since such distributions are symmetric [1] and are of no particular interest.

A decrease in the cross section for proton–neutron collisions is due primarily to the change in the isoscalar amplitudes. Upon changing the total contribution at an invariable asymmetry of the angular distribution of pions, it would be natural to expect a redistribution of the contributions of different partial waves. In order to extract isoscalar amplitudes, we have performed a global partial-wave analysis of the new data together with the data quoted in Ref. [1]. The formalism used was expounded in detail elsewhere [6–8] and is based on a spin–orbit expansion of the initial and final partial-wave amplitudes. In this connection, it was natural to employ the spectroscopic notation $^{2S+1}L_J$ for two-particle partial waves, where S is the intrinsic spin, L is the orbital angular momentum, and J is the total angular momentum.

We introduced the $\Delta(1232)3/2^+$ resonance and the $N(1440)1/2^+$ Roper resonance in order to describe the energy dependence in the πN system and used a modified effective scattering-length approximation in order to describe the NN interaction. Specific expressions can be found in Ref. [1]. In our analysis, we additionally included new data that were reported in Refs. [9–11] for pp inelastic reactions involving the productions of π^0 and π^+ mesons and which were measured at the proton-beam momenta of 1 581, 1 628 and 1 683 MeV/ c .

Owing to this, the contributions of isovector states at the high-energy boundary of the interval being studied could be determined more precisely, the unstable contributions of high-spin amplitudes being fixed by these data. The results of this global fit are represented by the solid curves in the figures. The improvement of agreement between the experimental data and the results of the partial-wave analysis can clearly be seen. This systematic improvement is evinced by a change in χ^2 , which decreased from 3.64 to 2.52 per degree of freedom for 473 fitted points. Concurrently, the description of the differential cross sections obtained in the measurements with a continuous neutron beam underwent virtually no change: the likelihood function became worse by only 30 for 8 155 points. At the same time, the total cross section

decreased by 5 to 6%, and this made it possible to describe the new data. The contribution of the isoscalar amplitudes is represented by the dashed curves. It is substantially smaller than the isovector contribution. Figures 4 and 5 give the contributions of various isovector and isoscalar amplitudes to the reaction $pn \rightarrow pp\pi^-$ versus the incident beam energy.

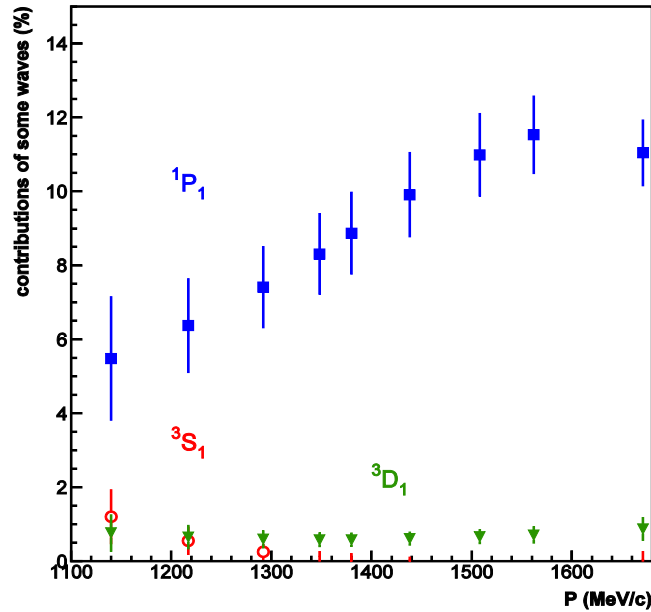


Fig. 4. Contributions (in percent) of the most important isoscalar waves to the reaction $pn \rightarrow pp\pi^-$

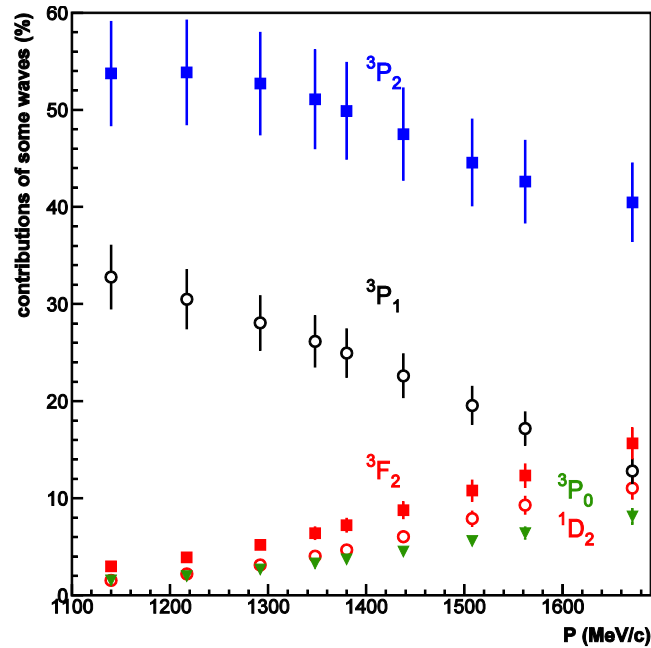


Fig. 5. Contributions (in percent) of the most important isovector waves amplitudes

4. Conclusion

We have compared new experimental data on the production of negatively charged pions in pn collisions with the results of the partial-wave analysis performed earlier and based on the data obtained with a continuous neutron beam. The inclusion of the new experimental data in the global fit permitted refining

the contributions of various partial waves, especially the contribution of isoscalar amplitudes. The data and the results of the analysis agree satisfactorily, confirming a small contribution (less than 12%) of isoscalar partial waves in the energy region below 1 GeV.

References

1. V.V. Sarantsev, K.N. Ermakov, L.M. Kochenda *et al.*, *Eur. Phys. J. A* **43**, 11 (2010).
2. V.P. Andreev, A.V. Kravtsov, M.M. Makarov, *et al.*, *Phys. Rev. C* **50**, 15 (1994).
3. V.V. Sarantsev *et al.*, *Eur. Phys. J. A* **21**, 33 (2004).
4. COSY-TOF Collab., S.A. El-Samad *et al.*, *Eur. Phys. J. A* **30**, 443 (2006).
5. L.G. Dakhno, A.V. Kravtsov, E.A. Lobachev *et al.*, *Sov. J. Nucl. Phys.* **36**, 83 (1982).
6. A.V. Anisovich, E. Klempt, A.V. Sarantsev, U. Thoma, *Eur. Phys. J. A* **24**, 111 (2005).
7. A.V. Anisovich, A.V. Sarantsev, *Eur. Phys. J.* **30**, 427 (2006).
8. A.V. Anisovich, V.V. Anisovich, E. Klempt *et al.*, *Eur. Phys. J. A* **34**, 129 (2007).
9. K.N. Ermakov, V.I. Medvedev, V.A. Nikonov *et al.*, *Eur. Phys. J. A* **50**, 98 (2014).
10. K.N. Ermakov, V.I. Medvedev, V.A. Nikonov *et al.*, *Eur. Phys. J. A* **47**, 159 (2011).
11. K.N. Ermakov, V.A. Nikonov, O.V. Rogachevsky *et al.*, *Eur. Phys. J. A* **53**, 122 (2017).

PNPI Participation in the LHC Detectors Upgrade

CMS ENDCAP MUON SYSTEM UPGRADE

PNPI participants of the CMS Collaboration: A.A. Vorobyev, V.T. Kim, Yu.M. Ivanov, A.Iu. Egorov, G.E. Gavrilov, V.L. Golovtsov, E.V. Kuznetsova, V.A. Murzin, V.A. Oreshkin, I.B. Smirnov, D.E. Sosnov, V.V. Sulimov, L.N. Uvarov, S.S. Volkov

1. Introduction

The compact muon solenoid (CMS) (Fig. 1) is a general-purpose detector at the Large Hadron Collider (LHC) located at CERN, Geneva [1]. It is one of the most ambitious scientific projects designed to investigate a wide range of high energy physics. The recent discovery of the Higgs boson is one of the major CMS achievements. The next step is the search for dark matter candidates and for any manifestation of physics beyond the Standard Model.

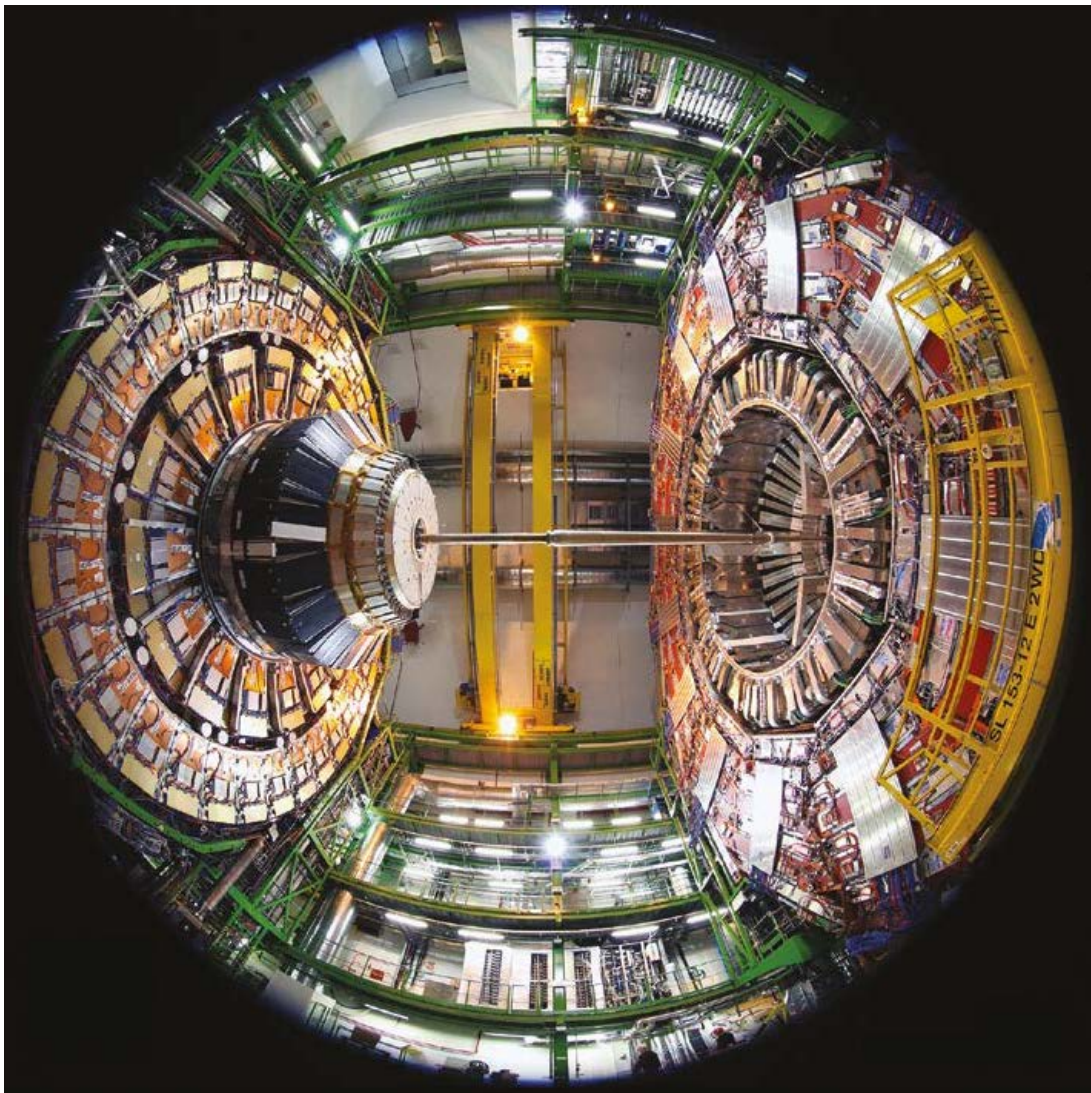


Fig. 1. The open CMS detector from below

Since the beginning of the CMS project, PNPI participated in the design, construction and operation of the endcap muon system (EMU). During the construction phase (2001–2007), 120 six-layer multiwire cathode strip chambers (CSC) were produced at PNPI for the EMU stations ME2, 3, 4/1. Another important

contribution was the design and production at PNPI of a 10 000-channel high voltage (HV) supply system for the EMU CSCs, with independent control and regulation of each HV channel. Also, PNPI participated in the design and construction of the track finding processor (TFP), which was an essential part of the EMU trigger system, and in the design and testing of the front-end electronics for the CSCs. Later, in 2011–2013, 76 large CSCs were constructed for the EMU station ME4/2. The production was organized at CERN with active participation of PNPI engineers. In 2014, the ME4/2 chambers were installed into the CMS detector, thus completing construction of the whole EMU system. An additional 2 400-channel HV supplier for the ME4/2 CSCs was produced at PNPI.

PNPI shares responsibility for the maintenance and operation of the EMU system. This system showed very reliable performance during the whole running period (2009–2022). Initially, CMS was designed to operate with an instantaneous luminosity of $1 \cdot 10^{34} \text{ cm}^{-2} \cdot \text{s}^{-1}$. This luminosity was reached already in 2012. By the end of 2018, the peak luminosity was increased to $2 \cdot 10^{34} \text{ cm}^{-2} \cdot \text{s}^{-1}$, and the integrated luminosity reached 200 fb^{-1} .

During all this period, the gas gain in the CSCs remained practically unchanged. Several CSCs suffered from appearance of the “Malter effect” (uncontrolled self-sustaining discharges) in some sectors of the CSCs. However, this does not influence the CSCs total efficiency due to very high redundancy of the system. Each CSC contains six layers of independent gas gaps. In addition, each layer in most CSCs is separated into several (up to five) sectors with independent HV supply channels. Therefore, switching off one sector (or reducing the HV in this sector) does not change noticeably the efficiency of the whole CSC.

According to the existing plans [2] for the next 15 years, CMS must be ready to operate after Long Shutdown 2 (LS2) with the peak luminosity gradually increasing up to $5 \cdot 10^{34} \text{ cm}^{-2} \cdot \text{s}^{-1}$. After LS3 (2026–2028), the luminosity of $5 \cdot 10^{34} \text{ cm}^{-2} \cdot \text{s}^{-1}$ will be maintained during the entire beam fill due to implementation of the luminosity leveling, with the 25 ns bunch spacing. This should allow to use the beam time more efficiently. The goal is to deliver $3\,000 \text{ fb}^{-1}$ of the integrated luminosity. To meet the new requirements, all subsystems of the CMS detector are to be upgraded. The upgrade program was formulated also for the CMS EMU system. Due to the endcap location, CSCs will experience a significant increase in the detector occupancy. The most affected will be the stations located in the region of large pseudorapidity, namely MEx/1. In order to fulfill the high luminosity LHC (HL–LHC) operation conditions, an upgrade of the CSC readout electronics is ongoing. Already during the LS2 period, an upgrade of on-chamber electronics was performed providing the optical trigger and data links for all MEx/1 chambers and increasing the data pipeline capacity to accommodate larger trigger latency. The corresponding upgrade of the back-end electronics responsible for the CSC trigger formation and data collection is ongoing and should be completed during LS3. Additionally, an upgrade of the ME1/1 HV supply was performed during LS2 in order to unify the CSC HV system and to improve resolution of the ME1/1 current monitoring.

The reliable performance of the CSCs, demonstrated during all previous years and dedicated studies performed prior the CSC construction in the beginning of 2000, gives good confidence that these chambers could operate in the next 15 years and accumulate the integrated luminosity up to $3\,000 \text{ fb}^{-1}$. Currently, additional R&D (Research and Development) is ongoing to study CSC longevity for the HL–LHC conditions. Presence of a greenhouse gas CF_4 in the CSC gas mixture provides good resistance to possible aging processes in the chamber, and the longevity of CSCs operating with the nominal gas mixture containing 10% CF_4 was confirmed. As the next step, an R&D on reduction of the CF_4 or even its replacement with more ecology-friendly gas has been started.

PNPI participates in the following items of the CMS EMU upgrade program: upgrade of the HV system, upgrade of the muon trigger, CSC aging studies.

2. Upgrade of the cathode strip chambers high voltage system

The present multichannel HV system for the CSCs was developed at PNPI in collaboration with the University of Florida (UF), and it was successfully used since the beginning of the CMS experiment. The system has a three-tier structure (Fig. 2). There are eight commercial Matsusada primary HV power supplies ($\text{HV}_{\text{max}} = 5\,000 \text{ V}$, $I_{\text{max}} = 60 \text{ mA}$). They provide the HV power to 50 master boards. Each master board has eight regulated outputs with the 1.5 mA maximum current in each of them. Both the primary HV supplies and

the crates with the master boards are located in the USC (underground service cavern, where there is no damage to the electronics circuits due to radiation). The master board outputs are routed to the distribution boards located near the CSCs (on the periphery of the endcap discs). There are two types of the distribution boards: the 30-channel boards serve the ME2/1, ME3/1, ME4/1, ME4/2 chambers (one chamber per board) and the 36-channel boards serve the ME2/1, ME3/1, ME4/1, ME1/2, ME1/3 chambers (two chambers per board). Each distribution board can provide the total current at its outputs up to 1.5 mA (limited by the master board) and the maximum current per channel not exceeding 100 μ A. The resolution of the current measurements in the individual channels is 100 nA. Table 1 summarizes the quantities of different hardware components in the present UF–PNPI HV system.

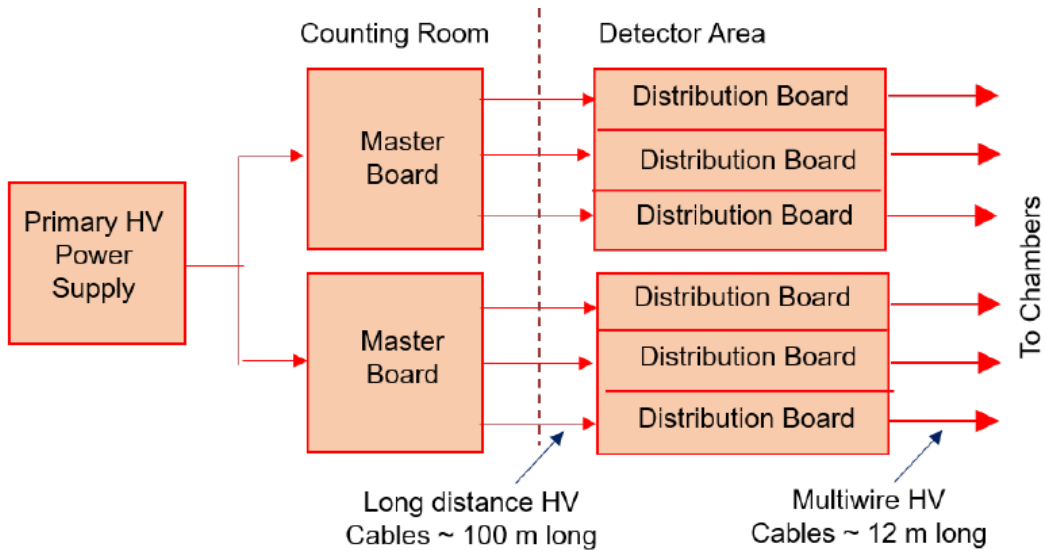


Fig. 2. UF–PNPI high voltage system structure

Table 1

Summary of hardware components in the present UF–PNPI high voltage system

Component	Quantity
Primary HV power supply	8
Master board	50
Distribution board – 30 channels	216
Distribution board – 36 channels	126
Independently regulated and monitored HV distribution channels	11 016

Besides the 11 016-channel UF–PNPI HV system, during Run-1 and Run-2 a commercial 432-channel CAEN HV supplier was used for ME1/1 chambers. It has sixteen HV boards (CAEN 1733BP) housed in the USC. Each channel can provide the maximum voltage up to 4 000 V and the maximum current up to 2 mA. Even though the nominal resolution in the current measurements in individual channels is 200 nA, the experience of operating this system showed significant noise in such measurements deteriorating the resolution.

For the future operation of the EMU system, the UF–PNPI HV supplier will be upgraded to have a sufficient margin to handle the current load expected at the LHC with a comfortable safety factor. During LS2, the CAEN HV supplier serving the ME1/1 chamber was replaced with the UF–PNPI HV system to provide precise current measurements needed for reliable monitoring of the chamber performance and for prompt diagnostics of possible operation problems during the HL–LHC operation.

The HV system upgrade plans include the following steps. In the UF–PNPI HV system, the commercial primary HV power suppliers will be withdrawn, and the present master boards will be replaced with thirty eight nine-channel master boards of a new design. Each channel in the upgraded boards will have its own HV power source, capable of outputting voltages from 0 to 4 000 V with the maximum current of 2.5 mA. This should be enough even at the ultimate LHC luminosity of $7.5 \cdot 10^{34} \text{ cm}^{-2} \cdot \text{s}^{-1}$. Another advantage of the new HV structure is more simple maintenance and operation of the two-tier system if compared with the three-tier system. The new master boards have been designed and successfully prototyped at PNPI. The ME1/1 HV subsystem has already been absorbed into the total UF–PNPI HV system. For the 432 HV channels of the ME1/1 station two upgraded master boards and twelve 36-channel distribution boards of the current design (Fig. 3) have been installed. Besides ensuring reliable current measurements, such a replacement makes the entire CSC HV system homogenous and simpler to operate and maintain. The master and distribution boards for the ME1/1 chamber are installed in a rack in the USC located near the racks that house the components of the existing UF–PNPI HV system. Table 2 summarized all modules of the upgraded UF–PNPI HV system.



Fig. 3. High voltage segmented power supply modules (*left*) and distribution boards DB36 (*right*)

Table 2

Summary of hardware components in the upgraded UF–PNPI high voltage system

Component	Quantity
Nine-channel master board	52
Distribution board – 30 channels	216
Distribution board – 36 channels	138
Independently regulated and monitored HV distribution channels	11 448

3. Cathode strip chambers aging studies

The general objective of the aging studies is to assess the radiation resistance of the muon chambers (CSC) in view of the planned increase of the integrated luminosity from the present value of 200 up to 3 000 fb^{-1} , with the accumulated charge level reaching $\sim 0.2 \text{ C}$ per 1 cm of an anode wire. Besides, there is an intention to modify the gas mixture of CSCs. At present, CSCs operate with the original mixture of 40% Ar + 50% CO_2 + 10% CF_4 . The main purpose to have CF_4 in the gas is to ensure the radiation resistance of the detector. However, CF_4 is considered as a dangerous gas for ecology. It is an extremely stable gas, which strongly absorbs infrared radiation at $\sim 8 \mu\text{m}$, and therefore it is capable to influence the greenhouse effect. The CF_4 emission in the CMS detector is being reduced over years by means of improvements of the CSC gas system. The CSC gas system operates in a closed loop mode with replenishment rate of 10%. The CF_4 recuperation system can reach up to 70% efficiency after a significant upgrade during LS2. However, even after the gas system upgrade the equivalent of a daily CF_4 emission in the global warming potential (GWP) units for all CSCs is about 12 t of CO_2 , with a lifetime of $\sim 50\,000$ years. Our goal is to consider a possibility either to reduce the amount of CF_4 in the gas mixture or to replace it with some ecology-friendly gas. In both cases, we should guarantee sufficient radiation resistance of CSCs.

Within this program, two CSC prototypes were manufactured at PNPI for the aging studies. The electric field structure and the construction materials are identical to those of the CSCs operating in the CMS detector.

One prototype was filled with the nominal CMS gas mixture 40% Ar + 50% CO₂ + 10% CF₄, while the mixture 37% Ar + 61% CO₂ + 2% CF₄ with the reduced fraction of CF₄ was used in the second prototype. The prototypes were irradiated with an intense β -source ⁹⁰Sr ($E_{\beta}^{\max} \approx 2.28$ MeV). The diameter of the irradiation area was about 4 cm.

In order to monitor the relative gas gain, regular measurements of the prototype response to a ⁵⁵Fe ($E_{\gamma} = 6$ keV) source were performed. During the measurements the source was placed above thin windows made in the cathode panels at three control points *D*, *E* and *F* along the irradiated anode wires. Point *E* was in the centre of the irradiation area, while points *D* and *F* were at distances of ± 6 cm from point *E*. The prototypes were irradiated up to 1.36 C/cm for the nominal CMS gas mixture and up to 0.39 C/cm for the modified gas mixture. The relative gas gain as a function of the accumulated charge was measured with a ⁵⁵Fe source. The results of the measurements are shown in Fig. 4. One can see that the gas gain remains stable in all monitored points up to the maximal accumulated charge. The *dark currents* measured during these aging tests did not demonstrate any increase significant for the detector performance. Later similar studies were performed at CERN with gas mixtures containing 5, 2 and 0 % CF₄. No performance degradation was seen in those tests as well up to the accumulated charge of 0.24 C/cm, as shown in Fig. 5, what is equivalent to a factor of two of the charge which is expected for HL–LHC operation of ME2/1 chamber type. However, the material analysis done for the irradiated anode wires showed a noticeable carbon deposition on the wire surfaces in the cases of 2 and 0% CF₄ while no significant surfaces modification was seen for the 5% CF₄ gas mixture (Fig. 6). At the moment, a gas mixture 40% Ar + 55% CO₂ + 5% CF₄ is considered as promising, and the final irradiation tests with the produced CSCs and a closed loop gas system are ongoing at the Gamma Irradiation Facility at CERN. In order to investigate the possibility to replace the greenhouse CF₄ with a more ecology-friendly gas, investigations of the new gas mixtures were started. As a first trial, the gas which is being carefully studied as a potential replacement of tetrafluoroethan R134a in resistive plate chambers, namely 1,3,3,3-Tetrafluoropropene, HFO1234ze (CF₃CH=CHF), has been chosen due to its wide availability, sufficient presence of fluorine atoms in the molecule and the low GWP < 1.

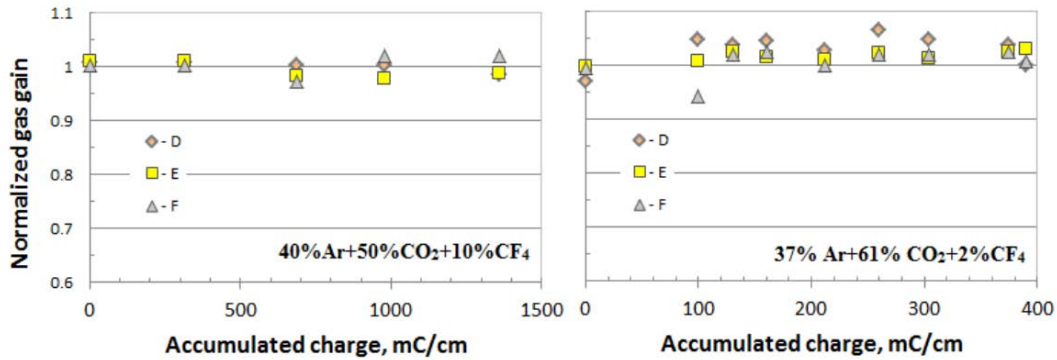


Fig. 4. Dependences of the gas gain on the accumulated charge for two aging runs: with a standard CSC gas mixture (left) and with a modified gas mixture with the five times reduced fraction of CF₄ (right)

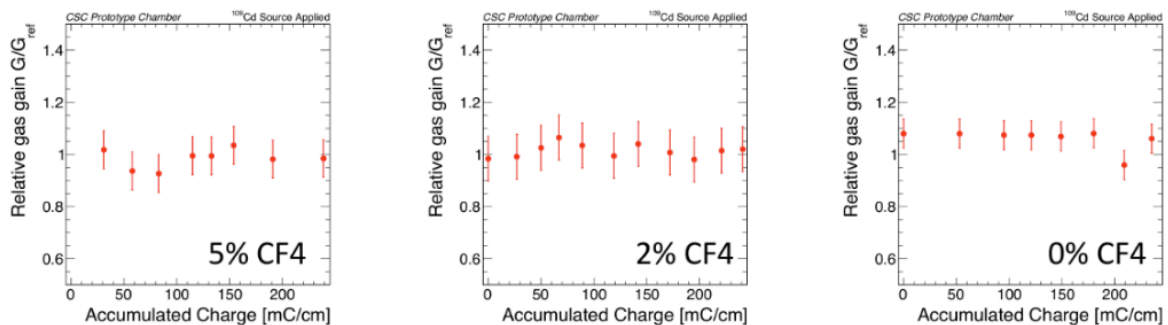


Fig. 5. Relative gas gain as a function of the accumulated charge measured with a ¹⁰⁹Cd source in the irradiation tests with 5, 2 and 0% CF₄ in the gas mixture

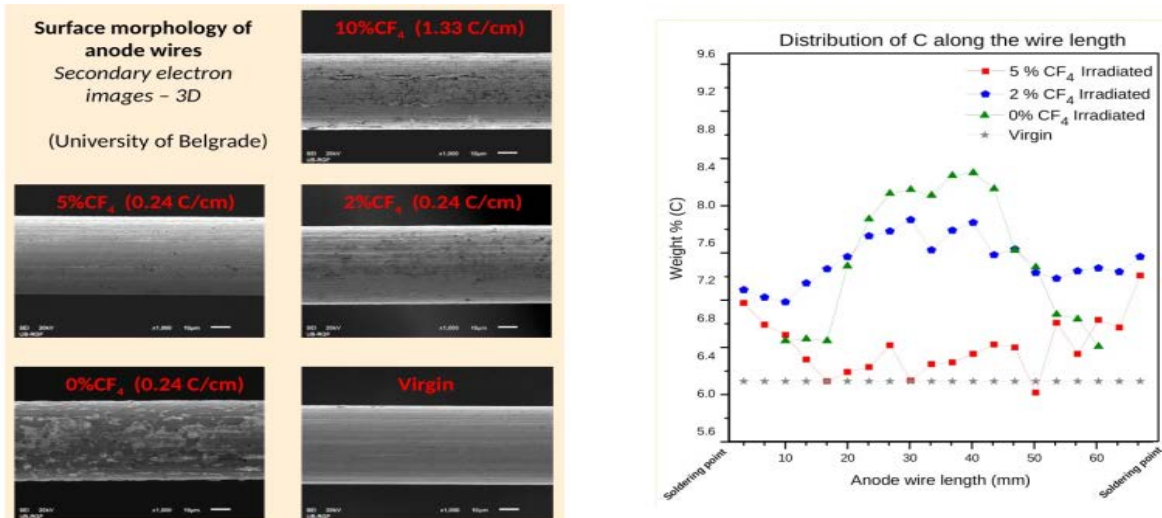


Fig. 6. Scanning electron microscope (SEM) images of anode wires extracted from the CSC prototypes irradiated with different fractions of CF₄ in the gas mixture compared to a non-irradiated (“virgin”) wire (*left*). The weight fraction of carbon detected on the wire surface along the irradiated and non-irradiated anode wires measured with energy dispersive X-ray spectroscopic technique (EDS); the increase in the carbon concentration along the wire corresponds to the irradiation area (*right*)

Using a CSC prototype, a gas mixture 38.8% Ar + 58.2% CO₂ + 3% C₃H₂F₄ was studied. Figure 7 (*left*) shows the current induced with a ⁹⁰Sr source, the corresponding gas gain and the dark current measured as a function of the high voltage for the new gas mixture. The gas gain was evaluated as the ratio of the ⁹⁰Sr current in the gas amplification mode (HV > 1000 V) to the corresponding ionization current at HV ≈ 700 V. Figure 7 (*right*) shows the chamber response to a ⁵⁵Fe source measured as event count rate as a function of the applied HV and demonstrates the operation efficiency plateau. A working point for this gas mixture is achieved at HV ≤ 3850 V with the gas gain equal to 5 · 10⁵. It is completely compatible with operation conditions and the capabilities of the high voltage system and readout electronics of the CSC operating within the CMS muon system.

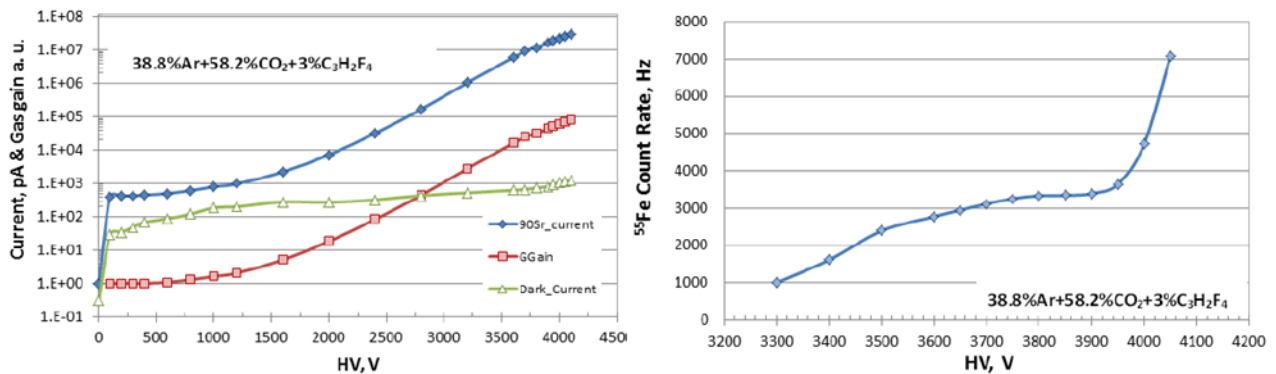


Fig. 7. Prototype current measured with a ⁹⁰Sr source, the evaluated gas gain and the *dark current* versus the high voltage (*left*). ⁵⁵Fe count rates versus the high voltage (*right*). Both measurements were performed with a 38.8% Ar + 58.2% CO₂ + 3% C₃H₂F₄ gas mixture

An amplitude spectrum of the ⁵⁵Fe X-rays obtained at HV = 3850 V is shown in Fig. 8 (*left*). The position of the 6 keV peak corresponds to the collected charge of 800 fC. Figure 8 (*right*) demonstrates the dependence of the gas gain on the fraction of C₃H₂F₄ in the gas mixture. It follows from this figure that, in order to be within the limits of the existing CMS HV system (HV_{max} = 4000 V), the fraction of C₃H₂F₄ in the gas mixture should not exceed 3%.

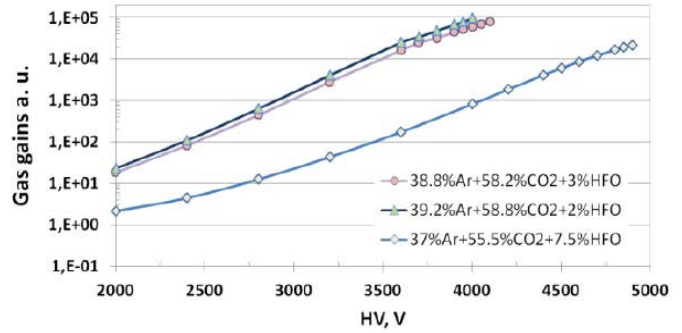
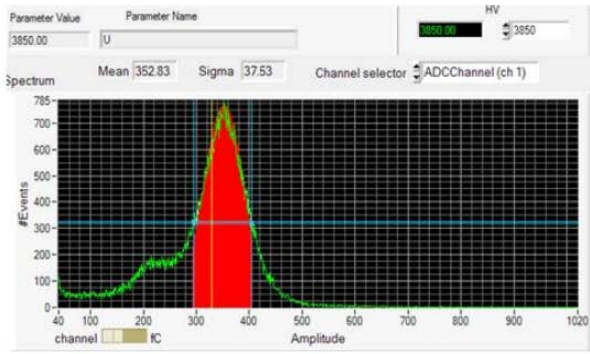


Fig. 8. Amplitude spectrum of ^{55}Fe X-rays ($E = 6$ keV) measured at the HV = 3 850 V (*left*). Gas gain versus high voltage for different fractions of $\text{C}_3\text{H}_2\text{F}_4$ in the gas mixture (*right*)

Preliminary longevity studies with the potential gas mixture containing 2% HFO1234ze have been performed up to the accumulated charge of 1.2 C/cm. As shown in Fig. 9, the relative gas gain did not change, however a strong increase in the dark current was observed. Further studies, including material analysis of the irradiated electrodes and additional longevity tests, are ongoing with the HFO1234ze gas as well as searches for other potential CF_4 alternatives.

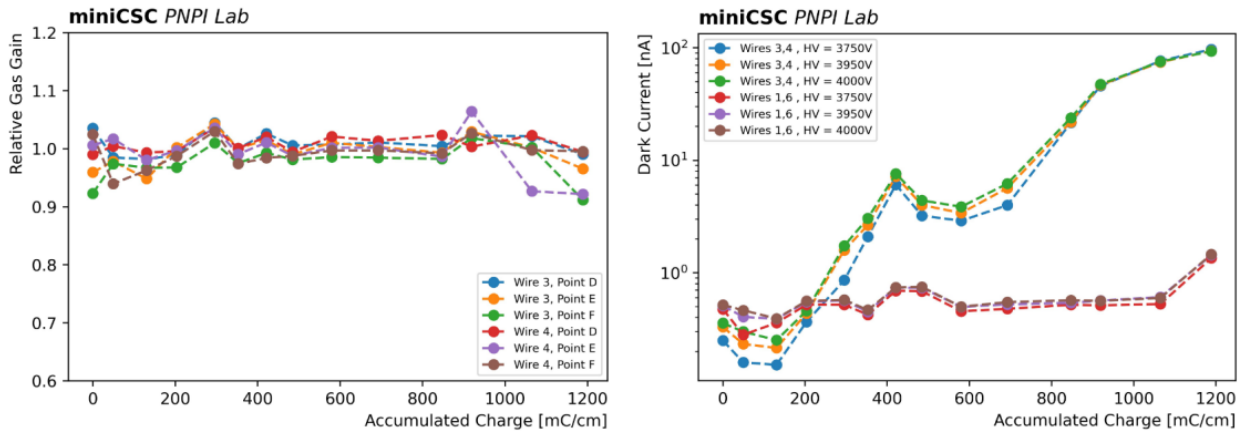


Fig. 9. The results of the preliminary longevity test done with the 40% Ar + 58% CO_2 + 2% HFO1234ze gas mixture: *left* – relative gas gain measured for a mini CSC as a function of the accumulated charge; the relative gas gain of the irradiated chamber area was defined as a ratio of the ^{55}Fe peak positions in the spectra measured at the irradiated area and at the non-irradiated points. *Right* – *dark currents* measured from anode wires of the mini CSC as a function of the accumulated charge. The measurements were done for anode wires experienced irradiation (wires 3, 4) and for reference wires located far from the irradiation area (wires 1, 6). A significant rise of the *dark current* was observed for the irradiated wires, exceeding the current from the reference wires by about an order of magnitude already at 400 mC/cm

4. Summary

PNPI has made important contributions to the design and construction of the EMU of the CMS detector and shares responsibility for the EMU maintenance and operation. During the whole running period of the LHC (2009–2022), EMU demonstrated very reliable operation at the luminosity up to $2 \cdot 10^{34} \text{ cm}^{-2} \cdot \text{s}^{-1}$, which exceeds the initially designed value by a factor of two. In fact, EMU proved to be one of the most reliable systems in the CMS detector.

The goal of the EMU upgrade program is to prepare EMU to work for the next 15 years with higher luminosity (up to $7 \cdot 10^{34} \text{ cm}^{-2} \cdot \text{s}^{-1}$). PNPI participates in this program in the following tasks:

- Upgrade of the HV system,
- Aging studies of the muon chambers,
- Search for a new eco-friendly gas mixture for the muon chambers.

References

1. CMS Collab., JINST **3**, S08004 (2008).
2. CMS Collab., Techn. Report CERN-LHCC-2017-012 CMS-TDR-016 (2008).

UPGRADE PROGRAMME OF THE ATLAS DETECTOR AT THE LARGE HADRON COLLIDER

PNPI participants of the ATLAS Collaboration: S.G. Barsov, O.L. Fedin, A.E. Ezhilov, M.P. Levchenko, V.P. Maleev, Yu.G. Naryshkin, D. Pudzha, V.A. Schegelsky, V.M. Solovyev

1. Introduction

The Large Hadron Collider (LHC), located at the European Organization for Nuclear Research (CERN) for a long time will remain the accelerator that provides the highest energy of proton–proton collisions, which ensures the novelty and relevance of the experimental results obtained with its help. The LHC was stopped from December 2018 till July 2022 for internal upgrades of the system, and this led to an increased luminosity up to $3 \cdot 10^{34} \text{ cm}^{-2} \cdot \text{s}^{-1}$. The increase of luminosity directly affects the detector ATLAS located at one of the LHC interaction points: a significant increase in the radiation background is expected in the ATLAS detector, primarily in the areas close to the interaction point of the LHC proton beams. The part of the muon system known as Small Wheels (SW) is not capable of operating at such a high rate, and its efficiency is expected to decrease. To solve these limitations, it was decided to replace the old SW by new detector structures – New Small Wheels (NSW) [1]. The detector technologies that were chosen for NSW are small-strip thin gap chambers (sTGC) [2] and Micromegas (MM).

2. Construction at PNPI

The PNPI team was involved in the construction and design of the largest type of sTGC – QL3. At the end of 2020, the PNPI team assembled all needed 32 quadruplets of sTGCs + 4 spares. Photos from construction sites can be seen in Fig. 1.



Fig. 1. Photos, illustrating different assembly steps of sTGCs at PNPI

For quality control of the manufactured detectors, dedicated tests were carried at different steps of the production: high voltage (HV) tests to ensure that the chambers can withstand 3 200 V (400 V more than the working point) without trips or dark current for a long time; X-ray scanning (shown in Fig. 2) for verification

of the gas gain uniformity; pulser tests to track down possible channels with distorted signals from them; a special test to check for possible shorts between the readout channels; and the final step in checking the performance of the assembled sTGC module was to measure the performance of each detector channel using cosmic muons (an example of the test output can be seen at Fig. 3).



Fig. 2. X-ray stand at PNPI

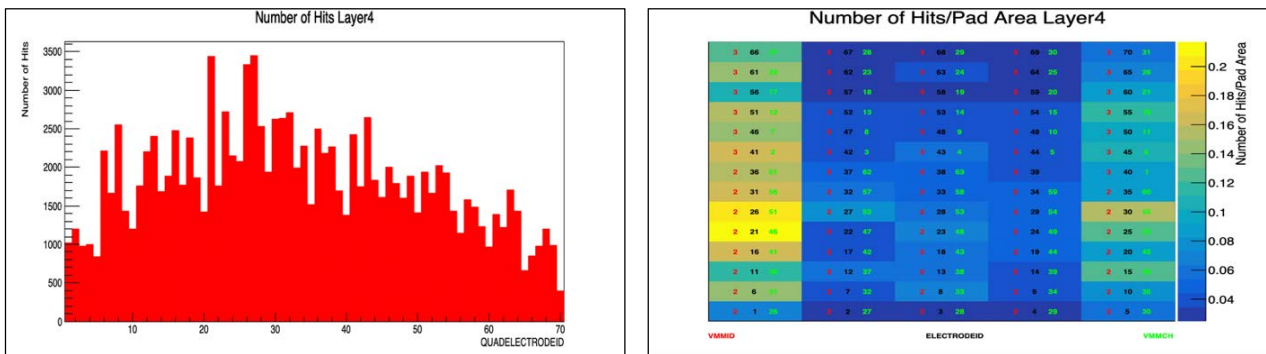


Fig. 3. Number of hits in each pad on one of the quadruplet layers, within the allowed time window and exceeded threshold

3. New Small Wheels assembly

In 2020–2021, the PNPI team participated in the assembly of the NSW detector at CERN. The quadruplets that arrived at CERN underwent an inspection, which consisted of a visual inspection, a leak test, and a HV test. The main goal of the HV test was to check the integrity of the anode wires which could be broken during transportation. It consisted of applying a high voltage of up to 2.8 kV to each chamber in the module filled with CO₂. The modules that passed the input control were then sent for a high radiation test, which was carried out at the installation GIF++ (gamma irradiation facility) [3] – a unique place where high energy charged particle beams are combined with a 14 TBq ¹³⁷Cs source. During the test, the chamber was filled with the working gas mixture (CO₂ + 45% C₅H₁₂) and the nominal voltage was applied. If there were no trips or high current within 10 min, then the radiation source was switched on. The current was recorded in the chamber under irradiation for 30 min, then the source was turned off and the current was monitored for another 10 min. The criteria for passing the test were the absence of trips and the absence of current variations of more than 1%. Figure 4 shows QL1 type modules on the radiation stand (*left*) and the result of the test (*right*). In the test results plot, the *blue line* shows the voltage in Volts and the *red line* shows the current in the chamber in μA.

The chambers that successfully passed the test were sent for assembly [4]. At the first stage, modules of three types were glued together on a special slipway and pasted over with a reinforcing frame (Fig. 5 on the *left*). The electronics was installed on the sector, HV cables were soldered and temperature sensors were installed, as well as position sensors for building the detector (see Fig. 5 on the *right*). Then a long-term HV

test was carried out and the electronic noise was measured to verify the correctness of the ground. If necessary, additional grounding was done.

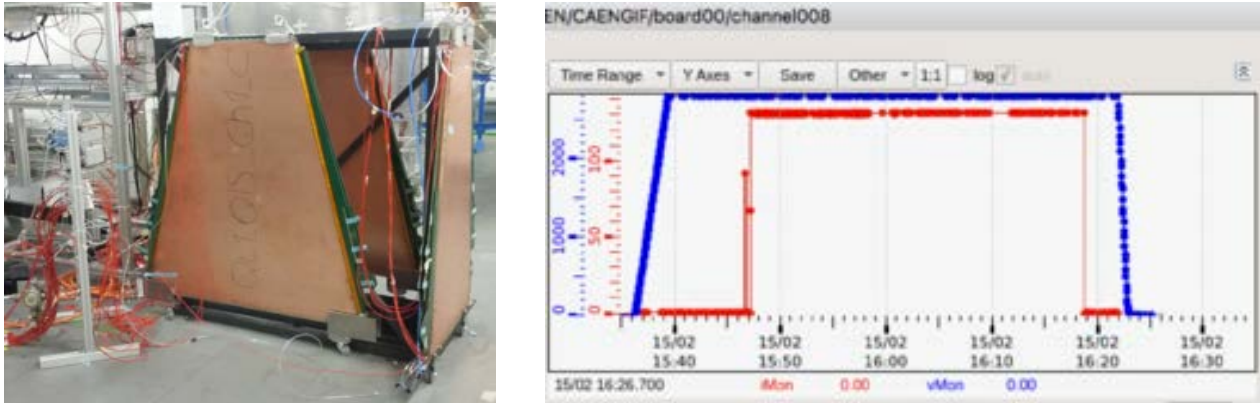


Fig. 4. QL1 quadruplets mounted on the radiation stand (*left*) and results of the test (*right*). The *blue line* shows the voltage in Volts and the *red line* shows the current in the chamber in μA

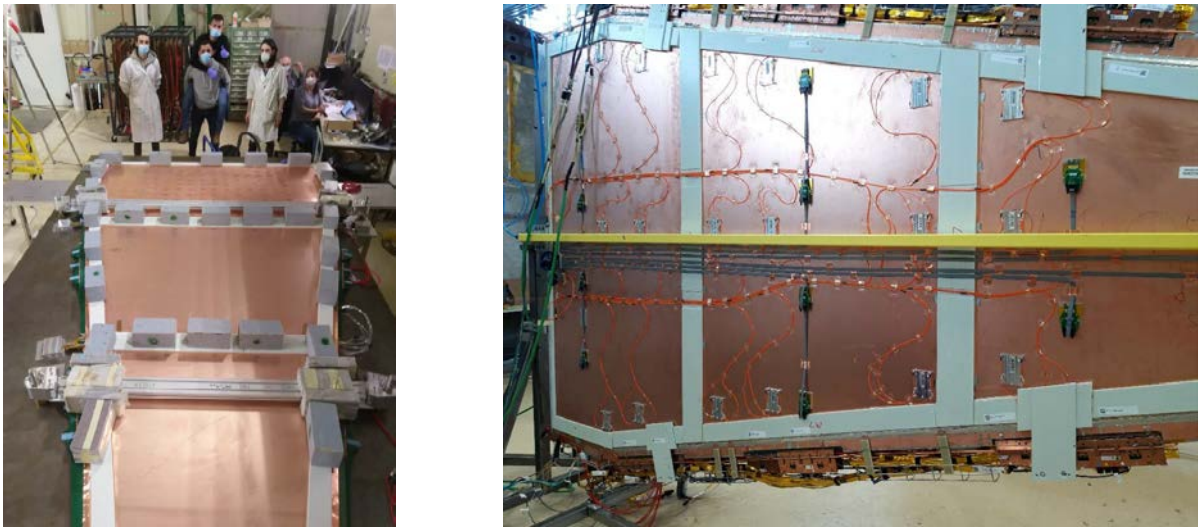


Fig. 5. Process of gluing modules at the initial stage of assembly of the NSW detector sector (*left*) and the sector with the installed electronics and sensors (*right*)

The X-ray scan [5] was performed after the long-term HV test and before the electronics installation. However, it could be done either before or after the long-term HV test. The goal of the survey was to locate the relative position of the sTGC strips with respect to the position of the alignment source plates. This is possible because the alignment platforms are precisely positioned on the wedge surface using the brass “V” and “I” features of the uppermost sTGC cathode strip boards as a reference.

The method is based on the irradiation of the wedges using an X-ray beam provided by an Amptek Mini-X X-ray tube. The X-ray gun is equipped with a gold anode which is operated (during the survey) at 40 kV / 95 μA peak voltage and current, respectively. A 280 μm thick copper foil is placed at the tip of the collimator to filter out low-energy X-rays. The X-rays produced at this working point are sufficiently energetic to enable the irradiation of all layers of an sTGC quadruplet simultaneously.

Differences observed between the measured and expected positions correspond to local misalignments of the sTGC strips occurring during the module assembly or non-conformities during the strip board fabrication. The centroid position of strip charge clusters during a typical X-ray run with a collimator is shown in Fig. 6. After the completion of all tests, the prepared wedge was sent for integration. At this stage, the wedges of sTGC and MM were combined into a sector: an sTGC pivot wedge, two MM wedges in the middle and an

sTGC confirm wedge. A hit registered in a pivot wedge prompts a search for the corresponding hit in a confirm wedge. After integration, the sector was mounted on the NSW structure. The installed sectors were again tested for high voltage, and electronic noise measurements were carried out.

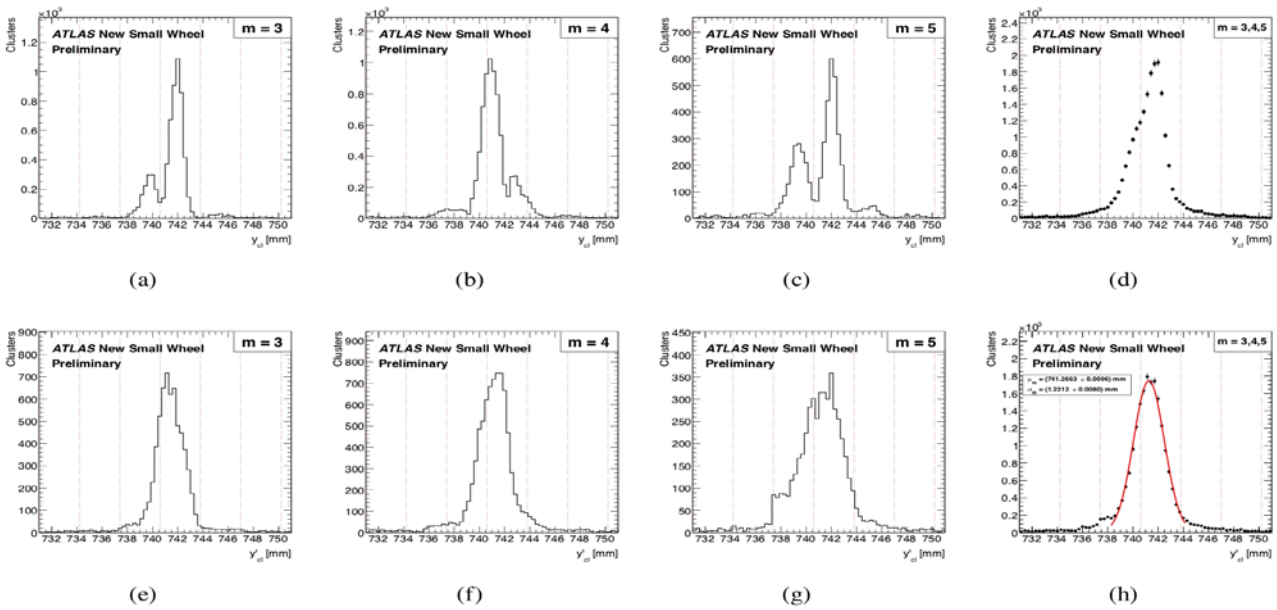


Fig. 6. Centroid position of strip charge clusters during a typical X-ray run with a collimator for strip multiplicities of (a–e) 3, (b–f) 4, and (c–g) 5, as well as for clusters multiplicities (d–h) 3 to 5 combined. The raw centroid positions, denoted y_{cl} , are shown in (a–d) and the centroid positions corrected for differential non-linearity, denoted y'_{cl} , are shown in (e–h)

4. New Small Wheels integration

After testing was completed, the finished disks were installed on the transport platforms and were transported to the ATLAS experiment cavern. Figure 7 on the *left* shows the installation of the last sector on the NSW C structure and on the *right* – the transportation of the NSW C to the cavern of the ATLAS experiment.

In the cavern, the NSW must go through a list of hardware checks: low voltage (LV) for digital and analog lines are correctly plugged and working, temperature sensors give reasonable values, ground points are correctly done and all services are in place on the wheel.

LV connectivity checks consist of verification that 300 V from the generator patch panel, located under sector 13, can reach the correct LV distributors intermediate conversion stage (ICS). The next check is to verify the connection of ICS to LV distribution boards located on the wedge. After that, one should check that communication between the final state machine is established and the switching on the desired sector will result in the current increase of around 4 A for digital channels and around 6 A for analog channels.

In order to monitor detector temperatures, dedicated monitored-drift-tube device modules [6] were installed during commissioning period on the surface and these sensors were checked in the cavern. After checking all service connections, both wheels were tested for HV capability on both CO₂ and n-pentane gas mixtures. If a certain chamber showed problems, then additional checks were carried out. At the end of the tests, all non-working chambers were documented.

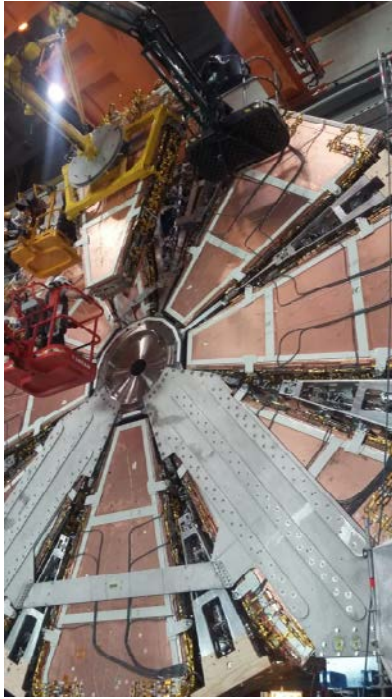


Fig. 7. Installation of the last sector on the disk of the NSW C detector (*left*). Transport of the NSW C detector from the assembly area to the ATLAS experiment shaft (*right*)

Having established the correct operation of the temperature sensors to monitor the adequacy of the cooling system and LV being delivered to front-end-boards – one can start the data acquisition (DAQ) system commissioning. In order to characterize each of the electronic channels, several types of tests are carried:

- Baseline run – records several hundred times the baseline level of each electronic channel *via* a slow control adapter;
- Trimmer run – a threshold value is set for each channel based on the pedestal values and noise levels obtained from the baseline run. At first, a global threshold is set and then it can be tuned by a trimmer for each channel individually;
- Noise run – recording data with random triggering to estimate noise level with pre-set thresholds;
- Pulser runs – an internal pulser that simulates a charge in each electronics channel. It allows one to validate all the phases within the electronics card.

As a first step, all readout cards are configured *via* the level-1 data driver card to return temperature readings for all electronic components. These temperatures, as well as those of the LV power supplies, are recorded for several hours to validate the cooling system. This is a necessary check for commissioning of the electronics. If any of the cards cannot be configured, certain corrective actions should be taken to fix it. Depending on the signature of the fault, the problem could be a failed twinax connection, or an unplugged LV connector, or a damaged or disconnected fiber optic cable, or even a failure of the electronic card itself. Despite the difficulty of accessing the electronic components when installing a sector on the NSW, any such problem will be corrected to the extent possible before commissioning the readout electronics. In some cases, the corresponding element was beyond repair and removed from the sector's DAQ configuration.

The next step is to record baselines for all channels in the sector. This is a critical test for measuring electronic noise levels at different locations in the detector and for characterizing low or noisy responses from all individual channels. This is also a time-consuming step as the baseline reading goes through the slow control adapter. In addition, any other channel with an unexpectedly low root mean square baseline value is characterized as a dead channel.

Once the noise levels are measured and found to be within expectations, thresholds are set for each electronic channel and then fixed frequency trigger runs are performed using these thresholds to test them. Thresholds are set initially on each readout chip (named VMM) and then adjusted individually for each of the

64 corresponding channels to obtain the most uniform response by setting the 32 analog-to-digital converter samples to the threshold value that is allowed to change for a channel within the VMM. As soon as the thresholds are set, a noise run is recorded using the full acquisition and triggering procedure at a fixed frequency of 1 kHz.

After successful integration, the NSW participated in several special ATLAS runs, including 2022 May splashes, where the pad trigger system for side C was fully included, except for one sector with cooling issues. The results can be seen in Fig. 8.

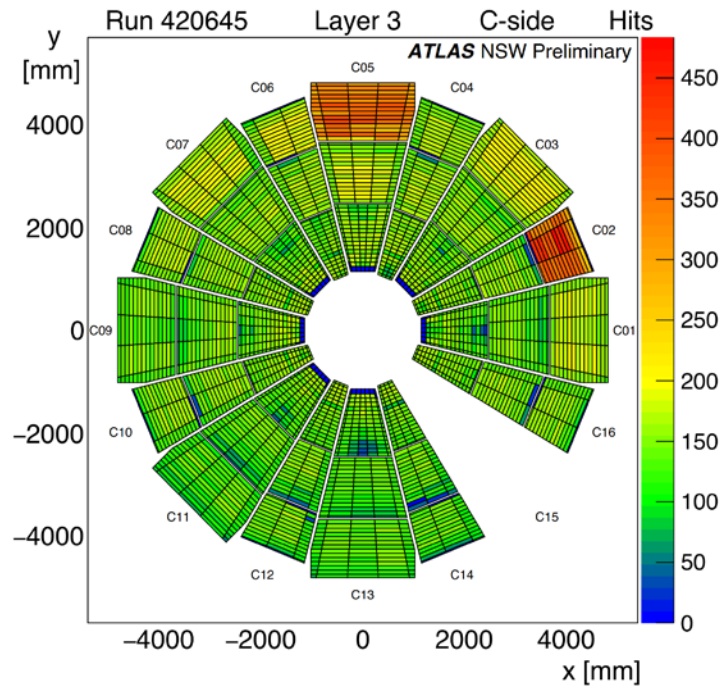


Fig. 8. The sTGC pad occupancy during the run that spans through the ATLAS splashes. The pad trigger operates in standalone self-trigger mode and sends out a packet of all the hits when both pivot and confirm sTGC quadruplets have hits in 3 out of 4 layers. Sector C15 has been excluded due to cooling issue at the time. Sectors C02 and C05 are taken with preliminary thresholds, therefore the noise level is higher

5. Summary

A crucial upgrade to improve muon triggering and tracking in the forward region of the ATLAS detector was performed by replacing old SW by NSW. The PNPI team was responsible for the construction of the largest sTGC modules, and all of them were assembled in 2020. After performing all necessary checks at PNPI, the team was sent to CERN to continue the work there with reception tests of quadruplets; wedge construction and integration; sector assembly and integration; final commissioning in the cavern of the ATLAS experiment. A huge amount of work has been done which allowed ATLAS to join first collision runs in 2022 and, therefore, to enter the new Run-3 data taking period.

References

1. ATLAS Collab., CERN-LHCC-2013-006 (2013). <https://cds.cern.ch/record/1552862>
2. D. Pudzha, J. Instrum. **15** (09), C09064 (2020).
3. M.R. Jaekel *et al.*, PoS TIPP2014 **102** (2014). <http://pos.sissa.it/cgi-bin/reader/conf.cgi?confid=213>
4. I. Trigger, sTGCWedgeAssembly-PRR, edms:1826389, v. 3 (2018). <https://edms.cern.ch/document/AT1-MW-AP-0002/3>.
5. B. Lefebvre, J. Instrum. **15**, C07013 (2020). <https://doi.org/10.1088/1748-0221/15/07/c07013>
6. C. Paraskevopoulos, PoS LHCP2021 **169** (2021).

UPGRADE PROGRAMME OF THE LHCb DETECTOR AT THE LARGE HADRON COLLIDER

PNPI participants of the LHCb Collaboration:

G.D. Alkhozov, N.F. Bondar, B.V. Bochin, A.D. Chubykin, V.V. Chulikov, S.A. Gets, A.A. Dzyuba, D.S. Ilyin, S.N. Kotryakhova, V.S. Kozlov, O.E. Maev, N.R. Sagidova, A.A. Vorobyev

1. Introduction

LHCb is an international collaboration of more than 1500 physicists from 83 institutions and 19 countries, who have designed, built and operated a collider detector at the CERN Large Hadron Collider (LHC).

Main physics goals are precision tests of the Standard Model (SM) in the heavy quark sector *via* studies of rare decays of heavy hadrons and constraining measurements of the parameters of the quark mixing matrix Cabibbo–Kobayashi–Maskawa (CKM). Another goal of the LHCb experiment is the precision spectroscopy of heavy hadrons helping to understand the quantum chromodynamics (QCD) – the theory of the strong interaction.

During Run-1, the LHC was operated at the pp centre-of-mass energy of 7 and 8 TeV, and the LHCb Collaboration collected the experimental data corresponding to 1 and 2 fb^{-1} of an integrated luminosity, respectively. During Run-2, the LHC was operated at the pp centre-of-mass energy of 13 TeV, which allowed LHCb to collect a data sample corresponding to more than 6 fb^{-1} of an integrated luminosity. Now, the upgraded LHCb detector is finishing the commissioning phase to be ready to take physics data in Run-3 at the pp centre-of-mass energy of 14 TeV and aiming to collect about 30 fb^{-1} during 2023–2025. Then, after Phase-2 Upgrade, planned in the period of 2026–2028, LHCb should enrich the total statistics with about 50 fb^{-1} more of data during Run-4 (2029–2032).

PNPI was involved in the LHCb project through the design, construction, commissioning, maintenance and operation of the LHCb muon system. PNPI physicists took part in the data analysis, including QCD, charm and B -physics studies. Among main LHCb physics results are the discovery of 56 new heavy particles (including “exotic” particles), high precision measurements of the parameters of the CKM matrix, studies of rare decays of heavy hadrons, as well as studies of the heavy hadrons spectroscopy. During Upgrade I (U1) of LHCb, the PNPI team played a key role in most of the activities on modernization and then on commissioning of the muon system to be ready for the data taking in Run-3. This report presents a new LHCb detector as a result of U1 performed during 2018–2022. Also, many ideas for the basic conception of the future Upgrade II (U2) planned in 2033–2034 were proposed by the PNPI team, but now the future PNPI status in the collaboration is unclear and depends on political decisions by CERN and LHCb.

2. LHCb detector

The LHCb detector is a forward spectrometer [1, 2]. The angular distribution for the charm and beauty hadrons, produced in collisions of high-energy protons, is boosted into the forward direction, where the products of their decays are registered in the 10 to 250 mrad range of the polar angle. A schematic view of the LHCb experiment before and after of U1 [3] is in Fig. 1.

The LHCb detector is a single-arm forward spectrometer covering the pseudorapidity range $2 < \eta < 5$. The detector includes a high-precision tracking system comprising a silicon-strip before U1 and pixel now vertex locator (VELO) surrounding the pp interaction region, a large-area silicon-strip system (TT) located upstream of a dipole magnet with a bending power of about 4 Tm , three stations of silicon-strip subdetectors and straw drift tubes outer tracker (T1–T3) before U1 placed downstream of the magnet, which were replaced with stations of scintillating fibers (SciFi) now. The tracking system provides measurements of the momentum, p_{tot} , of charged particles with a relative uncertainty that varies from 0.5% at low momentum to 1.0% at $200 \text{ GeV}/c$. The minimum distance of a track to a primary vertex, the impact parameter, is measured with a resolution of $(15 + 29/p_T) \mu\text{m}$, where p_T is the component of the momentum transverse to the beam, in GeV/c . Different types of charged hadrons are distinguished using information from two ring-imaging Cherenkov detectors (RICH1 and RICH2). Photons, electrons and hadrons are identified by

a calorimeter system consisting of scintillating-pad and preshower detectors (SPD/PS) which were removed for U1, an electromagnetic calorimeter (ECAL), and a hadronic calorimeter (HCAL). Muons are identified with a system composed of alternating layers of iron and multiwire proportional chambers (M1–M5), where M1 was also removed for U1. The online event selection was performed by a trigger, which consists of a hardware stage, based on information from the calorimeter and muon systems, followed by a software stage, which applies a full event reconstruction for Run-1 and Run-2 and now is replaced with a fully software trigger.

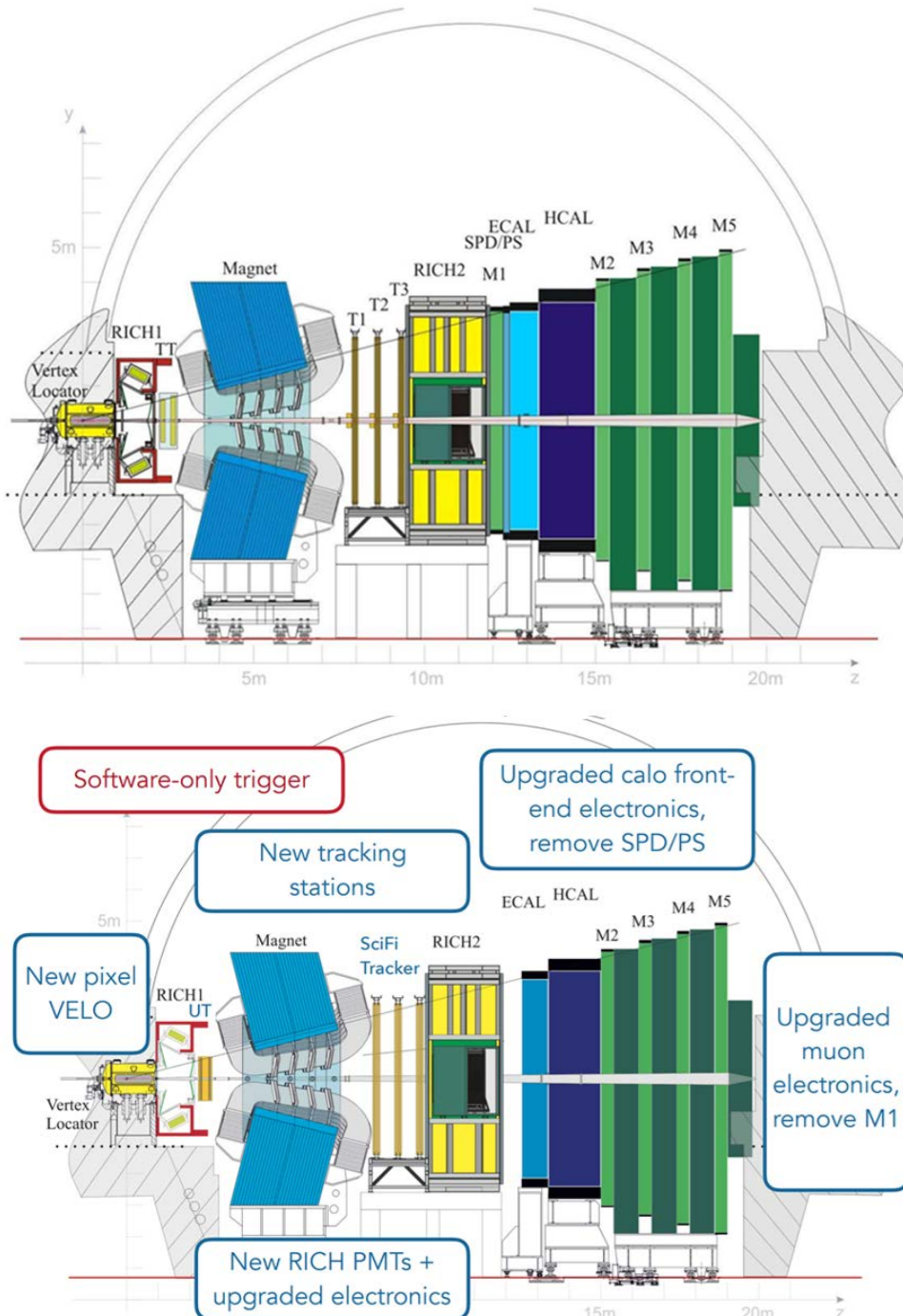


Fig. 1. Schematic view of the LHCb experiment: *top* – before of Upgrade I; *bottom* – after of Upgrade I

3. Physics case for the LHCb upgrades

The main goal of the LHCb upgrades is to drastically increase a precision in study of heavy flavour physics (Table 1) with jumping the rate of the data taking by ~ 5 times with the U1 LHCb detector. Instantaneous luminosity (L) was increased from $4 \cdot 10^{32} \text{ cm}^{-2} \cdot \text{s}^{-1}$ to $\sim 2 \cdot 10^{33} \text{ cm}^{-2} \cdot \text{s}^{-1}$. Then, it will be increased by ~ 10 times more to $L \approx (1.5-2) \cdot 10^{34} \text{ cm}^{-2} \cdot \text{s}^{-1}$ with U2 LHCb. The schedule of LHCb vs integrated and instantaneous luminosities is presented in Fig. 2. The trend includes 9 fb⁻¹ of data already collected during Run-1 & Run-2 and spreads over 20 years into the future with expectations for upgraded detector for Run-3 & Run-4 and also, after the future U2 for Run-5 & Run-6.

Table 1

Key observables [4] in flavour physics of LHCb with the precision reached in the analysis of the data collected in Run-1 & Run-2 and expected with the integrated luminosities collected with the detector after U1 and U2

Observable	Current LHCb (up to 9 fb ⁻¹)	Upgrade I (23 fb ⁻¹) (50 fb ⁻¹)		Upgrade II (300 fb ⁻¹)
CKM tests				
$\gamma (B \rightarrow DK, \text{ etc.})$	4°	1.5°	1°	0.35°
$\phi_s (B_s^0 \rightarrow J/\psi\phi)$	32 mrad	14 mrad	10 mrad	4 mrad
$ V_{ub} / V_{cb} (A_b^0 \rightarrow p\mu^-\bar{\nu}_\mu, \text{ etc.})$	6%	3%	2%	1%
$a_{\text{sl}}^d (B^0 \rightarrow D^-\mu^+\nu_\mu)$	36×10^{-4}	8×10^{-4}	5×10^{-4}	2×10^{-4}
$a_{\text{sl}}^s (B_s^0 \rightarrow D_s^-\mu^+\nu_\mu)$	33×10^{-4}	10×10^{-4}	7×10^{-4}	3×10^{-4}
Charm				
$\Delta A_{CP} (D^0 \rightarrow K^+K^-, \pi^+\pi^-)$	29×10^{-5}	13×10^{-5}	8×10^{-5}	3.3×10^{-5}
$A_\Gamma (D^0 \rightarrow K^+K^-, \pi^+\pi^-)$	11×10^{-5}	5×10^{-5}	3.2×10^{-5}	1.2×10^{-5}
$\Delta x (D^0 \rightarrow K_s^0\pi^+\pi^-)$	18×10^{-5}	6.3×10^{-5}	4.1×10^{-5}	1.6×10^{-5}
Rare Decays				
$\mathcal{B}(B^0 \rightarrow \mu^+\mu^-)/\mathcal{B}(B_s^0 \rightarrow \mu^+\mu^-)$	69%	41%	27%	11%
$S_{\mu\mu} (B_s^0 \rightarrow \mu^+\mu^-)$	—	—	—	0.2
$A_\Gamma^{(2)} (B^0 \rightarrow K^{*0}e^+e^-)$	0.10	0.060	0.043	0.016
$A_\Gamma^{\text{Im}} (B^0 \rightarrow K^{*0}e^+e^-)$	0.10	0.060	0.043	0.016
$A_{\phi\gamma}^{\Delta\Gamma} (B_s^0 \rightarrow \phi\gamma)$	$^{+0.41}_{-0.44}$	0.124	0.083	0.033
$S_{\phi\gamma} (B_s^0 \rightarrow \phi\gamma)$	0.32	0.093	0.062	0.025
$\alpha_\gamma (A_b^0 \rightarrow A\gamma)$	$^{+0.17}_{-0.29}$	0.148	0.097	0.038
Lepton Universality Tests				
$R_K (B^+ \rightarrow K^+\ell^+\ell^-)$	0.044	0.025	0.017	0.007
$R_{K^*} (B^0 \rightarrow K^{*0}\ell^+\ell^-)$	0.12	0.034	0.022	0.009
$R(D^*) (B^0 \rightarrow D^{*-\ell^+\nu_\ell)$	0.026	0.007	0.005	0.002

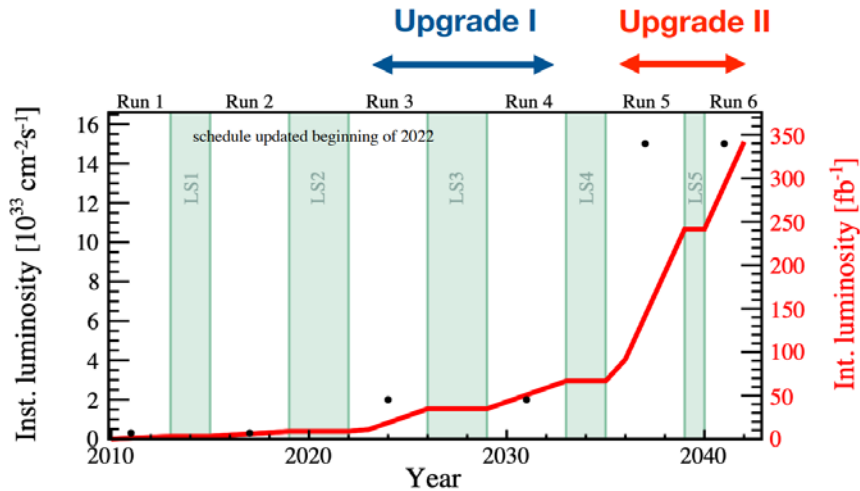


Fig. 2. LHCb schedule vs instantaneous (*black points*) and integrated (*red curve*) luminosities

4. LHCb Upgrade I

As it has been already mentioned above, the goal of U1 was a drastically increase in the rate of the collecting statistics with increasing the level of average number of the visible events per collision (μ) from ~ 1.1 during Run-2 to ~ 5 . This ambitious plan requested big changes on the detector side including full replacement of the trigger, detector readout electronics and data acquisition (DAQ) system with new ones and increasing the granularity of subdetectors in the most occupied regions. Most of the LHCb systems were replaced with new ones, see Fig. 3, where some of them were replaced also because of the factor of aging.

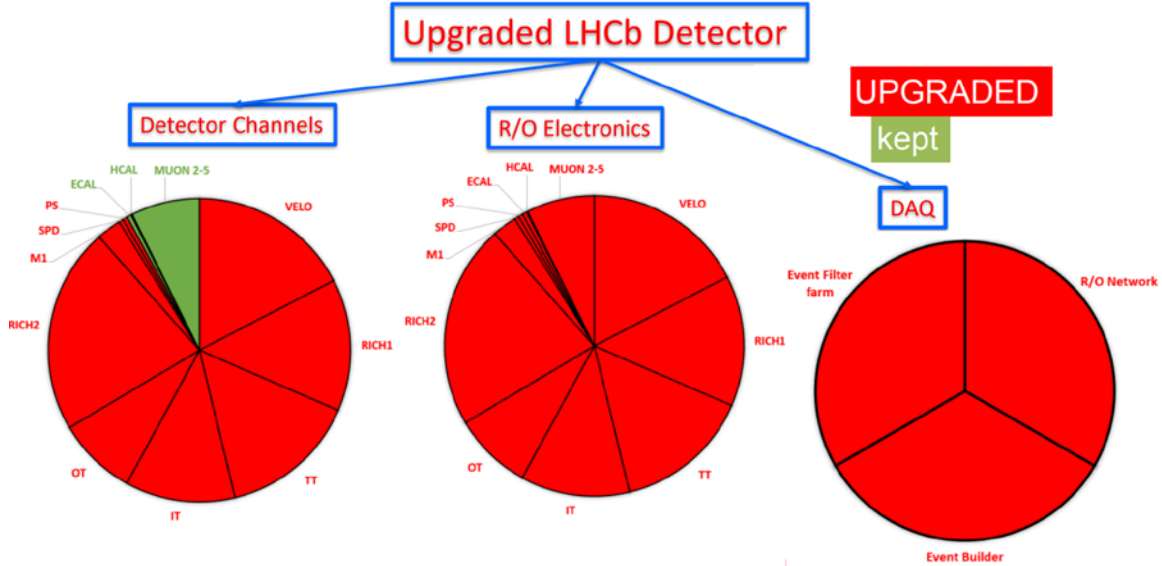


Fig. 3. LHCb after U1, where parts of the kept subsystems are shown in *green*, while upgraded ones – in *red*

Some details about the upgraded LHCb subsystems are presented below in short.

4.1. Trigger and online systems

One of the main and general tasks of LHCb in U1 was the replacement of the L0 (level 0) hardware (HW) trigger, which provided 1 MHz readout with high E_T/p_T thresholds on reconstructed events in muon, calorimeters and majority in SPD [5], see an example of the used trigger lines for 2015–2017 years of Run-2 operation in Table 2, with a full soft-ware (SW) trigger [6], or in other words with a so-called trigger-less readout system, see Fig. 4 (*top*).

Table 2

The L0 thresholds for the different trigger lines used to take the majority of the data for each indicated year

L0 trigger	E_T/p_T threshold			SPD threshold
	2015	2016	2017	
Hadron	> 3.6 GeV	> 3.7 GeV	> 3.46 GeV	< 450
Photon	> 2.7 GeV	> 2.78 GeV	> 2.47 GeV	< 450
Electron	> 2.7 GeV	> 2.4 GeV	> 2.11 GeV	< 450
Muon	> 2.8 GeV	> 1.8 GeV	> 1.35 GeV	< 450
Muon high p_T	> 6.0 GeV	> 6.0 GeV	> 6.0 GeV	none
Dimuon	> 1.69 GeV ²	> 2.25 GeV ²	> 1.69 GeV ²	< 900

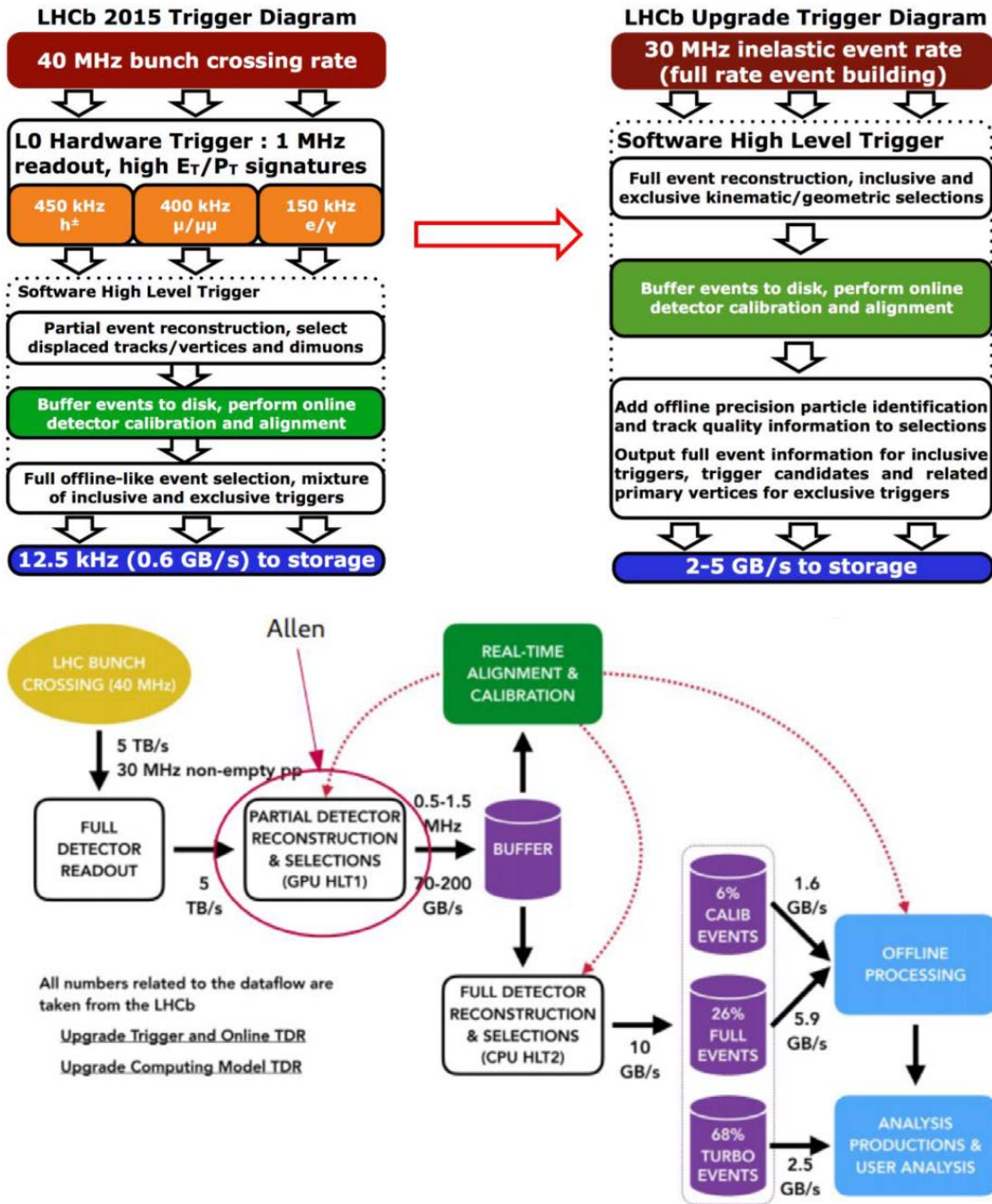


Fig. 4. Simplified diagrams show the transition from the old trigger based on the L0 HW trigger to the new so-called trigger-less readout system (*top*). Simplified diagram where main elements of the new data processing and the upgraded trigger scheme (*bottom*)

As it is shown in the simplified scheme in Fig. 4 *bottom*, a full stream of about 30 MHz non-empty pp collisions data pass through the first high level trigger (HLT1) based on graphical processor units (GPUs), named Allen after Frances E. Allen, where a partial detector reconstruction and the selection are performed in the buffer. Then, HLT2 starts the full detector reconstruction and selection processing, and in parallel, a program of real-time alignment and calibration is performed for subdetectors where it is needed. The events

pass through the offline processing and an additional selection with the so-called TURBO-processing [7], which allows to significantly reduce the size of the events and make them ready for an analysis. It is worth to mention that in order to realize such an ambitious challenge, a new Data Centrum based on modern technologies was designed and constructed near the LHCb experiment on the surface. Previously, the main computing facilities were located underground in the LHCb cavern.

4.2. Tracking system

The LHCb tracking system, which is a core of the experiment, comprises three subdetectors (SDs). All of them have been fully renewed in U1, see Fig. 5. Silicon strips VELO surrounding the pp interaction region was replaced with a silicon pixel detector [8] to provide much better event reconstruction near the interaction point. Old silicon strip upstream tracker (UT) called as a tracker turicensis located upstream of a dipole magnet has been replaced in 2023 with a new one [9] with a similar technology but with increased granularities and with better radiation hardness needed to accept much higher occupancies in Run-3 & Run-4. Gaseous straw tube outer tracker (OT) also comprises microstrip inner tracker (IT) located in the innermost part of the detector has been replaced with a full coverage of scintillating fibers SciFi detector [9] with the same geometry. The new detector will provide much better spatial and time resolution at much higher occupancy conditions. All three detectors are equipped with a new readout and DAQ electronics to be compatible with 40 MHz rate readout and 5 times higher luminosity.

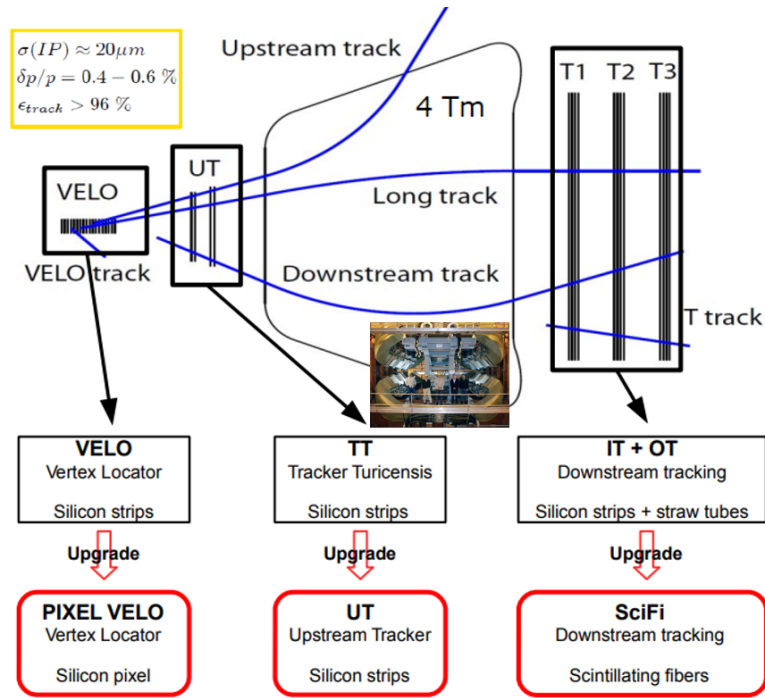


Fig. 5. Simplified scheme of the LHCb tracking system before and after U1. Vertex locator and upstream tracker are located upstream of the LHCb magnet, which is shown in the middle, the outer tracker is right after the magnet

4.3. RICHs and calorimeters

Two RICH detectors, RICH1 and RICH2, located upstream and downstream of the magnet respectively, together with the calorimeters and the muon system, which is described in more detail in the next section, are part of the LHCb particle identification system. All three systems have kept their configuration in general unchanged for U1, concentrating on replacement of the readout and DAQ electronics [10].

At the same time, the upgrade of the RICHs practically was a complete renewal of both detectors. Namely, only the mirrors in RICH2 were reused from the old system. The most important changes were an

increasing the focal length of the spherical mirror in RICH1 from 2.7 to 3.7 m to reduce an occupancy on the photodetectors, and old hybrid photon detectors [11] were replaced by Hamamatsu R13472 multianode photomultipliers (MaPMT) [12] with external brand-new front-end electronics in both subdetectors.

The PS/SPD subsystem used in the past for L0 HW trigger was removed in the calorimeters, and, as in all other SDs, the readout and DAQ electronics was 100% replaced to sustain U1 luminosity and data rate conditions [10].

4.4. Muon system

A large part of the LHCb muon system was under responsibility of PNPI from the very beginning of the LHCb experiment starting from the basic ideas of the project. The PNPI team played a key role in the design, construction, maintenance and operation of the muon detector. The same strategy was continued during the upgrade and commissioning period, until the cooperation was interrupted by the collaboration for political reasons in 2022.

The muon system [1, 13–15] was successfully operated during LHC Run-1 and Run-2 keeping tracking inefficiencies at a very minor level of 1 and 2.6%, respectively. The upgrade of the muon system [16] was needed to work at the new LHCb requested luminosity, which will increase by a factor five, and to allow the readout electronics to sustain the full event readout at the rate of 40 MHz.

The original muon system, see Fig. 6, was composed of five stations M1 to M5 comprising 1 368 multi-wire proportional chambers (MWPC) and 12 gas electron multiplier (GEM) chambers for a total area of 435 m². Four stations M2–M5 alternating with 80 cm thick iron absorbers are located downstream of the calorimeter systems and consist of four gaps MWPCs [17] see Fig. 7 to achieve a high efficiency and a high redundancy. Their data are used to trace and identify penetrating muons. The station M1, comprising 12 GEMs and 264 two-gaps MWPCs, was located upstream of the calorimeters and was intended to serve in the L0 trigger system. Each station is divided into four regions, R1 to R4, moving from the central beam axis outwards. The linear dimensions and the segmentations of the four regions scale with the factors 1, 2, 4 and 8 in order to uniformly distribute the particle flux and the channel occupancy across each station.

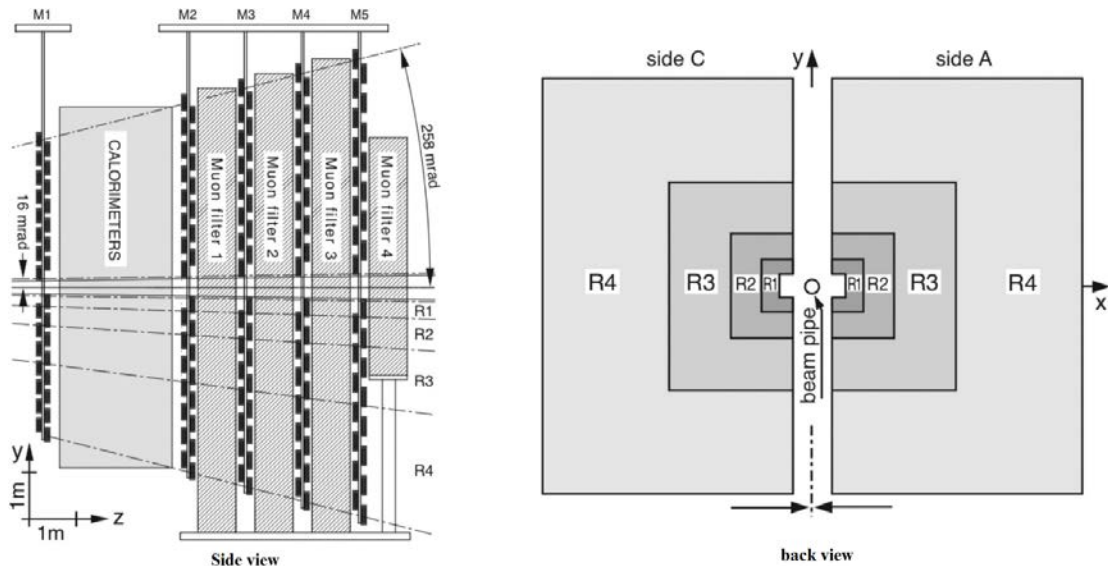


Fig. 6. Side view of the LHCb muon detector and the station layout with the four regions R1–R4 indicated

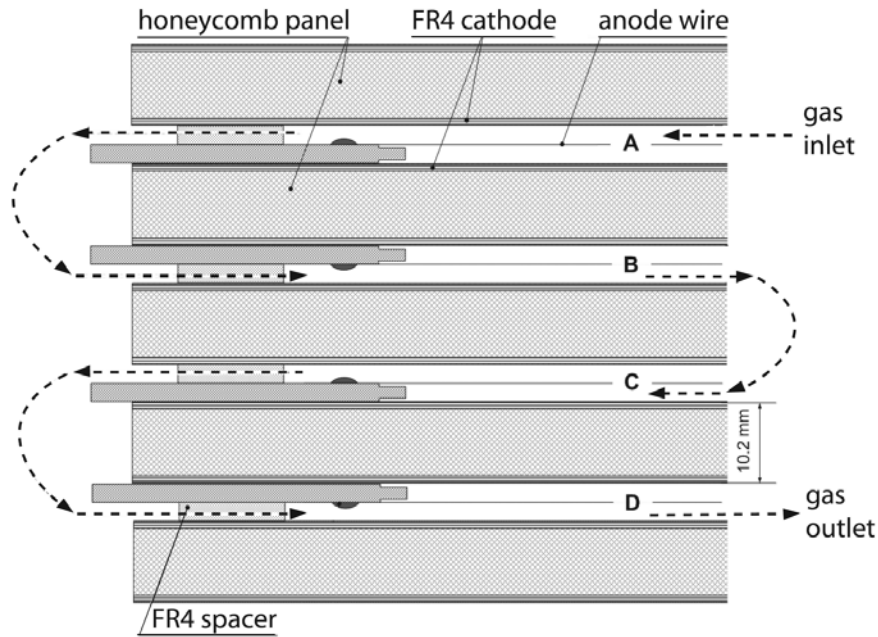


Fig. 7. Cross section of a MWPC with four gaps indicated by A, B, C and D. The direction of the gas flow is shown by the *dashed lines*

The muon specific front-end electronics installed directly on MWPCs was designed to guarantee high redundancy and to convert the analog signals extracted from the detectors physical pads into digital logical horizontal and vertical channels, survived with off detector electronics, to prepare the information needed by the L0 muon trigger and to send the data to the DAQ system.

High rates expected in Run-3 will result in high inefficiencies of the old detector. The new software trigger and the expected increased occupancies make useless and inefficient the most irradiated station M1, which was removed in U1 due to these reasons. The other four stations have been kept in the upgrade and follow the studies conducted in the perspective of using the current chambers in Run-3 and Run-4 at the LHC [18], and a large fraction of these chambers likely also in Run-5 and Run-6. In order to mitigate the high rate inefficiencies for the next Runs, there were installed additional shielding in the calorimeters, and the granularity of portion of both the detector and the readout channels was increased.

The front-end electronics, which digitizes the signals from the detector, was designed to be radiation tolerant up to 10 MRad. Accordingly, with the conditions foreseen for the upgrade, the current front-end electronics was kept unchanged. It would be important to mention that the muon system is the only subdetector in LHCb who passed U1 with keeping the detectors (MWPCs) unchanged and will operate with the original front-end electronics.

At the same time, the readout and the monitoring and control electronics was completely redesigned to cope with the new full event readout at the rate of 40 MHz and to interface with the new back-end electronics system. Despite significant changes required, the new electronics was redesigned to be back-compatible with the original architecture and its environment in order to minimize the cost allowing the reuse of the original crates, cabling, and power supplies.

High rates expected in Run-3 will result in high inefficiencies of the original detector. The particle flux in the innermost region of station M2 is expected to be very high, about 1 MHz/cm², with a consequent efficiency drop of about 25% in the region closest to the beam pipe. To reduce the inefficiencies an additional shielding was installed around the beam-pipe before M2 [19]: a rate reduction of about 50% in region R1 of M2 has been estimated by simulation.

Also, new pad detectors with increased granularity [20] were proposed for innermost regions in M2 and M3 stations to mitigate inefficiency from the dead time of the front-end electronics. First prototype for a M2R2 chamber, see Fig. 8 on the *left*, was designed and constructed at PNPI in 2016. A prototype for R1 of M2 and M3 stations, see Fig. 8 on the *right*, was made in 2020 also at PNPI. Both prototypes successfully

passed necessary tests and were accepted for the mass production. New pad chambers for M2R1 region were produced at PNPI in 2022 and were planned for the installation in the detector during Run-3.

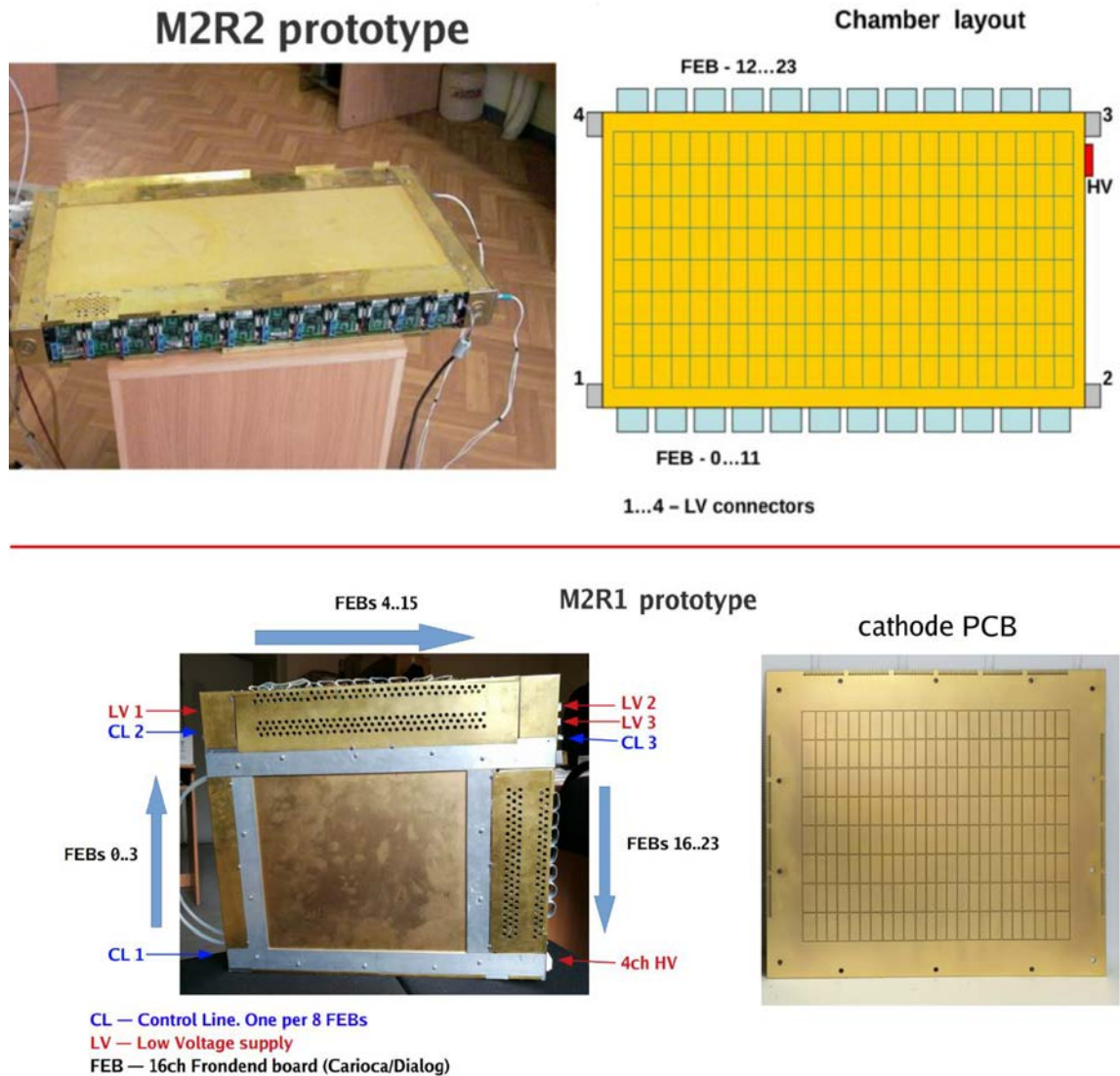


Fig. 8. Prototypes of the new pad chambers for M2R2 (on the *top*) and M2R1 (on the *bottom*) regions

Conclusion

The LHCb detector was performing well with a high data taking efficiency during Run-1 and Run-2. Many new physics results on different topics were obtained. By the middle of 2022, the number of publications reached 634. The data analysis will be continued, as only a part of the collected data has been analysed by now. During 2019–2022, the LHCb detector was almost fully upgraded and is now under commissioning to be able to operate with five times higher luminosity in 2023. All the details of the upgrade will be published soon [21]. The PNPI team played a key role in the design, construction and operation during Run-1 and Run-2 of the LHCb muon detector and continued with the same status during U1. In addition, the PNPI team proposed some basic ideas for the future upgrade U2, which are well described in the framework technical design report [3]. Unfortunately, the future status of PNPI in the LHCb Collaboration is unclear and will depend on political decisions made by LHCb and by CERN in general. By present, PNPI has been already moved out from the U2 activity.

References

1. A. Augusto Alves Jr. *et al.*, JINST **3**, S08005 (2008).
2. A. Augusto Alves Jr. *et al.*, JINST **8**, P02022 (2013).
3. Framework TDR for the LHCb Upgrade II, CERN-LHCC-2021-012 (2022); LHCb-TDR-23 (2022).
4. R. Aaij *et al.*, Physics Case for an LHCb Upgrade II, CERN-LHCC-2018-027 (2018); LHCb-PUB-2018-009 (2018).
5. R. Aaij *et al.*, JINST **14**, P04013 (2019).
6. LHCb Collab., LHCb Upgrade Software and Computing Technical Design Report, CERN-LHCC-2018-007 (2018); LHCb-TDR-017 (2018).
7. R. Aaij *et al.*, JINST **14**, P04006 (2019).
8. LHCb Collab., LHCb VELO Upgrade Technical Design Report, CERN-LHCC-2013-021 (2013); LHCb-TDR-013 (2013).
9. LHCb Collab., LHCb Tracker Upgrade Technical Design Report, CERN-LHCC-2014-001 (2014); LHCb-TDR-015 (2014).
10. LHCb Collab., LHCb Particle Identification Upgrade Technical Design Report, CERN-LHCC-2013-022 (2013); LHCb-TDR-014 (2013).
11. T. Gys, *et al.*, Nucl. Instr. Meth. A **567**, 176 (2006).
12. Hamamatsu Photonics, 314-5 Shimokanzo, Toyookavillage, Iwatagun, Shizuokaken, 438-0193 Japan. <http://www.hamamatsu.com>
13. LHCb Collab., LHCb Muon System. Technical Design Report, CERN-LHCC-2001-010 (2001); LHCb-TDR-4 (2001).
14. LHCb: Addendum to the Muon System Technical Design Report, 1 (2003).
15. LHCb: Second Addendum to the Muon System Technical Design Report, 4 (2005).
16. LHCb Collab., LHCb PID Upgrade Technical Design Report, CERN-LHCC-2013-022 (2013); LHCb-TDR-14 (2013).
17. A. Kachtchouk *et al.*, Design and Construction of the Wire Chambers for the LHCb Muon System, LHCb-MUON 2001-026 (2001).
18. P. Albicocco *et al.*, JINST **14**, P11031 (2019).
19. B. Schmidt, Engineering Design Review for the Improved Shielding of the LHCb Muon System: Tech. Rep. (2017).
20. M. Palutan, H.S. Kuindersma, Considerations on Muon Detector Granularity at Upgrade: Tech. Rep. (2017).
21. LHCb Collab., The LHCb Upgrade I, LHCb-DP-2022-002 (2023).



Nuclear and Atomic Physics

SEARCH FOR MUON CATALYZED $d^3\text{He}$ FUSION

PNPI participants of the MuSun Collaboration:

V.D. Fotev, V.A. Ganzha, K.A. Ivshin, P.V. Kravchenko, P.A. Kravtsov, E.M. Maev, A.V. Nadtochy, A.N. Solovev, I.N. Solovyev, A.A. Vasilyev, A.A. Vorobyov, N.I. Voropaev, M.E. Vznuzdaev

1. Introduction

We report here the results of an experiment aimed at observation of the muon catalyzed $^3\text{He}d$ fusion, which might occur after a negative muon stop in the $\text{D}_2 + ^3\text{He}$ gas mixture. The nuclear fusion reaction



is interesting for various reasons: as a mirror reaction of the $d + t \rightarrow ^4\text{He} + n$ fusion process and as a perspective source of thermonuclear energy. This fusion process was involved in the primordial nucleosynthesis of light elements in the early Universe. For these reasons, it is important to know the cross section for this reaction at low collision energies $E < 10 \text{ keV}$. The phenomenon of muon catalysis of fusion reactions opens an opportunity to study this reaction at practically zero collision energy when fusion occurs in the $^3\text{He}\mu d$ mesomolecule:

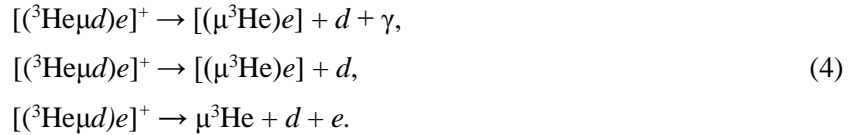


1.1. Formation of the $^3\text{He}\mu d$ molecules

Formation of the $^3\text{He}\mu d$ molecule occurs in collisions of slow μd atoms with ^3He atoms:



This process was predicted by Y.A. Aristov *et al.* [1] in 1981 as an intermediate step in the muon transfer from deuteron to helium nuclei $\mu d + ^3\text{He} \rightarrow d + \mu^3\text{He}$:



According to Ref. [1], such a scheme provides a high rate of the muon transfer, while the direct muon transfer is suppressed because of a specific structure of the energy terms in the μd - ^3He system. This prediction was confirmed in 1993 in an experiment at the PNPI [2]. The measurements were performed with the $\text{D}_2 + ^3\text{He}$ gas mixture at room temperature. The measured muon transfer rate $\lambda_{d^3\text{He}} = (1.24 \pm 0.05) \cdot 10^8 \text{ s}^{-1}$ proved to be in agreement with the theoretical prediction [1]. Later this muon transfer rate was measured at low temperatures in two experiments at the Paul Scherrer Institute (PSI) [3, 4]. The experimental results are summarized in Table 1. The theoretical predictions [1] are shown in Table 2 for comparison. One can see that the experimental data are in agreement with the theoretical predictions, both in the absolute values and also in the temperature dependence. The described scheme of the $^3\text{He}\mu d$ molecule formation was also supported by observation [5] of the 6.8 keV X-rays from the $(^3\text{He}\mu d)^*$ decay and precision measurement of the width of this peak in agreement with the theoretical calculations [6, 7].

Table 1Experimental results in measurements of $\lambda_{d^3\text{He}}$ *

Experiment. Ref.	Year	$\Lambda_{d^3\text{He}}, 10^6 \text{ s}^{-1}$	Experimental conditions			
			Gas filling	$T, \text{ K}$	$\varphi, \%$	$C^3\text{He}, \%$
D.V. Balin <i>et al.</i> [2]	1993	124(5)	$\text{D}_2 + ^3\text{He}$	300	5.5	11
E.M. Maev <i>et al.</i> [3]	1999	233(16)	$\text{HD} + ^3\text{He}$	39.5	9.21	5.6
B.Gartner <i>et al.</i> [4]	2000	186(8)	$\text{D}_2 + ^3\text{He}$	30.5	7.0	9.13

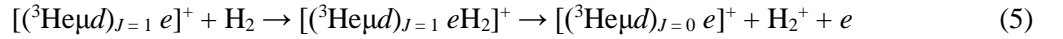
* $C^3\text{He}$ is the atomic concentration of ^3He in the gas mixture. The density φ and the rates are given relative to the liquid hydrogen density $\text{LHD} = 4.25 \cdot 10^{22} \text{ atoms} \cdot \text{cm}^{-3}$.

Table 2Theoretical prediction by Y.A. Aristov *et al.* [1] for $\lambda_{d^3\text{He}}$. ϵ_0 is the collision energy of μd and ^3He atoms

$\epsilon_0, \text{ eV}$	$4 \cdot 10^{-3}$	$4 \cdot 10^{-2} (T \approx 300 \text{ K})$	0.1	1	10
$\lambda_{d^3\text{He}} \cdot 10^6 \text{ s}^{-1}$	177	148	122	47	10

1.2. Fusion process

The discovered formation process of the $^3\text{He}\mu d$ molecules allows one to search for the muon catalyzed $d^3\text{He}$ fusion. However, a serious complication arises from competition of this fusion reaction with very fast decay of the $^3\text{He}\mu d$ molecule through the channels shown by Eq. (4). According to the theoretical considerations [8–10], the total decay rate of the $^3\text{He}\mu d$ molecule is $\lambda_{\text{decay}}(^3\text{He}\mu d) \approx 7 \cdot 10^{11} \text{ s}^{-1}$. The nuclear fusion rate $\Lambda_F(J)$ in the $^3\text{He}\mu d$ molecule depends strongly on the angular momentum (J) of the $^3\text{He}\mu d$ as $\Lambda_F(J=0) \approx 2 \cdot 10^5 \text{ s}^{-1}$ and $\Lambda_F(J=1) \approx 6.5 \cdot 10^2 \text{ s}^{-1}$ [11, 12]. Unfortunately, the great majority of the initially produced $^3\text{He}\mu d$ molecules are in the $J=1$ state. However, according to M. Faifman and L. Men'shikov [13], the spin flip $(^3\text{He}\mu d)_{J=1} \rightarrow (^3\text{He}\mu d)_{J=0}$ is possible in collisions of the $[^3\text{He}\mu de]^+$ complex with deuterium molecules *via* formation of a molecular cluster $[(^3\text{He}\mu d)e\text{D}_2]$ and its decay:



with the formation and the transfer rates of this cluster $\Lambda_1 \approx 3 \cdot 10^{13} \varphi \text{ s}^{-1}$ and $\Lambda_2 \approx 5 \cdot 10^{11} \text{ s}^{-1}$, respectively, where φ is the H_2 density. Here H_2 stands for D_2 or HD . Such an estimate shows that one can expect quite efficient $(^3\text{He}\mu d)_{J=1} \rightarrow (^3\text{He}\mu d)_{J=0}$ transfer and, as a consequence, detectable $^3\text{He}\mu d$ fusion process with an “effective” rate

$$\Lambda_F(^3\text{He}\mu d) = P(J=0) \cdot \lambda_f(J=0) + P(J=1) \cdot \lambda_f(J=1), \quad (6)$$

where $P(J)$ is the population of the $^3\text{He}\mu d$ molecule state with the angular momentum J .

1.3. Previous experiments

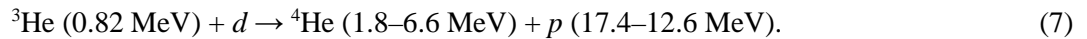
The first experimental limit on the “effective” muon catalyzed $d^3\text{He}$ fusion rate $\Lambda_F(^3\text{He}\mu d) \leq 4 \cdot 10^8 \text{ s}^{-1}$ was set at PNPI in 1990 in an experiment with the $\text{D}_2 + ^3\text{He}$ (5%) gas mixture. Next measurements were carried out in 1996 using the $\text{HD} + ^3\text{He}$ (5.6%) gas mixture. During a short test run in the intense muon beam at PSI, the upper limit for the $^3\text{He}\mu d$ fusion rate was moved down to $\Lambda_F(^3\text{He}\mu d) \leq 1.6 \cdot 10^6 \text{ s}^{-1}$. In 1997, there was a run at PSI aimed at observation of the muon catalyzed $d^3\text{He}$ fusion in the $\text{HD} + ^3\text{He}$ (5.6%) gas mixture. This experiment resulted with a new upper limit for the effective fusion rate $\Lambda_F(^3\text{He}\mu d) \leq 6 \cdot 10^4 \text{ s}^{-1}$ [14].

At the same time, another collaboration at PSI has undertaken in 1998 a search of the muon catalyzed $d^3\text{He}$ fusion in the $\text{D}_2 + {}^3\text{He}$ (5%) gas mixture. The reanalyzed results of that experiment were published in 2006 [15]. The authors declared the first observation of this process with the measured effective fusion rates $\Lambda_F({}^3\text{He}\mu d) = (4.5 + 2.6 / - 2.0) \cdot 10^5 \text{ s}^{-1}$ and $\Lambda_F({}^3\text{He}\mu d) = (6.9 + 3.6 / - 3.0) \cdot 10^5 \text{ s}^{-1}$ at the gas density 5.21 and 16.8%, correspondingly. Such a fusion rate exceeded by an order of magnitude the upper limit set in experiment [14]. This striking difference might be related with problems in Ref. [15] of taking into account the background reactions, which could simulate the searched reaction (2). The main background of this type is due to the so-called ${}^3\text{He} + d$ fusion-in-flight. It comes from collisions with D_2 of the ${}^3\text{He}$ (0.82 MeV) nuclei produced in the $d\mu d$ fusion reaction. This background is more important in the $\text{D}_2 + {}^3\text{He}$ gas mixture than in the $\text{HD} + {}^3\text{He}$ gas mixture used in Ref. [14]. On the other hand, the difference between the results of these two experiments might be also due to possible difference in the formation and transfer rates Λ_1 and Λ_2 in the $[({}^3\text{He}\mu d)_{J=1}e\text{HD}]^+$ and $[({}^3\text{He}\mu d)_{J=1}e\text{D}_2]^+$ clusters.

Fortunately, the MuSun experiment, performed at PSI [16], gives us an excellent possibility to clarify the situation. This very high statistics experiment is using pure D_2 gas. This gives a possibility to control the level of the dd fusion background expected in the presented here experiment.

2. Experimental set-up

Our experiment was performed exploiting the set-up of the MuSun experiment. The main goal of MuSun is to measure the muon capture rate in deuterium. For that, the lifetime of negative muons stopped in ultra clean D_2 gas is measured with high precision (10^{-5}). That required 10^{10} detected decays of the muons which stopped in the sensitive volume of the MuSun active target. In the main MuSun run of 2015 (Run-8), $1.2 \cdot 10^{10}$ such events were taken. Besides muons, the active target can detect also the products of the reactions initiated by muons, including the products of the ${}^3\text{He} + d$ fusion-in-flight:



MuSun can serve as a high statistical background experiment for the experiment aimed at searches of the muon catalyzed ${}^3\text{He}d$ fusion. Having this in mind, the decision was taken by the MuSun Collaboration to perform an additional Run-9 with the active target filled with $\text{D}_2 + {}^3\text{He}$ (5%) gas mixture, keeping all experimental conditions identical to those in Run-8. The results of these studies are presented below.

The scheme of the MuSun experiment is shown in Fig. 1. The incoming muons are detected first with a scintillator counter μSC and a wire proportional chamber μPC . Then they pass through a 0.4 mm thick hemispheric beryllium window and stop in the sensitive volume of the time-projection chamber (TPC). The TPC is filled with ultrapure protium-depleted deuterium gas at $T = 31 \text{ K}$ and $P = 5 \text{ bar}$. The TPC operates as an active target in the ionization mode. Its main goal is to select the muon stops within the fiducial volume well isolated from the chamber materials.

The trajectory and the arrival time of the muon decay electrons are measured with two cylindrical wire chambers $e\text{PC}1$, $e\text{PC}2$ and with a double layer scintillator hodoscope $e\text{SC}$ consisting of 32 plastic scintillators. The geometrical acceptance of the electron detector is 70%.

The ionization electrons produced in the TPC drift towards the anode plane in the electric field of 11 kV/cm with the velocity of 5 mm/ μs . The total drift space (the cathode – grid distance) is 72 mm. The anode plane is subdivided into 48 pads making a pad matrix of six pads (horizontal direction X) by eight pads (beam direction Z). The size of the pads is 17.5 mm (X) \times 15.25 mm (Z). About 50% of the muons passing through the μSC stop within the fiducial volume of the TPC (Fig. 2). All anode pads have independent readout channels with fast (100 MHz) amplitude to digital converters allowing to measure the time and the energy of the signals with a threshold of 80 keV and a resolution of 20 keV at any pad in the time window 0–25 μs . The μSC signal triggers the “muon-on-request” system, which switches off the muon beam thus excluding arrivals of other muons in the registration time window. The TPC measures the ionization produced by the entering TPC muon and products of muon reactions, including ${}^3\text{He}$, ${}^4\text{He}$ and protons from dd and ${}^3\text{He}d$ fusion.

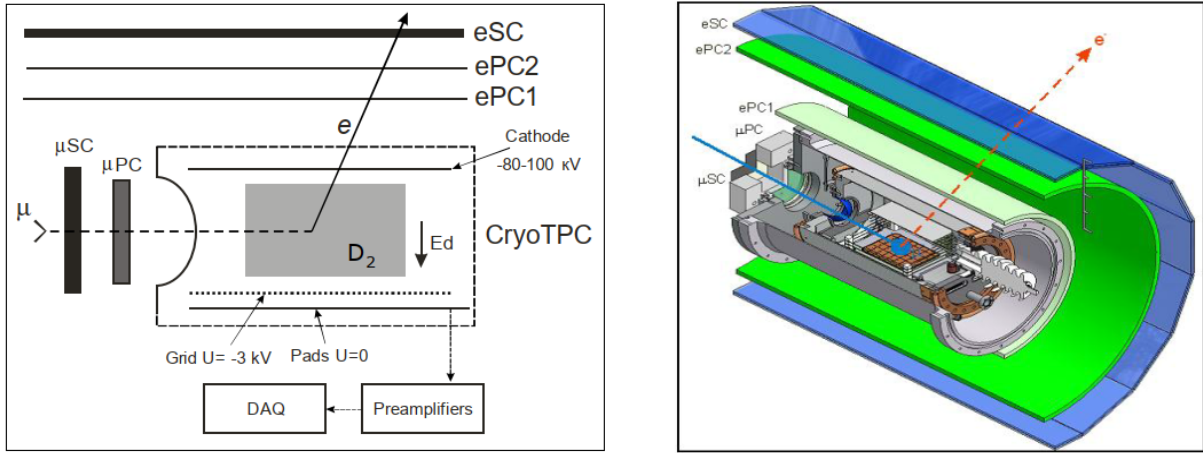


Fig. 1. Scheme of the MuSun experiment. The *shadowed area* shows the fiducial volume with muon stops far enough from all materials

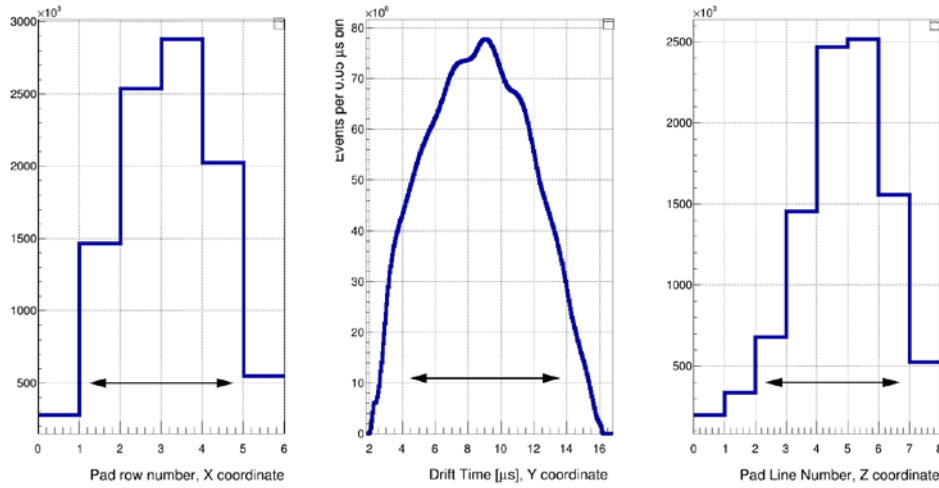


Fig. 2. The measured muon stop distribution inside the TPC. The arrows show the fiducial volume selected in the present analysis

3. Experimental data and analysis

Table 3 compares the experimental conditions of the TPC in Run-8 and Run-9.

Table 3

Experimental conditions in Run-8 and in Run-9

Run	Gas filling	T , K	P , bar	ϕ , % LHD	C_d , %	$C_{^3\text{He}}$, %	Gas purity
8	D_2	31	5	6.5	100		$< 2 \cdot 10^{-9}$ (N_2)
9	$\text{D}_2 + ^3\text{He}$	31	5	6.5	95	5	$< 2 \cdot 10^{-9}$ (N_2)

3.1. Processes after a negative muon stops in the $\text{D}_2 + ^3\text{He}$ gas mixture

Figure 3 shows a scheme of processes initiated by a muon stop in the $\text{D}_2 + ^3\text{He}$ gas mixture. For the goal of this experiment, it is important to know the yield of the $^3\text{He}\mu\text{d}$ molecules leading to possible muon catalyzed $^3\text{He}\text{d}$ fusion and the number of the ^3He (0.82 MeV) nuclei responsible for the background reaction

fusion-in-flight. ${}^3\text{He}\mu d$ yield can be calculated, as the parameters needed for such calculations are known with high enough accuracy. Table 4 presents the main parameters of the $d\mu d$ fusion taken from the review article [17], while other parameters are presented in the Fig. 3 caption.

Table 4

Parameters of the $d\mu d$ fusion at $T = 31\text{ K}^*$ [17]

Parameter	$\Lambda_{d\mu d}(3/2), \text{ s}^{-1}$	$\Lambda_{d\mu d}(1/2), \text{ s}^{-1}$	$\lambda_{21}, \text{ s}^{-1}$	$R(3/2)$	$R(1/2)$	$\omega_{\mu^3\text{He}} / \omega^{3\text{He}}$
Value	$4.05(6) \cdot 10^6$	$0.051(1) \cdot 10^6$	$37.1(3) \cdot 10^6$	1.43	1.05	0.121(1)

* $\lambda_{d\mu d}(3/2)$ and $\lambda_{d\mu d}(1/2)$ are $d\mu d$ formation rates from the μd ($F = 3/2$) and μd ($F = 1/2$) spin states, respectively. The rates are normalized to LHD. $R = (\omega_{\mu^3\text{He}} + \omega^{3\text{He}}) / \omega$, where ω , $\omega_{\mu^3\text{He}}$ and $\omega^{3\text{He}}$ are probabilities of the $d\mu d$ fusion channels (Fig. 3).

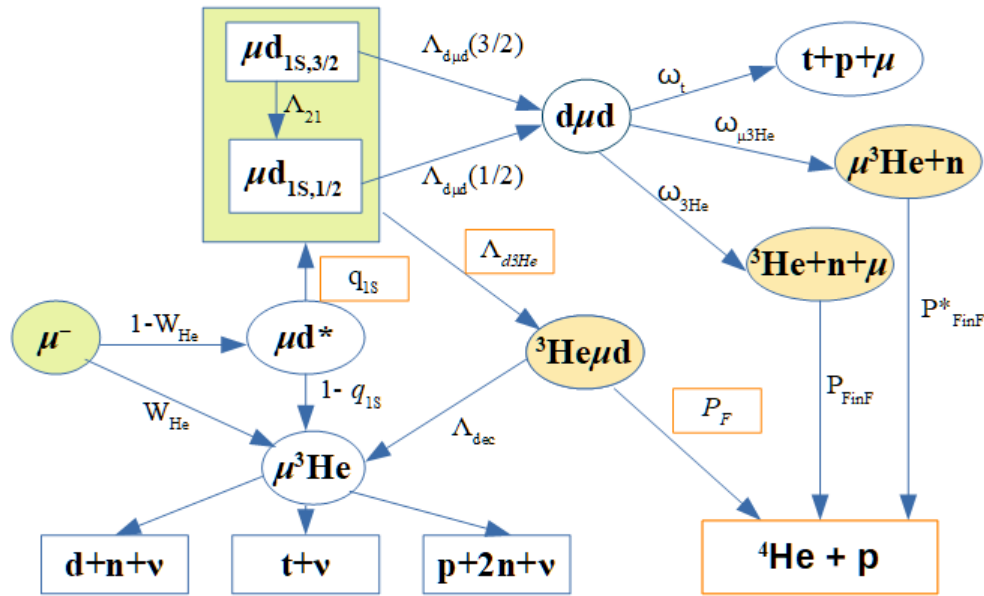


Fig. 3. Scheme of the processes initiated by the negative muon in the $\text{D}_2 + {}^3\text{He}$ gas mixture. The parameters related to the $d\mu d$ fusion are presented in Table 4. The $d\mu d$ formation rate $\Lambda_{d\mu d} = \lambda_{d\mu d} \phi C_d$. The spin-flip rate in the μd atoms $\Lambda_{21} = \lambda_{21} \phi C_d$. P_{FinF} and P^*_{FinF} are the ${}^3\text{He} + d$ fusion-in-flight probabilities for the ${}^3\text{He}$ (0.82 MeV) and ${}^3\text{He}\mu$ (0.80 MeV) particles, respectively. W_{He} is the probability of direct muon capture by ${}^3\text{He}$. The parameter q_{1s} is the probability of the muon transfer from μd^* to μd_{1s} . $\Lambda_{d^3\text{He}} = \lambda_{d^3\text{He}} \phi C^{3\text{He}}$ is the ${}^3\text{He}\mu d$ formation rate. The ${}^3\text{He}\mu d$ formation rate $\Lambda_{d^3\text{He}}$, as well as the probability q_{1s} , are determined in the presented here analysis of the experimental data. P_F is the yield of the muon catalyzed ${}^3\text{He}\mu d$ fusion

3.2. Energy and time distributions of the $d\mu d$ fusion products

Figure 4 shows the energy distributions of the ${}^3\text{He}$ and $\mu^3\text{He}$ particles produced in the $d\mu d$ fusion reaction. The largest peak in the energy spectrum of the dd fusion events is due to the ${}^3\text{He}$ (0.82 MeV) particles from the $d\mu d \rightarrow {}^3\text{He} + n + \mu$ fusion channel. The next peak is due to the $\mu^3\text{He}$ (0.80 MeV) particles from the $d\mu d \rightarrow \mu^3\text{He} + n$ fusion channel. Both peaks proved to be shifted from 0.82 and 0.80 MeV to lower energies because of the electron-ion recombination, the effect being larger for doubly charged ${}^3\text{He}^{++}$ ions than for singly charged $\mu^3\text{He}^+$ ions. The difference between the peak positions in Run-8 and in Run-9 is due to the difference in the effect of recombination which is by 9% lower in the $\text{D}_2 + {}^3\text{He}$ (5%) gas mixture than in the pure D_2 gas. The third peak is due to pileup of the ${}^3\text{He}$ signals with the ${}^3\text{He}$ or $\mu^3\text{He}$ signals from the next fusion cycle.

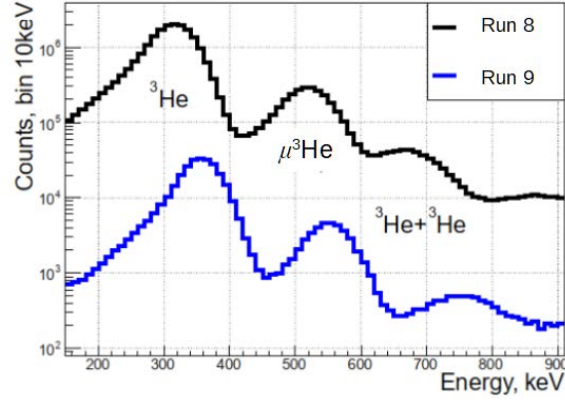


Fig. 4. Energies of the ${}^3\text{He}$ and $\mu^3\text{He}$ particles measured in D_2 gas (Run-8) and in $\text{D}_2 + {}^3\text{He}$ (5%) gas mixture (Run-9)

Figure 5 (*left panel, blue line*) presents the measured time distributions of the ${}^3\text{He}$ and $\mu^3\text{He}$ signals registered in Run-8 and selected in the energy range 150–620 keV. The drop below $t^* = 1.28 \mu\text{s}$ is related with overlapping of the fusion with the muon signals. Figure 5 (*right panel, blue line*) shows the time distribution of the ${}^3\text{He}$ signals registered in Run-9 and selected in the energy range 200–460 keV.

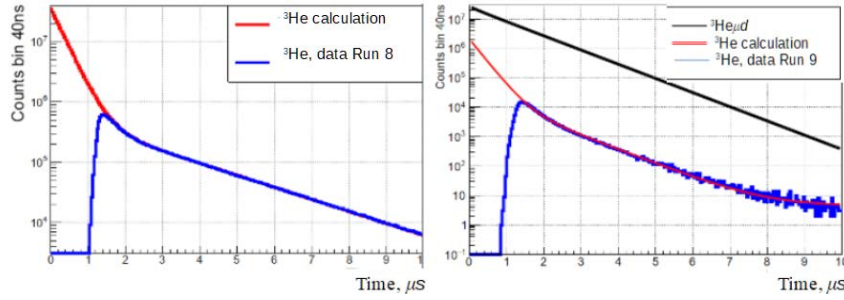


Fig. 5. The times of the ${}^3\text{He}$ (0.82 MeV) and $\mu^3\text{He}$ (0.80 MeV) particles from the $d\mu d$ fusion in Run-8 (*blue line, left panel*) and the times of the ${}^3\text{He}$ (0.82 MeV) particles in Run-9 (*blue line, right panel*). The red lines in both panels present the results of the calculations according to the scheme of Fig. 3. The black line (*right panel*) shows the calculated times of the ${}^3\text{He}\mu d$ molecules

3.3. Formation of the $d\mu d$ and ${}^3\text{He}\mu d$ molecules and q_{1s}

The measured time distributions were analysed according to the scheme presented in Fig. 3. At the first step, the experimental data from Run-8 (pure D_2 gas) were fitted with an exponential function

$$N^{{}^3\text{He}+\mu^3\text{He}}(t) = \varepsilon_{\text{FC}} \cdot N_{\mu} \cdot (\omega^{{}^3\text{He}} + \omega_{\mu^3\text{He}}) \cdot K_{\text{sel}} \cdot \Lambda_{d\mu d}(1/2) \cdot \exp[-(\Lambda_0 + \Lambda_{d\mu d}(1/2))t]. \quad (8)$$

Here, $N_{\mu} = 1.054 \cdot 10^{10}$ is the number of the selected muon stops, $\omega^{{}^3\text{He}} = 0.45$ and $\omega_{\mu^3\text{He}} = 0.062$ are the probabilities of the corresponding $d\mu d$ fusion channels, $\Lambda_0 = 0.45517 \cdot 10^6 \text{ s}^{-1}$ is the muon decay rate, and $\Lambda_{d\mu d}(1/2) = \lambda_{d\mu d}(1/2) \varphi C_d$ is the $d\mu d$ formation rate from the low spin state of $d\mu$ atom. K_{sel} is the selection factor of the ${}^3\text{He}$ (0.82 MeV) and $\mu^3\text{He}$ (0.80 MeV) particles in the region 150–620 keV. Also, it takes into account some losses of the events with small muon signals on the muon stop pad below some threshold value (muon stops in between the pads). The calculated value of this factor is $K_{\text{sel}} = 0.88(1)$. $\varepsilon_{\text{FC}} = 0.96$ is a correction factor following from the full kinetics analysis. The rate $\lambda_{d\mu d}$ was a free parameter in these fits. To check the stability of the obtained results, the fitting procedure was repeated in various fit windows in the time interval 2.5–10 μs . The results are presented in Table 5.

Table 5

The $d\mu d$ formation rate $\lambda_{d\mu d}(1/2)$ determined from the time distribution of the ${}^3\text{He} + \mu^3\text{He}$ particles (Run-8). The fitting procedure was repeated for various time intervals

Fit window, μs	$\lambda_{d\mu d}(1/2) \cdot 10^5 \text{ s}^{-1}$
2.5–10	0.5271(2)
2.5–8	0.5268(2)
2.5–6	0.5263(2)
2.5–4	0.5267(2)
3–10	0.5280(2)
5.5–10	0.5280(2)
4–10	0.5275(2)

As an average of Table 5, we take: $\lambda_{d\mu d}(1/2) = 0.527(7) \cdot 10^5 \text{ s}^{-1}$. The indicated here error is dominated by the estimated uncertainty in K_{sel} . This result agrees with the $d\mu d$ formation rate presented in Table 4: $\lambda_{d\mu d}(1/2) = 0.051(1) \cdot 10^6 \text{ s}^{-1}$. Such an agreement demonstrates the validity of all parameters entering the $d\mu d$ fusion scheme. With these parameters, the time distribution of the ${}^3\text{He} + \mu^3\text{He}$ particles was calculated according to the kinetics scheme shown in Fig. 3. The results are presented in Fig. 5 (*red line, left panel*). The calculated time distribution proved to be in perfect agreement with the experimental data. Note that these calculations reproduce the absolute yield of the ${}^3\text{He} + \mu^3\text{He}$ particles without introducing any free normalization factor.

A similar analysis of the Run-9 data ($\text{D}_2 + {}^3\text{He}$) includes two more parameters. One of them is the formation rate of the ${}^3\text{He}\mu d$ molecule $\Lambda_{d^3\text{He}} = \lambda_{d^3\text{He}} \phi C^3\text{He}$. The other one is the probability K_{fast} for the fast muon transfer to ${}^3\text{He}$ either *via* the direct muon capture by ${}^3\text{He}$ or in the μd^* de-excitation process. This factor can be expressed as $K_{\text{fast}} = N^3\text{He-fast} / N_{\mu} = (1 - N_{\mu d\text{-fast}}) / N_{\mu}$. Here N_{μ} is the number of the selected muon stops, $N^3\text{He-fast}$ and $N_{\mu d\text{-fast}}$ are the numbers of the $\mu^3\text{He}$ and μd atoms after the μd^* de-excitation process. $N_{\mu d\text{-fast}}$ is the sum of the statistically populated μd ($F = 3/2$) and μd ($F = 1/2$). $\Lambda_{d^3\text{He}}$ and K_{fast} were free parameters in this analysis. As concerns K_{fast} , it was determined by $N_{\mu d\text{-fast}}$ obtained in the fitting procedure.

The time distribution of the ${}^3\text{He}$ particles calculated according to the kinetics scheme in Fig. 3 was fitted to the experimental ${}^3\text{He}$ time distribution in various fit windows in the time interval 2.5–7 μs . Unlike the Run-8 data, the ${}^3\text{He}$ time distribution in Run-9 contains some background, though at a very low level. Presumably, this background is due to the $\mu^3\text{He}$ break up reactions: $\mu^3\text{He} \rightarrow t + \nu$ and $\mu^3\text{He} \rightarrow d + p + \nu$. This background is rejected by requirement of the decay electron coincidence. Only a small part remains due to some accidental signals in the electron detector. This background was included as a constant and determined from the counts in the time interval 8–10 μs : 4.5 events per 40 ns bin.

This analysis allowed us to determine the formation rate of the ${}^3\text{He}\mu d$ molecule $\lambda_{d^3\text{He}}$, the fast muon to ${}^3\text{He}$ transfer probability K_{fast} , and the yield of the ${}^3\text{He}\mu d$ molecules. The results are presented in Table 6.

Table 6

The results of the description of the Run-9 data according to the kinetics scheme of Fig. 3*

Fit window, μs	$\lambda_{d^3\text{He}} \cdot 10^6, \text{ s}^{-1}$	$K_{\text{fast}}, \%$	χ^2/NDF	$N^3\text{He}\mu d (4\pi)$
2.5–7	194(2)	24.5(1.8)	1.37	$0.96 \cdot 10^8$
2.7–7	192(2)	26.5(2.0)	1.37	$0.94 \cdot 10^8$
2.9–7	191(2)	26.8(2.3)	1.4	$0.93 \cdot 10^8$
3.1–7	191(3)	27.7(2.7)	1.4	$0.92 \cdot 10^8$
3.3–7	189(3)	29.0(3.0)	1.4	$0.91 \cdot 10^8$
3.5–7	189(4)	29.4(3.7)	1.36	$0.90 \cdot 10^8$

* $\lambda_{d^3\text{He}}$, K_{fast} and the total number of the produced ${}^3\text{He}\mu d$ molecules were determined from fitting to the measured ${}^3\text{He}$ time distribution in various fit windows.

The results proved to be practically independent of the chosen fit window, and finally we take:

$$\lambda_{d^3\text{He}} = 192(3) \cdot 10^6 \text{ s}^{-1}; K_{\text{fast}} = 27(3)\%; N^3\text{He}\mu d(4\pi) = 0.93(3) \cdot 10^8 \text{ molecules.}$$

We can determine the q_{1S} probability of the muon transfer from μd^* to μd using the following relation:

$$q_{1S} = (1 - K_{\text{fast}}) / (1 - W_{\text{He}}), \quad (9)$$

where W_{He} is the probability of direct muon capture by ^3He . According to Ref. [18], $W_{\text{He}} = AC^3\text{He}/(1 - AC^3\text{He})$ with $A = 1.7$. This gives $W_{\text{He}} = 9.3\%$ for $C^3\text{He} = 5.0\%$. Then we have: $q_{1S} = 0.80(3)$. The measured formation rate of the $^3\text{He}\mu d$ molecule proved to be in close agreement with the result of B. Gartner *et al.* [4]: $\lambda_{d^3\text{He}} = 186(8) \cdot 10^6 \text{ s}^{-1}$. The q_{1S} probability was reported by M. Augsburg *et al.* [5] as $q_{1S} = 0.69(3)$. This value was obtained for the gas density $\varphi = 7\%$ and $C^3\text{He} = 9.13\%$, $\varphi C^3\text{He} = 64 \cdot 10^{-4}$, compared to $\varphi C^3\text{He} = 32.5 \cdot 10^{-4}$ in our experiment. Therefore, to be compared with our result, the value $(1 - q_{1S})$ from Ref. [5] should be reduced by a factor of 2.0. This gives $q_{1S} = 0.84(3)$. We conclude that both results are in good agreement.

3.4. Yields of the ^3He (0.82 MeV) particles, $^3\text{He}\mu d$ molecules and fusion-in-flight events

In our analysis, we normalize the yields of the $^3\text{He}\mu d$ molecules and the fusion-in-flight events to the yield of the ^3He (0.82 MeV) particles (the first peak in Fig. 4) in the energy range 150–460 keV (Run-8) and 200–620 keV (Run-9). Table 7 presents the number of the ^3He (0.82 MeV) particles and the $d\mu^3\text{He}$ molecules at the time $t^* \geq 1.28 \mu\text{s}$, together with the number of the selected muon stops.

Table 7

Statistics from Run-8 and Run-9*

Run	N_{μ}	$N(^3\text{He})$	$N(^3\text{He}\mu d)$	$N_{\text{FinF}}(4\pi)$
8	$6.3 \cdot 10^9$	$1.28 \cdot 10^7$	–	518 ± 26
9	$1.0 \cdot 10^9$	$3.34 \cdot 10^5$	$0.9 \cdot 10^8$	14 ± 0.7

* N_{μ} is the number of the selected muon stops; $N(^3\text{He})$ is the number of the registered ^3He (0.82 MeV) signals; $N(^3\text{He}\mu d)$ is the number of the produced $^3\text{He}\mu d$ molecules; N_{FinF} is the number of the expected fusion-in-flight events.

The probability $F(^3\text{He})$ to produce a FinF event by a ^3He (0.82 MeV) particle was calculated using the available $^3\text{He} + d$ fusion cross sections in the ^3He energy range below 1 MeV [19]. The calculated value is $F(^3\text{He}) = 2.70(13) \cdot 10^{-5}$. One should add to this value the weighted probabilities to produce the FinF events by the $\mu^3\text{He}$ (0.8 MeV) particles and by the $^3\text{He} + ^3\text{He}$ pairs. These weights are:

$$w(^3\text{He}) / w(\mu^3\text{He}) / w(^3\text{He}^3\text{He}) = 0.842 / 0.125 / 0.033. \quad (10)$$

The relative fusion-in-flight probabilities for these types of events are:

$$F(^3\text{He}) / F(\mu^3\text{He}) / F(^3\text{He}^3\text{He}) = 1.0 / 2.3 / 2.0. \quad (11)$$

The probability $F(\mu^3\text{He})$ is larger than $F(^3\text{He})$ proportionally to the length of the tracks: $R(^3\text{He}) = 0.28 \text{ mm}$ and $R(\mu^3\text{He}) = 0.64 \text{ mm}$. The total probability $F^*(^3\text{He})$ to produce a FinF event per one registered ^3He (0.82 MeV) signal is given by the following expression:

$$F^*(^3\text{He}) = F(^3\text{He}) \times [w(^3\text{He}) + 2.3w(\mu^3\text{He}) + 2w(^3\text{He}^3\text{He})] / [w(^3\text{He})\epsilon(^3\text{He})] = 4.04 \cdot 10^{-5}. \quad (12)$$

The obtained value of $F^*(^3\text{He})$ can be used to calculate the expected yield of the FinF events from the measured number of the ^3He (0.82 MeV) signals. The total ^3He (0.82 MeV) yields in Run-8 and in Run-9 were found to be $N(^3\text{He}) = 1.28 \cdot 10^7$ and $N(^3\text{He}) = 3.34 \cdot 10^5$, respectively. Then, the expected yield of the $^3\text{He}d$ fusion-in-flight events in the time $t \geq 1.28 \mu\text{s}$ can be calculated as:

$$N_{\text{FinF}} = N(^3\text{He}) F^*(^3\text{He}) = 518 / 14 \text{ events in Run-8 / Run-9.} \quad (13)$$

These numbers are presented in Table 7 with 5% errors dominated by the error in calculations of $F(^3\text{He})$.

3.5. Selection of the candidates for the muon catalyzed $d^3\text{He}$ fusion events

The full data set from Run-8 and Run-9 was analysed with the goal to identify the $^4\text{He} + p$ events produced in the muon catalyzed $^3\text{He}d$ fusion reaction. The muon stops were selected to be inside the TPC fiducial volume (see Fig. 2) accompanied by the Michel electrons. At the first step, the selection of the candidates for the $^4\text{He} + p$ events was done with the following criteria:

- There should be a signal at the muon stop pad P0 ($E_{P0} \geq 1.0$ MeV) separated in time from the muon signal and accompanied with two signals at a sequence of two neighbour pads P1 and P2;
- The pulses on pads P0, P1 and P2 should overlap in time to form a continuous track;
- There should be only one active P1 pad in between P0 and P2.

Figure 6 demonstrates an example of a registered candidate. The further selection of the candidates for the $^4\text{He} + p$ events was done using information on the energy deposits on pads P0, P1 and P2 taking into account the electron–ion recombination in the tracks.

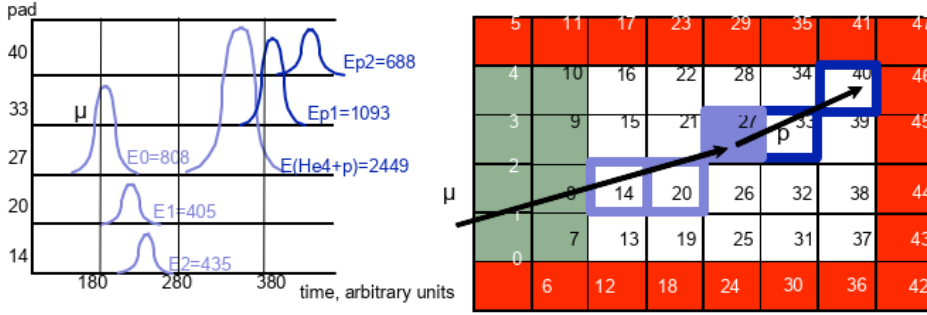


Fig. 6. The candidate of $^3\text{He}d$ fusion event. Muon stop on pad 27. The deposited energies are expressed in MeV

The recombination effect reveals itself as a difference between the measured energy of the signal E_{meas} and the real energy of the particle E : $E_{\text{meas}} = E - E_{\text{recomb}}$ (see Fig. 7b). The value of E_{recomb} was determined using the measured signals from the alpha sources, ^{240}Pu ($E_{\alpha} = 5.156$ MeV) and ^{241}Am ($E_{\alpha} = 5.48$ MeV) and from the ^3He (0.82 MeV) peak using for interpolation the following expression:

$$E_{\text{recomb}} = E (A\Theta^{1/2} + B\Theta), \text{ where } \Theta = Z^2M/E. \quad (14)$$

Here Z and M are the charge and the mass of the particle. The fit parameters were found to be $A = 6.26(15) \cdot 10^{-3}$, $B = -0.0095(15) \cdot 10^{-3}$ (Run-9). Figure 7a shows the Monte Carlo (MC) energy spectrum for the $^3\text{He} + d \rightarrow ^4\text{He} + p$ fusion-in-flight events and for the muon catalyzed $^3\text{He}d$ fusion events (pad P0). Figure 7c presents the energies on P0 pad of the $^4\text{He} + p$ particles (Run-8) according to the above mentioned criteria.

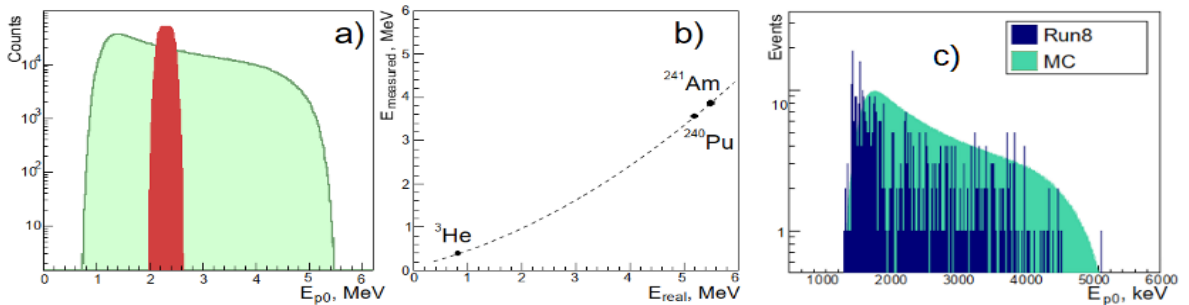
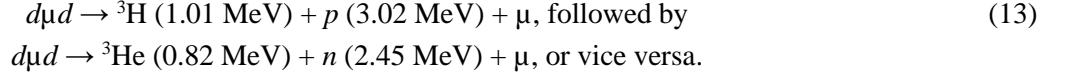


Fig. 7. MC energy spectra on pad P0 for the fusion-in-flight events in Run-8 (green) and for the muon catalyzed $^3\text{He}d$ fusion events in Run-9 (red) (a). The measured energy versus the real energy of the $^3, ^4\text{He}$ particles in Run-9; the dashed line represents the results of calculations using expression (14) with the parameters $A = 6.26 \cdot 10^{-3}$ and $B = -0.0095 \cdot 10^{-3}$ determined from the fit to the measured ^{241}Am and ^{240}Pu α -peak positions and to the ^3He (0.82 MeV) peak position (b). Energy spectrum on pad P0 of the 455 candidates of $^4\text{He} + p$ particles selected in Run-8 (c)

3.6. Detection efficiency and background

The next step includes the analysis of the energy spectra on pads P1 and P2. The range of the 14 MeV protons in the TPC is $R_p = 23$ cm with $dE/dx = 0.35$ MeV/cm. The energy deposited by a proton in the zone of pads P1 and P2 should be around 0.5 MeV. Therefore, we use the region $E_{P1} \leq 1$ MeV, $E_{P2} \leq 1$ MeV for selection of the candidates for the ${}^4\text{He} + p$ events. This resulted in 182 events in Run-8 and in 6 events in Run-9. Figure 8a displays the $E_{P1} \times E_{P2}$ plot of the 455 ${}^4\text{He} + p$ candidates, with 182 events in the region $E_{P1} \leq 1$ MeV, $E_{P2} \leq 1$ MeV. One can see that, besides the ${}^4\text{He} + p$ events, there is some background with a very special distribution ending sharply at $E_{P1} = 2.5$ MeV and at $E_{P2} = 1.8$ MeV. The nature of this background is understood. It is due to pile up of two successive dud fusion reactions:



Such events can produce signals on P0 (due to the 1.1 MeV ${}^3\text{H}$ and 0.82 MeV ${}^3\text{He}$), on P1 (due to the 3.02 MeV proton with $R_p = 13$ mm), and on P2 (due to scattering of the 2.45 MeV neutron on deuterons). The experimental data available in Run-8 allow one to reproduce directly this background by collecting the events with signals on P0 and P1 accompanied by signals on the pads which are not joining the pads P0 and P1. Figure 8b presents the $E_{P1} \times E_{P2}$ plot of such events. To separate the ${}^4\text{He} + p$ events from the dd fusion pileup events, the number of events in the $E_{P1} \times E_{P2}$ plot (Fig. 8b) in the region $E_{P1} \geq 1$ MeV, $E_{P2} \geq 1$ MeV was normalized to the number of events in the corresponding region in Fig. 8a, and the number of the dd fusion pileup events in the zone $E_{P1} \leq 1$ MeV, $E_{P2} \leq 1$ MeV was determined: $N_{\text{pileup}}(\text{R8}) = 25$. Then the number of the registered d ${}^3\text{He}$ fusion-in-flight events was obtained: $N_{\text{FinF}}(\text{R8}) = 182 - 25 = 157$. Comparison of this number with the expected number of the ${}^3\text{He} + d$ fusion-in-flight events gives the registration efficiency of the fusion-in-flight events: $\epsilon_F = 157 / 518 = (30 \pm 3)\%$. This value is valid also for the registration efficiency of the muon catalyzed $d^3\text{He}$ fusion. The quoted error is determined by the error in the number 182 and by the error in the calculated probability to produce a fusion-in-flight event $F({}^3\text{He})$.

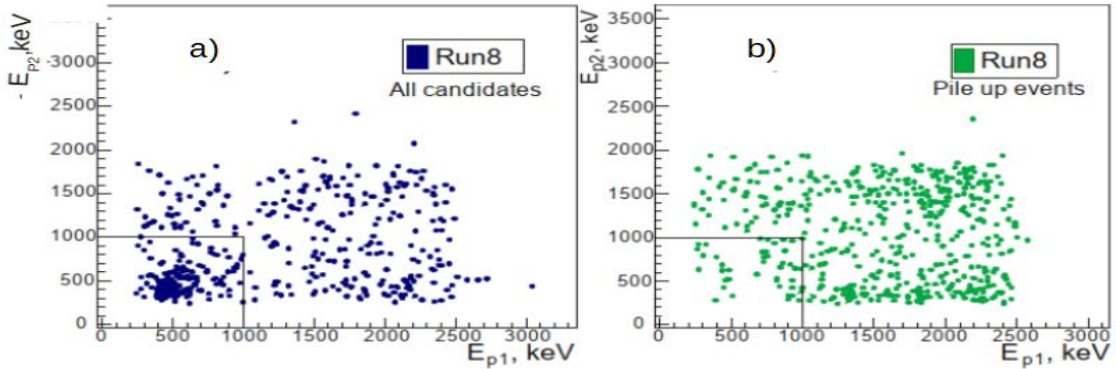


Fig. 8. Energy distribution on pads P1 and P2 of the 455 ${}^4\text{He} + p$ candidates in Run-8 (a). Energy distribution of the dd fusion pileup events on pads P1 and P2 (506 events) in Run-8 (b)

The considered above two types of events constitute the main background in Run-9 aimed at observation of the muon catalyzed fusion reaction ${}^3\text{He}d \rightarrow {}^4\text{He} + p$. Based on the results obtained in Run-8, we can calculate the expected background in Run-9 using the following expressions:

$$N_{\text{FinF}}(\text{R9}) = N_{\text{FinF}}(\text{R8}) \cdot N({}^3\text{He})_{\text{R9}} / N({}^3\text{He})_{\text{R8}} \cdot C_d(\text{R9})/C_d(\text{R8}), \quad (14)$$

$$N_{\text{pileup}}(\text{R9}) = N_{\text{pileup}}(\text{R8}) \cdot N({}^3\text{He})_{\text{R9}} / N({}^3\text{He})_{\text{R8}} \cdot P_{\text{pileup}}(\text{R9})/P_{\text{pileup}}(\text{R8}), \quad (15)$$

$$N_{\text{bgr}}(\text{R9}) = N_{\text{FinF}}(\text{R9}) + N_{\text{pileup}}(\text{R9}), \quad (16)$$

where the ratio of the registered ${}^3\text{He}$ signals $N({}^3\text{He})_{\text{R9}} / N({}^3\text{He})_{\text{R8}} = 0.026$; the ratio of the D_2 densities $C_d(\text{R9})/C_d(\text{R8}) = 0.95$; and the ratio of the dd fusion pileup probabilities $P_{\text{pileup}}(\text{R9})/P_{\text{pileup}}(\text{R8}) = 0.61$. The calculated in this way background predictions for Run-9 are as follows: $N_{\text{FinF}}(\text{R9}) = 3.87 \pm 0.3$,

$N_{\text{pileup}}(\text{R9}) = 0.39 \pm 0.08$, $N_{\text{bgr}}(\text{R9}) = 4.3 \pm 0.4$. The quoted error in $N_{\text{bgr}}(\text{R9})$ is determined mostly by the statistical error in $N_{\text{FinF}}(\text{R8})$. We can further reduce $N_{\text{bgr}}(\text{R9})$ by cutting the low energy part in the energy spectrum on pad P0 presented in Fig. 8a. The expected position of the signals from the muon catalyzed $d^3\text{He} \rightarrow ^4\text{He} + p$ reaction is above $E_{\text{P0}} = 2.4$ MeV (see Fig. 7a). Therefore, we can set the low energy cut at the energy up to $E_{\text{P0}} = 2.0$ MeV without noticeable decrease in the registration efficiency of the muon catalyzed $d^3\text{He} \rightarrow ^4\text{He} + p$ reaction. Table 8 presents the background predicted for Run-9 for various E_{P0} cuts.

Table 8

Total number of the selected $^4\text{He} + p$ candidates N_{tot} , the number of fusion-in-flight events N_{FinF} , and the number of dd fusion pile up events N_{pileup} registered in Run-8 and extrapolated to Run-9 for various cuts on the energy deposited on pad P0

$E0$ cut, MeV	Run-8			Run-9			
	N_{tot}	N_{FinF}	N_{pileup}	N_{tot}	N_{FinF}	N_{pileup}	$N_{\text{bgr}} = N_{\text{FinF}} + N_{\text{pileup}}$
1	182	157	25	6	3.87 ± 0.31	0.39 ± 0.08	4.3 ± 0.4
1.6	117	93	24	3	2.30 ± 0.23	0.37 ± 0.08	2.7 ± 0.3
2	99	77	22	2	1.90 ± 0.22	0.34 ± 0.07	2.2 ± 0.3

Another source of background in Run-9 might be the breakup reactions $\mu^3\text{He} \rightarrow d + n, p + 2n$. However, the energy deposit on pad P0 being rather small in such events, they could simulate the muon catalyzed $d^3\text{He} \rightarrow ^4\text{He} + p$ fusion events only when piling up with the $dd \rightarrow ^3\text{H} + p$ events. The calculated probability of such process is $0.5 \cdot 10^{-7}$ per muon stop. In addition, it is suppressed by three orders of magnitude to a negligible level by requiring detection of the muon decay electron. The muon capture on high Z gas could be disregarded, taking into account very high purity of the D_2 gas in this experiment. Finally, two candidates for the muon catalyzed ^3Hed fusion were registered with the predicted background of 2.2 ± 0.3 events.

3.7. Upper limit for fusion decay probability of the $d\mu^3\text{He}$ molecules

Based on this observation, an upper confidence limit for the number of the muon catalyzed ^3Hed fusion events was calculated by the method described in Refs. [20, 21]. This determines an upper limit for the probability for the fusion decay of the $d\mu^3\text{He}$ molecule in our gas mixture:

$$P_F(^3\text{Hed}\mu \rightarrow ^4\text{He} + p + \mu) = N_F/N(^3\text{Hed}\mu)\epsilon_F, \quad (17)$$

where $N_F \leq 3.1$ events is the upper limit at 90% CL for the number of detected muon catalyzed ^3Hed fusion events, $N(^3\text{Hed}\mu) = 0.93 \cdot 10^8$ is the number of the produced $^3\text{Hed}\mu$ molecules, and $\epsilon_F = 0.30$ is the detection efficiency for the ^3Hed fusion events. This gives: $P_F(^3\text{Hed}\mu \rightarrow ^4\text{He} + p + \mu) \leq 1.1 \cdot 10^{-7}$. One should stress here that the obtained result is model independent. It relies only on the experimentally measured parameters including the fusion-in-flight background and the detection efficiency. Using the measured P_F and involving the theoretical value for the total $^3\text{Hed}\mu$ total decay rate, $\Lambda_{\text{dec}} = 7 \cdot 10^{11} \text{ s}^{-1}$, one can deduce the ‘‘effective’’ $^3\text{Hed}\mu$ fusion decay:

$$\Lambda_F = \Lambda_{\text{dec}} \cdot P_F \leq 7.7 \cdot 10^4 \text{ s}^{-1} \text{ at } 90\% \text{ CL}. \quad (18)$$

4. Conclusion

This experiment was aimed at the search of the muon catalyzed $d^3\text{He}$ fusion. An important advantage of these measurements was a possibility to determine the level of the background and the registration efficiency using data from the high statistical MuSun experiment. This allowed us to determine in a model independent way the upper limit for the probability P_F of the fusion decay of the $^3\text{Hed}\mu$ molecule in the $\text{D}_2 + ^3\text{He}$ (5%) gas mixture at 6.5% LHD density at 31 K temperature: $P_F(^3\text{Hed}\mu \rightarrow ^4\text{He} + p + \mu) \leq 1.1 \cdot 10^{-7}$.

Using this value of P_F and involving the theoretical value for the total $^3\text{Hed}\mu$ total decay rate, $\Lambda_{\text{dec}} = 7 \cdot 10^{11} \text{ s}^{-1}$, we deduce an upper limit for the ‘‘effective’’ $^3\text{Hed}\mu$ fusion rate Λ_F : $\Lambda_F \leq 7.7 \cdot 10^4 \text{ s}^{-1}$

at 90% CL. This obtained limit for Λ_F is close to the result of the experiment [14] $\Lambda_F \leq 6.0 \cdot 10^4 \text{ s}^{-1}$ and disagrees strongly with the reported in Ref. [15] rate $\Lambda_F \approx 6 \cdot 10^5 \text{ s}^{-1}$, and thus rules out the statement made in Ref. [15] on observation of the muon catalyzed $d^3\text{He}$ fusion. This excludes also, as a possible explanation of the observed earlier in Refs. [14] and [15] large difference in Λ_F , an assumption of a large difference in the formation rates (according to Eq. (5)) of the clusters $[(^3\text{He}\mu d)e\text{D}_2]^+$ and $[(^3\text{He}\mu d)e\text{HD}]^+$. We present here also two complimentary results obtained in this experiment: $\lambda_{d^3\text{He}} = 192(3) \cdot 10^6 \text{ s}^{-1}$ and $q_{1S} = 0.80(3)$. These results proved to be in good agreement with measurements reported in Refs. [4] and [5].

Acknowledgments

The authors express their gratitude to M.P. Faifman and L.N. Bogdanova for fruitful discussions of theoretical aspects of the muon catalyzed $^3\text{He}d$ fusion.

References

1. Y.A. Aristov *et al.*, *Yad. Phys.* **33**, 1066 (1981).
2. D.V. Balin *et al.*, *Muon. Atoms Mol.* **25** (1993).
3. E.M. Maev *et al.*, *Hyperfine Interact.* **119**, 121 (1999).
4. B. Gartner *et al.*, *Phys. Rev. A* **62**, 012501 (2000).
5. M. Augsburger *et al.*, *Phys. Rev. A* **68**, 022712 (2003).
6. V. Belyaev *et al.*, *Z. Phys. D. Mol. Clusters* **41**, 239 (1997).
7. W. Czaplinski *et al.*, *Phys. Lett. A* **233**, 403 (1997).
8. Y. Kino, M. Kamimura, *Hyperfine Interact.* **82**, 195 (1993).
9. A.V. Kravtsov *et al.*, *Z. Phys. D* **29**, 49 (1994).
10. S.S. Gershtein, V.V. Gusev, *Hyperfine Interact.* **82**, 205 (1993).
11. L.N. Bogdanova, V.I. Korobov, L.I. Ponomarev, *Hyperfine Interact.* **118**, 187 (1999).
12. D.I. Abramov, V.V. Gusev, L.I. Ponomarev, *Hyperfine Interact.* **119**, 127 (1999).
13. M.P. Faifman, L.I. Men'shikov, *Hyperfine Interact.* **119**, 127 (1999).
14. E.M. Maev *et al.*, *Hyperfine Interact.* **118**, 171 (1999).
15. V.M. Bystritsky *et al.*, *Europ. Phys. J. D* **38**, 455 (2006).
16. V.A. Ganzha *et al.*, PNPI. High Energy Physics Division. Main Scientific Activities 2007–2012, 106 (2013).
17. D.V. Balin, V.A. Ganzha, S.M. Kozlov *et al.*, *Phys. Part. Nuclei* **42**, 185 (2011);
D.V. Balin, V.A. Ganzha, S.M. Kozlov *et al.*, *Part. Nuclei* **42**, 361 (2011).
18. V.M. Bystritsky, *Phys. At. Nucl.* **58**, 631 (1995).
19. W.E. Kunz, *Phys. Rev.* **97**, 456 (1955); R.M. White, R.W.D. Resler, G.M. Hale, *Tech. Rep. IEAE NDS* **177** (1997).
20. T.M. Huber *et al.*, *Phys. Rev. D* **41**, 2709 (1990).
21. R.D. Cousins, V.L. Highland, *Nucl. Instr. Meth. A* **320**, 331 (1992).

OBSERVATION OF A NEW PHENOMENON OF THE HIGHLY EXCITED LONG-LIVED ATOMIC ISOMERS

PNPI participants of the PENTATRAP Collaboration: S.A. Eliseev, P.E. Filianin, Yu.N. Novikov

1. Introduction

Most of the optical transitions are E1 or M1 type, with lifetimes on the level of ms, but some are highly forbidden and can have extremely long lifetimes up to millions of years as predicted theoretically [1]. A few of them with lifetimes in the range from milliseconds to seconds have been found and investigated using storage rings and ion traps, but hitherto no method allowed a direct observation of the excitation energy of extremely long-lived metastable states. It was not expected so far that the excitation energy of these states would exceed 10 eV. Therefore, it turned out to be completely unexpected when long-lived highly excited atomic states with energies higher than 100 eV were detected in experiments with rhenium and osmium ions.

2. Experimental method

Mass measurements have been performed with the novel high-precision Penning trap PENTATRAP at the Max Planck Institute for Nuclear Physics at Heidelberg (Germany) [2]. Highly charged ions (HCI) produced in an electron beam trap are extracted in a buncher with a kinetic energy of a few keV/ q , mass to charge (m/q) selected by a 90° dipole magnet, and sent into the Penning trap. The 4 K cold bore of the superconducting magnet houses five cylindrical Penning traps. Two of them (traps 2 and 3, Fig. 1) are used for measuring the trap frequencies of the ions of interest. Traps 1 and 4 serve to store ions, while trap 5 allows monitoring of fluctuations of the trap potentials and the magnetic field. The stabilization of the room temperature, the helium pressure inside the magnet bore and the active shielding of the magnet considerably reduce fractional changes of the magnetic field and hence of the cyclotron frequency drift. A relative mass measurement of the two HCI states with an unprecedented precision of $1 \cdot 10^{-11}$ is hereby achieved by determining the cyclotron frequency $\nu_c = qB/2\pi m$ of the HCI with the mass m and charge q in a strong magnetic field ($B \approx 7$ T) and a weak electrostatic harmonic potential of the Penning trap. The cyclotron frequency is derived by measuring the ion trap frequencies ν_+ , ν_z and ν_- (modified cyclotron (16 MHz), axial (700 kHz) and magnetron frequency (10 kHz)) and applying the invariance theorem $\nu_c^2 = \nu_+^2 + \nu_z^2 + \nu_-^2$.

The axial, magnetron, and cyclotron amplitudes of cooled $^{187}\text{Re}^{29+}$ ions are approximately 10, 2 and 2 μm , respectively [3]. Great care is taken to prepare just a single ion of interest in each trap as the presence of another undesired ion in the trap would disturb the motion of the ion of interest and hence alter its motional frequencies. The main experimental phase is devoted to the measurement in traps 2 and 3. The measurement cycle consists of a set of sub-measurements. First, the cyclotron motion is excited to an amplitude of approximately 10 μm with a subsequent measurement of its phase (reference phase). It is followed by the re-cooling of all three motions. After that, the cyclotron motion is again excited to the same amplitude and is let to freely evolve its phase for 40 s with its subsequent measurement (measurement phase). Ten measurement cycles constitute a measurement run. A unique feature of PENTATRAP is that during each run, the frequency measurements are performed simultaneously in synchronized traps, for instance on ion 1 in trap 2 (*upper blue ion* in Fig. 1) and ion 2 (*red*) in trap 3, respectively, for approximately 12 min [3]. After that, the ion species are swapped between traps 2 and 3 by moving the three ions one trap up. Then, a measurement run is carried out with ion 2 in trap 2 and ion 3 (*lower blue ion*) in trap 3. Lastly, the ion species are swapped back by moving the three ions one trap down again. After each change of the configuration of ions in the traps the ion motions are cooled for 20 s. In this way, one alternately determines the cyclotron frequencies of ions in ground and metastable states in each measurement trap. This measurement sequence is repeated until the measurement is stopped, as, even though the vacuum allows for several hours to days of storage times, ions are then lost due to charge exchange reactions with background gas. If no determination of the metastable state is possible anymore, the traps are emptied and a new set of ions is loaded. The full set of measured cyclotron frequencies is divided in a set of groups. The group length

must be as short as possible such that it can be described by a low-order polynomial, but must contain substantially more data points than the polynomial degrees of freedom. Thus, each group is chosen to be approximately 2-hour long and to contain a total of 10 cyclotron-frequency points (five points correspond to the ion in the ground state and the other five points correspond to the ion in the metastable state), see *middle* of Fig. 1. We use third-grade polynomials since this is the lowest order that has at least one inflection point. Data points from the ions in both the metastable and the ground state are fitted with the same polynomial with global fitting parameters. The polynomial for the data points from the ion in the ground state is scaled with an additional fitting parameter R , which corresponds to the frequency ratio. This yields three quantities: 1) the frequency ratio R , 2) its uncertainty ΔR , 3) the reduced χ^2 . The final ratio R is obtained as a weighted mean of the frequency ratios from all groups and measurement traps. Its statistical uncertainty ΔR is the larger one of the internal and external errors, see *right side* of Fig. 1.

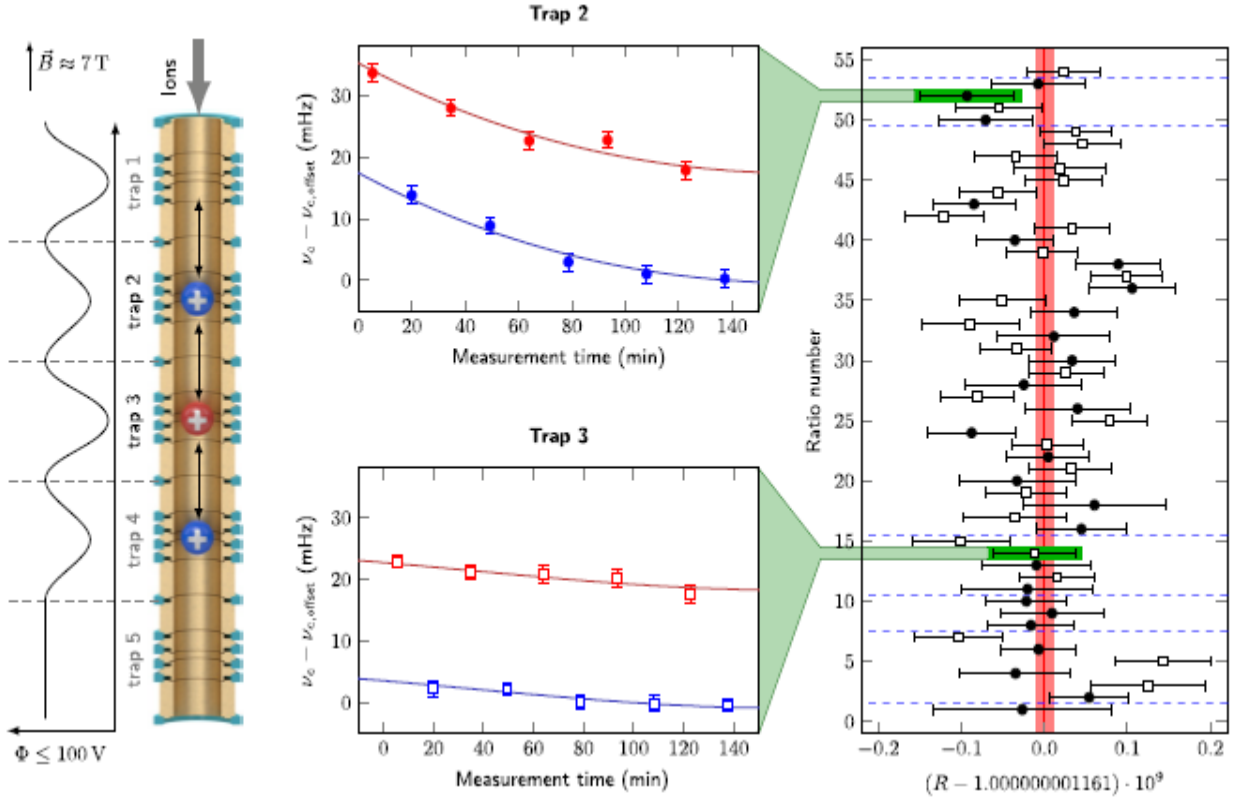


Fig. 1. Procedure of the Re frequency measurements at PENTATRAN. *Left* – three $^{187}\text{Re}^{29+}$ ions (ion 1 – blue, ion 2 – red and ion 3 – blue) are loaded from the top into the trap stack. The potentials are nominally identical to the neighbouring traps for each of the measurement traps, *i. e.* the potential of trap 2 is also applied in trap 4. The magnetic field points along the direction of the trap axis. *Centre* – shifting the ions one trap down or up after a cyclotron frequency determination results in measurements with the blue (ion 1) and red ion (ion 2) in trap 2 and red and second blue ion (ion 3) in trap 3. Here, the red ion is in the ground state, the other two are in the metastable electronic state. *Right* – all ratios determined over seven measurement campaigns (divided by the dashed lines) display the stability of the system. The results for trap 2 (filled) and trap 3 (empty) exhibit similar behaviour. The final averaged value is shown in red

3. Results

Analyses yield external errors of $8 \cdot 10^{-12}$ and internal errors of $7 \cdot 10^{-12}$ resulting in a Birge ratio of 1.14 and final ratio $R - 1 = 1.161(10)_{\text{stat}} \cdot 10^{-9}$ [3]. The systematic uncertainties in the final ratio, as it was carefully investigated [3], are well below the statistical uncertainty and hence can be neglected. From the final ratio, the energy of the metastable (isomeric) state in $^{187}\text{Re}^{29+}$ with respect to the ground state can be

calculated using $\Delta E_{\text{Re}} = m(^{187}\text{Re}^{29+})(R-1)c^2 = 202.2(17) \text{ eV}$ [3]. The similar frequency-ratio measurements of the same metastable state in Os^{30+} , which is isoelectronic to Re^{29+} give $\Delta E_{\text{Os}} = 207(3) \text{ eV}$.

To find out the nature of this isomeric state, theoretical calculations have been performed by groups of Max Planck Institute for Nuclear Physics (Heidelberg) and University of Heidelberg and Sorbonne [3]. They apply three different fully relativistic approaches, namely, the multiconfiguration Dirac–Hartree–Fock (MCDHF) method in two different implementations, and the configuration interaction method employing Kohn–Sham orbitals, as implemented by the many-body script language Quanyt (for details see Ref. [3]). Since the experimental half-life of the metastable state in ^{187}Re was estimated as > 7 days, the observed state can't be the short-lived $^3\text{P}_0$ state and should be characterized by the $4d^9 4f^3 \text{H}_5$ – configuration which can decay to the ground state by an E5-transition. Decay to the levels just below, *i. e.*, to the $^3\text{P}_0$, $^3\text{P}_1$ and $^3\text{P}_2$ states (Fig. 2), have very low probabilities because of their high multiplicities (M5, E4 and M3, respectively) and small photon energies. The half-life of the metastable level was estimated as 130 days, and the obtained energies with the mentioned above theoretical methods are shown in Fig. 2 in comparison with the shaded in pink experimental value.

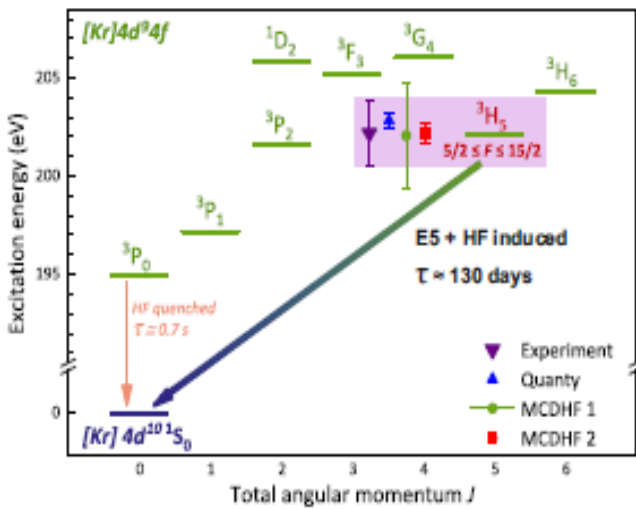


Fig. 2. The $4d^{10}$ ground state and relevant $4d^9 4f$ excited electronic states of the $^{187}\text{Re}^{29+}$ ion. Comparison of the experimental result and theoretical values obtained using multiconfiguration Dirac–Hartree–Fock approaches in two different implementations (MCDHF 1 and 2) and by means of a configuration–interaction (Quanyt) calculation is shown in the shaded region, which shows the experimental result

Such very long-lived and highly excited metastable states in atoms are observed for the first time. These characteristics of states lead to a very high quality factor $Q = \nu/\Delta\nu$, which is a leading factor in the choice of the relevant candidate for the frequency standard (modern clock). Highly charged ions are largely insensitive to external perturbations in contrast to neutral atoms and singly charged ions, which are presently used as optical clocks. Figure 3 shows a comparison of Q -factors for Re and other existing clocks which are widely used in science and technique. Superiority of rhenium is obvious, and the disadvantage in belonging the isomeric transition wavelength beyond the optical region is ridded by the possibility of accessing with frequency combs.

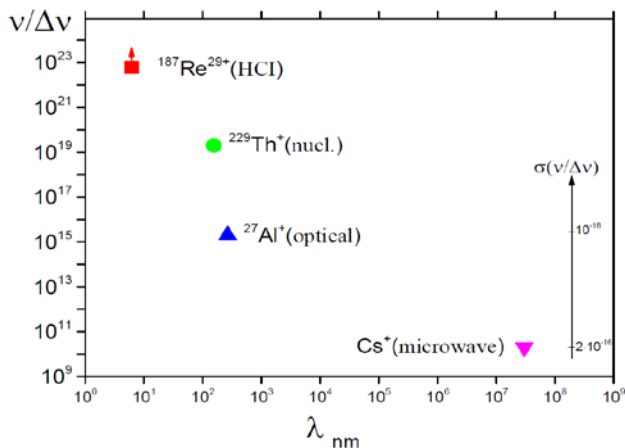


Fig. 3. Comparison of quality factors $\nu/\Delta\nu$ for the clocks obtained by different methods of experimental observation. For microwave and optical methods the best values achieved are shown with indication of their precision on the right vertical axis for Cs and Al, respectively. The lower limit of Q for ^{187}Re is given assuming the experimental half-life > 7 days and the experimental energy of metastable state of 202 eV [3]

4. Conclusion

In summary, the phenomenon of the unusually high energy long-lived isomerism, known very well in nuclei, has been firstly observed also in atoms. It was carried out by means of the new PENTATRAP system, which synchronously operates five individual traps for simultaneous mass measurements. High energy electron-metastable states in highly charged ions of $^{187}\text{Re}^{29+}$ and $^{187}\text{Os}^{30+}$ have been observed by direct measurement of their masses in comparison to ground states determined with an unprecedented precision of the absolute mass of $1 \cdot 10^{-11}$. Observation of the same isoelectronic states in both Re and Os and their strong confirmation by different theoretical approaches is an excellent crosscheck of the results. For the metastable state energy of 202.2 ± 1.9 eV in Re^{29+} and 207 ± 3 eV in Os^{30+} and the experimental lifetime of these states longer than seven days the electronic quality factor of $> 10^{22}$ has been obtained, which has ever been characterized experimentally. These states can be used for creation of a new more exact atomic clock. This creation will be more successful for the atoms with the same isoelectronic states that are already observed in rhenium and osmium, however with the lower energy which are being searched for at the PENTATRAP installation headed by Professor Dr. Klaus Blaum.

References

1. M. Safronova *et al.*, Rev. Mod. Phys. **90**, 025008 (2018).
2. A. Rischka *et al.*, Phys. Rev. Lett. **124**, 113001 (2020).
3. R.X. Schüssler *et al.*, Nature **581**, 42 (2020).
4. S. Brewer *et al.* Phys. Rev. Lett. **123**, 033201 (2019).

STUDY OF THE STRUCTURE OF LIGHT EXOTIC NUCLEI BY PROTON ELASTIC SCATTERING IN INVERSE KINEMATICS USING THE ACTIVE TARGET IKAR

G.D. Alkhazov, A.V. Dobrovolsky, A.G. Inglessi, A.V. Khanzadeev, G.A. Korolev, L.O. Sergeev,
A.A. Vorobyov, V.I. Yatsura

1. Introduction

The study of nuclei far from stability has shown that these nuclei may have exotic structures such as a neutron skin or a halo. The neutron skin describes an excess of neutrons on the nuclear surface and is quantitatively determined as the difference between the neutron R_n and proton R_p root-mean-square (rms) radii of radial nucleon density distribution. A neutron halo arises due to the tunneling penetration of a loosely bound neutron (or neutrons) through a potential barrier and manifests itself as an extended distribution of nuclear matter outside a compact core.

A necessary condition for the halo formation is considered to be a low neutron separation energy ($S_n \leq \sim 1$ MeV). It is with a decrease of the separation energy of one or several valence nucleons in neutron-rich nuclei that the shape of the nucleus, in which the halo is formed, changes. Another important criterion for the halo appearance is the configuration of the valence nucleon. The orbit in which it is located should have a low angular momentum of relative motion ($l = 0, 1$). The existence of the neutron halo leads to an increase in the rms radius of the nuclear matter distribution. This is manifested in an increased value of the total reaction cross section (σ_R), or the interaction cross section (σ_I), which was the first sign of the halo formation in exotic nuclei such as ${}^6\text{He}$, ${}^{11}\text{Li}$, ${}^{11}\text{Be}$ and ${}^{14}\text{Be}$. Another important feature of the halo nucleus is a narrow momentum distribution of the reaction products during fragmentation of exotic nuclei in comparison with stable nuclei. The cross section for knocking out one neutron can also be an indicator of a nucleus with a halo.

The nuclear size and the shape of the radial distribution of nuclear matter are fundamental characteristics of the nucleus and reflect the basic properties of nuclear forces. The experimentally determined radii and the shape of the distribution of nuclear matter are used to test theoretical models describing the nuclear structure. The most reliable information on the distribution of nuclear matter in stable nuclei was obtained by the method of elastic scattering of intermediate energy protons (about 1 GeV). At such an energy, the interaction process can be described by the Glauber theory of diffraction scattering, which makes it possible to relate rather accurately the measured scattering cross sections to the sought distributions of nuclear matter. To study the structure of exotic nuclei it was proposed at PNPI [1] to perform experiments on small-angle proton–nucleus elastic scattering in inverse kinematics. In this case, a beam of exotic nuclei can be scattered on a hydrogen target, which is the ionization spectrometer IKAR developed at PNPI [2, 3]. Earlier, the experimental set-up with the spectrometer IKAR was successfully used in studies of elastic scattering of hadrons at small angles [4–6].

The measurement of the absolute differential cross sections $d\sigma/dt$ for small-angle elastic scattering of protons on the nuclei under study was the purpose of the experiments performed in the secondary beams of the accelerator complex of GSI (Darmstadt) using the IKAR set-up. A cross-section analysis with the Glauber theory allows one to obtain information not only on the nuclear rms radii, but also on the shape of the radial distribution of the nuclear matter. Indeed, the analysis of the shape of the measured cross sections makes it possible for us to determine both the rms radius R_c of the core and the radius R_v (R_h) of the valence (halo) nucleon distribution. Note that the rms nuclear matter radius R_m is connected with R_c and R_v as

$$R_m = [(A_c R_c^2 + A_v R_v^2)/A]^{1/2}, \quad (1)$$

where A is the number of nucleons in the nucleus, A_c is the number of nucleons in the core, A_v is the number of valence (halo) nucleons; R_c and R_v are the core and the valence nucleons rms radii in the centre-of-mass of the nucleus.

In a series of experiments carried out at GSI by physicists of the PNPI–GSI Collaboration, the absolute cross sections $d\sigma/dt$ for elastic scattering of protons at an energy of 0.7 GeV/nucleon were measured in

the range of the momentum transfers $0.002 \leq |t| \leq 0.05$ (GeV/c)² on the ⁴He, ⁶He, ⁸He [7–9], ⁶Li, ⁸Li, ⁹Li, ¹¹Li [10], ¹²Be, ¹⁴Be [11], ¹²C, ¹⁴C, ¹⁵C, ¹⁶C, ¹⁷C [12], and ⁷Be, ⁸B [13, 14] nuclei.

In this review, we briefly describe the experimental set-up with the detector IKAR, discuss the method of the analysis of the experimental data, and present the main final results of the performed studies.

2. Experimental set-up

The experiments were carried out at the GSI accelerator complex. Figure 1 shows the layout of the experimental set-up.

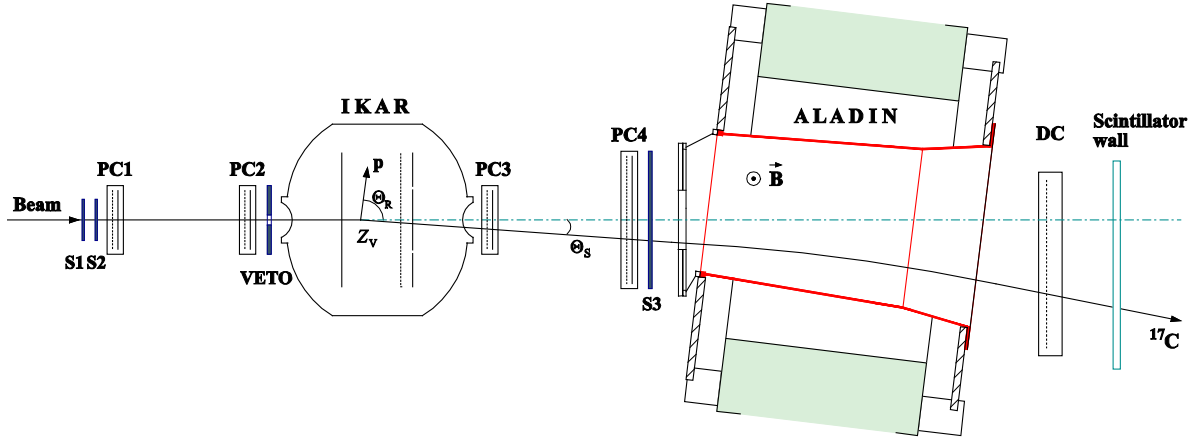


Fig. 1. Schematic layout of the experimental set-up [2]. IKAR – ionization chamber, which serves as a hydrogen target and a proton recoil detector. Only one of six IKAR modules is shown. The ionization chamber IKAR makes it possible to determine the energy T_R of the recoil proton, its outgoing angle Θ_R and the coordinate Z_V of the interaction vertex. PC1–PC4 – multiwire proportional chambers measuring the angle of scattering Θ_S of the incident particle. S1–S3 and VETO are scintillation detectors for particle identification and triggering. The ALADIN magnet with a drift chamber and a scintillation hodoscope is used for identification of the scattered particle

The beams of the nuclei under study interacted with the hydrogen nuclei of the ionization chamber IKAR filled with pure hydrogen at a pressure of 10 atm. The spectrometer IKAR was both a gaseous target and a recoil proton detector, *i. e.*, it was an active target. IKAR consists of six identical modules, which are axial ionization chambers with a grid. The signals from the electrodes give information about the recoil proton energy T_R , its scattering angle Θ_R and the point of interaction Z_V in the gap between the cathode and the grid. The square of the momentum transfer in the scattering process could be determined from the recoil-proton energy T_R measured in the IKAR spectrometer with the aid of the relation $|t| = 2mT_R$, where m is the recoil-proton mass. In order to ensure a better separation of useful events, the momentum transfer $|t|$ was also determined from the projectile scattering angle Θ_S , which was measured by a system of multiwire proportional chambers PC1–PC4 arranged downstream and upstream of the IKAR detector. The scintillation counters S1–S3 were used to identify beam particles by the time of flight and by dE/dx . The VETO scintillation detector that operated in the anticoincidence mode selected only those beam particles that propagated at a distance not larger than 10 mm from the chamber axis. The ALADIN dipole magnet and a system of scintillation detectors behind it permitted to separate the inelastic channels in which nuclei scattered in the reaction under study underwent break-up in the working volume of the ionization chamber. The energy calibration of the t scale was implemented with the aid of ²⁴¹Am α -particle sources deposited onto the chamber electrodes. The error in the calibration did not exceed 1%. The energy resolution σ_E , obtained for the α -line on anodes, varied within 45–55 keV. A high detection efficiency for both beam particles and elastic-scattering events in the chamber determined good accuracy of the absolute normalization of the measured differential cross sections (2 to 3%). A detailed description of the experimental set-up was given elsewhere [2]. In order to test the procedure used, the cross section for elastic p^4 He scattering in inverse kinematics was measured [8], and this cross section proved to be in good

agreement with the results of earlier precision measurements of the same cross section in direct kinematics [6]. The linearity and stability of the electronics channels were controlled using generator signals fed to the inputs of the preamplifiers.

3. Measurement of differential cross sections

The absolute differential cross sections for proton elastic scattering were found after the event selection by the formula

$$d\sigma/dt = dN/(dtMn\Delta L). \quad (2)$$

Here, dN is the number of elastic proton–nucleus scattering events in the interval dt of the four-momentum transfer squared t , M is the corresponding number of beam particles impinging on the target, n is the density of the hydrogen nuclei known from the measured gas pressure and temperature, and ΔL is the effective target length. The value of t was calculated as $|t| = 2mT_R$ for low momentum transfers, and was determined through the scattering angle Θ_s of the projectiles for higher momentum transfers.

The selection of useful elastic scattering events was carried out in several steps. Beam particles of the required isotope were identified using the time of flight and the energy loss of the projectiles in the S1–S3 scintillators. Then break-up events in the gas of the chamber were rejected with the help of tracking in the magnetic field. The correlation between the proton energy measured in IKAR and the scattering angle Θ_s of the incident particle was used to eliminate the background of random coincidences. The parameters of the proton signals in IKAR (*e. g.* width, amplitude, rise time, *etc.*) were also used to eliminate most of the background events.

Figure 2 shows the absolute differential cross sections (calculated by Eq. (2)) for elastic scattering of protons by nuclei of the ${}^6,8,9,11\text{Li}$ isotopes measured in inverse kinematics at an energy of about 0.7 GeV/nucleon [10]. Similar cross sections were also obtained for the isotopes ${}^4,6,8\text{He}$ [8], ${}^7\text{Be}$ [14], ${}^{12,14}\text{Be}$ [11], ${}^8\text{B}$ [13, 14] and ${}^{12,14,15,16,17}\text{C}$ [12].

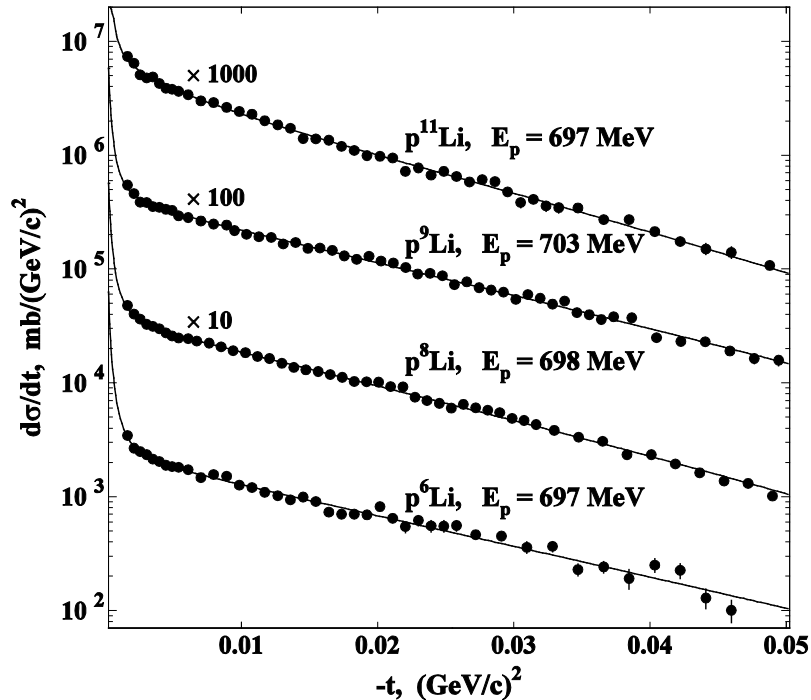


Fig. 2. Differential cross sections for elastic scattering of protons on nuclei of Li isotopes as functions of the four-momentum transfer squared [10]. The indicated energy corresponds to the equivalent proton energy for direct kinematics. The *solid lines* are the results of the cross section calculations using the Gaussian–oscillator nuclear matter distributions with fitted parameters

4. Data analysis

To obtain information about the nuclear matter density distributions from the measured cross sections, the Glauber multiple scattering theory was applied. The calculations were performed using the basic Glauber formalism for proton–nucleus elastic scattering and taking experimental data on the elementary proton–proton and proton–neutron scattering amplitudes as input. The cross sections calculated by the formulas of the Glauber theory were compared with the cross sections measured experimentally. In order to reduce the model dependence in the sought distributions of matter in the nuclei under study, several phenomenological parameterizations of the nuclear matter were used. Basically, four parameterizations were used, namely SF (symmetrized Fermi), GH (Gaussian–halo), GG (Gaussian–Gaussian) and GO (Gaussian–oscillator) [2, 9]. Each of these distributions contains two free parameters. In the case of the SF and GH parameterizations, it is assumed that all nucleons of the nucleus are described by the same distribution, while in the case of the GG and GO parameterizations, it is assumed that the nucleus consists of core nucleons and valence nucleons (halo nucleons) with different matter distributions. In both of these cases, the Gaussian distribution is used for the core–nucleon density, while a Gaussian distribution in the GG parameterization and a $1p$ -type harmonic oscillator distribution in the GO parameterization are used for the valence (halo) nucleons. The free parameters in the GG and GO distributions are the rms core radius R_c and the radius R_v of the valence nucleons. In the nuclei under study, the possibility of a halo of one or several nucleons was considered. It was assumed that the cores in ${}^6\text{He}$, ${}^8\text{He}$, ${}^6\text{Li}$, ${}^8\text{Li}$, ${}^9\text{Li}$, ${}^{11}\text{Li}$, ${}^7\text{Be}$, ${}^{12}\text{Be}$, ${}^{14}\text{Be}$, ${}^8\text{B}$, ${}^{15}\text{C}$, ${}^{16}\text{C}$ and ${}^{17}\text{C}$ have the same nucleon compositions as, correspondingly, in the nuclei ${}^4\text{He}$, ${}^4\text{He}$, ${}^4\text{He}$, ${}^7\text{Li}$, ${}^7\text{Li}$, ${}^9\text{Li}$, ${}^4\text{He}$, ${}^{10}\text{Be}$, ${}^{12}\text{Be}$, ${}^7\text{Be}$, ${}^{14}\text{C}$, ${}^{14}\text{C}$ and ${}^{16}\text{C}$. In the case of the ${}^{14}\text{Be}$ nucleus, the possibility of its structure consisting of the core ${}^{10}\text{Be}$ and a halo of four nucleons was also considered.

The parameters of the model density distributions were determined by fitting the calculated cross sections to the experimental data. The analysis of the data is described in detail in Ref. [9]. As a result of the data analysis, the density distributions and the rms radii of the nuclear matter for all investigated nuclei were determined. For a number of nuclei, the rms radii R_c of the core and those of the valence nucleons R_v were also determined. Figure 3 shows the radial nuclear density distribution $\rho(r)$ of the compact nucleus ${}^6\text{Li}$ and that of the halo nucleus ${}^{11}\text{Li}$. For the ${}^6\text{Li}$ nucleus, the SF, GH, GG and GO parameterizations give close results [10], only the GG distribution of the nuclear matter being shown in Fig. 3a. For comparison, the single-particle point distribution of protons obtained by measuring the cross section for electron scattering by the ${}^6\text{Li}$ nucleus is presented [10]. It is known that for nuclei with an equal number of neutrons and protons ($N/Z = 1$) the distributions of neutrons and protons are almost the same. The observed good agreement of these distributions in the ${}^6\text{Li}$ nucleus indicates the adequacy of the method used.

The final results of the data analysis are given in Table 1. The R_m values obtained by various groups of researchers from the measured reaction or interaction cross sections are also presented in Table 1. These data were taken from reviews [15, 16] (see also references in Ref. [2]). By combining the values of R_m and R_p , which were determined from the known values of the charge radii R_{ch} , the rms radii R_n of neutron distributions were obtained. Table 1 shows the corresponding values of the neutron skin $\delta_{np} = R_n - R_p$.

A characteristic feature of the described method for studying exotic nuclei is the ability to determine experimentally the sizes of the core and the halo. In the work of Grigorenko *et al.* [17], it was proposed to consider the ratio $\kappa = R_v/R_c$ as a quantitative characteristic of the halo. For light nuclei near the β -stability line, theory predicts the values of κ close to 1.20–1.25. The authors of Ref. [17] proposed to consider the cases when the ratio κ is sufficiently large ($\kappa \geq \sim 2.0$) as the cases of nuclei with a halo structure.

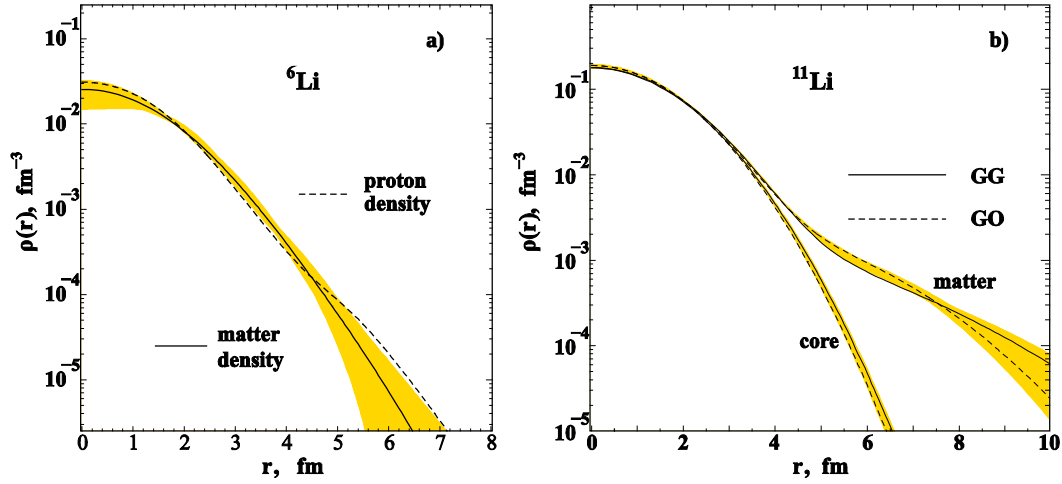


Fig. 3. Comparison of the one-particle density distribution of protons in the ${}^6\text{Li}$ nucleus, obtained from the analysis of data on scattering of electrons by ${}^6\text{Li}$ nuclei (*dashed curve*), with the one-particle density distribution of nuclear matter (protons and neutrons), obtained from the analysis of the $p{}^6\text{Li}$ scattering data [10] (*solid curve*) (a). The density distribution of the nuclear core and the total matter density (core + halo) in the ${}^{11}\text{Li}$ nucleus, obtained from the analysis of the data on $p{}^{11}\text{Li}$ scattering using the GG and GO nuclear density parameterizations [10]. The *shaded areas* denote the errors in the analysis of the proton scattering data (b)

Table 1

Results obtained for nuclei of the He [7, 9], Li [10], Be [11, 14], B [13, 14] and C [12] isotopes

Nucleus	Proton elastic scattering				Reaction (interaction) cross sections
	R_m , fm	R_c , fm	R_v , fm	δ_{np} , fm	R_m , fm
${}^4\text{He}$	1.49(3)	–	–	0.06(6)	1.57(4)
${}^6\text{He}$	2.45(10)	1.88(12)	3.31(28)	0.74(14)	2.50(5)
${}^8\text{He}$	2.53(8)	1.55(15)	3.22(14)	0.83(10)	2.52(3)
${}^6\text{Li}$	2.44(7)	2.11(17)	3.00(34)	–0.02(15)	2.36(3)
${}^8\text{Li}$	2.50(6)	2.48(7)	2.58(48)	0.46(12)	2.39(6)
${}^9\text{Li}$	2.44(6)	2.20(6)	3.12(28)	0.48(11)	2.34(6)
${}^{11}\text{Li}$	3.71(20)	2.53(3)	6.85(58)	1.72(26)	3.50(9)
${}^7\text{Be}$	2.42(4)	1.86(14)	3.01(19)	–0.23(10)	2.31(2)
${}^{12}\text{Be}$	2.71(6)	2.36(6)	4.00(28)	0.47(9)	2.59(6)
${}^{14}\text{Be}$	3.25(11)	2.77(6)	5.28(43)	1.12(15)	3.10(15)
${}^8\text{B}$	2.58(6)	2.25(3)	4.24(25)	–0.51(9)	2.61(8)
${}^{12}\text{C}$	2.34(5)	–	–	0.00(10)	2.35(2)
${}^{14}\text{C}$	2.42(5)	–	–	0.07(9)	2.33(7)
${}^{15}\text{C}$	2.59(5)	2.41(5)	4.36(38)	0.36(9)	2.54(4)
${}^{16}\text{C}$	2.70(6)	2.41(5)	4.20(26)	0.46(10)	2.74(3)
${}^{17}\text{C}$	2.68(5)	2.57(5)	4.05(47)	0.39(9)	2.76(3)

5. Results and discussion

The values of R_m obtained by the method of elastic scattering of protons within the limits of measurement errors basically agree with the results found in the analyses of the total reaction or interaction cross sections (see Table 1). However, in the case of the ${}^7\text{Be}$ nucleus, which is considered to be the core of the ${}^8\text{B}$ nucleus, our magnitude of R_m occurs to be significantly larger than that obtained from the reaction cross sections (see Ref. [15]). For the ${}^8\text{B}$ nucleus, the values of R_m measured by different researchers lie in

a wide range from 2.38(2) to 2.61(8) fm. Our result ($R_m = 2.58(6)$ fm) agrees with that determined in Ref. [18] ($R_m = 2.61(8)$ fm).

Measurements on the stable ${}^4\text{He}$, ${}^6\text{Li}$ and ${}^{12}\text{C}$ nuclei [8–10, 12], having equal numbers of protons (Z) and neutrons (N), for which the same distributions of protons and neutrons are assumed, were carried out for checking the correctness of operation of the technique used. The obtained values of R_m are very close to the known values of R_p for these isotopes.

In the studied nuclei, the largest neutron halo was observed in ${}^{11}\text{Li}$, for which the maximum value of $\kappa = 2.7(3)$ was obtained. A neutron halo, and, accordingly, a large value of κ was also found for the ${}^6\text{He}$ [9], ${}^{14}\text{Be}$ [11] and ${}^{15}\text{C}$ [12] nuclei. The ${}^8\text{He}$ nucleus, which is usually considered as a nucleus with a neutron skin, was described within the model of ${}^4\text{He}$ + four valence neutrons forming a neutron skin with the parameter $\kappa = 2.1(3)$. In the case of the ${}^{14}\text{Be}$ halo nucleus, two models were considered: (core ${}^{12}\text{Be}$ + 2 neutrons) and (core ${}^{10}\text{Be}$ + 4 neutrons). In both cases, a satisfactory description of the experimental cross section was achieved, though a somewhat better description of the experimental data was obtained for the ${}^{14}\text{Be}$ nucleus with a halo consisting of two neutrons.

A necessary condition for formation of a halo is a low separation energy of the valence nucleons and a low angular momentum of their motion. Table 2 shows the results of the analyses of the investigated nuclei in the model (core + 2 neutrons). The separation energy S_{2n} of two neutrons, the magnitude κ and the size of the neutron skin $\delta_{np} = R_n - R_p$ are given.

Table 2

Nuclei analysed using the model (core + 2n)

Nucleus	S_{2n} , MeV	$\kappa = R_v/R_c$	δ_{np} , fm
${}^{11}\text{Li}$	0.369	2.7(3)	1.72(26)
${}^6\text{He}$	0.973	1.8(3)	0.74(14)
${}^{14}\text{Be}$	1.336	1.9(2)	1.13(15)
${}^{12}\text{Be}$	3.670	1.7(2)	0.47(9)
${}^{16}\text{C}$	5.470	1.7(1)	0.46(10)
${}^9\text{Li}$	6.097	1.4(2)	0.42(11)

As predicted by theory, the size of the halo (the κ magnitude) increases with S_{2n} decreasing. The ${}^{11}\text{Li}$, ${}^6\text{He}$ and ${}^{14}\text{Be}$ nuclei, which are referred to as halo nuclei, are also characterized by a narrow momentum distribution of reaction products during their fragmentation. The ${}^{12}\text{Be}$ and ${}^{16}\text{C}$ nuclei, although they have a significant value of κ , have a high separation energy S_{2n} of two neutrons and a rather wide momentum distribution of reaction products during fragmentation, which does not allow one to consider them as nuclei with a halo. These nuclei with a large excess of neutrons, like the ${}^9\text{Li}$ nucleus, have a large neutron skin. Obviously, there is no clearly defined and quantitatively fixed boundary between halo nuclei and non-halo nuclei (which are usually called nuclei with a large neutron skin). Therefore, sometimes both ${}^{12}\text{Be}$ and ${}^{16}\text{C}$ are called halo nuclei.

Among the neutron-rich isotopes of carbon ${}^{14-17}\text{C}$ studied by this method, a significant halo is observed in the ${}^{15}\text{C}$ isotope. It is interesting to compare the structure of the nuclei of the ${}^{15}\text{C}$ and ${}^{17}\text{C}$ isotopes (Table 1). Though the binding energy S_n in the ${}^{17}\text{C}$ nucleus ($S_n = 0.728$ MeV) is lower than that in the ${}^{15}\text{C}$ nucleus ($S_n = 1.218$ MeV), the value of κ , corresponding to the halo existence is determined for ${}^{15}\text{C}$ ($\kappa = 1.8(2)$), but not for ${}^{17}\text{C}$ ($\kappa = 1.6(2)$). The absence of a halo in the ${}^{17}\text{C}$ nucleus is explained by the fact that in ${}^{17}\text{C}$ the valence neutron is in the d -state. Note that the momentum distribution of reaction products during fragmentation of the ${}^{15}\text{C}$ nucleus is much narrower than that of the ${}^{17}\text{C}$ nucleus. As already noted, a low binding energy of the valence nucleon is a necessary but not sufficient condition for formation of a halo in the nucleus.

The question of the existence of a halo in the ${}^8\text{B}$ nucleus is interesting in connection with the fact that formation of a proton halo in this nucleus is prevented by the Coulomb barrier. The study of the structure of the proton-rich ${}^8\text{B}$ and ${}^7\text{Be}$ nuclei is also important for nuclear astrophysics. An essential role in formation of solar neutrinos is played by these nuclei. ${}^8\text{B}$ nuclei are produced in the Sun in the ${}^7\text{Be}(p, \gamma){}^8\text{B}$ reaction with

emission of high energy neutrinos, which can be detected in terrestrial laboratories. The rate of the proton capture in ${}^7\text{Be}$ depends on the ${}^8\text{B}$ structure. The size of the ${}^8\text{B}$ nucleus and the shape of the proton density distribution in it at large distances determine the rate of the proton capture and can be used in theoretical calculations of the solar neutrino flux. The structure of the ${}^8\text{B}$ nucleus was analysed within the model (core ${}^7\text{Be} + p$). In the ${}^8\text{B}$ nucleus, the existence of a proton halo is observed, and its size is determined as $\kappa = 1.9(1)$. Note that the size of the proton halo in the ${}^8\text{B}$ nucleus is comparable to the neutron halo in the ${}^{15}\text{C}$ nucleus.

In many theoretical investigations, the proton-rich ${}^8\text{B}$ nucleus is described together with its mirror partner ${}^8\text{Li}$. It seems natural to expect similar matter distributions in these nuclei. However, the analysis of our proton scattering data shows that the matter distributions in these nuclei are significantly different (Fig. 4). As a matter of fact, this analysis provides clear evidence for a proton halo in ${}^8\text{B}$, and gives no evidence for a neutron halo in ${}^8\text{Li}$.

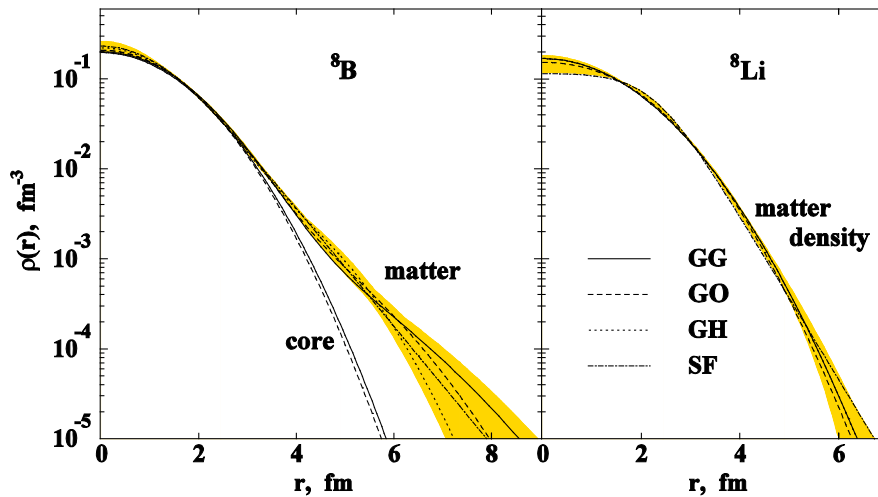


Fig. 4. Comparison of the matter density distributions in ${}^8\text{Li}$ and ${}^8\text{B}$ obtained in the analyses of the proton scattering data using the GG, GO, GH and SF density parameterizations [13]. The core density distribution in the case of ${}^8\text{B}$ is also shown

6. Conclusion

The method proposed at PNPI for studying the structure of light exotic nuclei proved to be highly efficient and made it possible for us to study the size and the structure of the ${}^4, 6, 8\text{He}$, ${}^6, 8, 9, 11\text{Li}$, ${}^7, 12, 14\text{Be}$, ${}^8\text{B}$ and ${}^{12, 14, 15, 16, 17}\text{C}$ nuclei. The halo structure was found in ${}^{11}\text{Li}$, ${}^{14}\text{Be}$, ${}^8\text{B}$ and ${}^{15}\text{C}$. By combining our results with existing data on charge radius, we have obtained information on the neutron distribution in the studied nuclei and about the size of the neutron skin in them. The measured cross sections can be used to test various theoretical density distributions.

In preparations for the experimental studies with the IKAR facility, during measurements and analysis of the obtained data at different stages of the experimental program, the following physicists took part in addition to the authors of this review article: employees of the HEPD of PNPI M.N. Andronenko, G.E. Gavrilo, A.A. Zhdanov, O.A. Kiselev, A.A. Lobodenko, G.E. Petrov, D.M. Seliverstov, L.O. Sergeev, N.A. Timofeev, GSI employees F. Aksouh, A. Bauchet, L. Chulkov, I. Dillmann, P. Egelhof, A. Estradé, F. Farinon, S. Fritz, H. Geissel, M. Gorska, C. Gross, S. Ilieva, H. Irnich, R. Kanungo, Y. Ke, G. Kraus, J. Kurcewicz, Yu.A. Litvinov, G. Münzenberg, S.R. Neumaier, F. Nickel, C. Nociforo, A. Prochazka, T. Schäfer, C. Scheidenberger, W. Schwab, H. Simon, T. Suzuki, M. Takechi, S. Tang, H. Weick, as well as M. Mutterer, J.P. Theobald, V.A. Volkov (Institut für Kernphysik, Technische Universität Darmstadt) and G. Colò (Dipartimento di Fisica, Università degli Studi di Milano and INFN).

References

1. G.D. Alkhazov, A.A. Lobodenko, JETP Lett. **55**, 379 (1992).
2. G.D. Alkhazov, A.A. Vorobyov, A.V. Dobrovolsky *et al.*, Phys. Part. Nucl. **53**, 655 (2022).
3. A.A. Vorobyov, G.A. Korolev, V.A. Schegelsky *et al.*, Nucl. Instr. Meth. **119**, 509 (1974).
4. A.V. Dobrovolsky, A.V. Khanzadeev, G.A. Korolev *et al.*, Nucl. Phys. B **214**, 1 (1983).
5. A.A. Vorobyov, G.A. Korolev, A.V. Dobrovolsky *et al.*, Nucl. Instrum. Methods Phys. Res. A **270**, 419 (1988).
6. O.G. Grebenyuk, A.V. Khanzadeev, G.A. Korolev *et al.*, Nucl. Phys. A **500**, 637 (1989).
7. G.D. Alkhazov, M.N. Andronenko, A.V. Dobrovolsky *et al.*, Phys. Rev. Lett. **78**, 2313 (1997).
8. S.R. Neumaier, G.D. Alkhazov, M.N. Andronenko *et al.*, Nucl. Phys. A **712**, 247 (2002).
9. G.D. Alkhazov, A.V. Dobrovolsky, P. Egelhof *et al.*, Nucl. Phys. A **712**, 269 (2002).
10. A.V. Dobrovolsky, G.D. Alkhazov, M.N. Andronenko *et al.*, Nucl. Phys. A **766**, 1 (2006).
11. S. Ilieva, F. Aksouh, G.D. Alkhazov *et al.*, Nucl. Phys. A **875**, 8 (2012).
12. A.V. Dobrovolsky, G.A. Korolev, S. Tang *et al.*, Nucl. Phys. A **1008**, 122154 (2021).
13. G.A. Korolev, A.V. Dobrovolsky, A.G. Inglessi *et al.*, Phys. Lett. B **780**, 200 (2018).
14. A.V. Dobrovolsky, G.A. Korolev, A.G. Inglessi *et al.*, Nucl. Phys. A **989**, 40 (2019).
15. A. Ozawa, T. Suzuki, I. Tanihata, Nucl. Phys. A **693**, 32 (2001).
16. I. Tanihata, H. Savajols, R. Kanungo, Prog. Part. Nucl. Phys. **68**, 215 (2013).
17. L.V. Grigorenko, B.V. Danilin, V.D. Efros *et al.*, Phys. Rev. C **57**, 2099(R) (1998).
18. G.W. Fan, M. Fukuda, D. Nishimura *et al.*, Phys. Rev. C **91**, 014614 (2015).

LOOKING FOR THE ELECTRON BRIDGE IN ^{229m}Th

A.V. Popov, Yu.I. Gusev, T.V. Koneva, Yu.V. Nechiporenko, Yu.N. Novikov

1. Introduction

The maximum accuracy of currently existing frequency standards devices that determine the entire way of our life does not exceed 10^{-16} . At the same time, the solution of pressing issues of fundamental physics, for example, checking the stability of fundamental interaction constants over time, as well as problems of the GLONASS system and other applications, requires an accuracy of 10^{-18} – 10^{-19} and higher. A nuclear clock based on the 8.11 ± 0.12 eV (152.7 ± 2.1 nm) transition in the ^{229}Th isomer just makes it possible to achieve an accuracy of 10^{-19} in singly charged and 10^{-21} in triply charged ions.

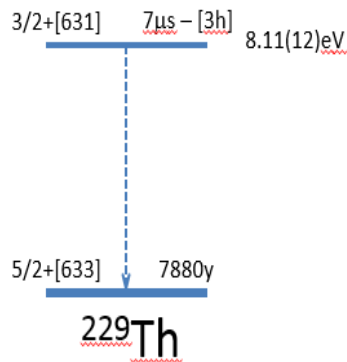


Fig. 1. Transition in the ^{229}Th isomer

In addition, the energy of this transition is sufficiently low to allow for nuclear laser spectroscopy, an inherent requirement for a nuclear clock. The small size of the nucleus, which is five orders of magnitude smaller than an atom size, and the screening of the nucleus by electrons significantly neutralize the effect of external fields on the nuclear transition frequency. This makes it possible to operate the oscillator in a dense medium and, as a result, leads to the possibility of creating compact solid-state devices as frequency standards [1, 2]. The energy of an isomeric transition is mainly determined by the contribution of the strong interaction. In all currently existing frequency standards, the electromagnetic interaction is decisive. The combination of clocks based on electromagnetic and strong interactions makes it possible to study the stability of world fundamental constants in time.

2. Method for isomer observation

A method for isomer observation based on the interaction of laser radiation and the hyperfine structure of the ion in an ion trap is being developed at a number of laboratories [3–5]. Along with such obvious advantages as high selectivity and high efficiency, this method requires a relatively high intensity of the ion beam containing the ^{229}Th isomer. To enjoy the unique features of this isomer, we must develop methods for populating this state, which can be monitored either through the registration of particles or photons emitted upon its decay or by analysing the hyperfine structure of the ionic states. It should be noted that the ways of measuring the energy of conversion electrons in Refs. [6–8] or of photoelectrons emitted from the surface of a solid in Refs. [9, 10] are quite difficult to grasp and are unlikely to provide accurate energy estimates. This is due to the nonuniformity of the work function, the complexity of the electron spectrum below the Fermi level, and the strong dependence of the photoelectron spectrum on the surface quality. To compare the calibration photoelectron spectra from an ultra violet radiation source and the spectrum of conversion electrons correctly, we need identical depth and surface distributions of the sources of conversion electrons and photoelectrons. Differences between the angular distributions of conversion electrons and photoelectrons can induce a Fermi shift (steps in the electron spectra). It is also important to maintain the same geometry for the

measured and calibrating photons when detecting photons of the isomeric transition. Registration of the electromagnetic radiation of the 8.1 eV transition is hampered by the long partial lifetime, since it increases the time required for registration and degrades the background conditions. Registration of the photons accompanying the process of the isomer decay [11] using atomic states (electron bridges) could meet difficulties associated with the broad range of photon energies and thus poor background conditions.

A set-up for recording and measuring the energy of the direct electromagnetic transition in ^{229m}Th was described in Ref. [12]. This set-up used a gas ion-source based on ^{233}U . The main objective of the set-up was the ultraviolet optical spectroscopy of an isomer implanted into ionic crystals. The expected dominance [11] of the electron conversion channel in the neutral atom of the ^{229}Th isomer and the high efficiency of electron detection in combination with fast decay make conversion electrons the most interesting tool for the initial detection of decay, and for use as a monitor in the feedback scheme of the frequency standard. The energy of the isomeric state exceeds the binding energy of the outer electron in a neutral thorium atom. An evaluation of the conversion factor for the $M1$ transition in a neutral thorium atom [11] yields $\alpha(M1) \approx 10^9$ with the isomer lifetime shrinking to a value of $\sim 10^{-5}$ s. This virtually eliminates the possibility to detect the direct electromagnetic transition if the atom is in its neutral state or in an environment with a small gap between the energy bands. Early attempts to observe conversion electrons [13] were limited to the direct implantation of recoil atoms into a substrate after α -decay, and to the monitoring of electron emission. Unfortunately, as noted by the author of Ref. [13], the energy of recoil atoms after α -decay results in a considerable depth (~ 30 nm) of the implantation into the substrate; this exceeds the path of the electron in the media and thus eliminates the possibility of its registration. The considerable background from the α -decay of ^{233}U , and from its daughter and impurity nuclides, creates additional difficulties.

3. Design of the spectrometer

The energy of the isomeric state imposes significant restrictions on the electronic configuration of the atoms that can be used for isomer registration, due to possible decay *via* the electron conversion and electron bridge channels. To suppress competition with background, thorium isomer atoms should be stored in the ionized state, either in the form of free ions or in the composition of ionic crystals with wide forbidden zones. In our case, the ^{229}Th isomer ions are injected into a multipole radio frequency (RF) trap, thermalized, and held there until they are neutralized in charge-exchange reactions with neutral atoms added to the working helium medium. A conversion electron from a neutral atom is emitted within a few microseconds after neutralization. It is highly likely that the atom remains within the trap at this moment. Electrons are transported away from the trap along the magnetic field lines parallel to the axis of the trap. Electric-field deceleration with magnetic collimation (MAC-E) is proposed for determining the electron energy. A similar set-up combining a multipole trap and a MAC-E spectrometer was used in spectroscopic studies of electrons produced in molecular processes [14]. A sketch of the spectrometer is presented in Fig. 2.

The isomer ions are produced by α -decay of the ^{233}U nuclide. The population probability of the isomeric state is about 2%. The isomer is populated by the converted transition at 29.18 keV (the coefficient of the internal electron conversion is $\alpha_L \approx 100$), with the formation of vacancies in the L -shell, the filling of which is accompanied by the emission of Auger electrons. As a result, there is a high probability of formation of thorium ions with a charge $q = 1-5$. The ions are thermalized in helium at a pressure of 10^{-3} Torr. The maximum possible charge of the resulting ion (3+) is limited by the mechanism of charge exchange on helium atoms. In addition to using a gas flow, the extraction of thorium ions from the gas environment requires that we impose an electric field. Techniques for extracting ions from the gas cell, their transport in the radio-frequency potential, and the potential generated by injected cloud of electrons were determined in preliminary studies [15]. A uranium layer $2 \mu\text{g} \cdot \text{cm}^{-2}$ thick is deposited using electrodeposition on foils with an area of $\sim 600 \text{ cm}^2$. The foils are placed into a chamber filled with helium at a pressure of ~ 10 Torr. Low voltage (a few volts) which decreases towards the output electrodes of the camera is applied to the source foils. A system of electrodes with radio frequency transport, or with electron injection, will be used for extraction of the thermalized ions [16]. A vacuum scheme of the ion generator is shown in Fig. 3.

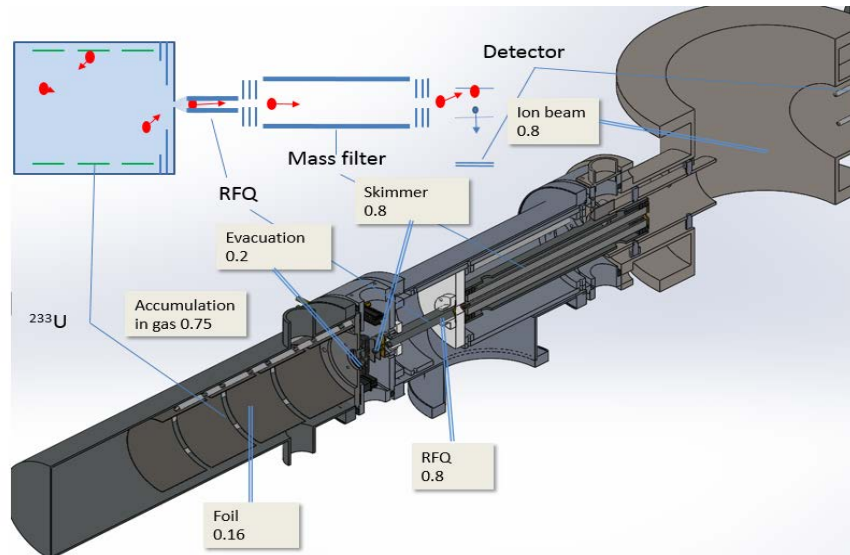


Fig. 2. Sketch of an electron spectrometer

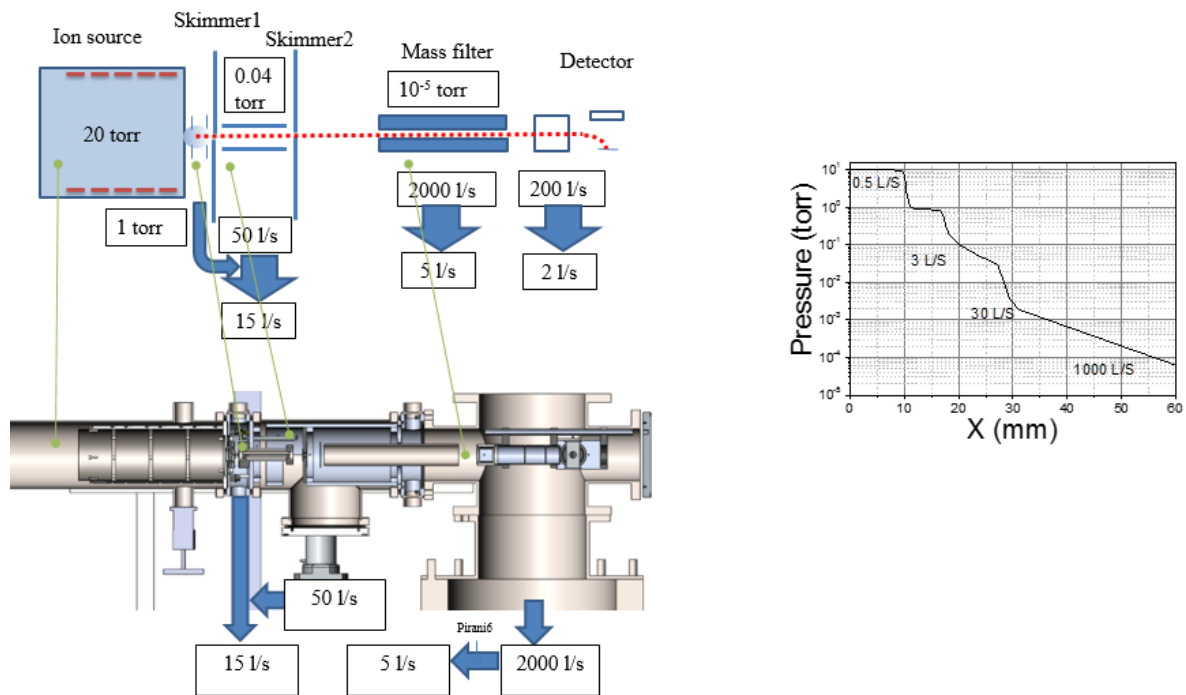


Fig. 3. Vacuum scheme of the ^{229}Th ions generator

A multipole with 22 electrodes was modeled. A pattern of the simulated spectrometer is presented in Fig. 4. This multipole (the diameter of 15 mm and the length of 40 mm) is mounted inside a solenoid that produces a field of several hundred Gauss. Disk-shaped magnetic screens 10 mm thick are positioned at the edges of the trap to confine the field. An additional cylindrical screen minimizes the magnetic field in the region of the analysing spectrometer electrodes. The need to establish the conditions for the ion deceleration inside the multipole, and the ion and electron transport outside it imposes constraints on the gas flows and thus the input and output trap apertures. Injected and thermalized ions are neutralized in interactions with impurity atoms added to helium. A hard-sphere model of interaction with gas was used to simulate the operation of the ion trap. Ions are injected into the trap with an energy of 1 eV and lose energy in collisions with atoms of helium

(the working medium). The time of thermalization is a few fractions of a millisecond. The ions are trapped by the effective potential produced in an RF field in a viscous medium.

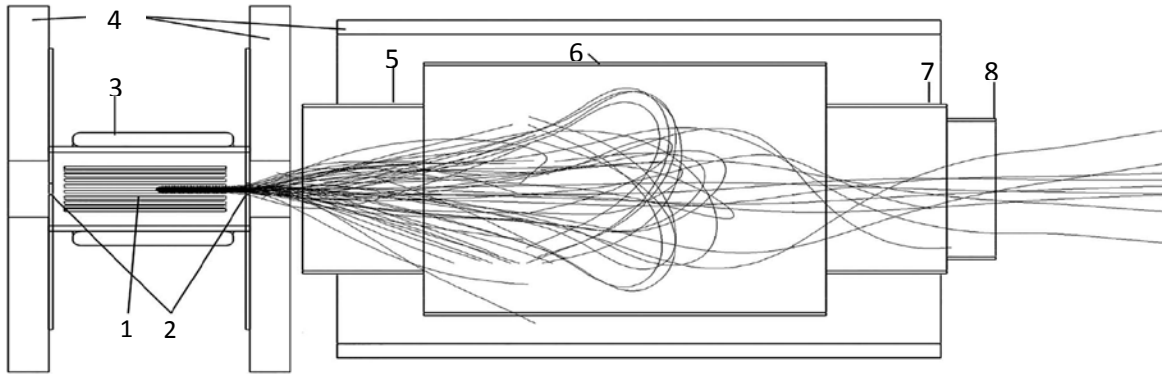


Fig. 4. Design of the electron spectrometer: 1 – gas-filled multipole; 2 – input and output aperture; 3 – solenoid; 4 – magnetic Fe screens; 5–8 – analyser electrodes

The distributions of ions over the energy and the distance from the axis are shown in Figs. 5 and 6, respectively. The mean energy of ions in the trap was ~ 0.04 eV; the corresponding mean displacement of an atom in the interval from the ion neutralization to the electron emission ($10 \mu\text{s}$) was ~ 2 mm. Data on the ion position in the trap and the ion velocity were used to estimate the distribution of atoms positions at the moment of electron emission. It was assumed that there was ergodicity, so the trajectory of a single ion was used instead of estimated momentary positions of a number of ions. After the presumed neutralization, an atom continues to move with the velocity of an ion. The emission of an electron occurred at a random point in time, according to an exponential distribution with a time constant corresponding to the isomer lifetime. The distribution of atoms at the moment of electron emission is represented by the filled symbols in Fig. 6. We can see that the distribution of the initial positions of electrons remains close to that of the trapped ions up to a radius of ~ 3 mm. If the spectrometer aperture diameter is set to 6 mm, this distribution limits the efficiency to $\sim 40\%$. The corresponding efficiency at a diameter of 3 mm is $\sim 10\%$. This aperture diameter appears to be acceptable if the pressure in the trap is kept at 0.5 Pa and sufficient vacuum-pump capacity is provided.

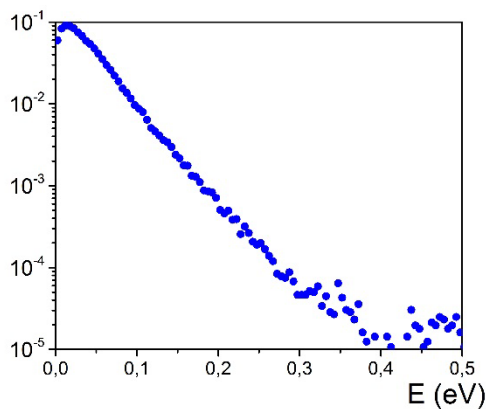


Fig. 5. Energy distribution of ions (mean energy of ions, $E \approx 0.04$ eV)

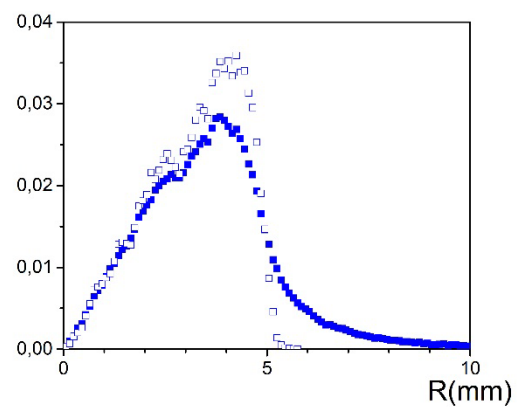


Fig. 6. Probability of finding an ion (*empty squares*) and an atom at the moment of electron emission (*full squares*) at the distance R from the multipole axis

Electron trajectories were calculated using the SIMION package [17] in the RF field of the multipole, combined with static electric and magnetic fields. The CST2017 code was used to calculate the magnetic field [18]. The elastic scattering of electrons off helium was also modeled. It should be noted that although the

probability of scattering was high, it had a negligible effect on the final electron energy in the analyser. This is attributable to the great difference between the masses of an electron and a helium atom, and the transporting effect of the magnetic field. The modeled spectrum for electrons with an energy of 2 eV yields an estimate of the resolution of the system: ~ 0.15 eV. Electrodes 5 and 7 were at zero potential, and a potential of +20 V was applied to electrode 8.

4. Results and discussion

The neutralization rate constant in a typical charge-exchange reaction is $\sim 10^{-9}$ cm³ · s⁻¹ [19]. The mean reaction time can vary from several milliseconds to seconds as the concentration of impurity oxygen varies from 10^{-1} to 10^{-4} . As a result of charge exchange and several other processes, thorium ions interacting with impurity molecules can both lose charge (with the production of molecules) and form molecules in an ionized state [19, 20]. For example, the most intense lines of thorium compounds in the mass spectrum correspond to thorium ions and oxides [21]. The energy of ThO ionization is 6.6026(2) eV [22] (0.3 eV higher than that of Th). We may therefore ignore the production of thorium oxide in the trap when making an initial estimate of the isomer energy. A more accurate estimation can be obtained by varying the concentration and nature of impurity molecules. It should be noted that the energy of molecular ion dissociation is relatively low (see, *e. g.*, Ref. [23]). An additional channel for the discharge of the ²²⁹Th isomer can thus be opened. Note that the pressure in our study (0.5 Pa = 0.005 mbar) was several orders of magnitude lower than 40 mbar in the set-up used in Ref. [7]. This has an important physical consequence that should help to understand the electron bridge mechanism better. When there is de-excitation *via* reverse resonance conversion, the lifetime of a nuclear isomer is proportional to the width of the intermediate atomic level, which is prone to the collisional broadening. According to Ref. [24], this broadening can be enhanced by a factor of 10 at $p = 45$ mbar (45 Pa). At $p = 0.5$ Pa, it is negligible. Lifetime data obtained at different facilities could therefore demonstrate experimentally the dependence of the lifetime of nuclear isomers on the ambient conditions.

5. Conclusion

The possibility of measuring the energy of electrons of conversion decay of the first excited ²²⁹Th state was considered. The technique is based on detecting conversion electrons produced during the neutralization of the ²²⁹Th isomer ions held in an RF multipole trap. It was proposed that deceleration in the electric field of a spectrometer with magnetic collimation (MAC-E) be used to measure the energy of electrons. The results from modeling show that a resolution of 0.1 eV can be achieved at an efficiency of several percent; the corresponding accuracy of energy measurement is at the level of 10^{-2} eV. This technique is specific in that the atom is isolated at the moment of electron emission, thus providing an opportunity to determine the energy of the isomeric state accurately, based only on known values of the electron energy and the electron bonding energy.

Acknowledgements

The work on this project was financially supported by Russian Science Foundation from 2022 (Grant No. 22-22-00090).

References

1. E. Peik, Ch. Tamm, *Europhys. Lett.* **61**, 181 (2003).
2. B.R. Beck, J.A. Becker, R. Beiersdorfer *et al.*, *Phys. Rev. Lett.* **98**, 142501 (2007).
3. B. Tordoff, J. Billowes, C.J. Campbell *et al.*, *Hyperfine Interact.* **171**, 197 (2007).
4. V. Sonnenschein, I.D. Moore, S. Raeder *et al.*, *Eur. Phys. J. A* **48**, 52 (2012).
5. S. Raeder, V. Sonnenschein, T. Gottwald *et al.*, *J. Phys. B: At. Mol. Opt. Phys.* **44**, 165005 (2011).
6. Y.I. Gusev, Y.N. Novikov, A.V. Popov, V.I. Tikhonov, *Bull. Rus. Acad. Sci. Phys.* **80** (8), 875 (2016).
7. B. Seiferle, L. Von der Wense, P.G. Thirolf, *Eur. Phys. J. A* **53**, 108 (2017).
8. S. Stellmer, Y. Shigekawa, V. Rosecker *et al.*, *Phys. Rev. C* **98**, 014317 (2018).
9. L. Wense, P.G. Thirolf, D. Kalb *et al.*, arXiv: 1211.0710 [nucl-ex].
10. P.V. Borisyyuk, E.V. Chubunova, N.N. Kolachevsky *et al.*, arXiv:1804.00299 [nucl-th].
11. F.F. Karpeshin, M.B. Trzhaskovskaya, *Phys. Rev. C* **76**, 054313 (2007).
12. L.V.D. Wense, P.G. Thirolf, D. Kalb, M. Laatiaoui, *J. Instrum.* **8**, 03005 (2013).
13. J. Burke, in *Proc. EMMI Workshop on Th-229* (2012).
14. P. Jusko, S. Roucka, R. Plasil *et al.*, *Int. J. Mass Spectrom.* **352**, 19 (2013).
15. C.J. Campbell *et al.*, *Phys. Rev. Lett.* **108**, 120802 (2012).
16. A.N. Litvinov, V.I. Romanenko, L.P. Yatsenko *et al.*, *New J. Phys.* **14**, 083019 (2012).
17. SIMION. <http://simion.com/>
18. CST Studio Suite: Electromagnetic Field Simulation Software. <http://www.cst.com/>
19. L.R. Churchill, M.V. De Palatis, M.S. Chapman, *Phys. Rev. A* **83**, 012710 (2011).
20. R.M. Cox, M. Citir, P.B. Armentrout *et al.*, *J. Chem. Phys.* **144**, 184309 (2016).
21. L. Von der Wense, B. Seiferle, M. Laatiaoui *et al.*, *Nature* **533**, 47 (2016).
22. V. Goncharov, M.C. Heavena, *J. Chem. Phys.* **124**, 064312 (2006).
23. J.K. Gibson, R.G. Haire, J. Marcalo *et al.*, *Eur. Phys. J. D* **45**, 133 (2007).
24. F.F. Karpeshin, M.B. Trzhaskovskaya, *Nucl. Phys. A* **969**, 173 (2018).

SHAPE-STAGGERING EFFECT IN MERCURY NUCLEI

PNPI participants of the IS598 Collaboration:

A.E. Barzakh, D.V. Fedorov, P.L. Molkanov, V.N. Panteleev, M.D. Seliverstov

1. Introduction

Since the mid-1970s, an unexpected large difference in the mean-square charge radius between ^{187}Hg and ^{185}Hg was observed by measuring the isotope shift in a radiation detection of optical pumping (RADOP) experiment performed at ISOLDE [1, 2]. Similarly to ^{185}Hg , the $^{181}, ^{183}\text{Hg}$ isotopes were found to exhibit a large isotope shift from their even-mass neighbours $^{182}, ^{184}, ^{186}\text{Hg}$ [3, 4]. Ever since these measurements, the observed pattern became known as “shape staggering.” Studying the levels at low excitation energy in more detail, different shapes were identified in close vicinity to the ground state, and the mercury isotopes are now one of the most illustrative examples of shape coexistence [5]. The experimental findings sparked extensive interest in studying this region of the nuclear chart from both experimental and theoretical points of view [5]. The large radius staggering was interpreted as transitions between weakly deformed, oblate ground states and strongly deformed, prolate ground states [6]. Since then, the isotopic chain of mercury has been studied with a multitude of complementary techniques: Coulomb excitation [7–9], in-beam γ -ray spectroscopy with recoil-decay tagging [10–13], mass measurements [14], and α/β -decay spectroscopy [15–21]. However, isotope shift and hyperfine-structure measurements had only been extended down to ^{181}Hg [2, 4]. While the ground-state deformation has been indirectly inferred for neutron-deficient mercury isotopes from in-beam recoil-decay tagging measurements, hinting toward less-deformed shapes for $A < 180$ [10–13], this had not been confirmed by a direct ground-state isotope-shift measurement. The missing mean-square charge-radii data for the lighter mercury isotopes left the key question of where the shape staggering ends. In order to address this key question, a measurement campaign was undertaken at the radioactive ion-beam facility ISOLDE [22] performing in-source laser resonance-ionization spectroscopy of 15 mercury isotopes, ranging from the neutron-deficient to the neutron-rich side ($^{177-185}, ^{198}, ^{202}, ^{203}, ^{206-208}\text{Hg}$) with the goal of measuring their isotope/isomer shifts (IS) and hyperfine structures (HFS).

The large isotopic span was made possible by using the resonance ionization laser ion source (RILIS) [23] in a novel target-ion source combination [24], together with three different ion counting techniques tailored to the isotope under investigation [25]: α -decay spectroscopy for short-lived isotopes with small production rates (down to 0.1 ion/s) using a “windmill”-type implantation station (WM) [26–28], multi-reflection time-off-flight mass spectrometer/separator (MR–ToF MS) [29–33] for high-resolution, and single-ion counting and Faraday cup (FC) ion-current measurements for high-intensity (>1 pA) mercury beams. A dedicated paper will provide a detailed discussion of the neutron-rich isotopes [34] also measured in the same experimental campaign.

2. Experimental technique

Mercury isotopes were produced at the CERN–ISOLDE facility [22] *via* spallation reactions induced by a 1.4-GeV proton beam from the PS-Booster synchrotron impinging on a molten-lead target. The neutral reaction products effused from the heated target *via* the transfer line ($\sim 700^\circ\text{C}$ target and $\sim 400^\circ\text{C}$ transfer line heating) into the versatile arc discharge laser ion source (VADLIS) cavity [24], which was operated in RILIS mode [24]. In this mode, lasers are used to resonantly ionize the isotopes of interest. The photo ions were extracted and accelerated by a 30-kV potential difference and mass separated by ISOLDE’s general purpose separator (GPS) dipole bending magnet before being sent to one of three measurement devices (FC/WM/MR–ToF MS). The choice of a molten-lead target was based on results obtained from a preparatory experiment in similar conditions at ISOLDE, where the mercury production of a molten-lead was compared with a UCx target. While the production rates of the lightest mercury isotopes were of a similar order of magnitude for both cases, the use of a molten-lead target significantly reduces the isobaric contamination of surface-ionized contaminants. This was especially important for the heavy mass region discussed in Ref. [34]. Furthermore, the production rate of the heavy mercury isotopes was significantly

higher for the molten-lead target. Resonance ionization of the mercury isotopes was accomplished using a three-step ionization scheme (Fig. 1) with a measured ionization efficiency of 6% [35]. Laser spectroscopy was performed on the 253.65-nm $6s^2\ ^1S_0 \rightarrow 6s6p\ ^3P_1$ transition. Well-resolved HFS spectra were obtained by scanning the frequency-tripled wavelength of the Ti:sapphire laser with a bandwidth of ~ 1.5 -GHz full width at half-maximum (FWHM) after tripling. At the second step (313.18 nm), the frequency-doubled output of the dye laser (Credo Dye model by Sirah Lasertechnik GmbH) was used. The third step was a non-resonant 532-nm transition driven by a Nd:YVO4 laser.

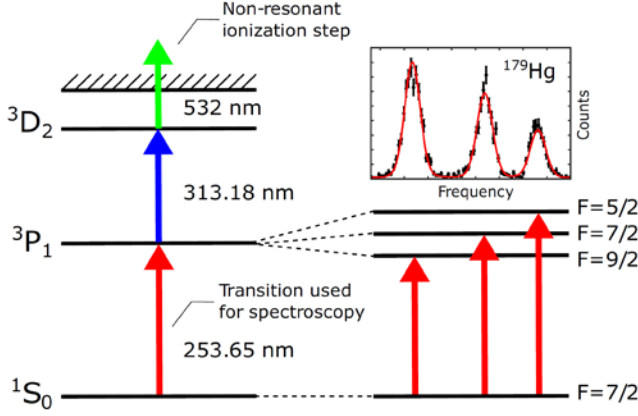


Fig. 1. Ionization scheme for mercury developed in Ref. [35] using the same transition for spectroscopy as in Refs. [1] and [36]. The right-hand side shows the splitting of the 3P_1 level states with different total angular momentum $F = I + J$ for an $I = 7/2$ nuclear spin with a corresponding exemplary HFS spectrum of ^{179}Hg . Energies and level splitting are not displayed to scale

3. Results

Information on the difference in the mean-square charge radius $\delta\langle r^2 \rangle_{A_0, A}$ between two nuclei with mass A and A_0 of the same isotopic chain is extracted from the difference in the positions of the centres of gravity of their respective HFS, ν_0 , *i. e.*, their isotope shift of a certain transition. The nuclear electromagnetic moments (magnetic dipole, electric quadrupole) dictate the relative position of the atomic-state hyperfine-splitting component with respect to ν_0 *via* the relation

$$\nu^F = a \frac{K}{2} + b \frac{\frac{3}{4} K(K+1) - I(I+1)J(J+1)}{2(2I-1) \cdot (2J-1)IJ}, \quad (1)$$

where the dipole and quadrupole hyperfine splitting parameters are given as a and b , ν^F represents the energy difference of the hyperfine component with total angular momentum $F = I + J$, with respect to ν_0 [37], and $K = F(F+1) - I(I+1) - J(J+1)$. Fitting of the spectra was performed with the open-source Python package SATLAS [38] and cross-checked with a similar fitting routine in ROOT [39] and the fitting procedure that was used in our previous HFS studies as, for instance, in Ref. [27]. To monitor the stability of the whole system, reference scans of ^{198}Hg were performed regularly. The spectra were fitted separately and the weighted mean of the fit results is taken as a final value. Results of the fits are shown in the Table. The experimental errors on the IS include both the fit errors and the spread of individual scan results. For ^{177}Hg , where only a single full spectrum was obtained, the typical dispersion in the extracted HFS centroid position for the other isotopes was added as an additional uncertainty. As the nuclear spin of $^{177, 179}\text{Hg}$ could not be determined directly by counting the hyperfine components from the present measurements due to the low angular momentum of the electronic state ($J = 1$) of the upper level of the studied transition (see Fig. 1), we report the IS and hyperfine splitting constant values assuming both possible options for the ground-state nuclear spin of $^{177, 179}\text{Hg}$ (7/2 and 9/2). Within the experimental uncertainties, good agreement on the IS and a and b parameters compared to the previous measurements was obtained.

Table

Isotope shifts ($\delta v_{198,A}$) and hyperfine splitting parameters (a and b) for the $6s6p\ ^3P_1$ level in mercury atoms and deduced mean-square charge radii ($\delta\langle r^2 \rangle_{198,A}$) and electromagnetic moments (μ and Q) in $^{177-185}\text{Hg}$ isotopes^a

Isotope	I^π	$\delta v_{198,A}$, MHz	a , MHz	b , MHz	$\delta\langle r^2 \rangle_{198,A}$, fm ² b	$\mu(\mu_N)$	$Q_S(b)$	Reference
^{177}Hg	$(7/2^-)$	54 580(390)	-4 320(180)	-410(600)	-1.067(8){78}	-1.025(48) ^c	0.57(83)	This work
	$(9/2^-)$	55 170(390)	-3 460(180)	-875(600)	-1.083(8){78}	-1.035(60) ^c	1.21(91)	This work
^{178}Hg	0^+	49 500(290)	-	-	-0.968(6){71}	-	-	This work
^{179}Hg	$(7/2^-)$	46 310(240)	-3 990(80)	-550(200)	-0.905(5){70}	-0.948(24) ^c	0.76(28)	This work
	$(9/2^-)$	46 820(230)	-3 150(70)	-1 050(210)	-0.915(5){70}	-0.947(27) ^c	1.45(31)	This work
^{180}Hg	0^+	41 330(240)	-	-	-0.808(5){60}	-	-	This work
^{181}Hg	$1/2^-$	5 390(280)	15 030(120)	-	-0.111(6){11}	0.515(4)	-	This work
		5 560(200)	14 960(250)	-	-0.114(4){10}	0.5071(7)	-	[2, 4]
^{182}Hg	0^+	33 350(260)	-	-	-0.653(5){48}	-	-	This work
^{183}Hg	$1/2^-$	3 100(260)	15 190(160)	-	-0.065(5){7}	0.521(6)	-	This work
		3 310(100)	15 380(130)	-	-0.069(2){6}	0.524(5)	-	[2, 4]
^{184}Hg	0^+	27 680(270)	-	-	-0.542(6){40}	-	-	This work
^{185}Hg	$1/2^-$	3 350(300)	14 930(340)	-	-0.069(6){7}	0.51(1)	-	This work
		3 710(30)	14 960(70)	-	-0.0764(6){63}	0.509(4)	-	[4]
$^{185}\text{Hg}^m$	$13/2^+$	27 780(190)	-2 286(25)	110(300)	-0.543(4){40}	-1.01(1)	-0.15(41)	This work
		27 770(110)	-2 305(19)	-140(230)	-0.543(2){42}	-1.017(9)	0.20(33)	[4]

^a Results of both optional ground-state spin assignments $I = 7/2$ and $I = 9/2$ for $^{177, 179}\text{Hg}$ are shown. The literature data for $\delta\langle r^2 \rangle_{198,A}$ in this table are recalculated from the experimental IS [4].

^b Statistical errors are given in parenthesis. Systematic errors stemming from the indeterminacy of the F factor (7%) [4] and M_{SMS} are shown in curly brackets.

^c Corrected in accordance with hyperfine anomaly estimation.

The isotope shift $\delta v^{A,A'}$ between two isotopes of the same isotopic chain with mass A and A' , results from the mass and field shifts noted $\delta v_M^{A,A'}$ and $\delta v_F^{A,A'}$, respectively:

$$\delta v^{A,A'} = \delta v_F^{A,A'} + \delta v_M^{A,A'} = F\lambda^{A,A'} + (M_{\text{NMS}} + M_{\text{SMS}}) \cdot \frac{A - A'}{AA'}. \quad (2)$$

The mass shift is described as the sum of the so-called normal and specific (NMS and SMS) mass shifts, where the NMS is related to the ratio of the electron and proton masses m_e and m_p and to the transition frequency ν as

$$M_{\text{NMS}} = \frac{\nu}{(m_p / m_e)}. \quad (3)$$

The field shift is proportional to an electronic F factor and nuclear parameter $\lambda^{A, A'}$, related to the change in nuclear mean-square charge radius between the two isotopes as

$$\lambda^{A, A'} = K \delta \langle r^2 \rangle^{A, A'}, \quad (4)$$

where $\lambda^{A, A'}$ takes into account the influence of the higher-order radial moments. It was shown [40] that the difference between λ and $\delta \langle r^2 \rangle$ can be accounted for by the single correction factor $K(Z)$. The F and M factors used, as well as the higher radial moments correction $K(Z)$, were taken from Ref. [41], resulting from a combined analysis of data from optical spectroscopy, muonic atoms, and elastic electron scattering. The used values are $F = -53(4)$ GHz/fm², $M_{\text{SMS}} = (0 \pm 0.5) M_{\text{NMS}}$ and $K(Z) = 0.927$.

The magnetic moments, μ , of the discussed mercury isotopes were calculated using the relation

$$\mu_A = \mu_{A_0} \cdot \frac{I_A}{I_{A_0}} \cdot \frac{a_A}{a_{A_0}} \cdot (1 + {}^{A_0}\Delta^A), \quad (5)$$

where we use ${}^{199}\text{Hg}^m$ as a reference ($A_0 = 199$, $\mu_{A_0} = -1.0147(8) \mu_N$ [42], $a_{A_0} = -2298.3(2)$ MHz [43]). The hyperfine anomaly is defined as

$${}^1\Delta^2 = \frac{a_1}{g_{I,1}} \cdot \frac{g_{I,2}}{a_2} - 1, \quad (6)$$

where g_I is the nuclear g factor and the indices 1 and 2 refer to two different isotopes. The hyperfine anomaly arises from the differences in charge and magnetization distribution within the nucleus, through the ‘‘Breit–Rosenthal’’ (BR) [44] and ‘‘Bohr–Weisskopf’’ (BW) [45, 46] effects, respectively.

We applied the Moskowitz–Lombardi (ML) [47–50] rule to estimate the BW correction for the magnetic moments of ${}^{177, 179}\text{Hg}$, taking into account the description of the experimental hyperfine anomaly by this rule for the variety of neutron single-particle states in mercury nuclei with the mass spanning a rather large range. For previously measured isotopes and isomers the maximal deviation of the experimental ${}^{199}\Delta^A$ from the ML calculation is equal to $2.5 \cdot 10^{-3}$. We conservatively estimated the error of ML prediction for the hyperfine anomaly in ${}^{177, 179}\text{Hg}$ as $5 \cdot 10^{-3}$. The BR correction was estimated by scaling the calculated ${}^{199}\Delta_{\text{BR}}^{201}$ [49, 51]. The uncertainty of this correction was estimated to be 10%. These corrections are taken into account in the Table.

The spectroscopic quadrupole moments were calculated using the relation

$$Q_{s, A} = \frac{b_A}{b_{\text{ref}}} Q_{s, \text{ref}} \quad (7)$$

with the reference values for ${}^{201}\text{Hg}$: $Q_{s, \text{ref}} = 0.387(6)$ b, $b_{\text{ref}} = -280.107(5)$ MHz taken from Refs. [52] and [53], respectively. The resulting spectroscopic quadrupole moments are shown in the Table.

4. Discussion

The change in the nuclear mean-square charge radius, $\delta \langle r^2 \rangle$, for lead [54–58] and mercury (Ref. [4] and this work) isotopes are plotted with respect to $N = 126$ at the top of Fig. 2. Three distinctly different regions are observed in the mercury charge radii. Mercury isotopes with $N > 105$ follow a smooth trend, identical to the one of the isotopic chain of lead. At $100 < N < 106$, in the neutron midshell region between the closed

shells at $N = 82$ and $N = 126$, a large shape staggering is observed. Here, ground-state radii of the odd- A mercury isotopes deviate substantially from the trend of the lead isotopes, which were found to keep their near-spherical shape at and beyond the neutron midshell [56, 57]. See also Fig. 2b, where the difference in $\delta\langle r^2 \rangle$ between mercury and lead isotones is shown. From the data obtained in the present work, it is observed that the staggering stops at ^{180}Hg and $\delta\langle r^2 \rangle$ for mercury isotopes returns to the trend of lead. In-beam recoil-decay tagging measurements [10–12, 59–61] showed that the band-head energies of strongly prolate deformed intruder bands in even- A isotopes increase rapidly for mercury isotopes with decreasing neutron number at $N < 101$.

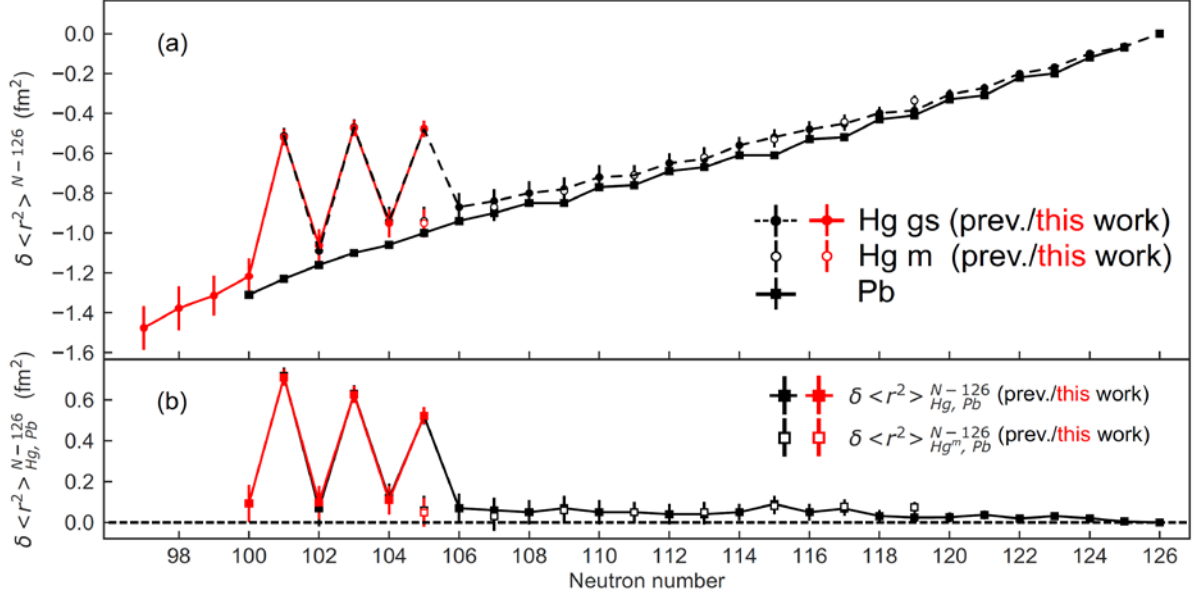


Fig. 2. Comparison of the change in mean-square charge radius for mercury and lead isotopic chains as a function of neutron number N , using $N = 126$ as a reference (a). Difference between the mercury and lead changes in charge radii; data points shown in red and black correspond to this work and previous work, respectively (Ref. [58] for lead and Ref. [4] for mercury) (b)

The in-beam studies by Kondev *et al.* [60] and ^{181}Pb α -decay analysis by Jenkins *et al.* [16] have shown that a pronounced structural change takes place when moving from $^{181, 183}\text{Hg}$ to ^{179}Hg . Based on their decay scheme deduced in Ref. [60], the authors proposed that the ground state of ^{179}Hg is near spherical with a possible weak prolate deformation rather than a strong prolate deformation. A similar interpretation was proposed for lighter odd- A mercury isotopes with $A = 173$ – 177 [12, 13, 62]. While those different studies had shown some indications of the shape of the ground state, our data provide a direct measurement of the ground-state charge-radii changes. The return of the lightest mercury nuclei to the trend of the weakly deformed mercury isotopes with $N > 105$ (and to the near-spherical trend in lead nuclei) delineates the region of shape staggering to near the neutron midshell region at $100 < N < 106$.

The ground-state spin and parity of ^{179}Hg was previously assigned $I^\pi = (7/2^-)$, based on experimental data obtained for the α decay of ^{183}Pb and subsequent α decays to daughter (^{175}Pt) and granddaughter (^{171}Os) nuclei [11, 16]. The same assignment, $I^\pi = (7/2^-)$, was proposed for the ground state of ^{177}Hg , based on decay properties of the $13/2^+$ isomeric state in this nucleus [12] and α decay of ^{181}Pb [20]. As was indicated in Sec. 3, we also tested $I = 9/2$ as a possible assignment, since the $\nu f_{7/2}$ and $\nu h_{9/2}$ orbitals are assumed to play a dominant role in the negative-parity states around $N = 97, 99$. The quality of fitting is the same for both assumptions. However, the measured large and negative magnetic moments of $^{177, 179}\text{Hg}$ rule out a $\nu h_{9/2}$ hole configuration, as this is expected to give a large positive magnetic moment $\mu_{\text{th}}(\nu h_{9/2}) = +0.69 \mu_N$ [63]. Two plausible origins of the $^{177, 179}\text{Hg}$ spins and magnetic moments are considered: 1) they arise from the strong Coriolis mixing of the Nilsson states of $\nu f_{7/2}$ and $\nu h_{9/2}$ parentage at very low deformation ($\beta_2 \approx 0.05$ – 0.07) or 2) they may be regarded as spherical $\nu f_{7/2}$ -hole states.

Let us first focus on the explanation (a). In Ref. [11], two likely candidates for the ground-state Nilsson configuration of ^{179}Hg were proposed: the $7/2^- [514]$ and $7/2^- [503]$ orbitals, arising from the $\nu h_{9/2}$ and $\nu f_{7/2}$ neutron shell-model states, respectively. These orbitals come close to the Fermi level only for small prolate deformations ($\beta_2 < 0.15$). In ^{175}Pt , the α -decay daughter of ^{179}Hg , the $\nu h_{9/2}$ $7/2^- [514]$ orbital was chosen as preferable for the ground-state band [12]. However, several measured magnetic moments of the $7/2^- [514]$ Nilsson state of deformed $N = 105$ nuclei ($^{183}\text{Pt}^m$, ^{177}Hf , ^{175}Yb) are close to $\mu \approx +0.8 \mu_N$ [64]. Nilsson-model calculations describe these experimental data fairly well [65]. The calculations with the same approach predict positive moments for $^{177, 179}\text{Hg}$ even at rather low deformation [$\mu(7/2^- [514], ^{179}\text{Hg})_{\text{th}} = +0.46 \mu_N$ and $+0.34 \mu_N$ at $\beta_2 = 0.15$ and 0.10 , respectively]. Coriolis mixing might, however, play a role as the lowest states in the lightest mercury isotopes display a high spin at low deformation. At $\beta_2 < 0.15$, contributions of the different Nilsson orbitals stemming from the $\nu f_{7/2}$ and $\nu h_{9/2}$ orbitals to the lowest $7/2^-$ state become nearly equal. This mixing would bring the magnetic moment down in value with respect to a pure $7/2^- [514]$ configuration and might be a possible explanation of the measured magnetic moments of $^{177, 179}\text{Hg}$.

Let us now discuss option b) and explore the interpretation of the ground states of $^{177, 179}\text{Hg}$ as spherical $\nu f_{7/2}$ -hole states. Magnetic moments of $^{177, 179}\text{Hg}$ come comparatively close to the single-particle estimation for spherical neutron shell $\nu f_{7/2}$: $\mu_{\text{s.p.}} = -1.3 \mu_N$ (with the commonly adopted renormalization of the neutron g factors: $g_{\text{eff } s} = 0.6 g_{\text{free } s}$ and $g_{\text{eff } l} = -0.05$). It is instructive to compare the magnetic moments of the presumed $7/2^-$ $^{177, 179}\text{Hg}$ ground states with the measured magnetic moments of the ground states of $N = 83$ isotones with one neutron in the $f_{7/2}$ shell. This comparison is shown in Fig. 3. One can see that $\mu(^{177, 179}\text{Hg})$ corresponds to $\mu(\nu f_{7/2})$ in the $N = 83$ isotones for which all show a rather large negative magnetic moment value. If this interpretation is valid, then the ground states of $^{177, 179}\text{Hg}$ could be regarded as holes in the $\nu f_{7/2}$ orbital within a simple shell-model picture. This means that for the light mercury isotopes, the state arising from a neutron hole in the $\nu f_{7/2}$ orbital lies above that arising from a neutron hole in the $\nu h_{9/2}$ orbital. As a consequence, the state ordering for $Z = 80$ and $N < 100$ is reversed with respect to the $N = 83$ isotones in the vicinity of the stable isotopes, where the $\nu f_{7/2}$ orbital is filled first after the $N = 82$ shell closure. Surprisingly, with the increase of Z after ^{80}Hg , the normal ordering is restored in ^{81}Tl and ^{82}Pb .

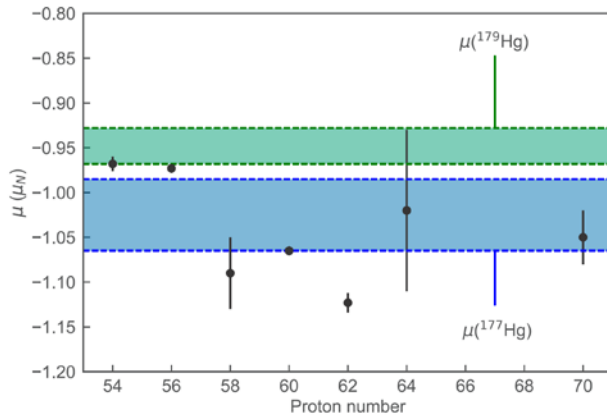


Fig. 3. Comparison of magnetic moments for $N = 83$ isotones, having one neutron in the $(\nu f_{7/2})$ shell above the closed shell $N = 82$, with the measured $\mu(^{177}\text{Hg})$ and $\mu(^{179}\text{Hg})$ indicated by shaded boxes. Data from Refs. [64] and [66] and references therein

The ground-state spin and parity of $^{181}\text{Pb}_{99}$ was determined as $9/2^-$ due to a hole in $\nu h_{9/2}$ shell arising from the complete depletion of the $i_{13/2}$ and $p_{3/2}$ shells lying above the $N = 100$ spherical subshell closure [20]. Similarly, the odd neutron state in $^{180}\text{Tl}_{99}$ was assumed to be a $\nu h_{9/2}$ -hole state on the basis of its magnetic moment value [17, 67]. Thus, for $Z > 80$ the $\nu h_{9/2}$ shell appears to be situated above the $\nu f_{7/2}$ shell. It was shown that the energy differences between the lowest-lying $9/2$ and $7/2$ states for the $N = 83$ and $N = 85$ isotones show a rapid drop above $Z = 64$ (see Ref. [68] and references therein). According to Bianco *et al.* [68], this drop reflects the gradual approach in energy of the $\nu h_{9/2}$ and $\nu f_{7/2}$ neutron single-particle orbitals. The presumed convergence of the $\nu h_{9/2}$ and $\nu f_{7/2}$ neutron levels also provides a natural explanation for the anomalous absence of charged-particle emission from the high-spin isomer of ^{160}Re [69]. This shell evolution was explained in Ref. [68] by the influence of the tensor part of the nucleon–nucleon interaction [70]. It was predicted in Ref. [68] that the energies of the neutron single-particle orbitals may

become inverted for high Z . The interpretation of the $^{177, 179}\text{Hg}$ ground states as $\nu f_{7/2}$ shell-model states and their first excited states as predominantly $\nu h_{9/2}$ states [11, 12] is in agreement with this description.

5. Conclusion

To summarize, we report on an experimental and theoretical study of the neutron-deficient mercury isotopes. By measuring for the first time the IS and HFS of $^{177-180}\text{Hg}$ and validating previous measurements along the chain of heavier mercury isotopes, the end point of shape-staggering in the neutron-deficient direction was found to be at ^{180}Hg . Not only the $\delta\langle r^2 \rangle$ of $^{177-180}\text{Hg}$ but also the magnetic and quadrupole moments of $^{177, 179}\text{Hg}$ support the inference of their small deformation.

References

1. J. Bonn *et al.*, Phys. Lett. B **38**, 308 (1972).
2. J. Bonn *et al.*, Z. Phys. A: At. Nucl. **276**, 203 (1976).
3. T. Kühn, P. Dabkiewicz *et al.*, Phys. Rev. Lett. **39**, 180 (1977).
4. G. Ulm *et al.*, Z. Phys. A: At. Nucl. **325**, 247 (1986).
5. K. Heyde, J. Wood, Rev. Mod. Phys. **83**, 1467 (2011).
6. S. Frauendorf, V.V. Pashkevich, Phys. Lett. B **55**, 365 (1975).
7. N. Bree *et al.*, Phys. Rev. Lett. **112**, 162701 (2014).
8. L.P. Gaffney *et al.*, Phys. Rev. C **89**, 024307 (2014).
9. K. Wrzosek-Lipska *et al.* (Unpublished).
10. R. Julin, K. Helariutta, M. Muikku, J. Phys. G: Nucl. Part. Phys. **27**, R109 (2001).
11. F. Kondev *et al.*, Phys. Lett. B **528**, 221 (2002).
12. A. Melarangi *et al.*, Phys. Rev. C **68**, 041301 (2003).
13. D. O'Donnell *et al.*, Phys. Rev. C **85**, 054315 (2012).
14. S. Schwarz *et al.*, Nucl. Phys. A **693**, 533 (2001).
15. J.D. Cole *et al.*, Phys. Rev. C **30**, 1267 (1984).
16. D.G. Jenkins *et al.*, Phys. Rev. C **66**, 011301 (2002).
17. J. Elseviers *et al.*, Phys. Rev. C **84**, 034307 (2011).
18. J. Sauvage *et al.*, Eur. Phys. J. A **49**, 109 (2013).
19. E. Rapisarda *et al.*, J. Phys. G: Nucl. Part. Phys. **44**, 074001 (2017).
20. A.N. Andreyev *et al.*, Phys. Rev. C **80**, 054322 (2009).
21. A.N. Andreyev *et al.*, J. Phys. G: Nucl. Part. Phys. **37**, 035102 (2010).
22. R. Catherall *et al.*, J. Phys. G: Nucl. Part. Phys. **44**, 094002 (2017).
23. V. Fedosseev *et al.*, J. Phys. G: Nucl. Part. Phys. **44**, 084006 (2017).
24. T. Day Goodacre *et al.*, Nucl. Instrum. Methods B **376**, 39 (2016).
25. B.A. Marsh *et al.*, Nucl. Instrum. Methods Phys. Res., Sect. B **317**, 550 (2013).
26. A.N. Andreyev *et al.*, Phys. Rev. Lett. **105**, 252502 (2010).
27. M.D. Seliverstov *et al.*, Phys. Rev. C **89**, 034323 (2014).
28. J.G. Cubiss *et al.*, Phys. Rev. C **97**, 054327 (2018).
29. S. Kreim *et al.*, Nucl. Instrum. Methods B **317**, 492 (2013).
30. B. Lommel *et al.*, Nucl. Instrum. Methods A **480**, 199 (2002).
31. R.N. Wolf *et al.*, Int. J. Mass Spectrom. **349**, 123 (2013).
32. F. Herfurth *et al.*, Nucl. Instrum. Methods A **469**, 254 (2001).
33. B. Marsh *et al.*, Nat. Phys. **14**, 1163 (2018).
34. T. Day Goodacre *et al.* (Private Communication).
35. T. Day Goodacre *et al.*, Hyperfine Interact. **238**, 41 (2017).
36. J. Bonn *et al.*, Z. Phys. A: At. Nucl. **272**, 375 (1975).
37. E.W. Otten, in *Treatise on Heavy Ion Science* **8**, 517–638 (1989).
38. W. Gins *et al.*, Comput. Phys. Commun. **222**, 286 (2018).
39. R. Brun, F. Rademakers, Nucl. Instrum. Methods A **389**, 81 (1997).

40. G. Torbohm, B. Fricke, A. Rosén, Phys. Rev. A **31**, 2038 (1985).
41. B. Fricke, K. Heilig, in *Nuclear Charge Radii*, 1–9 (2004).
42. R.J. Reimann, M.N. McDermott, Phys. Rev. C **7**, 2065 (1973).
43. O. Redi, H.H. Stroke, Phys. Rev. A **2**, 1135 (1970).
44. J.E. Rosenthal, G. Breit, Phys. Rev. **41**, 459 (1932).
45. A. Bohr, V.F. Weisskopf, Phys. Rev. **77**, 94 (1950).
46. A. Bohr, Phys. Rev. **81**, 331 (1951).
47. J. Persson, At. Data Nucl. Data Tables **99**, 62 (2013).
48. P. Moskowitz, M. Lombardi, Phys. Lett. B **46**, 334 (1973).
49. H.J. Rosenberg, H.H. Stroke, Phys. Rev. A **5**, 1992 (1972).
50. T. Fujita, A. Arima, Nucl. Phys. A **254**, 513 (1975).
51. A. Mårtensson-Pendrill, Phys. Rev. Lett. **74**, 2184 (1995).
52. J. Bieron *et al.*, Phys. Rev. A **71**, 012502 (2005).
53. R.H. Kohler, Phys. Rev. **121**, 1104 (1961).
54. M. Anselment *et al.*, Nucl. Phys. A **451**, 471 (1986).
55. S.B. Dutta *et al.*, Z. Phys. A: At. Nucl. **341**, 39 (1991).
56. H. De Witte *et al.*, Phys. Rev. Lett. **98**, 112502 (2007).
57. M.D. Seliverstov *et al.*, Eur. Phys. J. A **41**, 315 (2009).
58. I. Angeli, K. Marinova, At. Data Nucl. Data Tables **99**, 69 (2013).
59. M.P. Carpenter *et al.*, Phys. Rev. Lett. **78**, 3650 (1997).
60. F.G. Kondev *et al.*, Phys. Rev. C **62**, 044305 (2000).
61. F.G. Kondev *et al.*, Nucl. Phys. A **682**, 487 (2001).
62. D. O'Donnell *et al.*, Phys. Rev. C **79**, 051304 (2009).
63. R. Bauer *et al.*, Nucl. Phys. A **209**, 535 (1973).
64. N. Stone, At. Data Nucl. Data Tables **90**, 75 (2005).
65. C. Ekström, H. Rubinsztein, P. Möller, Phys. Scr. **14**, 199 (1976).
66. A.E. Barzakh *et al.*, AIP Conf. Proc. **610**, 915 (2002).
67. A.E. Barzakh *et al.*, Phys. Rev. C **95**, 014324 (2017).
68. L. Bianco *et al.*, Phys. Lett. B **690**, 15 (2010).
69. I. Darby *et al.*, Phys. Lett. B **695**, 78 (2011).
70. T. Otsuka, T. Matsuo, D. Abe, Phys. Rev. Lett. **97**, 162501 (2006).

SHELL EFFECT AND ODD-EVEN STAGGERING IN CHARGE RADII AROUND THE $N = 126$ SHELL CLOSURE

PNPI participants of the IS598 Collaboration:

A.E. Barzakh, D.V. Fedorov, P.L. Molkanov, V.N. Pantelev, M.D. Seliverstov

The kink in the relative mean square charge radii ($\delta\langle r^2 \rangle$) at the $N = 126$ shell closure (the so called shell effect in radii) has long been considered as a benchmark for testing theoretical calculations. Standard nonrelativistic mean field approaches were incapable of reproducing the kink at ^{208}Pb [1], while, conversely, relativistic mean field approaches were demonstrated to be successful in this [2].

Traditionally, the lead isotopic chain was employed in testing different theoretical models. New experimental results for the mercury isotopic chain reported in the present work, offer the opportunity to broaden this benchmark. This work also employs these new results, together with the existing lead data, to compare relativistic Hartree–Bogoliubov (RHB) and nonrelativistic Hartree–Fock–Bogoliubov (NR–HFB) approaches in description of the shell effect in radii.

Mercury isotopes were produced at the CERN–ISOLDE facility [3] by impinging a 1.4-GeV proton beam from the proton synchrotron booster onto a molten-lead target. The neutral reaction products effused into the anode cavity of the new modification of the ion source, versatile arc discharge and laser ion source (VADLIS) [4]. Laser light from the ISOLDE resonance ionization laser ion source (RILIS) complex [5] was used to excite three sequential atomic transitions for the resonance ionization of the mercury isotopes [6]. The photo ions were extracted and mass separated by the ISOLDE general-purpose separator and then directed to either a Faraday cup for direct photo ion detection or to the ISOLTRAP Paul trap [7] and multireflection time-of-flight mass spectrometer (MR–ToF MS) [8] for single-ion counting and discrimination from isobaric contamination.

The first of the three atomic transitions ($5d^{10}6s^2\ ^1S_0 \rightarrow 5d^{10}6s6p\ ^3P_1$, 253.65 nm) was probed by scanning a frequency-tripled titanium-sapphire laser (full-width-at-half-maximum bandwidth of less than 1 GHz before tripling) [9]. Isotope shifts (IS) in the frequency of this transition were measured for mercury nuclei with $A = 202, 203, 206, 207$ and 208 relative to the stable reference isotope with $A_0 = 198$. Sample spectra are presented in Fig. 1. Details of the scanning and fitting procedures can be found in Refs. [10, 11] and [10, 12], respectively, with further information on the data analysis in Ref. [13]. The relative changes in the mean-square charge radius, magnetic (μ) and quadrupole (Q) moments of the studied nuclei were derived from the experimental data by applying standard methods. The results are presented in Fig. 2 and in the Table, together with literature data ($^{202, 203, 206}\text{Hg}$) for comparison.

The nuclear spin of ^{207}Hg could not be determined unambiguously because the spectroscopic transition is between the atomic states with electronic spins $J = 0$ and $J = 1$. $I^\pi = 9/2^+$ was assumed for the analysis of the ^{207}Hg measurements based on [14]. The extracted isotope shifts for $^{202, 203}\text{Hg}$ are in good agreement with literature. The same is true for the neutron deficient isotopes that were remeasured during this experimental campaign [15]. The general agreement of the extracted $\delta_{V_A, 198}$ and hyperfine a and b factors with the previously published literature values further validates the method of the in-source resonance ionization spectroscopy with a VADLIS ion source.

The characteristic kink in the charge radii at the $N = 126$ neutron shell closure has been revealed, along with the odd-even staggering (OES), where an odd- N isotope has a smaller charge radius than the average of its two even- N neighbours (see Fig. 2).

The analysis of the magnetic moments (μ) for the nuclei with $N = 127$ [$\mu(^{207}\text{Hg})$ included] demonstrated that their Z -dependence is determined by the particle–quadrupole–vibration coupling mechanism. In the second order of perturbation theory the g -factor, $g = \mu/I$, correction due to particle–vibration coupling (PVC) is proportional to the inverse square of the energy of the lowest vibrational 2^+ state in the even-even nucleus with the same proton number, $E(2^+)^{-2}$. The agreement of the $g(vg_{9/2})$ and the $E(2^+)^{-2}$ evolution with Z (Fig. 3) supports the interpretation of the mechanism behind the variation in the g factors of the $N = 127$ isotones.

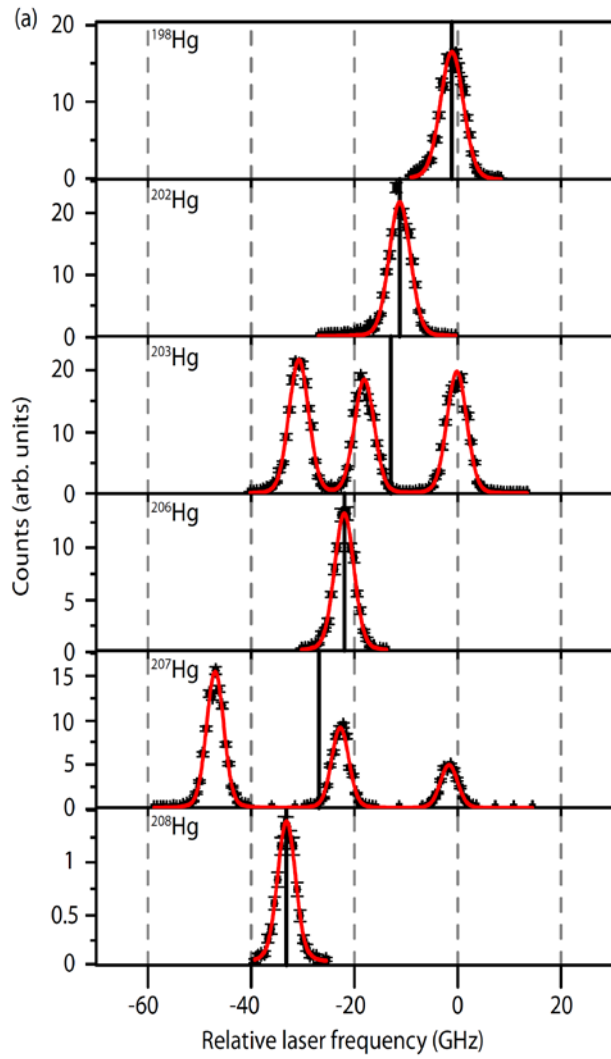


Fig. 1. Hyperfine structure spectra of the measured isotopes; the centroids are indicated with *solid black lines*

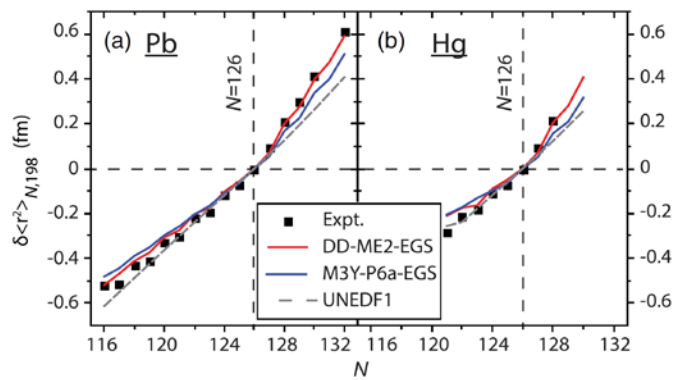


Fig. 2. Panels (a) and (b) show $\delta\langle r^2 \rangle$ of lead and mercury isotopes relative to ^{208}Pb and ^{206}Hg ($N = 126$), respectively. *Squares* – experimental data. Description of theoretical approaches (shown as *lines*) see in text

Table

Extracted isotope shifts in the 254-nm line with respect to ^{198}Hg , hyperfine a and b factors of the $5d^{10}6s6p\ ^3P_1$ state, and literature values recalculated from the compilations of Refs. [16, 17]*

A	I^π	$\delta v_{A, 198}$, MHz	a , MHz	b , MHz	$\delta \langle r^2 \rangle_{A, 198}$, fm ²	$\mu(\mu_N)$	$Qs(b)$	Reference
202	0	-10 100(180)	–	–	0.197(3){14}	–	–	This work
	–	-10 102.4(4.2)	–	–	–	–	–	[16]
203	$5/2^-$	-11 870(200)	5 070(90)	-20(250)	0.232(5){17}	0.843(15)	0.03(35)	This work
		-11 750(180)	4 991.33(4)	-249.2(3)	0.2296(35){180}	0.8300(7)	0.40(4)	[16, 17]
206	0	-20 930(160)	–	0.409(3){30}	–	–	–	This work
	–	-20 420(80)	–	0.3987(16){308}	–	–	–	[16]
207	$9/2^+$	-25 790(190)	-4 500(60)	530(250)	0.503(4){38}	-1.373(20)	-0.73(37)	This work
208	0	-32 030(160)	–	–	0.625(3){47}	–	–	This work

* The spin assignment of ^{207}Hg is discussed in the text. Statistical uncertainties are listed in parentheses and the systematic uncertainties related to F and M are listed in curly brackets.

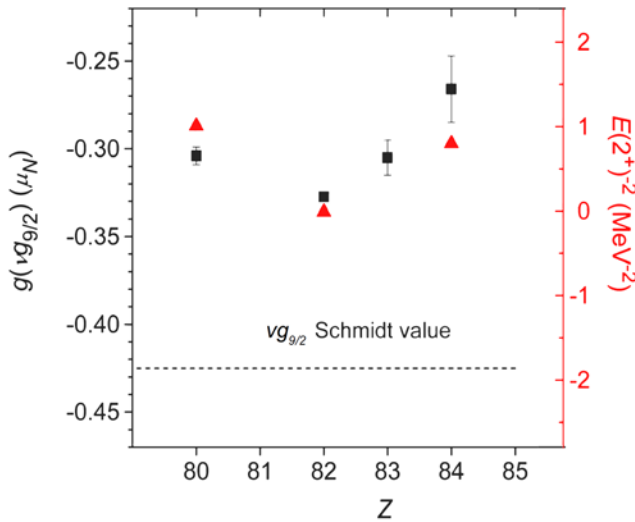


Fig. 3. g -factors of isotones at $N = 127$: squares – experimental values of g -factors; dashed line – the Schmidt value for $vg_{9/2}$ shell; triangles – $E(2^+)^{-2}$ (see the corresponding scale on the right-hand side of the figure)

The analysis of the magnetic moments (μ) for the nuclei with $N = 127$ [$\mu(^{207}\text{Hg})$ included] demonstrated that their Z -dependence is determined by the particle–quadrupole–vibration coupling mechanism. In the second order of perturbation theory the g -factor, $g = \mu/I$, correction due to PVC is proportional to the inverse square of the energy of the lowest vibrational 2^+ state in the even-even nucleus with the same proton number, $E(2^+)^{-2}$. The agreement of the $g(vg_{9/2})$ and the $E(2^+)^{-2}$ evolution with Z (see Fig. 3) supports the interpretation of the mechanism behind the variation in the g factors of the $N = 127$ isotones.

Special indicators are commonly used to facilitate the quantitative comparison of the experimental results with those from theoretical calculations. The first is the three-point indicator

$$\Delta \langle r^2 \rangle^{(3)}(N) = \frac{1}{2} \left[\langle r^2 \rangle(N-1) + \langle r^2 \rangle(N+1) - 2 \langle r^2 \rangle(N) \right],$$

which quantifies OES in charge radii. OES is absent when $\Delta \langle r^2 \rangle^{(3)}(N) = 0$. To quantify the shell effect at $N = 126$, a special kink indicator was used:

$$\Delta R^{(3)}(A) = 0.5 \cdot [R(A+2) + R(A-2)] - R(A),$$

where $R(A) = \langle r^2 \rangle^{1/2}(A)$ is the charge radius of the isotope with mass A of the element under consideration. The shell effect is absent when $\Delta R^{(3)}(A) = 0$.

To interpret the data, a new RHB code was developed, which enables the blocking of selected single-particle orbitals and allows for fully self-consistent calculations of the ground and excited states in odd- A nuclei. A separable version of the Gogny pairing was used [18], with the pairing strength of Ref. [19]. The NL3*, DD-PC1, DD-ME2 and DD-ME δ (see Ref. [19]) covariant energy density functionals (CEDF) were employed, the global performance of which was tested in Ref. [19]. The functionals achieved a comparable description of the kink and the OES; thus, only the DD-ME2 results are discussed below.

The NR-HFB calculations were performed assuming spherical symmetry with the semirealistic M3Y-P6a interaction, the spin-orbit properties of which were modified [20] to improve the description of the charge radii of proton-magic nuclei [20, 21]. Here for the first time, we apply it to the mercury isotopic chain. We consider only spherical nuclei, *i. e.*, nuclei for which $\langle\beta^2\rangle^{1/2} < 0.1$ where $\langle\beta^2\rangle^{1/2}$ is the mean-square deformation deduced from experimental $\delta\langle r^2\rangle$ using the droplet model. This restriction corresponds to $N > 116$ and $N > 121$ for lead and mercury isotopes, respectively.

Two different procedures labeled as “LES” and “EGS” are used for the blocking in odd- A nuclei, and the results of the respective calculations are labeled by the “Functional-Procedure” labels (for example, DD-ME2-EGS). In the LES procedure, the lowest in energy configuration is used, which is similar to all earlier calculations of OES. In the EGS procedure, the configuration with the spin and parity of the blocked state corresponding to those of the experimental ground state is employed, although it is not necessarily the lowest in energy. For example, in the RHB (DD-ME2) calculations, the EGS configurations with a blocked $\nu 2g_{9/2}$ state are located at excitation energies of 137, 122 and 96 keV above the ground-state configurations with a blocked $\nu 1i_{11/2}$ state in $^{209,211,213}\text{Pb}$. At first glance, this contradicts experimental findings that the ground state is based on the $\nu 2g_{9/2}$ orbital in odd- A lead isotopes with $N > 126$. However, PVC lowers the energy of this state below that of the $\nu 1i_{11/2}$ one (see Fig. 5 in Ref. [22]) so that it becomes the lowest in energy in the PVC calculations. Note that PVC significantly improves the accuracy of the description of the energies of experimental states in model calculations [22, 23]. However, it is neglected in the present study since its impact on charge radii is still an open theoretical question.

The results of the RHB and NR-HFB calculations are presented in Fig. 2, together with the experimental results for the lead and mercury chains. In both cases, the kink at $N = 126$ is visibly better reproduced in the RHB (DDME2) calculations.

In Figure 4, we present the values of the kink and OES indicators calculated from the experimental results and theoretical calculations for both lead and mercury. It is evident in Figs. 4a and 4b that the magnitudes of the kinks in the isotopic chains are comparable, suggesting that the kink at $N = 126$ is broadly insensitive to the change of the occupied proton states when crossing $Z = 82$. Evidently, the RHB (DD-ME2) calculations best reproduce the kink, while the NR-HFB (M3Y-P6a) and NR-HFB (Fy(Δr)) [24] results underestimate and overestimate its magnitude, respectively.

In both approaches (DD-ME2 and M3Y-P6a), the OES is best reproduced if the EGS procedure is applied (see Figs. 4c, 4d and 5). If the LES procedure is applied, the experimental OES is significantly underestimated for all nuclei under study in the RHB calculations and for $N < 126$ nuclei in the NR-HFB calculations. Note that, for simplicity, we show only NR-HFB results with both procedures in Figs. 4c and 3d. For a better understanding of the underlying mechanisms of both the kink and OES, we also performed RHB calculations without pairing for lead isotopes. The labels identifying such results contain “np.” Significantly, a kink is still present in the results as depicted in Fig. 4a due to the occupation of the $\nu 1i_{11/2}$ orbital. This indicates an alternative mechanism to the one based on gradient terms in pairing interactions [24]. The RHB results with and without pairing are compared in Fig. 5. OES appears in these calculations (the curves labeled as “DD-ME2-EGS” and “DD-ME2-np-EGS”) under the condition that, in odd- A nuclei, the EGS procedure is used. One can see that the inclusion of pairing somewhat reduces this effect. However, OES is mostly absent if the LES procedure is used in odd- A nuclei.

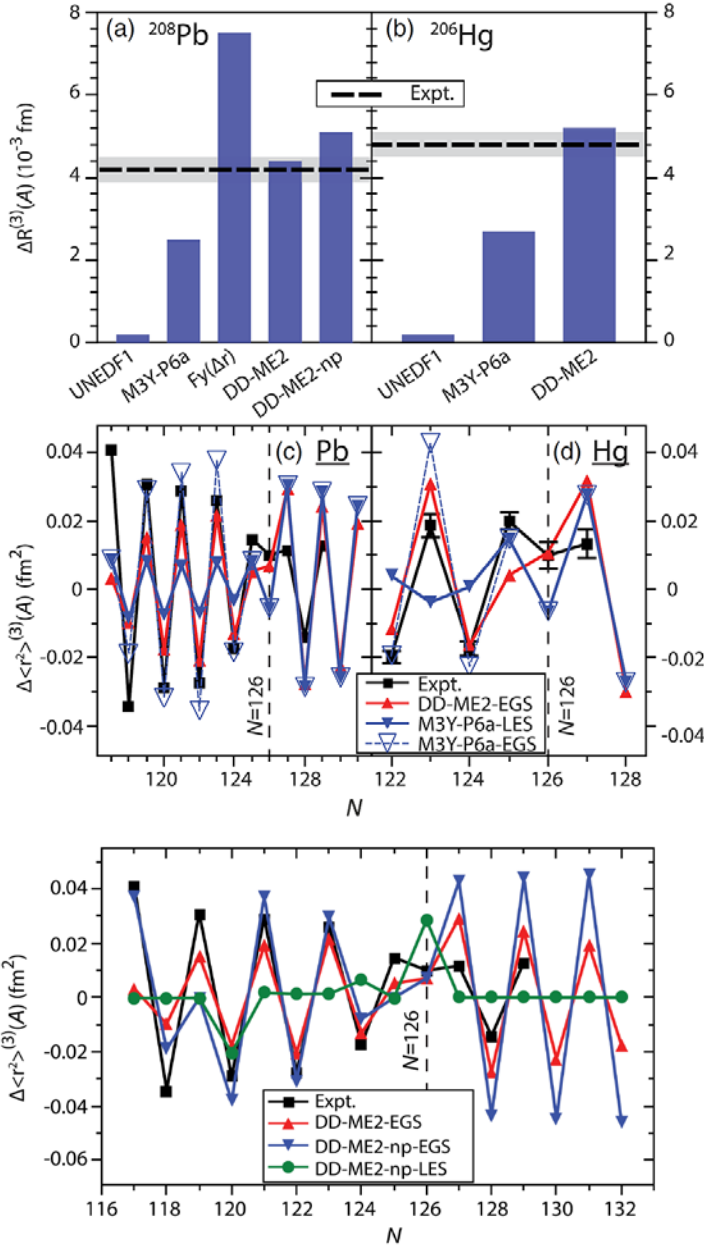


Fig. 4. Comparison of experimental and theoretical $\Delta R^{(3)}(A)$ and $\Delta \langle r^2 \rangle^{(3)}(A)$ values for isotopes of lead (a) and (c), respectively and mercury (b) and (d), respectively. Experimental values are shown as *squares*. The NR-HFB results with Fy(Δr) are taken from Ref. [8]. The description of theoretical results (shown by *lines*) are given in text

Fig. 5. Comparison of experimental and theoretical $\Delta \langle r^2 \rangle^{(3)}(A)$ values for lead isotopes. Experimental data are from Ref. [25]; theoretical results are from this work. See text for details

Let us consider the lead isotopes with $N \geq 126$ for a more detailed discussion of the origin of OES in the calculations without pairing. By designating the ground state of ^{208}Pb as a “core” and noting that PVC lowers the energy of the $\nu 2g_{9/2}$ state below $\nu 1i_{11/2}$ in odd- A nuclei [22], the sequence of the ground states in the $N \geq 126$ nuclei can be described as core (^{208}Pb), core $\times \nu(2g_{9/2})^1$ (^{209}Pb), core $\times \nu(2i_{11/2})^2$ (^{210}Pb), core $\times \nu(2i_{11/2})^2 (2g_{9/2})^1$ (^{211}Pb), and so on in the relativistic calculations without pairing. The $\nu 1i_{11/2}$ orbital has a smaller rms radius than the $\nu 2g_{9/2}$ orbital. However, because of the isovector nature of nuclear forces, its occupation leads to a larger charge radius as compared with the occupation of the $\nu 2g_{9/2}$ orbital. Thus, the staggering in their occupation between odd and even isotopes results in the OES seen in Fig. 5. On the contrary, in the majority of conventional nonrelativistic functionals, the $\nu 2g_{9/2}$ orbital is lower in energy than the $\nu 1i_{11/2}$ orbital. This is in agreement with experimental data on the structure of the ground states in odd-mass nuclei, but it creates a problem in the description of the kinks. In addition, in calculations with and without pairing, this leads to the sole or predominant occupation of the $\nu 2g_{9/2}$ state in even-even and odd-even nuclei with $N > 126$ and thus to a negligible or comparatively small OES. To address this, several prescriptions have been suggested over

the years to increase the occupation of the $\nu 1i_{11/2}$ orbital in the $N > 126$ lead nuclei. One approach includes a modification of the spin-orbit interaction, leading either to the inversion of the relative energies of these two states or to their proximity in energy. The NR–HFB results with M3Y–P6a shown in Figs. 2 and 3 are also based on a modification of the spin-orbit interaction, with the inclusion of a density-dependent term in the spin-orbit channel. Alternatively, the so-called Fayans functionals employ a specific form of the pairing interaction containing a gradient term [24]. Although this improves the general description of experimental data, discrepancies between theory and experiment still exist in the lead and tin isotopic chains [24]. Moreover, pairing becomes a dominant contributor to the kink and OES [24]. The present RHB interpretation of the kinks and OES differs from that suggested in Ref. [24], which is based on nonrelativistic Skyrme and Fayans functionals. In the RHB approach, the kink and OES are already present in the calculations without pairing. Thus, the evolution of charge radii with neutron number depends significantly on the mean-field properties. Pairing acts only as an additional tool that mixes different configurations and somewhat softens the evolution of charge radii as a function of the number of neutrons.

In conclusion, the determination of the $\delta\langle r^2 \rangle$ of $^{207,208}\text{Hg}$ has revealed a kink at $N = 126$ in the mercury nuclear charge radii systematics, with a magnitude comparable to that in the lead isotopic chain. These new data have been analysed *via* both RHB and NR–HFB approaches, together with the traditional magic- Z theoretical benchmark of the lead isotopic chain. We demonstrate that the kinks at the $N = 126$ shell closure and the OES in the vicinity are currently best described in the RHB approach without any readjustment of the parameters defined in Ref. [25]. According to the RHB calculations, the kink at $N = 126$ in $\delta\langle r^2 \rangle$ originates from the occupation of the $\nu 1i_{11/2}$ orbital located above the $N = 126$ shell gap. A new mechanism for OES is suggested, related to the staggering in the occupation of neutron orbitals between odd and even isotopes and facilitated by PVC in odd-mass nuclei. It is shown that pairing does not play an important role in the origin of OES and kink at $N = 126$. Thus, contrary to previous interpretations, it is determined that both the kink and OES in charge radii can be defined predominantly in the particle-hole channel.

References

1. R.C. Thompson, A. Hanser, K. Bekk *et al.*, *Z. Phys. A* **305**, 89 (1982).
2. M. Sharma, G. Lalazissis, P. Ring, *Phys. Lett. B* **317**, 9 (1993).
3. R. Catherall *et al.*, *J. Phys. G* **44**, 094002 (2017).
4. T.D. Goodacre *et al.*, *Nucl. Instrum. Methods Phys. Res., Sect. B* **376**, 39 (2016).
5. V. Fedosseev *et al.*, *J. Phys. G* **44**, 084006 (2017).
6. T.D. Goodacre *et al.*, *Nucl. Instrum. Methods Phys. Res., Sect. A* **830**, 510 (2016).
7. F. Herfurth *et al.*, *Nucl. Instrum. Methods Phys. Res., Sect. A* **469**, 254 (2001).
8. R.N. Wolf *et al.*, *Int. J. Mass Spectrom.* **123**, 349 (2013).
9. S. Rothe *et al.*, *Nucl. Instrum. Methods Phys. Res., Sect. B* **317**, 561 (2013).
10. S. Sels *et al.*, *Phys. Rev. C* **99**, 044306 (2019).
11. R.E. Rossel, A Distributed Monitoring and Control System for the laser Ion Source RILIS at CERN–ISOLDE: M. Sc. Thesis (2015).
12. M.D. Seliverstov *et al.*, *Phys. Rev. C* **89**, 034323 (2014).
13. T.D. Goodacre, Developments of the ISOLDE RILIS for Radioactive Ion Beam Production and the Results of Their Application in the Study of Exotic Mercury Isotopes: Ph. D. Thesis (2016). <https://cds.cern.ch/record/2254839>
14. T.L. Tang *et al.*, *Phys. Rev. Lett.* **124**, 062502 (2020).
15. B.A. Marsh *et al.*, *Nat. Phys.* **14**, 1163 (2018).
16. G. Ulm *et al.*, *Z. Phys. A* **325**, 247 (1986).
17. J. Bonn, G. Huber, H.J. Kluge, E.W. Otten, *Z. Phys. A* **276**, 203 (1976).
18. Y. Tian, Z.Y. Ma, P. Ring, *Phys. Lett. B* **676**, 44 (2009).
19. S.E. Agbemava, A.V. Afanasjev, D. Ray, P. Ring, *Phys. Rev. C* **89**, 054320 (2014).
20. H. Nakada, *Phys. Rev. C* **92**, 044307 (2015).
21. H. Nakada, T. Inakura, *Phys. Rev. C* **91**, 021302(R) (2015).

22. E.V. Litvinova, A.V. Afanasjev, Phys. Rev. C **84**, 014305 (2011).
23. A.V. Afanasjev, E. Litvinova, Phys. Rev. C **92**, 044317 (2015).
24. C. Gorges *et al.*, Phys. Rev. Lett. **122**, 192502 (2019).
25. M. Anselment *et al.*, Nucl. Phys. A **451**, 471 (1986).

HYPERFINE ANOMALY IN GOLD AND MAGNETIC MOMENTS OF $I^\pi = 11/2^-$ GOLD ISOMERS

PNPI participants of the IS534 Collaboration:

A.E. Barzakh, D.V. Fedorov, P.L. Molkanov, V.N. Pantelev, M.D. Seliverstov, Yu.A. Demidov, M.G. Kozlov

The magnetic dipole moment μ_A for a nucleus of mass number A and with a spin I can be calculated using the following expression:

$$\mu_A = \mu_{\text{ref}} \frac{I_A a_A}{I_{\text{ref}} a_{\text{ref}}}, \quad (1)$$

where a is a magnetic hyperfine constant and the subscript “ref” denotes a reference isotope with known μ and a values. However, Eq. (1) is based on a point-like approximation for the charge and magnetization in the nucleus. The finite size of the nucleus leads to a deviation of the hyperfine constant from the point-like value a_{pt} . Correspondingly, two parameters δ and ε were introduced to account for the charge and magnetization distribution within the finite-size nucleus. They are called the “Breit–Rosenthal” (BR) hyperfine anomaly (HFA) [1, 2] and “Bohr–Weisskopf” (BW) HFA [3], respectively. To account for these two effects, the hyperfine constant a should be expressed as

$$a = a_{\text{pt}}(1 + \delta)(1 + \varepsilon), \quad (2)$$

where δ and ε are small compared to unity. These corrections are isotope dependent and can be experimentally observed as small deviations of the a -factor ratios between different isotopes from the ratios of their magnetic moments. This deviation, known as a relative hyperfine anomaly (RHFA), is given by

$$\text{ref} \Delta^A \equiv \frac{a_{\text{ref}} I_{\text{ref}} \mu_A}{a_A I_A \mu_{\text{ref}}} - 1 = \text{ref} \Delta_{\text{BW}}^A + \text{ref} \Delta_{\text{BR}}^A \approx (\varepsilon_{\text{ref}} - \varepsilon_A) + (\delta_{\text{ref}} - \delta_A). \quad (3)$$

For heavy atoms Δ_{BR} is expected to be negligible compared to Δ_{BW} (${}^A \Delta_{\text{BR}}^{A+2} \approx 10^{-4}$ in the gold region [4], whereas in all cases relevant to the present work $\Delta_{\text{BW}} > 10^{-2}$; see below). Accordingly, in the following discussion we will ignore the BR contribution to the RHFA. Equation (1) needs to be modified to account for the finite size of the nucleus:

$$\mu_A = \mu_{\text{ref}} \frac{I_A a_A}{I_{\text{ref}} a_{\text{ref}}} (1 + \text{ref} \Delta^A) \approx \mu_{\text{ref}} \frac{I_A a_A}{I_{\text{ref}} a_{\text{ref}}} (1 + \varepsilon_{\text{ref}} - \varepsilon_A). \quad (4)$$

To determine the RHFA from Eq. (3) one should have independent values for the nuclear magnetic moments μ and a constants of the pair of isotopes under study, measured with high precision. Therefore, the available RHFA data are restricted mainly to stable and long-lived nuclei [5]. The lack of systematic experimental data for RHFA far from stability hampers the development of a theoretical analysis of this important nuclear observable, which is sensitive to the nuclear configuration [6]. One of the aims of the present study is to extend our knowledge of RHFA to short-lived isotopes, by the application of the method proposed in Refs. [7, 8] in combination with advanced atomic calculations.

Experimentally measured RHFA values are usually within the range of 10^{-2} – 10^{-4} [5]. For short-lived nuclei, $\text{ref} \Delta^A$ in Eq. (4) is typically neglected and the uncertainty of the extracted magnetic moments is increased by $\sim 1\%$. In most cases this approach is acceptable in view of the experimental uncertainties and nuclear physics inferences. However, there is a marked exception in gold isotopes, where ${}^{197}\Delta^{198} = 8.53(8)\%$ was reported in Ref. [9]. Such a large anomaly demands the estimation of the RHFA to obtain reliable magnetic moment values for gold isotopes far from stability. In the present work, we have deduced the magnetic moment values by Eq. (4) owing to the determination of the RHFA for the gold isotopes in question. The investigation presented in this paper is part of an experimental campaign at the ISOLDE facility (CERN) aimed at nuclear decay- and laser-spectroscopy studies of the neutron deficient gold isotopes. Partial results for ${}^{177, 179}\text{Au}$ were reported in Ref. [10]. In the present work we report the study of the hyperfine structure of the $I^\pi = 11/2^-$ isomers in the ${}^{177, 191, 193, 195}\text{Au}$ isotopes. With the RHFA determined in the present work for the first time, reliable

magnetic moments for the selected gold isomers have been derived. The deduced magnetic moments have enabled us to trace the evolution of the g factor ($g = \mu/I$) for the $\pi h_{11/2}$ orbital from $N = 82$ to $N = 126$.

The hyperfine anomaly reveals itself in the change in the ratio of the magnetic hyperfine structure (hfs) constants for different atomic states with quantum numbers $n_1 l_1$ and $n_2 l_2$. This ratio, $a_{n_1 l_1}^A / a_{n_2 l_2}^A$, depends on the atomic mass number A , because different atomic states differ in sensitivity to the nuclear magnetization distribution. This change can be related to the difference of the corresponding RHFA values by introducing differential HFA (DHFA):

$$\frac{{}^{A_1} \Delta_{n_1 l_1}^{A_2}}{\Delta_{n_2 l_2}^{A_2}} \equiv \frac{(a_{n_1 l_1}^{A_1} / a_{n_2 l_2}^{A_1})}{(a_{n_1 l_1}^{A_2} / a_{n_2 l_2}^{A_2})} - 1 = \frac{1 + {}^{A_1} \Delta^{A_2}(n_1 l_1)}{1 + {}^{A_1} \Delta^{A_2}(n_2 l_2)} - 1 \approx {}^{A_1} \Delta^{A_2}(n_1 l_1) - {}^{A_1} \Delta^{A_2}(n_2 l_2). \quad (5)$$

It was shown in Refs. [3, 11] that the BW anomaly may be represented in the single-particle nuclear shell model and one-electron approximation as the product of two factors, one of them being dependent only on the atomic structure, the second being dependent only on the nuclear properties. This atomic-nuclear factorization was confirmed in Refs. [6, 12, 13], where more-refined atomic and nuclear models were used. Due to this atomic-nuclear factorization, the ratio

$$\eta_{n_1 l_1, n_2 l_2} \equiv \frac{{}^{A_1} \Delta^{A_2}(n_1 l_1)}{{}^{A_1} \Delta^{A_2}(n_2 l_2)} \quad (6)$$

should be independent of A and is determined solely by the electronic wave function. The factor η can be determined experimentally for stable or long-lived nuclei where independent values of the magnetic moments are available. When the corresponding data are missing, this factor can be calculated by using advanced atomic approaches. With a known η factor, the RHFA value needed for the magnetic moment evaluation (see Eq. (4)) is deduced from the measured DHFA,

$${}^{A_1} \Delta^{A_2}(n_1 l_1) = \frac{{}^{A_1} \Delta^{A_2}(n_2 l_2) \eta_{n_1 l_1, n_2 l_2}}{1 / \eta_{n_1 l_1, n_2 l_2} - 1 - {}^{A_1} \Delta^{A_2}(n_2 l_2)}. \quad (7)$$

To summarize, it is possible to determine the RHFA without having independent measurements of magnetic moments, by measuring magnetic hyperfine constants for different atomic levels and deducing the corresponding η factor by either atomic calculations or (if possible) from the hfs measurements for isotopes with a known RHFA. This approach was first implemented for the gallium isotopes [7] (see also more general considerations on using DHFA for anomaly analysis in Ref. [8]). Subsequently, the same procedure was applied for thallium [14] and bismuth [15] nuclei. It is worth emphasizing, that in this way one can determine the RHFA for nuclei far from stability. Thus, this procedure allows us to gain insight into how the nuclear magnetization distribution of ground and isomeric states changes from one isotope to another.

The gold nuclei were produced in spallation reactions induced by the 1.4-GeV proton beam from the CERN PS Booster, impinging on a $50 \text{ g} \cdot \text{cm}^{-2}$ thick UC_x target. The reaction products diffused out of the high temperature target ($T \approx 2500^\circ \text{K}$) and effused as neutral atoms into the hot cavity of the ion source. Inside the cavity, the gold atoms were selectively ionized by the ISOLDE resonance ionization laser ion source installation (RILIS) [16, 17], with the laser beams frequency tuned to the three-step gold ionization scheme [18]. The ions were then extracted from the cavity using a 30-kV electrostatic potential and separated according to their mass-to-charge ratio by the general purpose separator of ISOLDE [19]. The mass-separated beam was then delivered to either the ISOLTRAP multireflection time-of-flight mass spectrometer (MR-ToF MS) [20] or the ‘‘Windmill’’ (WM) decay station [21, 22], for photoion monitoring during wavelength scans. Details of the scanning procedures can be found in Refs. [21, 22]. The hfs measurements were made upon the 267.7-nm atomic transition in gold ($6s \ ^2S_{1/2} \rightarrow 6p \ ^2P_{1/2}$), by scanning a frequency-tripled titanium-sapphire laser in a narrowband mode (bandwidth of $\sim 600 \text{ MHz}$ before tripling). Two broadband dye lasers (bandwidth of $\sim 20 \text{ GHz}$) were used for the second and third excitation steps. Examples of the experimental hfs spectra for the studied $I^\pi = 11/2^-$ gold isomers are shown in Fig. 1.

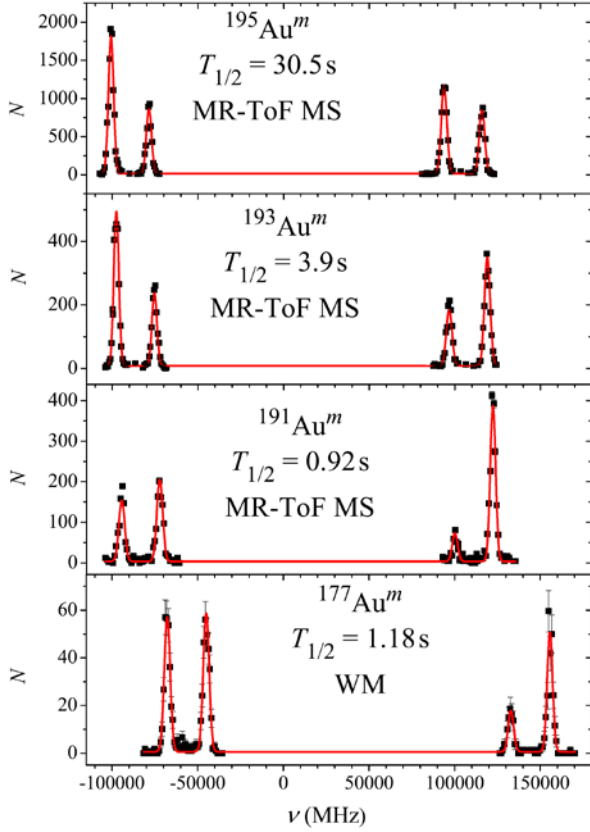


Fig. 1. The hfs spectra of selected Au isomers. The half-life and the method of the photoion current monitoring are shown for each isomer. The *solid lines* depict the Voigt-profile fit to the data. The zero point on the frequency scale corresponds to a wave number of $37\,358.90\text{ cm}^{-1}$

The positions of the hyperfine components as a function of the scanning laser frequency are determined by the formula:

$$\nu^{F,F'} = \nu_0 + a_{6p} \frac{K'}{2} - a_{6s} \frac{K}{2}, \quad (8)$$

where ν_0 is the centroid frequency of the hfs, the prime symbol denotes the upper level of the atomic transition, $K = F(F+1) - I(I+1) - J(J+1)$, F is the total angular momentum of the atomic level, I and J are the nuclear spin and the angular momentum for the electronic state, respectively, and a_{nl} is the magnetic hyperfine coupling constant for the atomic level with the quantum numbers n and l . For brevity, throughout the paper indices $6s$ and $6p$ will be related to the $6s\ ^2S_{1/2}$ and $6p\ ^2P_{1/2}$ states, respectively. In Table 1 the experimental hfs constants, a_{6s} , and a -constants ratios for the $11/2^-$ gold isomers are presented along with the DHFA values, calculated by Eq. (5). To convert the latter to RHFA one should know the $\eta_{6s, 6p}$ factor (see Eq. (7)). Unfortunately, there are no experimental data on a_{6p}^A / a_{6s}^A for $^{196, 198, 199}\text{Au}$ where the RHFA values were determined independently.

Therefore it is impossible to deduce a pure experimental value of the $\eta_{6s, 6p}$ factor. Accordingly, we used advanced atomic calculations to determine its value. We used many-body perturbation theory and coupled cluster approximations on top of the Hartree–Fock–Dirac method [23–26]. Correlation corrections were included within the random phase approximation with self-energy correction [27] and structural radiation correction [28]. As a final value for the $\eta_{6s, 6p}$ factor in gold we adopted the mean value of the results obtained in the frameworks of the different approximations with the uncertainty covering the dispersion of these results: $\eta_{6s, 6p} = 4.0(3)$.

Table 1

Experimental results

A	a_{6s}^A , MHz	a_{6p}^A / a_{6s}^A	${}_{6p}^{197}\Delta_{6s}^A$
177	33 414(34)	0.1142(9)	-7.7(8)
191	32 424(30)	0.1145(9)	-7.9(8)
193	32 391(30)	0.1141(7)	-7.6(6)
195	32 372(46)	0.1141(9)	-7.5(8)

In Table 2 and Fig. 2, the RHFA values for the selected $I^\pi = 11/2^-$ gold isomers are presented. The hyperfine structure of ${}^{189}\text{Au}^m$ was not measured in the present work and ${}^{197}\Delta^A(6s)$ value for ${}^{189}\text{Au}^m$ was calculated using the data from Ref. [29]. One can see that the ${}^{197}\Delta^A(6s)$ value for ${}^{177, 191, 193, 195}\text{Au}^m$ is constant within uncertainties. However, the value for ${}^{189}\text{Au}^m$ differs by just over 1.5σ , although there are no peculiarities in its nuclear structure compared to other $I^\pi = 11/2^-$ gold isomers, which could explain this deviation. Correspondingly, ${}^{197}\Delta^{189m}(6s)$ was not taken into account in the calculations of the mean value of the RHFA for the $I^\pi = 11/2^-$ gold isomers.

Table 2RHFA and magnetic moments for $I^\pi = 11/2^-$ gold isomers

A	${}^{197}\Delta^A(6s)$, %	$\mu(\mu_N)$	$\mu(\mu_N)^c$, literature	Reference	Methods
177	11.4(14)	6.519(38)	–	–	–
189	8.6(16)	6.365(38)	6.17(15)	[33]	NMR/ON
			6.186(20)	[29]	hfs
191	11.7(14)	6.326(37)	6.6(6)	[34]	NO
193	11.2(11)	6.320(37)	6.18(9)	[35]	NMR/ON
195	11.2(14)	6.316(37)	6.18(9)	[30]	NMR/ON

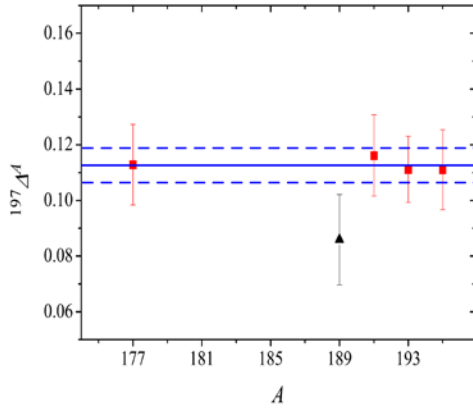


Fig. 2. Relative hyperfine anomaly for $11/2^-$ gold isomers: *squares* – present work; *triangle* ($A = 189$) – RHFA calculated by Eqs. (5–7) with the data from Ref. [29]; *lines* – weighted mean value for $A = 177, 191, 193, 195$ with the corresponding error bars

This weighted mean value, ${}^{197}\Delta^{(I=11/2)}(6s) = 0.1134(58)$, was used to deduce magnetic moments by Eq. (4) (see column 3 in Table 2). Nearly all previously derived magnetic moments in gold nuclei should be recalculated with correct accounting of the RHFA. Magnetic moments of the high-spin gold isomers were measured previously by the method of nuclear magnetic resonance on oriented nuclei (NMR/ON; see Table 2). The NMR/ON method relies upon the precise determination of the magnetic hyperfine splitting of radioactive nuclei in a ferromagnetic host lattice. To extract the magnetic moment, one should know the effective magnetic field B_{hf} seen by a nucleus embedded in a ferromagnetic host. This field depends on the nuclear magnetization distribution over the nuclear volume, which leads to a “NMR/ON” hyperfine anomaly. This anomaly is not equal to the hfs anomaly, due to the noncontact hyperfine field which should be taken into account in the

analysis of the NMR/ON experiments. The difference between these anomalies is believed to be small ($\sim 10\%$ according to the estimation in Refs. [30, 31]), and to determine B_{hf} , and thus the magnetic moments, the RHFA correction was taken into account in the corresponding publications.

In Ref. [30], the $^{198}\Delta^{195m}(6s)$ value was empirically estimated using the Eisinger and Jaccarino calculations [32], and strong assumptions on the nuclear configuration in ^{198}Au . The result, $^{198}\Delta^{195m}(6s)_{\text{emp}} = 0.004(15)$, differs noticeably from the value obtained by combining experimental values of $^{197}\Delta^{198}(6s)$ [9] and $^{197}\Delta^{(I=11/2)}(6s)$: $^{198}\Delta^{195m}(6s)_{\text{expt}} = ^{197}\Delta^{(I=11/2)}(6s)_{\text{expt}} - ^{197}\Delta^{198}(6s)_{\text{expt}} = 0.028(6)$. This means that even when assuming equal ‘‘NMR/ON’’ and hfs anomalies, the results and uncertainties of the NMR/ON measurements for the high-spin gold isomers should be reconsidered.

In Figure 3, the systematics of the g factors of the $\pi h_{11/2}$ states is presented. Along with the values for gold isomers determined in the present work, the experimental data for iridium ([35–37] and references therein), europium [38], holmium [39], thulium [40], gadolinium [41] and thallium [42] are shown. In the cases of ^{144}Gd and ^{205}Tl , $g(\pi h_{11/2})$ values were derived from the measured g factors for $I^\pi = 10^+(h_{11/2})^2$ and $I^\pi = 25/2^+(7^- \otimes h_{11/2})$ states, respectively [41, 42]. Thus, we have unique systematics of the single-particle g factors, spanning the whole range between the magic neutron numbers, $N = 82$ and $N = 126$. For such a wide range of proton number (from $Z = 64$ to $Z = 81$), the $g(\pi h_{11/2})$ values display a very regular N dependence: Starting from the maximal value at the magic number $N = 82$, it steeply decreases with the increase of N , approaching a constant value at $N > 110$. The value for ^{205}Tl demonstrates an increase to higher values, similar to those close to $N = 82$, although the g factor for the $\pi h_{11/2}$ state in ^{205}Tl was deduced by the additivity relation rather than measured directly [41]. Such a behaviour can be explained by the evolution of the first-order core-polarization correction (CP1) to the magnetic moment value [43] due to $\nu f_{7/2} \rightarrow \nu f_{5/2}$ core excitations [38]. The occupation of the $\nu f_{7/2}$ orbital starts at $N = 82$ and increases with increasing N , resulting in an enhancement of the core polarization and corresponding decrease of the magnetic moment. After the complete filling of the $\nu f_{7/2}$ orbital, the CP1 correction and g factor remain constant until the start of the $\nu f_{5/2}$ -orbital filling at $N = 118$. The population of this orbital leads to a blocking of the states available for the $\nu f_{7/2} \rightarrow \nu f_{5/2}$ excitations and, correspondingly, to a decrease in the CP1 correction for $g(\pi h_{11/2})$. The existing data support this qualitative interpretation. To substantiate these claims it is important to fill the gaps in the $g(\pi h_{11/2})$ systematics, namely, to measure magnetic moments for the long-lived $11/2^-$ states in $^{167-173, 193-197}\text{Ir}_{90-96}$, $^{116-120, 207}\text{Tl}_{126}$, $^{141}\text{Eu}_{78}$, $^{205}\text{Au}_{126}$.

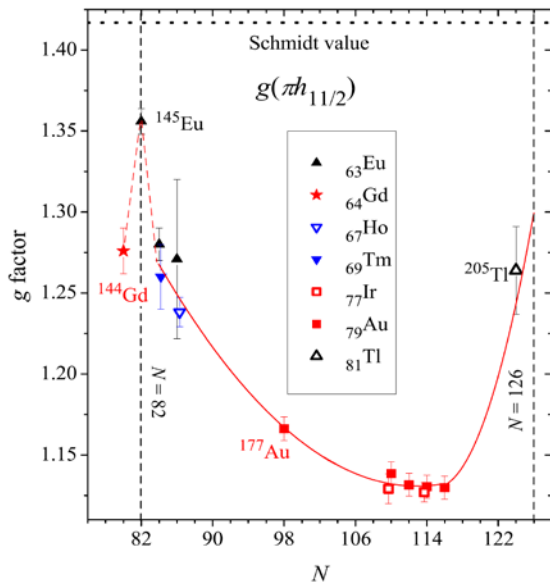


Fig. 3. g factors of the $\pi h_{11/2}$ states

To summarize, hyperfine structure constants of the $11/2^-$ gold isomers $^{177, 191, 193, 195}\text{Au}^m$ have been measured using the 267.7-nm atomic transition. The differential hyperfine anomaly has been determined for these nuclei by comparing the ratios of the magnetic hyperfine constants of the ground and excited atomic states for different isotopes and isomers. The obtained DHFA values have been converted to the relative hyperfine anomaly using advanced atomic calculations. Magnetic dipole moments have been deduced taking

into account the corresponding RHFA values. The applied method of the RHFA determination can be used for other far-from-stability nuclei. The magnetic moments previously calculated should be reevaluated with proper accounting for the hyperfine anomaly. Systematics of the nuclear g factor for the $\pi h_{11/2}$ states spanning the whole range between the magic neutron numbers, $N = 82$ and $N = 126$, can be qualitatively explained by the first-order core-polarization correction with the leading role of the $\nu f_{7/2} \rightarrow \nu f_{5/2}$ core excitations.

References

1. J.E. Rosenthal, G. Breit, Phys. Rev. **41**, 459 (1932).
2. M.F. Crawford, A.K. Schawlow, Phys. Rev. **76**, 1310 (1949).
3. A. Bohr, V.F. Weisskopf, Phys. Rev. **77**, 94 (1950).
4. H.J. Rosenberg, H.H. Stroke, Phys. Rev. A **5**, 1992 (1972).
5. J.R. Persson, At. Data Nucl. Data Tables **99**, 62 (2013).
6. T. Fujita, A. Arima, Nucl. Phys. A **254**, 513 (1975).
7. V.J. Ehlers, Y. Kabasakal, H.A. Shugart, O. Tezer, Phys. Rev. **176**, 25 (1968).
8. J.R. Persson, Eur. Phys. J. A **2**, 3 (1998).
9. C. Ekström, L. Robertsson, S. Ingelman *et al.*, Nucl. Phys. A **348**, 25 (1980).
10. J.G. Cubiss *et al.*, Phys. Lett. B **786**, 355 (2018).
11. C. Schwartz, Phys. Rev. **99**, 1035 (1955).
12. A.-M. Mårtensson-Pendrill, Phys. Rev. Lett. **74**, 2184 (1995).
13. H.H. Stroke, R.J. Blin-Stoyle, V. Jaccarino, Phys. Rev. **123**, 1326 (1961).
14. A.E. Barzakh, L.Kh. Batist *et al.*, Phys. Rev. C **86**, 014311 (2012).
15. S. Schmidt *et al.*, Phys. Lett. B **779**, 324 (2018).
16. V. Mishin, V. Fedoseyev *et al.*, Nucl. Instrum. Methods B **73**, 550 (1993).
17. V. Fedosseev, K. Chrysalidis *et al.*, J. Phys. G **44**, 084006 (2017).
18. B.A. Marsh, V.N. Fedosseev, P. Kosuri, Hyperfine Interact. **171**, 109 (2006).
19. R. Catherall *et al.*, J. Phys. G **44**, 094002 (2017).
20. R.N. Wolf *et al.*, Int. J. Mass Spectrom. **349–350**, 123 (2013).
21. M.D. Seliverstov *et al.*, Phys. Rev. C **89**, 034323 (2014).
22. J.G. Cubiss *et al.*, Phys. Rev. C **97**, 054327 (2018).
23. V.A. Dzuba, V.V. Flambaum, M.G. Kozlov, Phys. Rev. A **54**, 3948 (1996).
24. M.G. Kozlov, S.G. Porsev *et al.*, Comput. Phys. Commun. **195**, 199 (2015).
25. M.G. Kozlov, Int. J. Quant. Chem. **100**, 336 (2004).
26. M.S. Safronova, M.G. Kozlov, W.R. Johnson, D. Jiang, Phys. Rev. A **80**, 012516 (2009).
27. V.A. Dzuba, V.V. Flambaum, M.G. Kozlov, S.G. Porsev, Sov. Phys.–JETP **87**, 885 (1998).
28. M.G. Kozlov, S.G. Porsev, W. Johnson, Phys. Rev. A **64**, 052107 (2001).
29. K. Wallmeroth, G. Bollen *et al.*, Nucl. Phys. A **493**, 224 (1989).
30. E. Hagn, E. Zech, G. Eska, Phys. Rev. C **24**, 631 (1981).
31. P.T. Callaghan, W.M. Lattimer, P.D. Johnston, N.J. Stone, Hyperfine Interact. **2**, 288 (1976).
32. J. Eisinger, V. Jaccarino, Rev. Mod. Phys. **30**, 528 (1958).
33. E. Van Walle, D. Vandeplassche *et al.*, Phys. Rev. B **34**, 2014 (1986).
34. E. Van Walle, J. Wouters *et al.*, Hyperfine Interact. **22**, 507 (1985).
35. E. Hagn, E. Zech, Nucl. Phys. A **399**, 83 (1983).
36. G. Eska, E. Hagn, T. Butz *et al.*, Phys. Lett. B **36**, 328 (1971).
37. K.S. Krane, W.A. Steyert, Phys. Rev. C **9**, 2063 (1974).
38. W. Klinger, R. Böhm, W. Sandner, W. Witthuhn, Nucl. Phys. A **350**, 61 (1980).
39. G.D. Alkhozov, A.E. Barzakh *et al.*, Nucl. Phys. A **504**, 549 (1989).
40. A.E. Barzakh, I.Ya. Chubukov *et al.*, Phys. Rev. C **61**, 034304 (2000).
41. O. Häusser, P. Taras *et al.*, Phys. Rev. Lett. **42**, 1451 (1979).
42. K.H. Maier, J.A. Becker *et al.*, Phys. Rev. Lett. **48**, 466 (1982).
43. A. Arima, H. Horie, Prog. Theor. Phys. **11**, 509 (1954).

LARGE SHAPE STAGGERING IN NEUTRON-DEFICIENT Bi ISOTOPES

PNPI participants of the IS608 Collaboration:

A.E. Barzakh, D.V. Fedorov, P.L. Molkanov, V.N. Panteleev, M.D. Seliverstov, L.V. Skripnikov, A.V. Oleynichenko, A.V. Zaitsevskii

1. Introduction

Description of shape coexistence and shape evolution in nuclei is one of the most intriguing and complicated problems in contemporary nuclear physics [1]. The richest manifestation of these phenomena is observed in the lead region. The isotopic behaviour of the nuclear shape differs substantially for different Z values in this region. In the ^{80}Hg isotopic chain, a strong odd-even shape staggering was observed at $N < 106$ [2, 3], whereas for ^{84}Po and ^{85}At nuclei a gradual increase in deformation was found at $N < 113$ [4, 5]. At the same time, the neutron-deficient ^{82}Pb and ^{81}Tl nuclei preserve sphericity down to and beyond the neutron midshell at $N = 104$ [6–8]. The ^{83}Bi isotopic chain is intermediate between the lead ($Z = 82$) and polonium ($Z = 84$) chains with different shape evolution patterns.

On the other hand, Tl and Bi isotopic chains are “mirrors” with respect to the filled proton shell ($Z = 82$), and one might expect the similarity of the corresponding nuclear structures. However, in contrast to Tl isotopes with their nearly spherical ground states down to $N = 98$ [8], neutron-deficient Bi isotopes demonstrate some indications of the possible structural changes below $N = 110$ – 108 (see Refs. [9–12]). In particular, the noticeable deviation from the isotopic trend of the charge radii in the lead isotopic chains was observed for the Bi nuclei at $N < 111$. This deviation was interpreted as an indication of the possible onset of quadrupole deformation [12].

Observables that give model-independent information on the nuclear shape are charge radius changes which can be obtained by atomic spectroscopy *via* isotope shift (IS) measurements. Besides, atomic spectroscopy gives information on the spins and nuclear electromagnetic moments *via* hyperfine structure (hfs) analysis. So far, atomic spectroscopy measurements are limited for $^{189-198}, ^{202-213}\text{Bi}$ [12–15]. It should be noted that the accuracy of the IS measurement for ^{189}Bi is insufficient for unambiguous conclusions [12]. It is important to perform systematic IS and hfs studies for the Bi isotopic chain at $N < 107$ in order to trace the possible structural changes in neutron-deficient bismuth isotopes.

2. Experimental details

The experiments were performed at the ISOLDE facility (CERN) [16]. The bismuth nuclei were produced through spallation reactions induced by the 1.4 GeV proton beam from the CERN PS Booster impinging on a UC_x target (50 g/cm^2 of ^{238}U). The spallation products effused out of the high-temperature target ($T \approx 2050^\circ\text{C}$) as neutral atoms into the cavity of the resonance ionization laser ion source (RILIS) [17]. The bismuth atoms were resonantly ionized within this cavity when the laser beams were wavelength-tuned to the three-step ionization scheme using the laser light with the wavelengths of 306.9, 555.4 and 532 nm [18]. For more details of the RILIS laser system see Ref. [19].

The hyperfine splitting at the first excited state is large (about 30 GHz), while a typical bandwidth of the second-step ($\lambda_2 = 555.21 \text{ nm}$) broadband dye lasers is about 15 GHz. To enable the saturation of all hyperfine components in the second-step transition the broadband laser bandwidth was increased by removing a pair of prisms in the intracavity beam-expander, which resulted in a bandwidth of about 750 GHz. The atomic spectroscopy measurements have been performed for the $6p^3 \ ^4S_{3/2} \rightarrow 6p^2 7s \ ^4P_{1/2}$ ($\lambda_1 = 306.77 \text{ nm}$) transition, by scanning the frequency of the first-step narrowband titanium–sapphire (Ti:Sa) laser [19], whereas the photoion current was monitored by the detection of characteristic α decays of the isotopes in question using the “Windmill” decay station [20]. Examples of the hfs spectra are shown in Fig. 1. The zero point on the frequency scale corresponds to a wave number of $16\,294.11 \text{ cm}^{-1}$.

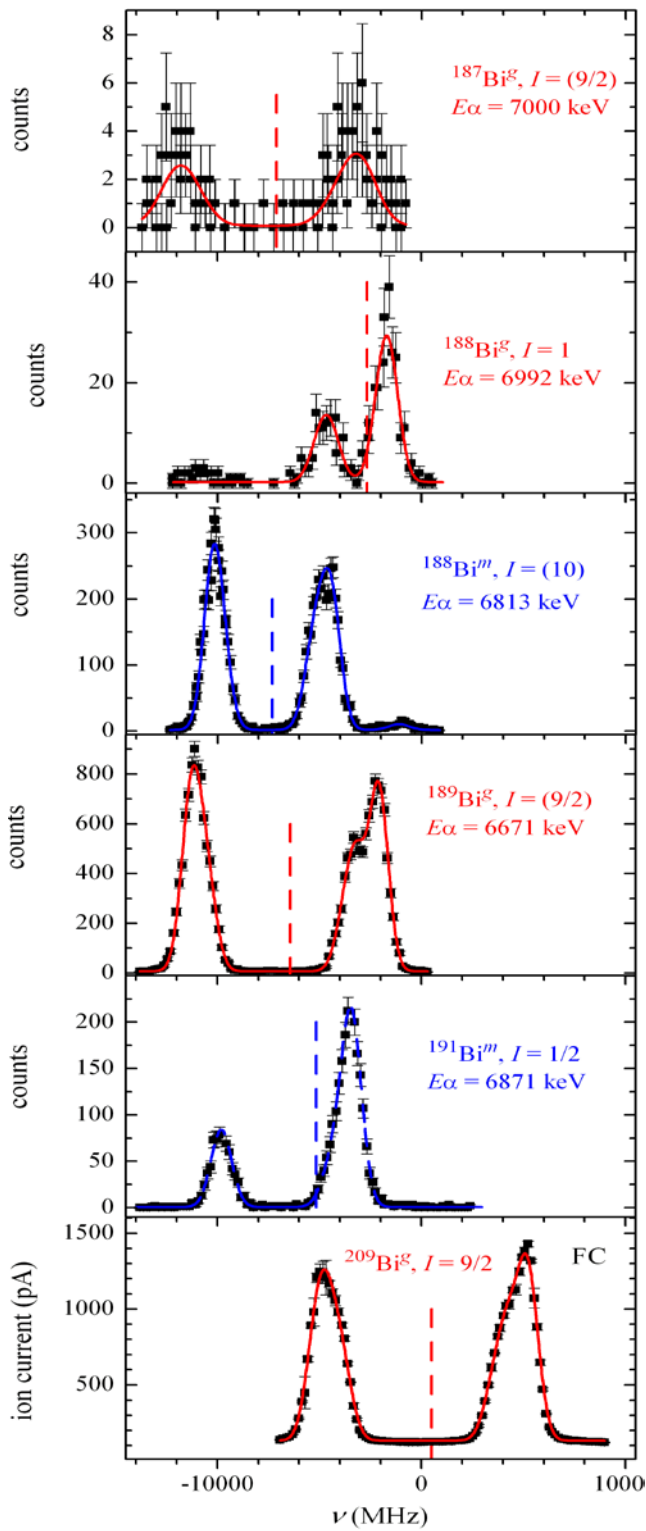


Fig. 1. The hfs spectra of the selected Bi isotopes. In the insets the spin of the corresponding nuclide and the energies of the α -decay lines used for the photoion current monitoring are shown. The *solid lines* depict the Voigt-profile fit to the data. The *vertical dashed lines* mark the centre of gravity of the corresponding hfs

3. Results

3.1. Spin determination

For the spin determination, the “integration method” was used [21, 22]. It is based on comparison of the ratio of areas under each resolved peak with theoretically predicted values for different spin assumptions (sum of the calculated from angular-momentum coupling intensities of each hyperfine component which formed that peak).

In our case, we always have two resolved peaks and the distance between them corresponds to the hyperfine splitting of the atomic excited state. Each peak is a sum of several unresolved components and the distance between them corresponds to the hyperfine splitting of the atomic ground state. It was shown [22] that the ratio of areas under each resolved peak should be equal to the ratio of the sums of the theoretical intensities of all hyperfine components buried under each observed peak independently of the saturation conditions. This theoretical ratio r_{theor} depends only on the nuclear spin:

$$r_{\text{theor}}(I) = \frac{I+1}{I}.$$

For spin assignments of $I = 1$ and 2, the theoretical ratio values are $r_{\text{theor}} = 2$ and 1.5, respectively. The weighted mean value, $r_{\text{exp}} = 2.00(12)$, for the six hfs spectra available for $^{188}\text{Bi}^g$ indicates a strong preference for an $I = 1$ assignment.

This assignment contradicts to the previous one, $I^\pi = (3^+)$, made by analogy with the heavier odd-odd Bi nuclei [9]. It should be noted that the $I^\pi = (3^+)$ assignment was proposed in Ref. [9] with caution. Indeed, authors stressed that in $^{188}\text{Bi}^g$ there are certain quantitative deviations from the decay pattern of the heavier odd-odd Bi isotopes. Such deviations, according to Ref. [9], might indicate a change in the configuration of $^{188}\text{Bi}^g$ and a possibility of an oblate-prolate shape coexistence at low excitation energy.

The same integration method was applied in Ref. [22] to $^{191}\text{Bi}^m$ spin assignment. Comparison of $r_{\text{exp}}(^{191}\text{Bi}^m) = 3.15(15)$ with theoretical predictions $r_{\text{theor}} = 3, 1.67$ for $I = 1/2, 3/2$ spin assignment strongly supports the adopted $I = 1/2$ assignment [23].

When fitting the hfs spectra for other Bi isotopes, the spins were fixed in accordance with the adopted assignments based on the α - and β -decay systematics [23].

3.2. Fitting procedure

The positions of the hyperfine components in the spectrum of the isotope with the atomic number A are determined by the well-known formulas [24] with four parameters: the isotope shift relative to the stable ^{209}Bi ($\delta v_{A, 209}$), the magnetic hfs constants (a_1 and a_2) for the first ($6p^3\ ^4S_{3/2}$) and the second ($6p^2\ 7s\ ^4P_{1/2}$) excitation levels, and the electric quadrupole hfs constant (b) for the first level (the b constant for the second level is equal to zero due to the electronic spin of this level $J = 1/2$). Experimental data were fitted by the Voigt profile. Due to limited resolution, the hfs of the excited atomic level was not resolved and in the fitting procedure the ratio $\rho \equiv a_2/a_1$ should be fixed. This ratio depends on the atomic mass number because different atomic states differ in sensitivity to the nuclear magnetization distribution. However, it was shown that for isotopes with the same spin, close magnetic moments and similar structure the ρ value is constant in the limits of 0.3% [25]. This conclusion was reaffirmed in the high-resolution hfs measurement for a number of bismuth isotopes [26]. In particular, it was found that for $9/2^-$ ground states of $^{209, 205, 201, 197}\text{Bi}$, $\rho = -11.01(2)$, for 10^- isomers $^{196, 198}\text{Bi}^m$, $\rho = -10.96(2)$, and for $1/2^+$ isomer ^{201}Bi , $\rho = -11.10(3)$ [26]. Correspondingly, in the fitting procedure the following fixed values of ρ were used: for $^{187, 189, 191}\text{Bi}^g$ ($I^\pi = 9/2^-$) $\rho = -11.01$, for $^{188}\text{Bi}^m$ ($I^\pi = 10^-$) $\rho = -10.96$ and for $^{191}\text{Bi}^m$ ($I^\pi = 1/2^+$) $\rho = -11.10$. A possible variation of ρ in the limits of 0.3% was included in the deduced a -constant uncertainties. There are no heavier isotopes with the structure similar to $^{188}\text{Bi}^g$. Therefore, $\rho = -11.01$ was fixed with a possible variation of this value in the limits of 1%. Other details of the fitting procedure can be found in Ref. [22].

The final results along with the literature data for $^{191}\text{Bi}^g$ and ^{189}Bi [12] are presented in Table 1.

Table 1

Isotope shifts and magnetic hfs constants for Bi isotopes studied in the present work

A	$\delta v_{A, 209}$, MHz	a , MHz	b , MHz
187	-22 990(250)	-397.7(2.5)	-912(400)
188	-8 370(160)	-489(25)	620(270)
188 <i>m</i>	-23 667(50)	-122.4(6)	-1 220(300)
189	-20 823(50)	-400.8(2)	-1 160(14)
	-19 900(1100) ^a	-405(30) ^a	-
191	-19 610(50)	-407.1(6)	-1 023(65)
	-19 370(230) ^a	-404(5) ^b	-1 130(560) ^a
191 <i>m</i>	-16 979(50)	-1463.3(65)	-

^a Reference [12].^b Recalculated from Ref. [12] with correct $\rho = -11.01$.

3.3. Magnetic moments evaluation

The nuclear magnetic-moment μ_A of the isotope with the atomic number A is connected with the magnetic hfs constant a_A by the following relation (see Ref. [24]):

$$\mu_A = \mu_{209} \frac{I_A a_A (6p^2 7s^4 P_{1/2})}{I_{209} a_{209} (6p^2 7s^4 P_{1/2})} \left[1 + {}^{209}\Delta^A (6p^2 7s^4 P_{1/2}) \right], \quad (1)$$

where ${}^{209}\Delta^A(6p^2 7s^4 P_{1/2})$ is a relative hyperfine anomaly (RHFA) for the indicated atomic state.

The following reference values were used: $a_{209}(6p^2 7s P_{1/2}) = 4 922.3(20)$ MHz [27] and $\mu_{209} = 4.0900(15) \mu_N$ [27]. The values of RHFA were estimated using RHFA's for heavier bismuth isotopes with the same spin and parities [26]. For ${}^{188}\text{Bi}^g$, the possible uncertainty due to the unknown RHFA was estimated as 2%. The magnetic moments calculated using Eq. (1), are presented in Table 2.

In order to extract other nuclear observables from the measured hfs constants and IS's, the atomic calculations are needed.

Table 2

Changes in mean-square charge radius ($\delta\langle r^2 \rangle_{A, 209}$), magnetic (μ) and quadrupole (Q_s) moments for the investigated Bi nuclei

A	I^π	$\delta\langle r^2 \rangle_{A, 209}$ ^a	$\mu(\mu_N)$ ^a	Q_s (b)
187 <i>g</i>	(9/2 ⁻)	-0.916(10){64}	3.639(24)	-1.26(55)
188 <i>g</i>	1 ⁺	-0.325(6){23}	0.994(51){19}	0.85(38)
188 <i>m</i>	(10 ⁻)	-0.944(4){66}	2.488(13){50}	-1.68(41)
189	(9/2 ⁻)	-0.830(2){55}	3.668(2){74}	-1.60(2)
191 <i>g</i>	(9/2 ⁻)	-0.782(2){54}	3.725(6){70}	-1.408(89)
191 <i>m</i>	1/2 ⁺	-0.676(2){47}	1.488(7){30}	-

^a The errors in parentheses are the statistical experimental uncertainties. The systematic errors are given in the curly brackets and stem for μ from the uncertainty in the hyperfine anomaly and for $\delta\langle r^2 \rangle$ from the uncertainty in the electronic factors used for extraction of $\delta\langle r^2 \rangle$ from experimentally measured IS.

3.4. Atomic calculations

The hyperfine constant b is related to the spectroscopic quadrupole moment Q_s via the following equation: $b = eQ_s V$, where V is the electric field gradient (EFG) produced by the electrons at the site of the nucleus. Thus,

when Q_s is known for a reference isotope ^{209}Bi , its value for other isotopes can be determined by the scaling relation:

$$\frac{Q_s(^A\text{Bi})}{Q_s(^{209}\text{Bi})} = \frac{b(^A\text{Bi})}{b(^{209}\text{Bi})}. \quad (2)$$

There are two independent Q_s measurements for ^{209}Bi made in the 1970s: $Q_s = -0.37(3) b$ (muonic X-ray, Ref. [28]) and $Q_s = -0.50(8) b$ (pionic X-ray, Ref. [29]). The noticeable difference between these values, their large uncertainties and a multitude of corrections needed in order to reliably estimate Q_s by these methods (Refs. [28, 30]), prevent us from using muonic or pionic result as a reference value. The alternative way is to calculate the EFG, and based on the measured $b(^{209}\text{Bi})$ to deduce $Q_s(^{209}\text{Bi})$. However, a complicated electronic structure makes accurate calculations for atomic bismuth a challenging problem. The first *ab initio* calculations by the multiconfiguration Dirac–Fock method [31] gave the reference value $Q_s(^{209}\text{Bi}) = -0.516(15) b$ adopted in the recent compilation [32]. However, subsequent advanced molecular calculations resulted in $-0.420(8) b$ [33] and $-0.415 b$ [34], questioning this value. To overcome this longstanding discrepancy, we summarized the results of 33 atomic and molecular calculations for ^{209}Bi , either published in the last decade (2013–2021) [33–37], or made specifically for this study. In these calculations a variety of advanced theoretical methods [38–44] with various computational strategies [45–49] were used by several independent groups on five continents. Combining the measured values of the hfs constant b of several electronic states in the neutral ^{209}Bi atom, the $^{209}\text{Bi}^+$ ion, as well as in several diatomic molecules (BiN, BiP, BiF, BiI, BiO, BiCl), with the calculated EFG values for those particular systems, we obtained a sample of 33 values of $Q_s(^{209}\text{Bi})$. The “world average” $Q_s(^{209}\text{Bi}) = -0.420(17) b$ was deduced by taking the average of all these results, and the uncertainty was evaluated as a standard deviation of this sample. The quadrupole moments for $^{187, 188, 189, 191}\text{Bi}$ calculated using Eq. 2, the “world average” $Q_s(^{209}\text{Bi})$ and $b_1(^{209}\text{Bi})$ from Ref. [50], are presented in Table 2. The details of the methods and calculations will be published elsewhere. The electronic factors F and M needed to extract $\delta\langle r^2 \rangle$ from the measured IS were determined similarly to the calculations performed in Refs. [51, 52]: $F = 23 : 8(10) \text{ GHz} \cdot \text{fm}^{-2}$ and $M = -750(100) \text{ GHz} \cdot \text{u}$.

In Figure 2, the $\delta\langle r^2 \rangle_{A, 209}$ values for bismuth nuclei are compared with the data for isotonic lead and mercury isotopes. For all three isotopic chains, one observes the similar smooth trend until $N = 106$ along with the small and well-known odd-even staggering (OES). Surprisingly, a huge staggering in radii appears for $^{187-189}\text{Bi}$ isotopes manifested by a drastic increase for $^{188}\text{Bi}^g$ in comparison with the neighboring $^{187, 189}\text{Bi}^g$ and with $^{188}\text{Bi}^m$. This dramatic change happens at the same neutron number, $N = 105$, where the famous Hg shape staggering starts [2, 3]. The latter was interpreted as a sharp change between nearly spherical shapes in the even- N cases and strongly-prolate deformed configurations in the odd- N isotopes.

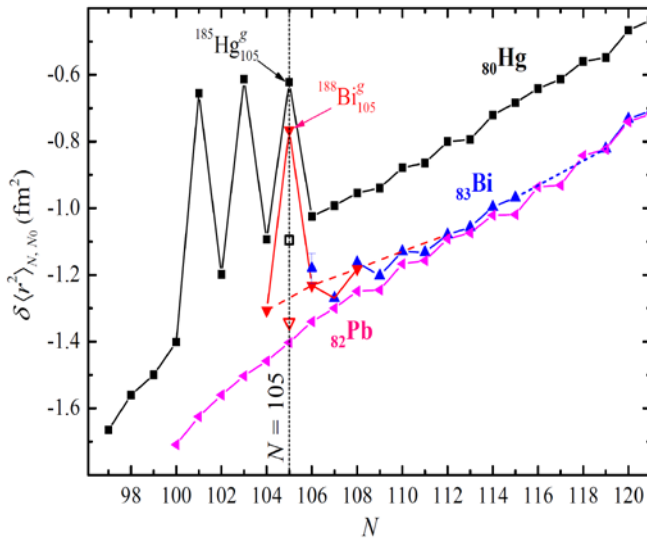


Fig. 2. Changes in the mean-square charge radii for Bi (downward triangles – present work; upward triangles – [27, 53]), Pb (leftward triangles – [5]) and Hg (squares – [10–12]) isotopes. Full and hollow symbols label the ground states and isomers, respectively. The data for each chain are shifted along the Y axis to improve visibility. Red dashed line connects the data for the even- N $9/2^-$ Bi ground states to demonstrate the deviation from the Pb trend

In contrast to the mercury isotopes with spin 0 or 1/2 for which $Q_s = 0$, for $^{188}\text{Bi}^g$ one can directly check this interpretation using the measured Q_s values. Indeed, in the strong coupling scheme the quadrupole moment can be related to the quadrupole deformation parameter β . Using this relation one obtains $\beta(^{188}\text{Bi}^g) = +0.25(7)$ whereas $\beta(^{188}\text{Bi}^m) = -0.08(2)$, $\beta(^{189}\text{Bi}) = -0.10(1)$, $\beta(^{187}\text{Bi}) = -0.08(4)$. Thus, $^{188}\text{Bi}^g$ is strongly prolate deformed, whereas its 10^- isomer and the adjacent isotopes with lower radii have a small deformation. It was noted in Ref. [8] that the $\delta\langle r^2 \rangle$ values of the $9/2^-$ Bi ground states follow the same trend as the radii of the spherical Pb isotopes down to $N = 112$, but start to deviate at $N = 110$. This was interpreted as a possible onset of deformation in $^{193, 191}\text{Bi}^g$. Our new data confirm this deviation from sphericity down to ^{187}Bi ($N = 104$). This is consistent with suggestions from extensive nuclear-spectroscopy data on the possible structural changes in the $N < 110$ bismuth isotopes (see Refs. [9, 10, 53]).

4. Conclusion

To summarize, the IS's and hfs's have been studied for neutron deficient bismuth isotopes using the ultra-sensitive (down to 0.1 ion/s) in-source resonance-ionization spectroscopy technique. A striking staggering in radii has been observed for $^{188}\text{Bi}^g$ relative to $^{187, 189}\text{Bi}^g$ at the same neutron number ($N = 105$) as in the Hg case. It is only the second example of such unusual behaviour throughout the nuclide chart. The quadrupole moment of $^{188}\text{Bi}^g$ confirms the strong prolate deformation in this nucleus with the newly established spin and parity of $J^\pi = 1^{(+)}$.

References

1. K. Heyde, J.L. Wood, Rev. Mod. Phys. **83**, 1467 (2011).
2. G. Ulm *et al.*, Z. Phys. A: At. Nucl. **325**, 247 (1986).
3. B.A. Marsh *et al.*, Nat. Phys. **14**, 1163 (2018).
4. T.E. Cocolios *et al.*, Phys. Rev. Lett. **106**, 052503 (2011).
5. J.G. Cubiss *et al.*, Phys. Rev. C **97**, 054327 (2018).
6. M.D. Seliverstov *et al.*, Eur. Phys. J. A **41**, 315 (2009).
7. A.E. Barzakh *et al.*, Phys. Rev. C **88**, 024315 (2013).
8. A. Barzakh *et al.*, Phys. Rev. C **95**, 044324 (2017).
9. A.N. Andreyev *et al.*, Eur. Phys. J. A **18**, 39 (2003).
10. A.N. Andreyev *et al.*, Phys. Rev. C **69**, 054308 (2004).
11. A. Hürstel *et al.*, Eur. Phys. J. A **15**, 329 (2002).
12. A.E. Barzakh, D.V. Fedorov *et al.*, Phys. Rev. C **95**, 044324 (2017).
13. M.R. Pearson *et al.*, J. Phys. G: Nucl. Part. Phys. **26**, 1829 (2000).
14. A. Barzakh *et al.*, Phys. Rev. C **94**, 024334 (2016).
15. A. Barzakh *et al.*, Phys. Rev. C **97**, 014322 (2018).
16. R. Catherall *et al.*, J. Phys. G **44**, 094002 (2017).
17. V.N. Fedosseev *et al.*, J. Phys. G **44**, 084006 (2017).
18. S. Rothe *et al.*, Nucl. Instr. Meth. B **376**, 91 (2016).
19. S. Rothe *et al.*, Nucl. Instr. Meth. B **317**, 561 (2013).
20. M. Seliverstov *et al.*, Phys. Rev. C **89**, 034323 (2014).
21. R.D. Harding *et al.*, Phys. Rev. C **102**, 024312 (2020).
22. M. Seliverstov *et al.*, Hyperfine Interact. **241**, 40 (2020).
23. National Nuclear Data Center. <https://www.nndc.bnl.gov/ensdf/>
24. E.W. Otten, in *Treatise on Heavy Ion Science* **8**, 517 (1989).
25. J.R. Persson, At. Data Nucl. Data Tables **99**, 62 (2013).
26. M. Bissel, unpublished (2021).
27. S. Schmidt *et al.*, Phys. Lett. B **779**, 324 (2018).
28. W. Lee, M. Chen, S. Cheng *et al.*, Nucl. Phys. A **181**, 14 (1972).
29. R. Beetz *et al.*, Z. Phys. A **286**, 215 (1978).
30. R. Beetz *et al.*, Nucl. Phys. A **300**, 369 (1978).

31. J. Bieron, P. Pyykko, Phys. Rev. Lett. **87**, 133003 (2001).
32. N. Stone, At. Data Nucl. Data Tables **111–112**, 1 (2016).
33. T.Q. Teodoro, R.L.A. Haiduke, Phys. Rev. A **88**, 052504 (2013).
34. A. Shee, L. Visscher, T. Saue, J. Chem. Phys. **145**, 184107 (2016).
35. J. Liu, Y. Shen, A. Asthana, L. Cheng, J. Chem. Phys. **148**, 034106 (2018).
36. J. Liu, X. Zheng, A. Asthana *et al.*, J. Chem. Phys. **154**, 064110 (2021).
37. L.V. Skripnikov, A.V. Oleynichenko, A.V. Zaitsevskii *et al.*, Phys. Rev. C **104**, 034316 (2021).
38. I.P. Grant, Relativistic Quantum Theory of Atoms and Molecules: Theory and Computation (2007).
39. C. Froese Fischer, M. Godefroid, T. Brage *et al.*, J. Phys. B: Atom. Mol. Opt. Phys. **49**, 182004 (2016).
40. C. Froese Fischer, G. Gaigalas, P. Jonsson, J. Bieron, Comp. Phys. Commun. **237**, 184 (2019).
41. M. Elantkowska, J. Ruczkowski, J. Dembczynski, Eur. Phys. J. Plus **130**, 14 (2015).
42. M. Kallay, P.G. Szalay, P.R. Surjan, J. Chem. Phys. **117**, 980 (2002).
43. V.A. Dzuba, V.V. Flambaum, P.G. Silvestrov, O.P. Sushkov, J. Phys. B: Atom. Mol. Phys. **18**, 597 (1985).
44. V.A. Dzuba, V.V. Flambaum *et al.*, J. Phys. B: Atom. Mol. Phys. **20**, 1399 (1987).
45. J. Bieron, L. Filippin, G. Gaigalas *et al.*, Phys. Rev. A **97**, 062505 (2018).
46. J. Bieron, C. Froese Fischer, P. Indelicato *et al.*, Phys. Rev. A **79**, 052502 (2009).
47. A. Papoulia *et al.*, Phys. Rev. A **103**, 022815 (2021).
48. M. Elantkowska, J. Ruczkowski, S. Wilman, M. Suski, Eur. Phys. J. Plus **136**, 330 (2021).
49. L.V. Skripnikov, A.V. Titov, J. Chem. Phys. **142**, 024301 (2015).
50. R.J. Hull, G.O. Brink, Phys. Rev. A **1**, 685 (1970).
51. F.P. Gustafsson *et al.*, Phys. Rev. A **102**, 052812 (2020).
52. E. Kahl, J. Berengut, Comp. Phys. Comm. **238**, 232 (2019).
53. A. Hürstel *et al.*, Eur. Phys. J. A **21**, 365 (2004).

STUDY OF NUCLEON CORRELATIONS IN NUCLEI BY THE INCLUSIVE (p, p') -REACTION AT 1 GeV

O.V. Miklukho, V.A. Andreev, G.V. Fedotov, A.A. Izotov, A.Yu. Kisselev, N.G. Kozlenko, D.V. Novinskiy, A.V. Shvedchikov, S.S. Volkov, A.A. Zhdanov

1. Introduction

The study of the nuclear structure using a 1 GeV proton beam in high resolution experiments is traditional at the PNPI synchrocyclotron [1]. In Ref. [1] we reported results of inclusive (p, p') -experiments aimed at studying nucleon correlations (NCs) in the nuclei ^{40}Ca [2–7], ^{12}C [4–7], ^{28}Si [5–8] and ^{56}Fe [5–8]. These experiments were performed using the magnetic spectrometer MAP (Fig. 1) equipped by a proton polarimeter with a carbon analyser. The differential cross section for the reactions $\sigma^{\text{incl}} = d^2\sigma/(d\Omega dK)$ and the secondary proton polarization P were measured at the scattering angle of 21° in narrow intervals of the scattered proton momentum K (10 MeV/c). These measurements were performed in a wide range of K covering the pN quasielastic peak with its maximum at $K = K_{pN} \approx 1480$ MeV/c and a high momentum region ($K > 1530$ MeV/c) up to the momentum corresponding to elastic scattering off the nucleus under investigation. The momentum resolution of the MAP spectrometer was about ± 2.5 MeV/c [4].

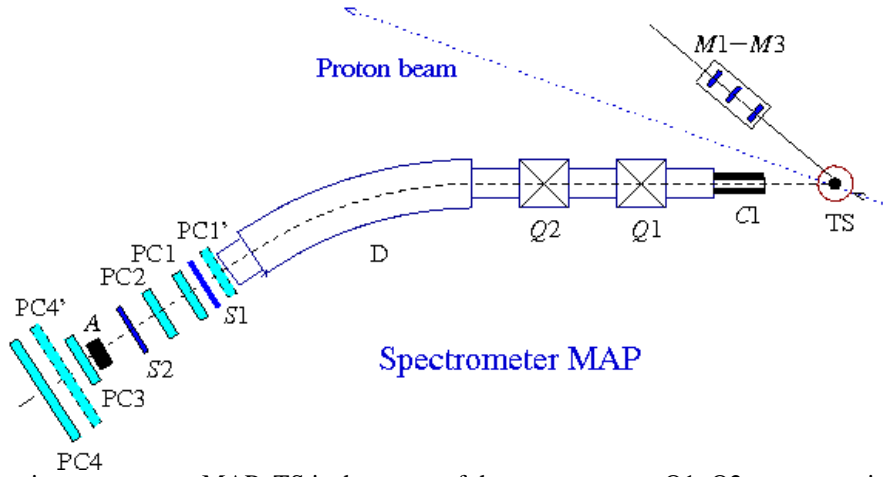


Fig. 1. The magnetic spectrometer MAP. TS is the target of the spectrometer; Q1, Q2 are magnetic quadrupoles; D is a dipole magnet; C1 is a collimator; S1, S2 and M1–M3 are scintillation counters; PC1–PC4, PC1', PC4' and A are multiwire proportional chambers and a carbon analyser of the MAP polarimeter

A structure in the polarization and the cross section for the (p, p') inelastic reaction with the nuclei ^{12}C [4], ^{28}Si [8], ^{40}Ca [4] and ^{56}Fe [8] at 1 GeV at a laboratory scattering angle of $\Theta = 21^\circ$ was observed. Different momentum intervals of the observed structure can be related to the in-medium elastic scattering on two-nucleon, three-nucleon, and four-nucleon correlations inside the nuclei under investigation. A dip in the polarization P in a range of K around the momentum $K \approx 1450$ MeV/c for all investigated nuclei [1] can be due to inelastic scattering by a two-nucleon short-range correlation [9] leading to its decay into two nucleons [7]. The scaling of the scattering cross section ratios off the nuclei under investigation (a value of the ratio is independent of the secondary proton momentum K) was observed in the high momentum range of $K = 1560\text{--}1635$ MeV/c [1].

Here we report some results of new inclusive polarization experiments in which the ^9Be , and ^{90}Zr nuclei were studied at the scattering angle of 21° [10]. We also present the high-momentum spectra in the inclusive scattering on the nuclei ^9Be and ^{12}C at the angles of 21 and 24.5° [11, 12].

2. Experimental data and observations

In Figure 2, the secondary proton polarization P (*blue squares*) and the cross sections σ^{incl} (*circles*) of the (p, p') inclusive reaction with the ${}^9\text{Be}$ nucleus at the scattering angle of 21° are presented as a function of the scattered proton momentum K [10]. The left and right vertical axes refer to the polarization and the scattering cross section, respectively.

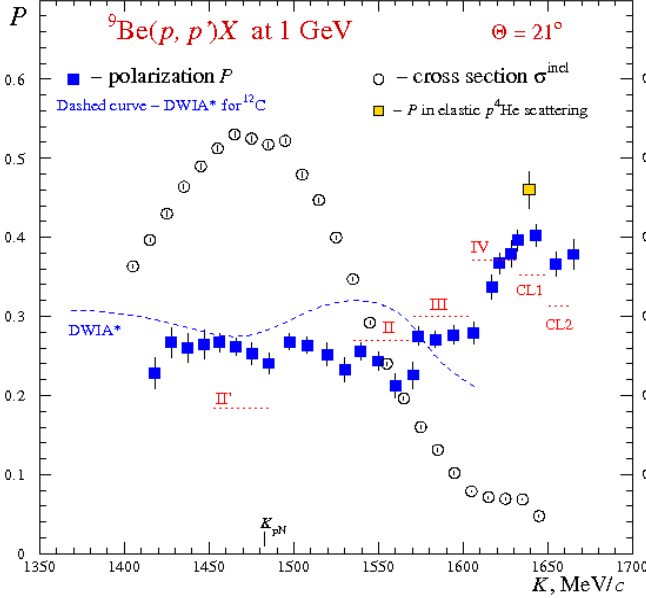


Fig. 2. Polarization (*blue squares*) and cross section (*circles*) of the ${}^9\text{Be}(p, p')X$ reaction at the angle of $\Theta = 21^\circ$ versus the scattered proton momentum K [10]. The *gold square* is the polarization in free elastic $p^4\text{He}$ scattering. Momentum intervals II–IV, II', CL1, CL2, the corresponding *dotted-line segments*, and the momentum K_{pN} are defined in the text. The *dashed blue curve* is the result of the polarization calculation for the ${}^{12}\text{C}$ nucleus in the framework of the spin-dependent distorted wave impulse approximation taking into account the relativistic distortion of the nucleon spinor in the nuclear medium [1, 10]

The observed structure in the polarization (Fig. 2, see also Ref. [11]): momentum intervals II, III and IV, indicated by segments of the *dotted line*, corresponds predominantly to the quasielastic scattering of ${}^9\text{Be}(p, p' \text{ NC})X$ by compact two-nucleon, three-nucleon and four-nucleon correlations inside the ${}^9\text{Be}$ nucleus similar to the light nuclei ${}^2\text{H}$, ${}^3\text{He}$ (${}^3\text{H}$) and ${}^4\text{He}$. It is possible that in interval II' (according to the model of short-range correlations [9]), a significant contribution is made by quasielastic scattering on two-nucleon correlation with its subsequent decay into two nucleons with equal and opposite momenta exceeding the Fermi momentum ($k_F \approx 250 \text{ MeV}/c$). The momentum interval CL1 possibly corresponds to the quasielastic scattering of ${}^9\text{Be}(p, p' X)Y$ on the residual nuclei (X) ${}^7\text{Li}$, ${}^6\text{He}$ (${}^6\text{Li}$) and ${}^5\text{He}$ in the reactions noted above. In this interval, there is a broad structure in the momentum distribution of the scattered protons shown in Fig. 3, *left panel* (see also Ref. [12]). According to kinematical calculations [12], the momentum interval CL2 corresponding to a narrower structure in the momentum distribution is possibly associated with the quasielastic scattering of ${}^9\text{Be}(p, p' {}^8\text{Be})n$ on an eight-nucleon (${}^8\text{Be}$) cluster. This structure was also observed at the scattering angle of 24.5° (Fig. 3, *right panel*) [12]. These observations (at two angles of the scattered proton [12]) confirm the model of the ${}^9\text{Be}$ nucleus in which this nucleus consists of a compact core, similar to the ${}^8\text{Be}$ nucleus, and a weakly bound neutron (n) [13]. The secondary proton polarization (see Fig. 2) was for the first time measured in the elastic scattering of protons on this core [11, 12]. Note that the values of the measured polarizations in the quasielastic scattering on the ${}^4\text{He}$ -like correlation at $K = 1621.3 \text{ MeV}/c$ (interval IV [10]) and on the ${}^8\text{Be}$ -like cluster at $K = 1654.6 \text{ MeV}/c$ (interval CL2, Refs. [10, 12]) are almost equal and amount to 0.367 ± 0.013 and 0.366 ± 0.015 , respectively.

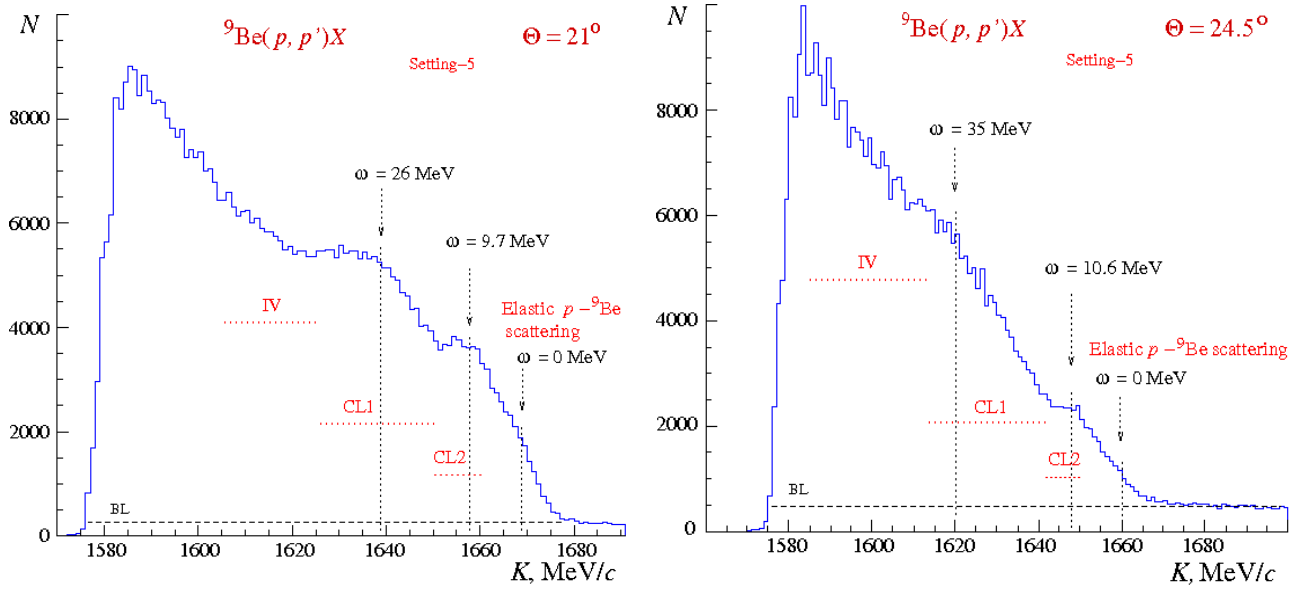


Fig. 3. Momentum distributions of protons scattered at the angle of 21° (left panel) and 24.5° (right panel) in the reaction ${}^9\text{Be}(p, p')X$ [10, 12] in a range from 1 585 to 1 700 MeV/c (Setting-5). ω is a difference of the scattered proton energy calculated for the elastic scattering off the nucleus under investigation and measured in the experiment. The momentum intervals IV, CL1, CL2 and the corresponding *horizontal red dotted-line segments* are defined in the text. The segment of the *black horizontal dashed line* shows the background level in the reaction

In Figure 4, the measured momentum distributions of the secondary protons produced in the reaction ${}^{12}\text{C}(p, p')X$ with the carbon nucleus at the scattering angles $\theta = 21^\circ$ (left panel) and $\theta = 24.5^\circ$ (right panel) are shown [12]. The calculated momenta of secondary protons in the elastic scattering of protons ${}^{12}\text{C}(p, p' \text{NCL})\text{NC}$ by nucleon clusters (NCLs) at rest (${}^9\text{Be}$, ${}^9\text{B}$, ${}^{10}\text{B}$ or ${}^8\text{Be}$) inside the carbon nucleus, where NC is the corresponding few-nucleon correlation (${}^3\text{He}$, ${}^3\text{H}$, ${}^2\text{H}$ or ${}^4\text{He}$), are marked in the figure by segments of the *red vertical dotted line*. A narrow peak is clearly visible in Fig. 4, *left panel* (*right panel*), in the momentum interval CL2. This peak at the transferred energy to the carbon nucleus $\omega = 15.6$ MeV ($\omega = 18.4$ MeV) and secondary proton momentum $K = 1\,658.8$ MeV/c ($K = 1\,648.2$ MeV/c) most likely corresponds to the quasielastic scattering ${}^{12}\text{C}(p, p' {}^8\text{Be}){}^4\text{He}$ on a ${}^8\text{Be}$ -like nucleon cluster inside the carbon nucleus. Note that the latter momenta almost coincide with the similar momenta for the case of the quasielastic scattering ${}^9\text{Be}(p, p' {}^8\text{Be})n$ on a ${}^8\text{Be}$ -like nucleon cluster (see Fig. 3). The secondary proton polarization in the reaction ${}^{12}\text{C}(p, p' {}^8\text{Be}){}^4\text{He}$ at the scattering angle of 21° was measured in a narrow momentum interval CL2 (Fig. 4, *left panel*). A value of this polarization ($P = 0.356 \pm 0.026$) is close to that in the reaction ${}^9\text{Be}(p, p' {}^8\text{Be})n$ reported above (Fig. 3, *left panel*).

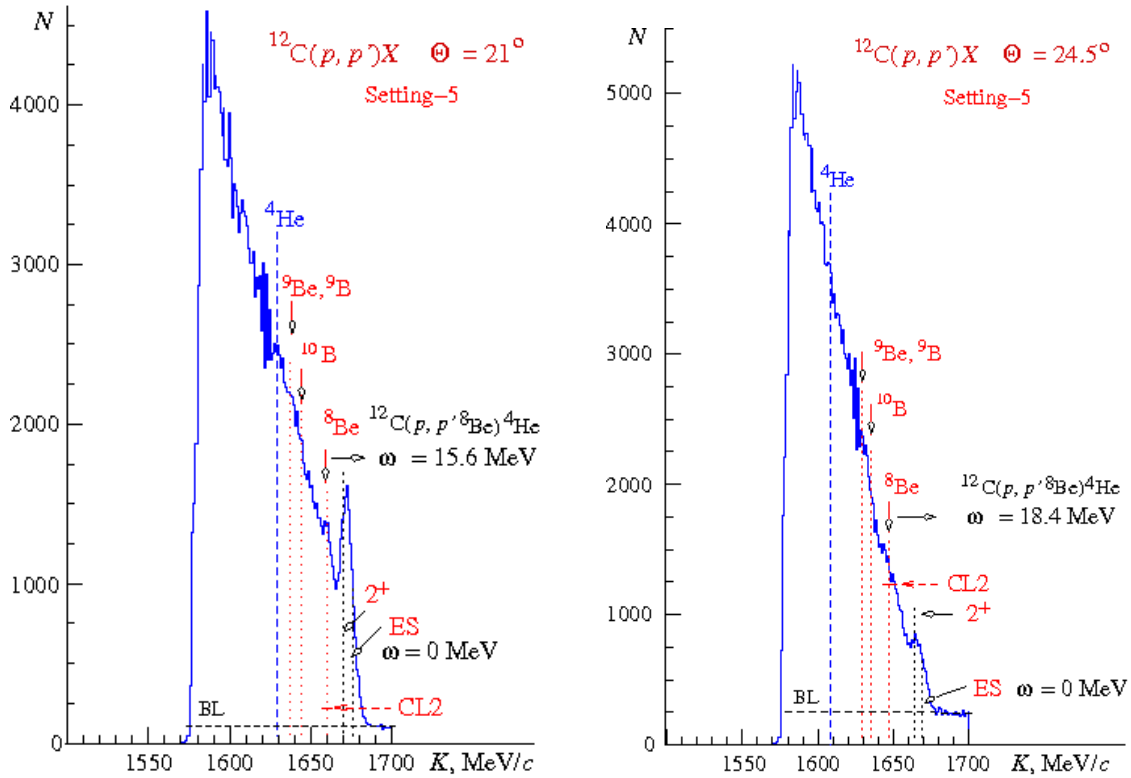


Fig. 4. Momentum distributions of protons scattered in the $^{12}\text{C}(p, p')X$ reaction at the angles of 21° (left panel) and 24.5° (right panel) [12] with the momenta from 1 585 to 1 700 MeV/c (Setting-5, the channel width in the distributions is equal to 1 MeV/c). The segment of the *blue vertical dashed line* indicates the calculated secondary proton momentum corresponding to the maximum of the quasielastic peak in scattering off an immovable ^4He -like correlation with a mass equal to the mass of the free ^4He nucleus. The segments of the *red vertical dotted line* are defined in the text. ω is defined in the caption to Fig. 3. The segments of the *black vertical dotted lines* correspond to elastic scattering by the ^{12}C nucleus in the ground state (ES) and in the excited state (2^+). A narrow momentum interval CL2 marked by the *red horizontal solid line* segment is defined in the text

3. Conclusion

We observe a structure in the momentum distribution of the secondary protons scattered in the inclusive (p, p') -reactions with the nuclei ^9Be and ^{12}C at the angles of 21° and 24.5° [10, 12]. We interpret this structure to be due to the proton elastic scattering on a ^8Be -like nucleon correlation inside the nuclei under study.

The secondary proton polarizations has been for the first time measured in the elastic $(p, p' \ ^8\text{Be})$ -reaction with the ^9Be and ^{12}C nuclei at the scattering angle of 21° [10–12]. The values of the polarizations are almost equal and amount to 0.366 ± 0.015 and 0.356 ± 0.026 , respectively.

All of the above confirms the model of the ^9Be nucleus, in which the nucleus consists of a compact core, similar to the ^8Be nucleus, and a weakly bound neutron (n) [13].

A list of participants of the present work:

G.M. Amalsky, V.A. Andreev, S.G. Barsov, G.V. Fedotov, V.V. Fedulov, G.E. Gavrilov, D.S. Ilyin, A.A. Izotov, A.Yu. Kisselev, N.G. Kozlenko, P.V. Kravchenko, D.A. Maysuzenko, O.V. Miklukho, V.A. Murzin, V.I. Murzin, D.V. Novinsky, A.V. Shvedchikov, V.A. Stepanov, S.S. Volkov, A.A. Zhdanov.

Acknowledgments

The authors of the paper are grateful to the staff of the PNPI 1 GeV proton accelerator for the stable beam operation and also to A.A. Vorobyov and S.L. Belostotski for their support of the work and fruitful discussions.

References

1. O.V. Miklukho, V.A. Andreev, A.A. Izotov *et al.*, PNPI. High Energy Physics Division. Main Scientific Activities 2013–2018, 290–297 (2019).
2. O.V. Miklukho, A.Yu. Kisselev, G.M. Amalsky *et al.*, e-Print: arXiv:1103.6113v1 [nucl-ex] (2011).
3. O.V. Miklukho, A.Yu. Kisselev, G.M. Amalsky *et al.*, JETP Lett. **102** (1), 11 (2015).
4. O.V. Miklukho, A.Yu. Kisselev, G.M. Amalsky *et al.*, Phys. Atom. Nucl. **80** (2), 299 (2017).
5. O.V. Miklukho, A.Yu. Kisselev, G.M. Amalsky *et al.*, Pis'ma v ZhETF **106** (2), 63 (2017).
6. O.V. Miklukho, A.Yu. Kisselev, G.M. Amalsky *et al.*, JETP Lett. **106** (2), 69 (2017).
7. O.V. Miklukho, A.Yu. Kisselev, G.M. Amalsky *et al.*, J. Phys.: Conf. Ser. **938**, 012013 (2018).
8. O.V. Miklukho, A.Yu. Kisselev, G.M. Amalsky *et al.*, Phys. Atom. Nucl. **81** (3), 320 (2018).
9. L. Frankfurt, M. Sargsian, M. Strikman, arXiv:0806.4412v2 [nucl-th] (2008).
10. O.V. Miklukho, A.Yu. Kisselev, G.M. Amalsky *et al.*, Phys. Atom. Nucl. **83** (3), 431 (2020).
11. G.M. Amalsky, V.A. Andreev, S.G. Barsov *et al.*, PNPI Scientific Highlights 2020, 62 (2021).
12. O.V. Miklukho, A.Yu. Kisselev, G.M. Amalsky *et al.*, e-Print: arXiv:2102.04109v1 [nucl-ex] (2021).
13. V. Chavchanidze, Usp. Fiz. Nauk **43** (1), 106 (1951) (in Russian).

μSR STUDIES OF MULTIFERROICS AND FERROFLUIDS AT THE NRC “KURCHATOV INSTITUTE” – PNPI

A.L. Getalov, E.N. Komarov, S.A. Kotov, G.V. Shcherbakov, S.I. Vorob'ev

1. μSR study of the dynamics of internal magnetic correlations in the Tb(Bi)MnO₃ multiferroic in magnetically ordered and paramagnetic states

A disk Tb_{0.95}Bi_{0.05}MnO₃ ceramic sample with a diameter of 35 mm and a thickness of 5 mm was fabricated for the study by solid phase synthesis. The X-ray diffraction analysis indicated that the sample was single-phase and characterized by the space group *Pbnm*. The composition of the sample was determined by the X-ray fluorescence method. The sample was examined at the μSR facility [1] located at the output of the muon channel of the synchrocyclotron at the PNPI (Gatchina, Russia). A muon beam with the mean momentum $p_\mu = 90$ MeV/*c* and the momentum dispersion $\Delta p_\mu/p_\mu = 0.02$ (FWHM) had the longitudinal polarization $P_\mu = 0.90$ – 0.95 . The sample under study was placed in a blowing thermostat, which allowed setting the temperature with an accuracy of about 0.1 K in the temperature range of 10–290 K. The external magnetic field on the sample was created by Helmholtz coils with a stability of about 10^{-3} . The nonuniformity of the magnetic field in the sample region was estimated on a copper sample. The low relaxation rate (0.0053 ± 0.0035) μs^{-1} of the polarization of muons stopped in the copper sample indicated that the magnetic field in the sample volume was quite uniform. The time spectra of the positrons from the decay of muons were measured simultaneously in two ranges (0–10 and 0–1.1 μs) with a channel width of 4.9 and 0.8 ns, respectively.

It is noted [2] that the relaxation function measured in the paramagnetic state in an external magnetic field in a temperature range of 70–150 K is split into two components with different relaxation types (Lorentzian and Gaussian) of the muon polarization on the internal local magnetic fields. Lorentzian relaxation is associated with the effect of local fields with high dynamics on the muon, when $\tau_c \ll t$, where τ_c is the correlation time of the magnetic moment of the muon with these fields and t is the measurement (observation) time. Here, the polarization relaxation rate is determined as $\lambda_1 = \sigma^2 \tau_c$, where σ is the parameter of the distribution of magnetic fields in the sample. In this case, the polarization relaxation function has a Gaussian form $\exp(-\sigma^2 \tau_c t) \equiv \exp(-\lambda_1 t)$. In the second case, where $\tau_c \geq t$, the relaxation function has the form $\exp(-\sigma^2 t^2) \equiv \exp(-(\lambda_2 t)^2)$.

Figure 1 demonstrates that the amplitudes of the muon spin precession a_1 and a_2 with relaxation rates λ_1 and λ_2 , respectively, in the temperature range of 80–150 K in the external magnetic field of $H = 290$ G are approximately equal to each other (each about 50%). This means that two types of sources of the local magnetic field with significantly different dynamics exist in approximately equal quantities in the sample in the external magnetic field in this temperature range. In the absence of the external magnetic field, all sources of the local magnetic field have the same dynamics (Fig. 2). The short-range magnetic order regions in the original crystal matrix containing Mn³⁺–Mn³⁺ ion pairs, as well as the phase separation regions containing Mn³⁺–Mn⁴⁺ ion pairs and electrons recharging them, can serve as sources of local internal magnetic fields in Tb_{0.95}Bi_{0.05}MnO₃ at 80–150 K. The character of correlations of the magnetic moment of the muon with the internal fields of these pairs in two phases depends on the temperature of the sample differently, and their responses to the applied magnetic field are different. The short-range magnetic order regions in the matrix of the original crystal have strong internal magnetic fields whose state weakly depends on a magnetic field of 290 G (see Figs. 3 and 2 for TbMnO₃ in Ref. [3]). The relaxation of the muon polarization in such regions has a Lorentzian shape. At the same time, ferromagnetic correlations are characteristic of the phase separation regions at all temperatures. At temperatures $80 \text{ K} < T < 150 \text{ K}$, the phase separation regions are isolated, and the ferromagnetic moments of Mn³⁺–Mn⁴⁺ ion pairs in zero field are disoriented. When the field $H = 290$ G is applied, these moments are oriented along the field. This strongly increases the probability of electron transfer between the phase separation regions in the case of their hopping conductivity by double charge exchange, increasing the correlation between them. Studies of the dielectric and magnetic properties of Tb_{0.95}Bi_{0.05}MnO₃ at these temperatures showed that the application of an external magnetic field led to residual long-term effects and temperature hysteresis of the states of local phase separation regions. The relaxation of the muon polarization in these regions has a Gaussian form. Thus, we can conclude that an external field of 290 G in

the temperature range of 80–150 K weakly affects the states of the short-range magnetic (mostly antiferromagnetic) order in the original matrix (which was typical of pure TbMnO_3 [3]) and significantly affects the phase separation regions with ferromagnetic correlations, which coexist in $\text{Tb}_{0.95}\text{Bi}_{0.05}\text{MnO}_3$ with the short-range order regions in equal ratios (see Fig. 1). Consequently, Mn^{3+} and Mn^{4+} ions constitute fractions of 3/4 and 1/4, respectively, in $\text{Tb}_{0.95}\text{Bi}_{0.05}\text{MnO}_3$ in the ideal variant when the phase separation regions contain only $\text{Mn}^{3+}\text{--Mn}^{4+}$ ion pairs and the original matrix contains only Mn^{3+} ions. As mentioned above, the phase separation regions are formed near Bi^{3+} ions substituting Tb^{3+} ions. Bi^{3+} ions, which are large and contain separated pairs of $6s^2$ electrons, are responsible for structural distortions not only in the immediate environment. In this case, Mn^{4+} ions can substitute Mn^{3+} ions on a length of several lattice constants. Correspondingly, the number of appearing Mn^{4+} ions can significantly exceed the concentration of Bi^{3+} ions (5%).

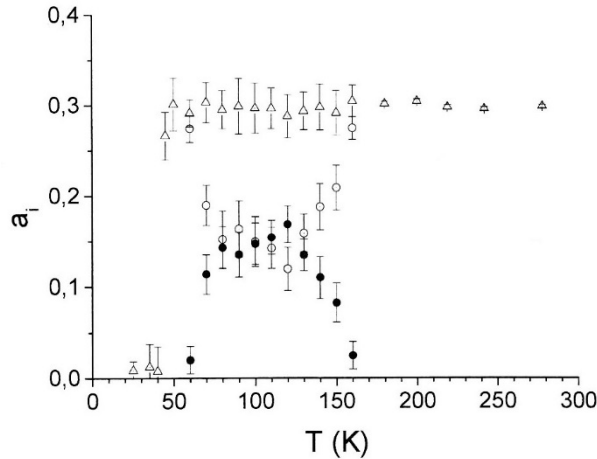


Fig. 1. Temperature dependences of the partial amplitudes of the muon spin precession in a magnetic field of $H = 290$ G. Open and closed circles are the amplitudes a_1 and a_2 for the phases described by Lorentzian and Gaussian relaxations, and open triangles are $a_1 + a_2$ for $T \leq 160$ K and a_F for $T > 160$ K

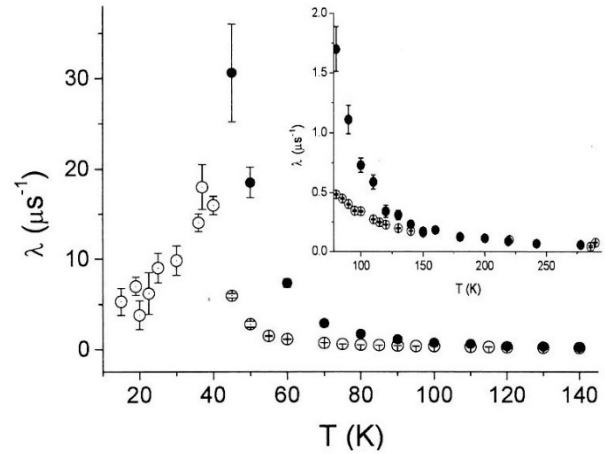


Fig. 2. Temperature dependence of the relaxation rates of the muon polarization (open circles) λ_s in zero magnetic field and (closed circles) λ_F in a magnetic field of $H = 290$ G

Structural distortions caused by Bi^{3+} ions and by the partial substitution of Mn^{4+} ions for Mn^{3+} ions also occur in the phase separation regions in the temperature range $80 \text{ K} < T < 150 \text{ K}$. It is noteworthy that changes in the lattice parameters were observed in $\text{Tb}_{0.95}\text{Bi}_{0.05}\text{MnO}_3$ single crystals in neutron diffraction studies [4] in this temperature range.

It is important to note that the sum of the partial amplitudes $a_1 + a_2$ is equal to a_F for all the temperatures of the studied sample above the Néel temperature (Fig. 3). This indicates that no other relaxation channels of polarization than those indicated above exist in the temperature range $80 \text{ K} < T < 150 \text{ K}$.

In the region of critical fluctuations, in the temperature range $40 \text{ K} < T < 70 \text{ K}$, the frequencies of the muon spin precession (Fig. 4), as well as the polarization relaxation rates (Fig. 5), increase noticeably for both phases: the short-range order regions of the original matrix, which are weakly sensitive to the field H , and the phase separation regions, which are oriented by the magnetic field. In Figures 3 and 2, the asymmetry parameter a_s and the relaxation rate λ_s (at $H = 0$) refer to the short-range order regions, whereas the parameters a_F and λ_F (at $H = 290$ G) refer to the phase separation regions.

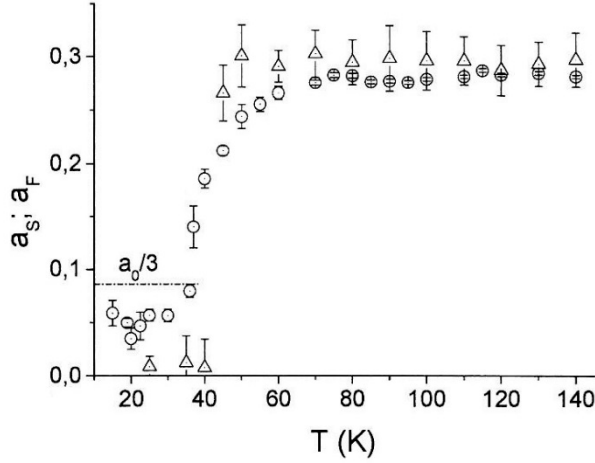


Fig. 3. Temperature dependence of asymmetries (*open circles*) a_s and (*closed circles*) a_F in a magnetic field of $H = 290$ G

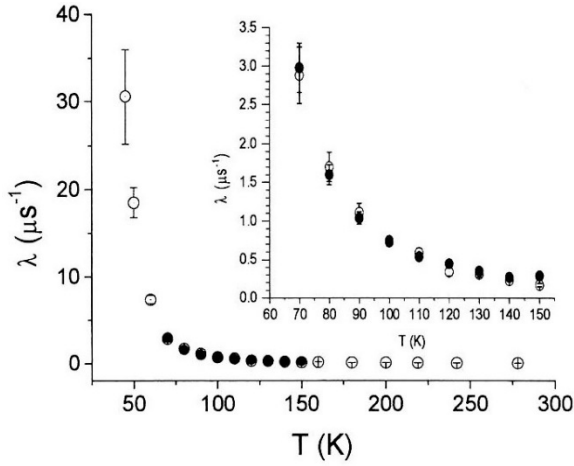


Fig. 4. Temperature dependence of the frequencies of the muon spin precession (*open circles*) F_1 and (*closed circles*) F_2 in a magnetic field of $H = 290$ G

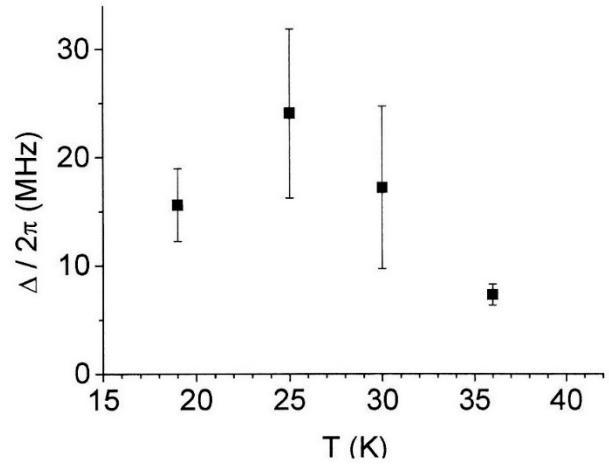


Fig. 5. Temperature dependence of the relaxation rates of the muon polarization (*open circles*) λ_1 and (*closed circles*) λ_2 in a magnetic field of $H = 290$ G

A comparative analysis of the temperature dependence of the parameters λ_s and λ_F (see Fig. 2) shows that these parameters are the same in the temperature range of 150–290 K, and the difference between them appears below $T = 150$ K. The difference $\lambda_F - \lambda_s$ increases with a decrease in the sample temperature (see Fig. 2). This can be due to the effect of the external magnetic field on the dynamics of the sources of local magnetic fields. Weakening of the dynamics of local fields leads to an increase in τ_c , which in turn increases λ_F . Note that the weakening of the dynamics in the applied magnetic field refers to both phase separation regions and short-range order regions. First, the formation of one-dimensional superlattices with ferromagnetic layers begins when the temperature approaches 70 K; these superlattices also exist at $T < T_N$. Second, the short-range order regions are enlarged and their properties approach those observed in TbMnO_3 at $T < T_N$ [3].

A magnetically disordered state occurs in the $\text{Tb}_{0.95}\text{Bi}_{0.05}\text{MnO}_3$ sample below the temperature $T_N = 40$ K. The asymmetry a_s observed in zero field was significantly lower than the expected value of $a_0/3$ (see Fig. 3). Muons lose polarization; we attribute this process to the appearance of an additional rapid muon depolarization channel. A rapidly relaxing muonium atom $\text{Mu} = \mu^+e^-$ is formed when the muon stops near $\text{Mn}^{3+}\text{--Mn}^{4+}$ pairs between which e_g electrons are transferred at the double exchange. In this case, muons bind these electrons, forming Mu atoms. The polarization of such muons relaxes in a time less than the time resolution of the facility. Thus, the loss of polarization occurs when muons stop in the phase separation regions. This effect was previously observed in RMn_2O_5 samples [5–7], which are characterized by the formation of phase separation regions. The qualitative difference in the relaxation of muon polarization in the phase separation regions in magnetically disordered and paramagnetic (in the applied magnetic field) states is remarkable. At $T < 40$ K,

the phase separation regions are one-dimensional superlattices, where the tunneling conduction mechanism prevails and e_g electrons are predominantly concentrated within these phase separation regions.

In this case, the probability of formation of rapidly relaxing muonium atoms is maximal, which leads to the loss of polarization. The hopping conduction between the isolated phase separation regions oriented by the magnetic field prevails in the temperature range of 80–150 K. This increases the correlation between these regions through the double exchange, significantly slowing the relaxation of muon polarization.

A muon channel of polarization relaxation of a different nature occurs when muons stop near pairs of the same valence manganese ions ($\text{Mn}^{3+}\text{--M}^{3+}$) in the original $\text{Tb}_{0.95}\text{Bi}_{0.05}\text{MnO}_3$ matrix. The muon alternately interacts with two e_g electrons of these ions, whose spins make an angle of $\Theta = 0.28\pi$.

The double exchange between neighbouring $\text{Mn}^{3+}\text{--M}^{3+}$ ions ($J_{\text{de}} = t \cos(\Theta/2)$) is weakened slightly in the cycloid compared to the ferromagnetic state ($\cos(\Theta/2) \approx 0.9$), and a quasimuonium can be formed. The characteristic frequency for the double exchange with $J_{\text{de}} \approx 270$ MeV is $\nu = 6.6 \cdot 10^{13}$ Hz. The hyperfine splitting frequency in the free muonium atom is $\nu_0 = \omega_0/2\pi \approx 4.46 \cdot 10^9$ Hz. In the case of a fast exchange, when, the hyperfine bond in the muonium is broken; the direct interaction of the muon spins with the internal magnetic fields of the cycloid appears. The high frequency of reorientation of the e_g electron spins at the appearance and disappearance of the hyperfine interaction in the muonium leads to the exponential relaxation of the longitudinal polarization of muons. The following expression was obtained for the relaxation rate λ_s of the longitudinal component at $\nu \gg \nu_0$:

$$\lambda_s = (\omega_0^*)^2/4\nu, \quad (1)$$

where ω_0^* is the hyperfine splitting frequency of the muonium in the medium and ν is the frequency of reorientation of the electron spin in the muonium.

Figure 2 demonstrates that the relaxation rate λ_s decreases from 15 to 5 μs^{-1} as the temperature decreases in the temperature range of the magnetically ordered state of the sample. This corresponds to a change in the exchange frequency from $1.2 \cdot 10^{13}$ to $3.6 \cdot 10^{13}$ Hz (the characteristic double-exchange frequency is $\nu = 6.6 \cdot 10^{13}$ Hz). A calculation by Eq. (1) was performed under the assumption that $\omega_0^* = \omega_0$, while the hyperfine splitting frequency of the muonium in the medium can be less than that in the vacuum ($\omega_0^* \leq \omega_0$). A similar mechanism of the relaxation of muon polarization was observed in TbMnO_3 [3] in a magnetically disordered state and in the temperature range of the existence of short-range magnetic order regions. This depolarization mechanism is observed in about 50% of muons stopped in the $\text{Tb}_{0.95}\text{Bi}_{0.05}\text{MnO}_3$ sample (see Fig. 3). The second half of the muons relax in the phase separation regions with loss of polarization.

The muon spin precession frequency is observed in the transverse component of the relaxation function in the local fields of the cycloid with a large standard deviation (Figs. 6 and 7). As the temperature decreases, the frequency increases, and the standard deviation remains quite large and hardly changes in the entire temperature range below the temperature T_N .

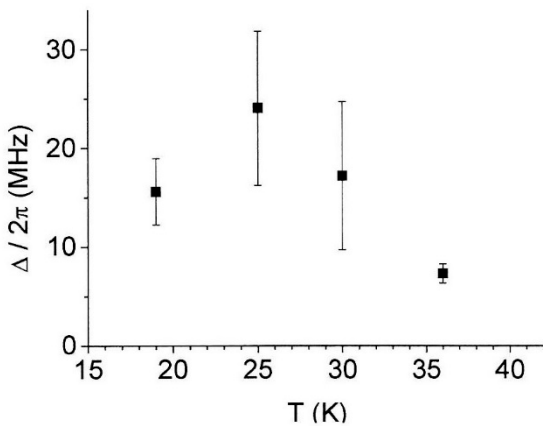


Fig. 6. Temperature dependence of the standard deviation Δ in a zero magnetic field

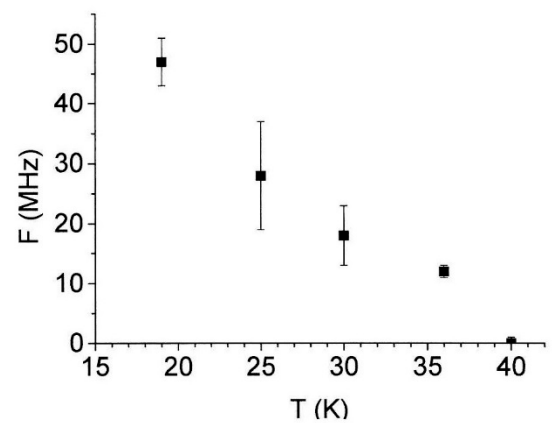


Fig. 7. Temperature dependence of the muon spin precession

The μ SR study of the $\text{Tb}_{0.95}\text{Bi}_{0.05}\text{MnO}_3$ multiferroic has revealed a number of features that were not observed in the study of other multiferroic manganites, including TbMnO_3 . In particular, the sample subjected to a weak magnetic field of about 300 G is separated into two fractions in the dynamics of internal magnetic correlations in the temperature range of 80–150 K. In one fraction (50% of the sample) attributed to the phase separation regions, the lifetime of correlations exceeds the measurement time (10 μ s). The phase separation is caused by the appearance of Mn^{3+} and Mn^{4+} ions in the sample doped with Bi^{3+} ions. The second fraction in the same temperature range is formed by the Mn^{3+} – Mn^{3+} correlations in the short-range magnetic order regions in the matrix of the original crystal, which is weakly sensitive to a magnetic field of 290 G. This state was observed previously in TbMnO_3 .

Two muonium relaxation channels of the muon polarization have been observed in the temperature range $T < T_N = 40$ K of the magnetically disordered state. The first channel is associated with the formation of muon ferromagnetic complexes (Mn^{3+} – Mu – Mn^{4+}) in the phase separation regions. In these complexes, the muon loses polarization due to the hyperfine interaction in the muonium in a time less than 10^{-8} s. The second channel is caused by the formation of quasimuonium with the broken hyperfine bond in the original matrix of the sample. In this case, the polarization relaxation rate is high, but the muon remains quasi-free when interacting with the local magnetic fields of the cycloid. The contributions to the depolarization of muons in these two channels are approximately the same.

2. μ SR study of a 3% CoFe_2O_4 nanoparticle concentration ferrofluid

In studies of CoFe_2O_4 nanoparticles, a ferrofluid sample composed of a 3% volume concentration of magnetic nanoparticles in water, stabilized using sodium dodecyl sulfate, $\text{CH}_3(\text{CH}_2)_{11}\text{SO}_4\text{Na}$, with a density of $\rho = 1.01$ g/cm³, and lauric acid, $\text{C}_{11}\text{H}_{23}\text{COOH}$, with a density of $\rho = 0.88$ g/cm³, was used as a double surfactant layer. One milliliter of ferrofluid contained 0.17 g of cobalt ferrite, and for every 1 g of CoFe_2O_4 nanoparticles, 0.25 g of surfactant was used.

The investigated sample was synthesized at the Institute of Technical Chemistry of the Ural Branch of the Russian Academy of Sciences. Preliminarily, a double separation of nanoparticles by the size was carried out with a Biofuge 15R centrifuge for 60 min at 6 000 rpm. The particle size distribution was studied at the Centre for Advanced Technologies (Moscow State University, www.nanoscopy.ru) using a LEO 912 AB OMEGA high-resolution transmission electron microscope with an accelerating voltage of 120 kV. The size distribution of nanoparticles was approximated by a lognormal distribution function, and the following parameter values were determined: $D_0 = 7.8 \pm 0.1$ nm, $\sigma = 0.40 \pm 0.01$ nm, with the mathematical expectation value of $\overline{D} = D_0 \exp(\sigma^2 / 2) = 8.5$ nm.

The sample was studied using the μ SR set-up [1]. The principles of μ SR and the use of various relaxation (depolarization) functions of the muon spins to describe the time spectra of the μ SR signals are presented in the studies which have become references in the field. At this facility, we have previously conducted studies of ferrofluids based on Fe_3O_4 [8]. A beam of positively charged muons with an average momentum $p_\mu = 90$ MeV/c and the momentum dispersion $\Delta p_\mu / p_\mu = 0.02$ (FWHM) had a longitudinal polarization $P_\mu = 0.90$ – 0.95 . The ferrofluid sample, packed in a copper cell 80 mm in diameter and 10 mm in height, was placed in a blowdown cryostat, which made it possible to set the temperature with an accuracy of ~ 0.1 K in the temperature range 10–290 K. The time spectra of the positrons from the muons decay were measured simultaneously in two ranges (0–10 and 0–1.1 μ s) with the channel widths of 4.9 and 0.8 ns, respectively.

The measurement procedure consisted of cooling the sample in a zero external magnetic field (ZFC) to a temperature of 25 K [9]. After that, a magnetic field of 527 G, transverse to the magnetic moment of the muon, was switched on, and ZFC measurements were recorded as the sample was heated to room temperature (290 K). Then, the sample was again cooled to a temperature of 30 K in the same transverse magnetic field of 527 G, and FC measurements were performed.

The experimental data (time spectra) were approximated using the function

$$N(t) = N_0 \exp(-t / \tau_\mu) [1 + a_s G_s(t) + a_b G_b(t)] + B, \quad (2)$$

where N_0 is a normalization constant, τ_μ is the muon lifetime (2.197 μs), B is the background of random coincidences, determined by the form of the time spectrum in the part before the beginning t_0 of the decay spectrum, a_s and $G_s(t)$ are the asymmetry and relaxation functions of the observed muon component of the muon spin precession in the sample, respectively. The term $a_b G_b(t)$ corresponds to the contribution of the constructive background to the observed asymmetry. The constructive background itself is mainly associated with the decay of muons stopped in the copper walls of the container with ferrofluid, and its contribution can be described as follows:

$$a_b G_b(t) = a_b \cdot \cos(2\pi F_b t) \cdot \exp(-\lambda_b t). \quad (3)$$

The parameters F_b and λ_b , the precession frequency and the relaxation rate, respectively, are determined from the processing of the time spectrum measured on a copper sample. The a_b parameter was obtained from the joint processing of two spectra measured on the ferrofluid sample in an external magnetic field ($H \neq 0$) and in a zero magnetic field ($H = 0$):

$$a_s G_s(t) = a_H \cdot \cos(2\pi F_H t) \cdot \exp(-\lambda_H t) + a_L \cdot \cos(2\pi F_L t) \cdot \exp(-\lambda_L t) \text{ for } H \neq 0, \quad (4)$$

$$a_s G_s(t) = a_1 \cdot \exp(-\lambda_H t) + a_2 \cdot \exp(-\lambda_L t) \text{ for } H = 0, \quad (5)$$

In this case, the following requirement is imposed:

$$a_1 + a_2 = a_H + a_L. \quad (6)$$

The amplitude a_2 of a weakly damped exponent is chosen as a_b .

The indices (H, L) on the parameters (a, λ) correspond to the observed frequencies of the precession of the muon spin F_H and F_L , where $F_H > F_{Cu} > F_L$. The value F_{Cu} corresponds to the rotation frequency of the muon spin in the pure copper sample. Using the relaxation function (Eq. (2)), and taking into account Eqs. (3) and (4), made it possible to accurately describe the experimental data of FC and ZFC measurements in a wide temperature range of the samples. In the temperature range of 26–100 K, the time spectra obtained in ZFC measurements are fairly well described using the following single-frequency relaxation function:

$$a_s G_s(t) = a_H \cdot \cos(2\pi F_H t) \exp(-\lambda_H t). \quad (7)$$

Even in the absence of an external magnetic field, μ^+ will precess around the internal dipolar field. At a sample temperature of 290 K, two measurements were performed in a zero external magnetic field. One measurement was performed before turning on the external field, as at $T = 41$ K, and the second one was carried out immediately after turning on the magnetic field with a value of $H = 527$ G. In both measurements, the relaxation functions did not differ from each other within the error limits.

Figure 8 displays the behaviour of the relaxation function $G(t)$ at sample temperatures of 290 and 41 K in a zero external magnetic field. This indicated that the external magnetic field did not lead to the spatial displacement of nanoparticles.

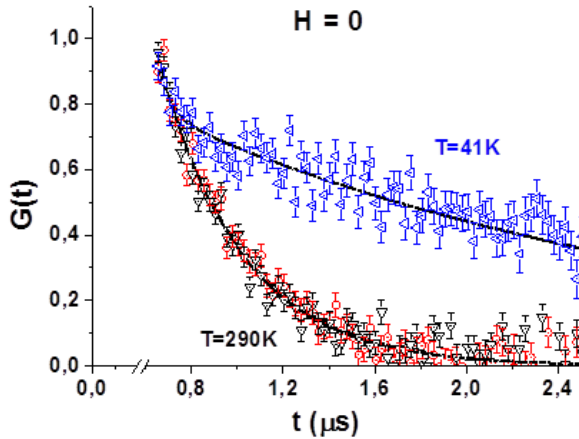


Fig. 8. Relaxation function $G(t)$ in a magnetic field $H = 0$ at $T = 41$ K (blue triangles) and $T = 290$ K (light red dots and squares)

The relaxation function at a temperature of 41 K had two components, which sharply differed in terms of the decay rates $\lambda_1 = 0.41 \pm 0.02 \mu\text{s}^{-1}$ and $\lambda_2 = 23 \pm 11 \mu\text{s}^{-1}$. The rapidly decaying component was apparently associated with the presence of muon stops in the near zone of the scattered fields of nanoparticles, where the inhomogeneity of the magnetic field was high. The separation of the sample volume into near and far zones occurred only at low temperatures when the rotation or oscillation of nanoparticles stopped. At a temperature of 290 K, the entire sample volume was homogeneous in terms of the relaxation rate. This behaviour of the relaxation functions was associated with the presence of a significant anisotropy of the magnetic properties of the nanoparticle itself.

Further, the sample was measured at room temperature with magnetic field values in the range of up to ~ 600 G. Figures 9–11 demonstrate the behaviour of the frequencies, decomposition rates, and populations as functions of the external magnetic field at the sample temperature of 290 K.

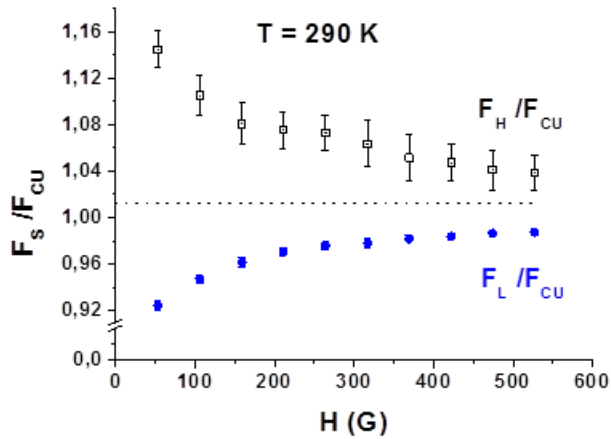


Fig. 9. Dependence of the precession frequencies of the muon spin F_s ($s = H, L$) in the sample on the external magnetic field at a temperature of 290 K (F_H – light points; F_L – dark blue points)

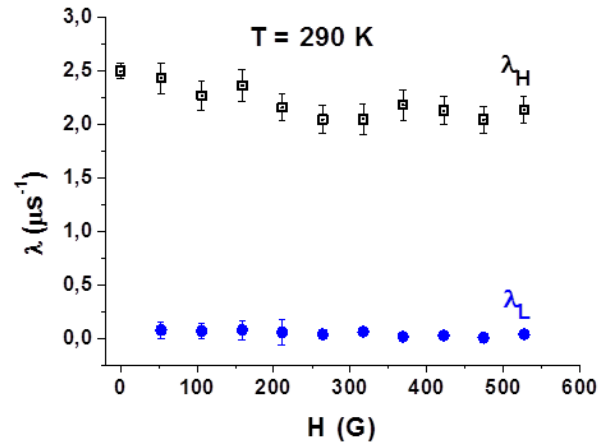


Fig. 10. Dependence of the muon relaxation rates on the magnitude of the external magnetic field at a temperature of 290 K (λ_H – light squares; λ_L – dark blue points)

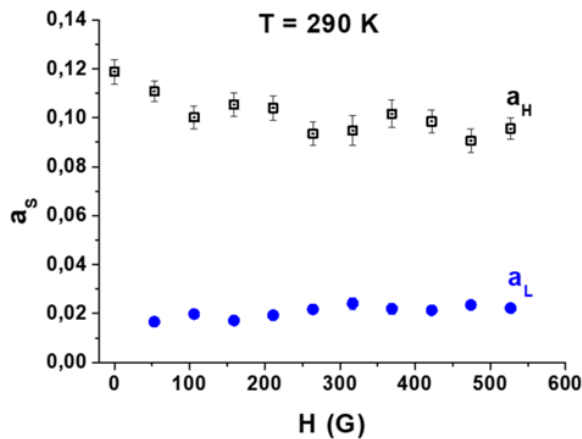


Fig. 11. Dependence of the amplitudes of the muon spin precession (populations) on the external magnetic field at a temperature of 290 K (a_H – light points; a_L – dark blue points)

For all external magnetic fields in the range of 50–527 G, the sample under study exhibited muon spin precession at two frequencies, F_H and F_L , in the order $F_H > F_{Cu} > F_L$ (see Fig. 9). The value F_{Cu} corresponds to the rotation frequency of the muon spin in the pure copper sample.

Additional magnetization was observed in 80% of the sample volume (see Fig. 11), which, at room temperature (~ 300 K), corresponded to an additional $\Delta H = 20 \pm 1$ G, when the external magnetic field was more than 300 G (see Fig. 9). In addition, there was a much less noticeable diamagnetic contribution $\Delta H = 6.7 \pm 0.2$ G in 20% of the sample volume (see Figs. 9 and 11). The relaxation rates λ_H and λ_L , as well as the populations a_H and a_L , practically do not depend on the value of the external magnetic field (Figs. 10

and 4). The values of λ_L in Fig. 10 are in the range of 0.09–0.12. The behaviour of systems with nanoparticles depends on the conditions in which they were cooled. At the FC procedure, the sample is cooled in the magnetic field, whereas the ZFC sample is cooled first in the absence of magnetic field and then the magnetic field is switched on. Figs. 12–15 present the results of processing the time spectra measured on a ferrofluid sample in an external magnetic field $H = 527$ G in the sample temperature range of 26 to 290 K. In the FC measurement mode, two muon spin precession frequencies, F_H and F_L , were observed over the entire temperature range (see Fig. 12).

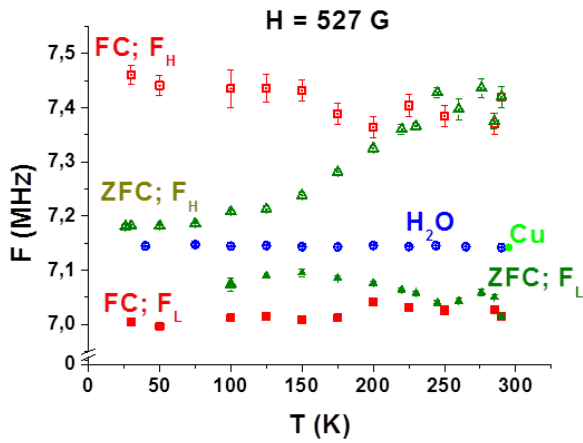


Fig. 12. Temperature dependence of the muon spin precession frequencies in a magnetic field of $H = 527$ G (FC mode: a_H – light red squares; a_L – dark red squares. ZFC mode: a_H – light olive triangles; a_L – dark olive triangles. H_2O – light blue points; Cu – dark green dot)

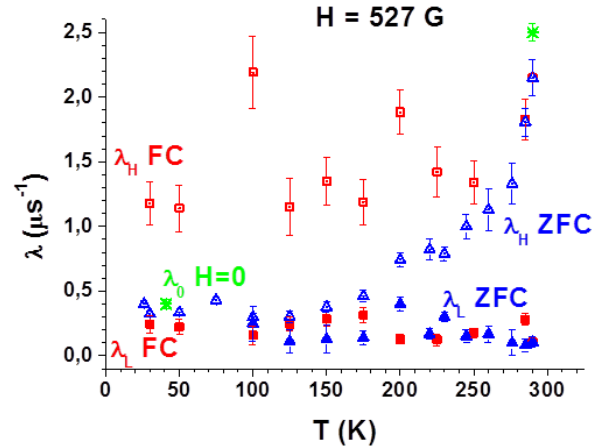


Fig. 13. Temperature dependence of the relaxation rates of muon polarization, λ_H and λ_L , in a magnetic field $H = 527$ G (FC mode: λ_H – light red squares; λ_L – dark red squares. ZFC mode: λ_H – light blue triangles; λ_L – dark blue triangles; λ_0 in $H = 0$ (green star))

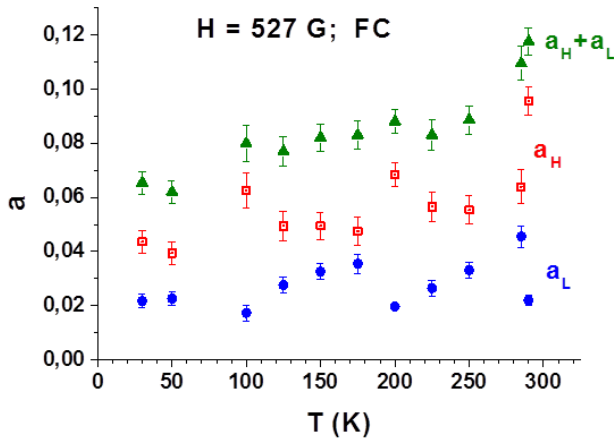


Fig. 14. Temperature dependence of the populations of the upper F_H and lower F_L frequencies in a magnetic field $H = 527$ G in the FC mode (a_H – light red squares; a_L – dark blue dots; and $a_H + a_L$ – dark olive triangles)

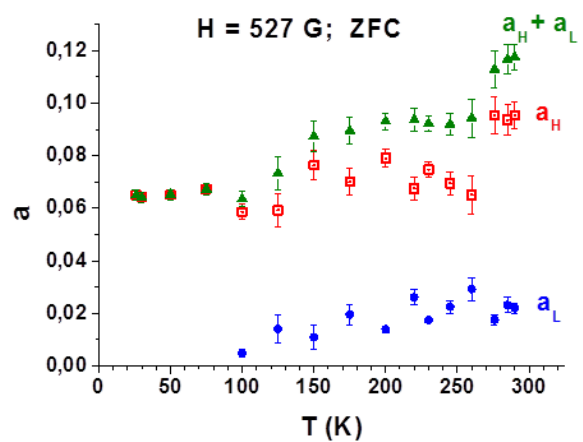


Fig. 15. Temperature dependence of the populations of the upper F_H and lower F_L frequencies in a magnetic field $H = 527$ G in the ZFC mode (a_H – light red squares; a_L – dark blue dots; and $a_H + a_L$ – dark olive triangles)

In the ZFC measurement mode, in the temperature range of 26–100 K, only one precession frequency of the muon spin was observed. With an increase in the sample temperature, starting from $T = 100$ K, two muon spin precession frequencies, F_H and F_L , appeared; moreover, the F_H frequency began to increase noticeably. For comparison, the same figure (see Fig. 12) shows the behaviour of the precession frequency of muons in a sample of H_2O and Cu . The relationship $F_H > F_{Cu, H_2O} > F_L$ is maintained throughout the entire temperature regime.

Figure 13 shows the behaviour of the parameters λ_H , λ_L and λ_0 in the sample temperature range of 26 to 290 K. Here, λ_0 is the relaxation rate of muon polarization in a zero external magnetic field. A noticeable difference of the parameter λ_0 at $T = 290$ K from the value at $T = 41$ K is associated with the dynamics of nanoparticles in the medium at $T = 290$ K. In the FC measurement mode, the values of λ_H and λ_L were practically independent within the error limits at the sample temperature. In the ZFC measurement mode in the temperature range 26–125 K, $\lambda_H \approx \lambda_0$ (see Fig. 13). At these temperatures, the sample behaviour was paramagnetic (see Fig. 12 and 13). With a further increase of the sample temperature, the parameter λ_H began to increase noticeably, and was practically comparable with the value of λ_0 at $T = 290$ K.

Figures 14 and 15 display the behaviour of the populations of the upper F_H and lower F_L frequencies (a_H and a_L) versus the sample temperature in FC and ZFC measurements.

A significant excess of a_H over a_L was observed over the entire temperature range. This difference was especially large at room temperature, when the solution was a real ferrofluid, and not ice. Definite structures of the temperature dependence of the quantities a_H and a_L were observed in FC measurements.

The sum of the partial amplitudes at all temperature points was almost 20% less than the amplitude of the precession obtained in water (H_2O), Fig. 16. This difference can be explained by the fact that some of the muons stop in places with large inhomogeneity in the field. This leads to their rapid depolarization, and the oscillation of their spins is not observed. The behaviour of positive muons in water was well studied previously. Nevertheless, we conducted our own measurements in our cryostat for confirmation.

The relaxation function $G(t)$ for the sum of spectra in the temperature range 26–100 K, obtained in the ZFC mode in an external magnetic field $H = 527$ G, and its satisfactory fitting curve obtained within the framework of the two-frequency hypothesis presented in Eq. (4), are depicted in Fig. 17.

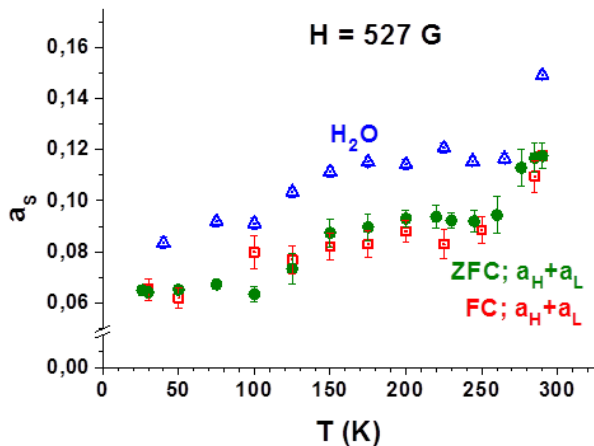


Fig. 16. Temperature dependences of the fraction of the asymmetry of the muon component in a transverse magnetic field $H = 527$ G in the FC mode ($a_H + a_L$ – open red squares), in the ZFC mode ($a_H + a_L$ – dark olive points) and for the water sample (H_2O – light blue triangles)

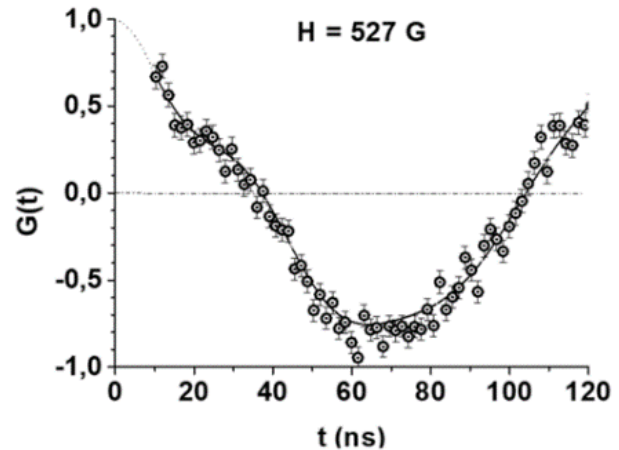


Fig. 17. Function $G(t)$ in the ZFC mode in an external magnetic field $H = 527$ G; the spectra are added at temperatures from 26 to 100 K

Therefore, in addition to the main contribution characterized by the amplitude $a_L = 0.099 \pm 0.001$, the relaxation rate $\lambda_L = 0.35 \pm 0.03 \mu s^{-1}$, and the frequency $F_L = 7.167 \pm 0.002$ MHz, corresponding to a magnetic field value of $H = 528.76 \pm 0.14$ G, a small supplementary contribution is determined with the parameters $a_H = 0.027 \pm 0.007$, $\lambda_H = 24 \pm 6 \mu s^{-1}$, and $F_H = 26.5 \pm 0.6$ MHz, corresponding to a magnetic field value of $H = 1.96 \pm 0.44$ kG. This contribution is associated with the muon stopping in the immediate vicinity of nanoparticles and inside nanoparticles. Thus, a direct measurement of the magnetization of the nanoscale object was carried out.

In conclusion, a muon spectroscopy study of a ferrofluid with a 3% volume concentration of $CoFe_2O_4$ magnetic nanoparticles dispersed in H_2O has been reported. New information on the magnetic properties of the system has been determined or confirmed using a new method. It has been shown that the structure and the

value of the magnetization of a ferrofluid with CoFe_2O_4 nanoparticles depend on the viscosity of the liquid itself. At room temperature (~ 290 K), when the sample was a superparamagnetic system, from the experimentally determined magnetization an average magnetic field of 20 G was obtained. A small fraction of the sample with negative magnetization, characteristic for diamagnetic systems, has been also determined. At low temperatures (~ 30 K), the sample exhibits paramagnetic behaviour in a magnetic field. The magnetic field inside and in the immediate vicinity of the CoFe_2O_4 nanoparticles was first measured by the μSR method, and its value is $B = 1.96 \pm 0.44$ kG.

References

1. S.G. Barsov, S.I. Vorob'ev, V.P. Koptev *et al.*, *Instrum. Exp. Tech.* **50**, 750 (2007).
2. S.I. Vorob'ev, A.L. Getalov, E.I. Golovenchits *et al.*, *JETP Lett.* **110**, 133 (2019).
3. D.S. Andrievskii, S.I. Vorob'ev, A.L. Getalov *et al.*, *JETP Lett.* **106**, 295 (2017).
4. I.V. Golosovsky, A.A. Mukhin, V.Yu. Ivanov *et al.*, *Eur. Phys. J. B* **85**, 103 (2012).
5. S.I. Vorob'ev, E.I. Golovenchits, V.P. Koptev *et al.*, *JETP Lett.* **91**, 512 (2010).
6. S.I. Vorob'ev, A.L. Getalov, E.I. Golovenchits *et al.*, *Phys. Solid State* **55**, 466 (2013).
7. S.I. Vorob'ev, D.S. Andrievskii, S.G. Barsov *et al.*, *J. Exp. Theor. Phys.* **123**, 1017 (2016).
8. M. Balasoiu, S.G. Barsov, D. Bica *et al.*, *JETP Lett.* **88**, 210 (2008).
9. S.I. Vorob'ev, M. Balasoiu, D. Buzatu *et al.*, *Magnetochemistry* **7**, 104 (2021).

LABORATORY BALL LIGHTNING–PLASMOID – NEW TYPE OF THE GAS DISCHARGE

G.D. Shabanov, A.G. Krivshich

1. Introduction

For several decades, the mystery of the mechanism of ball lightning (BL) formation excited the minds of numerous researchers, pushing them to put forward various hypotheses, which were extremely difficult to prove experimentally due to impossibility to generate a BL and to perform its systematic investigation in the laboratory conditions. Therefore, a mass interview of eyewitnesses became the main source of information on this natural phenomenon. The systematization and analysis of subjective evidence, rich in conjectures and fantasies, have given rise to many hypotheses regarding its nature. Thanks to some researchers, the most general features inherent in the original BL have become known.

Several major steps were taken in the study of the nature of BL:

- A review with almost 1 900 references on natural BL was presented in a monograph by J.D. Barry [1];
- I.P. Stakhanov collected about 2 000 different observations of the natural BL using a special technique and subjected these data of various observations to critical analysis and built a picture of this natural phenomenon [2, 3];
- B.M. Smirnov, using more of observational material, constructed an average observational model of the natural BL [4];
- A undoubted contribution to understanding of the mechanism of the natural BL formation was a significant improvement in the ideas about atmospheric electricity, namely, about the mechanisms of existence of the linear lightning leader channel [5–7].

Considering the improbability that scientific equipment can be applied to the natural BL, we took the path of creating a gas discharge in the laboratory that has the properties of the natural BL.

More than 20 years ago (in 2000 year), an experimental facility was constructed at the PNPI that allows generating a new type of the gas discharge – “plasmoids”, which outwardly resemble the natural BL. These luminous spherical objects, formed with the help of this set-up, we (participants of this article) called the Laboratory Ball Lightning–Plasmoid or “LBL–P”. It is fundamentally important that the reproduction efficiency of the “LBL–P” is about 100%. With the help of this set-up, more than 3 000 “plasmoids” were generated and a systematic analysis of their physical properties was carried out. The results obtained are presented in our publications in scientific journals, which became possible after the discovery and careful study of this new type of the gas discharge [7–24]. So, the set-up design can be assembled according to its description [9–14]. A comparison of the physical properties of the LBL–P with the natural BL and the main hypotheses of the natural BL are presented in Refs. [11–13, 15–16, 22–24].

It is important to note that over the past 10–15 years, many experimental groups (from Europe, the USA, China, *etc.*) created experimental set-ups for investigation of the “Gatchina Gas Discharge” in detail, applying their own diagnostic methods, including high resolution emission spectroscopy, various plasma probes, schlieren-images, *etc.* This long-term interest around the world is associated with the similarity of the LBL–P with the natural BL. We would like to note only some of them [23–40], covering 2007–2021. For example, researchers from the Max Planck Institute for Plasma Physics and the Humboldt University of Berlin reproduced under laboratory conditions the formation of a BL (plasmoid) according to the Gatchina method. Plasmoids have a low intrinsic temperature and do not even ignite the brought paper. Gerd Fußmann refers to the achievements of the research group from Gatchina, which, in his opinion, turned out to be much closer to reproducing the phenomenon observed in their natural conditions than the Israelis. Moreover, it were the Gatchina experiments that inspired the German group to conduct its own research [25–26].

Having considered the mechanisms necessary for the formation and existence of a natural BL, we were convinced that it is an analogue of the natural BL that is observed in our laboratory. We believe that the phenomenon of the BL is quite complex and requires further study. Therefore, we are trying to describe only general features of the phenomenon and do not pretend to a complete understanding of this process. Our goal is to show the relationship between the main factors that determine the formation of the LBL–P and its development.

The main objectives of this article are the following:

- We describe an experimental set-up that can generate an LBL-P in the laboratory and allows its systematic studies;
- We present experimental data illustrating some properties of the new type of the gas discharge – the “plasmoid”, or LBL-P.

2. Experimental set-up to generate the LBL-P discharge

The layout of the PNPI experimental facility is shown in Fig. 1.

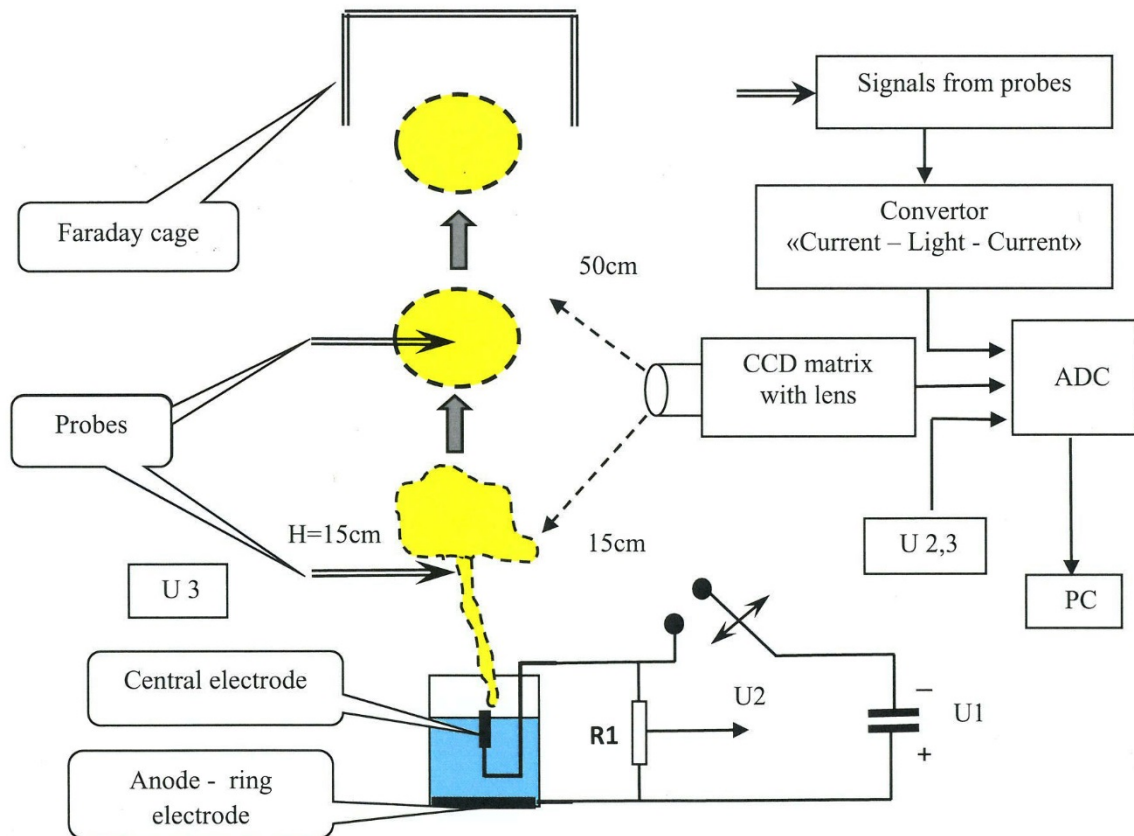


Fig. 1. Block-scheme of the experimental set-up. The yellow object is an LBL-P

The set-up is based on a capacitor bank with a capacity of 0.6 mF, which can be charged up to the voltage of 5.5–6.0 kV. In this case, the amount of electricity involved in the discharge is roughly one or two orders of magnitude smaller than that in the natural phenomenon, but at the same time the consequences of random breakdowns are less disastrous. A cylindrical vessel of 18 cm in diameter is filled with water to a height of 15 cm. A copper ring electrode with positive polarity (anode) is placed at the bottom of the vessel. The central graphite electrode has a diameter of 6 mm and it is placed inside a quartz tube tightly covering this electrode. The end of this tube is above the water surface by 3–4 mm, while the upper end of the graphite electrode is below the end of the quartz tube by 2–3 mm. The electrical resistance of the water contained between the immersed electrodes is about 1.2 kOhm.

When the discharger is rapidly “closed” and “opened”, a plasma jet flies out of the electrode with a slight “pop” sound, and then a luminous “plasmoid” separates itself from the jet and begins to float in the air surrounding the set-up. In more detail, this process looks like as follows.

After the capacitor bank is connected up to the discharge gap, a creeping discharge appears on the water surface, and a plasma jet, which actually represents the leader of the strip lightning, flies up. After 80 ms, the discharger is “opened” (residual voltage is about 3 kV) and a plasma jet, separating from the electrode, forms a “plasmoid” – LBL. Usually, 60–100 ms after the end of the discharge, the LBL looks like a jelly matter. Sometimes the LBL may be shaped as an ideal ball.

In order to investigate physical properties of both the plasma jet and the LBL–P, the following recording equipment was used. To measure the time behaviour of the high voltage drop between the electrodes, a resistor $R1 = 100 \text{ k}\Omega$ was connected in-parallel, from a part of which the voltage was fed to the amplitude-digital converter (ADC). The LBL–P luminosity was measured by a photo-sensor – silicon photo matrix ($24 \times 36 \text{ mm}$) with a lens. The photo sensor spotted the path of the LBL–P beginning from the height of $H = 15 \text{ cm}$ up to the height of $H = 50 \text{ cm}$.

In order to measure both the sign of the LBL–P charge and the internal charge distribution correctly, various types of electric probes ordinarily used in plasma physics were investigated: a Langmuir probe, a double probe and a dipole antenna. During this work a special approach for nondestructive measurements of the “plasmoid” internal charge distribution was developed. As a result, we came to the conclusion [12] that a dipole antenna is best suited for this purpose. A Faraday cell and a dipole antenna were used to measure the electric charge of the LBL–P [17].

3. Experimental results

3.1. The main stages of the LBL–P formation

Three sequences of the stages of the origin and development of the “plasmoid” – a new type of the gas discharge – are presented in Fig. 2:

- At the first stage (Fig. 2a), a discharge of the “plasma sheet” type with the subsequent appearance of a plasma stream spreads over the water surface;
- In Fig. 2b, a typical formation process of a new type of discharge is shown at that transient moment when the streak lightning leader still exists, but its upper part has been already transformed into an LBL–P;
- In Fig. 2c, the third stage of the “plasmoid” formation is shown. The leader channel has already disappeared. In most cases, the lifetime of the generated “plasmoids” is about 0.6 s, but sometimes it can reach even 1 s.

This type of “plasmoid” corresponds to about 80% of the observed natural BL [1], that is, most of the observed natural BL. We believe that for the remaining 20% of a natural BL, the amount of electricity involved in the discharge is one or two orders of magnitude greater than for the laboratory discharge, and therefore their behaviour is the subject of a separate consideration.

The voltage behaviour, measured both on the central electrode (graph 1), and in the vicinity of the upper part of the leader (graph 2), is shown in Fig. 3. As one can see, these two curves have a good correlation and their absolute values are very close to each other (this area is marked with a dashed line in Fig. 3). This means that the leader takes the potential of the central electrode and transports it almost without a loss through the air to a height of 15 cm. It is important to note that the “plasmoid” takes not only the potential, but also the electric charge from the upper part of the leader, which is negative in sign. The observed glow of the “plasmoid”, measured when a single probe and a dipole antenna were introduced into the “plasmoid”, is shown in Fig. 3 and Fig. 4 (curves 3), respectively. Curves 3 show that the brightness in the first case is much less than in the second one, and the duration of the glow in the second case is much longer than in the first one. This is due to the fact that the Langmuir probe almost completely destroys the LBL–P, and, on the contrary, the dipole antenna practically does not interact with the LBL–P.

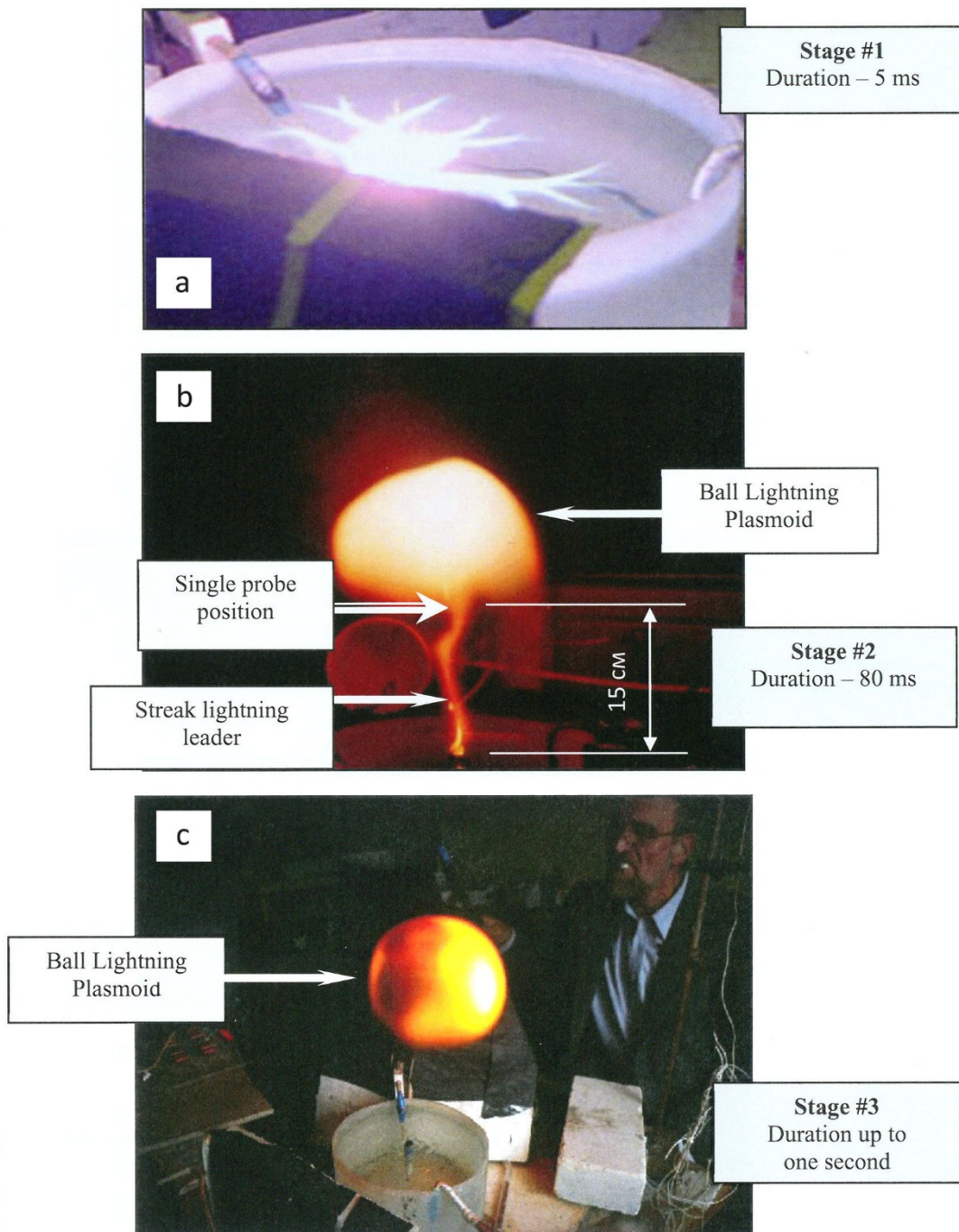


Fig. 2. Three main stages of the LBL-P development: *a* – creeping discharge is spreading along the water surface; *b* – streak lightning leader and the formation of the ball lightning plasmoid after the leader stopping; *c* – ball lightning plasmoid

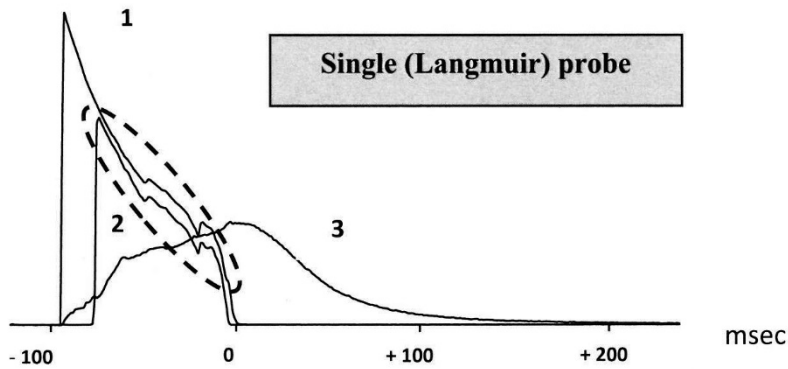


Fig. 3. Development of the streak the lightning leader transforming into the LBL-P when a single probe was introduced inside the “plazmoid”: 1 – discharge gap voltage; 2 – voltage from the probe that is placed on the height of about 15 cm in the vicinity of the leader, the probe is connected to the earth with a 100 kΩ resistor; 3 – “plasmoid” luminosity in relative unities

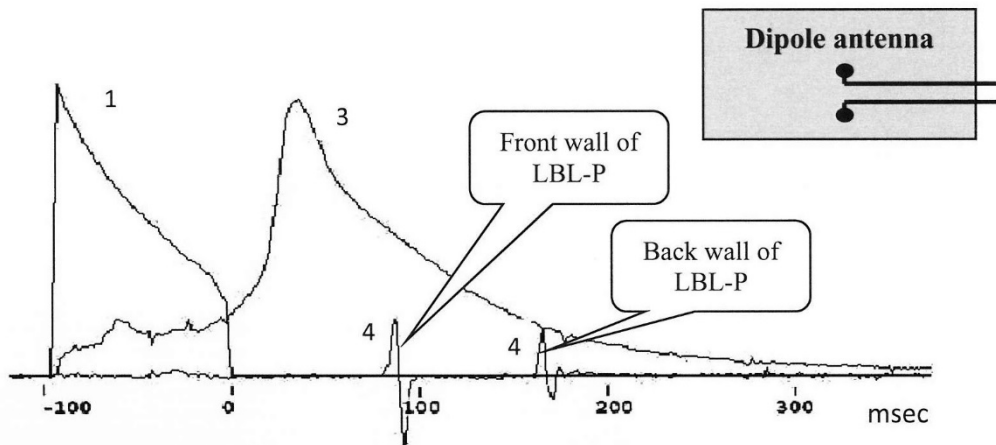


Fig. 4. The LBL-P is passing through a dipole antenna: 1 – discharge gap voltage; 3 – the “plasmoid” luminosity in relative unities; 4 – the signals received from the antenna while the upper and lower edges of the LBL-P intersect it

3.2. Investigation of the LBL-P internal charge distribution

The data presented in Fig. 4 were obtained by using a dipole antenna. The first bipolar pulse is observed at that moment when the LBL soars up and touches the probe by its upper edge. The second bipolar current pulse corresponds to the lower edge of the LBL-P. Video recordings of the “plasmoid” and the data presented in Fig. 4 make it possible to measure simultaneously the diameter of the LBL-P (10–18 cm), its vertical velocity (about of 1.6 m/s) and the lifetime.

As can be seen from the current data, the LBL-P structure looks like a soap bubble, the main electric charge of which is concentrated in a very thin spherical layer less than 3 mm thick. In the centre of the LBL-P, the electric charge is small. The visible observation of the LBL-P is in good agreement with these data (Fig. 5). As one can see, the external structure of the “plazmoid” consists of a bright thin shell surrounded by a “corona” of different colour. Since the apparent size of this shell is almost the same as the electrical one, it can be assumed that the LBL-P charge is concentrated namely in this yellow core.

The visible colours of the “plasmoids” corona strongly depend both on the composition of the substance involved in the discharge and on different brightness of the external illumination (Fig. 6). The colour of the “plasmoids” emitted by a wet metal electrode is usually determined by the spectrum of the electrode material. The lilac central part of the “plasmoid” is surrounded by a blurry yellowish shell. A small

admixture of sodium or calcium salts gives the plasmoid nucleus a yellow or even orange colour. These results are discussed in more detail in Refs. [10, 14].

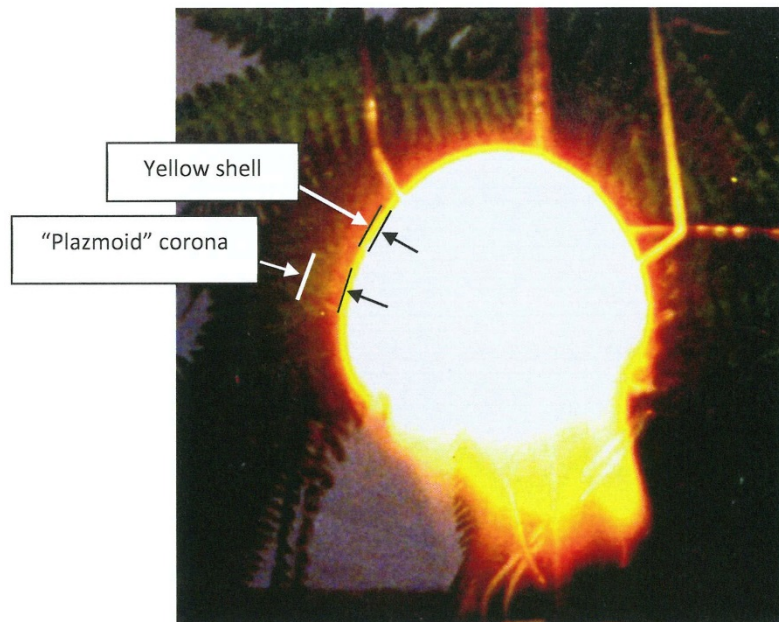


Fig. 5. Visual observation of the LBL-P. The “plazmoid” has an external structure that consists of a bright thin core surrounded by a shell of a different colour



Fig. 6. “Plazmoids” generated under the same charge conditions have quite different colours only because of different brightness levels of external lighting: *a* – the lab. window was closed; *b* – the lab. window was open

3.3. The LBL-P charge measurement

In order to make the correct measurement of the LBL-P charge, first of all, the charge calibration of the dipole antenna and the mathematical modeling of the shape of the induced charge were performed (Fig. 7). Using these data one could properly treat the signal received from the dipole antenna [12]. During the measurements, a LBL-P was generated in such a way that it passed at the closest distance to the dipole antenna. The obtained data allow us to conclude that the LBL charge is negative and its value is about $2 \cdot 10^{-7}$ C. This charge is related to the time moment when the LBL-P existed in a free running mode more than 100 ms. It is important to note that the LBL-P charge can considerably exceed the mentioned above value depending on the discharge conditions, the amount of the accumulated energy and *etc.*

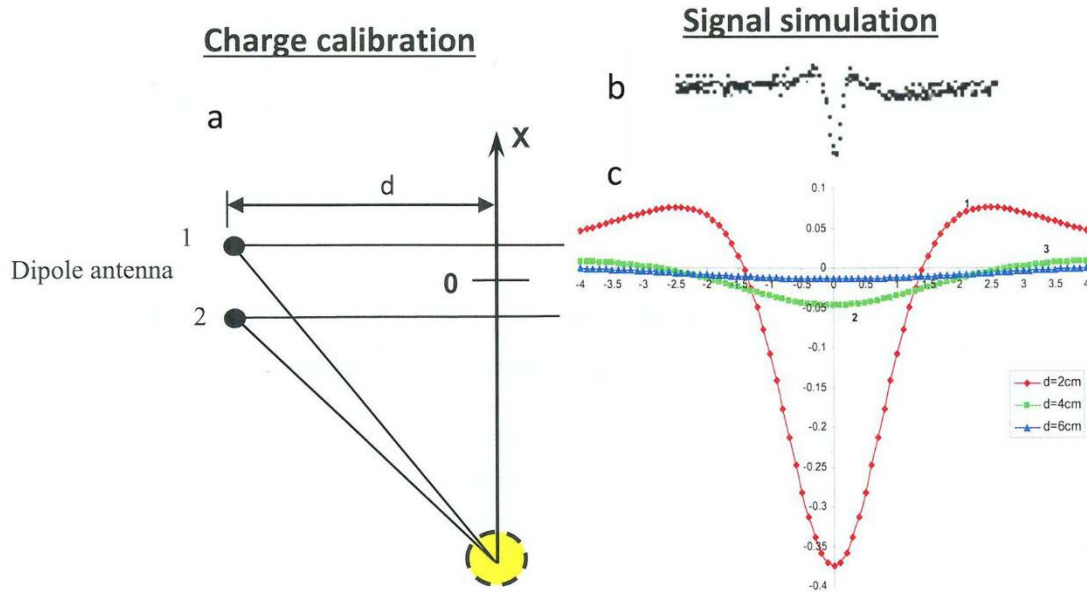


Fig. 7. Calibration procedure of the dipole antenna: *a* – shows the calibration procedure for a probe charge; *b* – a signal from the dipole antenna; *c* – a mathematical simulation of this signal

3.4. “Plasmoid” energy

The phase state of free charges generated by the electric field is determined by the parameter G [12, 22], which in its physical sense is the ratio of the potential LBL–P energy to the kinetic energy. An estimation made shows that under the conditions of our experiment this parameter is about $G \geq 1$. There are reasons to believe that on average [4] for the natural BL this parameter reaches a value of $G \geq 10$. This leads us to the assumption that the energy in the most of the LBL is stored in the form of the potential energy of the electric field formed by a negatively charged sphere [12].

3.5. Additional experimental evidences of the “plasmoid” close relationship with the natural BL

Our experiments have shown that the LBL–P has a common set of average parameters, which are very similar to the parameters of the natural BL described in Refs. [1–4]. One has to add the following properties of the observed “plasmoids” that gave us an additional proof of their close relationship with the natural BL.

These are:

- Absence of interaction with dielectrics (Fig. 8a);
- Strong interaction with conductors (Fig. 8b). Copper and nichrome wires were located on the LBL–P path. They were partially dispersed, and even melted directly in the “plasmoid” itself. We keep in mind that spraying a unit volume of metal requires more energy than melting. The ends of the extracted wire fragments have characteristics of melted balls. The diameters of the balls are very different: from 0.2 to 0.5 mm, which require from 0.03 to 1 J of energy for their formation, respectively. It is important to note that the conductors are fixed in space on two dielectric filaments and do not have contacts with the ground;
- The “plasmoid” has good enough transparency (Fig. 8c);
- The LBL penetration through a hole displaced from the discharge axis and smaller than that of the LBL (Fig. 8d). The diameter of the hole was 5 cm and it was shifted from the discharge axis by 3 cm. As a result, after passing through the hole, the discharge restored its spherical shape;
- The average temperature of the LBL is close to the room temperature (about 330 K) [14, 17]. In these investigations, the LBL–P temperature was estimated from the rate of the vertical rise. These data can be used to calculate the average temperature of warm moist air containing luminous plasma.

The specified temperature differs significantly from the colour temperature of the shell, which can reach 1 000–2 000 K, depending on the added allowances.

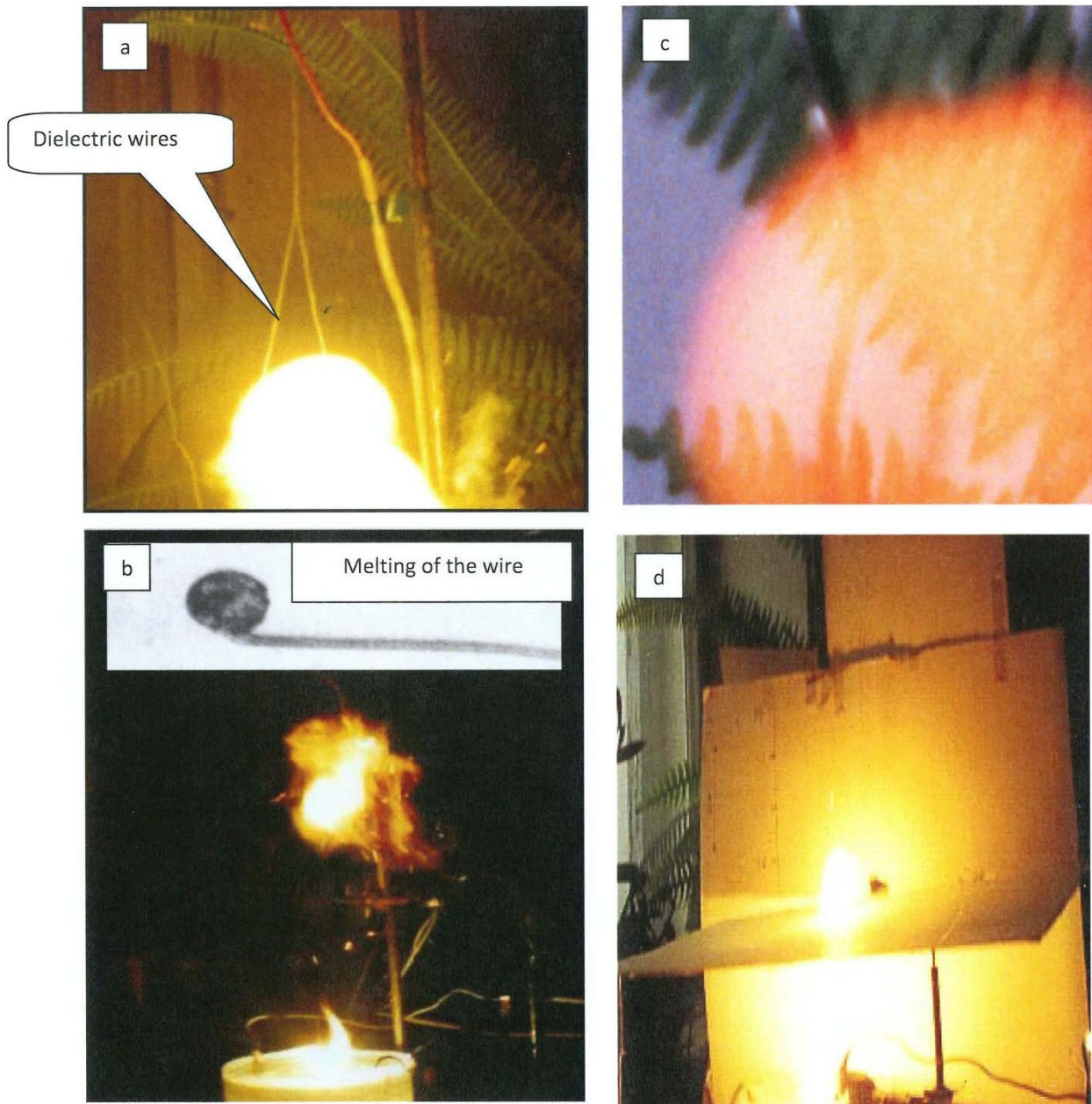


Fig. 8. Additional proof of close relationship of the observed “plasmoid” with the natural BL: *a* – absence of interaction with dielectrics; *b* – strong interaction with conductors; *c* – good transparency; *d* – penetration through a hole displaced from the discharge axis and smaller than that of the LBL

4. Conclusion

At the Institute of PNPI, an experimental set-up was constructed, on which for the first time a new type of the gas discharge was discovered, which we called “plasmoid”. It looks like a compact luminous formation with a diameter of 10–18 cm and a lifetime up to one second.

The reproduction efficiency of the LBL–P is about 100%, which allows systematic studies of “plasmoids” in the laboratory. A special method was developed for non-destructive measurements of the electric charge distribution of the “plasmoid”. The dipole antenna is the best technique for this purpose.

It has been shown that the new type of the gas discharge LBL–P has the following features:

- It develops in the zone between the water surface and further in the atmospheric air;
- It has three stages of development – the development of a discharge of the “plasma sheet” type on the surface of the water; formation of a leader in the space “water-air”; formation of a “plasmoid” in the air and its autonomous existence without external energy replenishment;
- The discharge shell has a multilayer structure, which as a whole has an uncompensated negative charge created by a thin plasma layer. Most of the energy of the “plasmoid” is stored in the electric field formed by this sphere of charged particles. This energy is potential in its nature. The thickness of this layer is less than 3 mm;
- The dynamics of the formation of this discharge and its radiation are highly dependent on the contributions of both chemical processes and external electric and magnetic fields.

The whole set of characteristics observed in “plasmoids” allow us to indicate a high probability that we are observing an object whose physical parameters make us believe that it has the properties of a natural BL. Thus, the obtained experimental data for LBL–P even allowed us to predict a number of critical properties for the natural BL. In particular, the latter has a negative shell which is kept balanced by dielectric layers formed by the discharge in the atmosphere. For the first time, a natural BL and its laboratory analogue created in our experiments have no paradoxes: the observed properties of the ball lightning are compatible with theoretical concepts and experiment.

References

1. J.D. Barry, *Ball Lightning and Bead Lightning: Extreme Forms of Atmospheric Electricity*, 298 (1980).
2. I.P. Stakhanov, *On the Physical Nature of Ball Lightning*, 208 (1985).
3. I.P. Stakhanov, *On the Physical Nature of Ball Lightning*, 264 (1996).
4. B.M. Smirnov, *Sov. Phys. Usp.* **35** (8), 650 (1992).
5. E.M. Bazelyan, Yu.P. Raizer, *Phys. Usp.* **43**, 701 (2000).
6. E.M. Bazeljan, Yu.P. Raizer, *Physics of Lightning and Lightning Protection*, 320 (2001).
7. G.D. Shabanov, O.M. Zhrebtsov, *J. Opt. Technol.* **71**, 4 (2004).
8. G.D. Shabanov, *Technical Phys. Lett.* **28**. (2), 164 (2002).
9. G.D. Shabanov, in *Proc. of the 3rd Int. Conf. on Natural and Anthropogenic Aerosols*, 368 (2001).
10. A.I. Egorov, S.I. Stepanov, G.D. Shabanov, *Phys. Usp.* **47** (1), 99 (2004).
11. N.G. Shabanova, G.D. Shabanov, *New Energy Technol.* **4** (19), 71 (2004).
12. G.D. Shabanov, B.Yu. Sokolovsky, *Plasma Phys. Rep.* **31** (6), 512 (2005).
13. G.D. Shabanov, O.M. Zhrebzov, B.Yu. Sokolovsky, *Chem. Phys.* **25** (4), 74 (2006).
14. A.I. Egorov, S.I. Stepanov, *Tech. Phys.* **47** (12), 1584 (2002).
15. G.D. Shabanov, A.G. Krivshich, B.Yu. Sokolovsky, O.M. Zhrebtsov, in *Proc. of the 9th Int. Symposium on Ball Lightning*, 202 (2006).
16. G.D. Shabanov, A.G. Krivshich, B.Yu. Sokolovski, O.M. Zhrebtsov, in *Proc. of the VI Rus. Conf. on the Atmospheric Electricity*, 157 (2007).
17. A.I. Egorov, S.I. Stepanov, *Tech. Phys.* **53**, 688 (2008).
18. G.D. Shabanov, A.G. Krivshich, B.Yu. Sokolovski, O.M. Zhrebtsov, *Plasma Phys. Rep.* **35** (7), 611 (2009).
19. G.D. Shabanov, A.G. Krivshich, G.E. Gavrilov *et al.*, in *Proc. of 11th Int. Symposium on Ball Lightning*, 160 (2010).
20. G.D. Shabanov, A.G. Krivshich, G.E. Gavrilov *et al.* *Int. J. Unconvent. Electromagn. Plasmas* **4** (1–2), 141 (2012).
21. S.I. Stepanov *Tech. Phys.* **59** (1), 107 (2014).
22. G.D. Shabanov, *Phys. Uspekhi* **62** (1), 92 (2019).
23. Shixin Zhaoa, Chengxun Yuana, A.A. Kudryavtsev *et al.*, *Techn. Phys.* **66** (7), 1081 (2021).

24. Sh. Zhao, Ch. Yuan, A.A. Kudryavtsev *et al.*, *Techn. Phys.* **67** (2), 171 (2022).
25. B. Juettner, S. Noack, A. Versteegh, G. Fussmann, in *Proc. of 28th ICPIG, Int. Conf. on Phenomena in Ionized Gases*, WA6, 5P12-05 (2007).
26. A. Versteegh, K. Behringer, U. Fantz *et al.*, *Plasma Sources Sci. Technol.* **17**, 024014 (2008).
27. S.E. Emelin, A.M. Astafiev, A.L. Pirozerski, in *Proc. of 10th Int. Symposium on Ball Lightning*, 42 (2008).
28. V.B. Yuferov, E.V. Muffle, V.I. Tkachev *et al.*, *Bulletin of NTU “KhPI”* **4**, 103 (2011).
29. V.L. Bychkov, N.P. Savenkova, S.V. Anpilov, Yu.V. Troshchiev, *IEEE Trans. Plasma Sci.* **40** (12), Part 1, 3158 (2012).
30. M.I. Baranov, *Elektrotekh. Elektromekh.* **5**, 56 (2013).
31. U. Fantz, S. Kalafat, R. Friedl, S. Briefi, *J. Appl. Phys.* **114** (4), 043302 (2013).
32. K.D. Stephan, S. Dumas, L. Komala-Noor, J. McMinn, *Plasma Sources Sci. Technol.* **22** (2), 025018 (2013).
33. V.I. Bychkov, S.V. Anpilov, N.P. Savenkova, *Rus. Journ. Phys. Chem. B* **8** (1), 50 (2014).
34. U. Fantz, S. Briefi, R. Friedl *et al.*, *IEEE Trans. Plasma Sci.* **42** (10), 2624 (2014).
35. U. Fantz, R. Friedl, S. Brief, *J. Appl. Phys.* **117** (17), 173301 (2015).
36. M. Jacobs, W. Gekelman, P. Pribyl *et al.*, *Phys. Plasmas* **28**, 052114 (2021).
37. S.E. Dubowsky, A.N. Rose, N.G. Glumac, B.J. McCall, *Plasma*, **3** (3), 92 (2020).
38. V. Stelmashuk, P. Hoffer, *IEEE Trans. Plasma Sci.* **45**, 3160 (2017).
39. M.L. Shmatov, K.D. Stephan, *J. Atmosphere. Solar-Terrestrial Phys.* **195**, 105115 (2019).
40. R. Friedl, U. Fantz, I. Pilottek *et al.*, *J. Phys. D: Appl. Phys.* **54**, 095205 (2021).

New Projects

IRINA PROJECT AT THE REACTOR PIK

V.N. Panteleev, A.E. Barzakh, D.V. Fedorov, P.L. Molkanov, M.D. Seliverstov

1. Introduction

At present, valuable information about the structure of nuclei and the characteristics of the nuclear state has been obtained as a result of experiments on ISOL (isotope separator on-line) facilities. In addition, experiments at ISOL installations provide information for astrophysics, when ideas about the creation of chemical elements in the universe and evolution of stars can be tested experimentally by the interaction of radioactive nuclear beam (RNB) with a hydrogen target, for solid state physics where radioactive ion implantation is used to investigate the material properties, and for modern medicine as well, providing a fast and harmless disease diagnosis and therapy. Currently, about twenty ISOL facilities operate over the world and new ones are planned for construction within the next few years.

At the PNPI, the ISOL installation IRIS (investigation of radioactive isotopes at synchrocyclotron) [1, 2] has been operating for nearly fifty years. In studies carried out at this facility more than 300 nuclides were obtained (17 of them were produced and investigated for the first time). During the operation of the IRIS facility, a lot of new approaches and methods of production and investigation of short-lived isotopes have been developed and applied. One of them is the method of selective laser ionization of atoms of different elements in a hot cavity, called laser ion source, which was developed and firstly successfully used at the IRIS facility [3, 4]. It makes possible to get the isobaric pure radioactive isotope beams of a large number of chemical elements.

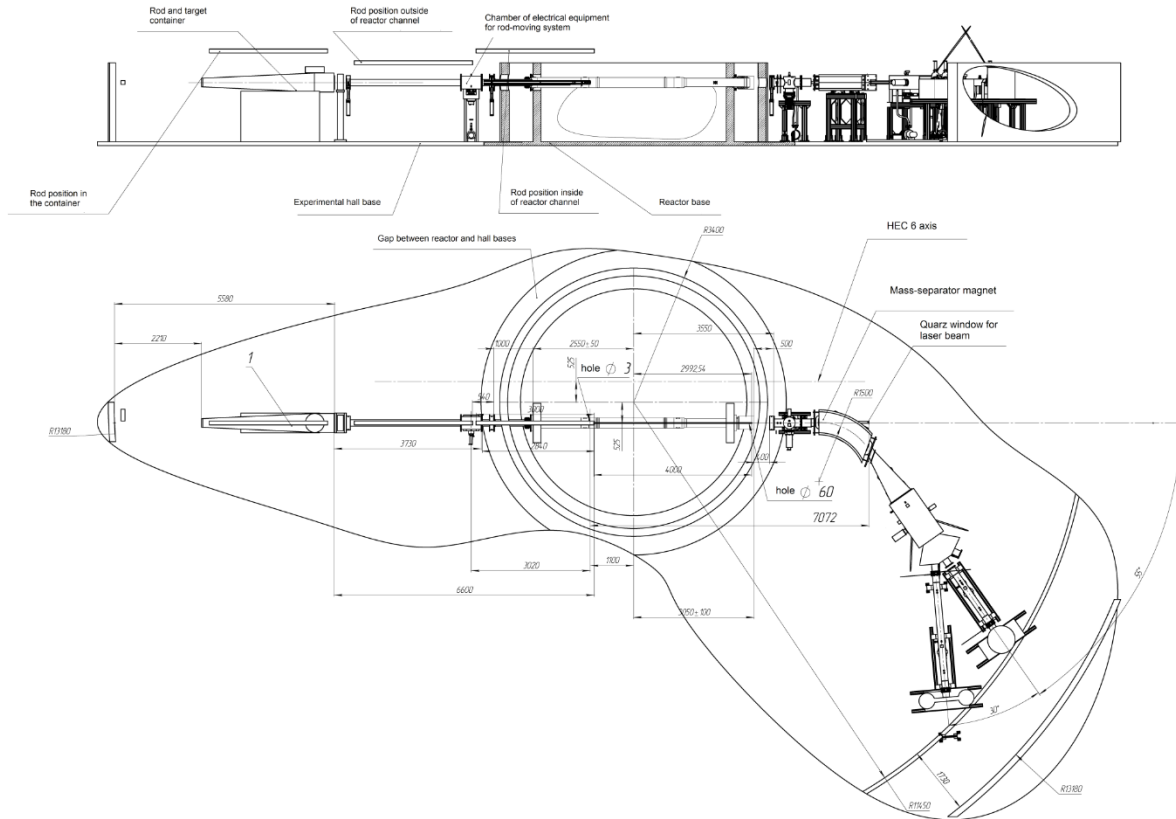
The use of 1 GeV protons as bombarding particles gives the possibility to produce mainly neutron-deficient nuclei, making use of different types of targets. There is also a possibility with protons of this energy to produce neutron-rich isotopes as well in the fission reaction of ^{238}U . For this purpose, a high density uranium carbide target was developed and successfully used to produce neutron-rich isotopes of Ag, Cd, In, Sn and others [5]. This target has demonstrated very good characteristics during prolonged (three months) on-line tests at a high working temperature (2 000–2 100°C).

In spite of rather successful utilization of a high density ^{238}U carbide target at the proton beam [6, 7] for neutron-rich isotope production, the use of a high flux of thermal neutrons from reactors gives the possibility to increase considerably the production yields of isotopes with a large neutron excess [8, 9]. For this purpose, a high density ^{238}U carbide target will be utilized. According to preliminary calculations, the yield of ^{132}Sn (double-magic, far from β -stability), considered as a reference nuclide for ISOL facilities, at the neutron beam of the reactor PIK (thermal neutron flux of $3 \cdot 10^{13} \text{ cm}^{-2} \cdot \text{s}^{-1}$, target – 4 g of ^{235}U) can be of about $1 \cdot 10^{11}$ particles per second. At present, the operating ISOL systems IRIS (PNPI) and ISOLDE (CERN) are able to provide 10^7 and 10^8 of ^{132}Sn nuclides per second, correspondingly. The maximum yield of this isotope at the perspective ISOL installation SPIRAL-2 (GANIL, France) will not exceed 10^9 nuclides per second.

Presently, at PNPI (Gatchina) the project IRINA (investigation of radioactive isotopes with a neutron facility) [10] of an ISOL installation for the high intensity exotic neutron-rich isotope production at thermal neutrons of the high flux reactor PIK is being developed. The IRINA facility is expected to provide the most intensive beams of neutron-rich nuclei in the world. The main directions of studies of neutron-rich exotic nuclei at the IRINA facility will be the studies of the “magic numbers conservation” in the nuclides far from stability, which are of importance for nuclear physics and also directly connected to astrophysics. Recently obtained data point to a change of the magic number values for such nuclei. This leads to a considerable revision of the magical number concept itself. Also, a very important direction is the measurement of the ground state properties of short-lived nuclei (spins, mean square charge radii, electromagnetic moments, *etc.*), making use the method of resonant laser spectroscopy in a laser ion source. Such a possibility is of great importance for traditional area of the laser-nuclear spectroscopy application – for the isotope shift and hyperfine splitting measurements. Mean square charge radii, spins and electromagnetic moments can be evaluated from these experimental data. A description of the physical program of the IRINA installation was presented in Ref. [11]. Additionally, it is planned to construct a special ion beam line of the IRINA mass-separator for production and collection of high purity isotopes with rather long life-times. It can be used for the solid-state physics and for the nuclear medicine purposes. The use of high-flux neutron reactors for these purposes looks very promising.

2. IRINA facility project

A schematic view of the IRINA set-up in the reactor PIK experimental hall of horizontal channels is demonstrated in the Figure. This figure does not show the installation for the resonant laser ionization of the produced isotopes, which is located in a specially equipped room outside the experimental hall. The isotope mass-separator is one of the main parts of the IRINA facility. The target-ion source device with the ion-optic system of the mass-separator is placed inside the reactor channel horizontal experimental channel (HEC) 5-5' on the thermal neutron flux of $(3-5) \cdot 10^{13} \text{ cm}^{-2} \cdot \text{s}^{-1}$. This neutron flux irradiates the target material and heats it up to 2200°C . As the planned final target position is about 0.9 m from the central point of the channel HEC 5-5', there is a principle possibility to increase the neutron flux through the target almost one order of magnitude. But in that case a very serious problem with the power dissipation of about 30 kW should be solved.



Layout of the IRINA facility at the experimental hall of the reactor PIK

The operation of the IRINA facility at the beam of thermal neutrons of the reactor PIK can be described as follows. Fission products (atoms of neutron-rich isotopes) are thermally released at a high temperature ($\sim 2200^\circ\text{C}$) from the target material due to diffusion and ionized inside the internal volume of the target. Ions are extracted through the exit hole of the target capsule, accelerated to 30–40 kV by extraction–acceleration electrical field and are formed into a beam with an angular divergence of about $2 \cdot 10^{-2} \text{ rad}$. After that, the ion beam passing the focusing lens is transferred into an almost parallel one. The formed ion beam enters into the mass-separator magnet normally to the magnetic field lines and is focused in vertical and horizontal planes. The ion beam cross-section in the focal plane of the mass-separator magnet in the collector chamber is about 1 mm (vertical plane) and 1.5 mm (horizontal plane). The central trajectory curvature in the magnetic field is equal to $R = 1500 \text{ mm}$ and provides the distance between the neighbour masses equal to $D_{\text{rect}} = R/A \text{ mm}$, where A is the mass number. For instance, for $A = 100$ the dispersion $D_{\text{rec}} \approx 15 \text{ mm}$. The mass-separated ion beams are transported from the collector chamber to the beam bending and distributing chamber – the vacuum chamber with electrostatic deflectors bending the ion beam by $+30$ and -30° from the direct central beam

trajectory. The selected ion beams are directed to the experimental hall with the ion guide systems. Focusing triplet electrostatic lenses are installed along the ion beam lines to focus the ion beam at detection posts of the experimental set-ups. The ion beam cross-section in the implantation point is about $2 \times 2 \text{ mm}^2$. The vacuum system should provide the pressure of about $(2-4) \cdot 10^{-6} \text{ mbar}$ in all parts of the mass-separator vacuum chamber. The ion beam transmission from the ion source to the detection posts should be in the range of 60–90% (depending on the ion source type and the beam focusing quality).

A fast tape station with α -, β - and γ -detectors for identification and investigation of rare isotopes will be placed at the main ion guide. A neutron 4π detector for the delayed neutron registration will be installed on the second ion guide. All detection posts, the tape station and the mass-separator will be controlled with the mainframe computer.

3. Target-ion source unit development for the IRINA facility

As a prototype of the combined target–ion source for the IRINA mass-separator, the target construction developed at the IRIS facility will be used as an effective high-temperature target unit for on-line production of short-lived radioactive isotopes. The construction of the target unit allows one to avoid cold spots usually arising in the target–ion source assemblies in the places of the target–transfer tube and transfer tube–ion source connections. The peculiarity of the developed target unit is the absence of the ion source [10], since the ionization process happens in the target volume itself. This avoids an additional delay time due to the effusion inside the transfer tube and the ion source. This target construction could be especially useful for production of short-lived isotopes of elements with a long sticking time, such as isotopes of Co, Ni, Sn and others hardly volatile elements. The only difference will be the replacement of tantalum foils as a target material by a high-density mono carbide of ^{235}U . A detailed description of the target-ion source unit developed for the IRINA facility was given in Ref. [11].

4. Target material investigation for the IRINA facility

During the latest thirty years, there has been a trend at the ISOL facilities to develop fast uranium carbide targets for the on-line production of rare nuclides. Since the beginning, a growing interest in the development of uranium carbide targets has been stimulated by the study of exotic neutron-rich nuclei far from stability produced in fission reaction of ^{238}U by energetic protons. In addition, these targets enable the production of a wide range of neutron-deficient heavy nuclei by means of fragmentation reactions. Presently, an increasing demand for targets containing large fractions of ^{238}U has been enhanced by the new projects concerning ISOL facilities with intensive proton beams as projectile particles. At the IRINA facility, as it was pointed above, 4 g of ^{235}U (90% enrichment) in the form of the uranium monocarbide at the beam of thermal neutrons will be exposed. As physical and chemical properties of the target material do not depend on what uranium isotope it contains, preliminary target tests were carried out at the proton beam of the IRIS facility, making use of targets containing ^{238}UC of a high density. The target for the IRINA facility will be prepared from the identical target material containing a highly enriched ^{235}U . We used for the targets a special uranium carbide with the density of 11 g/cm^3 , that is rather close to its theoretical monocrystal value (13.6 g/cm^3) [7]. In order to measure their characteristics, long term tests about three months have been carried out at the IRIS facility. The yields and delay times were obtained that have demonstrated the reproducibility of the relevant values after three month heating of the target at a temperature $2\,000\text{--}2\,100^\circ\text{C}$.

As it was shown in the experiments at the IRIS facility, the delay characteristics of the IRIS monocarbide high density target (diffusion and effusion delay times) are much shorter than similar characteristics of the ISOLDE uranium carbide target. It gives two order of magnitude higher yields of short-lived francium isotopes in millisecond region of isotope half-lives. Additionally, in series of off-line and on-line experiments carried out at the IRIS facility it was demonstrated that the target can be maintained for more than 2400 h at a temperature of about $2\,100^\circ\text{C}$ without appreciable changes in its main characteristics. It is very important, as the developed target will be utilized at the reactor beam during the reactor working cycle which is about one month period. Another important result is a good reproducibility of the yields and release times for the

nuclides investigated for the long period of the target maintenance. So, presently we consider this target and the target material to be a good prototype for the designed target unit of the IRINA facility.

5. Current state of the project IRINA

The design documentation for units of the IRINA facility is presently prepared by the contractors of the project. The mass-separator, which is one of the main parts of the installation, with its ion optic system, ion beam transmission chambers and ion beam pipes is being designed and manufactured by the D.V. Efremov Institute of Electrophysical Apparatus (Rosatom, Saint-Petersburg). The mass-separator target, which is a complex unit, containing a cylinder made of a high density ^{235}U monocarbide, will be designed and constructed by Luch Scientific Production Association (Rosatom, Podolsk). The laser unit of the IRINA installation for resonant selective ionization of atoms of the produced neutron-rich isotopes will be designed and manufactured by the DMK Laser Microsystems Co. In accordance with the work plans, the production of the working design documentation for all parts of the installation should be completed in 2023.

6. Conclusion

The project IRINA at the reactor PIK opens new possibilities for production and investigation of neutron rich nuclei. It will be able to compete with and in some cases to surpass the current and other projected ISOL installations. The use of a combination of a high flux reactor of thermal neutrons, the mass-separator and the laser resonance ionization facility enables one to overcome the inevitable difficulties in production and investigation of extremely neutron rich nuclei with a very low production rate. It is expected that the IRINA facility will provide the most intensive beams of neutron-rich nuclei in the world. The main directions of studies of neutron-rich exotic nuclei at the IRINA facility will be the studies of the “magic numbers conservation” in the region of neutron rich nuclides far from stability, which are of importance for nuclear physics and also directly connected to astrophysics. Note that recently obtained data indicate a change in the values of the magic number for such nuclei. This leads to a considerable revision of the magical number concept itself. Also, a very important direction is the measurement of the ground state properties of short-lived nuclei (spins, mean square charge radii, electromagnetic moments, *etc.*) by using the method of resonant laser spectroscopy in a laser ion source. Such a possibility is of great importance for the traditional area of the laser-nuclear spectroscopy application – for the isotope shift and hyperfine splitting measurements. Mean square charge radii, spins and electromagnetic moments can be evaluated from these experimental data. Additionally, it is planned to construct a special ion beam line of the IRINA mass-separator for production and collection of high purity isotopes with rather long life-times. It can be used for the solid-state physics and for the nuclear medicine purposes. The use of the high-flux neutron reactor PIK for these purposes looks very promising.

References

1. E.Ye. Berlovich *et al.*, *Izv. Akad. Nauk SSSR, Ser. Fiz.* **40**, 2036 (1976).
2. V.N. Panteleev *et al.*, *Rev. Sci. Instrum.* **73** (2), 738 (2002).
3. G.D. Alkhazov *et al.*, *Nucl. Instr. Meth. A* **306**, 400 (1991).
4. A.E. Barzakh *et al.*, *Rev. Sci. Instrum.* **83**, 02B306 (2012).
5. A. Andrighetto *et al.*, *Nucl. Instr. Meth. Phys. Res. B* **204**, 267 (2003).
6. H.L. Ravn *et al.*, *Nucl. Instr. Meth. B* **70**, 107 (1992).
7. V.N. Panteleev *et al.*, *Nucl. Instr. Meth. Phys. Res. B* **240**, 888 (2005).
8. J.A. Pinston *et al.*, *Nucl. Instr. Meth. Phys. Res. B* **126**, 22 (1997).
9. V.N. Panteleev *et al.*, *PNPI. High Energy Physics Division. Main Scientific Activities 2007–2012*, 274 (2013).
10. V.N. Panteleev *et al.*, in *Proc. of XXIII Int. Seminar on Interaction of Neutron With Nuclei Dedicated to the Centenary of the Birth of Feodor L. Shapiro (1915–1973)*, 32 (2015).
11. V.N. Panteleev *et al.*, *PNPI. High Energy Physics Division. Main Scientific Activities 2013–2018*, 336 (2019).

AMBER – A NEW FACILITY AT THE CERN SPS

PNPI participants of the AMBER Collaboration: A.A. Dzyuba, A.G. Inglessi, K.A. Ivshin, E.M. Maev, O.E. Maev, A.N. Solovyev, I.N. Solovyev, A.A. Vassiliev, **A.A. Vorobyev**, M.E. Vznuzdaev

1. Proton radius puzzle

The charge radius of the proton (r_p) is one of the fundamental physics constants. The so-called “proton” radius puzzle originated due to a striking discrepancy of 4% between the electric charge radius of the proton, extracted from muonic hydrogen Lamb-shift measurements ($r_p = 0.8409(4)$ fm) obtained in 2010–2013, compared to the CODATA value, based on electron–proton scattering experiments ($r_p = 0.877(7)$ fm), as well as on atomic transition measurements in electronic hydrogen ($r_p = 0.877(8)$ fm). Various reasons for the discrepancy of six standard deviations are discussed including possible systematic uncertainties of the measurements and lepton universality violation. A compilation of the results on the proton radius puzzle is presented in Fig. 1. The main part of the problem is the discrepancy between the results of ep scattering experiments and the muonic hydrogen measurements. The PRad Collaboration in 2019 measured the proton charge radius of 0.831(14) fm using the elastic electron–proton scattering on a windowless gas target, but the obtained dependency of the proton electric form factor (G_E) from the four-momentum transfer (Q^2) is inconsistent with the measurements performed by the A1 Collaboration. Therefore, new high precision ep and μp elastic scattering experiments in the region of low momentum transfers are necessary. They will reduce the probability of possible systematic uncertainty of the measurement and experimental data interpolation.

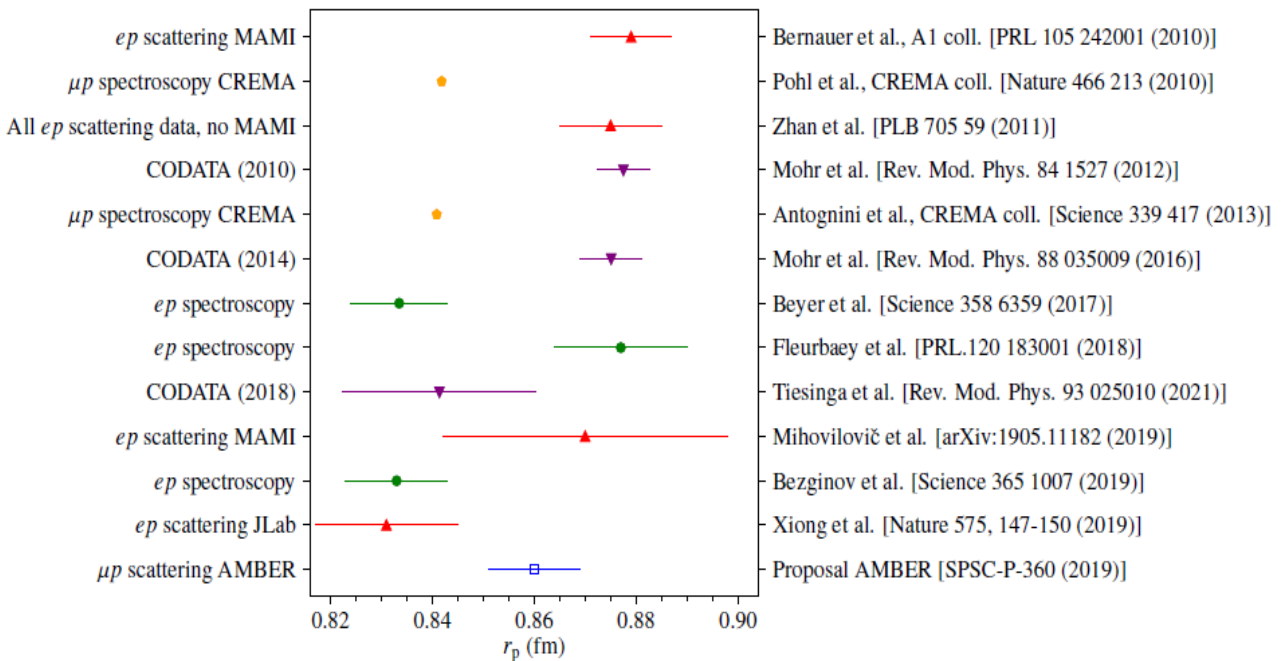


Fig. 1. Compilation of results on the proton–radius puzzle. Electron–proton scattering and spectroscopy (*red/green*), muon–proton spectroscopy (*orange*) and summary data (*purple*) are shown with the value of this proposed measurement (*blue*) arbitrarily placed at 0.86 fm, with the projected uncertainty. Error bars represent statistical and systematic uncertainties added in quadrature

The PNPI group within the framework of the new AMBER Collaboration proposed to perform a muon–proton experiment using high-energy muons of the CERN M2 beam line. This measurement will provide a new and completely independent result on the proton charge radius with a statistical accuracy of 0.01 fm or better and considerably smaller systematic uncertainty. The measurement will employ a time-projection chamber (TPC) filled with hydrogen. Advantages of high-energy muons as a probe are the following: low

values of the radiative corrections due to the high mass of muons, as well as due to the experimental method, and a possibility to test the principle of lepton universality in lepton–proton scattering.

2. Physics program of the AMBER experiment

AMBER (apparatus for meson and baryon experimental research) is a new CERN-based experiment aiming to address several questions about some of the proton’s most fundamental properties, such as its size, internal structure and intrinsic spin [1]. AMBER will be the next-generation successor of the COMPASS experiment, which is currently finishing its operation at the M2 beamline of the super proton synchrotron (SPS) accelerator. The M2 beamline is located in the north area of CERN and provides either secondary hadron beams or tertiary muon beams of both charges. These beams result from the interaction of SPS-extracted protons at 400 GeV/c momentum on a primary target. By means of a complex beam optics, the beam particles are transported along the 1100 m distance up to the EHN2 building, where the AMBER set-up will be located. The muon beam is obtained from the natural leptonic decays of pions and kaons over a path length of 600 m, the remaining hadronic component being stopped by an absorber placed upstream of the experiment. Both charges are available, for momenta up to 190 GeV/c. Presently, the M2 beamline is the only facility in the world providing muon beams of high energy and high intensity. Hadron beams with momenta in a range from 50 to 280 GeV/c are available in the M2 beamline. The energy spread of the beams is below 5% for the fixed beam momentum.

The first phase of the AMBER experiment (Phase-1) was approved in December 2020 by the CERN Research Board [2]. The reference number of the experiment is set to be NA66. The future experiment will use a part of the COMPASS detector, which, however, will be equipped with a new readout system capable of operating in a so-called triggerless mode. The physics program of the Phase-1 of AMBER consists of the following:

- Precise measurement of the elastic muon–proton scattering at 100 GeV beam energy for a measurement of the proton form factor at low momentum transfers and, consequently, of the proton radius;
- Determination of antiproton production cross-sections in proton–proton and proton–helium collisions in the energy range 20–280 GeV, as a valuable input for a dark matter search;
- Investigation of pion parton distribution functions (PDF) in Drell–Yan pair production employing a 190 GeV pion beam. In parallel to these studies, a high statistics dataset of J/ψ production will be recorded and will allow to conclude on the production mechanisms (gluon–gluon fusion vs quark–antiquark annihilation).

According to the current planning, the main data taking for the muon–proton elastic scattering will take place in 2023–2024, the antiproton production cross-section run is planned for 2023, and pion-induced Drell–Yan pair production will start in 2025.

The PNPI group is focused on the first topic of the physics program providing an expertise in the design, development and operation of a TPC, which is the core experimental technology used in the measurement. PNPI HEPD physicists also carry official roles in the AMBER Collaboration. For example, Alexander Inglessi was a Run coordinator for the 2021 AMBER Pilot Run, and Alexey Dzyuba is currently the chairman of the AMBER Publication Committee.

3. Set-up for proton radius measurements

A schematic view of the AMBER set-up for the proton radius measurement is presented in Fig. 2. The core part of the set-up is located in front of the magnetic spectrometer and consists of a TPC filled with hydrogen at high pressure (20 bar), two pipes with helium gas and four unified tracking stations. The TPC will serve as an active target, which means that the hydrogen will play a role of the target and detection medium for the recoil protons at the same time. The energy deposited in the TPC corresponds to the kinetic energy of the recoil proton and thus to the momentum transfer. According to theoretical predictions, radiative corrections associated with the lepton arm cancel out for the proposed scheme of measurements. Pipes filled with helium will reduce effects of multiple scattering of muons, which enter and leave the TPC. Each of four unified tracking stations consists of silicon pixel layers and scintillating fiber-based detectors. They will provide high

precision tracking for the incoming and outgoing muons. ALPIDE-based detectors are planned to be used for silicon pixel layers, and scintillating-fiber detectors will provide high precision timing information with an accuracy better than 1 ns. The total length of the target region is about 9 m.

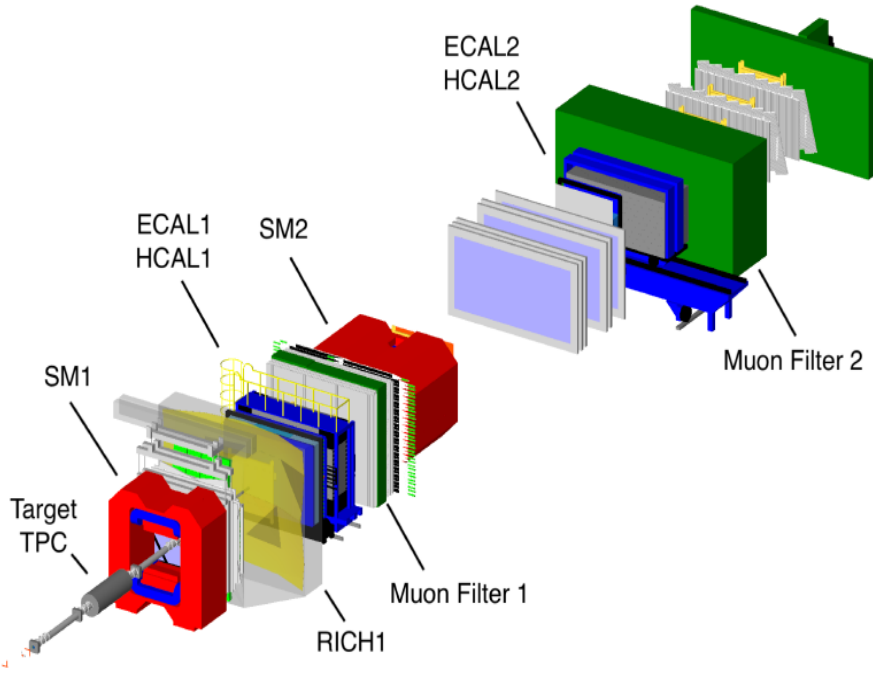


Fig. 2. The experimental set-up for the measurement of the proton charge radius. The M2 muon beam enters the set-up from the lower left corner, where the core set-up is visible in the target area (target TPC) with the corresponding labeled parts of the spectrometer

The magnetic spectrometer for the momentum reconstruction will use the magnet spectrometer magnet 2 (SM2) combined with tracking detectors. Mainly scintillating fiber detectors and novel GEM free-running detectors are used to cover the required small-angle part. The length of the core set-up for the proton radius measurement into the target area of the spectrometer is 9 m. The first dipole magnet spectrometer magnet 1 (SM1) will not be used to avoid influence of the fringe field on the small angle tracking in the target area. This change in magnet configuration especially downstream of the SM1 requires repositioning of the detectors for the data taking along the spectrometer with respect to the default configuration used in previous measurements. The muon identification will be provided by the muon filter 2. It uses absorber layers to stop incoming hadrons allowing only muons to pass through. Together with tracking and hodoscopes at the most downstream positions of the spectrometer the muon tracks can be identified. To measure the radiative effects or identify electrons, electromagnetic calorimetry is provided by the electromagnetic calorimeter 2 (ECAL2), in particular for small angles. Additional larger tracking detectors (multiwire proportional chamber – MWPC) and hodoscopes are foreseen to cover the central horizontal part of ECAL2 along the bending direction of the SM2 to allow a distinction between charged and non-charged tracks.

With this set-up, the goal is to collect a sample of 70 million elastic muon–proton scattering events in the momentum transfer Q^2 range from 0.001 to 0.04 GeV². This will take about one beamtime of 140 days, currently foreseen starting in 2023.

4. Feasibility studies (2018)

In 2018, a first feasibility test was performed as a part of the preparation for the final measurement. The goals to ensure the desired recoil proton energy resolution of the TPC and successful event matching with a tracking system were achieved. Additionally, beam ionization noise influence on the TPC performance was preliminarily studied.

To achieve these goals, a set-up consisting of a TPC prototype (ACTAF2 prototype – see Ref. [3]) and four silicon strip tracking detectors were prepared. The set-up was located in the downstream area of the COMPASS spectrometer with the measurement being performed in a parasitic mode. That resulted in a very wide beam size and a divergence covering the whole TPC and beyond. This made the event selection and beam noise studies more complicated as opposed to the narrow beam case. Due to the relatively slow performance of the TPC, it was read out with a data acquisition (DAQ) system independent from the rest of the set-up. The synchronization of two DAQ systems was made using a timestamp-based approach.

The set-up consisted of the ACTAF2 prototype TPC surrounded by four silicon strip tracking detectors, two placed upstream and two downstream of the TPC (Fig. 3). The TPC was filled with hydrogen at up to 8 bar pressure used to measure recoil proton energy. The circular anode was divided into 66 individually read-out pads. The anode–cathode space was 230 mm. For energy calibration and gas purity control, a ^{241}Am α -source was placed on the cathode.

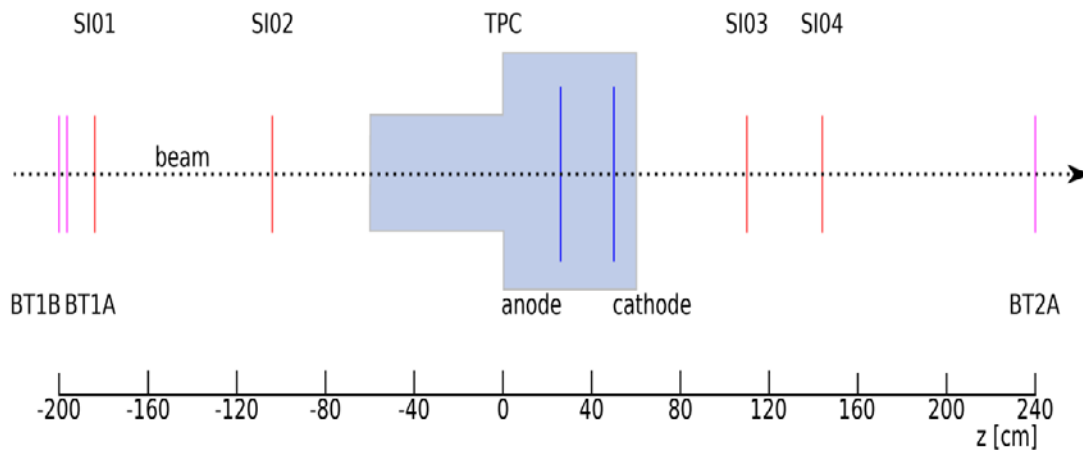


Fig. 3. The experimental set-up for the feasibility test of the proton charge radius measurement. The silicon strip detectors (SI01-04) are indicated in *red*, the beam trigger (BT1-2) – in *purple* and the TPC – in *blue*

Two silicon detectors upstream of the TPC were used to measure incoming muon tracks and two detectors downstream to measure the scattered tracks. They covered an area of $70 \times 50 \text{ mm}^2$ with a strip pitch of about $50 \mu\text{m}$. Each detector consisted of two coordinate planes: an XY plane and a UV plane rotated by five degrees with respect to each other. The readout was based on the APV25 chip. Spatial resolution of about $14 \mu\text{m}$ and time resolution of about 2 ns was achieved. A beam trigger system consisting of two scintillators in the beginning and the end of the set-up was used.

For each TPC and silicon tracker event, the timestamp difference was calculated. It was shown that correlated events took place within a certain time window corresponding to the TPC drift time of about $64 \mu\text{s}$ (Fig. 4a). Additionally, a correlation between the Z vertex and the drift time was clearly visible (Fig. 4b).

To calculate the total recoil proton energy in the TPC, the signals on the pads corresponding to the ionization track were summed up. The TPC data show a clear correlation of the measured energy with the energy kinematically reconstructed from the muon scattering angle (Fig. 5).

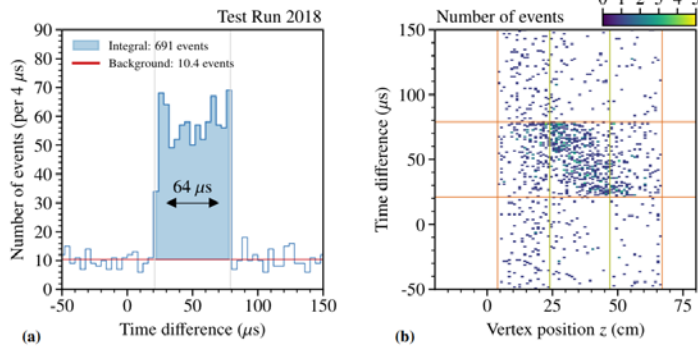


Fig. 4. Timestamp difference between TPC events and muon candidates (a); correlation between the time difference and the Z vertex (b)

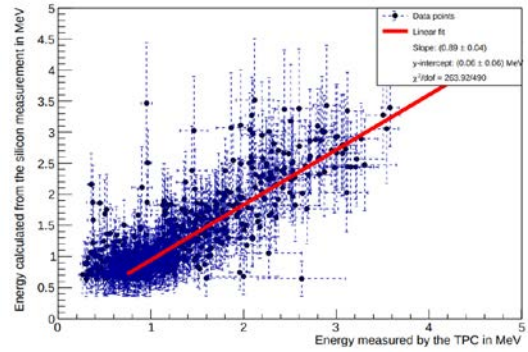


Fig. 5. Correlation between the proton energy measured in the TPC and that calculated using the muon kinematics

5. AMBER Pilot Run (2021)

In the end of 2021, a Pilot Run was carried out to further evaluate the performance of the detectors with the conditions closer to the final measurement. This run was approved by the CERN research board following the recommendation by the SPSC. The experimental set-up was located in the upstream region of the COMPASS experimental hall. The advantage of this position was the beam width of $\sigma = \sim 15$ mm and the possibility to utilize the COMPASS spectrometer for muon momentum measurements. The energy of the beam was about 100 GeV.

At the centre of the Pilot Run, the experimental set-up was IKAR ionization chamber with newly modified internal structure designed to replicate the geometry and anode segmentation to match the final TPC as closely as possible (Fig. 6). The IKAR TPC consisted of two cells with ~ 40 cm anode-cathode space equipped with field shaping rings placed around the active volume (Fig. 7). For energy calibration and gas purity control purposes, ^{241}Am α -sources were placed on the cathode and the grid. This made it possible to determine the electron attachment coefficient and the subsequent correction of the recoil proton energy. The TPC operated with hydrogen at up to 8 bar pressure.

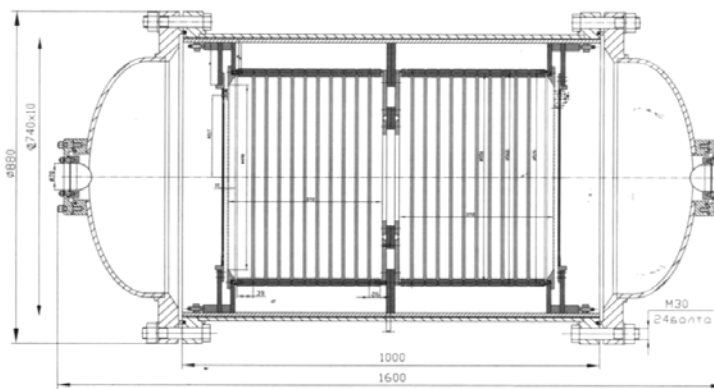


Fig. 6. The modified IKAR TPC with two drift cells

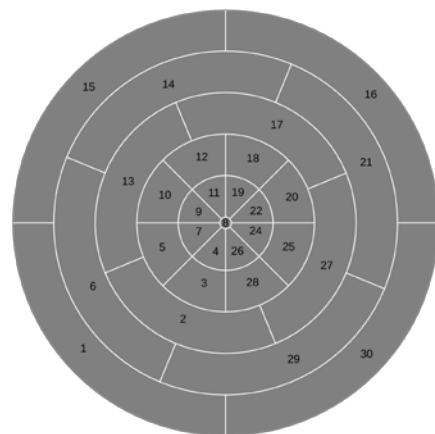


Fig. 7. Modified IKAR TPC anode plane segmentation (mapping for cell 1). The anode diameter is 40 cm

Additionally, a beam trigger system, silicon strip detectors, scintillating fiber detectors and a GEM detector were used (Fig. 8).

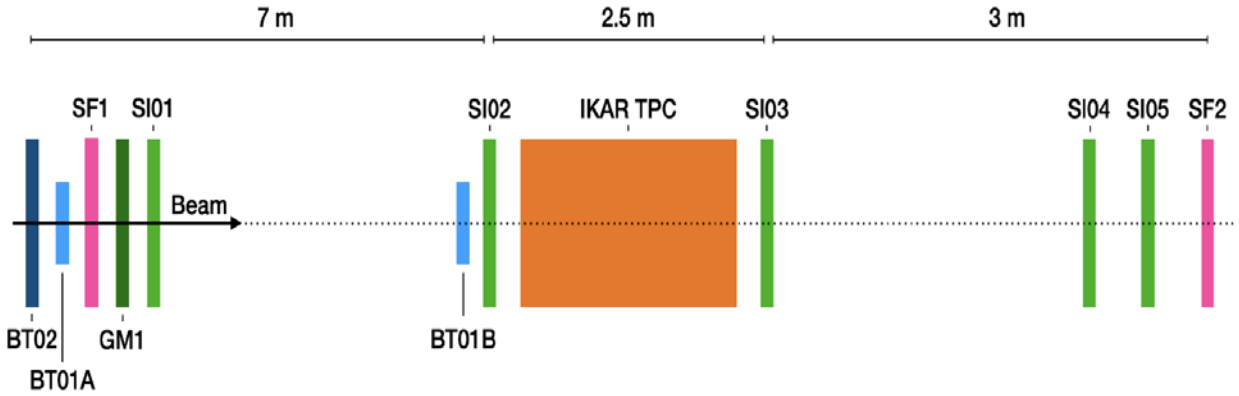


Fig. 8. The experimental set-up for the Pilot Run. The silicon strip detectors (SI01-05) are indicated in *green*, beam trigger (BT01-02) – in *blue*, scintillating fiber detectors (SF1-2) – in *pink*, GEM detector – in *dark green* and TPC – in *orange*

The synchronization of two DAQ systems was performed using a timestamp technique. The resulting timestamp difference between tracking and the TPC indicated a drift time of $145 \mu\text{s}$ (Fig. 9a). A correlation between the Z vertex and the drift time is clearly visible for both TPC active volumes (Fig. 9b).

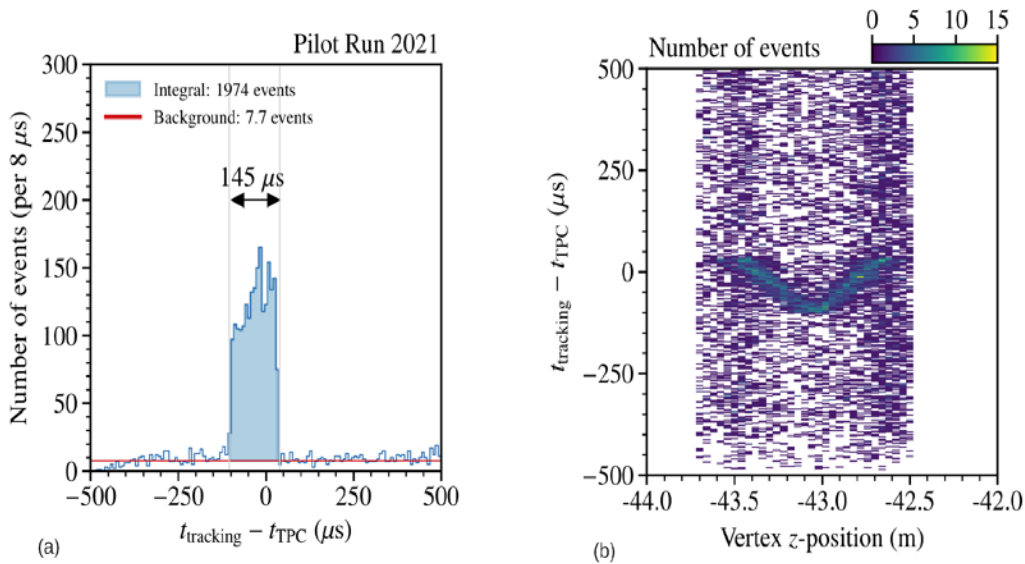


Fig. 9. Timestamp difference between TPC events and muon candidates (a); correlation between the time difference and Z vertex for two TPC cells (b)

To evaluate the influence of the beam intensity on the TPC energy resolution, a dedicated intensity scan measurement was performed. In this measurement, a test signal was sent to all channels of the TPC signal amplifiers. The fluctuation of the ionization produced by beam muons resulted in increased widths of energy distributions on anode pads. The beam intensity was measured with an ionization chamber located upstream of the TPC. The results show an acceptable level of beam noise even at high beam rates (Fig. 10).

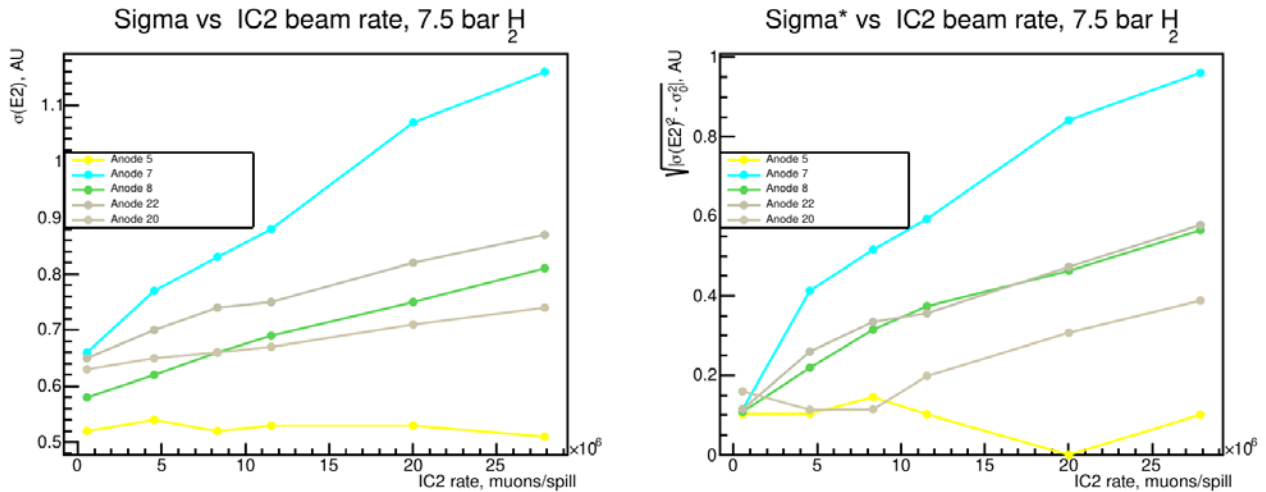


Fig. 10. Dependence of the energy resolution on the beam rate (with zero beam values subtracted on the *right plot*). 28 million muons per spill correspond to ~ 5.6 MHz rate. 1 AU (arbitrary unit) ≈ 30 keV. See Fig. 7 for anode pad numbers

6. Hardware development

The PNPI group is responsible for the design of the new AMBER high-pressure TPC of large radius. Currently two possible options are discussed. These are variants with two or with four drift cells. The shorter option is developed to optimize the cost of production, however, such a choice will double the required duration of the beamtime to achieve the desired precision of the proton radius measurement. Therefore, it is designed with a possibility to convert it into the four-cell variant in future. Drawings of the two-cell variant of the TPC are presented in Fig. 11.

The inner structure of the main TPC is also under the responsibility of the PNPI group. The major requirement for it is an ultrahigh uniformity of the electric field inside the drift cell. This can be achieved by the installation of high-precision correction coils. The test assembly of the drift cell was done at PNPI in 2022 (see *middle panel* of Fig. 11).



Fig. 11. A drawing of two-cell variant of a high-pressure TPC (*left panel*); a test assembly of the TPC inner structure (*middle panel*); a design of the gas purification unit (*right panel*)

A liquid nitrogen-based gas recirculation system is proposed by the PNPI group for the AMBER proton radius measurement program aiming to provide high purity hydrogen in the TPC. The system will operate the TPC at different pressures between 0 and 20 bar. The system is designed to keep a maximum pressure of 30 bars to satisfy safety requirements. The proposed scheme of the AMBER TPC consists of three main blocks: detector enclosure part, gas storage area (gas bottles, pressure reducer, MV10), gas system (mechanical compressor and purification units). An alternative to the temperature stabilization scheme with the detector

enclosure is a so-called density stabilization technique relying on an adjusting of a hydrogen flow to the measured temperature. Such a scheme was developed in the past for the MuCap experiment, where per mille precision was achieved. Moreover, simultaneous online measurement of the gas temperature and pressure allows to determine the target thickness with the required precision. The core part of the AMBER TPC gas system will be two liquid-N₂-based gas purification units designed at PNPI (see Fig. 11).

The expected admixtures to hydrogen are air components and water. These admixtures are a source of TPC signal degradation, which is caused by attachment of electrons during their drift. The level of admixtures will be controlled by water and oxygen sensors. The water level is assumed to be the main benchmark, as other admixtures known to be less. Chromatography can be an optional solution for control, but the elements which are controlled should be known beforehand.

7. Conclusion

The AMBER (NA66) experiment, recently approved at CERN, shall use the M2 beamline arriving at the EHN2 experimental hall, for a series of QCD-related studies addressing various aspects of the so-called emergence of hadron mass mechanism: the proton and mesons charge radii, the mesonic parton momentum distributions. The physics program will start in 2023, with a measurement of the proton radius from the muon–proton elastic scattering and antiproton production in proton–helium collisions. The PNPI group plays a key role in the measurement of the proton charge radius in muon–proton scattering using the active target technique. A series of pilot experiments was conducted in 2018–2021. A new high-pressure TPC and a gas system are designed. The design, as well as a test assembly of the TPC drift cell, was done.

References

1. AMBER: Proposal for Measurements at the M2 Beam Line of the CERN SPS. <https://cds.cern.ch/record/2676885/>
2. Minutes of the 235th Meeting of the CERN Research Board. <https://cds.cern.ch/record/2746325>
3. G.D. Alkhazov *et al.*, PNPI. High Energy Physics Division. Main Scientific Activities 2007–2012, 375 (2013).

THE SPASCHARM EXPERIMENT AT THE ACCELERATOR U-70 (IHEP, PROTVINO)

PNPI participants of the SPASCHARM Collaboration: V.A. Andreev, A.B. Gridnev, N.G. Kozlenko, V.S. Kozlov, V.A. Kuznetsov, D.V. Novinsky, V.I. Tarakanov, V.S. Temirbulatov

1. Introduction

A new world-class research in the SPASCHARM (spin asymmetry in charmonia) experiment has been constructed at the largest accelerator facility in Russia, the U-70 facility, at the Institute for High Energy Physics (IHEP, Protvino).

This project is aimed at studying such fundamental problems of modern particle physics as the spin structure of the proton and the mechanism of formation of spin asymmetries in the creation of particles. Solving the problem of the proton spin crisis is one of the important tasks of modern high energy physics. The study of charmonium at energies up to 45 GeV in a polarized beam gives access directly to the gluon distribution function. As part of the first stage of the experiment, the study of the spin properties of hadrons will take place in a beam of negatively charged hadrons on existing beamline 14 at the operating SPASCHARM set-up at the U-70 accelerator facility. With the SPASCHARM set-up, it is also possible to measure the transverse polarization of hyperons and elements of the spin density matrix of vector mesons. The spin structure of the nucleon will be investigated in the study of the quarkonium production to determine the contribution of gluons to the proton spin.

At the second stage, the production of polarized beams of protons and antiprotons is envisaged in beamline 24A of the U-70 accelerator facility. A polarized antiproton beam will certainly become a unique beam in the world. It is planned to measure single-spin asymmetries in dozens of reactions, both on hydrogen and on various nuclei. The presence of two types of polarized beams (p , \bar{p}) and eight types of unpolarized beams (π^\pm , K^\pm , p , \bar{p} , d , C), in combination with a polarized target, expands the range of studies of polarization phenomena and enhances the uniqueness of the project.

2. The perspective project at beamline 24A

Studies of the last few decades have shown the presence of significant spin effects in various physical processes. However, the observation of large spin effects has not yet been explained in terms of the standard perturbation theory of quantum chromodynamics (QCD), which assumes collinear kinematics. In this regard, further systematic experimental studies in this area are relevant, involving the measurement of several spin-dependent observables (one-spin and two-spin asymmetries, hyperon polarization, elements of the spin matrix of vector mesons) in dozens of different reactions.

A global analysis of the data obtained in this way will reveal general patterns of data behaviour, including a comparison of particle and antiparticle interactions with protons and nuclei, the role of colour forces, the spin structure of the nucleon, the dependence of spin effects on the isotopic spin and beam energy, the type of quarks, and the atomic weight of the target and the multiplicity of particles in the event. Previously, studies of this magnitude have not been carried out. Interactions of polarized particles are a unique tool for studying the mechanism of strong interactions in the confinement region, which cannot be done so far by studying collisions of unpolarized hadrons. To carry out the above studies, the creation of a world-class experimental facility and a polarized channel of protons and antiprotons is required.

The project of the SPASCHARM experiment on new 24A (Fig. 1) hadron particle channel, created at the U-70 accelerator, is aimed at studying the spin dependence of the strong interaction of matter (and antimatter) and the spin structure of the nucleon [1]. First of all, a survey polarization experiment will be carried out on antiproton and proton polarized beams at an energy of 15 GeV and a polarization of up to 45% with the measurement of the same large set of physical observable quantities. To study the spin structure of the nucleon, a research will be carried out on the formation of charmonium in the fragmentation region of a polarized beam. The polarization of gluons in a longitudinally polarized proton $\Delta G/G$ will be determined through the formation of charmonium states χ_{c1} (3 510 MeV) and χ_{c2} (3 555 MeV).

IHEP completed the draft design of new 24A hadron channel (total length of the channel is 180 m) from the target to the end of the channel. This project involves the transmission of a proton beam from its output from the U-70 to the primary target located in front of a special radiation-resistant magnet [2]. In channel 24A, the formation of polarized beams of protons and antiprotons is assumed. Their parameters were calculated. The intensity of the antiproton beam can reach 10^6 antiprotons per accelerator cycle when 10^{13} protons from U-70 are dropped onto the primary target. The polarized antiproton beam will undoubtedly be a unique beam in the world. Note that the FAIR (facility for antiproton and ion research) project in Germany is planning the appearance of an antiproton, high-intensity, but unpolarized beam with an energy of up to $E = 15$ GeV.

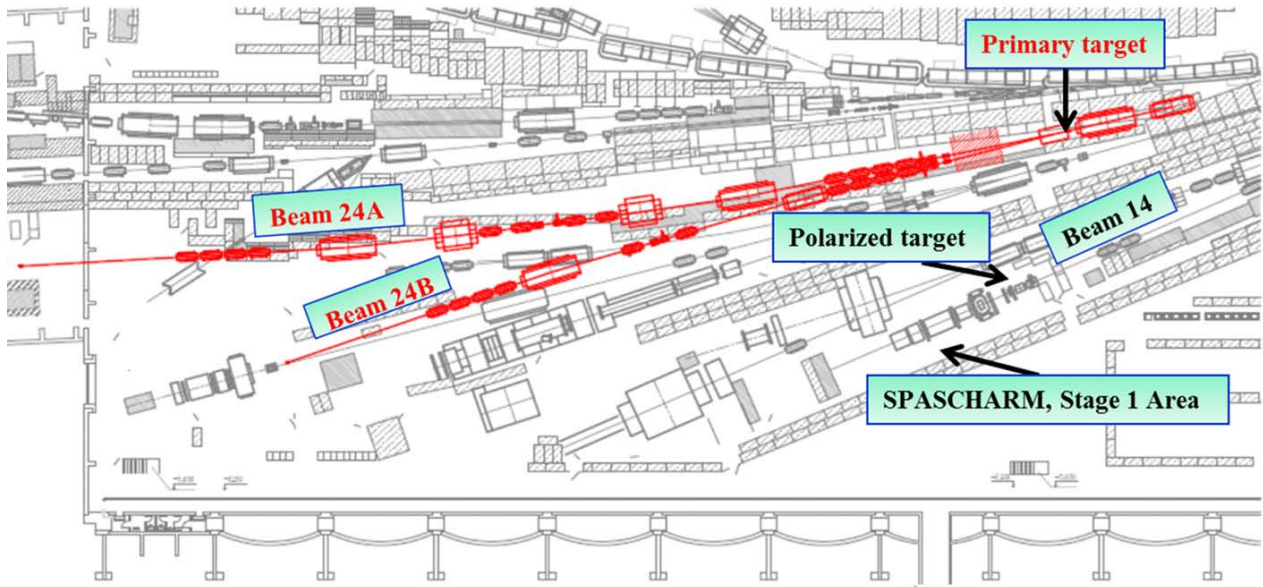


Fig. 1. Layout of channels 24A and 24B in the experimental hall of the U-70 accelerator

Unlike most previous polarization experiments, SPASCHARM will implement 2π -geometry in the azimuth angle, which can significantly improve the measurement accuracy of spin observables and, most importantly, minimize systematic measurement errors. The solid angle of the set-up ($\Delta\theta \approx 200$ mrad vertically and $\Delta\theta \approx 300$ mrad horizontally in the beam fragmentation region) allows measurements in a wide range of kinematic variables (p_T , x_F) and will make it possible to separate the dependences on these two variables, which is usually not possible in experimental set-ups with a small solid registration angle.

To carry out the research program, it is necessary to build a system of superconducting magnets, “Siberian snakes”, which ensures the rotation of the beam polarization on the target, as well as the cryogenic system of channel 24A. The installation requires the creation of a precision thin-segmented electromagnetic calorimeter of the “Shashlyk” type with a small cell, a wide-aperture multichannel Cherenkov detector of the ring image Cherenkov (RICH) type, the creation of a polarimeter system for measuring the absolute value of the beam polarization, and the presence of a polarized target with a vertical and horizontal spin orientation. A scheme of the installation, including the beam equipment, the polarized target, the magnetic spectrometer, the electromagnetic calorimeter, the hadron calorimeter, the system for detecting secondary particles, the trigger, and data acquisition system, is shown in Fig. 2.

The main purpose of the SPASCHARM physical program is to expand our knowledge in the field of strong interactions, the structure of hadrons, and the role of spin in the dynamics of strong interactions. The measurement of various spin observables (asymmetry A_N , polarization P_N , spin transfer D_{NN} , elements of the spin density matrix ρ_{ik} , etc.) opens additional opportunities for comparing experimental data and model predictions, which will eventually contribute to solving the above problems. In particular, the study of the ratios of the yields χ_{c1} and χ_{c2} will make it possible to verify a new theorem on scale invariance in the yields

of these mesons [3], the experimental validation of which was found in experiments at the Large Hadron Collider (LHC) [4].

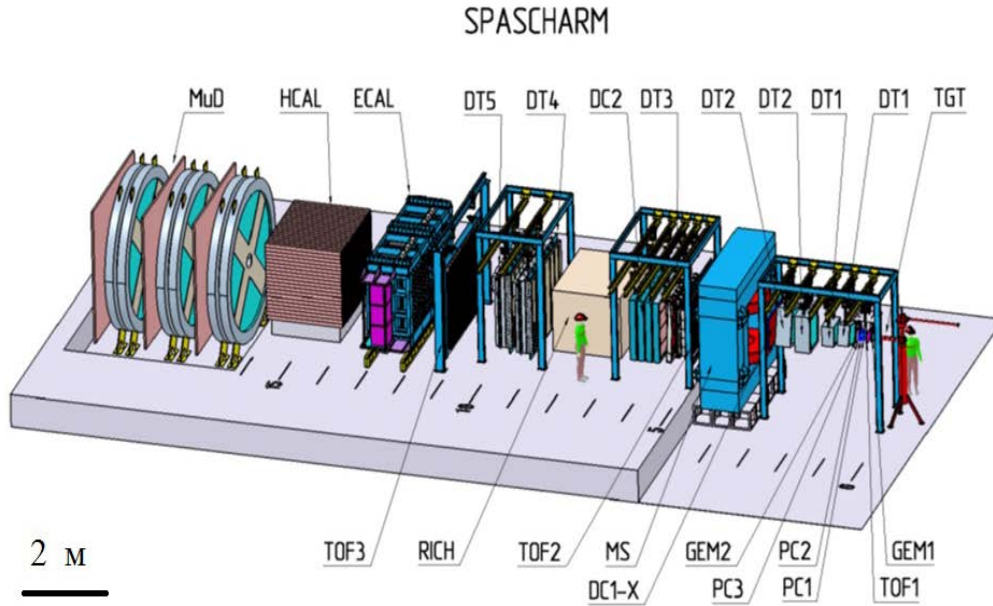


Fig. 2. Schematic view of the future experimental set-up SPASCHARM installation: TGT – the polarized target; GEM1–GEM2 – the GEM detectors; TOF1–TOF3 – the time-of-flight systems; PC1–PC3 – the proportional chambers developed at PNPI; DT1–DT5 – the drift tubes stations; ECAL – the electromagnetic calorimeter; RICH – the Cherenkov detector, HCAL – the hadron calorimeter; MuD – the muon detector

One of the possible ways to measure the polarization of partons (quarks and gluons in a proton) is to study the formation of particles ϕ , $f_2(1520)$, as well as χ_{c1} and χ_{c2} , which decay into J/ψ and a photon. It is well known that the formation of quarkonia involves three main processes at the parton level (Fig. 3): quark–gluon scattering (a), light quark annihilation (b) and gluon–gluon fusion (c) [5, 6]. In this case, in the considered energy range, the dominant contribution for the proton beam will come from the process of quark–gluon scattering, and for the antiproton scattering, from quark–antiquark annihilation.

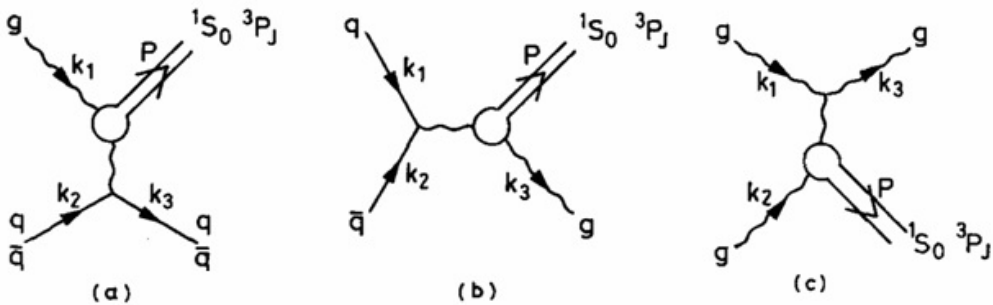


Fig. 3. The typical quarkonium formation diagrams

The SPASCHARM experiment will allow simultaneous measurements of the analysing powers of the beam A_B , of the target A_T , and of the spin correlation coefficient A_{NN} in the elastic pp -scattering. In the region of the diffraction cone $0.075 < -t < 0.6$ (GeV/c)² at a momentum greater than 12 GeV/c , there are no data for A_{NN} . In addition, it is possible to experimentally verify the obvious equality of A_B and A_T .

The purpose of research at the SPASCHARM set-up is to solve problems of studying the spin properties of the strong interaction, which no one in the world has yet tried to solve and is planning to do soon due to the difficulties and complexity of the research. The closest and supplementing the physical program

of the SPASCHARM experiment is the project of the SPD (spin physics detector) Collaboration created recently [7, 8] at the NICA (nuclotron-based ion collider facility) accelerator under construction at the Joint Institute for Nuclear Research (JINR).

3. The existing experimental set-up at U-70 channel 14

There is a significant backlog for the creation of the SPASCHARM facility up to the present. A wide-aperture spectrometric magnet has been assembled, tested and is already in operation. Two multichannel threshold Cherenkov detectors have been created and are being adjusted. They are quite capable of providing the first measurements on the antiproton beam, albeit in a limited solid angle compared to the full design configuration. The creation of a precision tracking system based on drift tubes is nearing completion. A hadron calorimeter is available. Beam equipment is being created, the new recording electronics and a data acquisition system in the EuroMISS* standard are being adjusted [9].

At the first stage of the research, the experimental set-up is commissioned with a limited number of detectors. Figure 4 shows a diagram of the experimental set-up for the present. The system of beam detectors located along the beam axis (beam) includes scintillation (S1–S3) and threshold Cherenkov counters (C1–C3, the first two Cherenkov counters are located upstream of the beam and are not shown in the diagram), as well as scintillation hodoscopes (H12, H2). The beam equipment also may include an anticoincidence counter (BK) and magnet-correctors of the set-up (KM1, KM2).

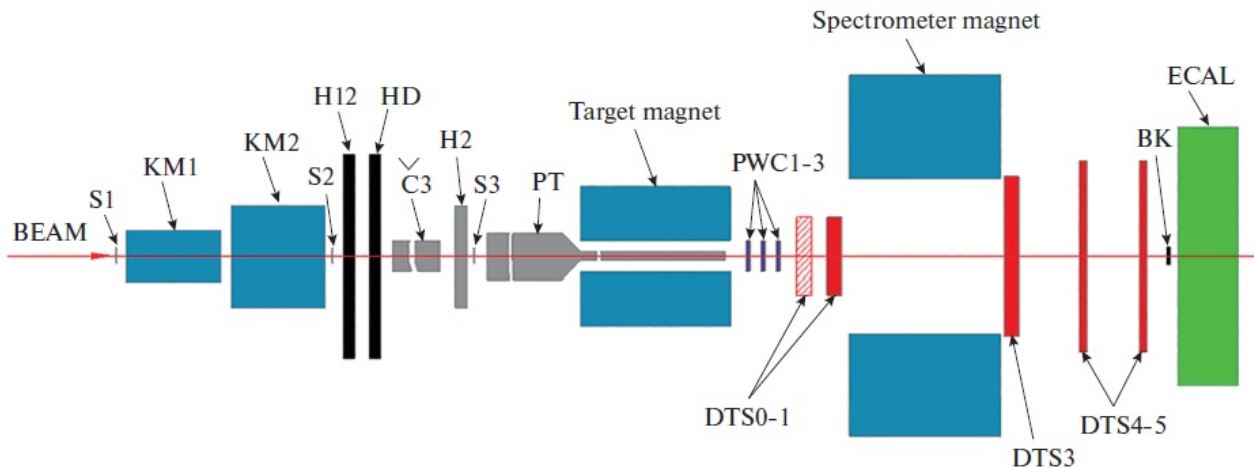


Fig. 4. Schematic diagram of the present SPASCHARM set-up

The spectrometer of the set-up in the current configuration consists of 57 planes of tracking detectors and a wide-aperture magnet; the set-up is primarily designed to detect charged particles. It is possible to supplement the set-up with six more planes. Detection of gamma quanta and electrons is carried out by an electromagnetic calorimeter based on lead glass. The main element of the set-up is a facility of proton polarized “frozen” target (PT), including a magnet with a field inhomogeneity of 10^{-4} . The target is surrounded by a protecting system to suppress background processes.

This scheme will be added in the nearest future by GEM-type tracking detectors, an identification system consisting of time-of-flight (ToF) detectors, a Cherenkov radiation detector RICH, and a muon detector, as well as a hadron calorimeter, and drift chambers produced at the PNPI for the EPECUR (the experiment for pentaquark search in the elastic scattering) experiment [10].

* The electronic system “EuroMISS” for creation of apparatus for IHEP experimental set-ups is the evolution of the system MISS (multichannel information high-speed system) and it bases on the Eurocard standard.

4. The running experiments on channel 14

These studies are the most complex in the SPASCHARM program and impose severe constraints on the requirements for the experimental set-up; in this case, at the early stages no fewer interesting tasks will be solved:

- Measurement of single-spin transverse (azimuthal) asymmetries A_N of hadrons consisting of light u , d , s quarks upon scattering of a transversely polarized beam on an unpolarized target, or an unpolarized beam on a transversely polarized target. Any particles (with spin $J = 0, 1/2, 1, \dots$) and even nuclei can be used as a detected particle. The detection of hadron resonances, in addition to the usually measured hadrons that are stable in terms of the strong interaction, will make it possible to significantly expand the list of reactions available for study. Previously, there were almost no measurements of A_N for resonances;
- Determination of transverse (with respect to the scattering plane) polarizations P_N of hyperons and antihyperons produced by unpolarized beams on unpolarized targets (a proton target and nuclear targets). The polarization P_N can be measured due to parity violation in weak two-particle hyperon decays. The parameters of the angular distribution of hyperon decay products are related to the polarization of the decaying particle. Comparison of A_N and P_N for hyperons (antihyperons) opens additional possibilities for choosing (or rejection) a specific model for generating significant A_N and P_N . Until now, there have been almost no simultaneous measurements of A_N and P_N for a given reaction;
- Measurement of alignment (of density matrix elements ρ_{ik}) of vector mesons (spin $J = 1$, parity P is negative), decaying into two particles, in the processes of collisions of unpolarized particles. As in the case of hyperons, the alignment and A_N can be measured and compared for vector mesons, which has never been done before, and which makes it possible to obtain additional constraints on the strong interaction mechanism.

4.1. Measurement of single-spin transverse asymmetries A_N of hadrons

Usually, the main motivation for research with a polarized target or beam is the problem of studying the structure of the proton. Spin effects can also be associated with such fundamental problems as spontaneous breaking of chiral symmetry, the appearance of mass in quarks and hadrons, the formation of quasiparticles in hadrons – constituent quarks [11]. The study of the spin structure of the nucleon is at the same time only one of the goals of the SPASCHARM experiment. Another important area of research is the study of the dynamics of strong interactions with allowance for spin.

One of the main physical observables is the transverse single-spin asymmetry A_N , which is proportional to the difference in the cross sections for opposite directions of the transverse polarization of the beam or target:

$$A_N = \frac{\sigma^\uparrow - \sigma^\downarrow}{\sigma^\uparrow + \sigma^\downarrow}, \quad (1)$$

or differences in the cross sections at angles of 90° (left) and -90° (right),

$$A_N = \frac{\sigma_{\text{left}}^\uparrow - \sigma_{\text{right}}^\uparrow}{\sigma_{\text{left}}^\uparrow + \sigma_{\text{right}}^\uparrow}, \quad (2)$$

relative to the direction of the proton polarization vector.

The “raw” single-spin asymmetry A_N^{meas} is defined as follows in terms of the measured quantities:

$$A_N^{\text{meas}} = \frac{D}{P \cdot \cos\varphi} \cdot \frac{(N^\uparrow - N^\downarrow)}{(N^\uparrow + N^\downarrow)}, \quad (3)$$

where P is the polarization of the beam or target, $\cos\varphi$ is the mean cosine angle between the normal to the scattering plane and the direction of the beam or target spin*. The value of D is called the dilution factor in a

* With full (2π) geometry, the azimuth angle is fitted with $\cos\varphi$.

polarized target*. The yields of the observed hadron h normalized to the number of beam particles for the upward or downward polarization of the beam or target are denoted as $N\uparrow$ and $N\downarrow$, respectively. According to the convention [12], A_N is considered positive if more hadrons h fly to the left for a beam with upward polarization†.

As shown in Ref. [1], it is no longer energy that comes to the fore in polarization studies, but the systematic study and analysis of data from a large number of different reactions. In the studies at the SPASCHARM facility, it is proposed to pay attention, first of all, to two aspects:

- Comparison of polarization effects in the interaction of particles and antiparticles with matter at the same energy and in the same kinematic region;
- Investigation of spin effects for a large class of reactions in a wide kinematic region.

4.2. Measurement of transverse polarizations P_N of hyperons and antihyperons

The SPASCHARM experiment will be the first one with the possibility of simultaneous measurements of A_N and P_N . Comparison of these values for hyperons (antihyperons) opens up additional possibilities for choosing (or discriminating) a specific model for generating significant A_N and P_N . The measurement of hyperon polarization is possible due to the presence of a weak decay that occurs with parity violation. So, in the case of the decay of a Λ -hyperon from a state with polarization P , into a π^- -meson and a proton, the dependence of the proton emission probability at an angle θ_p to the direction of the hyperon polarization vector \mathbf{P} has the form:

$$\frac{dN}{d\Omega} = \frac{1 + \alpha \mathbf{P} \mathbf{e}_p}{4\pi} = \frac{1 + \alpha P \cos \theta_p}{4\pi}, \quad (4)$$

where \mathbf{e}_p is a unit vector in the direction of proton motion in the hyperon's rest frame. The vector \mathbf{P} is directed, due to parity conservation in strong interactions, along the normal vector \mathbf{n} to the scattering plane, which is determined by the direction of the momentum of the incident baryon \mathbf{p}_a and the momentum of the resulting hyperon \mathbf{p}_c : $\mathbf{n} = (\mathbf{p}_a \times \mathbf{p}_c) / |\mathbf{p}_a \times \mathbf{p}_c|$. The asymmetry parameter $\alpha = 0.642 \pm 0.013$ of parity breaking weak decay is a measure of interference between s and p waves in the final state [13].

The transverse polarizations P_N of hyperons and antihyperons can be measured on any of the beams considered above, unpolarized and polarized. In the latter case, it will be necessary to average P_N over two polarizations. It is also possible to use the unpolarized part of the beam, which will be present and measured during the operation of the beam tagging system [14]. To estimate the statistical accuracy of measuring P_N of hyperons, one can use one of the formulas for determining the polarization:

$$P_N = \frac{2 \text{Up} - \text{Down}}{\alpha \text{Up} + \text{Down}}, \quad (5)$$

where "Up" and "Down" denote the integrals of the angular distribution corrected for the efficiency in the region of positive (Up) and negative (Down) values of the cosine of the angle θ_p , between the normal to the scattering plane and the direction of proton emission in the hyperon rest frame [15]. The statistical accuracy of measuring P_N of hyperons, by analogy with δA_N , is determined by the expression:

$$\delta P_N = 2 / [(1 - B/N_{EV}) \alpha \sqrt{N_{EV}}], \quad (6)$$

where $N_{EV} = \text{Up} + \text{Down} = S + B$ is the total number of events with a hyperon in the final state, B is the number of background events under the peak of the mass of the reconstructed hyperon. The parameter α for most hyperons has a significant value, on the order of 0.5, which makes it possible to obtain a high accuracy of P_N measurements.

* The dilution factor D is defined as the total number of interactions in the target divided by the number of interactions on polarized protons. When using a polarized beam, $D = 1$ is assumed.

† To compare single-spin asymmetries obtained in measurements with a polarized beam and A_N obtained on a polarized target, it is necessary to change the sign of A_N for measurements on a polarized target.

It is possible to measure the polarization at the SPASCHARM experiment not only of the Λ -hyperon, but also of other hyperons and antihyperons. Since the distance from the target centre to the last chamber in front of the spectrometric magnet is almost 3 m, most of the hyperon decays will occur in the area of the facility equipped with track detectors, and the parameters of hyperon decay tracks can be measured. The hyperon polarization measurements began in the 70s of the last century and gave an unexpected result: the Λ -hyperon polarization is large and does not decrease with energy [1].

Taking into account the statistics of hyperons and decay parameters [1], the statistical accuracy for most reactions will be no worse than 0.5%, and for the reaction $K^-p \rightarrow \Sigma^-X$ it will be 8%. Figure 5 presents the predictions for the polarization of antilambda hyperons in the pA interaction within the framework of the model of chromomagnetic polarization of quarks [16–18].

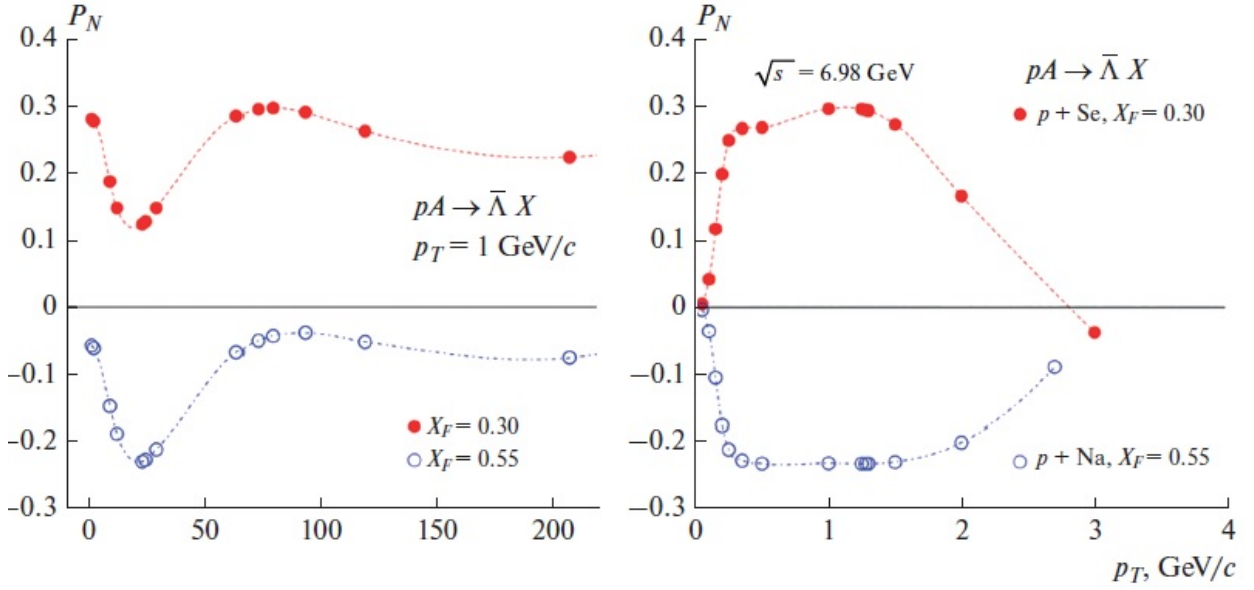


Fig. 5. Polarization predictions for antilambda hyperons in pA interaction within the framework of the model of chromomagnetic polarization of quarks

4.3. The elements of the density matrix ρ_{ik} of vector mesons measurements

As in the case of hyperons, for vector mesons the alignment and A_N can be measured and compared. The density matrix elements ρ_{ik} of vector mesons can be measured on any of the beams considered above, unpolarized and polarized. If single-spin effects are associated with the polarization of quarks and antiquarks prior to the process of their hadronization, then we should observe not only the polarization of hyperons, but also the polarization of vector mesons [19]. The alignment of vector mesons (V) is described by the elements $\rho_{mm'}$ of the spin density matrix ρ , where m and m' denote the spin components along the quantization axis.

The diagonal elements ρ_{11} , ρ_{00} and ρ_{-1-1} for the unit trace matrix are the relative intensities of the meson spin components m , take the values 1, 0 and -1 , respectively, which should be equal to $1/3$ for the case of unpolarized particles. Since vector mesons usually decay strongly into two pseudoscalar mesons, it is difficult to measure all elements of the matrix ρ . But some of them can be easily determined from measurements of the angular distributions of the decay products. It can be shown that in the rest frame of the vector meson V , for the decay $V \rightarrow h_1 + h_2$, where h_1 and h_2 are pseudoscalar mesons, the angular distribution $W(\theta, \varphi) = dN/d\Omega$ of the decay products has the form [19]:

$$\begin{aligned}
 W(\theta, \varphi) = & 0.75\{\cos 2\theta \rho_{00} + \sin 2\theta (\rho_{11} + \rho_{-1-1})/2 - \\
 & - \sin 2\theta (\cos \varphi \operatorname{Re}\rho_{10} - \sin \varphi \operatorname{Im}\rho_{10})/\sqrt{2} + \\
 & + \sin 2\theta (\cos \varphi \operatorname{Re}\rho_{-10} + \sin \varphi \operatorname{Im}\rho_{-10})/\sqrt{2} - \\
 & - \sin 2\theta (\cos 2\varphi \operatorname{Re}\rho_{1-1} - \sin 2\varphi \operatorname{Im}\rho_{1-1})\}/\pi.
 \end{aligned} \tag{7}$$

Here θ is the polar angle between the direction of motion h_1 and the quantization axis, ϕ is the azimuthal angle. Integrating over the angle ϕ , we obtain:

$$W(\theta) = 0.75\{(1 - \rho_{00}) + 3(\rho_{00} - 1) \cos 2\theta\}. \quad (8)$$

Similarly, integrating over the angle θ , we get:

$$W(\phi) = \frac{0.5\{1 - 2 \cos 2\phi \operatorname{Re}\rho_{1-1} + 2 \sin 2\phi \operatorname{Im}\rho_{1-1}\}}{\pi}. \quad (9)$$

The deviation of ρ_{00} from $\frac{1}{3}$ leads to an uneven distribution of the decay products over $\cos\theta$. By measuring $W(\theta)$, one can determine ρ_{00} . Other elements, ρ_{10} and ρ_{1-1} , can be studied by measuring $W(\theta, \phi)$. In a few cases, these measurements have already been made for hadron–hadron collisions, *e. g.*, in Refs. [20, 21]. It is possible to simultaneously measure the density matrix element ρ_{00} for a number of vector mesons (ρ , ω , ϕ and J/ψ) in the SPASCHARM experiment, in the mode of decay into pseudoscalar mesons and the parameter α in the modes of their decay into e^+e^- and $\mu^+\mu^-$. It is also possible to measure the single-spin asymmetry A_N for these vector mesons using a polarized target or a polarized beam.

Simultaneous measurement of three different polarization parameters of vector mesons at the same facility is a great advantage of the proposed research program, since it allows one to make a more significant discrimination of alternative models of the origin of polarization effects. Previously, such large-scale studies of spin effects for vector mesons were not planned.

5. Conclusion

The SPASCHARM polarization project features a global, systematic approach to the study of the antiproton–proton (nucleus) and proton–proton (nucleus) systems, including conducting a survey polarization experiment and simultaneously studying dozens of reactions and several physical observables that depend on many variables. The polarization of gluons in the proton (antiproton) in the region of their fragmentation will be determined from the study of the formation of charmonium. The expected high accuracy of measurements, minimum systematic errors, combined with a wide range of beams, targets, secondary charged and neutral particles distinguishes this project from other polarization projects. Note that the polarized antiproton and proton beams are truly unique tools in these studies.

References

1. V.V. Abramov *et al.* NRC “Kurchatov Institute” – IHEP Preprint 2019-12, 148 (2019).
2. V. Abramov *et al.*, Nucl. Instrum. Meth. Phys. Res. A **901**, 62 (2018).
3. G. Kane, J. Pumplin, W. Repko, Phys. Rev. Lett. **41**, 1689 (1978).
4. A.K. Likhoded, A.V. Luchinsky, S.V. Poslavsky, Phys. Rev. D **90**, 074021 (2014).
5. S.D. Ellis *et al.*, Phys. Rev. Lett. **36**, 1263 (1976); C.E. Carlson, R. Suaya, Phys. Rev. D **14**, 3115 (1976); C.E. Carlson, R. Suaya, Phys. Rev. D **18**, 760 (1978); R. Baier, R. Rucki, Z. Phys. C **19**, 251 (1983); V. Barger, A.D. Martin, Phys. Rev. D **31**, 1051 (1985).
6. V.V. Abramov *et al.*, arXiv:hep-ex/0511046 (2005).
7. SPD Collab., V.M. Abazov *et al.*, arXiv:hep-ph/2102.00442v3.
8. V. Abramov *et al.*, Phys. Part. Nucl. **52**, 1044 (2021), arXiv: hep-ph/2102.08477.
9. S.V. Ryzhikov, V.S. Petrov, P.A. Semenov, V.I. Yakimchuk. Instrum. Exp. Tech. **57** (6), 676 (2014).
10. I.G. Alexeev *et al.*, Instrum. Exp. Tech. **57** (5), 535 (2014).
11. D. Diakonov, Prog. Part. Nucl. Phys. **51**, 173 (2003).
12. A. Bacchetta *et al.*, arXiv:hep-ph/0410050.
13. Particle Data Group, C. Patrignani *et al.*, Chin. Phys. C **40**, 100001 (2016).
14. P.A. Semenov *et al.*, Int. J. Mod. Phys. Conf. Ser. **40** (01), 1660086 (2016).
15. G. Agakishiev *et al.*, Eur. Phys. J. A **50**, 81 (2014).
16. V.V. Abramov, Eur. Phys. C **14**, 427 (2000).
17. V.V. Abramov, Phys. Atom. Nucl. **70**, 2103 (2007).

18. V.V. Abramov, Phys. Atom. Nucl. **72**, 1872 (2009).
19. K. Schilling, P. Seyboth, G.E. Wolf, Nucl. Phys. B **15**, 397 (1970).
20. A.A. Minaenko *et al.*, Z. Phys. C **62**, 15 (1994).
21. EXCHARM Collab., A.N. Aleev *et al.*, Phys. Lett. B **485**, 334 (2000), hep-ex/0002054.

SHiP: SEARCH FOR HIDDEN PARTICLES

PNPI participants of the SHiP Collaboration: V.T. Kim, E.V. Kuznetsova, O.L. Fedin, G.E. Gavrilov, V.L. Golovtsov, N.V. Gruzinskiy, S.A. Nasybulin, V.P. Maleev, L.N. Uvarov, V.I. Yatsyura, A.V. Zelenov

1. Introduction

SHiP (search for hidden particles) at the European Organization for Nuclear Research (CERN) beam dump facility (BDF) is an ambitious experiment proposal [1–4] aimed at exploring the domain of very weakly interacting particles, which can, in particular, be constituents of the dark matter of the Universe. BDF–SHiP [2–6] is a state-of-the-art experimental set-up designed to perform a generic and exhaustive search for feebly interacting particles (FIPs) in a region of mass and coupling that is only accessible with a dedicated beam-dump configuration. The experiment aims at taking full advantage of the opportunities offered by the available but unused $4 \cdot 10^{19}$ protons at 400 GeV at the CERN super proton synchrotron (SPS) accelerator. The physics programme [7–9] includes a search for new physics through both decay and scattering signatures.

The Deliberation Document of the 2020 Update of the European Strategy for Particle Physics (ESPPU 2020) recognised the BDF–SHiP proposal as one of the front-runners among the new facilities investigated within the physics beyond colliders (PBC) studies. To respond to the financial constraints that prevented considering the project for approval in 2020, a continued programme of R&D (research and development) was launched as part of the CERN Medium Term Plan 2021–2025 with the objective for the BDF working group to review the design of the facility, aiming for an alternative implementation in an existing beam facility around the SPS in order to significantly reduce the cost with respect to the initial proposal while preserving the original physics scope and reach of the facility.

This effort has been accompanied by a revision of the detector layout by the SHiP Collaboration with the goal of reducing the size and the overall space required, in order to fit in existing underground areas. A dedicated collaboration agreement between the SHiP institutes and CERN was established through a Memorandum of Understanding in 2021 to ensure a coherent optimisation effort between the facility and the experiment. The result of this location and layout optimisation study identified ECN3 as the most suitable and cost-effective option. The decision of the CERN management to review the post Long Shutdown 3 physics programme in underground hall ECN3–TCC8 prompted the BDF–SHiP Collaboration to pursue the studies of the facility and of the SHiP detector aimed at ECN3, and to verify, by full simulation, the physics performance. The use of ECN3 for BDF–SHiP entails a major cost-saving when compared to the original proposal. The recent BDF–SHiP Letter of Intent [6] for a new chosen location reports on the results of the studies performed for ECN3 and formally expresses intent to construct BDF–SHiP in ECN3.

Why is the SHiP physics programme so timely and attractive? We have now observed all the particles of the Standard Model (SM), however it is clear that it is not the ultimate theory. Some yet unknown particles or interactions are required to explain a number of observed phenomena in particle physics, astrophysics and cosmology, the so-called beyond the Standard Model (BSM) problems, such as dark matter, neutrino masses and oscillations, baryon asymmetry, and the expansion of the Universe.

While these phenomena are well-established observationally, they give no indication about the energy scale of the new physics. The analysis of new Large Hadron Collider (LHC) data collected at 13 TeV will soon have directly probed the TeV scale for new particles with couplings at $O(1\%)$ level. The experimental effort in flavour physics, and searches for charged lepton flavour violation and electric dipole moments, will continue the quest for specific flavour symmetries to complement direct exploration of the TeV scale.

However, it is possible that we have not observed some of the hidden particles responsible for the BSM problems due to their extremely feeble interactions, rather than due to their heavy masses. Even in the scenarios in which BSM physics is related to high-mass scales, many models contain degrees of freedom with suppressed couplings that stay relevant at much lower energies.

Given the small couplings and mixings, and hence typically long lifetimes, these particles of hidden sector (HS) have not been significantly constrained by previous experiments, and the reach of current experiments is

limited by both luminosity and acceptance. Therefore, the search for low-mass BSM physics should also be pursued at the intensity frontier, along with expanding the energy frontier.

SHiP is designed to give access to a large class of interesting models with HS particles. It has discovery potentials for the major observational puzzles of modern particle physics and cosmology, and can explore some of the models down to their natural “bottom line”. SHiP also has the unique potential to test lepton flavour universality by comparing interactions of muon and tau neutrinos.

2. SHiP experimental set-up

Despite an active program of searches for HS particles in many experiments, SHiP remains a unique dedicated experiment capable of reconstructing the decay vertex of an HS particle, measuring its invariant mass and providing particle identification (PID) of the decay products in an environment of extremely low background. Moreover, SHiP is also optimised to search for light dark matter (LDM) through scattering signatures and for tau neutrino physics.

Following the technical proposal (TP) [2, 3] submitted in 2015, the subsequent three-year comprehensive design study (CDS) [4], and the recent study of BDF–SHiP [5, 6], the SHiP design went through a significant re-optimisation phase. Figure 1 shows the layout of the re-optimised SHiP detector in the newly proposed location at ECN3. While the overall set-up of the detector remains unchanged, the geometry and the detector composition has been significantly modified, and technological studies and test beams have brought maturity to the design. SHiP consists of a proton target, followed by a hadron stopper and an active muon shield that sweeps muons produced in the beam dump out of acceptance. Since the TP, the target has been extended from ten to twelve interaction lengths in order to reduce the hadronic background and to improve the acceptance of the spectrometers, and to reduce the weight and cost of the muon shield. A significant improvement was achieved by starting the first section of the muon shield within the hadron stopper by integrating a coil which magnetises the iron shielding blocks.

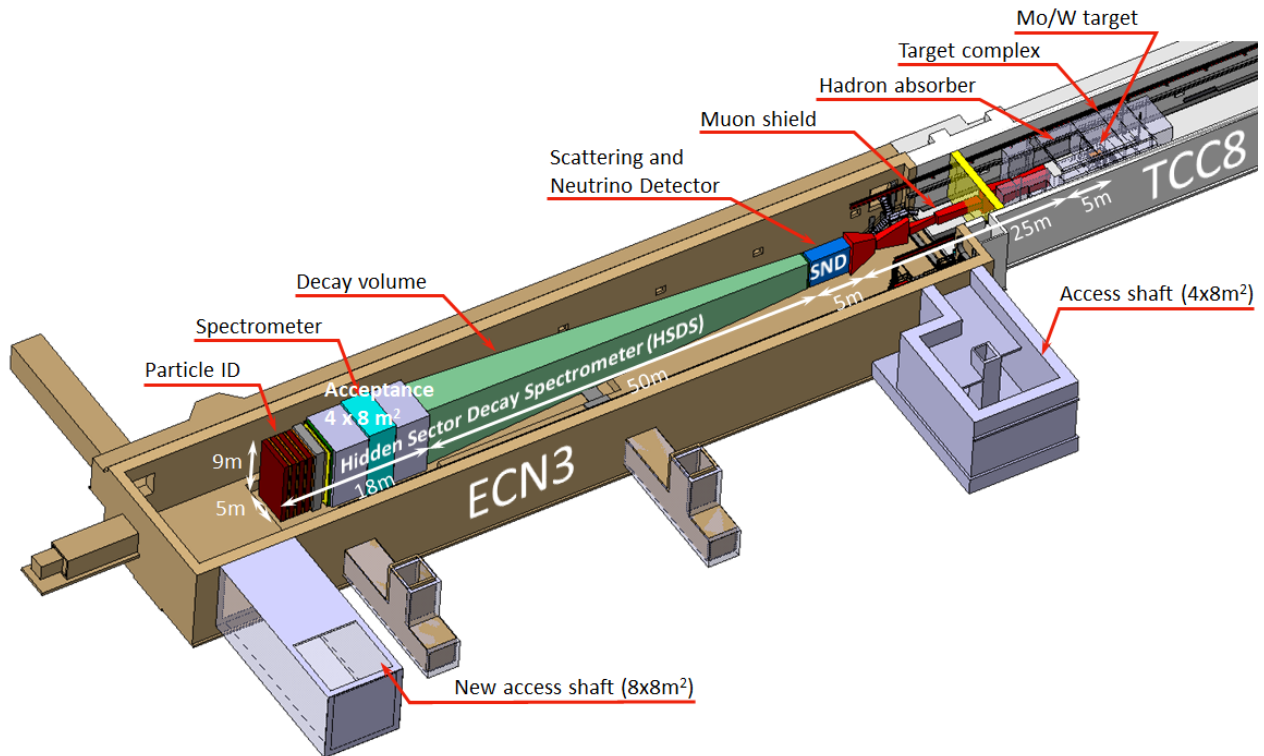


Fig. 1. Overview of the BDF–SHiP experimental set-up in the SPS TCC8–ECN3 beam facility

The SHiP detector itself incorporates two complementary apparatuses, the scattering and neutrino detector (SND), and the HS spectrometer. The SND will search for LDM scattering and perform neutrino physics. It is made of an emulsion spectrometer located inside a single long magnet with a field above 1.2 T in the entire volume, and a muon identification system. The emulsion spectrometer is a hybrid detector consisting of alternating layers of an absorber, nuclear emulsion films and fast electronic trackers. The absorber mass totals ~ 10 t.

The HS decay spectrometer aims at measuring the visible decays of HS particles by reconstructing their decay vertices in a 50 m long decay volume. In order to eliminate the background from neutrinos interacting in the decay volume, it is maintained at a pressure of $O(10^{-3})$ bar. To maximise the sensitivity to HS particles, the muon shield was shortened in combination with changing the shape of the decay volume from an elliptic cylinder to a pyramidal frustum. The decay volume is followed by a large spectrometer with a rectangular acceptance of 5 m in width and 10 m in height.

The main element of the HS decay detector is the spectrometer straw tracker (SST) designed to accurately reconstruct the decay vertex, the mass, and the impact parameter of the hidden particle trajectory at the proton target. The main change since the TP is the removal of the straw veto station that was located 5 m into the decay volume, and the increase of the straw diameter from 10 to 20 mm. Also, all tracker stations upstream and downstream of the magnet have now the same dimensions to ease construction and to reduce cost. The spectrometer dipole magnet is still based on a warm magnet with a fiducial aperture of $5 \cdot 10^2$ m² and a field integral of ~ 0.5 Tm, but the coil and the fitting of the coil have been updated in order to accommodate the rectangular vacuum tank of the spectrometer section.

A set of calorimeters and muon detectors provide particle identification, which is essential in discriminating between the very wide range of HS models. For the TP, the electromagnetic calorimeter (ECAL) was optimised to provide electron identification and π^0 reconstruction. It has now been decided to extend the ECAL requirements to include reconstruction of axion-like-particles (ALP) decaying to the two-photon final state that is the unique way to discriminate between an ALP and a dark photon or a dark scalar. The current version of ECAL, called SplitCal, is a longitudinally segmented lead sampling calorimeter consisting of two parts which are mechanically separated in the longitudinal direction. Each part is equipped with high spatial resolution layers in order to provide pointing with a resolution of ~ 5 mrad for photons originating from ALP decays. The longitudinal layer segmentation of SplitCal also improves the electron/hadron separation. This opens the possibility to remove the hadron calorimeter (HCAL) detector without compromising the PID performance, and only leave the absorber for the purpose of muon filtering.

The muon system consists of four stations interleaved by three muon filters. The ECAL converter material and the muon filters provide sufficient material budget to stop low momenta muons, such that the last muon station is only reached by muons with momenta exceeding 5.3 GeV/c. Since the TP, the muon system considers a new technology based on scintillating tiles with direct silicon photomultipliers (SIPMs) readout. This option provides better time resolution and is more robust against hit rate variations.

Since the key feature of the HS decay spectrometer design is to ensure efficient suppression of various backgrounds, the tracking and particle identification are complemented by a dedicated timing detector with ~ 100 ps resolution to provide a measure of time coincidence, in order to reject combinatorial backgrounds. The decay volume is instrumented by the surround background tagger (SBT) whose purpose is to detect neutrino and muon inelastic interactions in the vacuum vessel walls which may produce long-lived neutral particles decaying in the decay volume and mimicking the HS signal events. Similarly, tagging of interactions in the upstream material of the muon identification system of the SND detector is provided by the associated detector layers.

The muon shield and the SHiP detector systems are housed in an ~ 120 m long underground experimental hall ECN3-TCC8 at a depth of ~ 15 m. To minimise the background induced by the flux of muons and neutrinos interacting with material in the vicinity of the detector, no infrastructure systems are located on the sides of the detector, and the hall is 20 m wide along its entire length.

3. Hidden sector decay spectrometer

The HS decay spectrometer consists of a large vacuum vessel, a surrounding background tagger, a spectrometer straw tracker, together with a large spectrometer magnet with a total field integral of about 0.5 Tm, a timing detector (TD), an electromagnetic calorimeter and a downstream muon system.

The decay spectrometer has to perform precise measurements of charged particles and photons originating from decay vertices of hidden particles in the decay volume, measure their momenta and obtain PID information. Moreover, the decay spectrometer has to ensure a redundant background suppression using timing and track information from the TD and the SST, vetoing criteria from the upstream muon system of the SND and the SBT, and PID by the calorimeter and the muon systems.

The principal features and main parameters of the HS decay spectrometer subdetectors are implemented in FairShip, SHiP software framework based on FairRoot [2–4]. These parameters have been used in the simulation studies of the HS decay spectrometer performance. Specific proof-of-principle tests of prototypes have been undertaken in order to demonstrate that the expected detector performance can be achieved.

The purpose of the spectrometer straw tracker, a key element of the HS decay detector, is to measure track parameters and momentum of charged particles with high efficiency and accurate enough to reconstruct decays of hidden particles, and to reject background events. The precision of the extrapolated position of the tracks must be well matched with the segmentation of the timing detectors such that the high accuracy of the associated track time can be used to remove combinatorial background. The invariant mass, the vertex quality, the timing, the matching to background veto taggers and the pointing to the production target are crucial tools for rejecting background.

The spectrometer consists of a large aperture dipole magnet and two tracking telescopes, one on each side of the magnet and each composed of two tracking stations. The four stations are identical with a nominal acceptance of 5 m in X and 10 m in Y , and are based on ultrathin straw drift tubes oriented horizontally. Each station contains four views, in a $Y-U-V-Y$ arrangement, where U and V are stereo views with straws rotated by a small angle $\pm\theta_{\text{stereo}}$ around the z -axis with respect to the y -measuring straws.

The main change since the TP [2, 3] is the increase of the straw diameter D from 10 to 20 mm [6]. This change is motivated by the refined background rate simulations, which confirm that for $D = 20$ mm the rate per straw remains modest (< 7 kHz in the hottest straw).

Tools for producing 20 mm straws have been developed, and several prototype straws, using as before a 36 μm thick polyethylene terephthalate (PET) film coated with 50 nm Cu and 20 nm Au, have been produced with no new difficulty encountered compared to the fabrication of the original 10 mm straws. Several straws of 20 mm diameter and 5 m length were fabricated. The rupture over-pressure was measured on ten samples of 50 cm length and was found to be around 4.4 bar, as expected. This is considered a sufficient margin for operating the straws at a pressure of about 1 bar in vacuum. The torsion of 5 m long straws, cemented on one side and pressurised to 1 bar over-pressure, was measured. A rotation of 38° was found at the free end. A torque of about 0.076 Nm was needed to cancel the rotation. A 2 m long $D = 20$ mm straw was fabricated and its performance as a minimum ionizing particles (MIP) detector was characterised in a test run with beam in the SPS north area as a function of the wire offset at nominal conditions (~ 1.05 bar pressure, 70% Ar / 30% CO₂). First results indicate that a straw hit resolution of 120 μm is achievable with high hit efficiency over most of the straw diameter, independently of the wire offset. The drift time spectra for different wire offsets are being analysed, and methods to extract the local wire offset from the distinctive features of the spectra are being investigated. Alignment studies for the full detector, using Monte Carlo (MC) simulation, are being started, which should allow us to define the geometrical constraints for the mechanical engineering design.

4. Proton beam and experimental facility

At the CERN SPS, the optimal experimental conditions for SHiP are obtained with a proton beam energy of around 400 GeV. The SHiP operational scenario implies returning to full exploitation of the capacity of the SPS. The request for the proton yield is based on a similar fraction of beam time as the past CERN Neutrinos to Gran Sasso program. A nominal beam intensity of $4 \cdot 10^{13}$ protons on target per spill is assumed for the design of the experimental facility and the detector. In the baseline scenario for SHiP, the beam sharing delivers

an annual yield of $4 \cdot 10^{19}$ protons to the BDF and a total of 10^{19} to the other physics programs at the CERN North Area, while respecting the beam delivery required by the high luminosity LHC (HL–LHC). The physics sensitivities are based on acquiring a total of $2 \cdot 10^{20}$ protons on target, which may thus be achieved in five years of nominal operation.

5. SHiP physics performance

The physics performance of the SHiP experiment [7–9] is anchored in the emphasis on an extremely efficient and redundant background suppression, and a detector which is sensitive to as many decay modes as possible to ensure a model independent search for hidden particles. A set of common benchmark models is used below to illustrate the physics performance to HS particle decays and to LDM, including the neutrino physics performance.

5.1. Hidden sector particle decays

All benchmark HS models predict a signature with an isolated vertex in the HS spectrometer. Hence, HS signal candidates are required to form an isolated vertex in the fiducial volume. For fully reconstructed signal decays, where all particles coming from the decaying hidden particle are reconstructed in the spectrometer, it is required that the impact parameter (IP) to the target is less than 10 cm. This selection cut is very powerful in rejecting all background sources. Partially reconstructed final states (with one or more missing particles, *e. g.*, $N \rightarrow \mu^+ \mu^- \nu$) point back more loosely to the target. These final states are therefore more challenging to discriminate from the background. The signal candidates are required to have $IP < 250$ cm and, in addition, no associated activity in the SBT.

The background to the searches for hidden particles includes three main classes: neutrino and muon induced backgrounds resulting from inelastic interactions in the material of the detector and the cavern walls, and combinatorial muon background resulting from residual muons reconstructed as charged tracks in the SHiP decay spectrometer. As it was demonstrated in the SHiP TP [2, 3], backgrounds originating from cosmic muons can be reduced to a negligible level.

Large samples of neutrino and muon inelastic backgrounds, corresponding to about ten years and five years of SHiP nominal operation, respectively, were generated using FairShip, forcing all produced neutrinos and muons to interact with the material. The interaction points were distributed along the neutrino and muon trajectories, with weights according to the material density along the tracks.

While the background rejection and signal sensitivities presented here rely on linear cuts, multivariate techniques can be expected to further improve the performance of the final experiment. Expected background to the HS particle search at 90% confidence level for $2 \cdot 10^{20}$ protons on target is quite small: < 1 event from neutrino background and $< 6 \cdot 10^{-2}$ events from muon background.

All signal sensitivities are obtained using the FairShip simulation framework [2, 4, 6, 7]. The 90% confidence region is defined as the region in the parameter space where on average $N_{\text{events}} \geq 2.3$ reconstructed signal events are expected in the whole mass range, corresponding to a discovery threshold with an expected background level of 0.1 events.

5.2. Heavy neutral leptons

The neutrino portal consists of adding to the SM new gauge-singlet fermions – heavy neutral leptons (HNLs). Phenomenologically, HNLs are massive Majorana particles with mass M_N that possess “neutrino-like” interactions with W and Z bosons (the interaction with the Higgs boson does not play a role in our analysis and will be ignored). The interaction strength is suppressed as compared to that of ordinary neutrinos by flavour-dependent factors (known as mixing angles) $U_\alpha \ll 1$ ($\alpha = \{e, \mu, \tau\}$).

The dominant production channels for HNLs in the SHiP experiment occur through weak decays of flavoured mesons. For HNLs with masses $M \leq 500$ MeV/ c^2 kaon decays are the dominant production channel. While $O(10^{20})$ kaons are expected at SHiP, most of them are stopped in the target or hadron stopper before

decaying. As a consequence, only HNLs originating from charm and beauty mesons are included in the estimation of the sensitivity below. Figure 2 shows the production rates of HNLs used in this analysis.

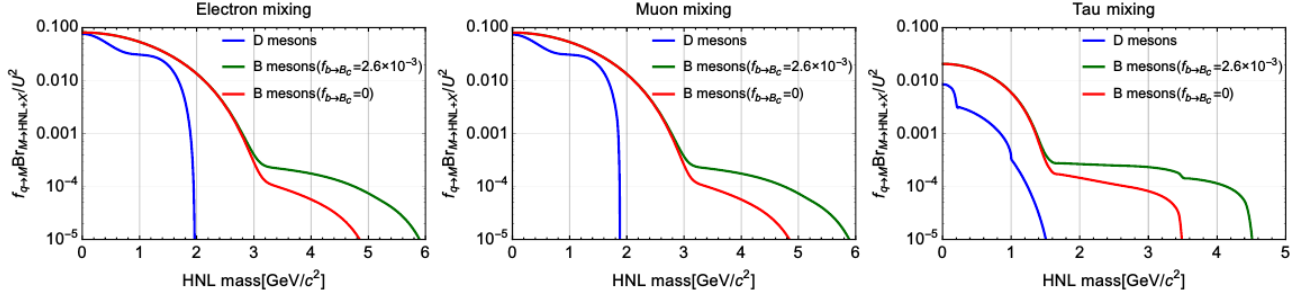


Fig. 2. Meson fragmentation fraction times branching fraction of meson decays to heavy neutral lepton as a function of the HNL mass. Contributions from D and B mesons are shown. To demonstrate the influence of B_C mesons, two cases are shown: the B_C fragmentation fraction at SHiP energies is equal to that as at LHC energies: $f(b \rightarrow B_C) = 2.6 \cdot 10^{-3}$ (maximal contribution) and $f(b \rightarrow B_C) = 0$

The production of HNLs through the decay of charm mesons dominates for HNL masses greater than the kaon masses. For HNL masses greater than charm meson masses, decays of beauty mesons are responsible for the production of HNLs at SHiP as shown in Fig. 2. For masses $M_N \geq 3 \text{ GeV}/c^2$ the contribution of B_C may become important and even dominant. The fraction of B_C mesons among all beauty mesons (*i. e.* the fragmentation fraction $f(b \rightarrow B_C)$ at SHiP energies is unknown. Given this uncertainty, two estimates were provided:

- Assuming that $f(b \rightarrow B_C)$ is the same as at the LHC energies $f(b \rightarrow B_C) = 2.6 \cdot 10^{-3}$;
- Assuming that $f(b \rightarrow B_C) = 0$.

The main decay channels of HNLs are considered in Refs. [6–9]. Signal events were simulated through FairShip for various masses and mixing angles U_i^2 with SM electron, muon and tau neutrinos as input parameters. The sensitivity to various HNL benchmark models is estimated by applying the reconstruction and selection criteria for partially reconstructed final states.

When estimating the contribution from HNLs produced through decays of B_C mesons, the angular distribution of B_C mesons is taken to be the same as that of B^+ mesons, based on comparisons performed with the BCVEGPY and FONLL packages. The energy distribution is obtained by re-scaling the energy distribution of the B^+ meson to account for the mass difference with the B_C .

Figure 3 presents the sensitivity curve for HNLs, with the benchmark assumption that the ratio between the three HNL mixing angles corresponds to $U_e^2 : U_\mu^2 : U_\tau^2 = 0 : 1 : 0$.

For completeness, both the conservative curves for the case $f(b \rightarrow B_C) = 0$, and the optimistic ones with $f(b \rightarrow B_C) = 2.6 \cdot 10^{-3}$ are shown in all sensitivity plots.

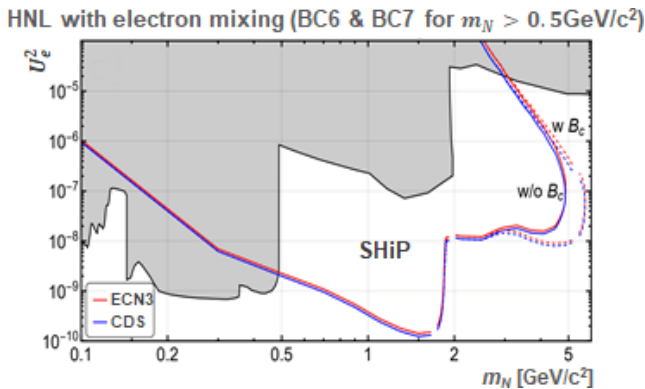


Fig. 3. Sensitivity curve for HNLs, with the benchmark assumption that the ratio between the three HNL mixing angles corresponds to $U_e^2 : U_\mu^2 : U_\tau^2 = 0 : 1 : 0$

5.3. Dark scalars

The scalar portal couples a gauge-singlet scalar S to the gauge invariant combination $H^\dagger H$ made of the SM Higgs doublet.

Further details on the phenomenology of the scalar portal are provided in Refs. [6, 7]. Dark scalars are produced from decays of kaons and B^\pm -mesons [6, 7]. However, as discussed for the HNLs, kaons are mainly absorbed in the hadron absorber in SHiP, and here only the production *via* B -mesons is considered.

The hadronic decay width of these scalars S is subject to large uncertainties for masses $M_S \sim 1 \text{ GeV}/c^2$, where neither chiral perturbation theory nor perturbative quantum chromodynamics (QCD) can provide reliable results.

The SHiP sensitivity is calculated within the FairShip simulation framework that allows us to apply reconstruction and selection criteria described in Refs. [2–4]. In contrast to the neutrino portal, the contribution of dark scalar production through B_C meson decays is negligible, thus there is no need to assess the B_C contributions to the sensitivity. The sensitivity of the SHiP experiment to dark scalars is shown in Fig. 4.

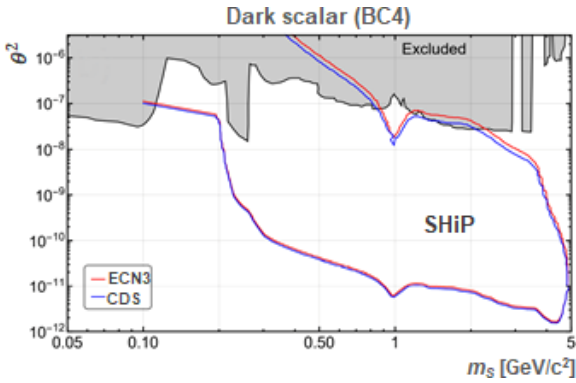


Fig. 4. Sensitivity of the SHiP experiment to dark scalars. Only contribution from B mesons is taken into account

5.4. Dark photons

The minimal dark photon (DP) model considers the addition of a gauge group $U(1)$ to the SM, whose gauge boson is a vector field called the DP. A kinetic mixing between the dark photon and the SM $U(1)$ gauge bosons is allowed [6–9], with a reduced strength parameterised by a coupling ϵ , also called the kinetic mixing parameter. In its simplest form, the knowledge of the mass of the dark photon m_{DP} and the kinetic mixing parameter ϵ is enough to characterise the model and calculate the production cross section and decay properties. Different mechanisms are possible for the production of such new particles at a fixed-target experiment. Three different modes are investigated for estimating the sensitivity of the SHiP detector (Fig. 5), considering only the primary proton–proton interactions (cascade production, which is included for HNL and the dark scalar is here ignored).

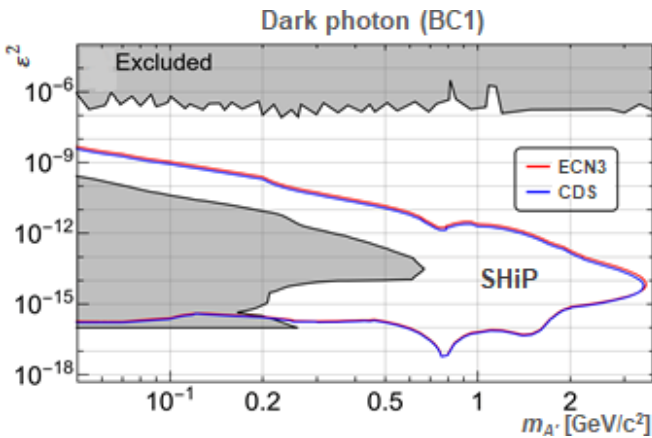


Fig. 5. Expected 90% exclusion region as a function of the dark photon mass and of the kinetic mixing parameter ϵ^2 , for the three production modes studied

DP with masses below $0.9 \text{ GeV}/c^2$ can mix with photons from neutral meson decays ($\pi^0, \eta, \omega, \eta'$), that are produced in non-diffractive interactions. The PYTHIA8.2 MC generator is used to obtain an estimate of the neutral meson production rate. For an incident beam momentum of $400 \text{ GeV}/c$ on fixed-target protons, the non-diffractive interactions represent 60% of the total proton–proton interactions. Branching ratios of mesons to DPs are calculated according to Refs. [7–9].

Proton–proton interaction can also lead to the emission of a DP *via* a bremsstrahlung process, dominant for DP masses in the range $0.4\text{--}1.3 \text{ GeV}/c^2$. An approach identical to that of Refs. [3–4] is followed to parameterise the probability density function for producing DPs with a given momentum and angle to the beam-line, and calculate the total production rate. Above this threshold, the dominant production mechanism happens through quark–quark annihilation into the DP. This process is simulated using the generic implementation of a resonance that couples both to SM fermion pairs and hidden particles as implemented in PYTHIA8.2 under the “Hidden valley” Z model [6–9]. The native cross section from PYTHIA8.2 is used for the normalisation of the process.

5.5. Axion-like particles

Pseudo-Nambu–Goldstone bosons can arise from spontaneously broken symmetries at high energies. A prime example is the axion introduced to solve the strong charge-parity problem in QCD with a mass of $\sim 10^{-5} \text{ eV}$. The SHiP experiment is not sensitive to QCD axions, however other pseudoscalar particles can feature very similarly to axions but with larger masses. These hypothetical particles are known as axion-like particles. Two cases were considered: the coupling of ALPs with photons and with fermions.

The ALPs coupling to fermions have an analogous production mechanism to that of dark scalars. The sensitivity for ALPs coupling to fermions, compared to previous experiments is shown in Fig. 6.

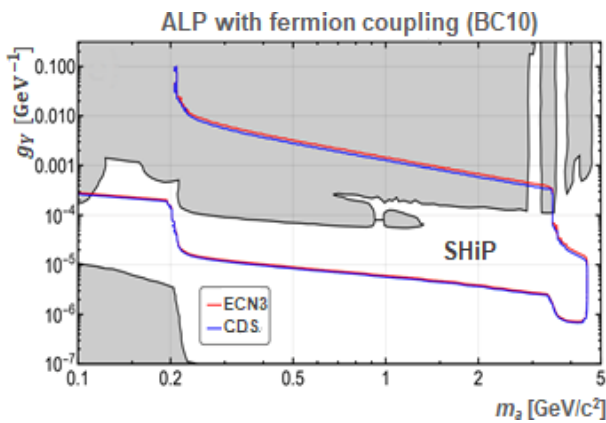


Fig. 6. SHiP sensitivity to axion-like-particles coupling to fermions

6. Project plan and cost

Timeline for the BDF–SHiP is shown in Fig. 7.

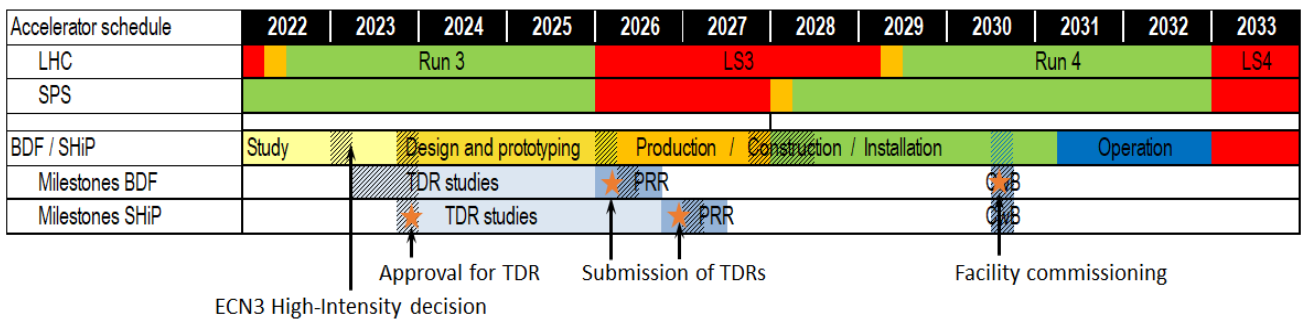


Fig. 7. Timeline for the BDF–SHiP

7. The SHiP Collaboration

SHiP is currently a collaboration of 33 institutes and 5 associated institutes, in total representing 15 countries and CERN.

PNPI joined the SHiP project in 2014 since preparation of the SHiP TP [2]. The PNPI team is involved in R&D of the spectrometer straw tracker, a key system of the SHiP experiment. Now PNPI scientists and engineers are taking part in spectrometer straw tracker optimisation of signal and background reconstruction, straw tube production R&D, and developing a conceptual design of the spectrometer straw tracker digital and analogue electronic readout for 18 000 channels.

8. Conclusion

The intensity frontier greatly complements the search for new physics at the LHC. In accordance with the recommendations of the last update of the European Strategy for Particle Physics, a multirange experimental programme is being actively developed all over the world. Major improvements and new results are expected during the next decade in neutrino and flavour physics, proton-decay experiments and measurements of the electric dipole moments. CERN will be well-positioned to make a unique contribution to exploration of the hidden-particle sector with the BDF–SHiP experiment at the SPS.

References

1. W. Bonivento *et al.*, arXiv:1310.1762.
2. SHiP Collab., M. Anelli *et al.*, Tech. Rep. CERN-SPSC-2015-016, SPSC-P-350 (2015), arXiv:1504.04956.
3. SHiP Collab., M. Anelli *et al.*, Tech. Rep. CERN-SPSC-2015-040, SPSC-P-350-ADD-2 (2015).
4. SHiP Collab., C. Ahdida *et al.*, Tech. Rep. CERN-SPSC-2019-049, SPSC-SR-263 (2019).
5. C. Ahdida *et al.*, 10.23731/CYRM-2020-002 (2019), arXiv:1912.06356.
6. BDF Working Group/SHiP Collab., O. Aberle *et al.*, CERN-SPSC-2022-032/SPSC-I-258 (2022).
7. S. Alekhin *et al.*, Rep. Prog. Phys. **79**, 124201 (2015), arXiv:1504.04955.
8. SHiP Collab., C. Ahdida *et al.*, JINST **14** (03), P03025 (2019), arXiv:1810.06880.
9. SHiP Collab., C. Ahdida *et al.*, JHEP **04**, 077 (2019), arXiv:1811.00930; SHiP Collab., C. Ahdida *et al.*, JHEP **04**, 199 (2021), arXiv:2010.11057; SHiP Collab., C. Ahdida *et al.*, Eur. Phys. J. C **81**, 451 (2021), arXiv:2011.05115.

PNPI IN THE MPD PROJECT AT NICA

PNPI participants of the MPD Collaboration: O.L. Fedin, D.A. Ivanishchev, A.V. Khanzadeev, L.M. Kochenda, D.O. Kotov, P.A. Kravtsov, E.L. Kryshen, M.V. Malaev, A.Yu. Ryabov, V.G. Ryabov, Yu.G. Ryabov, V.M. Samsonov, M.B. Zhalov

1. Introduction

The NICA (nuclotron based ion collider facility) is under construction at Joint Institute for Nuclear Research (Dubna), which is expected to come into operation in the end of 2023. The multipurpose detector (MPD) is one of two collider experiments at NICA, which is designed to search for novel phenomena in the baryon-rich region of the quantum chromodynamics (QCD) phase diagram by studying heavy nuclei collisions in the energy range from 4 to 11 GeV, where the energy is given for nucleon–nucleon collisions in the centre of mass system [1]. The MPD strategy is to perform a high-luminosity scan in energy and system size, looking for different signals, which are expected to accompany the phase transition and point to proximity of the critical point. The scans are going to be performed using the same apparatus with all the advantages of collider experiments such as the large and uniform acceptance and absence of the target parasitic effects. The Bi + Bi collisions at $\sqrt{s_{NN}} = 9.2$ GeV will be utilized for the first year(s) of operation of the MPD experiment. The choice of nuclei is driven by the current configuration of the ion source at the NICA accelerator complex, while the collision energy was chosen to match one of the energies previously used by STAR (solenoidal tracker at RHIC) in the beam energy scan program at the Relativistic Heavy Ion Collider for a more direct comparison of the first results.

The physical program of the MPD experiment has much in common with those of other heavy-ion experiments. It is intended to probe the equation-of-state of dense nuclear matter and to search for partonic degrees of freedom and critical activity at high baryon densities. The main contributions from PNPI in the MPD are the construction and support of the time projection chamber (TPC) gas system and development of analysis methods for the measurement of properties of short-lived hadronic resonances and neutral mesons.

Hadronic resonances are excited hadronic states with relatively small lifetime. The resonances are produced in hadronic and heavy-ion collisions and are widely accessible for experimental measurements in the dominant hadronic decay channels. Neutral mesons are copiously produced and can be reconstructed using their decay modes with photons in the final state. Measurements of resonances and neutral mesons can be used to study such phenomena as strangeness enhancement, development of the collective flow, parton recombination and energy loss, lifetime and density of the late hadronic phase. Different lifetimes, masses and quark contents of these particles help to disentangle different particle production mechanisms and competing processes that define the particle yields and transverse momentum (p_T) spectral shapes. Precise measurements of the neutral meson production are essential for direct photon, dielectron and heavy-flavour electron studies where the particles serve as the dominant source of background.

2. Reconstruction of resonances in the MPD

To estimate the MPD capabilities for reconstruction of short-lived resonances in Bi + Bi collisions at $\sqrt{s_{NN}} = 9.2$ GeV, the UrQMD [2] was used as event generator and the MpdRoot [3] was used for propagation of particles through the detector materials, simulation of the response of different detector subsystems, particle tracking and species recognition. Resonances were set as stable particles in UrQMD and were decayed by GEANT4, which is a part of the MpdRoot framework. Thus, no mass or width modifications were simulated for the particles. The Bi + Bi events were simulated with a wide z -vertex distribution ($\sigma_{z\text{-vertex}} = 23$ cm) and cut at $|z\text{-vertex}| < 50$ cm. In total $5 \cdot 10^6$ events were simulated and processed. The event centrality was estimated by track multiplicity measured in the TPC. The charged particle tracks were reconstructed in the TPC and propagated to the time-of-flight detector (ToF). Only tracks that had at least 20 hits measured in the TPC and matched to the primary vertex within 3σ were accepted for the analysis. The charged hadrons were identified by a 3σ cut on the measured value of ionization losses in the TPC. If a track is matched to the ToF, an additional requirement for a track to be identified by a 3σ cut on the measured value of β was imposed. The daughter track candidates were paired to accumulate $\pi^+\pi^-$, $\pi^\pm K^\pm$, $\pi^\pm K_s$, K^+K^- , pK^- and $\pi^\pm\Lambda$ invariant mass distributions.

For resonance decays with weakly decaying daughters, an additional step was required to reconstruct $K_s \rightarrow \pi^+\pi^-$ and $\Lambda \rightarrow p\pi^-$ decays using different topology cuts for the secondary vertex. The K_s and Λ candidates were selected by imposing a 2σ cut on the reconstructed particle masses. The Particle Data Group [4] masses of daughter particles and the reconstructed momenta were used in the reconstruction of parent resonances. Examples of K^+K^- and $\pi^\pm\Lambda$ invariant mass distributions accumulated for 0–20% central Bi + Bi collisions at $\sqrt{s_{NN}} = 9.2$ GeV are shown in the *top panels* of Fig. 1 with black histograms. The accumulated invariant mass distributions contain signals from the resonance decays and the combinatorial background. The uncorrelated combinatorial background was estimated by the mixed-event method when one of the daughter particles is taken for the same event and another daughter particle is taken from a different event with similar multiplicity and z -vertex. Thus accumulated invariant mass distributions were scaled to the invariant mass distributions measured for the same events at high mass and then subtracted. The scaled mixed event invariant mass distributions are shown with red histograms in the *top panels* of Fig. 1. The remaining distributions after subtraction contained clear peaks from the resonance decays and some remaining correlated background from jets and misreconstructed decays of heavier particles as shown in the *bottom panels* of Fig. 1. It was found that the remaining background is a smooth function of mass in the vicinity of the resonance peaks. To extract the resonance raw yields, the invariant mass distributions were fit to a combination of a second-order polynomial to describe the remaining background and the Voigtian function (Breit–Wigner function convolved with a Gaussian to account for the finite detector mass resolution) for the signal. Examples of the fits are shown in the same plots. The detector mass resolution was estimated as a function of transverse momentum and collision centrality for each decay mode under study equal to a width of the Gaussian fit to the distribution with the difference of the simulated and reconstructed resonance masses. The resonance raw yields (N_{raw}) were evaluated as Voigtian integrals in the physically allowed mass ranges.

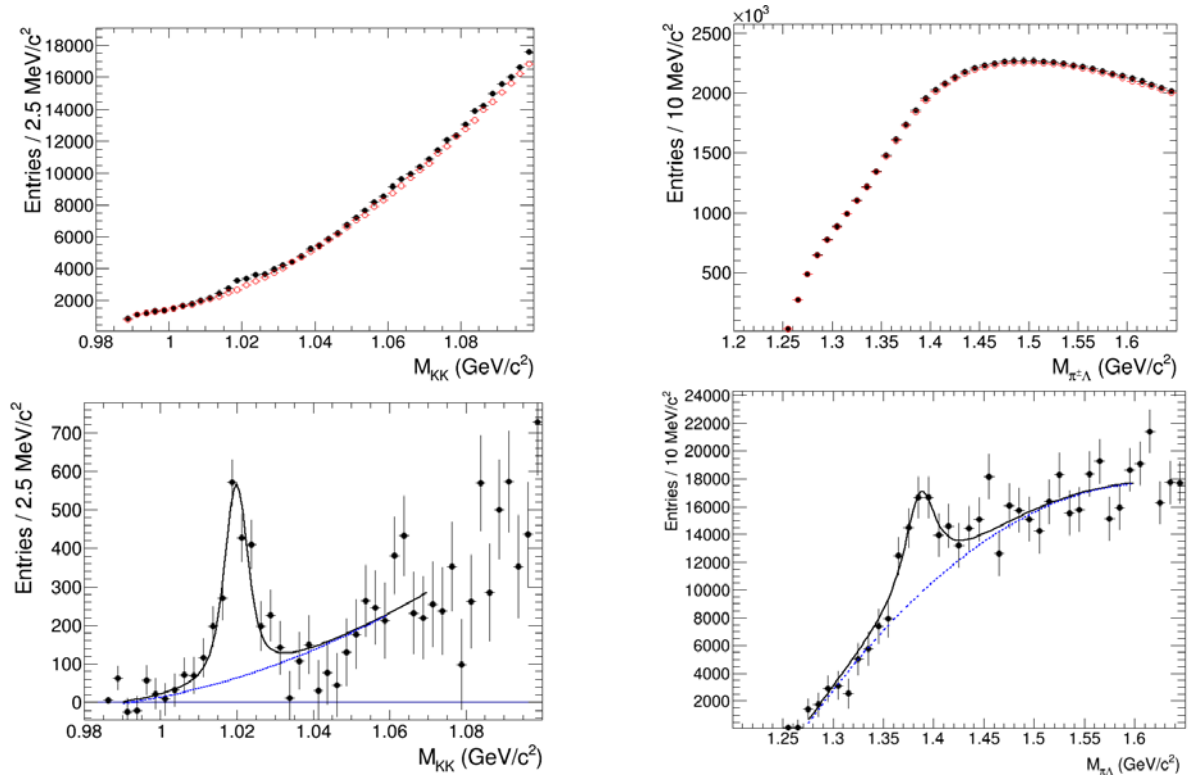


Fig. 1. The invariant mass distributions for K^+K^- (left) and $\pi^\pm\Lambda$ (right) pairs accumulated for the same and the mixed events. The *bottom panels* show the distributions after subtraction of the mixed-event background. The resulting distributions are fit to a combination of a second-order polynomial and the Voigtian function. Examples are shown for 0–20% central Bi + Bi collisions at $\sqrt{s_{NN}} = 9.2$ GeV in the transverse momentum intervals 0.2–0.4 (0–0.5) GeV/c for K^+K^- and $\pi^\pm\Lambda$ pairs

The efficiency of the resonance reconstruction at midrapidity $|y| < 1.0$ in the MPD detector was estimated as $A \cdot \epsilon = N_{\text{rec}}/N_{\text{gen}}$, where N_{rec} and N_{gen} are the numbers of reconstructed and generated resonances. The number of reconstructed resonances is determined after all event and track selection cuts, while the number of generated resonances is counted only for those particles that decay in a given channel. The evaluated efficiencies are significantly smaller for resonance decays with weakly decaying daughters since a larger number of particles should be reconstructed. The efficiencies decrease at low momentum, however, most of the resonances can be measured starting from zero transverse momentum due to a large difference between the masses of the resonances and the daughter particles. The efficiencies show a modest event centrality dependence; they are smaller in central collisions due to a higher detector occupancy.

The fully corrected transverse momentum spectra for the resonances were calculated as $\frac{d^2N}{dydp_T} = \frac{N_{\text{raw}}}{\Delta p_T \Delta y} \cdot \frac{1}{A \cdot \epsilon} \cdot \frac{1}{\text{BR}}$, where N_{raw} is the number of resonances reconstructed from the invariant mass distributions, Δp_T and Δy are the intervals in p_T and rapidity, $A \cdot \epsilon$ is the reconstruction efficiency, and BR is the decay branching ratio. The fully reconstructed transverse momentum spectra for $\rho(770)^0$, $K^*(892)^0$, $K^*(892)^\pm$, $\phi(1020)$, $\Sigma(1385)^\pm$ and $\Lambda(1520)$ resonances are shown with black circles in Fig. 2.

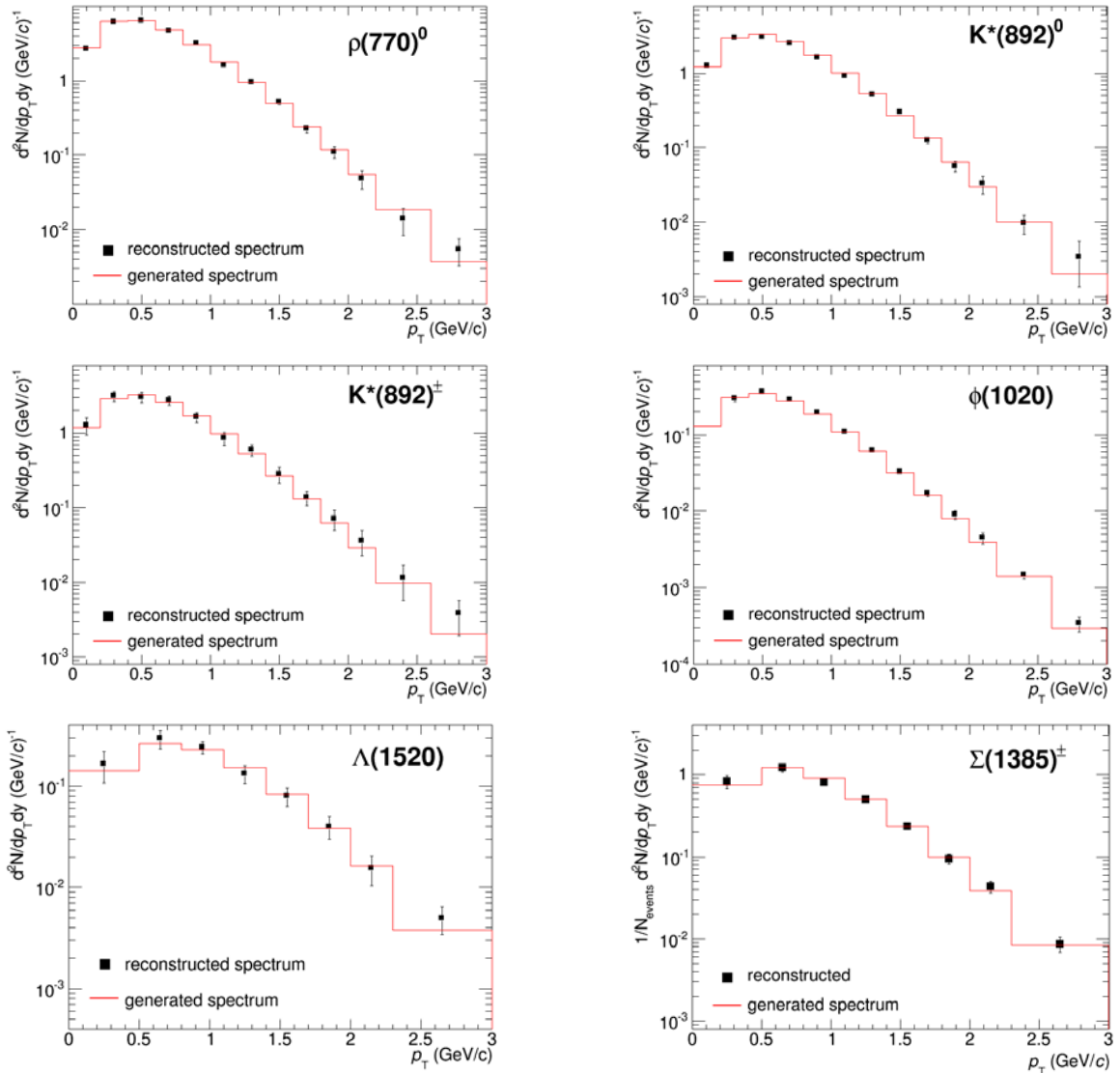


Fig. 2. The reconstructed (*black circles*) and truly generated (*red histograms*) transverse momentum spectra for $\rho(770)^0$, $K^*(892)^0$, $K^*(892)^\pm$, $\phi(1020)$, $\Sigma(1385)^\pm$ and $\Lambda(1520)$ resonances in Bi + Bi collisions at $\sqrt{s_{NN}} = 9.2$ GeV

The spectra are compared to truly generated spectra shown with red histograms in the same plots. The reconstructed spectra match the generated ones within the statistical uncertainties confirming the validity of the analysis chain. First measurements for resonances will be possible with $\sim 10^7$ sampled Bi + Bi collisions at $\sqrt{s_{NN}} = 9.2$ GeV. Most of the resonances except for $\phi(1020)$ can be measured starting from zero transverse momentum, which is very important for physics studies. The centrality-dependent studies would need $\sim 5 \cdot 10^8$ sampled events while detailed measurements for $\Xi(1530)^0$ may require up to $\sim 10^9$ sampled events.

3. Reconstruction of neutral mesons

For the first year of operation with an accumulated statistics of $\sim 10^7$ – 10^8 events, only reconstruction of $\pi^0 \rightarrow \gamma\gamma$ and $\eta \rightarrow \gamma\gamma$ decays can be realistically considered. Photons in the final state can be measured in the electromagnetic calorimeter (ECAL) or in the tracking system as e^+e^- pairs using the photon conversion method (PCM) in the beam pipe (0.3% X_0) and inner vessels of the TPC (2.4% X_0). All results reported in these proceedings for neutral mesons are for Bi + Bi collisions at $\sqrt{s_{NN}} = 9.2$ GeV simulated with UrQMD v.3.4 [2].

Figure 3 demonstrates examples of $\gamma\gamma$ -pair invariant mass distributions reconstructed with the ECAL and the PCM. In the former case, the distributions are shown after subtraction of the mixed event background. In all cases, we observe peaks from $\pi^0 \rightarrow \gamma\gamma$ decays on top of a combinatorial background. The π^0 raw yields are extracted by fitting the distributions to a combination of a Gaussian function for the signal and a polynomial of the second order for the background. The corresponding values of the signal-to-background ratios are 0.01(0.13) and 0.12(0.35) for the two p_T bins measured with the ECAL (PCM).

A detailed comparison of π^0 and η peak widths reconstructed with the two methods is shown in Fig. 4. One can see that the PCM provides much narrower peaks due to the better energy resolution of the tracking system compared to the ECAL.

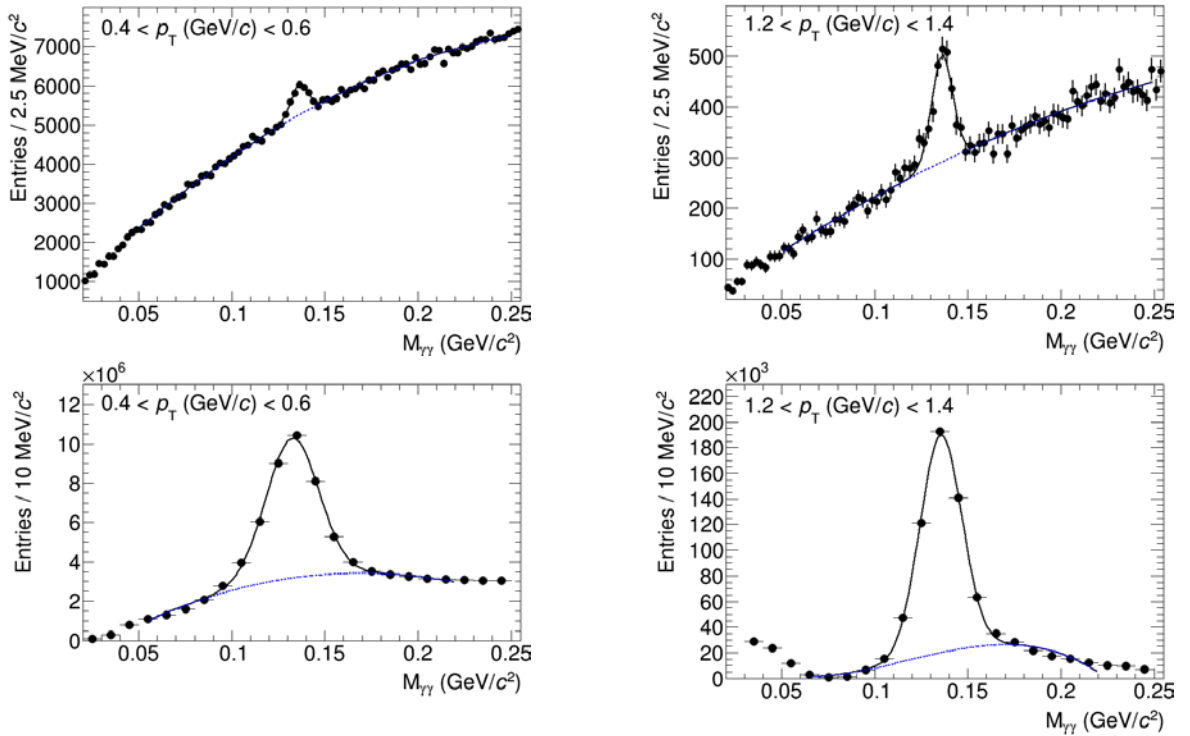


Fig. 3. Examples of $\gamma\gamma$ -pair invariant mass distributions reconstructed in Bi + Bi collisions at $\sqrt{s_{NN}} = 9.2$ GeV with the PCM (*top*, $2 \cdot 10^7$ events) and ECAL (*bottom*, $1.5 \cdot 10^7$ events) in two different p_T intervals. The distributions are fit to a combination of a Gaussian for the signal and a polynomial for the background

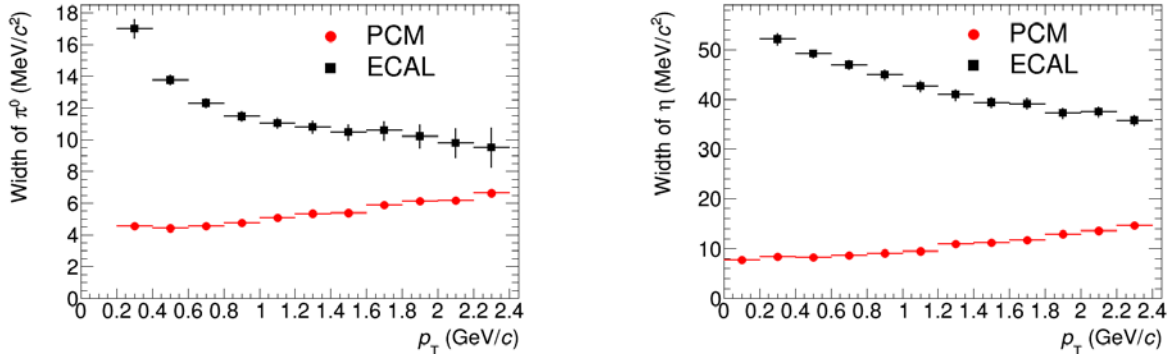


Fig. 4. Comparison of π^0 and η peak widths reconstructed with the ECAL and PCM as a function of p_T

Figure 5 shows results of a Monte Carlo closure test for π^0 and η measurements in the ECAL in Bi + Bi collisions at $\sqrt{s_{NN}} = 9.2$ GeV. The generated spectra are provided by the event generator. The reconstructed spectra were obtained by extracting the π^0 and η raw yields from the invariant mass distributions and correcting them for the reconstruction efficiencies. One can see that the generated and the reconstructed spectra are consistent within uncertainties thus validating the analysis chain. Neutral meson measurements are possible starting from $p_T \sim 50$ MeV/c and the high- p_T reach is limited by available statistics. Reconstruction of η mesons requires a much larger sample because they are produced at much lower rate at low momentum and have much wider reconstructed peak widths compared to π^0 . With 15 M sampled events, we can only observe η signals with the ECAL in rather wide p_T bins with large statistical uncertainties for the extracted yields.

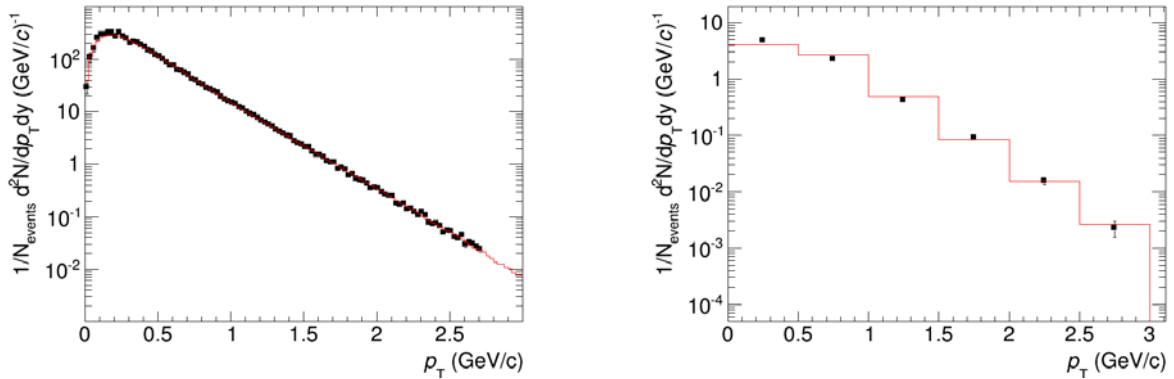


Fig. 5. The generated (*solid lines*) and reconstructed (*markers*) p_T -differential yields of π^0 and η mesons in $1.5 \cdot 10^7$ Bi + Bi collisions at $\sqrt{s_{NN}} = 9.2$ GeV

Figure 6 presents the expected raw yields of π^0 and η mesons reconstructed with the PCM. With $\sim 10^9$ sampled Bi + Bi collisions, we will be able to perform the multiplicity-dependent studies for π^0 , including measurements of flow coefficients, and to reconstruct the η meson spectrum starting from zero momentum.

To summarize, with the ECAL, first measurements for π^0 and η mesons will be possible with $\sim 1.5 \cdot 10^7$ sampled Bi + Bi collisions at $\sqrt{s_{NN}} = 9.2$ GeV in a range of transverse momenta from ~ 50 MeV/c up to ~ 3 GeV/c. For more precise measurements and multiplicity-dependent studies, we would need an order of magnitude higher statistics or $\sim 10^8$ events. The PCM is more statistics demanding, first measurements for π^0 will be possible with $\sim 2 \cdot 10^7$ sampled Bi + Bi collisions, while measurements of η would require $\sim 10^9$ events that is beyond the limits of one year running of the MPD detector. Measurements with the ECAL and PCM are going to be complementary. The ECAL will provide higher statistics while the PCM will benefit from much superior energy resolution at low-to-intermediate momenta.

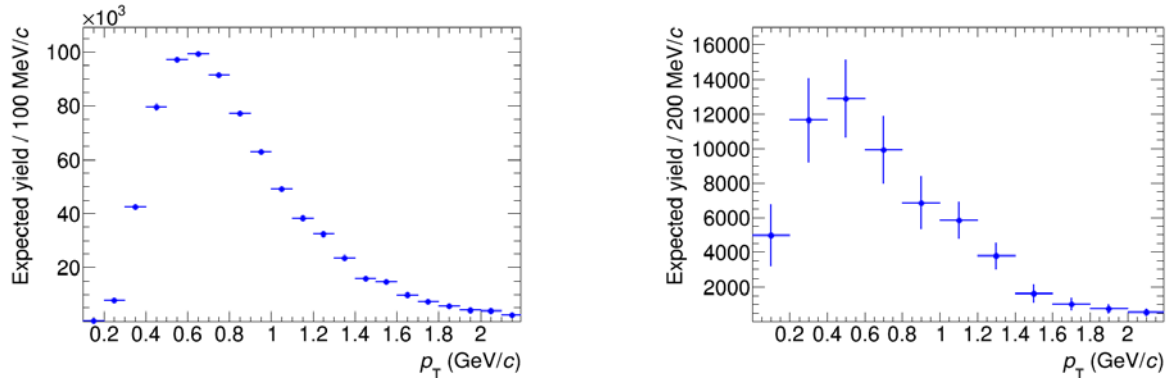


Fig. 6. Expected raw yields of π^0 and η mesons reconstructed with the photon conversion method using 10^9 Bi + Bi collisions at $\sqrt{s_{NN}} = 9.2$ GeV

References

1. V. Abgaryan *et al.*, Eur. Phys. J. A **58** (7), 140 (2022).
2. S.A. Bass *et al.*, Prog. Part. Nucl. Phys. **41**, 255 (1998).
3. S. Hnatic *et al.*, in *Proc. of the 9th Int. Conf. on Distributed Computing and Grid Technologies in Science and Education*, 75 (2021).
4. P.A. Zyla *et al.*, Prog. Theor. Exp. Phys. **2020**, 083C01 (2020).

SPD EXPERIMENT AT NICA: POLARIZED AND UNPOLARIZED STRUCTURE OF THE PROTON AND DEUTERON

PNPI participants: V.T. Kim, E.V. Kuznetsova, S.G. Barsov, S.A. Bulanova, O.L. Fedin, G.E. Gavrilov, V.L. Golovtsov, A.K. Kiryanov, V.P. Maleev, S.A. Nasybulin, D.E. Sosnov, L.N. Uvarov, A.V. Zelenov

1. Introduction

The nuclotron based ion collider facility (NICA) [1] at Joint Institute for Nuclear Research (JINR), Dubna, one of megascience projects in Russia, is devoted to relativistic nuclear, hadron and applied physics. The NICA complex, which is currently under construction, will accelerate different ions from proton to Au at the energies $\sqrt{s_{NN}}$ up to 27 GeV and 11 GeV/u, respectively. The beams will collide at two interaction points, where $\sim 4\pi$ detectors will be installed.

One of the detectors, the spin physics detector (SPD) [2, 3], will be dedicated to the physics with both polarized and unpolarized ion beams in the transition region between the perturbative and non-perturbative quantum chromodynamics (QCD). The major goal of SPD is to study the spin structure of the proton and deuteron and other spin related phenomena with polarized proton and deuteron beams at the luminosity up to $10^{32} \text{ cm}^{-2} \cdot \text{s}^{-1}$ and at the collision energy \sqrt{s} up to 27 GeV. A comprehensive study of the unpolarized and polarized gluon content of the nucleon at large Feynman- x using different complementary probes, such as charmonia, open charm, and prompt photon production processes, is the central point of the SPD physics program.

The kinematical region accessible at SPD covers the transition region from non-perturbative to perturbative QCD and it should help to shed light on 3D parton structure of proton and deuteron. The symmetries of the strong interaction, the properties of the QCD vacuum, basic properties of particles as mass and spin will be studied through different processes. The kinematical range together with the high performances expected from a modern $\sim 4\pi$ detector and availability of both polarized proton and deuteron beams make the scientific program at SPD unique [4, 5].

At the first stage of the SPD experiment with not very high intensity NICA collider beams, a broad physics program is also planned [5]. It is focused on investigations using both unpolarized and polarized proton–proton and light ion–ion collisions, in particular: antiproton production; production of exotic multi-quark resonance states and light nuclei [6]; multi-quark flucton (short-range nucleon correlations) [7–9]; study of diquark role in large- p_T baryon production [10], novel production mechanisms as multiparton scattering subprocesses, *e. g.*, double quark–diquark scattering [6], *etc.*

The SPD detector is supposed to be working with online event filters only, *i. e.*, without dedicated hardware triggers. High rate of SPD data will be comparable, for example, with the data rate of the LHCb experiment at the Large Hadron Collider (LHC). Therefore, the SPD computing requires grid computing capabilities like those which were done in Russia for the LHC Grid.

The PNPI group is involved in the SPD detector developments and physics simulations. It includes research and development (R&D) with modeling of the response of the central straw tracker and track reconstruction, test beam measurements for read-out electronics, straw tube production technology and studies with the SPD sensitivity to various physics signals, such as exotic resonance production, *etc.*

2. SPD physics program

QCD has remarkable success in describing the high-energy and large momentum transfer processes, where quarks and gluons, which are the fundamental constituents of hadrons, behave, to some extent, as free particles and, therefore, the perturbative QCD approach can be used. The cross-section of a process in QCD is factorized into two parts: the process-dependent perturbatively-calculable short-distance partonic cross-section (the hard part) and universal long-distance functions, parton distribution functions (PDFs), and fragmentation functions (the soft part). The parton distributions could be applied also to describe the spin structure of the nucleon that

is built up from the intrinsic spin of the valence and sea quarks (spin $-1/2$), gluons (spin -1), and their orbital angular momenta. A full description can be given in terms of the so-called transverse-momentum dependent (TMD) PDFs.

SPD is planned to operate as a universal facility for comprehensive tests of the basics of the QCD. The main goal of the experiment is the study of the unpolarized and polarized gluon content of the proton at large Bjorken- x , using different complementary probes such as charmonia, open charm, and prompt photon production processes, as well as large- p_T hadron correlations [4, 5]. The experiment aims at providing access to the gluon helicity, gluon Sivers, Boer–Mulders functions, and other TMD PDFs in the proton *via* the measurement of specific single and double spin asymmetries. The kinematic region to be covered by SPD (Fig. 1, *left*) is unique and has never been accessed purposefully in polarized hadronic collisions. Quark TMD PDFs, as well as spin-dependent fragmentation functions could also be studied. The results expected to be obtained by SPD will play an important role in the general understanding of the nucleon gluon content and will serve as a complementary input to the ongoing and planned studies at running and planned experiments with polarized protons both on a fixed-target and in a collider mode (Fig. 1, *right*).

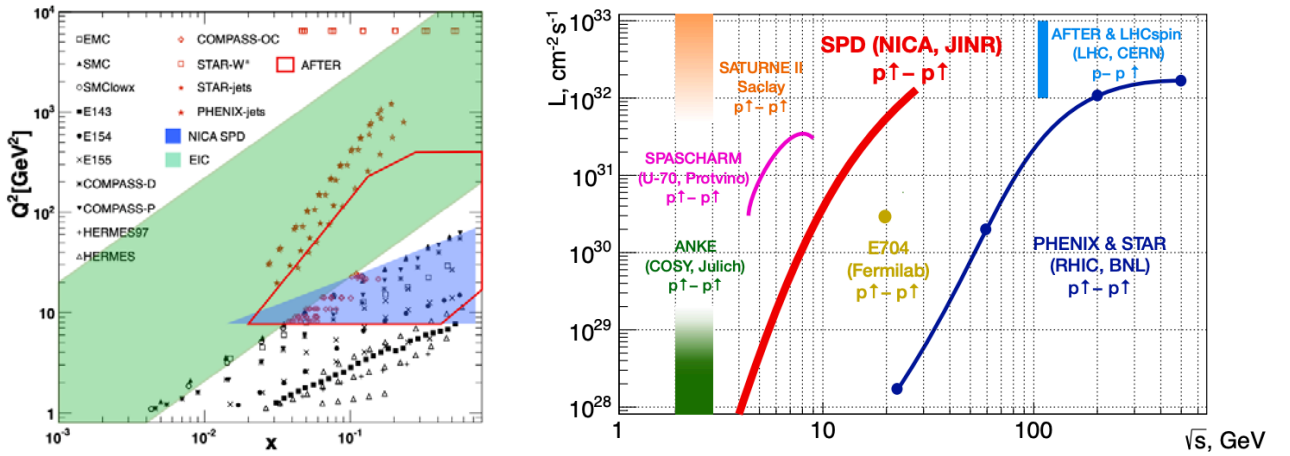


Fig. 1. Kinematic coverage of SPD in the charmonia, open charm and prompt photon production processes (*left*); NICA SPD capabilities in comparison with running and planned experiments with polarized protons both on a fixed-target and in a collider mode (*right*)

SPD has an extensive physics program [5] for the first stage of the NICA collider operation with reduced luminosity and collision energy of the proton and ion beams, devoted to comprehensive tests of various phenomenological models in the non-perturbative and transitional kinematic domain. It includes such topics as spin effects in elastic scattering, exclusive reactions as well as in hyperons production, multi-quark correlations and dibaryon resonances, charmonia and open charm production, *etc.*

PNPI team is currently involved in studies of the SPD sensitivity to the novel production mechanisms as large- p_T baryon production *via* diquark subprocess [5, 10], multiparton scattering, *e. g.*, double quark–diquark scattering, which would lead to enhanced production of exotic multi-quark resonance states and light nuclei [5, 6].

3. SPD experimental set-up

The SPD set-up [2, 3] is being designed as a universal 4π experimental set-up with advanced tracking and particle identification capabilities based on modern technologies. It is shown schematically in Fig. 2. SPD will have a cylindrical symmetry around the collider beam axis, set at the collision point, with longitudinal and transverse dimensions of ~ 8 m and 6.5 m, respectively. The size of the detector is limited by its weight to be less than 1 200 t.

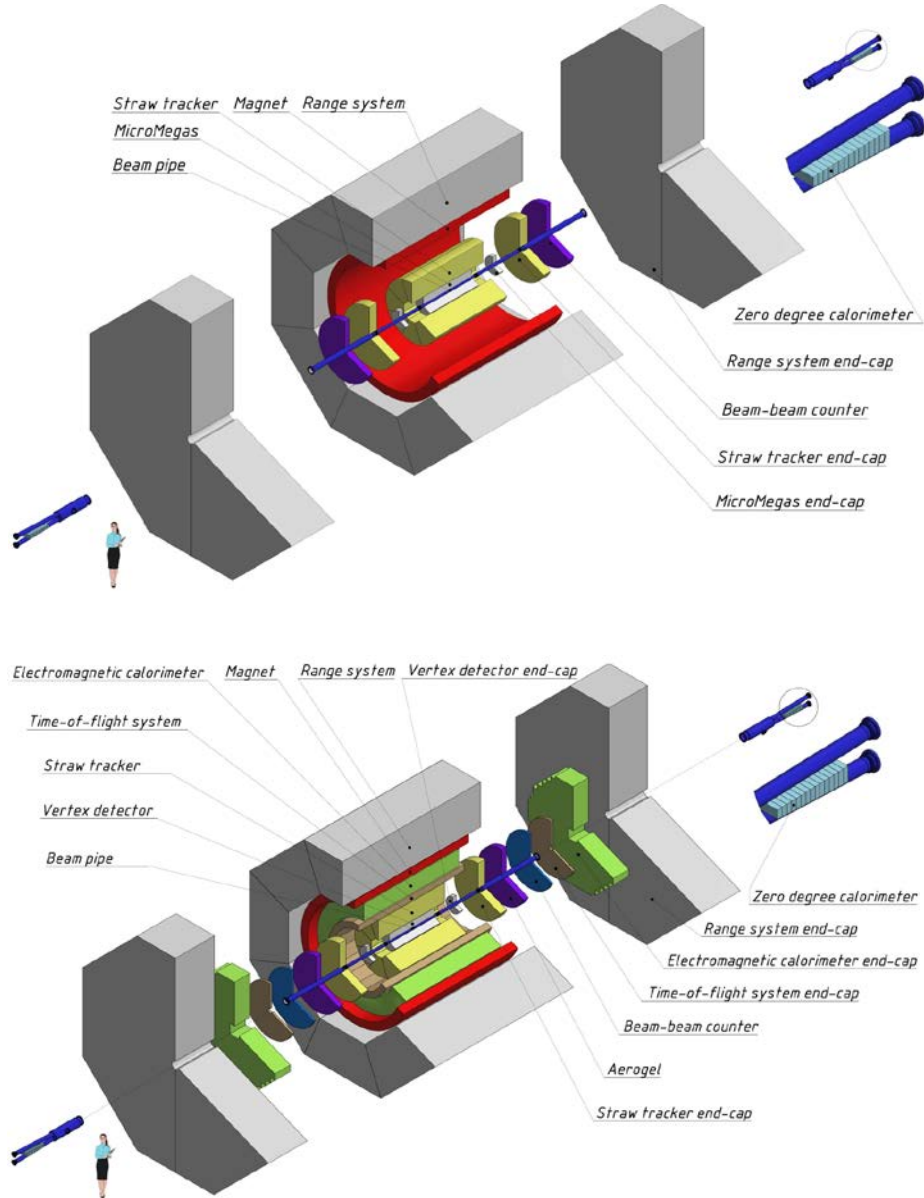


Fig. 2. General layout of the SPD set-up at the first stage (*top*); the final layout of the SPD detector (*bottom*)

The detector will be embedded in a solenoidal magnetic field of ~ 1 T at the axis. The main options of the magnetic system are the superconducting solenoid or a set of superconducting coils in a single cryostat that differs from the SPD conceptual design report option [2]. The silicon vertex detector (VD) with a low material budget will provide the resolution for the vertex position on the level of ~ 100 μm needed for reconstruction of secondary vertices of D -meson decays. VD will be placed as close as possible to the beryllium beam pipe (at distances of $5 \leq R \leq 25$ cm). The use of monolithic active pixel sensors designed and produced for ALICE with the pixel size of 29×27 μm improves the signal-to-background ratio of the D -meson peak by a factor of 3. Micromegas technology is considered for the vertex detector at the first stage of SPD operation.

The tracking system (straw tracker – ST) based on the straw mini-drift tubes and placed inside a solenoidal magnetic field should provide the transverse momentum resolution $\sigma_{p_T}/p_T \approx 2\%$ for a particle momentum of 1 GeV/c. Information on the charged particles energy losses will be used additionally to identify particles with the momenta ≤ 0.7 GeV/c.

The time-of-flight system with a time resolution of about 60 ps will provide 3σ π/K and K/p separation of up to about 1.2 and 2.2 GeV/c, respectively. The possible use of an aerogel-based Cherenkov detector could

extend this range. Detection of photons will be provided by a sampling electromagnetic calorimeter with the energy resolution $\sim 5\% / \sqrt{E}$. To minimize multiple scattering and photon conversion effects for photons, the detector material will be kept to a minimum throughout the internal part of the detector. The muon (range) system is planned for muon identification. It can also act as a rough hadron calorimeter. A pair of beam-beam counters and zero-degree calorimeters will be responsible for the local polarimetry and luminosity control. To minimize possible systematic effects, SPD will be equipped with a triggerless data acquisition (DAQ) system. A high collision rate (up to 4 MHz) and a few hundred thousand detector channels pose a significant challenge to the DAQ, online monitoring, offline computing system, and data processing software [2, 3].

4. SPD straw tracker read-out electronics

In 2018–2022, the PNPI team was involved in the SPD ST R&D: the straw-tube response signal simulation, test-beam studies with straw prototypes and the SPD software development related with the ST. The works are performing in close collaboration with a JINR group (T. Enik, V. Bautin, M. Demichev, K. Salamatin and Y. Kamar) with the help of the European Organization for Nuclear Research (CERN) RD51 Collaboration. Preliminary results were presented at conferences [11] and [12].

Nowadays, the trackers built of straw drift tubes are a perfect solution for precise track measurements in high energy and neutrino physics experiments operating at low and moderate event rate. ST will play crucial roles in such future detectors as the NICA SPD [2, 3] detector and also, at the hidden sector detector of the SHiP [13] and the near-detector complex of the DUNE [14] experiments. Performance requirements of ST and its read-out electronics are defined by the physics goals. Proper evaluation of the designed ST performance demands realistic simulation and studies with tracker prototypes. Preliminary results [11, 12] of the muon beam measurements done with straw tube chambers, which were equipped by multifunctional application specific integrated circuits (ASICs). The results obtained at the CERN super proton synchrotron (SPS) test beam line are compared to the predictions made with GARFIELD [15] simulation package interfaced to LTSpice [16] program for electronics circuit modeling.

The SPD ST will serve not only for coordinate measurements, but also for particle identification, exploiting the difference in the ionization energy losses of different particle kinds. This option requires measurements of both the drift time and charge of the straw signal. Two families of ASICs currently capable for those measurements are available: VMM3 [17]/VMM3a [18] and TIGER [19]. Figure 3 shows the basic features of the ASIC schematics and the Table compares their operation parameters.

GARFIELD package for detailed gas detector simulation is used to predict the straw response to a muon of 1 GeV energy. Figure 4, *left*, shows an example of the signal induced at the straw anode as it is simulated with GARFIELD. To model the corresponding signal at the output of the read-out electronics, LTSpice [11] software is used. The package allows to define a certain electronics circuit model and to predict its response to a custom input signal shape. A straw response generated with GARFIELD is used as a signal at the input of the VMM3 circuit model. The corresponding output signal is shown in Fig. 4, *right*.

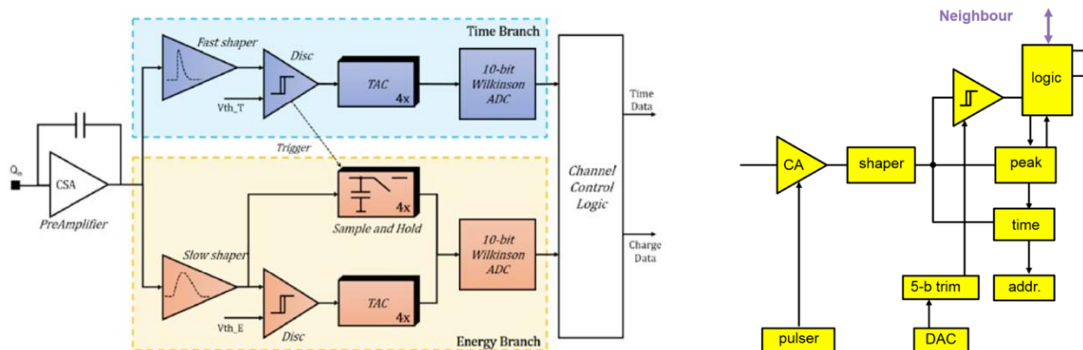


Fig. 3. Basic features of the ASIC schematics: TIGER (*left*) and VMM3/3a (*right*)

Table

Comparison of VMM3/3a and TIGER operation parameters

Parameter	VMM3	TIGER
Number of channels	64	64
Clock frequency	10–80 MHz	160–200 MHz
Input capacitance	< 300 pF	< 100 pF
Dynamic range	Linearity within $\pm 2\%$ up to 2 pC	50 fC
Gain	0.5, 1, 3, 6, 9, 12, 16 mV/fC	12 mV/fC
ENC (energy branch)	< 3 000	< 1 500
TDC binning	~ 1 ns	50 ps
Maximum event rate	140 kHz/ch	60 kHz/ch
Consumption	15 mW/ch	12 mW/ch

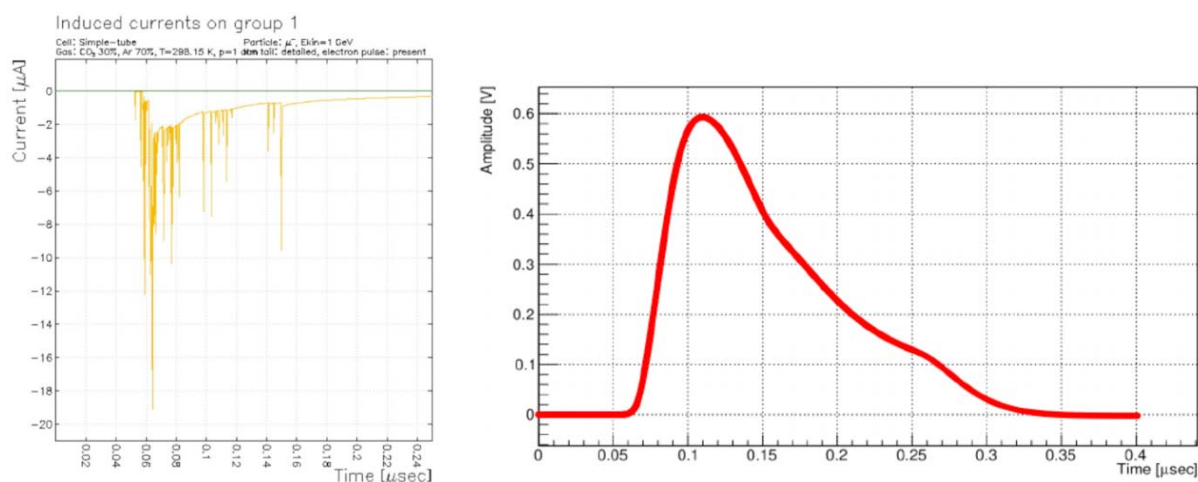


Fig. 4. A signal from the straw tube predicted by GARFIELD (*left*) and the corresponding response of the VMM3 amplifier and shaper emulated with LTSpice (*right*)

The combination of the GARFIELD and LTSpice packages allows to obtain realistic predictions of the measurements done with a straw tube and the VMM3-based read-out.

Three types of straw read-out electronics were tested with the SPS muon beam at CERN. To perform the measurements a test set-up has been developed. The set-up consists of:

- The reference tracking implemented with three Micromegas detectors measuring the track coordinate perpendicular to the straw axis and an additional one for control measurement of the track coordinate along the tube. All Micromegas have a pitch of 250 μm;
- The reference timing implemented with scintillators read out with silicon photomultipliers running in a coincidence mode. The time resolution of the reference timing was found to be better than ~ 1 ns;
- Straw tubes with a diameter of 6 mm operated with the 70% Ar + 30% CO₂ gas mixture and were read out with one of three types of the frontend electronics based on the VMM3a, VMM3 and TIGER ASICs.

A photo and a schematic diagram of the test set-up are shown in Fig. 5.

Measurements at the CERN SPS test beam were made with three different read-out electronics solutions for the straws. The first one, based on the VMM3a read-out, was done in November of 2021 [11]. VMM3a reliably operates in the so-called “time-at-peak” mode, when the time of the signal peak is measured, and performs well as a read-out of the ATLAS New Small Wheel [20]. This operation mode cannot be used in read-out of drift tubes, since the time of a threshold crossing rather than a signal peak time has to be measured. This possibility is implemented for VMM3/3a as well as a “time-at-threshold” mode, but has not been tested in detail. During the test beam measurements with the straw tubes, VMM3a was found to suffer of channel

latching while operated in the “time-at-threshold” mode, as can be seen in Fig. 6. The current information hints to an algorithmic issue in the cases when the time between the threshold crossing and signal peak is shorter than one clock period, which is often the case for the straw signals.

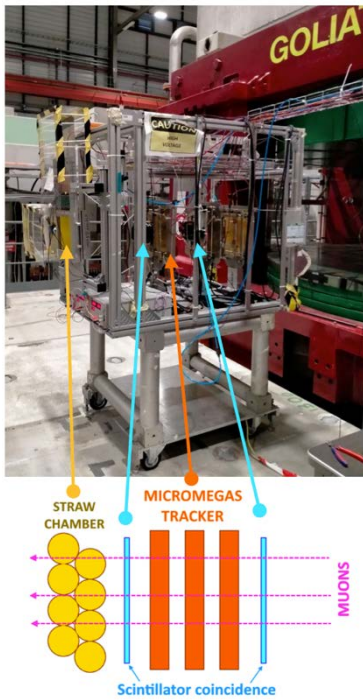


Fig. 5. Photo and schematic description of the test setup at CERN SPS

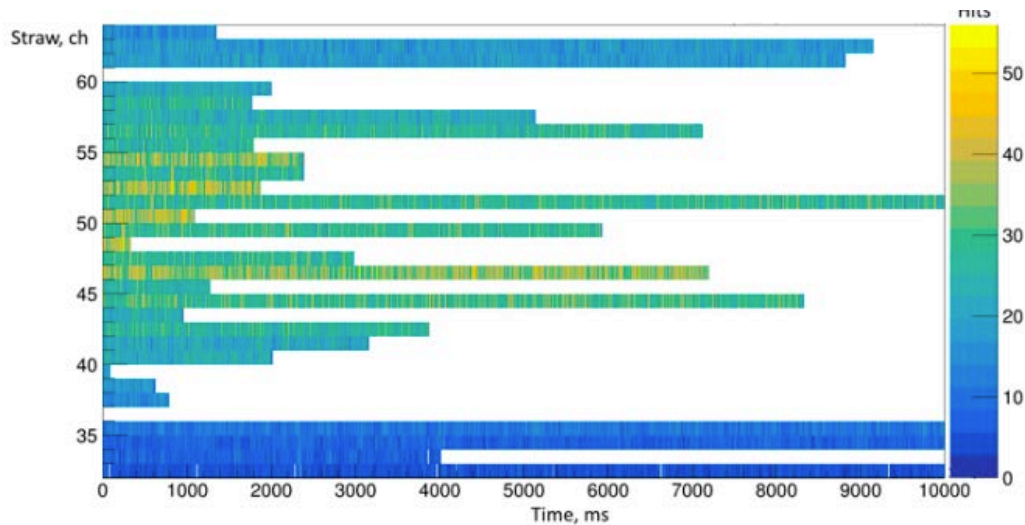


Fig. 6. VMM3a channels latching in the “time-at-threshold” mode – after several seconds of operation no response from most of VMM3a channels is observed

The observed problem makes it impossible to use VMM3a for straw read-out, so the previous version of the ASIC, VMM3, was tested as well. The measurements were performed in summer 2022 with SPS muon beams [12].

It was found that VMM3 has no such “latching” problem since implementation of the “time-at-threshold” mode slightly differs for VMM3 and VMM3a. Preliminary results of the data analysis are shown in Fig. 7, *left*. At this stage of the analysis, only one of three Micromegas, R , is used to reconstruct the track coordinates. The plot shows the drift time t_{drift} measured as the time of a signal threshold crossing with respect to the

scintillator coincidence signal as a function of the reference track coordinate. The muon flux is uniform across the straw tube.

Figure 7, *right*, compares the straw drift times obtained from the data analysis to the corresponding results of the GARFIELD simulation, followed by emulation of the read-out electronics in LTSpice. It can be concluded that the agreement between the model and data is quite good.

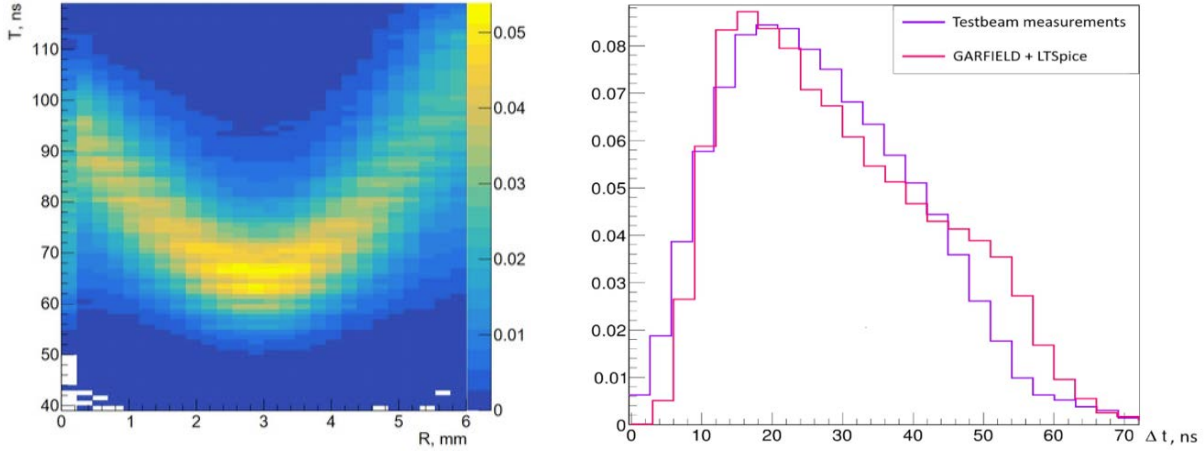


Fig. 7. Preliminary results of the $t_{\text{drift}}(R)$ measurements done with the VMM3-based read-out (*left*); a comparison of the drift time distribution obtained with the muon beam data (magenta) to the corresponding GARFIELD + LTSpice prediction (*red, right*)

Straw read-out based on the TIGER ASIC was tested at the SPS as well in autumn 2022. Preliminary results of the data analysis [12] are shown in Fig. 8, with the reduced reference tracking information as well. Work on the reference track reconstruction using all Micromegas detectors is ongoing. Improvement of the reference tracking will provide high precision of the $t_{\text{drift}}(R)$ distribution.

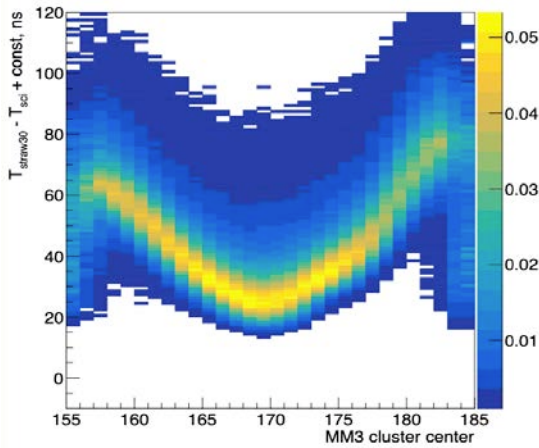


Fig. 8. Preliminary results of the $t_{\text{drift}}(R)$ measurements done with the TIGER-based read-out

To summarize, intensive searches of possible solutions for straw read-out electronics are ongoing. A synergy of muon beam measurements and straw response simulation provides a good base for exploring different straw read-out options in order to find a good solution for front-end electronics of the ST for the SPD experiment at the NICA collider.

As existing possibilities, VMM3a, VMM3 and TIGER ASICs were studied [11, 12]. VMM3a was discarded due to the observed latching problem in the “time-at-threshold” operation mode, while VMM3 was found to be operational in that mode. The analysis of the measurements performed with the VMM3 and TIGER-based straw read-outs is ongoing, as well as simulation studies with the combined GARFIELD and LTSpice software.

5. Conclusion

The SPD experiment at the future NICA accelerator facility [1] at JINR, Dubna, one of megascience projects in Russia, is focused to investigate spin structure of nucleons and various phenomena in collisions of longitudinal and transverse polarized protons and deuterons at \sqrt{s} up to 27 GeV and luminosity up to $10^{32} \text{ cm}^{-2} \cdot \text{s}^{-1}$. A comprehensive study of the unpolarized and polarized gluon content of the nucleon at large Feynman- x using different complementary probes such as charmonia, open charm, and prompt photon production processes is the central point of the SPD physics program [2, 3].

The SPD experimental set-up [2, 3] is planned as a multipurpose universal 4π detector with advanced tracking and particle identification capabilities, an electromagnetic calorimeter, and a muon (range) system. With the high luminosity polarized proton–proton collisions, the SPD experiment at NICA will cover the kinematic gap between the low-energy and high-energy measurements of running and planned experiments both on a fixed-target and in a collider mode. The possibility for NICA to operate with polarized deuteron beams at such energies is unique [4, 5].

The SPD conceptual design report was presented in the beginning of 2021 [2]. The SPD technical design report [3] was completed at the end of 2022. The future measurements at SPD have bright perspectives to make a unique contribution and challenge our understanding of the spin structure of the nucleon and the nature of the strong interaction.

The PNPI team is actively participating in the SPD ST developments and SPD physics program.

References

1. V.D. Kekelidze, V.A. Matveev, I.N. Meshkov *et al.*, Phys. Part. Nucl. **48**, 727 (2017).
2. V.M. Abazov *et al.*, SPD Conceptual Design Report (2021), e-Print: 2102.00442 [hep-ex].
3. V.M. Abazov *et al.*, SPD Technical Design Report (2022).
4. A.B. Arbuzov *et al.*, Prog. Part. Nucl. Phys. **119**, 103858 (2021).
5. V.V. Abramov *et al.*, Phys. Part. Nucl. **52** (6), 1044 (2021).
6. A.V. Efremov, V.T. Kim, JINR E2-87-74 (1987).
7. A.V. Efremov, V.T. Kim, G.I. Lykasov, Sov. J. Nucl. Phys. **44**, 151 (1986).
8. A.V. Efremov, A.B. Kaidalov, V.T. Kim *et al.*, Sov. J. Nucl. Phys. **47**, 868 (1988).
9. V.T. Kim, Phys. Part. Nucl. Lett. **15**, 384 (2018).
10. V.T. Kim, Mod. Phys. Lett. A **3**, 909 (1988).
11. V. Bautin *et al.*, Nucl. Instrum. Meth. A **1047**, 167864 (2023).
12. A. Zelenov *et al.*, in *Proc. of ICPPA-2022* (2023).
13. SHiP Collab., C. Ahdida *et al.*, Eur. Phys. J. C **82**, 486 (2022).
14. DUNE Collab., R. Acciarri *et al.*, (2016), e-Print: 1601.02984 [hep-ex].
15. R. Veenhof, in *Conf. Proc. C 9306149*, 66 (1993).
16. LTSpice Simulator, <https://www.analog.com/en/design-center/design-tools-and-calculators/ltspice-simulator.html>, Accessed: 2023-01-14.
17. ATLAS Muon Collab., G. Iakovidis, EPJ Web Conf. **174**, 07001 (2018).
18. G. Iakovidis, J. Phys. Conf. Ser. **1498**, 012051 (2020).
19. M. Greco *et al.*, PoS MPGD2017, 049 (2019).
20. T. Kawamoto *et al.*, Tech. Rep. (2013), <http://cds.cern.ch/record/1552862>

ENGINEERING DESIGN OF THE RICH AND MUCH DETECTORS FOR THE CBM EXPERIMENT AT FAIR

D.A. Ivanishchev, A.V. Khanzadeev, N.M. Miftakhov, V.N. Nikulin, E.V. Roshchin, A. Riabov, Yu.G. Ryabov, G.V. Rybakov, V.M. Samsonov, O.P. Tarasenkova, D.V. Tyts

1. Introduction

The goal of the CBM experiment research program at FAIR (GSI, Germany) is to explore the quantum chromodynamics phase diagram in the region of high baryon densities using high-energy nucleus–nucleus collisions [1]. As shown in Fig. 1, CBM apparatus consists of several detectors specially designed to register different signatures of dense and hot matter created in heavy ion collisions at the FAIR luminosity and energy.

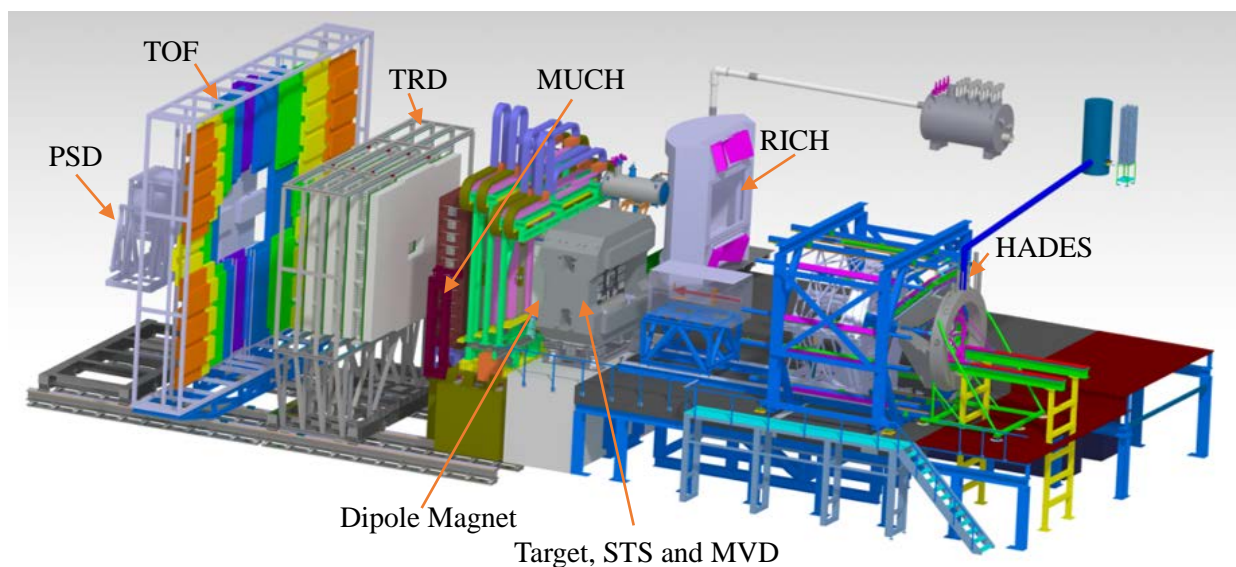


Fig. 1. Layout of the detectors of the CBM experiment

According to the international task sharing in CBM Collaboration, the PNPI participates in the design, production, delivery, assembling and testing of the ring-imaging Cherenkov (RICH) detector for detection of electrons [2] and the muon chamber (MUCH) detector for muon identification. The PNPI obligations are as follows:

- Design and production of the mechanical structure of the MUCH detector,
- Design and production of the mechanical structure of the RICH detector,
- Design and production of systems for supplying working gases to these two detectors.

2. Detector MUCH

The MUCH detector (Fig. 2, 3) is designed to identify muons among particles detected by the silicon tracker STS located inside the dipole magnet. MUCH consists of a series of absorbers (A1–A5), sandwiched with the tracking stations located in 30 cm thick gaps between them. Each of the tracking stations contains three layers of chambers. The transition radiation detector (TRD) is normally used as the last station. The first absorber is composed of 28 cm thick layer of carbon padded with 30 cm of concrete. The remaining four absorbers (20 + 20 + 30 + 100 cm thick) are made of steel.

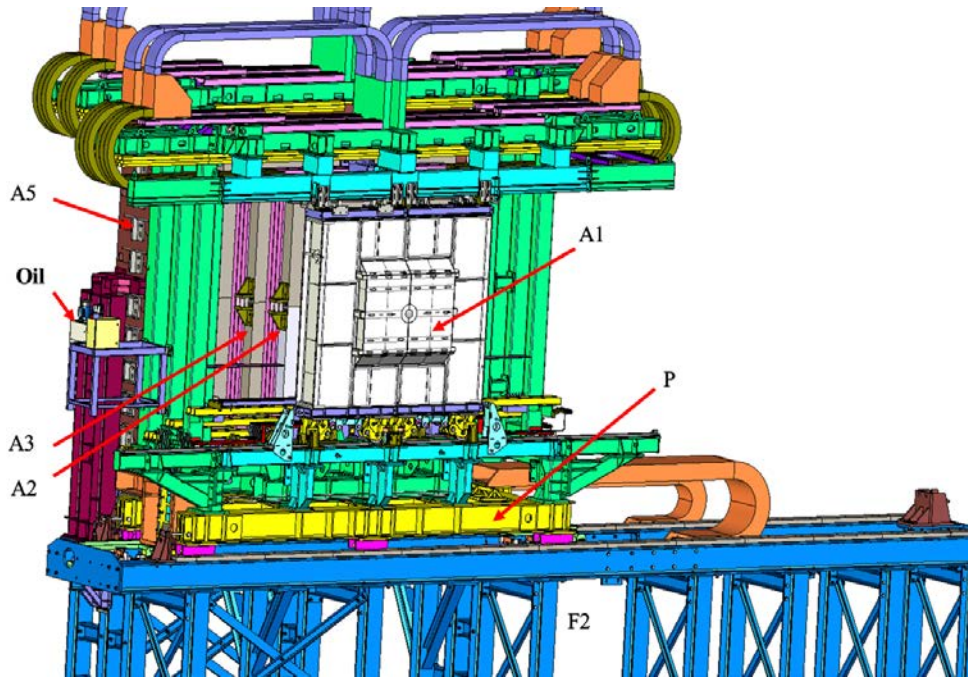


Fig. 2. General layout of MUCH in the operational (beam) position. Four absorbers (A1–A4) sit on a movable platform (P) that can roll on the rails installed on the foundation (F2). The hydraulic drive and its oil station (Oil) are removable. The fifth absorber A5 is installed on the dedicated foundation

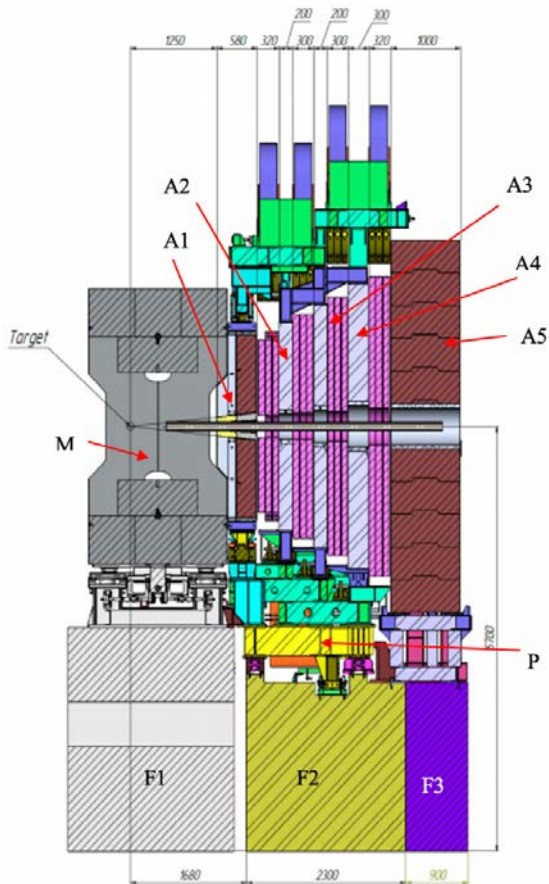


Fig. 3. Cut view of the MUCH detector with the dipole magnet (M). Four absorbers (A1–A4) sit on a movable platform (P) that can roll on the rails installed on the foundation (F2). The fifth absorber A5 is installed on the dedicated foundation (F3). The foundations F are shown schematically

The energy of the produced muons and, accordingly, their penetrating power depend on the beam energy. Therefore, it is necessary to carry out measurements in various MUCH configurations to identify both charmonium and low-mass vector mesons in the entire FAIR energy range. Special simulations were done and the following MUCH configurations were selected as the most efficient.

- For the lowest FAIR energies, MUCH consists of three absorbers and two tracking stations with a total thickness of 98 cm, which corresponds to the radiation length $X = 26.5 X_0$ or 3.7 nuclear interaction lengths λ_{int} . In this case, there are no absorbers 4 and 5, while the TRD detector moves closer to the MUCH detector.
- The MUCH design foresees the addition of a fourth absorber and supplemental stations for intermediate FAIR energies. In this case, the total thickness increases to 128 cm and the radiation length to $X = 43.6 X_0$ or $5.46 \lambda_{\text{int}}$.
- At maximal energies of the FAIR synchrotron SIS300 it should be possible to install a 1 m thick fifth absorber. The total length of the absorbers will be about 2.28 m, which corresponds to $96.3 X_0$ and 11 nuclear interaction lengths.

The first two tracking stations are gas electron multiplier based chambers with two-component gas mixture, while the third and fourth stations consist of several resistive plane chambers (RPC) operating with a three-component gas mixture.

MUCH and RICH detectors will share the beam on an alternate basis, *i. e.* after CBM operation in the muon mode, MUCH, built on a movable platform, will be displaced to the parking position near the cavern wall, while RICH will be installed in the beam to take data in electron mode. Therefore, the MUCH design must provide:

- The safe movement of MUCH to about 7 m with the reproducibility of the final position with an accuracy of about ± 1 mm;
- Permanent reliable connection of the required services (various cables, optical lines, pipes for the gas mixture and cooling water);
- The MUCH width limited to 6.4 m in parking position. Otherwise, it will not be possible to install RICH in operating position in the beam.

The longitudinal dimension of MUCH should be minimized in order to reduce the number of pion decays into muons. Such muons cause an additional background in the di-muon mass spectrum and degrade the detector performance in studies of rare processes.

Each of the tracking stations consists of three chambers divided into two planes (right and left). These planes are fixed in the operational position in the gap between the absorbers. Each plane can be moved individually outside the gap for maintenance.

It is important to have a permanent connection of the principal services to the detecting plane. Temporary disconnections of services are allowed using connectors that guarantee a quick and reliable reconnection, such as gas and water pipes on self-sealing quick-release connectors.

Since the RICH detector is moved to its parking position, which is far away from MUCH, in the muon mode of operation of the CBM, the constraint on the width of the detector is removed and it becomes possible to install removable extensions of the transverse beams.

The MUCH platform could be moved along the rails bolted to the RICH–MUCH foundation by means of a displacement system. Two flexible cable holders are used to provide secure guidance of the multiple services – various cables, water and gas pipes, optical links *etc.* – from the foundation to the patch panels on the platform.

The operation of the detection elements requires the supply of services – various kinds of cables, fiber optic lines, gas and cooling pipes. The service delivery system includes flexible cable layers that connect patch panels located near the exit point of the cable layers on the MUCH platform with patch panels located on the detecting layers and systems for their fastening.

Special attention was paid to guarantee safe operation of MUCH during eventual earthquakes. The MUCH detector, being a heavy (110 t), high device (6,5 m) with a relatively short support base and the centre of gravity shifted downstream, is unstable in case of an earthquake. To prevent its falling, pressure beams were provided, fixed on the foundation of the dipole magnet. Anchor bolts in the RICH–MUCH foundation must withstand a pull-out force of around 25 t. The brackets on the perimeter of the foundation

fix the detector during the earthquake. To prevent tipping over in the parking position, a dedicated frame fixed to the floor of the CBM cave and to the RICH–MUCH foundation was designed.

The performed stress, deformation and the behaviour during earthquakes analysis of MUCH design prove the correctness of the design.

3. Detector RICH

The detector RICH and several layers of the TRD detector are planned to be used in the CBM experiment for electron identification. With the SIS100 cyclotron, CBM is going to use the RICH detector and the first station of the TRD detector. However, with the SIS300 cyclotron the full inclusion of TRD is necessary to study vector mesons and possibly also detecting the photons through a single transformation ($\gamma \rightarrow e + e^-$) inside the target or the first STS station.

The RICH detector ensures electron identification and pion suppression at the momenta below 10 GeV/c. This is a gas detector with focusing mirror projection geometry and a photon detector. CO₂ is used as the gas-radiator. The detector will be located behind the dipole magnet approximately 1.8 m from the target, as shown in Fig. 4.

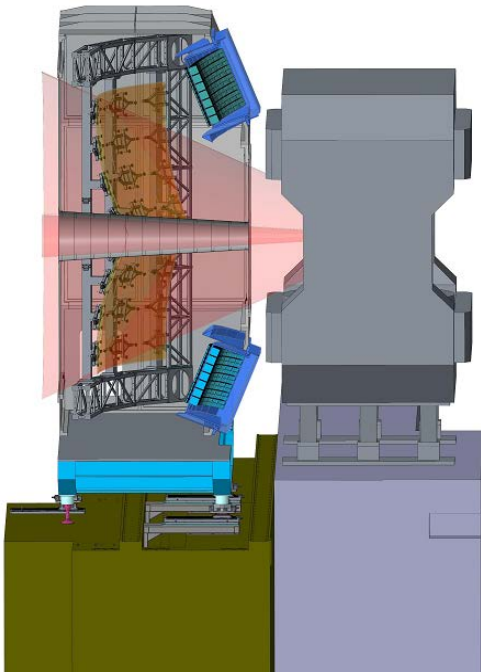


Fig. 4. Schematic view of the RICH detector

Focusing of the induced Cherenkov light is achieved using a large multisegment system of spherical mirrors with an area of 13 m² (two mirrors above and below the beam path) with a radius of curvature of 3 m (see Fig. 4). Glass mirror tiles ($\sim 40 \times 40$ cm², 6 mm thick) with an Al + MgF₂ reflective coating (85% reflectivity over a wide wavelength range) will be used.

The photon detection system covers a total active area of 2.4 m². Multianode photomultipliers (PMT) Hamamatsu H12700 with an ultra violet (UV) transparent window will be used. The use of a wavelength-shift coating applied to the PMT window is being considered to further improve the UV performance. The readout pixel size is 6 × 6 mm², which requires 55 000 readout channels. The residual magnetic field affects the operation of photomultipliers. To move the photon detectors to an area with lower magnetic fields, the mirror focusing system was tilted. Unfortunately, the shift of the photon detectors leads to a deterioration in the performance of the detector (the shape of the image rings begins to deviate from the circle, which reduces the efficiency of the ring finding algorithm). After intensive modeling and calculations, the optimal tilt angle of the optical system (about 12°) was chosen. But in this case, additional magnetic protection (iron) is

required around the photon detectors in order to reduce the magnetic field on the photocathodes to a value of 1–2 mT.

To comprehensively test the selected components, a full-scale prototype of the RICH detector was built, which was successfully tested during three test sessions on a test beam at European Organization for Nuclear Research (CERN). Tests have shown that 22 photons are measured per electron ring. In central Au + Au collisions, at a beam energy of 25 A · GeV, about 100 rings will be registered (due to the large amount of material in front of the RICH detector). However, due to the high granularity and large number of photons registered for one ring, according to the simulation results, it is expected that pion suppression by more than 100 times will be achieved.

The CBM experiment physics program assumes alternate use of the RICH and MUCH detectors (typical change period once a year) in the same place on the beam. Therefore, the mechanical structure of the RICH, with dimensions of about 2 × 5 × 6 m (length × height × width), should allow the mobility of the RICH detector with a crane or with rails. The RICH detector covers a range of scattering angles up to 35° in the horizontal (x - z) plane and up to 25° in the vertical (y - z) plane relative to the nominal target position. The length of the gas radiator (measured from the entrance window to the mirror surface) is 1.70 m (the total length is approximately 2 m). The remaining space is reserved for the mirrors, their mounts and support frames.

A general view of the mechanical structures of the RICH detector is shown in Fig. 5. The largest part of the RICH detector is the gas box (2). The box is filled with radiator gas. Inside the box is a focusing mirror system. The basis of the system is the mirror support frame (3), to which the mirror tiles are attached with special mounts and fixing of the mirror tiles. The gas box is mounted on a support platform with adjustable articulated supports (1), which in turn is mounted on the foundation, that allows the detector to be at the level of the beam axis, passing at a height of about 6 m from the level of the cave floor. Two photon detectors are installed on the front side of the box – above and below the beam pipe. Two photon detectors are surrounded by massive protective boxes (4) to protect the PMT from the residual magnetic field of the dipole magnet. The box is equipped with inlet (6) windows at the front and exit (7) windows at the back. In the centre of the gas box there is a tunnel for the beam tube (5). As part of the preparation for the engineering project, the PNPI group provided a detailed model of the magnetic shielding box for photomultipliers, a detailed design of the support platform, designed, manufactured, assembled and successfully tested a prototype of the adjustable supports. Testing of the built full-scale (in height) prototype of the mirror support frame continued to confirm the stability of the mirror system.

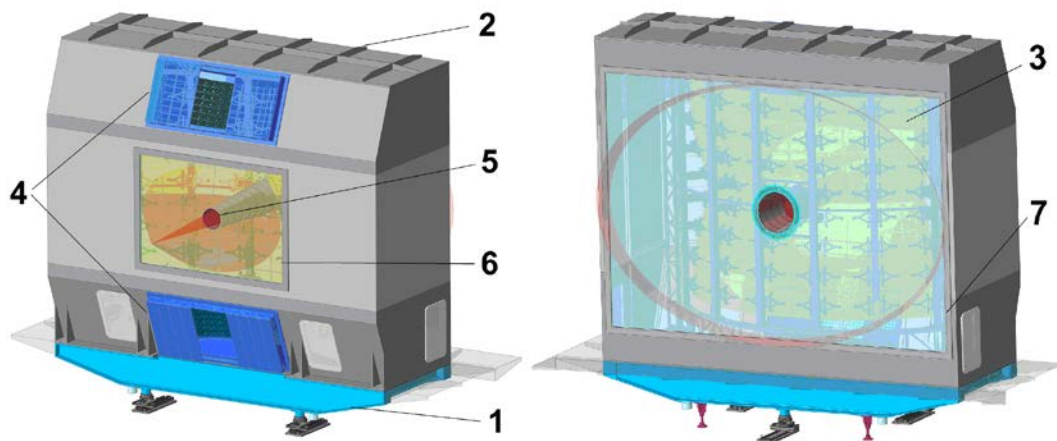


Fig. 5. General view of the mechanical structures of the RICH detector of the CBM experiment: 1 – support platform and adjustable supports; 2 – gas box; 3 – mirror support frame; 4 – magnetic shielding boxes; 5 – beam tube tunnel; 6 – inlet window; 7 – outlet window

The support platform ensures the stability of the installation of the entire detector in the working position (on the beam), and also provides the possibility of alignment on the beam axis in the cave of the CBM

experiment. The adjustment is carried out using adjustable hinged supports, which are pre-installed on the foundation. Lifting and rearrangement of the RICH detector is carried out by the support platform with a crane using a special traverse. The support platform is mounted on three adjustable supports, each of which is designed for 6000 kg static load. Some additional safety supports may be used to provide additional stability to the structure. The design is calculated based on a preliminary load estimate of 16 t. In the current concept, the support platform is made of an I-profile aluminum or steel profile (I-profile) with a height of 500 mm. A plate is fixed on top of the profile frame, which serves as the basis for fixing the gas box and for installing the mirror support truss. From below, hemispherical support elements are installed for installation on adjustable hinged supports.

The design of adjustable supports allows moving the detector vertically (*Y*-axis) within 15 mm, 100 mm horizontally (*X*-axis, across the beam) and 580 mm along the beam axis (*Z*-axis). This design of hinged supports allows the detector to be precisely positioned relative to the beam axis. The increased movement along the beam axis makes it possible to gain access to the beam tube between RICH and the magnet, as well as to secure crane operations with the detector when installing or removing it from its working position. We plan to use two types of adjustable supports. The support of the first type regulates movements in the transverse and vertical directions, has free longitudinal movement and all rotational degrees of freedom. The support of the second type regulates movements in the longitudinal and vertical directions and has free transverse movement and all rotational degrees of freedom. In the upper part of the supports there is a hemisphere providing rotational degrees of freedom. The movement of the supports is ensured by means of lead screws and linear guides (vertically by means of sliding wedges) manually. Due to the complexity of the design, three adjustable supports were produced and successfully tested under load (Fig. 6).



Fig. 6. Prototype of the upper part (for vertical movement) of the adjustable support (*a*) under load (*b*) and the bottom part (for horizontal movement) during testing under load (*c*, *d*)

Another important part of the detector is a mirror focusing system. Each of the two halves of the RICH mirror is divided into 40 rectangular segments (tiles). It is supposed to have four rows of ten tiles. Four types of tiles of different sizes are used. This segmentation scheme takes into account the reasonable dimensions of the glass mirror tiles tested on the prototype and provides acceptable gaps of 3–4 mm between the tiles. Specific requirements are imposed on the mirror support structure. On the one hand, the design should ensure the stability of the optical system even when transported by crane. On the other hand, the design should be as radiation-transparent as possible in order to prevent the operation of the detectors installed downstream of the RICH from being affected. To solve the problem, intensive calculations and studies were

carried out on about ten different options for the design of the frame to support the mirrors. As a result, the most promising option was chosen with the so-called pillars, carrying two rows of mirror tiles. Preliminary calculations showed that such a design can provide the required strength and rigidity, while ensuring a minimum of substance in the acceptance of the detector. The mirror mounting frame is assembled from aluminum parts and contains seats for mounts. Mirror tiles are attached to the frame with three adjustable mounts. Adjustable mounts allow us to orient the mirror tiles independently of each other, which allow ensuring sufficient convergence and focusing of the entire focusing mirror system. The concept of a three-point attachment (tripod) was chosen as the basic idea for installing the mirror tiles. Three mounts are glued to the mirror at three points, forming an equilateral triangle. This allows individual focusing for each mirror tile and eliminates its significant deformation.

The decision to produce a full-scale (in height) prototype of mirror supporting frame (with two pillars) (Fig. 7*c, d*) was made to test this concept.

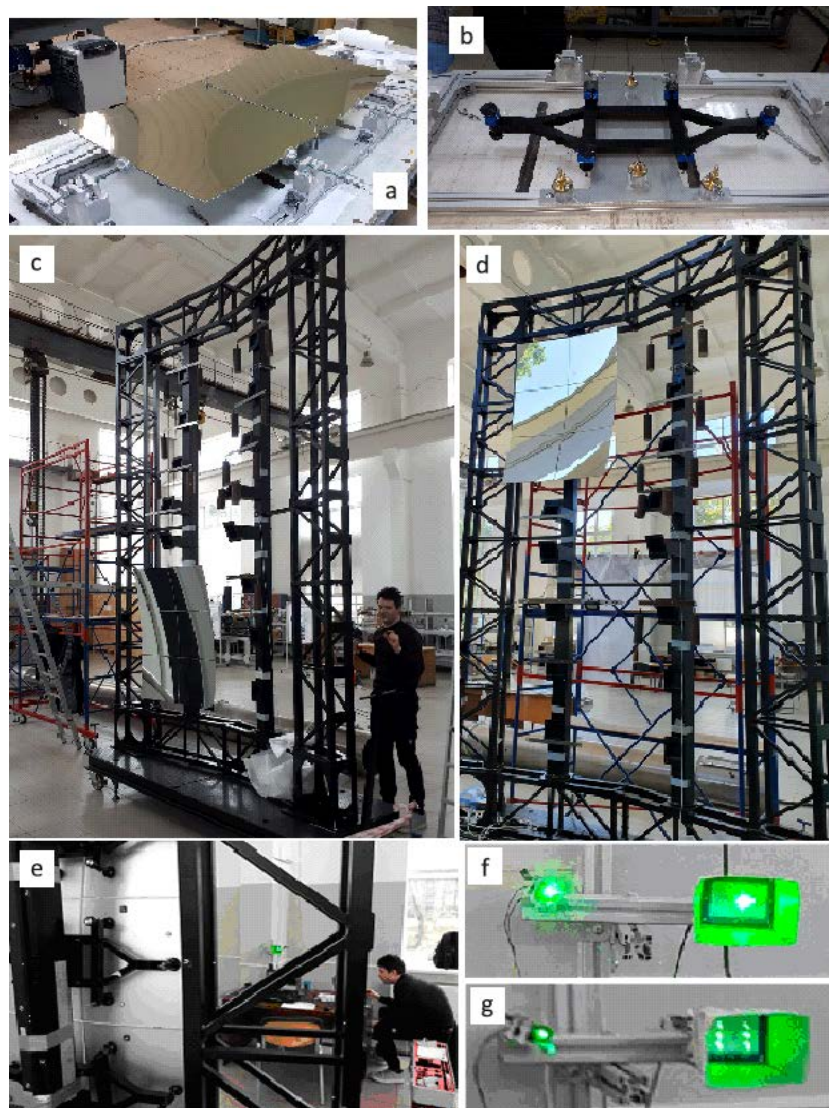


Fig. 7. The mirror tiles gluing process with specially assembled set-up (*a, b*); full size mirror support frame prototype with test mirror tiles installed (*c, d*); rear view showing small frames and mounts (*e*); reflective light spots from defocused laser for testing (*f, g*)

For the tests, four sets of frames for mirror tiles were designed, manufactured and assembled. Mountings for mirrors gluing were developed, produced and assembled. A special set-up for spherical mirror tiles gluing

was developed and assembled. Mirror tiles were successfully glued and installed in the prototype (see Fig. 7). A special laser stand was constructed to check the stability of the mirror system. The installed mirror tiles were used for long-term stability tests of the mirror system. The tiles were installed in different places of the frame (see Fig. 7c, d) and the position of the light spots from the lasers on the screen was measured for six months. The test results show good agreement between the calculations and real measurements and prove the correctness of the chosen option.

Also, as part of the engineering project preparation, the design of the gas box and magnetic protection was developed. The gas box is mounted on a rigid platform that can be adjusted. The box provides a gas-tight and light-tight enclosed space for the CO₂ radiator gas and supports the magnetic shielding boxes for the two photon detectors. The dimensions of the gas box are about 2.2 m long, more than 5 m high and about 6 m wide. The parts of the front and back walls of the box that are in acceptance of the CBM experiment should contain as little material as possible. For example, a portion of the front wall may be a window made from a Kapton-type film or the like, and the back wall may be made from a thin plastic sheet. The gas pressure of the CO₂ radiator inside the box will be continuously regulated by the gas system to 2 mbar above atmospheric pressure. Leakage of working gas from the box should not exceed 3 l/min. For ease of transportation and manufacturing, the gas box is supposed to be assembled from several aluminum parts, as shown in Fig. 8 (*left*). In the current concept, the gas box is also used as a supporting structure for heavy magnetic shield, which creates loads and leads to deformations, that can affect the focusing of the mirror system. To reduce this influence, the truss of the mirror system is not mechanically rigidly connected to the gas box. The proposed option satisfies the requirements.

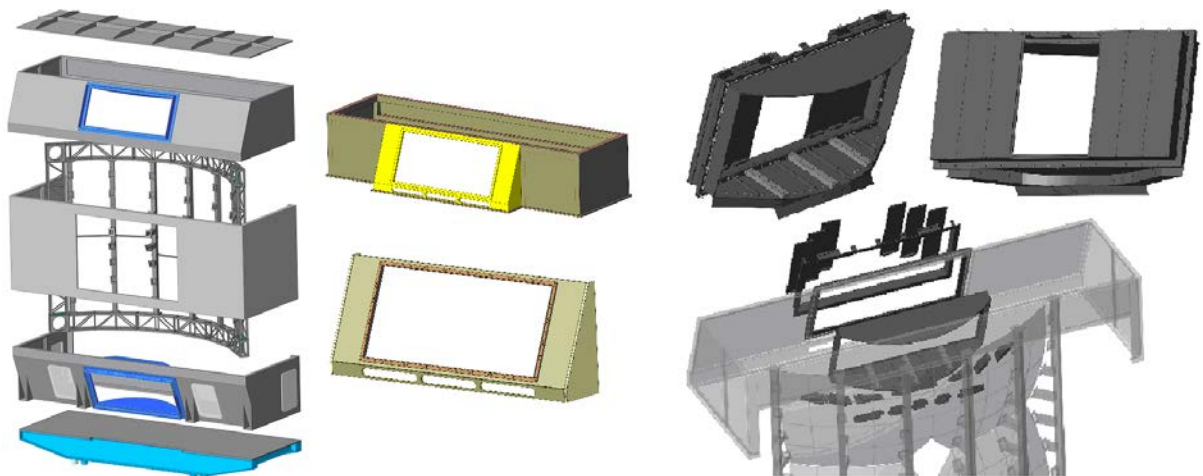


Fig. 8. Gas box components (*left*); composite structure of magnetic shielding boxes (*right*)

The magnetic shielding is the most important condition for correct working of PMT detectors located near the dipole magnet of the CBM experiment. With a maximum magnet field of 1 T, magnetic protection should reduce the residual magnetic field induction of 50–100 mT to a value of 1 mT in the area where the PMT photocathodes are located. Reading electronics is attached to the magnetic protection boxes. Therefore, a composite model of magnetic shielding boxes was created (Fig. 8, *right*). At the moment, it is assumed that the magnetic protection boxes will be entirely made of magnetic iron. To provide access to the readout electronics, the rear walls will be removable and made of lightweight parts to be removed and installed by hand. The design of shielding boxes will take into account the presence of cooling of the electronics, for example, holes for hoses will be made. The dimensions of the boxes correspond to the dimensions of the photon detectors.

4. Conclusion

The conceptual design report of the MUCH and RICH mechanical structures was approved by the collaboration in 2021. At the moment, materials for engineering design are in the final stage.

References

1. CBM Collab., Nucl. Phys. A **967**, 892 (2017).
2. CBM Collab., Nucl. Instrum. Meth. A **553**, 91 (2005).

STATUS OF THE FORWARD TIME-OF-FLIGHT DETECTOR FOR THE PANDA EXPERIMENT AT GSI

S.L. Belostotski, G.V. Fedotov, **A.A. Izotov**, S.I. Manaenkov, O.V. Miklukho, V.A. Stepanov, D.O. Veretennikov, S.S. Volkov, A.A. Zhdanov

1. Introduction

The PANDA (antiproton annihilation at Darmstadt) experiment is aimed at precise studies of $\bar{p}p$ annihilations and reactions of \bar{p} with nucleons of heavier nuclear targets using the \bar{p} beam of unprecedented quality [1, 2]. This beam will be provided by the high energy storage ring (HESR). The accelerator HESR is under construction at GSI, Darmstadt, Germany. The ring will operate in the momentum range from 1.5 to 15 GeV/c. In a high momentum resolution (HR) mode of HESR, the relative momentum spread of the beam is reduced to $5 \cdot 10^{-5}$ with 10^{10} circulating antiprotons at the peak luminosity of $2 \cdot 10^{31} \text{ cm}^{-2} \cdot \text{s}^{-1}$. In a high luminosity (HL) mode, the peak luminosity reaches $2 \cdot 10^{32} \text{ cm}^{-2} \cdot \text{s}^{-1}$ at the same target density. The relative momentum spread in this regime is expected to be about 10^{-4} . The HR and HL modes are established to meet the challenging requirements of the PANDA experimental program.

The main experimental subject matters of the PANDA program were widely presented, discussed and commonly approved by the international physical community [2–5]. The PANDA experiment plans to exploit an extraordinary physics potential of the projected high quality \bar{p} beams with unprecedented momentum resolution. Precise measurements of all states below and above the open charm threshold is of great importance for the quantum chromodynamics (QCD). All charmonium states can be formed directly in $\bar{p}p$ annihilation in the invariant mass range $2.25 < M(\bar{p}p) < 5.46 \text{ GeV}$. At full luminosity, PANDA will be able to collect several thousand $\bar{c}c$ states per day. By means of beam momentum scans, it will be possible to measure masses with accuracies of the order of 100 keV and widths to 10%, or better. The latter is crucially important for theoretical analyses. The search for pure gluonic excitations and exotic hadron states is another interesting topic. This is one of the main challenges of the modern hadron physics. A full description of future PANDA experimental activities can be found in Ref. [5].

The PANDA experiment is designed to achieve the 4π solid angle coverage, high resolution for tracking, good particle identification, high precision calorimetry. A high rate capability is planned with a versatile readout and a very good event selection. A detailed description of the PANDA detector can be found in Ref. [6]. The \bar{p} beam interacts with a cluster or pellet hydrogen target, or with a deuterium or heavy nucleus target. The detector is composed of two magnetic spectrometers: the target spectrometer (TS), based on a superconducting solenoid magnet and the forward spectrometer (FS) based on a dipole magnet. The TS is designed to provide the 4π solid angle coverage around the interaction point, while the FS is used to cover small polar angles in the forward region. The PANDA spectrometer comprises a variety of sub-detectors dedicated to measure tracks of produced particles, their energy deposit, Cherenkov light and timing. The most important characteristics of the PANDA spectrometer are presented in Ref. [1]. Time information is foreseen in several PANDA sub-detectors (*e. g.*, barrel detector of internally reflected Cherenkov light – DIRC or forward ring imaging Cherenkov – FRICH). The high time resolution at the picosecond level will be provided for the PANDA experiment with two dedicated time-of-flight (ToF) detectors: the barrel ToF in the TS and the forward ToF (FToF) wall in the FS. A side view of the PANDA spectrometer is shown in Fig. 1 [1].

The FToF wall was proposed and designed by the PNPI group. The detector consists of scintillation plates with the vertical and horizontal dimensions of 140 and 10 cm, respectively, with the plates thickness of 2.5 cm. So the FToF wall has a large sensitive area: 560 cm (width) by 140 cm (height). Every plate is controlled by two end-cap fast photomultipliers (PMT). One important function of the FToF wall is to measure the time of flight of forward charge particles emitted within the FS acceptance under laboratory angles below 5 and 10° in the vertical and horizontal directions, respectively. This detector is assumed to be positioned at 7.5 m downstream of the PANDA target behind the FS dipole and PANDA FRICH detector (see Fig. 1). In the off line analysis of the FToF wall data, the information on the particle momentum and track length provided by the dipole forward tracking (FT) system is used. With this information, the FToF

wall should identify the hadrons (pions, kaons and protons and their antiparticles) by the ToF criterion. As Monte Carlo analysis shows, a reliable proton/kaon and kaon/pion separation is possible at the momenta below 4.3 and 3 GeV, respectively, provided that the time resolution of the FToF detector is better than 100 ps [1]. Note that this low momentum range is typically below the FRICH thresholds where there is no guarantee for the hadron detection with a high efficiency. No dedicated start counter in the interaction point area is foreseen for the PANDA detector. Similar to the HADES experiment at GSI [7], the ToF information is assumed to be obtained by using the time correlations between the responses (time stamps) of two or more scintillation counters of the FToF wall. Besides, the combined information of the FToF wall and barrel ToF can be used in many cases. As mentioned above, no dedicated start counter is assumed in the PANDA spectrometer. On the other hand, the determination of the antiproton–target interaction time stamp (event start) t_0 is one of the crucial points for the data analysis. The time stamp of a particle detected with a FToF wall counter may be used for a rough on-line determination of t_0 [1].

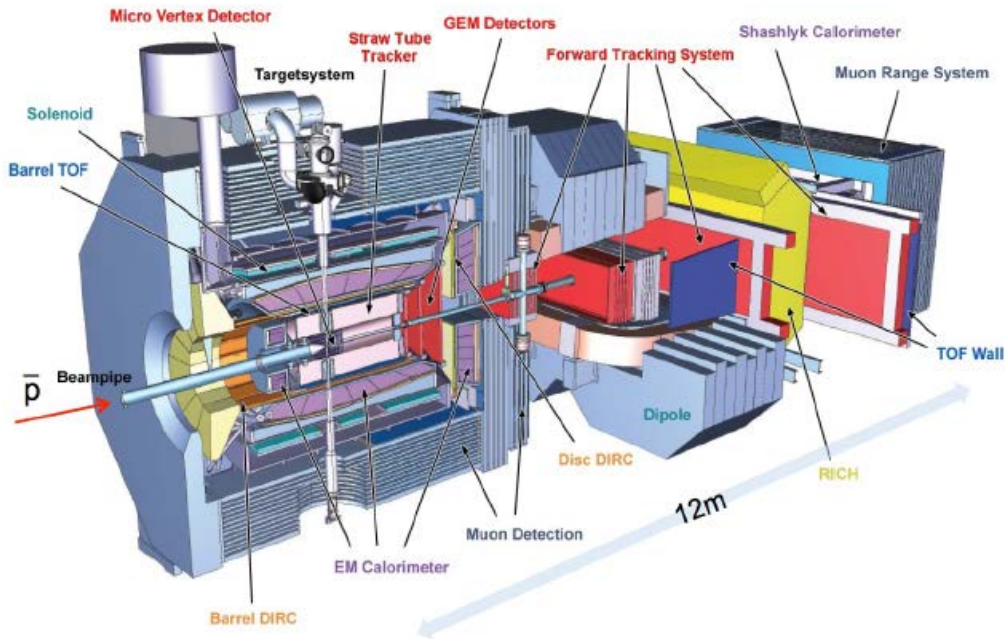


Fig. 1. Side view of the PANDA spectrometer with the target spectrometer (TS) on the *left side* and the forward spectrometer (FS) starting with the centre of the dipole magnet on the *right*. The \bar{p} beam enters from the *left*

Until 2019, studies were conducted on the time resolution of the FToF wall detector prototypes, using its commercially available components. Using the PNPI proton beam with an energy of 1 GeV, we tested slabs made from the Bicron-408 plastic scintillator with good timing characteristics, and coupled on both ends with fast photomultipliers PMT1 and PMT2. The dimensions of the scintillation slabs were $140 \times 5 \times 2.5$ (slab1) and $140 \times 10 \times 2.5$ (slab2) cm^3 . These slabs were planned to use in the central and side parts of the FToF wall, respectively [1]. We used the readout electronics – amplitude digital convertors (ADCs), and time digital convertors (TDCs) in the Versa Module Europa (VME) and computer automated measurement control (CAMAC) standards. After applying (off line) the amplitude and hit position corrections the best time resolution σ of 60–70 ps was obtained for the slab1 and slab2 coupled on both ends with the Hamamatsu PMTs R4998 and R2083, respectively [8]. Here σ is the weighted mean of both end PMTs: $1/\sigma^2 = 1/\sigma_{\text{PMT1}}^2 + 1/\sigma_{\text{PMT2}}^2$. It is important that the variation of σ with the hit position on the slab was found to be small.

Here we report about optimization of the FToF wall detector made after 2018. New design of the detector was accepted. For study of the time characteristics of the detector, a stand based on a picosecond laser was made. A prototype module was created to control these characteristics using a beam of laser photons in the course of a real experiment.

2. New design of the forward time-of-flight wall detector

The modified FToF wall detector, shown in Fig. 2, consists only of the scintillation slabs with a width of 10 cm (slab2, see above). Such a modification does not violate the basic requirements for the detector during its development [8]. The necessary experimental studies and Monte Carlo simulations were mainly carried out for the slabs with a width of 10 cm. The number of the slabs in the new design is equal to 56. Two slabs in the centre of the wall are cut to allow the beam vacuum tube to pass through.

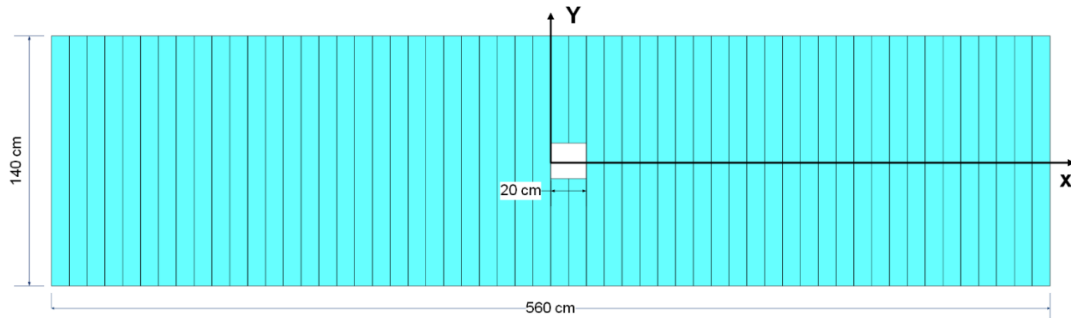


Fig. 2. New design of the FToF wall

3. Laser stand

The laser test room is shown in Fig. 3.



Fig. 3. Laser test room overview

In Figure 4, the $140 \times 10 \times 2.5$ cm slab with light guides and PMTs attached from both sides is shown.

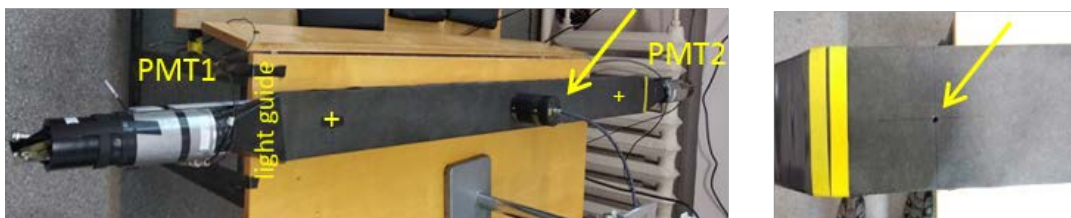


Fig. 4. The scintillation slab overview (*left panel*). Three 5 mm diameter holes in the wrapping materials like to that shown in the *right panel* of the figure were made along the slab (y). One in the centre of the slab and one (+) at a distance of 10 cm from each side. A laser head indicated by the yellow arrow is installed in the centre of the slab ($y = 70$ cm)

In Figures 5 and 6 the location of electronic equipment and the electronic flowchart in detector testing are shown, respectively.

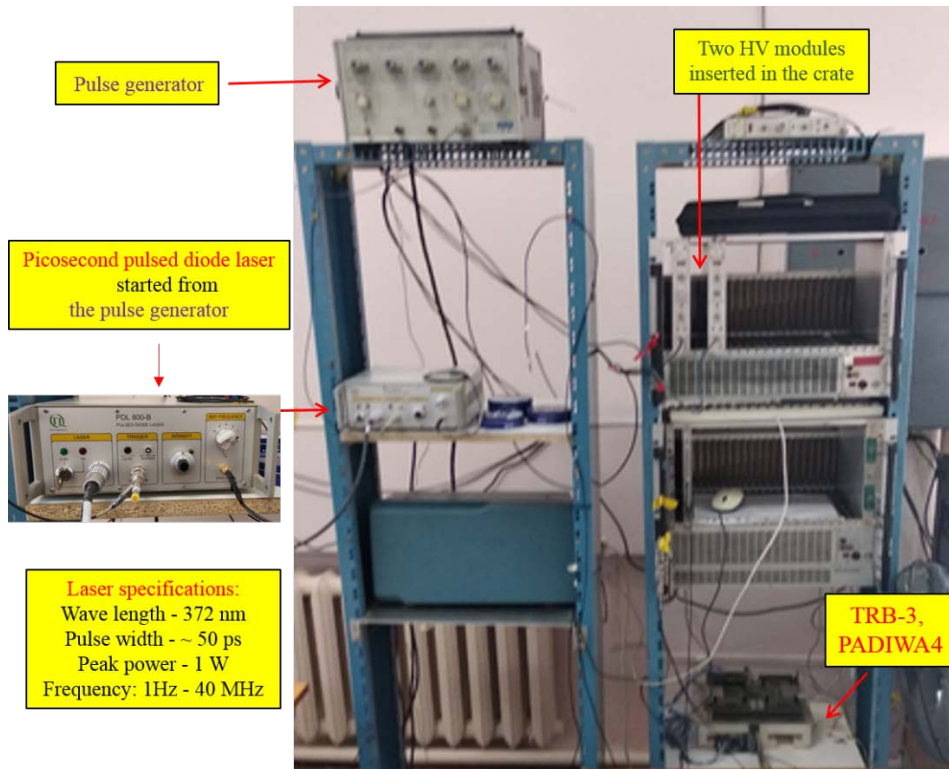


Fig. 5. Location of electronic equipment used in detector testing

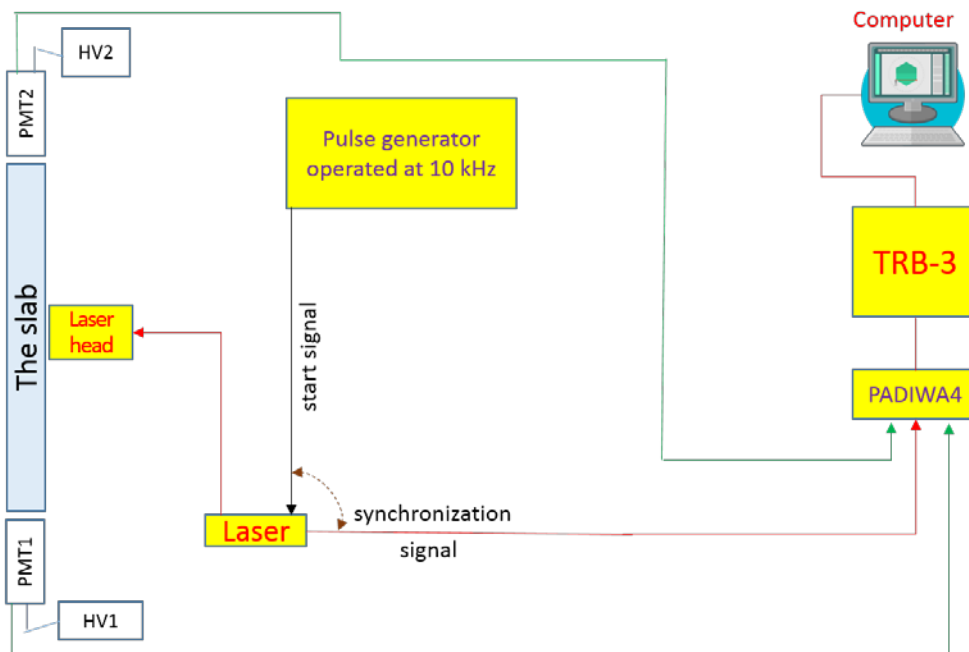


Fig. 6. Flowchart of the testing electronics. HV1 and HV2 are high-voltage modules for powering the active dividers of photomultipliers PMT1 and PMT2

The stand is based on a picosecond ultraviolet diode laser with the laser head LDH-P-C-375B (see Fig. 4, *left panel*, indicated by the yellow arrow, and see Fig. 6) and picoquant driver pulsed diode laser (PDL) 800-B (see Fig. 5). The main characteristics of the laser are given in Fig. 5. The beam of laser photons on the surface of the scintillation plate has an ellipsoidal shape with a maximum and minimum size of 3 and 2 mm. The absolute contribution to the time resolution (σ) from the finite transverse dimensions of the photon beam is approximately 10 ps.

The readout electronics is based on the field programmable gate array (FPGA) system with TRB-3 platform and PADIWA4 front-end interface modules (see Figs. 5 and 6) [8–11]. The TRB-3 platform is multipurpose trigger and readout board and contains 264 individual high timing resolution (8 ps) TDC channels for low voltage differential signal (LVDS) signals. The PADIWA4 module – a 16 channel discriminator – produces LVDS signals both by the front and trailing edge of a PMT pulse provided the height of the PMT pulse exceeds a fixed PADIWA threshold. The LVDS signals are sent to a TRB which provides a time-over-threshold (TOT) information. The overall time resolution of the PADIWA3 and TRB-3 based electronics was estimated in Ref. [8]. This resolution (σ) was about 20 ps.

4. The choice of photomultipliers for the forward time-of-flight wall detector (2019)

The results of investigating the time characteristics of the BC-408 scintillation bar at the laser stand are shown in Figs. 7 and 8. These data were obtained using various types of the fast Hamamatsu photomultipliers PMT1 and PMT2. The weighted mean time resolution (see Fig. 8) turned out to be significantly better when R13435 photomultipliers were used ($\sigma \approx 60$ ps).

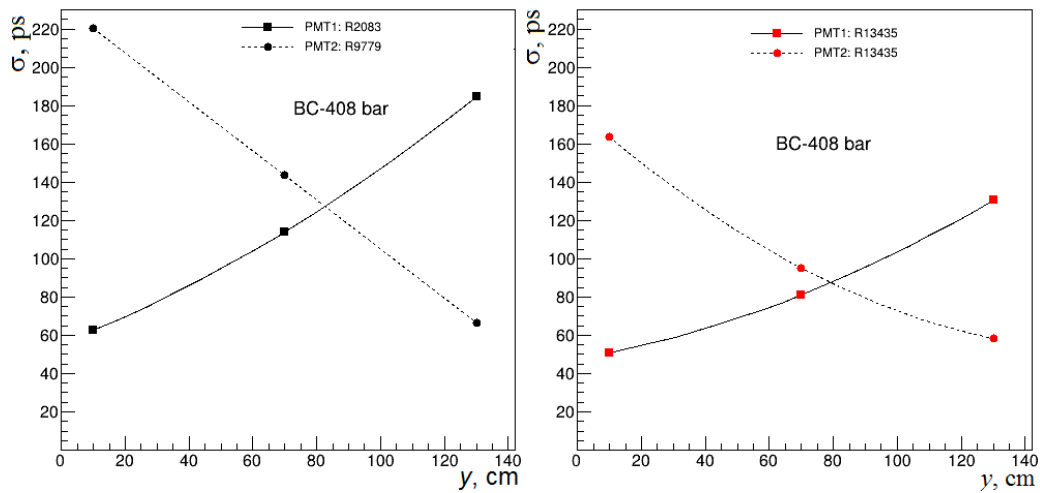


Fig. 7. The time resolution (σ) of a scintillation counter prototype with various PMTs versus the position (y) of the laser head along the BC-408 slab. *Left panel* – PMT1: R2083, PMT2: R9779. *Right panel* – PMT1 and PMT2: R13435. The supply voltage of the photomultipliers R13435 was the same and amounted to $V_{\text{PMT}} = 1.6$ kV

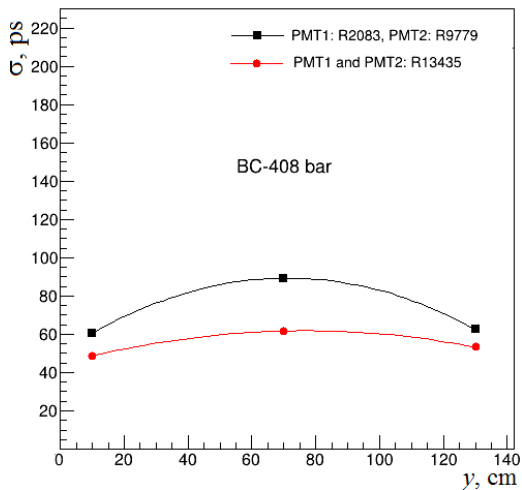


Fig. 8. The weighted mean resolution (σ) of a scintillation counter prototype with various PMTs versus the position (y) of the laser head along the BC-408 slab. $1/\sigma^2 = 1/\sigma_{\text{PMT1}}^2 + 1/\sigma_{\text{PMT2}}^2$. *Black squares* – PMT1: R2083, PMT2: R9779. *Red circles* – PMT1: R13435, PMT2: R13435. The supply voltage of the photomultipliers R13435 was the same and amounted to $V_{\text{PMT}} = 1.6$ kV

5. The choice of the scintillation material for the forward time-of-flight wall detector (2020)

The results of investigations of the time characteristics of the BC-408 and EJ-200 scintillation bars at the laser stand are shown in Figs. 9 and 10. These data were obtained using the same type of the fast Hamamatsu photomultipliers PMT1: R13435 and PMT2: R13435. The weighted mean time resolution (see Fig. 9, *right panel*) turned out to be significantly better when using the EJ-200 scintillation bar ($\sigma \approx 45$ ps). The time resolution $\sigma(t_0)$ (see Fig. 10) in this case is also significantly better ($\sigma(t_0) < 55$ ps).

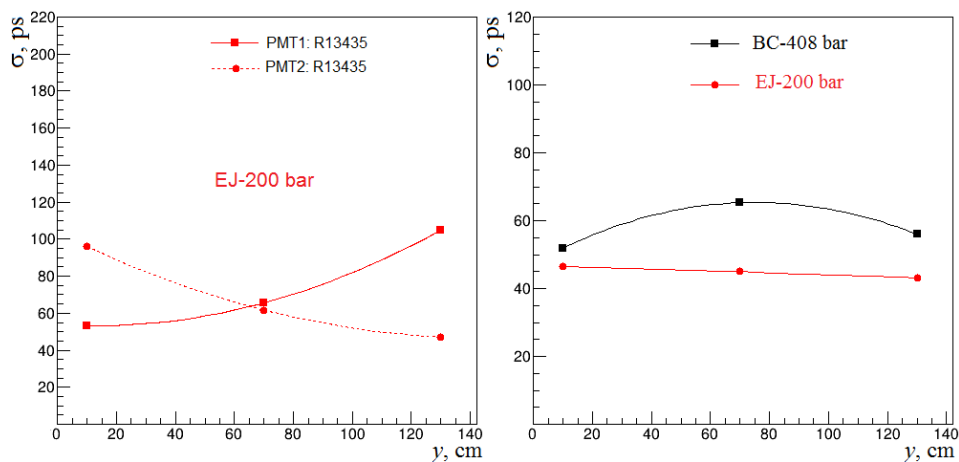


Fig. 9. The time resolution (σ) of a scintillation counter prototype with the same type of photomultipliers PMT1 and PMT2, R13435, versus the position (y) of the laser head along the EJ-200 bar. *Left panel* – the supply voltage of the PMTs was approximately the same and amounted to $V_{\text{PMT}} \approx 1.5$ kV. *Right panel* – the weighted mean time resolution (σ) with the same PMTs versus the position (y) of the laser head along the BC-408 bar (*black squares*) (see Fig. 8) and the EJ-200 bar (*red circles*)

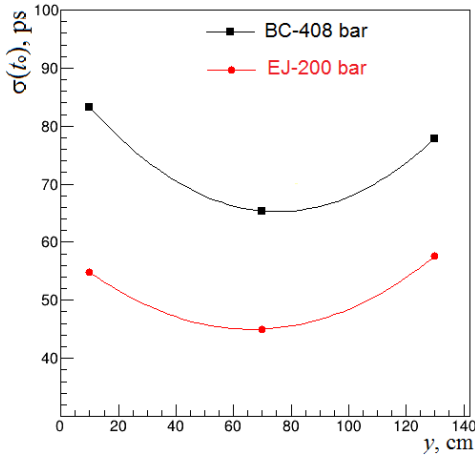


Fig. 10. The time resolution $\sigma(t_0)$, where $t_0 = (t_{\text{PMT1}} + t_{\text{PMT2}})/2$, at the same type of photomultipliers PMT1 and PMT2, R13435, versus the position (y) of the laser head along the BC-408 bar (*black squares*) and the EJ-200 bar (*red circles*)

6. The LEDIS laser for controlling the time characteristics of the forward time-of-flight wall detector (2021)

A powerful light source based on the fast ultrabright blue diode GN-3014BC (Fig. 11) was designed by the HEPD (PNPI) Electronics Department. The technical specification of the diode is given in the Table.



Fig. 11. The fast light-emitting diode GNL-3014BC

Table

Technical specification of the fast light-emitting diode GNL-3014BC

Parameter	Value
Width (FWHM) light pulses, ns	0.6
Number of photons per pulse	10^9
Emitted colour	Blue
Peak wavelength, nm	470
Maximum luminous intensity I_{max} , mCd	1 500
At current I , mA	20
Visible solid angle, deg	25
Lens colour	Colourless
Lens size, mm	3

The width of the light pulse generated by the diode and its light yield depend very little on the ambient temperature and persist for a long time. These important properties of the diode open up wide possibilities for creating the calibration and control system of physical experiments based on the scintillation technique. Figure 12 shows a prototype of the control system light-emitting diode investigation system (LEDIS) created on the basis of one GN-3014BC diode and providing two light beams at the output.

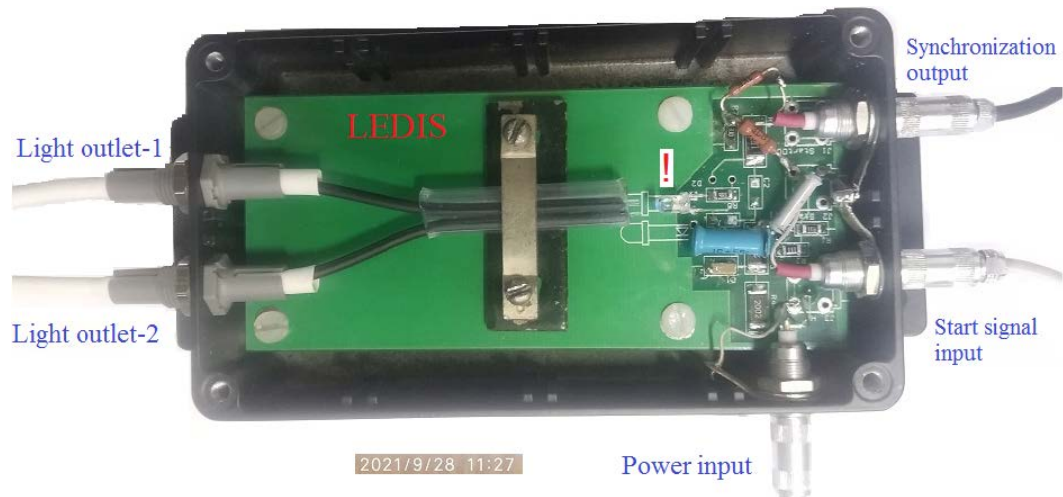


Fig. 12. Prototype of the time control system LEDIS of the FToF wall detector. Red symbol (!) indicates the position of the diode on the plateau of the LEDIS

The results of investigations of the time characteristics of the EJ-200 scintillation bar using the LEDIS laser photons are shown in Fig. 13. These data were obtained using the same type of the fast Hamamatsu photomultipliers PMT1: R13435 and PMT2: R13435.

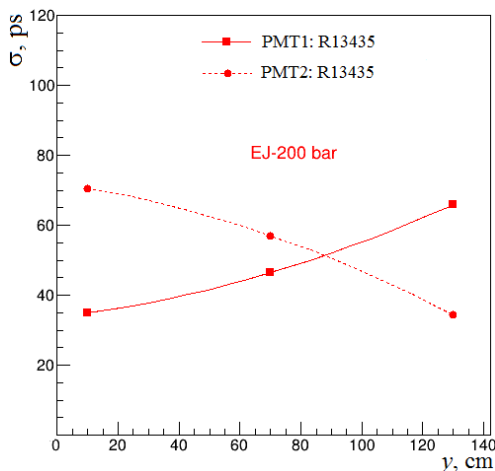


Fig. 13. The time resolution σ for the same type of photomultipliers PMT1 and PMT2, R13435, versus the position (y) of the LEDIS laser head along the EJ-200 bar. The supply voltage of the photomultipliers PMT1 and PMT2 was the same and amounted to $V_{\text{PMT}} = 1.23 \text{ kV}$

The observation of narrow time distributions ($\sigma \approx 40\text{--}70 \text{ ps}$) when the scintillation bar is irradiated by photons of the LEDIS laser (see Fig. 13) makes it possible to use the latter in an experiment to control the state of the FToF wall detector before using the beam particles from the accelerator.

7. Conclusion

We report about optimization (made after 2018) of the FToF wall project [8] for the PANDA experiment. New design of the detector was accepted (all scintillation bars in the wall now have the same dimensions $140 \times 10 \times 2.5 \text{ cm}^3$). A stand based on a picosecond laser was made. The laser tests have shown that the bar made of the EJ-200 scintillator and viewed from the side of its ends with the Hamamatsu R13435 photomultipliers gives a significantly better time resolution. A laser prototype (LEDIS) based on the fast ultrabright blue diode GN-3014BC was created to control the time parameters of the FToF wall detector in the experiment.

The list of participants of the present work:

- Laboratory of Few Body Systems, HEPD: S.L. Belostotski, G.M. Amalsky, G.V. Fedotov, V.V. Fedulov, A.A. Izotov, S.I. Manaenkov, O.V. Miklukho, V.A. Stepanov, D.O. Veretennikov, A.A. Zhdanov;
- HEPD Electronics Department: S.S. Volkov, S.V. Bondarev, N.B. Isaev, N.V. Gruzinsky;
- Other HEPD laboratories: V.A. Andreev, N.G. Kozlenko, V.I. Murzin, D.V. Novinsky, A.V. Shvedchikov.

References

1. S.L. Belostotski, A.A. Izotov, S.I. Manaenkov *et al.*, PNPI. High Energy Physics Division. Main Scientific Activities 2013–2018, 370–374 (2019).
2. M. Kotulla, B. Krusche, F. Zehr *et al.*, Strong Interaction Studies with Antiprotons: Letter of Intent for PANDA (2004).
3. N. Brambilla, U.-G. Meissner, arXiv:1512.03299 (2015).
4. B. Singh, W. Erni, B. Krusche *et al.*, Nucl. Phys. A **954**, 323 (2016).
5. M.F.M. Lutz, B. Pire, O. Scholten *et al.*, Physics Performance Rep. for PANDA: Strong Interaction Studies with Antiprotons (2009).
6. M. Kotulla, B. Krusche, F. Zehr *et al.*, Technical Progress Rep. for PANDA: Strong Interaction Studies with Antiprotons (2005).
7. G. Agakishiev, C. Agodi, H. Alvarez-Pol *et al.*, Eur. Phys. J. A **41**, 243 (2009).
8. PANDA Collab., S. Belostotski *et al.*, Technical Design Report for PANDA: Forward Time of Flight Detector (FToF Wall) (2018), https://panda.gsi.de/system/files/user_uploads/admin/RE-TDR-2016-004.pdf
9. A. Neiser, J. Adamczewski-Musch, M. Hoek *et al.*, JINST **8**, C12043 (2013).
10. I. Froehlich, C. Schrader, H. Strobele *et al.*, in *Proc. of 10th Conf., ICATPP 2007*, 973 (2008).
11. F. Gonnella, V. Kozuharov, M. Raggi, Nucl. Instrum. Meth. A **791**, 16 (2015).

PNPI IN THE R³B PROJECT AT FAIR

PNPI participants of R³B:

G.D. Alkhazov, V.A. Andreev, A.Yu. Arutyunova, A.V. Dobrovolsky, V.L. Golovtsov, D.S. Ilyin, A.G. Inglessi, V.V. Ivanov, A.V. Khanzadeev, G.A. Korolev, A.G. Krivshich, E.M. Maev, D.A. Maysuzenko, A.V. Nadtochiy, E.V. Roschin, V.V. Sarantsev, L.N. Uvarov, S.S. Volkov, V.I. Yatsura, A.A. Zhdanov

1. Introduction

A versatile reaction set-up R³B with high efficiency, acceptance, and resolution for kinematically complete measurements of reactions with high-energy radioactive beams [1] is under construction at GSI, Darmstadt. R³B is a part of the NuSTAR project. The R³B set-up will be located at the focal plane of the high-energy branch of the Super-FRS. The experimental configuration is based on the concept similar to the existing LAND reaction set-up at GSI introducing substantial improvements with respect to resolution and an extended detection scheme, which comprises additional detection of light recoil particles and a high-resolution fragment spectrometer. The set-up is adapted to the highest beam energies (corresponding to 20 Tm magnetic rigidity) provided by the Super-FRS capitalizing on the highest possible transmission of secondary beams. The experimental set-up is suitable for a wide variety of scattering experiments, *i. e.*, such as heavy-ion induced electromagnetic excitation, knockout and breakup reactions, or light-ion elastic, inelastic, and quasifree scattering in inverse kinematics, thus enabling a broad physics program with rare-isotope beams to be performed. The R³B set-up will cover experimental reaction studies with exotic nuclei far off stability, thus enabling a broad physics programme with rare-isotope beams with emphasis on nuclear structure and dynamics. Astrophysical aspects and technical applications are also concerned. The R³B programme will focus on the most exotic short-lived nuclei, which cannot be stored and cooled efficiently, and on reactions with large-momentum transfers allowing the use of thick targets. In order to cover such a large physics programme, several different detection subsystems (Fig. 1) as well as sophisticated data acquisition system and data analysis software are planned.

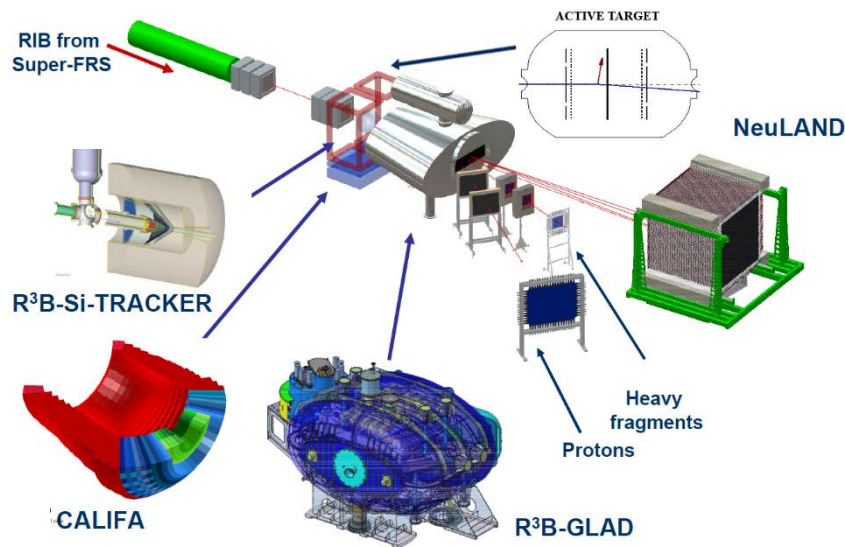


Fig. 1. The R³B detector set-up with its main components: the silicon tracker R³B-Si-TRACKER, the calorimeter CALIFA, the active target detector ACTAF, the dipole magnet R³B-GLAD, the protons and heavy fragments detectors, the neutron time-of-flight spectrometer NeuLAND

The incoming secondary beams are tracked and identified on an event-by-event basis. Measurements of the magnetic rigidity $B\rho$ (position measurement at the dispersive focus in the Super-FRS), time-of-flight (ToF), and energy loss ΔE provide unique isotope identification and momentum determination. After the secondary

target, the kinematically forward focused projectile residues are again identified and momentum analysed. The large gap of the dipole provides a free cone of ± 80 mrad for the neutrons, which are detected in forward direction by a large area neutron detector (NeuLAND). The target is surrounded by a γ -ray spectrometer. For elastic, inelastic and quasifree scattering experiments or charge-exchange reactions, liquid hydrogen or frozen hydrogen targets are considered. Recoiling protons and neutrons are detected by a Si-strip array and plastic scintillators, respectively. For measurements at low momentum transfers, the use of an active target is foreseen. For most of the experiments envisaged, a high-efficiency total-absorption spectrometer (cooled CsI or NaI) is the optimum solution, which is also used to measure the energy of recoiling protons. For specific experiments requiring ultimate energy resolution for γ -detection, the germanium spectrometer AGATA might be used alternatively.

High beam energies, in the range of a few hundred MeV/nucleon, allow a quantitative description of the reaction mechanisms, while also having experimental merits, such as the possibility of using relatively thick targets (in the order of 1 g/cm^2). Moreover, due to the kinematical forward focusing full-acceptance measurements are feasible with moderately sized detectors. This makes it possible to gain nuclear-structure information from reaction studies even with very low beam intensities, as low as about 1 ion/s . R³B will cover experimental reaction studies with exotic nuclei far off stability, with emphasis on nuclear structure and dynamics.

PNPI physicists participate in the R³B project in construction of the high voltage (HV) system for the detector new large area neutron detector (NeuLAND), the proton detector PAS for tracking protons and other light charged particles behind the R³B dipole magnet, and the active target (targets) ACTAF for detection of low-energy recoil particles, as well as in the physics program when the R³B set-up starts to collect data.

NeuLAND is the next-generation high-energy neutron detector (200 to 1 000 MeV) designed for R³B, which meets all requirements defined by the ambitious physics program proposed for the R³B facility. NeuLAND features a high detection efficiency, a high resolution, and a large multineutron-hit resolving power. This is achieved by a highly granular design of plastic scintillators, avoiding insensitive converter material. The detector will consist of 3 000 individual sub-modules with a size of $5 \times 5 \times 250 \text{ cm}^3$, arranged in 30 double planes with 100 submodules providing an active face size of $250 \times 250 \text{ cm}^2$ and a total depth of 3 m. NeuLAND can be divided into two detectors for special applications and will be placed at different distances from the target, in order to meet specific experimental demands. The main design goals of NeuLAND comprise a one-neutron detection efficiency above 95% in a wide energy range and a full acceptance corresponding to an angular coverage of 80 mrad. The desired resolutions for momenta and thus the excitation energies lead to the required spatial resolutions of $\sim 1.5 \text{ cm}$ and to the time resolution of $\sim 150 \text{ ps}$ for the standard distance between the detector and the target of 15.5 m. When placed at a distance of 35 m, an excitation-energy resolution of better than 20 keV will be reached for an excitation energy of 100 keV above threshold for a beam energy of $600 \text{ A} \cdot \text{MeV}$. Apart from the excellent energy resolution, NeuLAND has an enhanced multineutron recognition capability with an efficiency of up to 60% for reconstructed four-neutron events.

2. High voltage system for NeuLAND

In 2012, PNPI physicists presented to GSI a proposal for designing and manufacturing a HV distribution system (HVDS) for 6 000 photomultipliers (PMT) of the spectrometer NeuLAND.

The principle of operation of the proposed HVDS is individual down-regulation of the output voltage of a primary HV power supply for each PMT tube, Fig. 2. The advantages of this proposal are the following.

- The HV value from a primary power supply (PS) unit is individually down-regulated and then distributed to each PMT.
- The HV value is generated locally at the PMT base, the control levels and voltage and current monitoring values being delivered to/from the PMT *via* an analog interface.
- The HV value is generated the same way as above, but digital-to-amplitude convertor (DAC) and amplitude-to-digital convertor (ADC) are located on each PMT base as well.

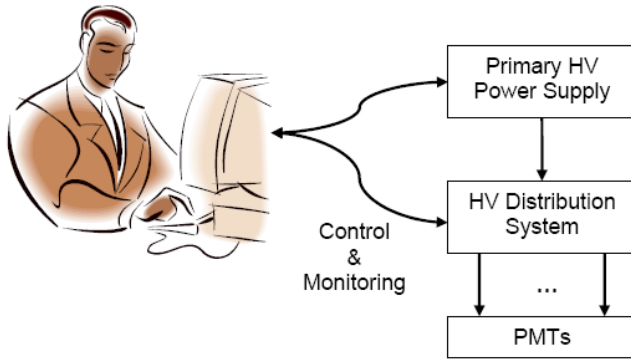


Fig. 2. High voltage distribution system for NeuLAND

The host computer controls HV settings of the primary PS and each out of 6 000 down-regulators of the HVDS. It also monitors the actual HV applied to each PMT and the current drawn by it. All control and monitoring operations are executed over Ethernet. Each PMT consumes 0.3 mA of current, a primary HV PS rated at 1 A can feed up to 3 000 PMTs, or one half of the NeuLAND detector. The proposed HVDS details are shown in Fig. 3.

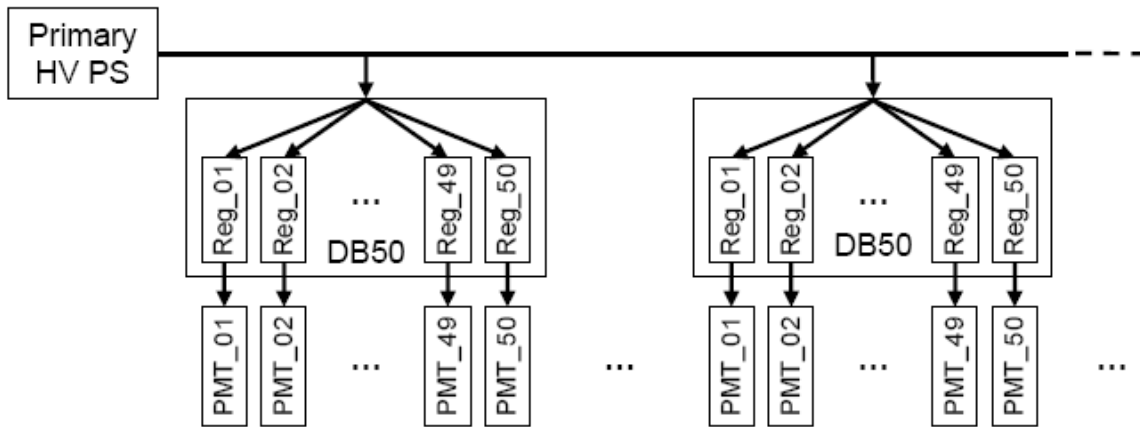


Fig. 3. High voltage distribution from a primary high voltage power supply

Each PMT is powered from an output of a separate regulator Reg_XX, where XX is a channel number spanning from 01 to 50. 50 regulators reside at a 50-channel distributor board (DB50). Only four DB50s are needed for a double plane of scintillator bars (containing 100 scintillator bars), with two DB50s sitting at each top corner of the double-plane frame. A single primary HV PS rated at 1 A can feed up to 15 double planes or up to 60 DB50s.

A host computer uses Ethernet to connect to the HV control board (HVCB) (Fig. 4). The HVCB features four outputs with RJ-45s for connecting control & monitoring buses (CMB). Each CMB is capable to control and monitor up to 16 DB50s. The high voltage control and monitoring (HVCM) serves up to 64 DB50s, which translates to 3 200 PMTs. The CMB is implemented as a Cat 5 network cable with four pairs of wires. Two pairs are used for downloading HV settings and two pairs – for receiving voltage and current monitoring data. Each DB50 has a pair of RJ-45s connected to the same bus. To add a new DB50 to the already existing bus, the user just needs to add a jumper cable from the last DB50 in the chain to a new one. Plugging in the CMB terminator in the last DB50 is optional and depends on the overall CMB length. The DB50 has a switch that sets its address (from 00 to 15 in decimal or from 0×0 to $0 \times F$ in hex). Of course, all DB50s on the same CMB should carry exclusive addresses. The HVCB carries an field programmable gate array (FPGA) that keeps the control and monitoring data for each HV regulator. There is also a sequencer that continuously updates control values in regulators and scans them for monitoring data.

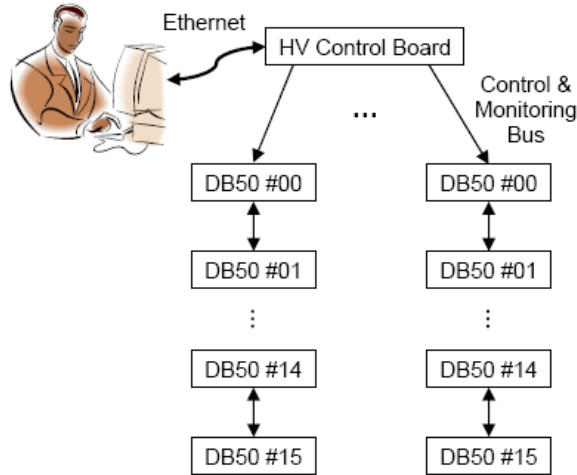


Fig. 4. High voltage distribution system control and monitoring

The output voltage is regulated from 0 to 1 600 V by a 10-bit DAC. The voltage is monitored by a 10-bit ADC for the same range. The current is monitored by a 10-bit ADC with a 1 nA resolution. The maximum output current to the load is 0.5 μ A. The system comes with a software package to perform control, monitoring and calibration tasks.

The production of the HV system was started in 2014. By the end of 2017, the HV system for 3 000 channels was fabricated. The production of the HV system with 6 000 channels was completed in 2021.

3. Proton arm spectrometer for the R³B set-up at FAIR

The tracking detectors for R³B are designed to be used in a wide variety of experiments with the R³B set-up, where beams of unstable nuclei up to 1 GeV/nucleon formed by the Super-FRS at FAIR impinge on a secondary target, the reaction products being magnetically analysed with the superconducting magnet GLAD. For multiparticle final states, the invariant mass is obtained from the momenta and relative angles of the outgoing particles.

Protons emitted in flight from excited fragments are bent in the dipole magnet GLAD and tracked using the dedicated proton arm spectrometer (PAS) that is placed inside of a large vacuum chamber.

A thick plastic scintillator wall, which is placed behind the PAS after the vacuum exit window of the GLAD magnet, will be used for timing, triggering and particle identification. It consists of vertically placed paddles read out by photomultiplier tubes covering the size of 2.7×1.2 m².

The PAS project was proposed by PNPI physicists and it received approvals of both the German (the expert council of the FAIR megaproject) and Russian parties (the expert council of the State Atomic Energy Corporation “Rosatom”). The proposed project [2] is basically different from that considered previously by the R³B Collaboration. The complex of following fundamental problems should be solved in the course of realization of the project.

- The tracking detector that previously registered X and Y coordinates of protons in one plane, *i. e.* in other words, it represented a hodoscope, now it will be a proton spectrometer (telescope), which registers the coordinates of the proton tracks at several points along the beam, providing a high angular resolution (better than 10 mrad).
- The detector aperture is increased from 500×500 mm² to $2\,300 \times 1\,100$ mm², the number of information recording channels is increased up to 2 000.
- The PAS will be installed inside the vacuum chamber behind the GLAD dipole magnet. To ensure reliable operation of the PAS under vacuum conditions and simultaneously achieve the required operating characteristics in a confined space in the vacuum chamber, the proton arm spectrometer will be based on straw-tube technology.
- The spatial resolution of a single straw tube should be better than 200 μ m. Two-track resolution of the PAS of time-correlated pair events should be less than 10 mm.

are located near the end of the track. Aluminum tubes are used in order to minimize the total leakage of the gas into the vacuum volume and to constrain the total cost of the array.

To facilitate access to PAS, the PAS detector is placed on a movable platform inside the large vacuum chamber behind GLAD. The electronic front-end readout cards, the gas system, the high- and low-voltage PS and other services of PAS are arranged at the detector and the mechanical frame structures.

Each STW of the PAS will consist of three layers of straw tubes filled with a gas mixture at the overpressure of about 1 bar. The tubes are glued together, each layer being shifted by one tube radius with respect to the previous layer. Then, for an orthogonal proton track, a lower detection efficiency close to the tube wall is always combined with high efficiency in the centre of the straw in the following (staggered) layer. Also, the track's left/right ambiguity from the wire can be disentangled in the next layer.

The straw tubes under the overpressure of the gas mixture (1–2 atm) in vacuum can be considered as this basic technology. This will ensure the required cylindrical shape of each tube and allows to build a self-sustaining detector design that does not require special strong supporting outer frames. On the other hand, the overpressure results in serious problems that should be solved during implementation of this project. The problems include:

- A possible instability of operation of each of the straw tubes (caused by a change in their length and diameter, and as a consequence a change in the tension of the anode wires) can result in structural deformations of a group of several hundreds of straw tubes combined together that form the STW-X1 detector station and, as a consequence, a serious deterioration of the detector operating characteristics;
- Different diffusion rate of the working gas components through the tube Mylar (Kapton) walls.

A 25 μm -diameter gold-plated tungsten anode wire is stretched by a weight of 70 g and placed in the copper pins (0.1 mm holes). At such a wire tension, the calculated gravitational sag for Y1 and Y2 should be smaller than 30 μm , which is below the projected spatial resolution of 200 μm .

The granularity (tube diameter) of 10 mm and the straws precise alignment allows a continuous tracking with a few hits per track, which is important in order to resolve complex track patterns. The position accuracy of the mounted STW relative to the precision alignment marks in the end angles of the PAS mechanical frame should be better than 100 μm . Due to the close packaging of the glued straws in a module with a precise tube-to-tube distance, the deviations in the position of a single straw is less than 100 μm . The overall mechanical precision in the X – Y plane will be below 200 μm .

Straw tubes are proportional counters that are used as drift chambers with the corresponding structure of the electric field inside. The PAS straws will be operated in the proportional mode. The drift time information can be converted to distance R from the particle track position to the anode wire by using the so-called X – T relation obtained from calibration experiments. The ideal gas mixture will present a linear X – T relation over the entire distance R in the straw. The optimal choice of the working gas mixture is still to be determined.

The straw tubes will work in intense radiation fields of complex composition (protons and heavy ions). The detector will detect not only protons with energies $E_p = 500$ – $1\,000$ MeV, but also the background of light and heavy ions. Dedicated studies of radiation resistance of the detector will allow to optimize the detector radiation resistance at the design and examination stage and will ensure the maximum lifetime of the detector in experiments.

The four STWs of the PAS consist of about 2 000 channels. The front-end electronics is placed in vacuum close to the straw-tube detectors for optimum performance in terms of noise. The electronics consists of two types of signal processing boards – DA16 and DD32 – and of a communication board DC2K for threshold control on the individual channel bases.

For the read-out of the STW signals, a TDC with $\sigma_t \leq 500$ ps time resolution will be used. The TDC will accept LVDS signals directly from the discriminator. The TDC modules must be fully compatible with the R³B DAQ standards. The PAS TDCs will run an internal clock for time measurement, which will be synchronized with a distributed clock signal (*e. g.* 100 MHz) from the R³B DAQ.

The PAS electronics will normally run with an external trigger provided by the R³B DAQ. However, for testing and commissioning, the PAS electronics should also be able to run in stand-alone mode. For this, an additional input for a reference signal (start counter) should also be foreseen.

The PAS electronics provides: the preamp/shaper peaking time – 10 ns; the digitizing rate – up to 1 000 MHz; the trigger rate, max – 25 kHz; the trigger latency, max – 100 μs ; the data flow, max – 750 kB/s.

The work on the design and fabrication of the PAS spectrometer was started at PNPI in 2015. The present status of the PAS construction is given in Ref. [3]. Also, the HV system for the PAS spectrometer is described in Ref. [4].

4. Active target ACTAF

The planned active target detector ACTAF (or ACTAF2 – active target for FAIR, version 2) is intended to identify the recoil particles in direct reaction studies with radioactive beams at small momentum transfers. The design is based on the first generation of the active target set-up IKAR used in previous experiments at GSI but is extended with respect to a larger variety of reactions and heavier beams up to uranium. The active target detector ACTAF for light (target-like) particles is supposed to be a part of the R³B set-up. It will allow registration of the recoil particles in coincidence with the heavy fragments, neutrons and γ -rays [5]. This set-up gives thus a unique possibility to study elastic, inelastic, charge-exchange, *etc.* reactions at low momentum transfers, and it will extend the possibilities of R³B in studies of nuclear structure of exotic short-lived nuclei. The active target detector ACTAF is an axially symmetric (Fig. 6) ionization chamber (IC) with an azimuthally angular acceptance 2π and with close to 100% registration efficiency for recoil particles (protons, deuterons and α -particles) at the energy interval of interest.

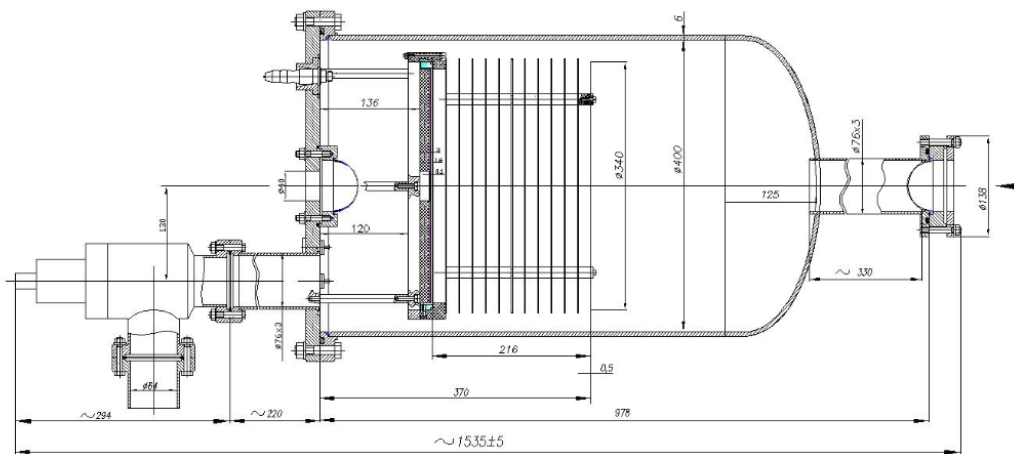


Fig. 6. A drawing of ACTAF2 (side view) with the inner structure of the electrodes of the ionization chamber

ACTAF is to be designed such that it fits inside the CALIFA γ detector. The maximum pressure in ACTAF is determined by the wall thickness, which is chosen to optimize the gamma efficiency for γ -rays detected in the CALIFA detector. The total energy of the recoil particle (T_R) is measured in the ionization chamber with the precision of $\sigma(T_R) = 20\text{--}30$ keV in the energy range from 0.3 to 20 MeV. The energy threshold is ~ 150 keV, which provides $\sim 100\%$ efficiency for the registration of recoil particles with $T_R > 300$ keV. The active target technique permits to detect the energy (T_R) of the recoil particles, the respective polar angles θ_R of the recoil and the Z-coordinates of the vertices along the chamber axis Z. The polar angles of the recoil particles (protons, deuterons or helium nuclei) can be measured with a precision (σ_θ) of a few mrad. The Z-coordinate of the point of interaction (along the beam axis) is measured with a precision (σ_z) better than 0.5 mm. It gives the possibility to select useful events inside the effective gas volume, and to eliminate background events due to interaction with the chamber walls on the level of $\sim 10^{-4}$. ACTAF provides the possibility to work with different gases (H_2 , D_2 , He, CH_4 , N_2 and Ar) at pressures from 0.1 to 10 bar. The construction of the ACTAF multisegmented anode plane gives the possibility to distinguish different types of recoil particles (p , d , t , ${}^3\text{He}$ and ${}^4\text{He}$) using the correlation between the energy deposit and the range of the recoil particles. The active target has a special multianode structure (Fig. 7) that provides the possibility to work with very heavy ionizing beams. The number of the segmented anodes is 70.

PNPI physicists fabricated a prototype of the active target ACTAF for studying inelastic ${}^4\text{He}$ -nucleus scattering in inverse kinematics. During 2012–2013 the prototype of the chamber ACTAF2 was constructed

and prepared for testing in GSI ion beams. In 2014–2018, three test experiments were performed at the GSI and MAMI (Mainz) accelerator facilities aiming to check the functionality of the detector ACTAF influence on the energy resolution of delta electrons emitted by heavy projectiles. The test experiment at GSI in 2014 (beam of ^{58}Ni ions) was the first implementation of an active target of this type having a beam of ions heavier than carbon. The experimental data obtained in these three test experiments with the ACTAF prototype proved the possibility of registration of different types of recoil particles with low energies (0.4 MeV) and the efficiency close to 100%, the energy resolution being 20–30 keV.



Fig. 7. The ACTAF2 segmented anode plane with the central Kapton part

The body of the ACTAF pressure vessel consists of a central cylinder, a forward convex wall, and a backward flange (see Fig. 6). The chamber walls are made of 6 mm aluminum alloy. The ACTAF pressure vessel is ~ 680 mm long (along the beam), the inner diameter is 400 mm, the total volume is about 80 l, and the total weight is about 100 kg. The operating pressure can be chosen up to 10 bar, pressure tests were performed at 12.5 bar. The backward flange carries the outlet Be window, HV connectors for the cathode and the grid (the voltage up to 50 and 10 kV, respectively), multipin connectors for the signal readout and a tube with flange for high pressure valve for pumping the chamber. In order to minimize the γ -abortion in the chamber walls, the cylinder part of the chamber is fabricated from aluminum alloy, the wall thickness being 6 mm. The backward flange is made of 20 mm stainless steel; its diameter is 480 mm. The forward convex part is also made of 6 mm aluminum alloy. The Be hemispheres of the windows are attached to stainless steel flanges by cold welding. They are attached to the IC body with Viton O-ring fittings. Other connectors and valves are attached with Viton O-rings too. The Be hemispheres of windows were used already at pressures up to 25 bar. Other components (HV connectors, multipin connectors) were used in our previous ionization chambers at pressures up to 50 bar. The inner structure of IC (electrodes) are mounted on the ACTAF2 backward flange. The chamber was tested at PNPI for achieving a vacuum down to 10^{-6} mbar and for a gas pressure up to 12.5 bar.

The readout electronics of the active target consists of a front-end part (charge-sensitive preamplifiers and shaping amplifiers), the flash analog-to-digital converters and a trigger/processing part. The front-end electronics is mounted directly on the detector and is optimized for low noise and low power consumption. The charge-sensitive preamplifiers and shaping amplifiers are designed at the PNPI. Both parts are combined in one unit in order to minimize pickup noise and cross-talk between the channels, often occurring due to the cables connecting two units. One electronic board consists of 16 individual channels. Each electronic channel was calibrated. The absolute accuracy of such calibration is better than 0.5% for all channels. Finally, we have now 192 channels of the front-end electronics. It is totally enough for the realization of the ACTAF project. Verification of combined operation of the detector ACTAF and front-end electronics was carried out at PNPI using specially arranged test station (gas, vacuum, HV systems and electronics). The acceptance test of the active targets consists of several measurements. The kind and sequence of them is based on the experience

with the IKAR active target used for several experiments at PNPI and GSI. The active target detector ACTAF (Fig. 8) has passed all tests and is considered as ready for operation within the R³B FAIR set-up.



Fig. 8. ACTAF in the test laboratory at PNPI

4. Concluding remarks

The experiment R³B at FAIR is devoted to the study of the nuclear structure of exotic nuclei using a universal experimental set-up with high efficiency, acceptance, and resolution for kinematically complete measurements of reactions with high-energy radioactive beams. PNPI physicists participate in construction of this set-up by fabricating the HV system for the NeuLAND detector, by designing and building the proton tracking detector PAS for measuring coordinates and angles of protons and light nuclei emitted in nuclear reactions, and the active target ACTAF2 for studying inelastic nucleus scattering on ⁴He and some other light nuclei. The experiment R³B will be a unique facility providing the capability for kinematically complete measurements of reactions with relativistic heavy-ion beams of short-lived nuclei up to about 1 A · GeV. The experimental results which will be obtained with the R³B set-up are expected to be very important for theory of the nuclear structure and nuclear reactions, and for solving open questions of modern astrophysics.

References

1. GSI. A Next Generation Experimental Setup for Studies of Reactions with Relativistic Radioactive Beams, <http://www.gsi.de/r3b>
2. Technical Report for the Design: Construction and Commissioning of the Tracking Detectors for R³B (2014), https://edms.cern.ch/ui/file/1865815/2/TDR_R3B_TrackingDetectors_public.pdf
3. G.D. Alkhazov, V.A. Andreev, V.L. Golovtsov *et al.*, Proton Arm Spectrometer (PAS) for the R³B SET-UP at FAIR. This Vol.
4. S.V. Bondarev, V.I. Golovtsov, N.V. Gruzinsly *et al.*, High Voltage Power Supply for the Proton Arm Spectrometer of the R3B Experiment at FAIR. This Vol.
5. ACTAF Technical Design Report (2017), https://edms.cern.ch/ui/file/1816116/1/TDR_R3B_ACTAF_public.pdf

CONCEPTUAL PROJECT OF THE PROTON BEAM LINES IN THE NUCLEAR MEDICINE COMPLEX OF THE “KURCHATOV INSTITUTE” – PNPI

D.A. Amerkanov, S.A. Artamonov, E.M. Ivanov, V.I. Maximov, V.A. Tonkikh

1. Introduction

The project of a nuclear medicine complex based on the isochronous cyclotron of negative hydrogen ions C-80 is being developed at the National Research Centre “Kurchatov Institute” – PNPI. The project provides for the design of a building, the creation of stations for the development of methods for obtaining new popular radionuclides and radiopharmaceuticals based on them. The commercial component is not excluded. The project also provides for the creation of a complex of proton therapy of the eyesight. For these purposes, the modernization of the beam extraction system of the cyclotron C-80 is planned: a project for the simultaneously two beams extraction systems is being developed. The one for the production of isotopes with an intensity up to 100 mA and an energy of 40–80 MeV and the other – for ophthalmology with an energy of 70 MeV and intensity up to 10 mA.

The initial conditions for both beams at the output window from the accelerator were obtained using the Orbita-1 program [1]. A blueprint of the project and beam transfer lines are shown in Fig. 1.

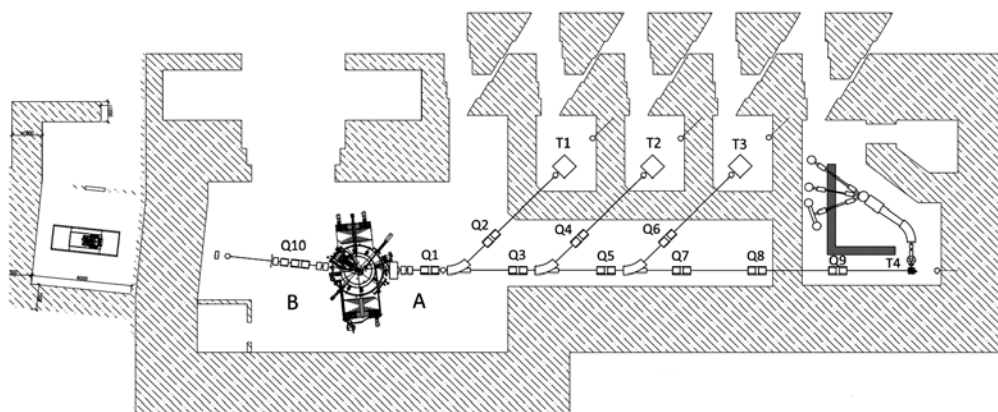


Fig. 1. Blueprint of the project and beam transfer lines: A – beam line for radioisotope part; Q1–Q9 – lens doublets; T1–T4 – target stations; B – beam line for the ocular oncology complex; Q10 – triplet lenses

2. Beam transport lines

2.1. Radio isotope complex

The isotope complex (direction A, Fig. 1) includes four target stations. Target stations will be equipped with special devices for removing highly radioactive targets, loading them into protective containers for safe transportation to storage sites or to hot chambers for further processing.

When designing the line for the production of radionuclides for each energy of the proton beam in the range of 40–80 MeV, the optimal parameters of the magnetic elements of the beam were found under conditions of minimal losses of particles in the transportation path, and so that the beam size on the target was at least 20 mm.

The optimization of the beam transfer lines was carried out using the Proton_MC program developed at the PNPI [2]. The calculation algorithm consists in tracing the proton beam trajectories along the transport channel from the source to hitting the experimenter's target or the aperture of the magnetic elements. The initial conditions of the particles are chosen random within normal distribution. The beam from the accelerator is presented in the form of a multidimensional Gaussian distribution in $x, x', z, z', \Delta p/p$ phase

space. In the case when an absorber is installed in the transport channel, the beam parameters after the absorber are calculated using the GEANT4 program [3].

The output file of this program may be used as the source for the program. The program includes a block for optimizing any beam parameters presented in a functional form. The random search method is used for obtaining the global maximum of a function of many variables.

Figure 2 shows the results of calculating the beam envelopes in the horizontal (X) and vertical (Z) planes for the target stations T1, T2, T3, T4, respectively. The energy of the protons is $E = 70$ MeV.

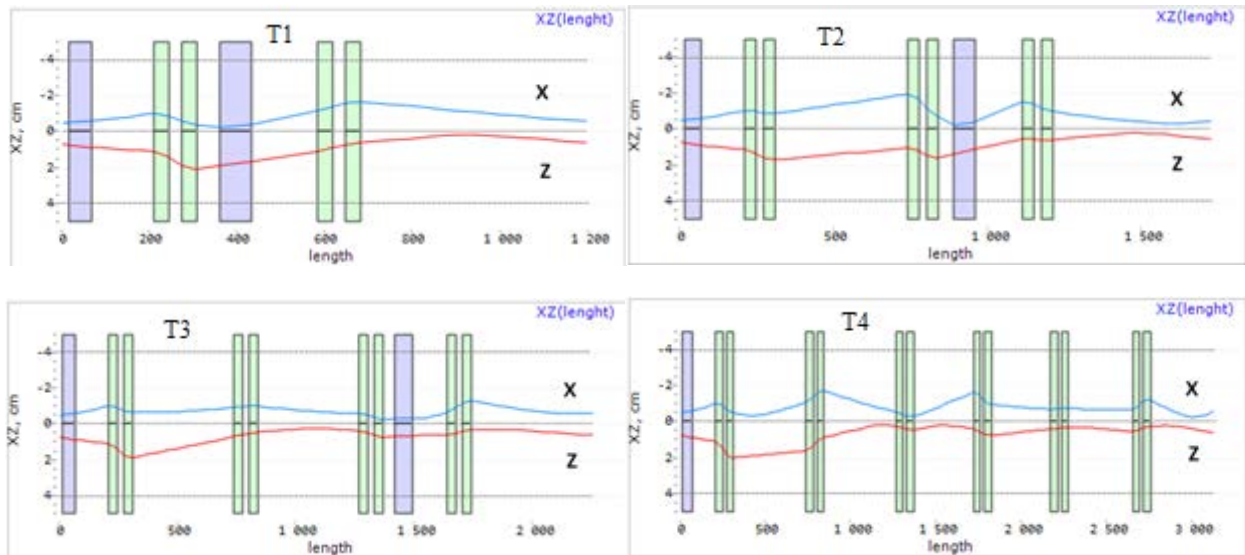


Fig. 2. Beam envelopes in horizontal (X) and vertical (Z) planes for stations T1–T4. The *upper and lower horizontal lines* are the beam aperture

Figure 3 shows a beam portrait for the most distant T4 direction as an example of the beam quality.

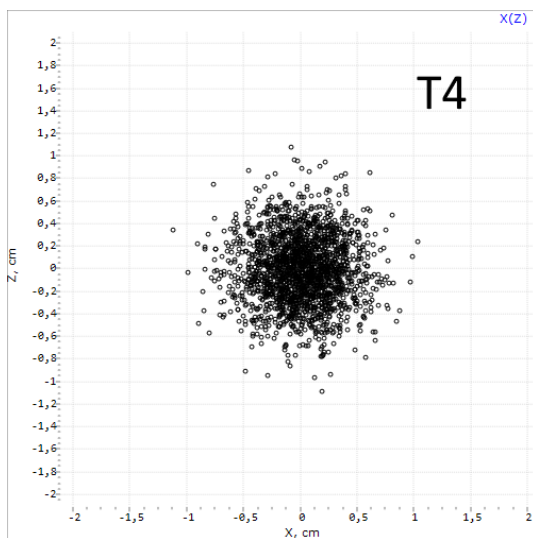


Fig. 3. Beam size on the T4 target

2.2. Ophthalmic oncology beam line

Another area of application of the C-80 cyclotron is proton therapy for oncological eye diseases. For this purpose, a beam line was designed for the formation and delivery of a proton beam from the cyclotron to the treatment room, where patients are irradiated (direction B, Fig. 1). The line meets special requirements:

the beam energy 60–70 MeV; the beam diameter at the entrance to the treatment room ≈ 60 mm; the beam divergence angle ≈ 1 mrad; the uniformity of the beam in the area of $\varnothing 60$ mm is not less than 90%.

A challenge in the design of medical tract was the requirement of medical physicists about the simultaneous and independent operation of the two beams of isotopes and medicine. On a cyclotron accelerating H^- ions, it became possible to ensure the simultaneous operation of two beams of different intensities and energies – one for the production of isotopes with an intensity of 100 μA and an energy of 40–80 MeV and the other – for ophthalmology with an energy of 60 MeV and an intensity of 10 mA.

To implement this idea, it turned out to be necessary to extract the beams in two directions (see Fig. 1) and select a complex configuration of stripping foils. To obtain a homogeneous beam, a well-known method of beam scattering and sampling of its homogeneous central part were applied. To fulfil these conditions, a beam line with a passive scatterer made of tantalum (Ta) foil 300 μm thick was constructed. The scheme of the beam path is shown in Fig. 4.

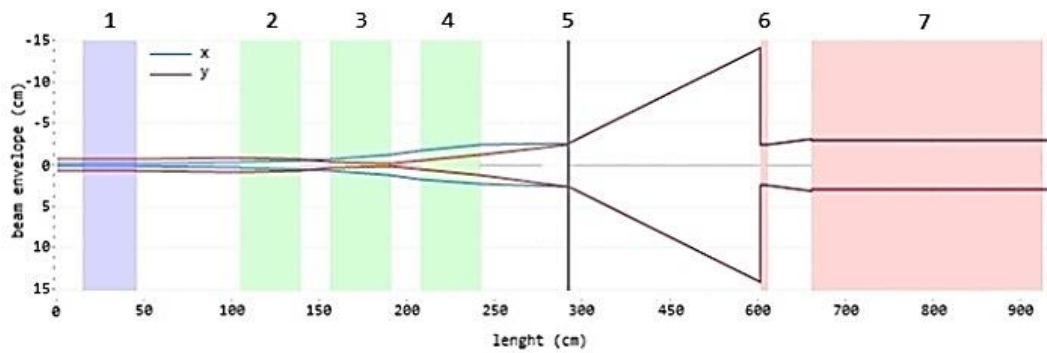


Fig. 4. Ophthalmic beam line scheme and beam envelopes: 1 – corrector magnet; 2–4 – triplet lenses; 5 – tantalum scatterer 300 μm thick; 6 – collimator; 7 – protective wall in front of the irradiation room

The proton beam $E = 70$ MeV, extracted from the accelerator, is transported to the Ta foil, on which a beam size of $\sim \varnothing 30$ mm is formed by a triplet lens. The optimization of the proton beam transport line in this section was also carried out using the Proton_MC program. The results of the passage of protons through a Ta foil with a thickness of 300 μm , obtained using the GEANT4 program, were the initial conditions of the Proton_MC program during further transport of the diverging proton beam in free space of ~ 3.7 m. The phase ellipses of the beam at the entrance and exit from the foil are shown in Fig. 5.

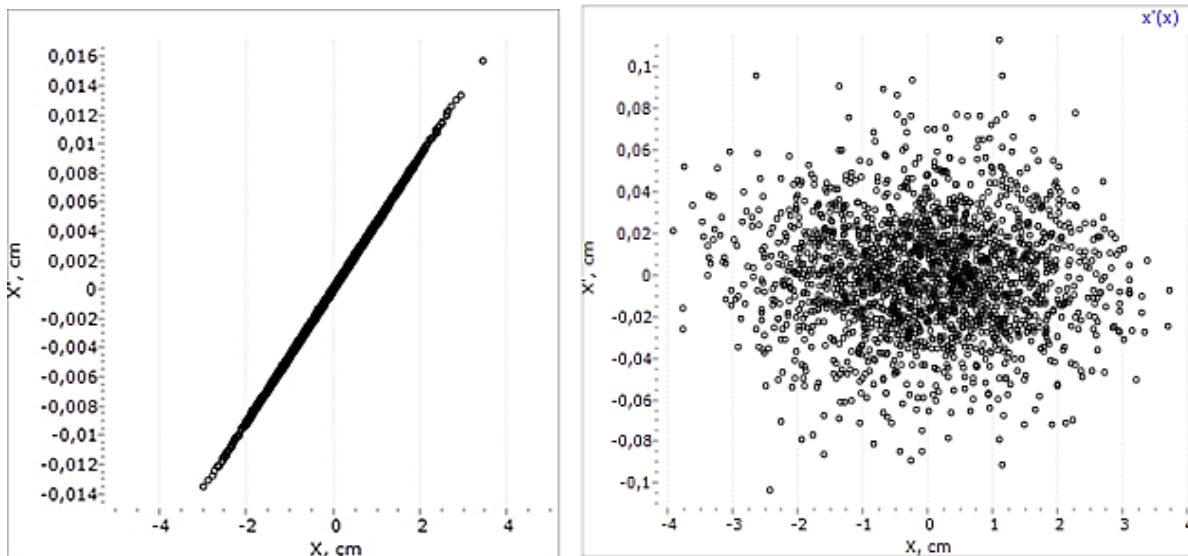


Fig. 5. Phase ellipses of the beam ($x-x'$) at the entrance and exit from the foil, respectively

A collimator with an optimal beam length of 100 mm and a diameter of 50 mm, installed in front of the protective wall, finally forms a beam with specified conditions as shown by Fig. 6.

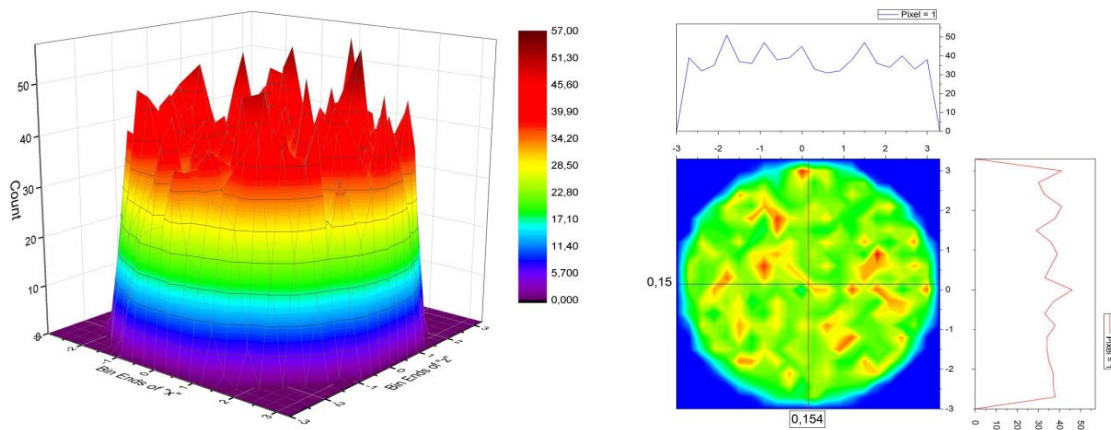


Fig. 6. Distribution of the intensity of the proton flux in the beam at the entrance to the irradiation room of patients

3. Conclusion

Within the framework of this project, the radioisotope and oncoophthalmological beam line for the transport of the proton beam were designed. We managed to place the necessary equipment within the allocated area. Calculations show that this configuration of the channels will provide a proton beam with the required parameters.

References

1. N.K. Abrosimov, G.A. Ryabov, A.N. Chernov, Preprint PNPI 2851 (2010).
2. D.A. Amerkanov, E.M. Ivanov, G.A. Ryabov, V.A. Tonkikh, in *Proc. of the 27th Rus. Particle Accelerator Conf. (RuPAC'21)* 262 (2021).
3. GEANT4, <https://geant4.web.cern.ch>

Methodical and Applied Research

INSTRUMENT BASE OF SYSTEMS FOR DIAGNOSTICS AND TRANSPORTATION OF PROTON AND NEUTRON BEAMS FOR RADIATION TESTING OF ELECTRONICS AT THE 1 GeV SYNCHROCYCLOTRON OF PNPI

D.A. Amerkanov, S.A. Artamonov, A.S. Vorobyov, **G.I. Gorkin**, E.M. Ivanov, S.V. Kosyanenko, **O.V. Lobanov**, V.G. Muratov, V.V. Pashuk, O.A. Shcherbakov, V.A. Tonkikh; V.S. Anashin, A.E. Kozyukov, P.A. Chubunov – United Rocket and Space Corporation – Scientific Research Institute of Space Instrumentation, Moscow

1. Introduction

The widespread use of semiconductor products of microelectronics as an element base of space electronic systems has made the problem of assessing and predicting the levels of failures of elements and assemblies to the radiation effects of outer space relevant. The requirements for these tests are due to the fact that in modern devices manufactured using micron and submicron technologies, new effects of radiation exposure have arisen associated with ionization effects and structural damage to products under the action of individual high-energy particles, the so-called single radiation effects, or single event effects.

Over the past 20 years, failures and breakdowns under the action of individual protons and neutrons have been studied at PNPI in the operation of various highly integrated products: memory elements, transistors, charge coupled devices (CCD) matrices. In this direction, PNPI actively cooperates with many organizations and enterprises in Russia.

Below is given a description of the instrumental base of the systems for diagnostics and transportation of proton and neutron beams, which are part of the stands for radiation tests, developed at PNPI in cooperation with the Institute of Space Instrumentation (Roscosmos), a branch of the United Rocket and Space Corporation [1].

2. Transportation system

The transportation system ensures the delivery of the proton beam from the output window of the accelerator to the workstations. The transportation system includes:

- Dispensing magnet SP-40 – for output to the required path;
- Correction magnets – to shift the proton beam vertically and horizontally;
- Collimators – to change the beam emittance;
- Magnetic lenses – for focusing and defocusing the proton beam;
- Absorber of variable thickness (0–530 mm) – for changing the beam energy in the range of 60–1 000 MeV [2].

The diagram of the proton beam transportation paths to the irradiation workstations is shown in Fig. 1.

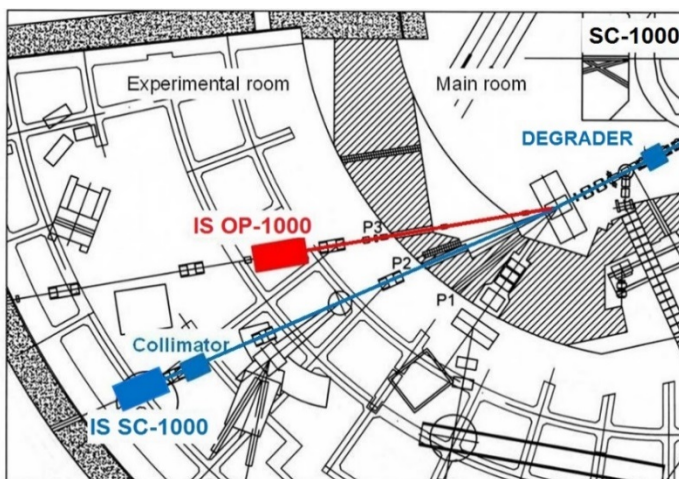


Fig. 1. Diagram of proton beam transport paths: P2 – protons with an energy of 1 000 MeV; P3 – protons with a variable energy of 60–1 000 MeV

The automated control system for setting and stabilizing the current in the magnetic elements is responsible for regulating the current in the magnets (Fig. 2). For output to the working path, an appropriate magnetic field is installed in the distributing magnet SP-40, which is located at the output wall of the “Main Hall”.

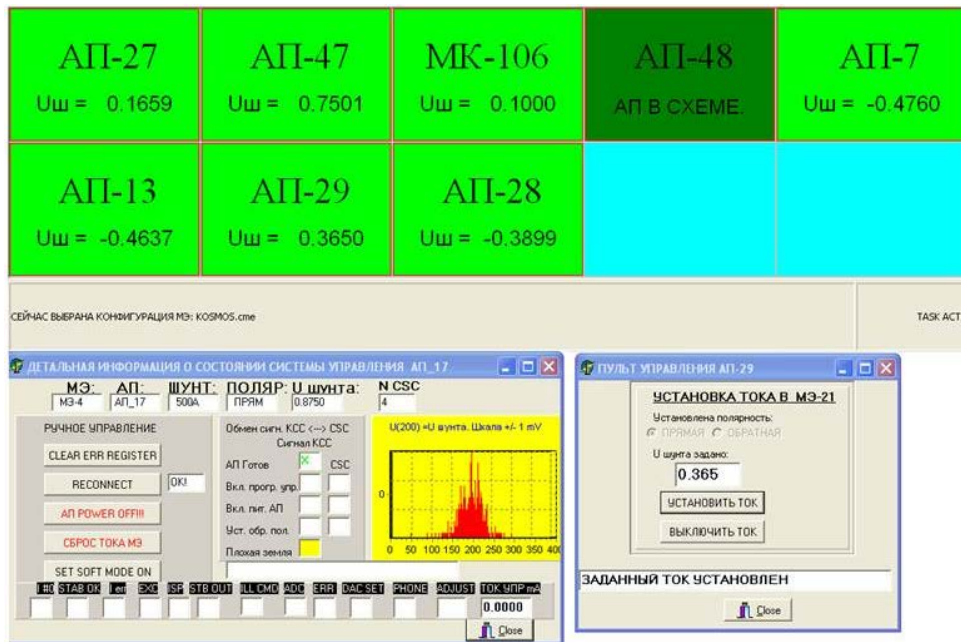


Fig. 2. Interface of the automated control system of the current in the magnetic elements

The fields in the main magnet E-9 of the synchrocyclotron and in the distributing magnet SP-40 are set and controlled by nuclear magnetic resonance (NMR) magnetometers, which makes it possible to reproduce the beam output with good accuracy (Fig. 3).

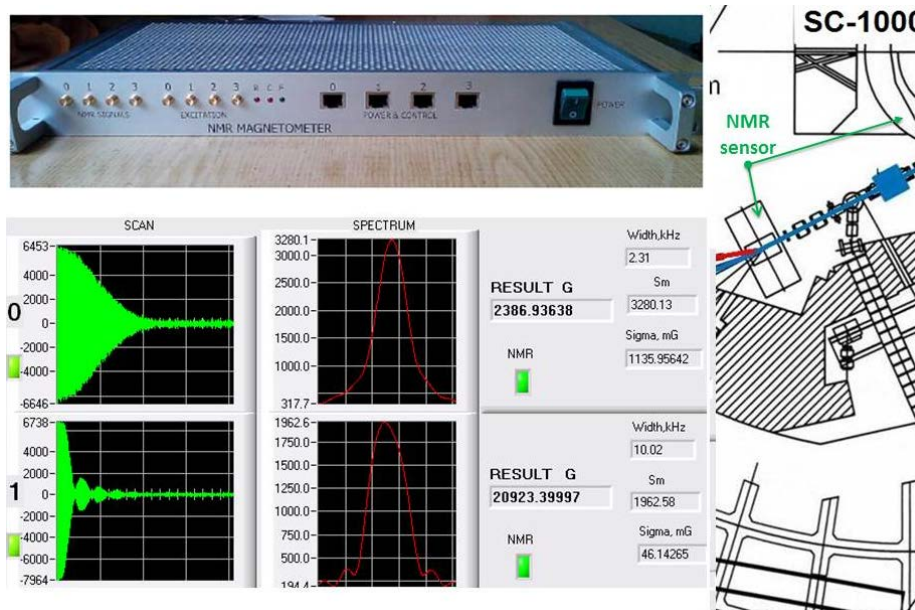


Fig. 3. Nuclear magnetic resonance magnetometer, its interface and location

The variable thickness absorber allows remote adjustment of the absorber thickness by placing a set of copper cylinders in the beam path (Fig. 4).



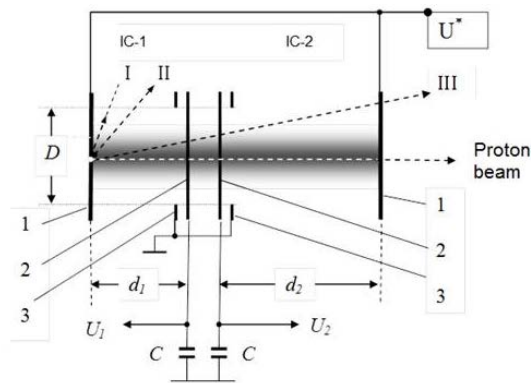
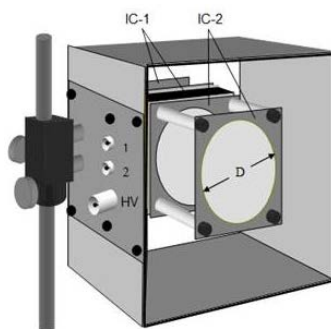
Fig. 4. The variable thickness absorber

3. Diagnostic system

The diagnostic system provides control of beam parameters and consists of the following tools:

- Two-channel semiconductor profilometer to determine the width of the beam and its centre of gravity;
- Scintillation profilometer with CCD-matrix – to obtain a proton beam profile with a resolution of 512×512 points;
- Two-section ionization chamber for online monitoring of the intensity of the proton flux [3];
- Fission ionization chamber to determine the intensity of the neutron flux;
- Two-axis position-sensitive multiwire proportional counter to obtain the distribution of neutrons in the beam.

A two-section ionization chamber design is shown in Fig. 5.



Effective range
 $10^6 - 10^9 \text{ p}\cdot\text{sec}^{-1}$

1. High-voltage electrodes
 2. Signal electrodes
 3. Aperture electrodes
- U^* – High-voltage source

Fig. 5. Two-section ionization chamber design

The results of measuring the beam width and particle distribution density are shown in Fig. 6.

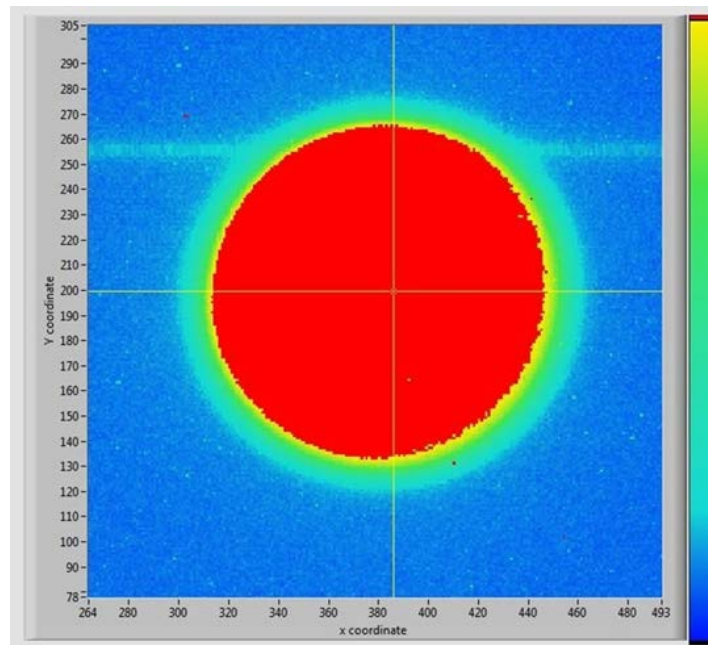


Fig. 6. The result of the work of a scintillation profilometer with a CCD-matrix to find the particle distribution density in the beam

4. Conclusion

The PNPI centre is equipped with all necessary systems of beams diagnostics and transportation to a target. These systems allow changing the shape, energy and direction of the proton beam, as well as measuring the profile and intensity of proton and neutron beams. There is also an instrument to vary the temperature of exemplars in a wide range.

The combination of these systems provides the necessary beam parameters for testing electronic components in proton beams with a variable energy of 60–1 000 MeV and in an atmospheric neutron beam with a wide energy range (1–1 000 MeV).

References

1. D.A. Amerkanov, S.A. Artamonov, E.M. Ivanov *et al.*, in *XXV Rus. Conf. on Particle Accelerators RUPAC 2016*, THCAMH01 Report, 105 (2016).
2. E.M. Ivanov, G.F. Mikheev, V.S. Anashin, An Automated Moderator of the Proton Beam of the Synchrocyclotron – a Degradar: Utility Model Patent No. 181147; Priority 03.30.2018.
3. D.A. Amerkanov, G.I. Gorkin, E.M. Ivanov *et al.*, *PTE* **3**, 11 (2016).

ABSOLUTE PROTON BEAM MONITOR BASED ON AN IONIZATION CHAMBER WITH A TRANSVERSE ELECTRIC FIELD

D.A. Amerkanov, E.M. Ivanov, **N.A. Ivanov**, **O.V. Lobanov**, V.V. Pashuk

1. Introduction

The physical properties of an absolute proton beam monitor operating in real time are investigated. The monitor detector consists of two air-filled ionization chambers (IC) combined into one module with a transverse electric field relative to the beam path. In the chambers, the signal electrodes have different lengths along the beam. High-voltage electrodes are located from the signal electrodes at a distance equal to or proportional to the length of the signal electrode. The ability to vary the length of the electrode allows one to quickly change the measured range of the proton fluxes.

2. Ionization chamber with a transverse electric field

When conducting radiation research at the PNPI synchrocyclotron, absolute monitors are used based on a plane-parallel dual-section ionization chamber (DIC) [1, 2] through which a beam of protons with energies of 50–1 000 MeV passes perpendicular to electrodes made of thin aluminium foils (10–20 μm). In order to expand the measured range towards higher values of proton fluxes, in this paper, we considered an ionization chamber monitor with a transverse electric field relative to the beam direction and, consequently, with no foils in the beam path, but designed in such a way as to preserve the method for determining the quantitative characteristics of the flux and the total number of protons, previously developed for the DIC monitor.

A beam detector with a transverse electric field relative to the beam path [3] consists of two ICs combined into one module with plane-parallel high-voltage and signal electrodes. The chambers differ in the lengths of the signal electrodes and are arranged in series along the beam path. In each IC, the distances between the high-voltage and signal electrodes are different in magnitude, and the lengths of the signal electrodes along the beam direction are equal or proportional to the inter-electrode distances of the corresponding ICs. Equal-rated capacitors are connected to each signal electrode, which are charged by induction currents of external circuits equal to the ion currents of the chambers. The number of protons passing through these chambers is calculated from the voltage measured simultaneously on the capacitors using a developed algorithm [1]. A technical drawing of a dual-chamber ionization detector (DID) is shown in the Figure.

The number of ion pairs n' , formed by N beam protons passing in the inter-electrode space IC_1 and IC_2 during the integration time T is

$$n'_{1(2)} = N \left[-\frac{dE}{dx} \right] L_{1(2)} \omega^{-1}, \quad (1)$$

where $[-dE/dx]$ is the specific ionization loss of a proton in air at normal pressure; $L_{1(2)}$ is the total length of the electrode ($L'' + L'$); ω is the energy spent by the proton on the formation of one pair of ions.

If $\left[\frac{L_{1(2)}}{d_{1(2)}} \right] = k$, then

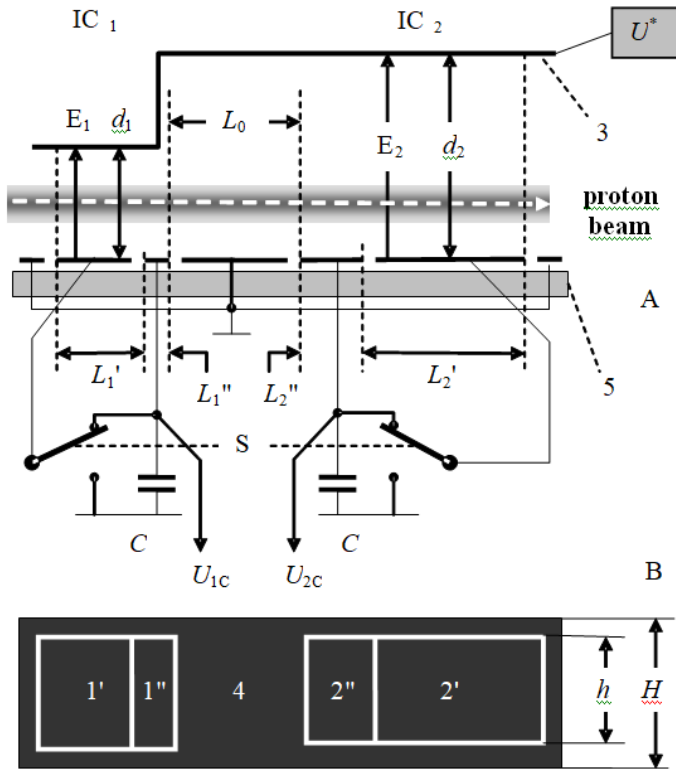
$$n_{1(2)} = N \left[-\frac{dE}{dx} \right] d_{1(2)} k \omega^{-1} \lambda_{1(2)}. \quad (2)$$

The voltage $U_{C_{1(2)}}$ on the capacitor $C_{1(2)}$ in the signal electrode circuit of each IC with inter-electrode distance $d_{1(2)}$ is equal to

$$U_{C_{1(2)}} = \frac{n_{1(2)} e}{C}. \quad (3)$$

The number N of beam protons passing through the chambers can be determined as

$$N = \frac{U_{C_{1(2)}} C}{\left[-\frac{dE}{dx} \right] d_{1(2)} k e \omega^{-1} \lambda_{1(2)}}. \quad (4)$$



Technical drawing of a dual-chamber ionization detector: A – frontal projection; B – top view of the board with the signal electrodes. IC₁ and IC₂ – the first and second ionization chambers; 1', 1'' – signal electrodes of length L_1' , L_1'' along the path of the beam in IC₁; 2', 2'' – signal electrodes of length L_2' , L_2'' along the path of the beam in IC₂; 3 – high voltage electrode; 4 – grounded electrode; 5 – printed circuit board with electrodes; d_1 and d_2 are the inter-electrode distances between the signal and high voltage electrodes in IC₁ and IC₂, respectively; E_1 and E_2 are the electric field strength vectors in IC₁ and IC₂; L_0 is the distance between the signal electrodes; U_{1C} and U_{2C} – the measured voltages on capacitors C; S – the key for switching the proton flux measurement range; h – width of the signal electrodes; H – width of the panel with signal electrodes

3. Results and conclusion

The operation of a DID with a transverse electric field with respect to the beam path and the principles for calculating the absolute value of the number of particles in a beam were tested at the PNPI synchrocyclotron using a collimated proton beam. It was shown that the experimental values of the proton flux measured using a two-chamber ionization detector and using a two-section ionization chamber at a constant current of a relative monitor located in the main hall of the accelerator coincide within 10%. Note that there are no physical restrictions for measuring large flows. By changing the length of the signal electrodes, as well as changing the capacitance of the capacitors and the integration time, it is possible to measure the proton flux over a wide range during the experiment.

An ionization detector of this design can be used in heavy particle accelerators, where the problems of correct measurements of fluxes are necessary and important, as well as in the cases where beam broadening is unacceptable (for example, in proton therapy, ophthalmology).

References

1. N.A. Ivanov, O.V. Lobanov, V.V. Pashuk, PTE **6**, 5 (2009).
2. D.A. Amerkanov, G.I. Gorkin, E.M. Ivanov *et al.*, PTE **3**, 11 (2016).
3. N.A. Ivanov, O.V. Lobanov, V.V. Pashuk, Two-Chamber Ionization Detector, Message No. 3012, 12 (2017).

IMPORTANT FOCUSING PROPERTIES OF THE MAGNETIC STRUCTURE OF ISOCHRONOUS CYCLOTRONS WITH HIGH SPIRALING ANGLE OF THE POLE TIPS

D.A. Amerkanov, S.A. Artamonov, E.M. Ivanov, G.A. Riabov, V.A. Tonkikh

1. Introduction

Magnetic structures with a large spirality angle of pole tips were investigated in a number of works and are used in superconducting cyclotrons, H^- ion cyclotrons, *etc.* With the design and construction of an 80 MeV isochronous H^- cyclotron, such studies were continued and extended. In this work, a relatively simple approach for analysing the spiral structure is proposed.

The magnetic structure with a large spirality angle of the pole tips is used in cases when vertical focusing from the flutter (field difference in the valley and the sector) is insufficient and it is necessary to add the angle focusing. This situation is typical for superconducting cyclotrons and for cyclotrons that accelerate negative hydrogen ions. Moreover, at Joint Institute for Nuclear Research (JINR) in Dubna, such structures were investigated and a cyclotron and a synchrocyclotron with sectors in the form of an Archimedes spiral with a maximum spirality angle of up to 70 degrees were built. Numerical calculations of the magnetic field for an isochronous superconducting cyclotron with spiral sectors in the approximation of their uniform magnetization were carried out [1].

Two effects were noted: a decrease in the flutter in the central region with the introduction of spirality and a mismatch between the spirality of the sector iron and the magnetic field. However, calculations made for a specific geometry are not applicable in the case of a different design. With the construction of an isochronous cyclotron for accelerating H^- ions up to 40–80 MeV [2, 3], studies of the focusing properties of spiral structures were continued and expanded. Modern 3D software codes simplify the design of the magnetic field of any configuration by using trial and error. However, to speed up the procedure and to reduce the number of options for a 3D analysis, it is useful to first perform a simplified and visual analysis of the system and estimate the importance of various parameters in the framework of a simpler 2D approximation.

2. Development of two-dimensional approximation

2.1. Optimization of the magnet gaps

As a first approximation, the hill ($2g_h$) and valley ($2g_v$) gaps for each fixed sector thickness (h_s) were selected using 2D POISCR calculations based on the proposed new fill factor method. In this method, a 3D problem is reduced to a 2D one. The iron rings or the so-called shims mounted on the magnet poles and providing an isochronous rise in the field are calculated using a 2D program with a reduced value of the magnetic permeability $\mu_{\text{new}}(B) = \mu(B) \cdot C$. The permeability is reduced by a factor $C(r)$ – the so-called filling factor equal to the ratio of the azimuthal length of the sector to the length of the periodicity element at each radius r . The gap of the magnet obtained in this way corresponds to the gap of the hill, and there is no additional shim in the valley. Thus, two variants of the gaps of the main magnet and the gaps of the hills and the valleys were analysed. The parameters of these variants are presented in the caption to Fig. 1.

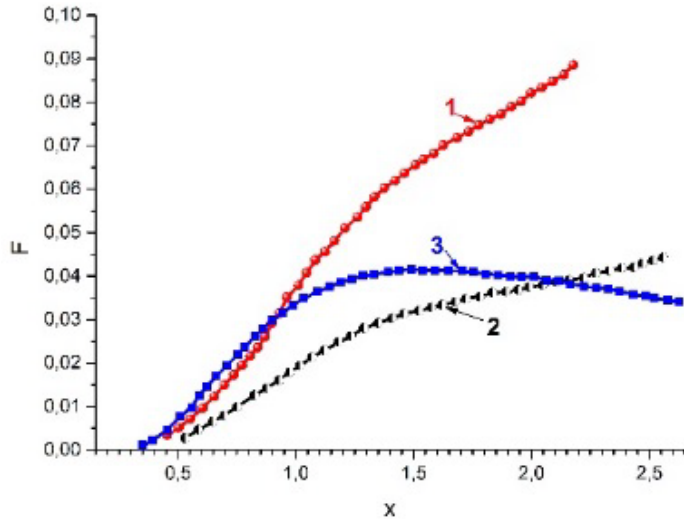


Fig. 1. The dependence of the flutter on the dimensionless parameter $x = r / N \cdot g_h$, where $N = 4$, for two options: 1 – $2g_v = 386$ mm, $2g_h = 170$ mm, $h_s = 108$ mm; 2 – $2g_v = 284$ mm, $2g_h = 145$ mm, $h_s = 69$ mm; 3 – a variant of uniform magnetization for the case of the geometry of the first variant

2.2. Flutter problem

The azimuthal variation of the magnetic field [1] is determined by the so-called flutter $F(r)$:

$$F(r) = \langle (B - \langle B \rangle)^2 \rangle / \langle B \rangle^2, \quad \langle \dots \rangle = (2\pi)^{-1} \int_0^{2\pi} \dots d\theta.$$

The flutter can be represented as a Fourier harmonics expansion of the azimuthal variation of the magnetic field. The fundamental contribution to the expansion is made by the general focusing harmonic associated with the number of sectors and periodicity elements (in our case, $N = 4$). If we denote the value of the fundamental focusing harmonic $f = B_N / \langle B \rangle$, then $F = f^2/2$.

An analytical calculation of the flutter is a complex and practically impossible problem, therefore, approximate methods were used. In particular, in Ref. [4], an expression was obtained for the general harmonic of the magnetic field variation in an isochronous cyclotron in the approximation of uniform magnetization of the sectors of the magnet,

$$B_N = 8M \sin(2\pi a/d) \exp(-2\pi g_h/d),$$

where $2a$ is the length of the sector along the azimuth for a given radius r ; $2g_h$ is the gap in the hill; d is the period of the structure, equal to the total length of the hill and valley, $4\pi M = 21$ kG. It follows from this expression that for an isochronous cyclotron with a period of the magnetic field structure equal to $d = 2\pi r/N$, where N is the number of sectors, the flutter grows with increasing radius according to the law

$$F \sim \frac{B_N^2}{2} \sim \exp(-2/x), \quad x = r/N \cdot g_h. \quad (1)$$

Although this approximation is insufficient for obtaining accurate quantitative estimates, it allows, in a unified manner, to get an idea of the relationship between different parameters of the magnetic structure. Moreover, the introduction of the dimensionless parameter x enables the comparison of different variants of the structures. In particular, the flutter rises as the gap in the hill decreases and falls as the number of sectors increases.

The maximum flutter value corresponds to the case when the azimuthal extent of the sector and the valley are equal. In this case, $a = 0.25d$ and $\sin(\pi/2) = 1$. For the case when the parameter x becomes less than 0.5, the flutter drops very sharply, *i. e.*, at radii $r \leq 0.5Ng_h$, the azimuthal variation becomes ineffective, and focusing tends to zero. The results of these calculations are shown with curve 3 in Fig. 1.

The dependence of the flutter on the radius can be calculated using 3D programs. However, they are usually a commercial product. Therefore, in our case, to speed up and simplify the calculations, we used 2D approximate calculations. The flutter can be estimated using a 2D program if we replace the calculation of the edge effect along the azimuth with the calculation of the edge effect along the radius of the two-dimensional magnet with a gap in the form of teeth and valleys along the radius. In this case, the gap variation of a 2D-

magnet along the radius corresponds to the length and gaps of the sector and valley along the azimuth of the investigated 3D magnet.

Simple estimates carried out for the C-80 cyclotron show that the structure with straight sectors does not provide the necessary vertical focusing; therefore, it is necessary to use the following effect.

2.3. Influence of the spirality effect

As it is well known, the frequency of vertical oscillations, which determines the vertical focusing, can be expressed using the following approximation:

$$v_z^2 \approx -k + F \cdot S(r, \gamma), \quad S(r, \gamma) = 1 + 2tg^2\gamma, \quad (2)$$

where k is the rate index of the average magnetic field growth along the radius,

$$k = \left(\frac{r}{\langle B \rangle} \right) \left(\frac{d \langle B \rangle}{dr} \right) \approx \frac{2W}{E_0}.$$

Here W is the kinetic energy, $E_0 = 938$ MeV is the rest mass of the proton, γ is the spirality angle. The frequency of axial oscillations is determined by two oppositely acting terms – the defocusing of the isochronous rise of the mean field and the focusing action of the azimuthal variation of the field. The task is to select F and γ for each value of the energy W so that v_z^2 remains greater than zero during acceleration. At the same time, to limit the dissociation of negative ions, it is necessary to strive for the lowest possible value of the magnetic field in the hill, *i. e.* to the minimum flutter value. The spiraling sector provides an increase in focusing force due to the non-perpendicular angle of particle entry into the sector region. Effectively, the flutter F is multiplied by the coefficient $S(r, \gamma)$; however, in a structure with a large spirality angle, the increase in focusing force is noticeably less [1] than could be expected from the above formula. This is due to a decrease of the flutter when the spirality angle is introduced and a mismatch between the iron and the magnetic spirality angles.

There is a simple geometric explanation for the first effect. With a large spirality angle, the difference between the sector length along the azimuth (AB in Fig. 2) and the width of the A_1B_1 sector determined from geometric considerations, becomes significant. In the case of straight sectors, the flutter is determined by the magnetic field difference in the hill and the valley. In this case, the field falls off along the azimuth. When a spiraling angle is introduced, the distance between the sectors along a line perpendicular to the centre-line of the sector is much smaller than the distance along the azimuth. This leads to a decrease in the effective length of the sector A_1B_1 and, accordingly, to a decrease in the length of the valley. From geometric considerations, we can conclude that the effective length of the A_1B_1 sector is approximately equal to the length of the sector along the azimuth AB multiplied by a factor equal to $\cos\gamma$, *i. e.* $A_1B_1 \approx AB \cos\gamma$. With a decrease in the length of the sector, the effective length of the valley and the period of periodicity decrease. In this case, the dimensionless parameter x , introduced in expression (1) and related to the length of the periodicity period, will also decrease and becomes $x_{\text{eff}} = x \cos\gamma$. According to Fig. 1, a decrease in the value of the parameter $x_{\text{eff}} = x \cos\gamma$ leads to a shift along the graph towards lower flutter values. At intermediate and large radii, the spirality causes an increase in the edge focusing and a decrease in the flutter, and the total effect leads to an overall increase in focusing. However, at small radii, the introduction of spiraling reduces the effective sector length and this can lead to a very sharp drop in the flutter and a total decrease in focusing. The total effect of the introduction of the spiral sectors can be characterized by a parameter that is the product of two factors: the flutter F and $S(r, \gamma)$. Since the flutter drops sharply at $x_{\text{eff}} < 0.5$, the introduction of spiraling in the central region leads to a decrease in focusing. For each radius, it is possible to calculate the limiting value of the spiraling angle, exceeding which spiraling does not give an increase in focusing. This value for each parameter x can be estimated by finding the solution for the following equation:

$$U(x, \gamma) = (F(x \cos\gamma)/F(x)) \cdot (1 + 2tg^2\gamma) - 1 = 0, \quad (3)$$

where $F(x)$ is a function of the type shown in Fig. 1.

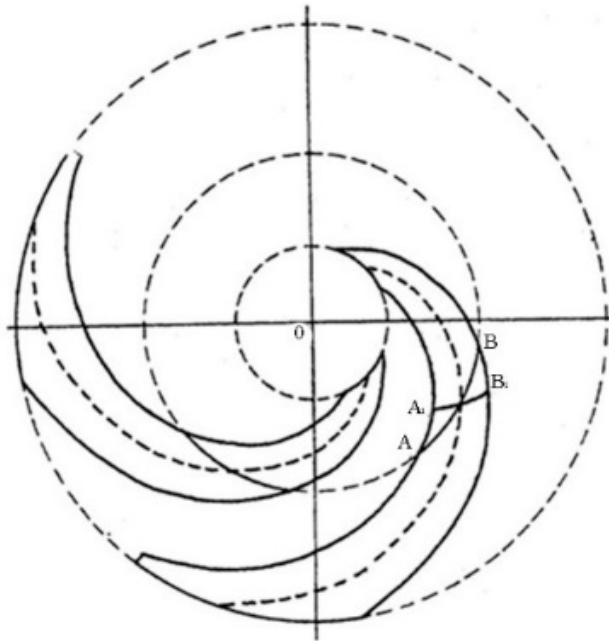


Fig. 2. There is a difference between the sector length along the azimuth AB and the “effective” length A_1B_1 at large spiraling angles. The effective sector width corresponding to its average line for a given r is equal to $A_1B_1 \approx AB \cos \gamma$

Figure 3 shows the limiting spiraling angle calculated by formula (3) as a function of the radius for the case of the C-80 cyclotron. According to Fig. 3, spiraling leads to decreasing of vertical focusing at radii smaller than 35 cm, and it is advisable to use a structure with a large spirality angle at radii greater than 35 cm. Thus, a structure with a large spiraling angle is effective only at radii larger than the hill gap value.

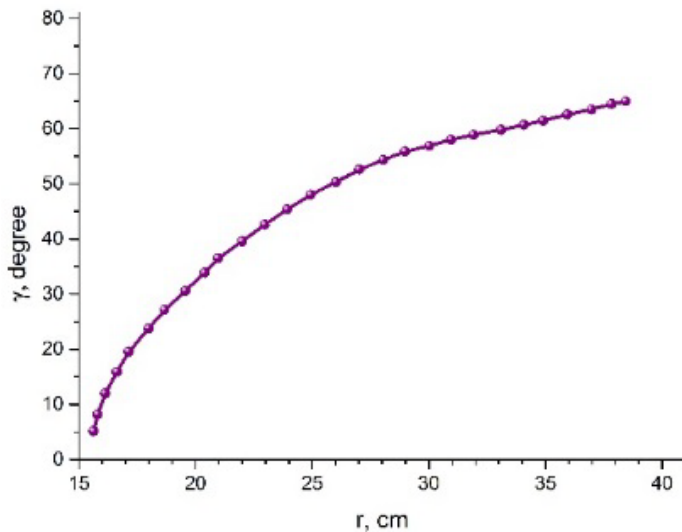


Fig. 3. Ultimate spirality angle for C-80 cyclotron in dependence on the radius for $2g_v = 386$ mm, $2g_h = 170$ mm, $N = 4$

3. 3D computation and experiment

When choosing the spiral angle in the cyclotron design, it is necessary to take into account the fact that the magnetic field does not completely repeat the iron sector geometry [5].

According to Fig. 4, there exists an effect of magnetic spirality “netration” into the region of straight sectors [6]. This effect leads to a decrease in vertical focusing at radii smaller than 35 cm. This explains the widespread use of direct sectors in the central region. It is also seen that at radii $\sim 75 \leq r \leq 88$ cm there is a “lag” between the magnetic field spiraling angle and the geometrical one. The maximum lag reaches 7° , which at a spirality angle of 65° leads to a 30% decrease in focusing.

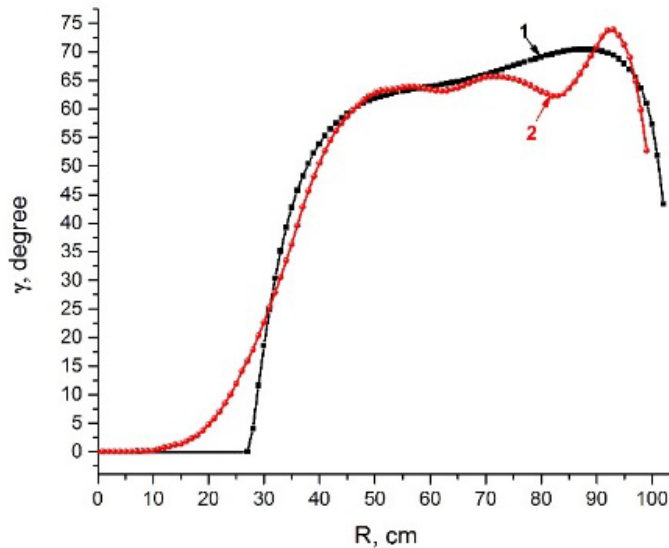


Fig. 4. The spirality angle γ (deg.) in dependence on the radius of the cyclotron: 1 – the data of the sector geometry spirality (*black*); 2 – the spirality of the fourth focusing harmonic of the magnetic field, obtained in 3D calculations and measurements of the magnetic field (*red*)

After preliminary assessments related to the choice of the parameters of the magnetic structure, the final variants were calculated in detail using the 3D MERMAID program.

In the calculations, to achieve the maximum accuracy, the magnetic structure was described using ~ 20.5 million straight prisms [7]. During the design process, two variants of the magnetic structure were considered at a finite radius: the flutter $F = 0.04$, the spirality angle $\gamma = 55^\circ$, and $F = 0.025$ with $\gamma = 65^\circ$, and the field variation amplitudes of 4.14 and 3.28 kG, respectively. Ultimately, the second option was adopted, providing a lower field in the hill, at which the loss of H^- ions due to electrodisassociation does not exceed 2.6% [8].

4. Conclusion

The analysis of the structure of the magnetic field of a cyclotron with a high spirality angle, presented in this work, makes it possible to investigate the effect of different parameters of the structure and promptly compare various options. Such an approach provides the means to qualitatively analyse the effect of a decrease in the vertical focusing of the spiral structure at the centre of the cyclotron. It is expedient to use the structure with a large spiraling angle only at radii larger than the gap in the hill. In the central region, it is advisable to use direct sectors. The paper presents a technique that was used in the design of the magnetic structure of the C-80 cyclotron. The use of the limiting large values of the spirality angle in the C-80 cyclotron made it possible to obtain the limiting energy as high as 80 MeV in a magnet with a diameter of 2 m at an extraction radius of 0.9 m. The magnetic structure allows us to limit the negative ions electrodisassociation to less than 2.6%.

References

1. H.G. Blosser, D.A. Jonson, Nucl. Instr. Meth. **121**, 301 (1974).
2. Yu.N. Gavrish *et al.*, in *Proc. 25th Rus. Part. Accelerator Conf. (RuPAC-2016)*, 180 (2016).
3. N.K. Abrossimov, S.A. Artamonov, V.A. Eliseev, G.A. Riabov, Preprint PNPI 2049, 1995.
4. V.I. Danilov, Preprint JINR-R-409 (1959).
5. S.A. Artamonov, E.M. Ivanov, G.A. Riabov, in *Proc. 26th Rus. Part. Accelerator Conf. (RuPAC-2018)*, 103 (2018).
6. D.A. Amerkanov, S.A. Artamonov, E.M. Ivanov *et al.*, in *Proc. 27th Rus. Part. Accelerator Conf. (RuPAC-2021)*, 219 (2021).
7. S.A. Artamonov, E.M. Ivanov, G.A. Riabov, N.A. Chernov, in *Proc. 23th Rus. Part. Accelerator Conf. (RuPAC-2012)*, 475 (2012).
8. S.A. Artamonov, D.A. Amerkanov, G.I. Gorkin *et al.*, in *Proc. of XX Int. Conf. Beam Dynamics & Optimization (BDO-2014)*, 18 (2014).

CALCULATION AND OPTIMIZATION OF HIGH ENERGY BEAM TRANSFER LINES BY THE MONTE CARLO METHOD

D.A. Amerkanov, S.A. Artamonov, E.M. Ivanov, G.A. Riabov, V.A. Tonkikh

1. Introduction

The calculation of high-energy beam lines consists of tracing of the proton beam trajectories along the transport channel from the source. There are many programs in the world for calculating the optics of high-energy beams [1, 2]. In most of them, the ion source is represented in the phase space in the form of a multidimensional ellipsoid, inside which particles and their initial parameters are uniformly distributed, while there are no particles outside. Moreover, it is assumed that the beam emittance is conserved during the transport of the beam along the channel, which means that there are no beam losses in the channel. In particular, it is not possible to compute the effect of collimators on the intensity and other parameters of the beam. These assumptions greatly facilitate the mathematical formulation of the problem, but they do not quite reflect the experimental situation. In this work, a more adequate representation of the ion source is proposed.

The Proton_MK program code has been developed to carry out such calculations using the Monte Carlo method. The beam from the accelerator is introduced in the form of a multivariate Gaussian distribution in $x, x', z, z', dp/p$ phase space. In the case when an absorber (absorber, air section, window in the channel, etc.) is installed in the transport channel, the beam parameters after the absorber are calculated using the GEANT4 code. The output file of this code can be used as input for the program. The program allows calculation of any beam parameters – intensity, spatial or phase density, energy distribution, etc. The program includes a block for the optimization of beam parameters presented in a functional form. Random search method with learning for search correction based on analysis of intermediate results (so-called statistical gradient method) is used for obtaining the global maximum of a function of many variables. The program has been tested in calculations of the beam transport lines for the IC-80 cyclotron and for the development of the beam line for ophthalmology.

2. Representation of sources

In the experiment, the beam profile *i. e.* the distribution of the beam intensity over the transverse coordinates is well approximated by the Gaussian distribution, and the beam spot, *i. e.* intensity distribution in x - z plane is an ellipse. This situation is typical for a multivariate Gaussian distribution, where any marginal or partial distribution along any axis is also described by a Gaussian distribution. Let us assume that the beam in the ion source can be described by a five-dimensional normal distribution with a distribution function in space (x, x', z, z', δ) in the form

$$f(X, Z, s, \delta) = \frac{1}{(2\pi)^{5/2} |\Sigma|^{1/2}} \exp \left\{ -\frac{1}{2} \begin{pmatrix} X \\ Z \\ \delta \end{pmatrix}^T \Sigma^{-1} \begin{pmatrix} X \\ Z \\ \delta \end{pmatrix} \right\}, \quad (1)$$

where Σ is a 5×5 symmetric matrix, which is the covariance matrix of the adopted distribution, *i. e.* the mathematical expectation of the distribution and its elements of interest, X is a vector (x, x') , Z is a vector (z, z') . The components of the matrix Σ have the form where $\sigma_{kl} = \langle y_k \cdot y_l \rangle$, y_k, y_l are the components of the random vector (x, x', z, z', δ) .

In most cases, the movements along x and z are independent and then $\Sigma_{xz} = 0$. In the case when the magnetic analysis takes place only in the x -plane, $\Sigma_{zp} = 0$. Based on the general properties of the multivariate normal distribution, it is possible to write the bivariate Gauss distribution in $x, -x'$ space in the form

$$f(X) = \frac{1}{(2\pi)^{|\Sigma_{xx'}|^{1/2}}} \exp\left\{-\frac{1}{2} X^T \Sigma_{xx}^{-1} X\right\}. \quad (2)$$

The elements of the correlation matrix Σ_{xx} are the mathematical expectations of the vector $(x_i x_j')$ *i. e.* $M(x_i x_j)$, where $i, j = 1, 2$ and $x_1 = x, x_2 = x'$. The matrix Σ_{xx} has the form

$$\Sigma_{xx} = \begin{pmatrix} M(x^2) & M(xx') \\ M(xx') & M(x'^2) \end{pmatrix} = \begin{pmatrix} \sigma_x^2 & \rho\sigma_x\sigma_{x'} \\ \rho\sigma_x\sigma_{x'} & \sigma_{x'}^2 \end{pmatrix}, \quad (3)$$

where $M(x, x') = \rho\sigma_x\sigma_{x'}$ by definition of the correlation coefficient ρ .

Then the bivariate Gaussian distribution on the plane takes the form

$$f(x, x') = \frac{1}{2\pi\sqrt{1-\rho^2}\sigma_x\sigma_{x'}} \exp\left\{-\frac{1}{2(1-\rho^2)}\lambda^2\right\}, \quad (4)$$

where $\sigma_x, \sigma_{x'}$ are the standard deviations and ρ is the correlation coefficient. From the general form of the probability density of two random variables, it follows that the probability density is constant in all points of the xx' plane at which

$$\lambda^2 = \left(\frac{x^2}{\sigma_x^2} - 2\rho\frac{xx'}{\sigma_x\sigma_{x'}} + \frac{x'^2}{\sigma_{x'}^2}\right), \quad (5)$$

where λ is an arbitrary value.

The curve on the xx' plane, defined by the equations above, is the so-called ellipse of equal probabilities. In the case of a Gaussian distribution, instead of one ellipse, there is a set of concentric ellipses each of which corresponds to the fraction of the beam particles lying inside the ellipse contour. Let us denote by $P(\lambda)$ the probability of a beam particle to fall inside an ellipse with a given value of λ parameter and $F(\lambda)$ the area of this ellipse in phase space:

$$P(\lambda) = \iint_{\lambda} f(x, x') dx dx' = 1 - \exp(-\lambda^2), \quad (6)$$

$$F(\lambda) = \iint_{\lambda} dx dx' = \sigma_x\sigma_{x'}\frac{\lambda^2}{\sqrt{1-\rho^2}}. \quad (7)$$

If δ is a fraction of particles outside the ellipse, then

$$P(\lambda) = 1 - \delta, \quad \lambda^2 = -2\ln\delta(1-\rho^2). \quad (8)$$

Gaussian distribution parameters can be determined by characteristic points of the ellipse. The ellipse of the beam and its three characteristic points x_1, x_2 and x_2' are shown in Fig. 1.

The sign of ρ corresponds to the sign of x_2 . If $x_2 > 0$ then the beam diverges, and $\rho > 0$. If $x_2 < 0$, then $\rho < 0$, and the beam converges. In the case of $\rho = 0$, the beam is described by a straight ellipse.

3. Geant code usage

Another way of generation of the particle source is used when an energy degrader, a scattering foil or a vacuum window is presented in the channel.

In this situation, the beam behaviour in the degrader material is calculated by using the GEANT code. On the output of the program, a file containing the energy, transverse coordinates and velocities of the particles is produced. The file is then used as input for further tracing of trajectories through the channel.

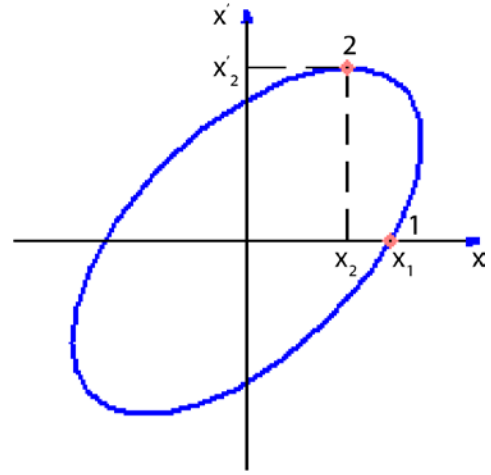


Fig. 1. Ellipse of the beam

4. The beam transport along a channel

The calculation algorithm is as follows: a five-dimensional vector $(x, x', z, z', dp/p)$ randomly generated according to the Gaussian distribution determines the initial conditions for a particle at the entrance of the channel. Then the particle with the chosen initial conditions is traced along the channel. The transport channel consists of standard magnetic elements located in different positions: quadruple lenses, various types of magnets, which provide deflection of the beam in different directions. In a linear approximation, the relationship between the input and output coordinates and velocities in the transport element can be obtained using the transition matrix, which is different for each element.

The mathematical expression for the transition matrices were formulated in many works. In this work, we used the coordinate system and the transition matrices from Steffen's monograph [3]. The calculation of the trajectory of a particle along the channel is carried out step-by-step by application of transition matrices for magnetic elements. At the output of each element, the x and z coordinates are compared with the apertures. If a particle falls out of the aperture, then its transport is stopped and it is counted as a lost particle. As a result of multiple repetitions of this procedure (several thousand times), the beam parameters are evaluated at the output of each element.

5. Optimization

In addition to the problem of calculating the beam parameters in a channel with a given configuration, it is often necessary to obtain the optimal value of some beam parameter by changing the configuration of the channel or by varying the magnetic field in the channel elements. This problem is solved in this work by using the Monte Carlo method. Different beam parameters such as intensity, energy distribution and so on are calculated using the above technique. In our case, one of the random search methods, the statistical gradient method, was used for optimization. The calculation algorithm is as follows. A sequence of random vectors is selected whose components are variable parameters with a normal distribution with dispersions σ_i and mean value X_0 .

$$\vec{X}^K = (x_1^K, x_2^K, x_3^K, \dots, x_n^K), \quad K = 1, 2, \dots, n. \quad (9)$$

For each set of randomly selected parameters, *i. e.* for each vector, the quality function $\Phi(\vec{X}^K)$ is calculated, the maximum $\Phi_m = \max \Phi(X)$ and the vector \vec{X}^M for which $\Phi = \max \Phi$ are found [4].

6. Algorithm realization

Based on the described algorithm, a code with a graphical interface Proton_MK has been developed. The program is written in C++ and can be compiled to produce an executable file for Windows. The interface Proton_MK provides the following opportunities:

- Calculation of the high energy beam transport lines which consist of quadruple lenses, bending magnets, free space, collimators;
- Generation of a particle source – a sample of N particles with the axial momentum of the channel p_0 and the parameters of the Gaussian distribution $\sigma_0, \sigma_x, \sigma_x', \sigma_z, \sigma_z', \rho_x, \rho_z, \Delta p/p$;
- Beam import after the absorber according to the GEANT4 calculation;
- The output of beam parameters at any channel element;
- Variation of the operation modes of a large number of optical elements of the channel to optimize the output beam parameters;
- The calculation results are presented in the output report.

The program was tested during the development of the beams with energy of 50–900 MeV by decelerating the primary proton beam with energy of 1 000 MeV in a copper absorber. Good agreement of calculation results with experimental data was achieved. Another example of the application of the program was the design of the beam for ophthalmology with a high degree of homogeneity [5] at the IC-80 accelerator. A beam with an intensity of 10 μA is extracted from the accelerator and then is focused onto a thin 300 μm tantalum scattering plate. The collimator after the foil preserves the central and uniform part of the scattered beam in such a way that a beam with a diameter of 60 mm and an intensity of 10^{10} s^{-1} falls into the patient's irradiation room with a 5% uniformity in intensity and a minimum divergence. The beam line for ophthalmology and the beam envelopes are shown in Fig. 2.

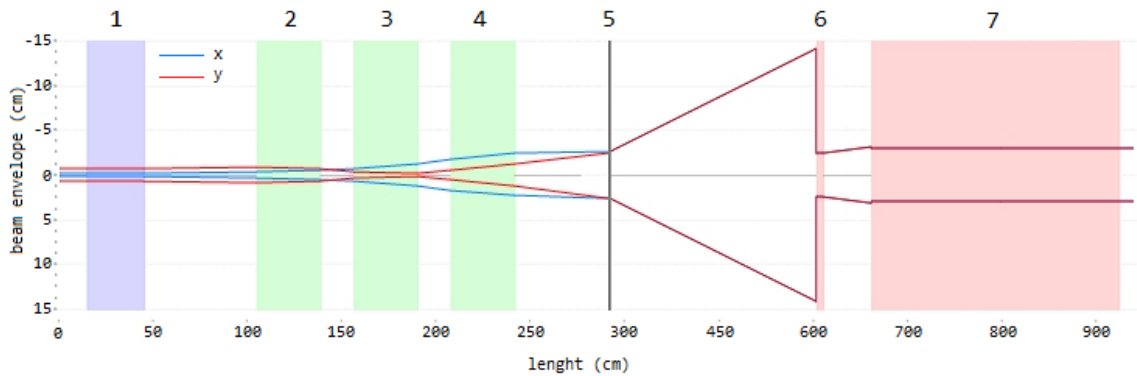


Fig. 2. Ophthalmic beam line and beam envelopes on the level 95% of the intensity: 1 – corrector magnet; 2–4 – quadruple lenses triplet; 5 – tantalum scattering foil 300 μm thick; 6 – collimator; 7 – radiation shielding wall in front of the irradiation room

References

1. K.L. Brown, A First and Second Order Matrix Theory for the Design of Beam Transport Systems and Charged Particle Spectrometers, SLAC Report No. 75, 71–134 (1968).
2. K.R. Crandall, D.P. Rusthoy, TRACE 3-D Documentation, LA-UR-97-886 (1997).
3. K.S. Steffen, High Energy Beam Optics, 211 (1965).
4. D.M. Kuzmenkov, V.I. Chernetsky, Method of Searching for Global Extreme in Linear and Nonlinear Programming Problems Under Arbitrary Constraints: Algorithms and Programs for Random Search ed. Knowledge, 145 (1969).
5. D.A. Amerkanov, S.A. Artamonov, E.M. Ivanov *et al.*, in *27th Rus. Part. Accelerator Conf. (RuPAC'21)*, MOPSA44 (2021).

THE CALCULATION METHOD AND OPTIMIZATION OF A PROTON BEAM LINE WITH COLLIMATORS BY USING COURANT–SNYDER FORMALISM

D.A. Amerkanov, S.A. Artamonov, E.M. Ivanov, V.A. Tonkikh

There are many ways to optimize and calculate the lines of charged particle beams. Calculation methods based on the approximation of the phase ellipse of the beam are widely used. The beam is represented by a 6×6 matrix defining a hyperellipsoid in six-dimensional phase space. The projection of this hyperellipsoid on any two-dimensional plane is an ellipse that defines the boundary of the beam in that plane. This hyperellipsoid can be mathematically specified by Courant–Snyder (or Twiss) parameters [1].

However, this method is not designed for the use of limiting apertures or collimators in the beam line. Therefore, an artificial technique was employed. The effect of the collimator on the phase portrait of the beam was taken into account as follows.

Let the z -axis of the reference system is directed along the beam axis, x is the horizontal coordinate, and y is the vertical one. Let the collimator be a square 3×3 mm. The collimator acceptance is imposed on the x and y phase ellipses of the beam at the entrance to the transport path. The acceptance is represented by two straight lines mapped using the collimator aperture transition matrix $x, y \leq 3$ mm onto the entrance of the beam line.

According to Ref. [2],

$$\vec{X} = M\vec{X}_0,$$

where $M = \begin{pmatrix} M_{11} & M_{12} & 0 & 0 \\ M_{21} & M_{22} & 0 & 0 \\ 0 & 0 & M_{33} & M_{34} \\ 0 & 0 & M_{43} & M_{44} \end{pmatrix}$, $\vec{X} = \begin{pmatrix} x \\ x' \\ y \\ y' \end{pmatrix}$, \vec{X}_0 are the coordinates and angles of motion of the particle at the entrance to the beam line.

It is obvious that particles whose coordinates satisfy the following relations will pass through the collimator:

$$\begin{aligned} |x| &= |M_{11}x_0 + M_{12}x'_0| \leq A, \\ |y| &= |M_{33}y_0 + M_{34}y'_0| \leq A. \end{aligned}$$

Here $|M_{11}x_0 + M_{12}x'_0| = A$ and $|M_{33}y_0 + M_{34}y'_0| = A$ are, respectively, parallel straight lines in the phase space of the beam x – x' and y – y' , which are the mapping of the collimator acceptance to the beam line entrance.

Further, a new ellipse is inscribed in the part of the phase space bounded by the input beam ellipses (vertical and horizontal ones at the input of the beam line) and the straight lines of the reflected collimator (this allows one to remain in the TRACE-3D formalism working with beam ellipses). This procedure makes it possible to find the ellipse and emittance of the beam passing along the beam line and through the collimator without losses. The ratio of the area of the inscribed phase ellipse to the area of the original ellipse determines the intensity reduction factor.

For example, let us consider one of projects for a beam line for the C-80 cyclotron. Its scheme is shown in Fig. 1. The effect of the collimator on the phase portrait of the beam is shown in Fig. 2.

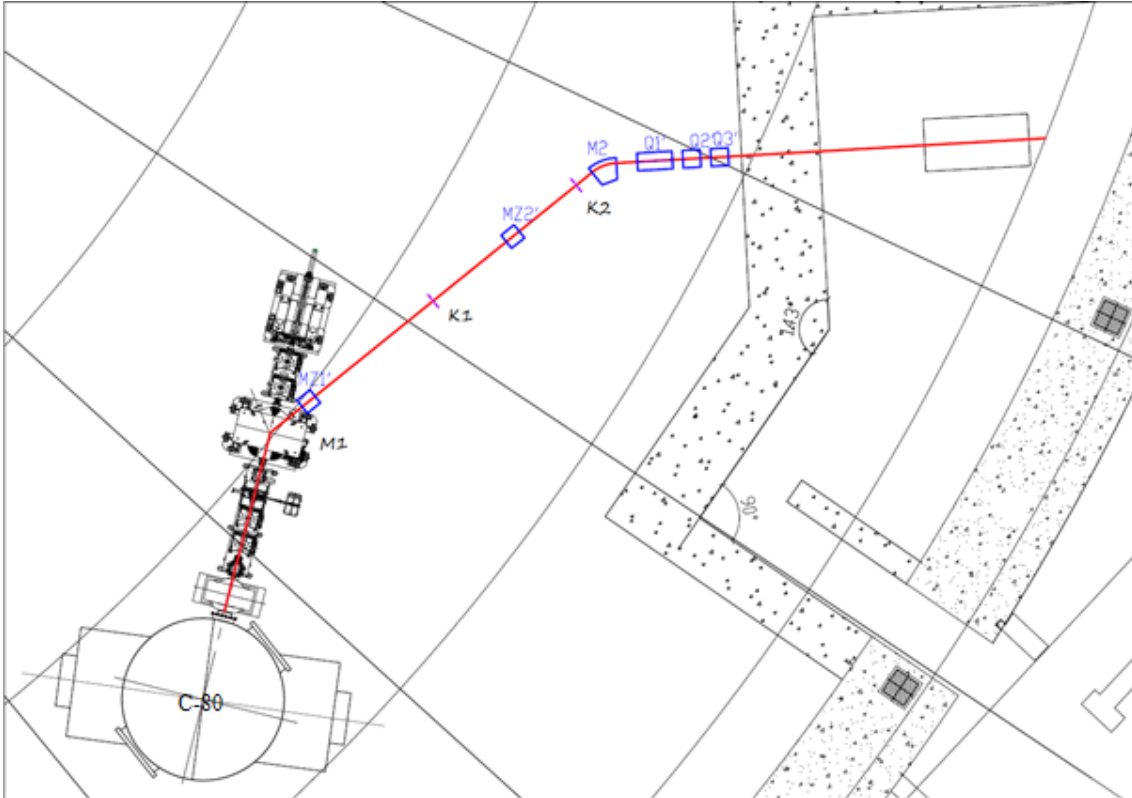


Fig. 1. Optimized beam transport path for ophthalmological needs. Here MZ1 and MZ2 are bending magnets in the vertical plane; M1 and M2 are bending magnets in the horizontal plane; K1 and K2 are collimators; Q1, Q2 and Q3 make up a triplet of quadrupole lenses

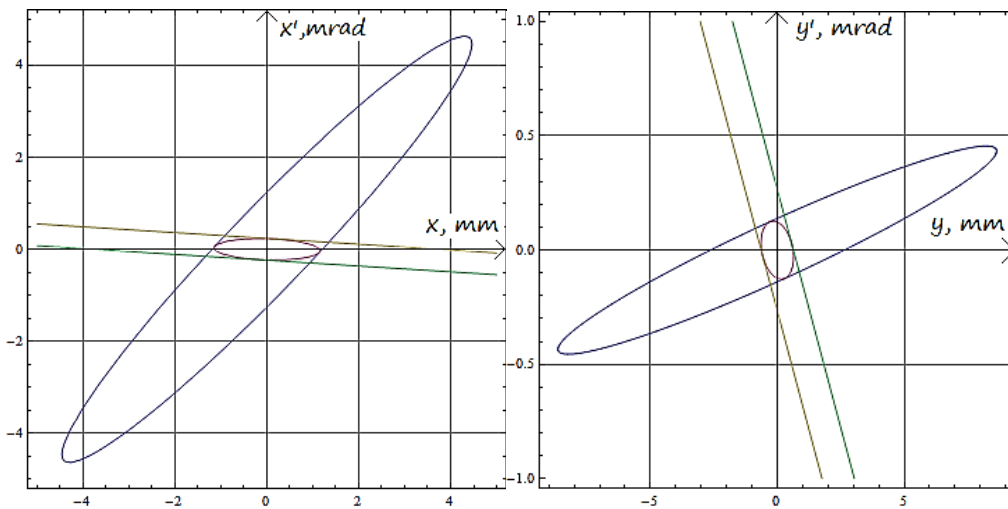


Fig. 2. Horizontal ellipse $x-x'$ (left); vertical ellipse $y-y'$ (right)

Figure 3 shows a screenshot of the result of the TRACE-3D software on optimizing the proposed beam line transportation. Above are the optimal values of the gradients of the magnetic fields of the quadrupole lenses. At the bottom of Fig. 4, the upper line corresponds to the horizontal beam envelope (in relation to the midline), and the lower line corresponds to the vertical beam envelope.

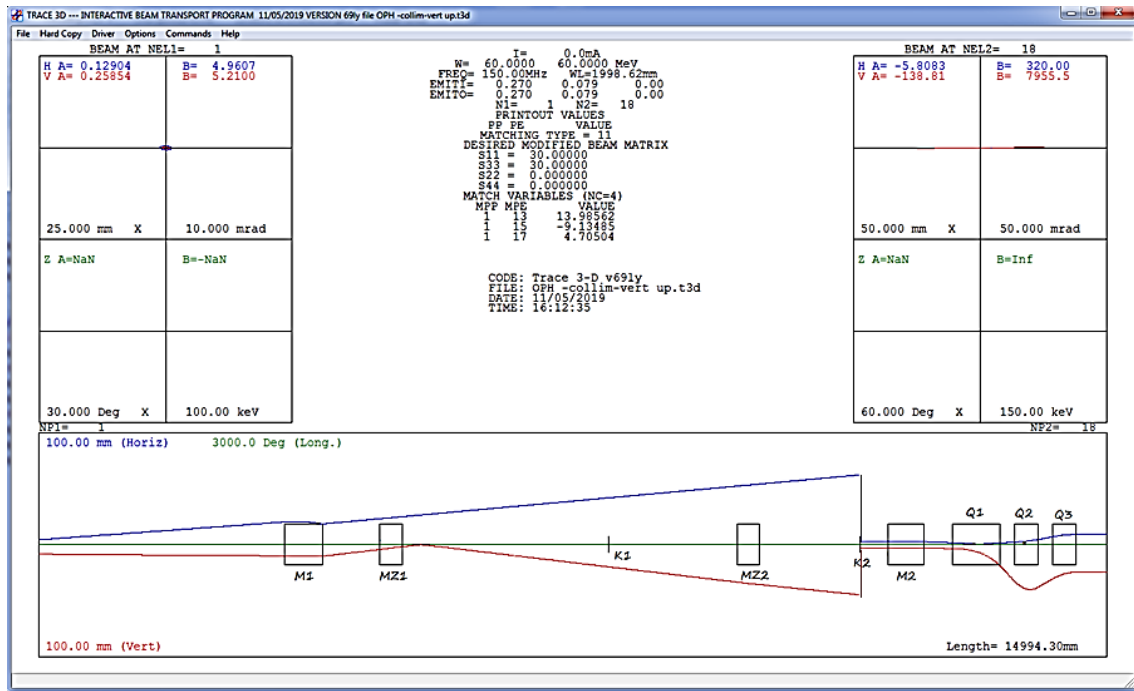


Fig. 4. TRACE-3D optimization calculation results and beam envelopes

References

1. K. Crandall, D. Rusthoi, TRACE 3-D Documentation, LA-UR-97-886, 106 (1997).
2. K.G. Steffen, High Energy Beam Optics (1965).

STRATEGY OF EQUIPPING THE PIK REACTOR EXPERIMENTAL STATIONS WITH DETECTION SYSTEMS

A.G. Krivshich, D.S. Ilyin

1. Introduction

Due to the appearance of new high-intensity neutron sources and new ways of application of high-performance neutron focusing optical systems, the intensity of neutron beams has increased significantly over the past 10–20 years. General technical progress and new ideas implemented into the construction of the experimental stations and creation of new detector systems allowed one to achieve great potential in the field of neutron scattering research, which recently seemed impossible.

The necessity to develop and apply new research methods for both the study of new class objects and the search for solutions of experimental tasks at the highest level requires equipping the PIK reactor instrumental infrastructure with state-of-art neutron detection systems produced in Russia and worldwide. The PIK reactor is being constructed at the PNPI.

The quality of information received within a modern experiment quite often depends directly on practical realization of a complex of interconnected (and sometimes mutually contradictory) maximum attainable characteristics of the detection systems. Namely, these specifications are the following: large registration area, high neutron rate requirements and spatial resolution, low noise level, high performance within the whole required wavelength range of neutrons, very low sensitivity to the background radiation, high stability of functional specifications, low cost and maintainability.

The aim of the present paper is to develop strategies of equipping the PIK reactor experimental stations with the detection systems based on three main factors:

- Analysis of experience accumulated by the leading neutron research centres over the last 40 years;
- Clear understanding of the current state over the last 10 years and ways of practical realization of the development trends of detection technologies;
- Estimation of the global trends of the development of detection technologies and definition of the concept of their further development for the next 10–15 years.

It is clear that the concept of development of neutron detectors for experimental stations of the PIK reactor should be based on the experience of the leading Russian and international neutron research centres, such as ILL (France), J-PARC (Japan), ESS (Sweden), FZ (Jülich, Germany), *etc.*

2. Analysis of experience of world research centres in the field of neutron detector construction

2.1. Over the last 40 years. Analysis of experience of the world research centre ILL, France

In order to produce neutron detectors for the experimental stations of the PIK reactor, it is essential to take into account the world experience, knowledge and achievements of specialists working in the field of development of various types of neutron detectors.

ILL is currently the unofficial world capital of neutron research (<https://www.ill.eu/instruments-support/instruments-groups>). Experience of neutron experiments was accumulated in this Institute for over 40 years with participation of world leading experts from many different countries contributing to it. Unique world-class experimental stations were created, and their parameters were optimized based on simulations and experiments.

According to its purpose, the structure of instrumentation base in the main neutron centres of the world is approximately the same as in ILL. The neutron flux density of the PIK reactor is expected to be similar to that of the high-flux reactor (HFR) at ILL, which essentially makes the PIK reactor a potential future successor of the HFR. For this reason, it would be reasonable to copy both the general instrumentation structure of ILL and appropriate types of neutron detectors, and to apply this knowledge to the PIK reactor installations. Various devices at ILL are brought to perfection, and their parameters are optimized basing on simulations, real testing and experiments.

Classification of the types of detectors used for ILL experimental stations and detection technologies are presented in Table 1.

Table 1

Classification of the types of detectors used at ILL

Detection technology	Type of detector	Amount
Gas-discharge detectors based on ^3He converters	Proportional counter (^3He)	9
	Multidetector and installation based on proportional counter	14
	Single- and multimodule microstrip detectors (micro strip gas chambers – MSGC)	6
	^3He 2D position sensitive detector	10
	Neutron beam monitor	4
	Total	43
Scintillation detectors based on solid-state converters (^6Li and ^{10}B)	Scintillation detector based on ZnS/LiF	2
	Scintillation detector ImagePlates	2
	Total	4

It is obvious that, despite the ^3He deficit, the leading European neutron research centre, ILL, uses detectors with ^3He as a converter gas in the vast majority of its experimental stations (43 out of 47).

2.2. Current status over PAST 10 years. Analysis of experience of the world research centre J-PARC, Japan

The materials and life science experimental facility (MLF) neutron research centre was founded in J-PARC (<http://j-parc.jp/index-e.html>). MLF uses a high-intensity pulsed spallation neutron source generated by the 3GeV proton beam with the current of 333 μA and the operating frequency of 25 Hz.

Implementation of new scientific and applied research programmes required new experimental stations equipped with new detectors. An analysis showed that in order to use ^3He -detectors it would be necessary to acquire more than 10 000 l of this gas. Taking into account the rise of its price, such acquisition will require a serious financial investment – more than 20 million dollars for a period of five years.

Taking into account this reason, it was decided to use scintillation technologies for detectors having the surface of complex geometry and a wide aperture (five stations). In order to comply with the required detector parameters, standard scintillators based on ZnS/ ^6LiF were dismissed in J-PARC and ceramic scintillators based on ZnS/ $^{10}\text{B}_2\text{O}_3$ were put into operation. This allowed one to improve the parameters of existing scintillation detectors with regard to enhancement of their operation speed, efficiency, decreasing their afterglow and so on. With these enhancements, the efficiency of such scintillation detectors achieved about 70% of the efficiency of ^3He -detectors (at 4 bars). This work required creation of a new “scintillation” infrastructure in J-PARC and more than 10 years of hard work. Currently, it can be said that the situation with the application of different types of detectors is balanced in the best way in J-PARC instruments. The proportion of experimental stations with different types of detectors is demonstrated in Fig. 1 (the stations with scintillation detectors are marked with yellow filling and the stations with ^3He -detectors – with red filling) [1]. It is obvious that the majority of detectors used are ^3He -detectors. They are used in order “to cover” large areas, to work in high-intensity neutron-beams – up to $1 \cdot 10^8 \text{ cm}^{-2} \cdot \text{s}^{-1}$, to work with relatively small apertures (up to $300 \times 300 \text{ mm}^2$) when the method of delay line readout is used (with only five channels of registration electronics), which significantly reduces the cost of the detector.

The J-PARC centre is equipped with more than 21 experimental stations, most of which (about 75%) use gas-filled ^3He -detectors.

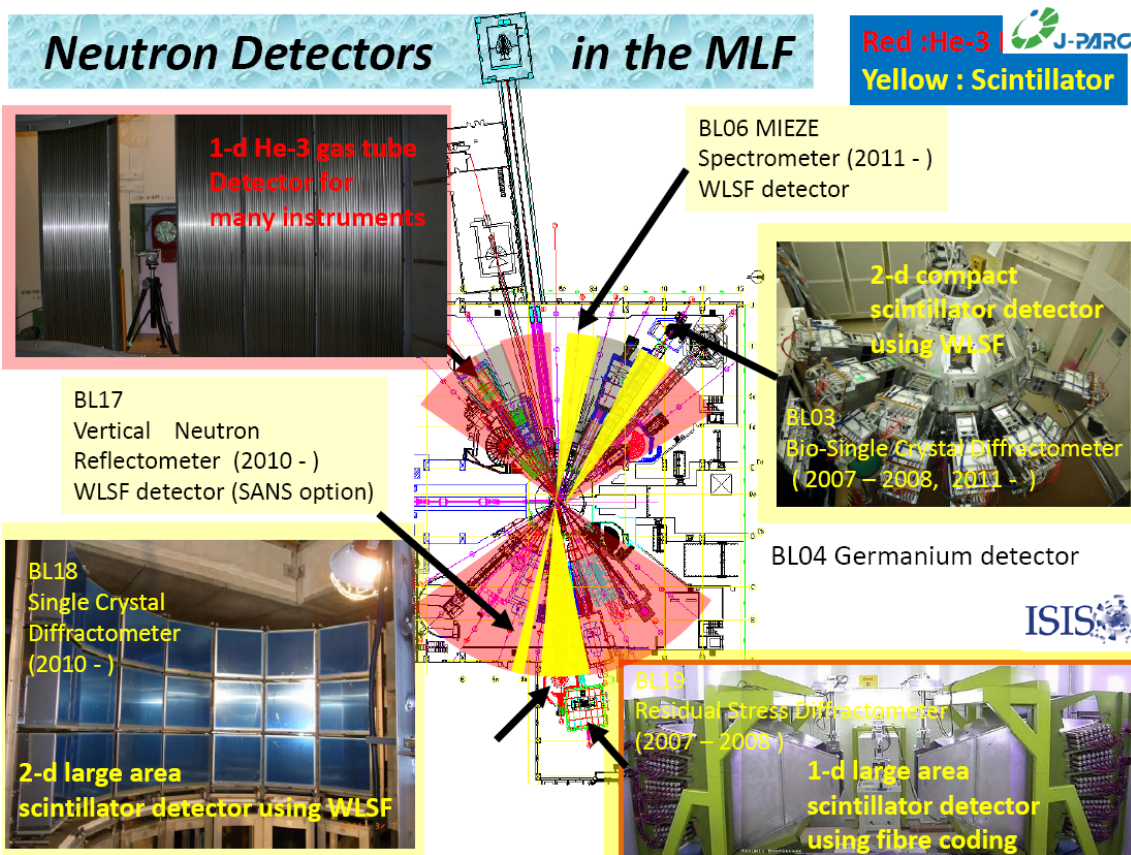


Fig. 1. Location and structure of neutron detectors at MLF experimental stations (J-PARC)

2.3. Estimation of the global trends for the next 10–15 years. Analysis of experience of the world research centre ESS, Sweden

European Spallation Source (ESS) is being actively built in Lund, Sweden. The first neutrons were planned to be generated in about 2020. It is also planned that ESS with its initial suite of experimental stations will be put into operation no later than in 2025. An international expert group was formed in order to perform an analysis of technical requirements for ESS experimental stations and the neutron detectors required for them [2]. The analysis presented here is based on the initial suite of 22 instruments, put forward in the ESS technical design report in 2013.

It appeared that the total area of neutron detectors exceed 280 m². More than a half of the area is reserved for three installations – three chopper spectrometer instruments (80, 50 and 30 m²). The total number of channels of registration electronics is quite large as well, it exceeds 60 000. It is worth noting that only two experimental stations should have the spatial resolution of 0.1 mm. The spatial resolution of other detectors should vary in the range of 1–10 mm, which is possible to achieve with the existing technology. In the course of the analysis, all detectors were divided into four categories according to their registration area: large-area detectors (two stations); high-resolution medium-area detectors (nine stations); small-area detectors with the area of 1 m² and less (nine stations) and ultrahigh-resolution detectors (two stations).

The detectors from the first two categories occupy about 90% of the total area of all the detectors. In order to produce them using the ³He-technology, it would be necessary to acquire more than 25 000 l of ³He, which is quite a large sum with respect to the current European prices – about 50 million dollars. The need to decrease the expenses involved in acquisition of ³He essentially defined the choice of the strategy of the detector production.

1. First two categories of detectors are to be based on detectors that do not use ³He.

2. Small area detectors (the third category) are to be based on the ^3He -detectors with the aim to ensure maximum attainable parameters. Such are 9 of 22 experimental stations (40%).
3. Ultrahigh-resolution detectors can be produced based on scintillation detectors or gas-filled detectors gas electron multiplier (GEM) or micromesh gaseous structure (Micromegas).

Production of detectors that do not use ^3He will be implemented in three basic directions. Their development requires significant financial investments and significant efforts of the international community [3]:

- $^6\text{LiF}/\text{ZnS}$ and $\text{B}_2\text{O}_3/\text{ZnS}$ scintillation detectors with the wave length shifting fibers readout;
- Gas detectors with ^{10}B solid converters;
- Position sensitive gas detectors based on BF_3 .

At ESS, the primary choice for ^3He replacement technology was decided to be gaseous detectors with a ^{10}B solid converter.

On the way to the creation of new detector technologies, there is a lot of open questions and difficult outstanding issues that should be solved for the technical parameters of new detectors to come as close as possible to the parameters of modern ^3He -detectors.

The developers will have to take into account the following parameters: efficiency of new detectors should be equivalent to that of ^3He -detectors; the capability of operating in high-intensity neutron beams; a low sensitivity to γ -background – the key factor for many experiments; an essential reduction of the cost of large area detectors.

2.4. Peculiarities of detector infrastructure in several other world leading scientific neutron centres

2.4.1. Current state of neutron detectors and trends of their development in Russian research centres

The neutron detectors that are currently most widely used in the Russian Federation can be divided into two main categories: gas-filled detectors and scintillation detectors.

Gas-filled detectors. Russian experts made a notice of favourable conditions for production of ^3He position sensitive detectors (PSD) up to $300 \times 300 \text{ mm}^2$ in Russia. The PNPI and Joint Institute for Nuclear Research (JINR) groups are successfully developing and producing such detectors and are experienced in this field. A group from the Institute for Nuclear Research of the Russian Academy of Sciences (INR RAS, Troitsk) works now with such detectors as well. Many years of activity in this direction have allowed one to develop stable technologies for production of gas-filled PSDs. Relative availability of ^3He in Russia and its lower price (in comparison with the global prices) act as a powerful motivation to continue the work with ^3He gas-filled PSDs.

Detection systems based on helium counters operate at the IBR-2M reactor of JINR Laboratory of Neutron Physics (further – LNP) as a part of the experimental stations NERA, SKAT, EPSILON, DN-12, DIN-2PI and at the reactor VVR-M of PNPI. The possibility to measure both coordinates by means of mutually orthogonal cathode planes in a proportional chamber allows one to use 2D PSDs in order to perform measurements using the methods of small-angle neutron scattering. Detectors of this type are used in spectrometers REFLEX, GREINS, DN-2 at LNP JINR and at INR RAS (Troitsk), *etc.*

For neutron beam monitors, low efficiency is needed – typically in the region of a tenth-thousandth of a percent. In order to reach such a low level of detection efficiency, the monitor was filled with a gas mixture of 50 mbar ^3He + 950 mbar CF_4 . The monitor was used to measure the profiles of the IBR-2M reactor beams. N_2 was added to the mixture as a converter-gas in order to be able to work with ultra-high fluxes ($\geq 10^7 \text{ cm}^{-2} \cdot \text{s}^{-1}$).

Scintillation detectors. Scintillation methods are particularly attractive in time-of-flight neutron spectrometers. This is caused by the fact that in scintillation detectors, the detection layer is by an order of magnitude thinner and, consequently, their time-of-flight resolution is better compared to the gas-filled detectors. A higher sensitivity of scintillation detectors to γ -background does not affect the results of time-of-flight experiments. In addition to a high efficiency of thermal neutron registration ($\lambda \leq 1 \text{ \AA}$) and time resolution of less than a microsecond, such detectors are capable of a spatial resolution of about 100 μm .

JINR and PNPI jointly developed a scintillation detector already in the end of 1990s. The design solution was further developed in the RASTR detector for a diffractometer ($\lambda \leq 1,53 \text{ \AA}$, the interplanar spacing resolution being $\Delta d/d = 0.2\text{--}0.3\%$) of the Institute of Metal Physics of the Ural Branch of the Russian Academy of Sciences. The experience of production of modern scintillation detectors gained by LNP JINR is the basis for the future joint PNPI and JINR developments, which will be used at the PIK reactor.

2.4.2. Forschungszentrum Jülich (FZ Jülich, Germany)

FZ Jülich possesses over 30 experimental stations, most of which are at FRM II in Germany, three of which are at ILL, three – at the spallation neutron source (SNS), two – under construction (http://www.fz-juelich.de/jcns/EN/Leistungen/InstrumentsNEW/_node.html). Several instruments are planned as a contribution to the ESS. The majority of these stations are designed for the investigation of processes of elastic (15 instruments) and inelastic (13 instruments) neutron scattering.

The analysis shows that more than 70% of the stations use ^3He -detectors that are implemented as 2D PSDs (with the aperture – up to $500 \times 500 \text{ mm}^2$, the spatial resolution – 2 mm) and proportional counters (from 100 to 1 000 mm long).

2.4.3. Brookhaven National Laboratory (BNL, USA)

BNL no longer has a research reactor, but implemented previously a research development programme focused on creation of high-precision thermal neutron PSDs and equipped with them the experimental stations of national research centres (USA), in particular for the SNS for structural biological and chemical research (http://www.inst.bnl.gov/programs/gasnobledet/neutrons/neutron_brochure.pdf).

All the BNL detectors are ^3He -detectors based on proportional chambers with the data readout from cathode strips.

2.4.4. Some other centres

In other centres, for instance Rutherford Appleton Laboratory (RAL, UK) at the spallation neutron source ISIS or Oak Ridge National Laboratory (ORNL, USA; SNS and the HFIR reactor), the correlation of gas-filled and scintillation detectors is a little more balanced. RAL successfully used scintillation technologies for neutron registration. The higher importance of the time resolution at a pulsed spallation source, along with the better efficiency for lower wavelength neutrons, is the primary motivation behind the higher fraction of scintillator detectors for spallation sources.

3. Final analysis of the global trends of neutron detector development

Basing on the analysed experience of the most significant Russian and international neutron research centres and on their development trends drawn out in the course of the analysis (some of them were mentioned above), one can propose a strategy for development of neutron detectors and equipping the experimental stations of the PIK reactor. The results of the analysis and prediction of the detection technology development based on it demonstrate clearly the development strategies of neutron detectors over the period of more than 60 years (40 years of past + “the current” period of the last 10 years + about the next 10 years of the future) based on three main international neutron centres.

1. Using the example of the ILL experimental stations, an analysis of the neutron detector structure established over the last 40 years is presented.

In the course of these 40 years, unique world-class experimental stations were created, and their parameters were optimized based on simulations and experiments. The absolute majority of detectors (90%) are gas-filled devices using ^3He as a neutron converter.

2. The current state and practical implementation of the “current” development trends of detection technologies (over the last 10 years) were analysed on the example of the MLF centre operating as part of the neutron research centre at J-PARC (Japan).

About 75% of the detectors are gaseous detector devices using ^3He as a neutron converter. Implementation of new scientific and applied programmes required creation of new complex experimental stations (five units) equipped with the detectors based on scintillation technology.

3. The estimation of the global trends of the detection technology development and generation of their development strategies (for the next 10 years) were considered based on the baseline ESS instrument suite from the technical design report as an example.

Small-aperture detectors (1 m² and less) are in many cases planned to be produced based on the ^3He -technology. Such are 9 of 22 experimental stations (40%).

Nine more detectors (40%) having medium and large aperture (from 1 to 80 m²) will be created based on the following technologies: scintillation detectors and gaseous detectors based on the ^{10}B solid converter. It is assumed that for the next 5–7 years these technologies will reach such a level that their parameters can come close to those of ^3He -detectors.

So, the gas-discharge ^3He -detectors will be the basic development direction at least for the next 10 years. This is connected with the outstanding combination of properties of the detectors using ^3He as a neutron converter, which defined the inclination of neutron centres towards the use of such detectors for their experimental stations throughout their history.

A transition to different detection technologies based on ^6Li and ^{10}B converters that are being currently developed is mostly caused by the necessity and has the aim to reduce the cost of devices by means of abandoning the use of ^3He in large volume detectors. At the same time, it should not cause an intention to upgrade all the detector knots of the instruments, since, on the one hand, it would require a significant financial investment, and on the other hand, it would guarantee a change of a number of characteristics of devices for the worth: registration efficiency, spatial resolution, γ -background sensitivity and so on.

It is necessary to perform a detailed and thorough analysis of applicability of different detection technologies to a specific physical task, to a specific physical instrument. For instance, scintillation detectors are effective in the cases when it is necessary to achieve a high spatial resolution ($\approx 100 \mu\text{m}$) and to build a complex geometry shape of the registration surface.

4. Analysis of the issue of ^3He deficit

An analysis of the ^3He demand for the equipment of neutron detectors operating as a part of the neutron scattering research at large international neutron centres has been presented (<http://dx.doi.org/10.1080/10448632.2012.725325>, <http://www.tandfonline.com/doi/full/10.1080/10448632.2012.725325>) see Table 2. It should be noted that this is a minimum estimate of a global ^3He demand. For instance, Table 2 does not include the information of ESS detectors requiring more than 25 000 l of ^3He .

Based on the comparative analysis of the data presented in Table 2, it is possible to state that the demand of experimental facilities of the PIK reactor for ^3He is relatively small, around 900 l, which is a great deal less than the amount required by any more or less significant national or international centre.

One can see (Tables 3 and 4) that about 70% of neutron detectors are ^3He -detectors, which corresponds well with the global development trends. The cost of ^3He for the PIK reactor is relatively low (one-time investments of ~ 0.9 million dollars USA) and the advantages gained by the PNPI international neutron research centre based at the PIK reactor are positively significant. Such as:

- Detectors based on ^3He have a generally accepted unique complex of performance characteristics;
- PNPI already possesses technologies necessary for development and production of neutron detectors with aperture of up to $300 \times 300 \text{ mm}^2$ (and larger), which guarantees compliance with the complex of requirements for modern neutron detectors. It does not require significant financial investment in technology. A technological modernization would be necessary due to creation of detectors with aperture of $1\,000 \times 1\,000 \text{ mm}^2$;
- There are almost no sources of ^3He acquisition in Europe, and its price there is rather high;
- For this reason, the European scientific community is actively searching for alternative neutron converters and conceptually new construction ideas in order to create detectors that could replace ^3He detectors.

^3He is available in Russia, and its price is several times lower than the European one. For this reason, detectors based on ^3He are our competitive advantage over Europe, which certainly should be used to the fullest extent.

Table 2

Analysis of ^3He demand in the leading neutron centres of the world

Neutron centers	Exploitation of detectors and research, l/year	New small-aperture detectors, l	New large-aperture detectors, l
ORNL (SNS)	100	1 300	25 000
ORNL (HFIR)	100	1 210	2 500
Los Alamos	100	1 994	12 362
NIST	100	560	40
BNL	50	180	–
FRM II	100	650	4 500
HZ Berlin	100	520	7 850
ILL	100	1 000	3 000
JCNS	40	15	7 200
LLB	50	600	600
PSI	50	–	2 000
STFC	100	400	11 300
J-PARC	100	40	16 100
JRR-3	31	71	–
KAERI	150	–	2 000
CSNS	200	–	21 000
Total	1 431	8 540	115 372
The PIK reactor	10	900	0

Table 3

Types of detectors proposed for applications at the PIK research complex and their quantity

Device / detector	Gas neutron converter (^3He)		Solid neutron converters (^6Li and ^{10}B)	
	Proportional counter and 2D-module based on LPSC counter	2D position sensitive detector	Scintillator	Solid-state detector
Powder diffractometer	3 (D1, D2, D3)	–	–	–
Crystal diffractometer	–	3 (DC1, DC3, DC5)	3 (DC3, DC4, DC6)	–
Inelastic scattering spectrometer	2 (IN4)	1 (IN2)	3 (IN1, IN3, IN5)	–
Small-angle instrument	2 (S2, S3)	3 (S1, S4, S5)	–	–
Reflectometer	4 (R1–R4)	4 (R1–R4) 2 (R2, R3)	–	–
Total number	11	13	6	–

Table 4

Detectors operating in neutron beams of different intensity at PIK

Intensity of neutron beams, s^{-1}	Experimental station	Number of detectors, un.	Detector technology
Up to $1 \cdot 10^5$	S1	1	2D PSD (^3He)
	D2, IN2, IN4 (2 un.)	3	^3He proportional counter and LPSC
	IN1, IN3	2	Scintillators
Up to $1 \cdot 10^6$	DC1–DC5, DC7, S3, S4, S5, R1, R2, R3, R4	12	2D PSD (^3He)
	D1, D3, S2, R1–R4	7	^3He proportional counter and LPSC
	DC3, DC6, IN5	3	Scintillator
Up to $1 \cdot 10^7$	Beam monitor (R2, R3)	2	2D PSD (^3He -technology)
	None	0	^3He proportional counter and LPSC
	None	0	Scintillator
–	Total	30	–

5. Analysis of the PIK reactor planned instrumental facility and recommendations on equipping the experimental stations with neutron detectors

An analysis of the PIK reactor instrumental facility with regard to compliance of the neutron detectors with all the required operation parameters has been performed based on the information on detectors and strategic trends of their development in the leading neutron research centres of the world and analogous centres in Russia [4].

Detectors that are planned to be used at the experimental stations of the PIK reactor are listed in Table 3. Requirements for the loading capability of detectors with ^3He -converter are presented in Table 4. The background level and the γ -background sensitivity are stated as the maximum loading capability/background count of $\geq 10^6$ and the minimum possible sensitivity to the γ -background ($< 1 \cdot 10^{-7}$).

It is clear from Tables 3 and 4 which detection technologies should be given a high priority for the development at PNPI.

^3He detection technologies necessary for equipping the majority of experimental stations of the PIK reactor either exist at PNPI or can be produced there since there are technological capabilities for their development and realization.

1. PNPI already possesses technologies necessary for development and production of neutron detectors with aperture up to $300 \times 300 \text{ mm}^2$ (and larger), which comply with the requirements of the current physical experiments (Fig. 2). Creation of such detectors does not require now any significant financial investments in their development stage. Based on these technologies, one can fabricate ^3He -detectors of different structural variations including the capacity to operate in vacuum.
2. Beam intensity: up to $1 \cdot 10^6 \text{ s}^{-1}$. For the existing 2D PSD ^3He -detectors to be able to work in intensive neutron fields, it is necessary to change the data readout method from a delay line readout to channel-by-channel readout from the cathode strips.
3. Beam intensity: up to $1 \cdot 10^7 \text{ s}^{-1}$ and higher. If the experiment requires the detector to operate in a counting mode with efficiency close to 100%, then it is necessary to perform a detailed analysis of new detection technologies such as, 2D linear position sensitive counters (LPSC), GEM-technology, pad-structural gas-discharge detectors, scintillation detectors, etc.
4. Neutron beam monitors have a very low efficiency, which allows them to work in neutron beams of very high intensity ($1 \cdot 10^8 \text{ s}^{-1}$).

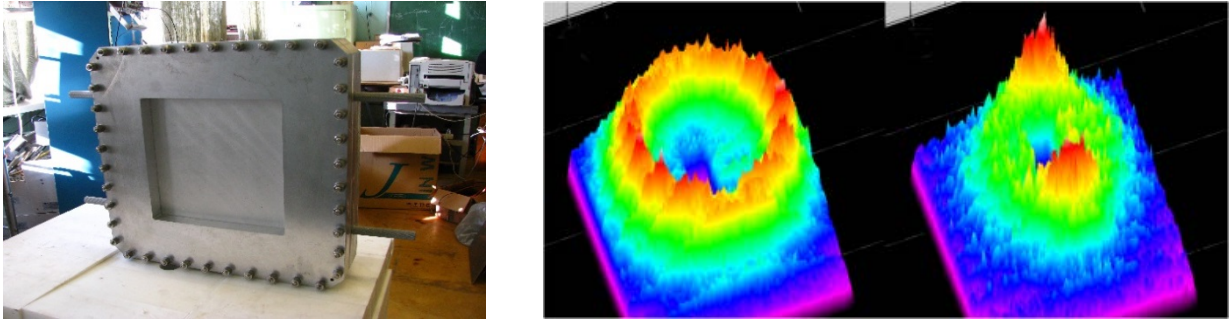


Fig. 2. Neutron detector (*left*); asymmetric scattering of neutrons on a fluoroplastic film before its deformation and after (*right*)

In order to create 2D detectors with aperture of $1\,000 \times 1\,000\text{ mm}^2$ based on LPSC, it is necessary to update the technological line, to develop prototype models and registration electronics.

The production of banana-type detectors based on LPSC-technologies (or microstrip gas chambers) requires a separate development.

Special attention should be paid to the development of scintillation detection technologies: the PIK reactor experimental stations are not yet fully equipped with such technologies, which are being actively developed in the world and have their own technological niche, such as:

- Fabrication of wide-aperture detectors of complex geometry;
- Neutron beam monitors;
- Practical applications of neutron tomography requiring the creation of detectors with high spatial resolution at the level of 0.1 mm (and higher), *etc.*

Taking into account the insufficient technological potential existing at PNPI in this field and quite significant financial investments needed to be done in the future, it is necessary to join efforts and support the joint activities of the developing collaboration of PNPI, JINR and INR RAS aimed at the applied development of scintillation technologies.

Neutron imaging for the purposes of tomography and radiography is a separate research field that is widely developing in modern sources, but is still not listed among the PIK reactor research stations.

The most advanced installations for neutronography and neutron tomography in Europe are located at the FRM II reactor in cold and thermal neutron beams and at the PSI – cold and thermal neutrons. The analogs are put in operation at the National Institute of Standards and Technology – NIST (USA).

Currently, the development of this field is possible only with the development of scintillation technologies.

6. Conclusion

An analysis of the PIK reactor instrumental facility with regard to compliance of the neutron detectors with all the required operation parameters has been performed based on the information on detectors and strategic trends of their development in the leading neutron research centres of the world and analogous centres in Russia over the period of more than 60 years (40 years of past + “the current” period of the last 10 years + about the next 10 years of future). We have come to the conclusion that the global trends for the next 10 years of creation of new neutron detection technologies are developing in several main directions (they are arranged in priority order):

- Modernization and development of gas detectors based on ^3He neutron converters;
- Development of gas detectors based on ^{10}B solid converters;
- Development of scintillation detectors based on spectrum-shifting optical fibers;
- For specific cases another type of detectors, such as GEM, Micromegas, solid state semiconductor detectors and so on.

Despite the high price of ^3He , a global neutron community still considers gas-discharge ^3He -detectors to be the basic development direction, first of all, for the detectors with aperture of up to 1 m^2 . The reason for

this is a unique combination of such properties as high efficiency for neutron registration and low γ -background sensitivity.

A possible transition to different detection technologies based on ^6Li and ^{10}B converters, which are being currently developed in Europe, is mostly caused by necessity and has the aim to reduce the cost of devices by means of abandoning the use of ^3He in large and medium volume detectors with aperture from 1 to 80 m² and larger.

He-3 detection technologies. These technologies necessary for equipping the majority (about 70%) of experimental stations of the reactor PIK either exist at PNPI or can be produced there, as there is a technological capability for their development and realization. The aperture of these detectors does not exceed 1 m² and consequently they do not require a large amount of ^3He (about 900 l). ^3He is available in Russia, and its price is several times lower than that in Europe. For this reason, detectors based on ^3He is Russia's competitive advantage over Europe, which certainly should be used to the fullest extent.

Scintillation detection technologies. Groups of experts professionally working with scintillation detectors and having some interesting activities have been formed at PNPI, JINR and INR RAS. The greatest experience in development of large-area ZnS(Ag) scintillation detectors was accumulated by JINR (LNP). Several such detectors have been created there and are successfully put into operation at some Russian scientific centres. In order to succeed with any further activity in this area, it is necessary to join efforts of at least three Russian scientific centres, and it is reasonable to base this joint activity on the experience of JINR (LNP) developments.

To perform a detailed and thorough analysis of applicability of different detection technologies (today's and future) and to guarantee the best realization of its advantages, its competitive strengths in comparison with other neutron sources in Russia and abroad, it is important to organize a fruitful collaborations between PNPI and the world leading scientific centres such as: ESS (Sweden), ILL (France), FZ Jülich (Germany), J-PARC (Japan).

In the process of development of the neutron detector technique, it is necessary to apply widely the ideas and technologies developed for charged-particle detectors in high energy physics (and other research fields). It is necessary to strive for unification of the equipment used and ready-made technological solutions. It is also reasonable to develop a unified detection electronics for the detection systems, as well as electronics for data accumulation and processing. It is necessary to standardize interfaces and software at a lower level.

Acknowledgements

Special thanks for our colleagues from JINR (Dubna, Russia) and from PNPI HEPD and NRD (Gatchina, Russia) for their fruitful discussions and assistance during preparation of this article.

References

1. K. Soyama, Basic Energy Sciences Neutron & Photon Detector Workshop (2012).
2. S. Peggs *et al.*, European Spallation Source Conceptual Design Report, ESS-2012-001 (2012);
S. Peggs *et al.*, European Spallation Source Technical Design Report, ESS-2013-001 (2013);
O. Kirstein *et al.*, PoS (Vertex2014) 029 (2014), arXiv:1411.6194.
3. Int. Collab. on Neutron Detectors, <http://icnd.org>;
K. Zeitelhack *et al.*, Neutron News **23** (4), 10 (2012);
T. Wilpert, Boron Trifluoride Detectors, Neutron News **23** (4), 14 (2012);
B. Guerard *et al.*, ^{10}B Multi-Grid Proportional Gas Counters for Large Area Thermal Neutron Detectors, Neutron News **23** (4), 20 (2012);
N.J. Rhodes, Scintillation Detectors, Neutron News **23** (4), 26 (2012).
4. A. Krivshich *et al.*, Reactor Complex PIK, Vol. II. Scientific Background for a Complex of Experimental Stations at the PIK Reactor, Detectors for the PIK Reactor Experimental Stations, 164 (2014).

PROTON ARM SPECTROMETER FOR THE R³B SET-UP AT FAIR

G.D. Alkhazov, V.A. Andreev, V.L. Golovtsov, D.S. Ilyin, A.G. Inglessi, V.Yu. Ivanov, N.N. Filimonova, L.M. Kochenda, P.A. Kravtsov, A.G. Krivshich, D.A. Maysuzenko, A.V. Nadtochiy, I.N. Parchenko, S.S. Volkov, L.N. Uvarov, V.I. Yatsura

1. Introduction

The R³B (reaction studies with relativistic radioactive beams) experimental facility for the study of reactions with relativistic radioactive beams is part of the FAIR project. The goal of the R³B Collaboration is to develop and create a universal reaction set-up with high efficiency, acceptance and resolution for kinematically complete measurements of reactions with high-energy radioactive beams. The installation will be located in the focal plane of the high-energy branch of the super fragment separator (Super-FRS). The installation is adapted to the highest beam energies up to 1 GeV/nucleon provided by the Super-FRS, which ensures the maximum possible transmission of secondary beams. The R³B facility will cover experimental studies of reactions with exotic nuclei that are far from stability, which will allow implementing a broad physical program with beams of rare isotopes with an emphasis on the structure and dynamics of nuclei. The work is carried out within the R³B Collaboration, which includes more than 50 different institutes from around the world. To cover such a large physical program, several different tracking detection subsystems are provided (Fig. 1a). One of these systems will be a spectrometer for determining the momentum of emitted protons with energies up to $E_p = 500\text{--}900$ MeV. Unstable nuclear beams formed by the Super-FRS hit a secondary target, the reaction products being magnetically analysed with the superconducting magnet GSI large acceptance dipole (GLAD). Protons emitted in flight from excited fragments are bent in the GLAD and tracked using the dedicated proton arm spectrometer (PAS), which creation is the subject of responsibility of PNPI.

In 2016, the FAIR scientific council approved the PAS detector design and concept proposed by the Tracking Detector Department (TDD) of the HEPD [1]. The TDD proposal calls for the PAS facility to be based on thin-walled drift tubes (DT), which have a small material budget ($X/X_0 \approx 0.05\%$ per tube) and operate in vacuum. PAS will consist of four straw tube walls (STW), two walls for horizontal (X1&X2) and two walls for vertical (Y1&Y2) particle coordinate detection. A schematic arrangement of the PAS STWs, which are placed on a moving platform inside a vacuum chamber, is shown in Fig. 1b.

Each STW of the PAS will consist of three layers of straw tubes filled with a gas mixture at an overpressure of about 1 bar. The tubes are glued together, each layer being shifted by one tube radius with respect to the previous layer. In this way, for an orthogonal proton track, a lower detection efficiency close to the tube wall is always combined with a high efficiency in the centre of the straw in the following (staggered) layer. Also, the track's left/right ambiguity from the wire can be disentangled in the next layer.

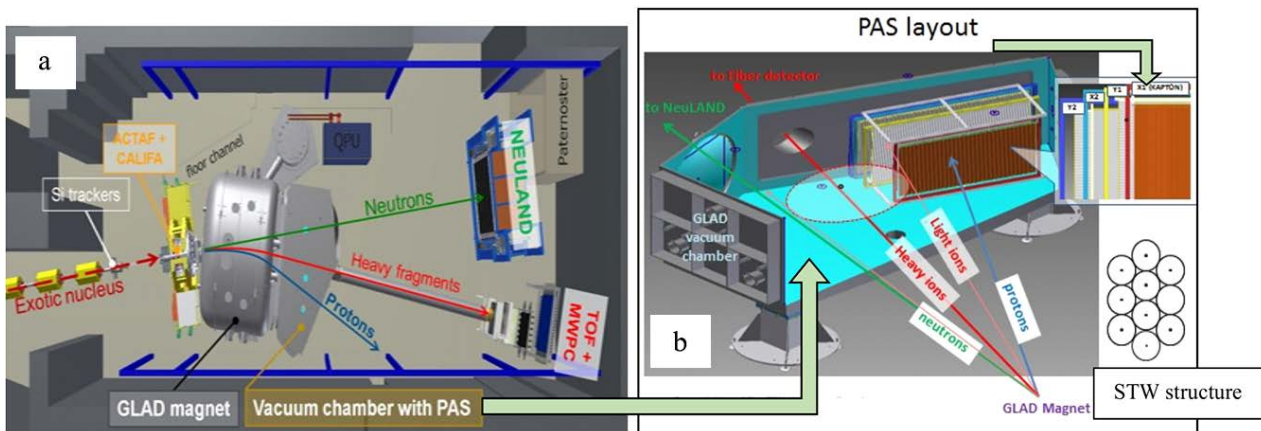


Fig. 1. R³B set-up (a); proton arm spectrometer lay-out (b)

As follows from the technical requirements, the PAS installation must have a minimum amount of substance to ensure small angular straggling of the passing particles. First of all, this requirement applies to the first STW-X1. Therefore, it was decided to make this plane from Mylar tubes with a wall thickness of 60 μm , and the other three planes from ultrathin aluminum tubes with a wall thickness not exceeding 300 μm . Although the angular straggling caused by these tubes is larger compared to the thin Mylar tubes, their influence on the angular resolution is small since they are located near the end of the track.

The front-end electronics is placed in vacuum close to the straw-tube detectors for optimum performance in terms of noise. The PAS infrastructure, such as the gas supply, high-voltage (HV) and low-voltage (LV) power supply will be located outside the vacuum chamber. The technical requirements for the PAS spectrometer were discussed in more detail in the previous edition of HEPD Main Scientific Activities.

2. Drift tubes technology at Tracking Detector Department

A thorough search showed that there is no production of aluminum tubes with such parameters in Russia. A similar production was found in Switzerland and Germany, however, the minimum wall thickness of European pipes is 400 μm . As a result, the company MedSpetsTrub LLC was found, which agreed to develop and debug the necessary tube technology on the basis of its production. Within three years, with the direct participation of experts from the TDD, a technology was developed for the production of tubes from aluminum alloys AMg-5 and AMg-6 with a wall thickness of 220–240 μm [2].

Below are the main technical parameters of the tubes manufactured by this technology [3]:

- Inner diameter – 9.50–9.70 mm;
- Wall thickness – 0.22–0.24 mm;
- Uniformity of the inner surface $R_a \approx 0.32 \mu\text{m}$;
- Straightness of tubes is not worse than 150 μm per one metre of length;
- Tube material corresponds to aluminum alloy Amg-5;
- The tube leak is on the level of no worse than $5 \cdot 10^{-6} \text{ mbar} \cdot \text{l/s}$.

On the basis of that technology, about 2 800 aluminum tubes (with a length of 2 750 mm) for the PAS spectrometer were manufactured. These tubes have passed through the output quality control (OQC) at the company (MedSpecTrub LLC) and the input quality control (IQC) at the TDD PNPI [2]. The mandatory incoming inspection of each tube included: visual inspection (the tube was rejected if any defects were found); mechanical machining of the tube ends; pressure steam washing; checking geometric parameters; checking the tube vacuum strength at overpressure of 4 bar.

After successfully passing through the IQC, the tube was cut out to the required length. Then this tube was used to manufacture the drift tube, which has its own procedure of certification including: gluing and checking of end pieces, leak test on a straw leak test station (SLTS) and HV tests with radioactive sources (^{55}Fe and ^{90}Sr) [3].

At the moment, about 1 400 drift tubes have passed through certification. Three prototypes and two working planes (STW-X2 and STW-Y2) for PAS were assembled from them. The gas leaks of these tubes did not exceed $2 \cdot 10^{-6} \text{ mbar} \cdot \text{l/s}$, which is an order of magnitude better than required.

3. The choice of the gas mixture for proton arm spectrometer

This activity was based on GARFIELD simulations of the drift tubes. The operating characteristics of a gaseous detector are highly dependent on the gas mixture. One can select it for one or more of the following criteria: stability; low tendency to spurious discharges; good detection efficiency; high amplification; the drift velocity can be either slow (for good position measurement) or fast, for small dead time; non-flammability for safety; low diffusion for better time and space resolution; minimum aging effects for longer operational life of the detector.

As a result of Monte Carlo modeling of PAS drift tubes functioning in the GARFIELD program package, 70% Ar + 30% C_2H_6 was selected as a working gas mixture. It was used in tests of both prototypes and directly in the PAS STWs.

4. Proton arm spectrometer prototyping

These works were performed to test the PAS technology, to determine the diameter and length of the anode wire, to investigate the drift tube behaviour under different pressures (1–3 bar). Three prototypes were assembled and tested: prototype 1 (X2, length – 1 000 mm), prototype 2 (Y2, length – 2 500 mm) and prototype 3 (length – 300 mm).

Prototype 1. We have fabricated and tested the detector module, structurally corresponding to the STW-X2. This detector performance was studied at PNPI with a β -source ^{90}Sr and a photon source ^{55}Fe , as well as a high-energy (600 MeV/u) beam of carbon ions at GSI. The gas mixture Ar + 30% C_2H_6 was used. A general view of the prototype 1 and its location on a carbon beam at GSI is shown in Fig. 2a. The space structure of the beam and its halo were measured, the time spectra of the drift tubes were obtained, and algorithms for event selection were worked out [4, 5].

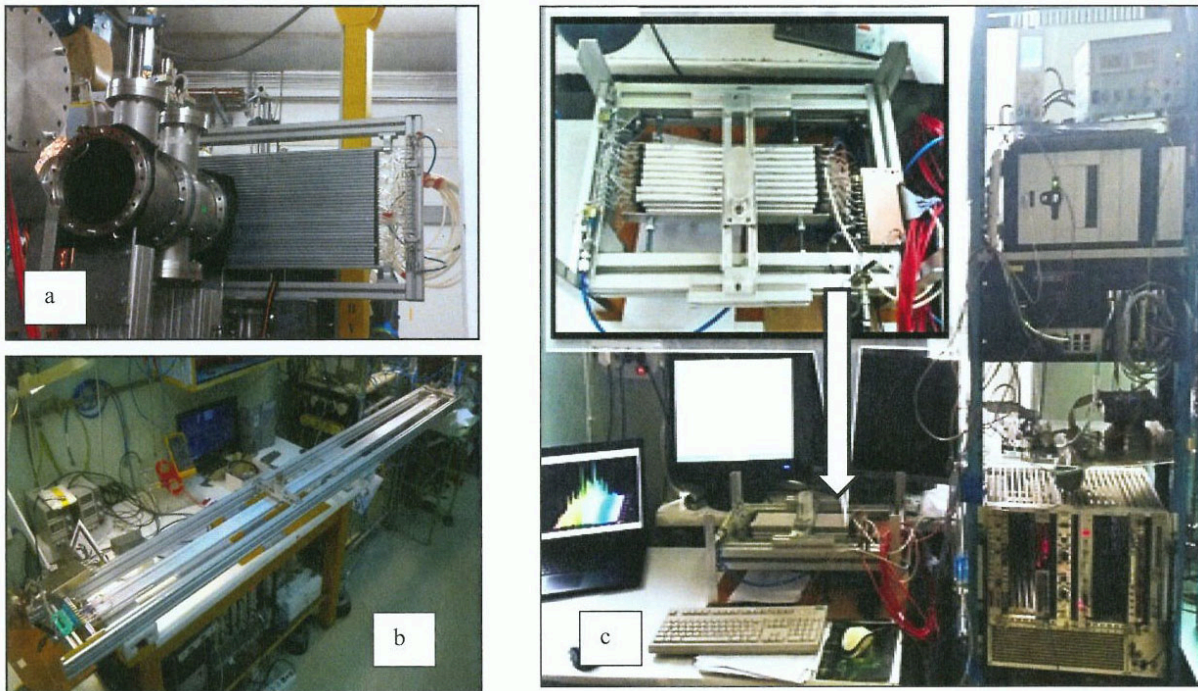


Fig. 2. Prototype 1 testing on a carbon beam at GSI (a); prototype 2 testing at PNPI (b); prototype 3 as a part of the proton arm spectrometer test station (c)

Prototype 2. We have fabricated and tested the detector module with the length $L = 2\,500$ mm, which is larger than the tubes in the longest plane STW-Y2 ($L = 2\,180$ mm). In addition, some of the drift tubes had anodes with different diameters – 30 and 35 μm with and without a special support. The operation of the detector with electronics was tested at a working gas pressure of 1–3 bar and different deformation of the drift tube [5].

Prototype 3. It was used to test the front-end electronics modules DT_ASD16 (amplifier/shaper/discriminator) and to study their interaction with the R³B data acquisition system using a special test station (Fig. 2c). The test station includes: a time-code converter (CLK-TDC-128) with a control personal computer (PC) and an auxiliary module EXPLODER, four DT_ASD16 modules with a drift-tube unit, a server PC for remote operation with the test station, LV and HV power supplies (LVPS, HVPS).

Based on the results of our research, the following conclusions were made: the diameter of all PAS anodes will be the same and equal to 35 μm ; the anodes of the drift tubes work confidently without special supports at pressures of 1–3 bar; the allowable deformation of the tubes is 300 μm [5].

5. Construction and testing of X2 and Y2 planes

A general view of the X2 and Y2 planes is shown in Fig. 3. (Note that in this paper we use symbols ST wall and ST plane, which are identical to each other.) In the upper right corner of the plane X2 one can see preamplifiers (two preamplifiers on each side) which are mounted on both sides of the frame.

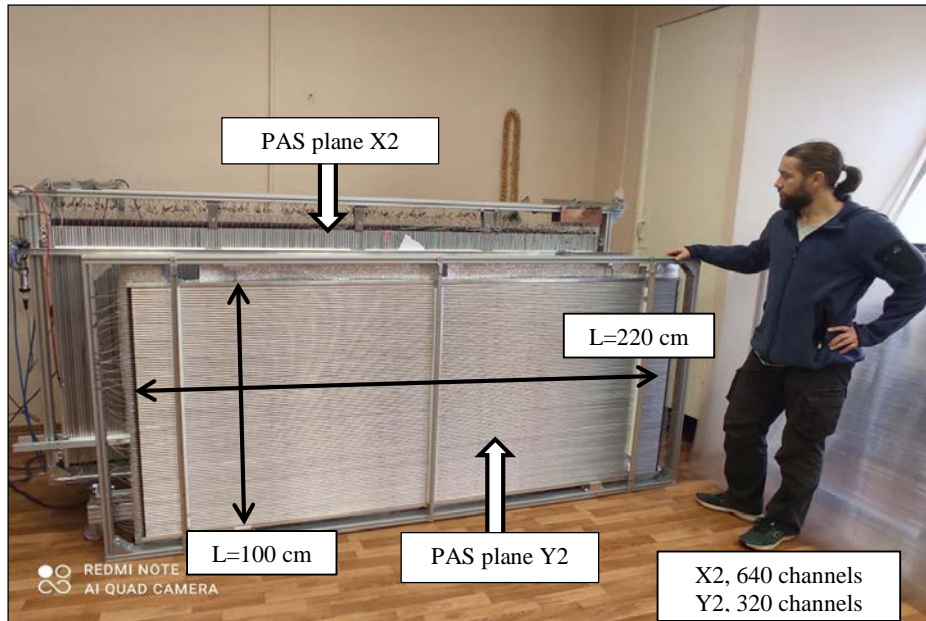


Fig. 3. General view of two proton arm spectrometer planes (X2 and Y2)

All drift tubes were tested for the vacuum leak (Fig. 4a) and after that their current and counting characteristics were measured. The tubes selected in this way were glued together in three layers by a specially developed technology and placed in a frame for the PAS spectrometer. The distance between the drift tubes for each of the planes was measured and shown in Fig. 4b. It is seen that the absolute position of these tubes in space has no deviation, and the accuracy of their positioning will be $10\,250 \pm 30 \mu\text{m}$, which is 2 times better than the technical requirements.

The vacuum leak was measured independently for each drift tube and plane. Since we do not have a vacuum chamber of sufficiently large dimensions, the gas leak rates were tested at a pressure much higher than the atmospheric pressure (not less than 2 bar). As a result, the gas leakage rates were tested at the following gas pressures:

- Hydrotesting of drift tubes $P = 4$ bar;
- Gas tests of drift tubes $P = 3$ bar;
- Gas tests of the plane from drift tubes $P = 2$ bar.

The pressure and temperature in the planes were recorded during seven days. The data obtained for the X2 and Y2 planes are shown in Fig. 4c. The temperature was practically constant in the range $22\text{--}25^\circ$, and so the density of the gas inside the tubes depended only on the behaviour of the pressure. As one can see, the pressure dropped down from 2 to 1.1 bar in X2 during $(74 - 16) / 24 \text{ h} = 2.4$ days and in Y2 during $(135 - 28) / 24 \text{ h} = 4.5$ days. These are upper estimates! The obtained data on the leak level in the planes differed by a factor of about two, which corresponded to the number of drift tubes in the X2 and Y2 planes. This allows us to state that the gas leaks in the planes are mainly associated with the gas connections between the tubes, and they are rather small.

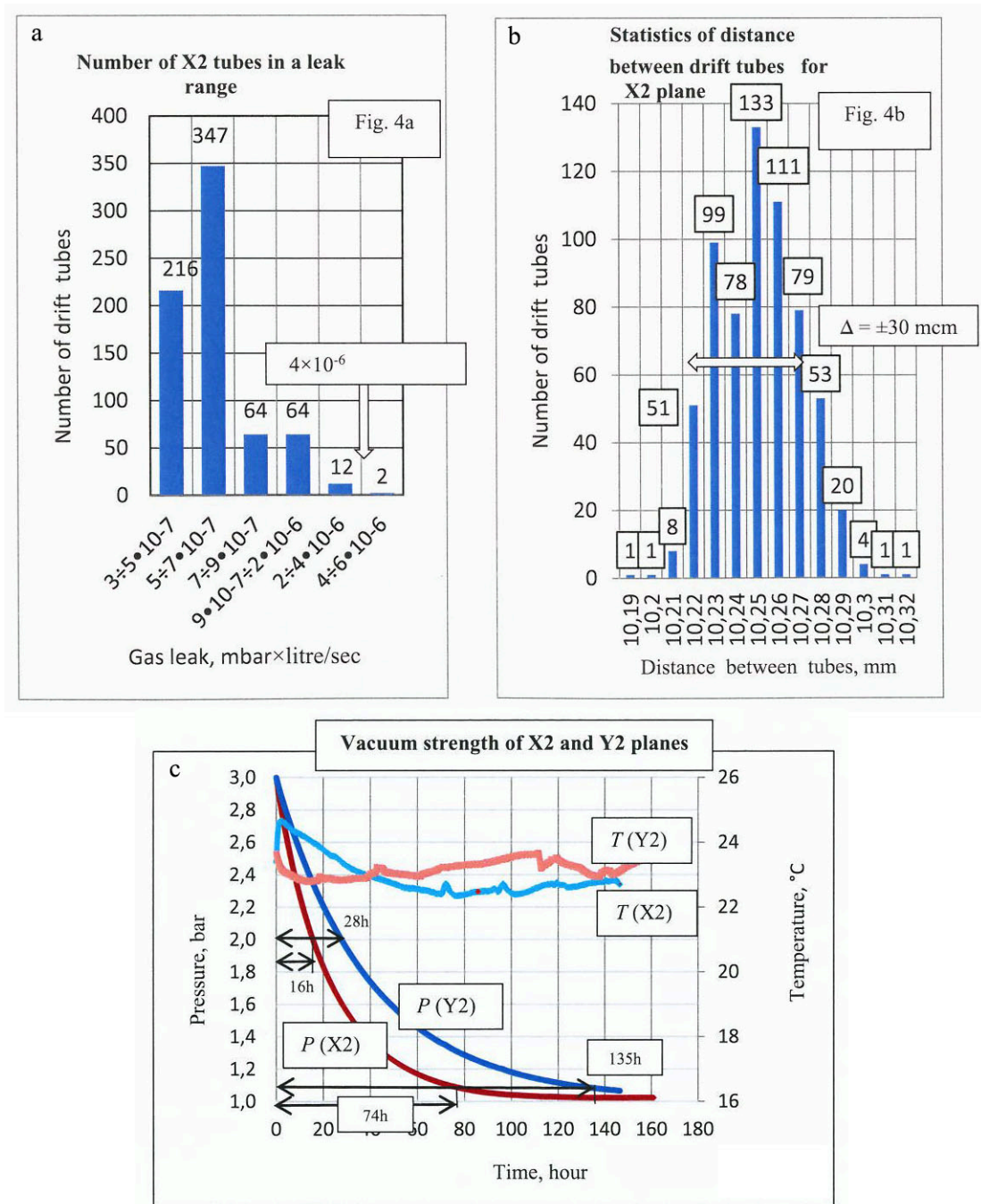


Fig. 4. Number of X2 tubes in a leak range (a); statistics of distance between drift tubes in STW-X2 (b); plane's pressure and temperature time behaviours (c)

6. The straw leak

To investigate the straw leakage, two methods were used by us. The first method was implemented on the basis of the straw leak test station (SLTS, Fig. 5) and answered the question of the gas leakage rate into vacuum. It had high sensitivity and allowed us to select drift tubes with small leakage. The second method was based on the behaviour of the tube in water. It had a slightly lower sensitivity, but it allowed to accurately spot the place where the leak occurred. By combining both methods, it was possible to efficiently select drift tubes with no leakage to vacuum under an absolute pressure of 4.0 bar. We worked with tubes leaking up to $4 \cdot 10^{-6}$ mbar · l/s.

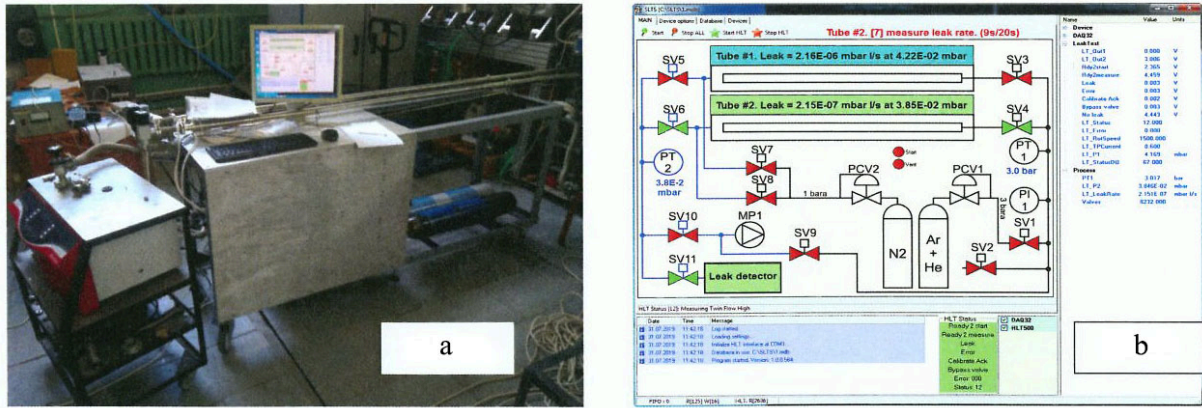


Fig. 5. Straw leak test station (a); straw leak test station software main window (b)

The main task of the SLTS was to measure the leak rates from the straw drift tubes into vacuum. The parameters of the system are listed below: the leak rate sensitivity – $\sim 1 \cdot 10^{-8}$ mbar · l/s; the straw working gas mixture – Ar + 8% He; the absolute pressure range was 0.5–5.0 bar; the maximum straw length was 3 m. The system was mounted in a special bench with two vacuum cartridges and a control console on top of the bench. All valves, a vacuum pump and gas cylinders were located inside the bench.

7. Proton arm spectrometer gas supply system

The main task of the gas system (Fig. 6a) is to provide a pure (70% Ar + 30% C₂H₆) mixture to the PAS detector at the chosen operating pressure. The gas supply system works in flushing mode, with the total flow rate of up to 4 litres per minute. The absolute pressure in the straw tube walls is stabilized in the range 1–3 bar with ~ 1% accuracy. The oxygen and moisture concentration in the mixture is kept at the 5 ppm level.

The wiring of the control and gas panels was finished. All sensors and control devices were checked. The control software of the gas system is shown in Fig. 6b. The software package consists of the main control program, the CHARTS program for online parameters visualization, the DBVIEWER program for handling the databases with the gas system parameters. The pressure stabilization in X1 plane (PT4) and in X2, Y1, Y2 planes (PT5) is shown in Fig. 6c.

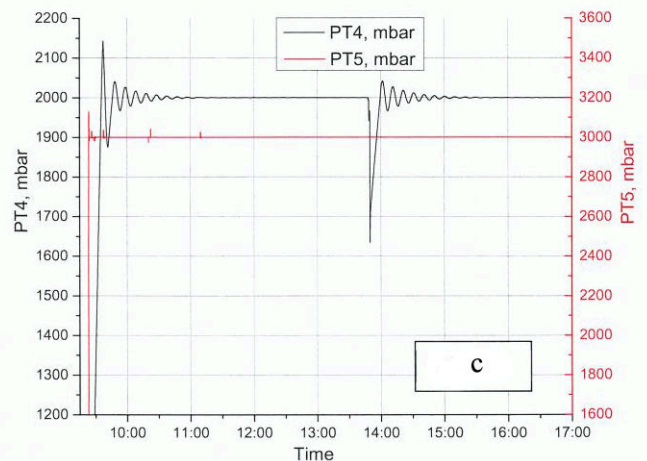
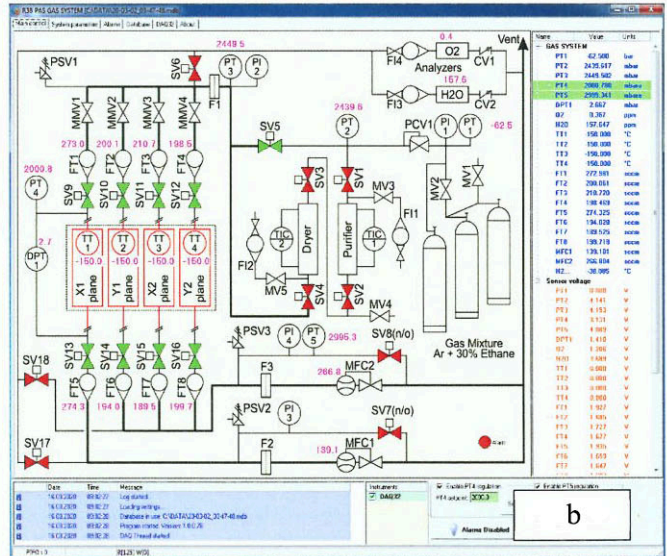


Fig. 6. Proton arm spectrometer gas supply system appearance (a) and system software main window (b); pressure stabilization in X1 plane (PT4) and in X2, Y1, Y2 planes (PT5) (c)

The pressure histogram for the X1 plane was measured during the stable operation of the system. The standard deviation of the pressure was only 0.22 mbar at the total pressure of 1999.99 mbar, so the stability is about 0.01%. This is very good, but should be checked again with the real detector planes. The gas system is ready to operate with the detector planes.

8. Front-end electronics

The Radio Electronics Department (RED) of the HEPD has developed a version of the front-end electronics that combines an amplifier, a shaper and a discriminator on one 16-channel DT_ASD16 card (amplifier, shaper, discriminator), see Fig. 7a–c. Its specification is in the Table. These cards are located directly on the STW frame in vacuum. The DT_ASD16 card is optimized to work with straw tubes manufactured by PNPI and has an output connector compatible with the CLK-TDC-128 digitizing module of the data acquisition system. These modules are produced at GSI.

The LVPS has a LV switchboard (not shown in Fig. 7a) located on the STW frame to supply power to each DT_ASD16 via a separate 3.8–4.5 V wire. (This is LV IN, see Fig. 7a.) Low dropout voltage regulators (LDOs) provide a nominal 3.3 V (LV OUT) voltage to power on-board circuits. LV switchboard combines up to 20 DT_ASD16 cards per one LVPS.

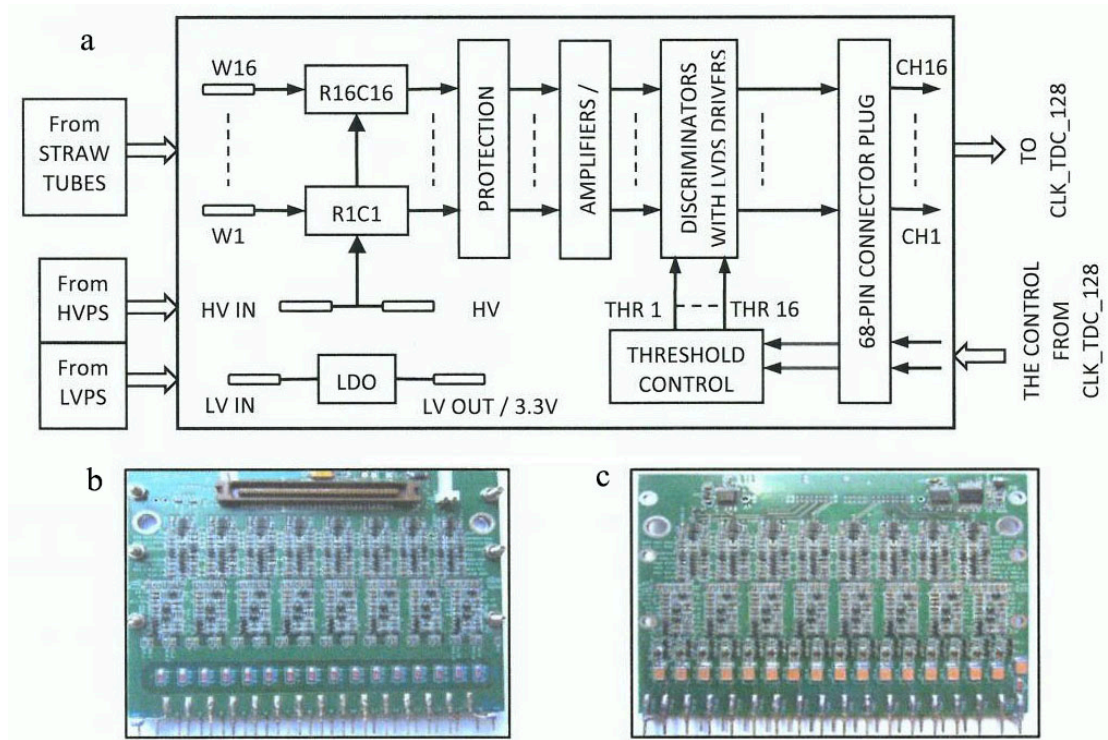


Fig. 7. DT_ASD16: *a* – block diagram; *b* – top view; *c* – bottom view

Table

DT_ASD16 specification

Parameter	Value
Board size	105 × 84 mm ²
Input	Charge sensitive
Input impedance	260 Ohm
Gain	5.4 mV/fC
Shaping	8.5 ns
Threshold control	Per channel
Supply Voltage	3.8–4.5 V
Output standard	Low voltage distribution system
Internal noise	2 fC
Double pulse resolution	100 ns
Output connector	68-pin 1.27 mm pitch low profile plug (by KEL Corporation)
Current consumption per card	240 mA

The HVPS comes from a HV switchboard (not shown in Fig. 7*a*), also located on the STW frame. The DT_ASD16 distributes the high voltage from the HV IN pin to each straw wire (W1... W16). The HV OUT pin allows multiple DT_ASD16 boards to be connected in series, allowing more straws to be powered per HV channel.

Placing the DT_ASD16 cards on both sides of the frame made it possible to achieve two important things: firstly, to minimize the couplings between the amplifier inputs and drift tubes, and secondly, to ensure efficient removal of the generated heat from the electronics, which should operate in vacuum. The measured temperature of the hottest elements on the DT_ASD16 card does not exceed 45°C, which should ensure long-term stable operation in vacuum without active cooling.

Up to eight DT_ASD16 cards are connected to one CLK-TDC-128 module, also located in vacuum on the inner wall of the vacuum chamber, which allows minimizing the length of the connecting flat cables to 6 m. Individual thresholds in each DT_ASD16 channel allow to compensate gain fluctuations in tubes and are set *via* the CLK-TDC-128 module.

All DT_ASD16 cards were tuned and quality controlled on the set-up shown in Fig. 8a. The LVPS of the preamplifiers was carried out from standard power supplies. The HVPS of the drift tubes was carried out through the preamplifier board by power sources developed in the RED. The modules of this power supply (HVCD MASTER and DB50) are shown in Fig. 8b.

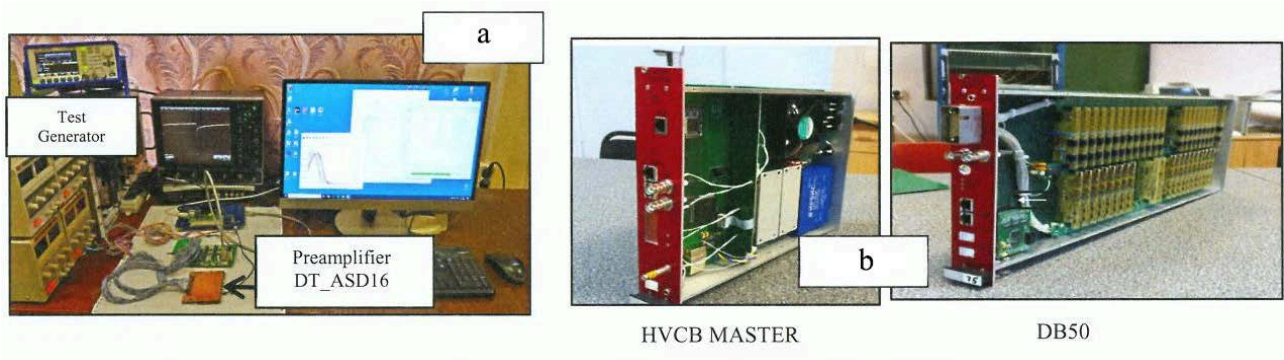


Fig. 8. The set-up for DT_ASD16 tests of quality (a); the modules of HVDS1600 (b)

The development of the HVPS HVDS1600 (high voltage distribution system) was performed in the RED in accordance with the parameters of the required technical specifications [6].

Tests of four DT_ASD16 modules at a test bench and a test station with the CLK-TDC_128 module showed that their characteristics comply with the technical specifications (Fig. 9). As a result, this version represents the final technical solution DT_ASD16 for PAS, which will be put into serial production.

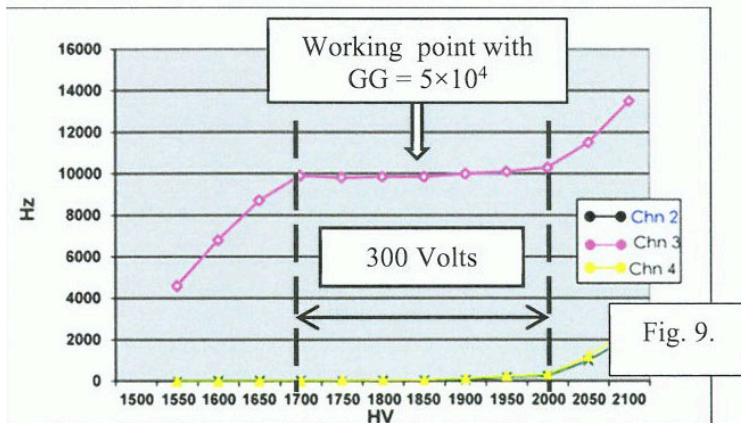


Fig. 9. The counting rate versus high voltage from ^{90}Sr source for different channels of DT_ASD16

The results of testing of four DT_ASD16 modules are presented below. The following parameters are ensured, which cover the entire range of lengths of the drift tubes (0.3–2.2 m) for PAS:

- The counting rate plateau is in the range of 1 700–2 000 V;
- The operating point is at 1 850 V, which corresponds to the gas gain (GG) factor of $GG = 5 \cdot 10^4$;
- The measured cross couplings within the plateau do not exceed 2.0%.

Currently, four DT_ASD16 modules are installed on the system test station and demonstrate stable operation with the CLK-TDC-128 module. These modules are reference ones and will be used for product tests during serial production. The threshold control is also provided by the CLK-TDC-128 module; thus no special threshold control unit is required.

9. Conclusion

1. The manufacturing technology of the PAS spectrometer based on long drift tubes with ultrathin walls for vacuum operation has been developed at PNPI.
2. The PAS spectrometer is in a high state of readiness:
 - The plane X2 is ready for work;
 - The plane Y2 is already done and ready to be equipped with electronics;
 - The plane Y1 is in the process of being assembled;
 - The plane X1 will be made from Mylar drift tubes. This technology has been developed at PNPI. The tubes for this plane were ordered in England, delivered to GSI and are ready to be sent to PNPI.

References

1. Technical Report for the Design, Construction, and Commissioning of Tracking Detectors for R³B, 101–117 (2014).
2. V.A. Andreev, M.I. Gasanov *et al.*, Preprint NRC “Kurchatov Institute” – PNPI 3052 (2021).
3. V.A. Andreev, V.Yu. Ivanov *et al.*, Preprint NRC “Kurchatov Institute” – PNPI 3059 (2021).
4. A.G. Krivshich *et al.*, Preliminary Results of the PAS Prototype Test with a ¹²C Beam: GSI Scientific Report 2016, 217 (2017). DOI:10.15120/GR-2017-1.
5. A.G. Krivshich, V.A. Andreev *et al.*, Preprint NRC “Kurchatov Institute” – PNPI 3062 (2022).
6. A.A. Fetisov, A.G. Krivshich, D.A. Maisuzenko, in *Contract Between FAIR and PNPI: Technical Specifications*, 1–7 (2018).

HIGH VOLTAGE POWER SUPPLY FOR THE PROTON ARM SPECTROMETER OF THE R³B EXPERIMENT AT FAIR

S.V. Bondarev, V.L. Golovtsov, N.V. Gruzinsky, N.B. Isaev, E.A. Lobachev, L.N. Uvarov, V.I. Yatsyura, S.S. Volkov

The design and construction of the high voltage power supply (HVPS) for the proton arm spectrometer (PAS) at FAIR further developed the ideas implemented in the design and construction of the high voltage distribution system (HVDS) for photomultiplier tubes (PMTs) for the new large-area neutron detector (NeuLAND) described in Ref. [1].

PAS [2, 3] consists of four straw-tube walls (STW), two pairs of which are either horizontal or vertical. The first STW (X1) is made of thin-walled Kapton (or Mylar) tubes. The remaining three STWs (Y1, X2, Y2) are made of aluminum tubes with a wall thickness of about 300 μm . Straw tubes require a higher input voltage but draw less current than PMTs. Each HVDS channel feeds one PMT, whereas each HVPS channel serves an array of 48 straws. Thus, the total number of high voltage (HV) channels for PAS is about 40 (with a total number of straws less than 2 000), while the total number of HV channels for NeuLAND is 6 000.

HVPS for PAS consists of two modules: high voltage control board – master (HVCB–MASTER) and distributor board (DB50), Fig. 1.

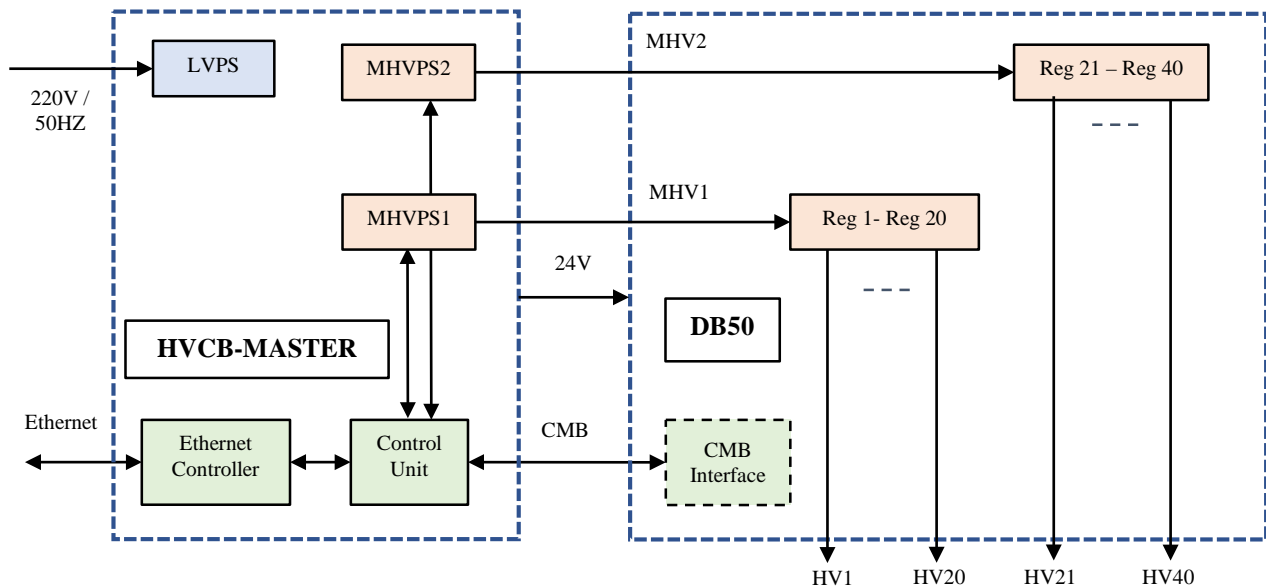


Fig. 1. High voltage power supply block diagram

HVCB–MASTER integrates in one module:

- Two Master HVPS (MHVPS1 and MHVPS2) based on the Spellman UM4P30/E 4 kV / 7.5 mA module;
- HVCB, which provides communication with the main computer and performs setting and monitoring of voltages and currents in MHVPSs and DB50 regulators;
- Low voltage power supply (LVPS, 24 V) for DB50 and itself.

The DB50 is a modified module originally designed for HVDS, containing HV regulators individually adjustable for each channel. Firstly, the two previously jumpered HV connectors are now separated, with each connector feeding exactly half of the regulators. Secondly, only 40 slots for the regulators are populated with modified 3 kV plug-in cards, since PAS requires only 40 HV channels.

The control and monitor bus (CMB) is a serial link between modules over an Ethernet patch cord with RJ45 connectors. HV cables with save HV (SHV) connectors carry the master HV (MHV) from the HVCB–MASTER to the DB50.

The HVCB–MASTER provides a 100 Mbps Ethernet connection to the host computer. The host software allows one to download required voltage setting and read back voltage and current monitor values to/from the

buffer memory of the control unit (CU). The finite state machine (FSM) in the CU field programmable gate array communicates directly with the MHVPSs in the HVCB–MASTER and *via* the CMB with the regulators in the DB50. The CMB interface on the DB50 converts serial CU commands and monitoring data back and forth. Every 20 ms, the FSM updates the voltage set values from the buffer memory to the MHVPS/regulators and the voltage and current monitor values from the MHVPS/regulators to the buffer memory. In this way, the host computer can promptly process trip conditions in the straw tubes.

The main system parameters are as follows:

- Control range of a single channel – 0 to 3.0 kV;
- Voltage setting and monitor step – 2 V;
- Output current, max – 240 μ A;
- Current monitor step, min (non-linear scale) – 0.1 μ A;
- Current trip level – under software control;
- Voltage ramp up and down rate – under software control.

HVPS modules are shown in Fig. 2*a–c*.



Fig. 2. Module: *a* – HVCB–MASTER; *b* – DB50; *c* – HVPS

The host computer runs software developed within the visual components library for Windows of the Delphi integrated development environment (IDE) to manage and monitor the HVPS. Delphi IDE uses the Delphi dialect of the Object Pascal programming language. New application libraries have been developed. The software has a friendly and intuitive graphical user interface. The software is described in detail in the “HVPS-40 Operating Manual”.

References

1. G.D. Alkhazov *et al.*, PNPI. High Energy Physics Division. Main Scientific Activities 2013–2018, 377–378 (2019).
2. G.D. Alkhazov, V.A. Andreev, A.V. Dobrovolsky *et al.*, PNPI in the R³B Project at FAIR, This Vol.
3. A.A. Fetisov, A.G. Krivshich, D.A. Maisuzenko, Description of the High Voltage System for the PAS R³B Detector: Technical Design Report, 7 (2018).

COMPREHENSIVE STUDY OF A PROPORTIONAL CHAMBER CATHODE'S SURFACE AFTER ITS OPERATION IN AN EXPERIMENT AT THE LARGE HADRON COLLIDER

G.E. Gavrilov, A.A. Dzyuba, O.E. Maev

1. Introduction

Radiation resistance of multiwire proportional chambers (MWPCs) in experiments at the Large Hadron Collider (LHC) remains a hot topic, due to the recent tenfold increase in the luminosity of the collider after its upgrading. The key motivation for this research is to maintain the stability of MWPCs for the next 10 years of the LHC operation with an expected jump in the ionization current and the already observed spontaneous self-sustaining current – Malter effect (ME) [1]. Spontaneous currents arising in MWPCs are ten times higher than the current from collisions of the proton beams in the collider and reach up to 30–40 μA [2]. This complicates operation of the readout electronics and overloads it with false responses. The ME current localized at a point on the cathode as well accelerates the aging of the anode wires located nearby.

It should be noted that the main source of the background in the muon detector of the LHCb experiment are fast neutrons with energies of up to several hundred MeV. They form photons with energies of 0.1–1 MeV as a result of nuclear interaction with the structural materials of the facility. Compton electrons are generated when photons pass through the gas volume of the MWPC, and their energy exceeds the threshold of the formation of radiation defects in metals ~ 0.5 MeV [3, 4].

The aim of studying the surface of the cathode of the MWPC was to determine the cause of ME currents in order to develop non-invasive ways of suppressing them.

2. Experiment

A module of the MWPCs of the muon detector of the LHCb experiment (type M5R4_FIR037), which operated at the LHC ($T \approx 3.2 \cdot 10^7$ s), was chosen for the study [2]. This module consists of four detecting planes (Gaps A, B, C and D) of MWPCs, and only Gap D's plane regularly displays spontaneous self-sustaining currents. It was from this plane that cathode samples were taken (disks 1 mm thick with radius of 23 mm).

As a result of the LHC operation with a working gas mixture of Ar 40% / CO₂ 55% / CF₄ 5%, the MWPC anode wires in the M5R4_FIR037 module accumulated charges of $Q \approx 1$ mC \cdot cm⁻¹ (or ~ 2.5 mC \cdot cm⁻²). After the module was dismantled from the muon detector, it was additionally studied at the gamma irradiation facility (GIF++) [5] using an Ar 40% / CO₂ 58% / CF₄ 2% gas mixture. As a result, a charge of $Q_1 \approx 0.5$ mC \cdot cm⁻¹ was additionally accumulated on the wires.

It should be noted that the charge Q_1 accumulated in a very short time (the current of the MWPC detecting planes was two orders of magnitude higher than that during operation as a part of the muon detector). The CF₄ content in the working mixture was 2% and the gas flow through the volume was reduced by 30%. Despite the tougher testing conditions, there were no new zones of spontaneous electron emission in the MWPCs. The already existing ME zone remained in its original place.

High voltage was not applied to one of the MWPC planes (Gap A) during operation on the collider (and at the facility). Like its counterparts, however, this plane was exposed to charged particles with an intensity of $R \approx 350$ Hz \cdot cm⁻². Since there was no electric field, the cathodes in the Gap A plane were not exposed to the plasma chemical effect of products of the dissociation of the gas mixture's components. The samples taken on this plane are therefore referred to below as control samples. They were compared to samples from the Gap D plane, which had experienced the entire set of radiation and plasma chemical effects. The characteristic fluence of minimum ionizing particles for the MWPC planes was $F \approx 5 \cdot 10^{13}$ cm⁻². The dose on the copper foil of the cathode (35 μm thick), calculated using the GEANT4 software package, was thus at a level of $D \approx 1.3$ Gy.

The count rates of Gap D anode wires combined into groups were measured to localize the zone of the ME current generation in the MWPCs during irradiation at the GIF++ facility. The zone of generation was

therefore found as a group of wires with a very high count rate. Here and below, the cathode samples taken along these wires are referred to as ME samples, while those taken outside the zone of the high count rate are non-ME samples.

Figure 1 (*upper part*) shows photographs of the M5R4_FIR037 cathode planes after disassembly. Photos of the Gap A and Gap D planes are on the left. The layout of the samples on the cathode is on the right. ME samples were taken in series along the Y axis (30 cm long) parallel to the anode wires with the highest count rate. Non-ME samples were also taken along the Y axis, but were offset by ~ 20 cm from the zone of spontaneous currents. Visual inspection of the MWPC module after disassembly showed that the cathodes of all the MWPC planes, except for the Gap A plane, were strongly oxidized (the *lower photo* of Fig. 1). However, since the ME was observed only on the Gap D plane, we can assume that the oxidation and reduction of copper are still not sufficient reasons for the emission currents on the cathode [6, 7], although it is known, that the island oxidation of copper surface with the formation of Cu_2O often leads to the emission currents in an electric field of $E \geq 50 \text{ kV} \cdot \text{cm}^{-1}$ [8].

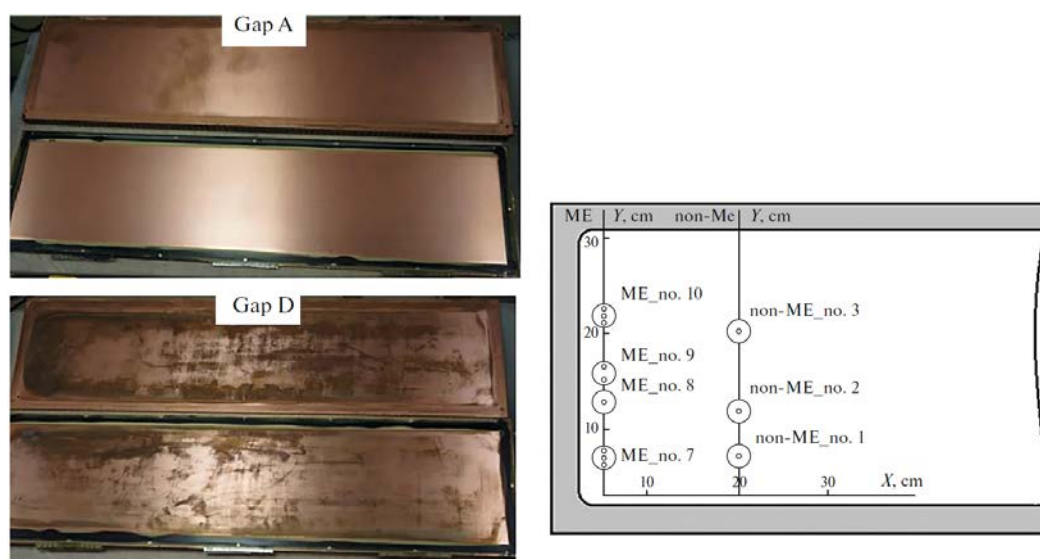


Fig. 1. Photos of the cathode planes Gap A and Gap D after the disassembly of the MWPC (*left*); the arrangement of samples (*dots*) on the cathode (*right*)

The surface morphology of the cathode samples was studied by atomic force microscopy (AFM) with Solver Next scanning probe microscope (OAO NT-MDT, Zelenograd, Russia). Surfaces were scanned by NSG10/TiN cantilevers in the tapping (topography and phase) and contact (current spectroscopy at air under normal conditions) modes. Elemental analysis of the samples surfaces was performed *via* Rutherford backscattering spectroscopy (RBS) on the Mikrozon component of the Mikrozon-EGP-10 complex at a beam energy of 4 MeV, a proton current 0.01 nA on the samples, and a beam size of $30 \times 30 \mu\text{m}^2$. The scanning area was $300 \times 300 \mu\text{m}^2$. The phase composition of samples was determined using a Shimadzu XRD-7000 X-ray diffractometer and copper anode radiation (wavelength, 1.542 Å), $V = 40 \text{ kV}$, $I = 30 \text{ mA}$.

The composition of microparticles and microstructured objects was analysed *via* Raman spectroscopy. A RamMics M532R Raman microscope was used that combined the capabilities of an EnSpectr R532R Scientific Edition Raman analyser and an Olympus CX-41 microscope.

3. Results and discussion

An analysis of the surface structure of samples taken from different sections of the cathode in the Gap D plane showed the nonuniformity of the radiation aging processes. Figure 2a (*upper part*) shows a scan of the surface of a control sample (Gap A plane). Figures 2b, c show scans of no-ME samples 2 and 3 (Gap D plane). The surface of the control sample has a weakly structured fibrous relief with zones of disorder

(technological defects) and single peaks. Primary defects most likely were formed on the cathode when bonding copper foils to fiberglass plates during production.

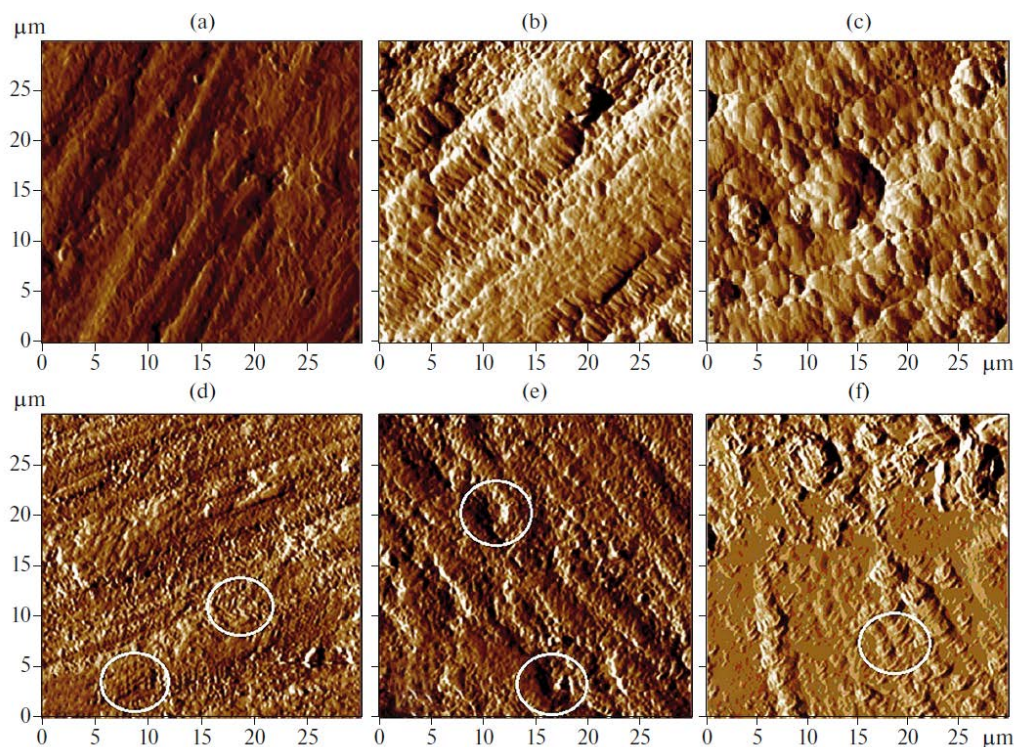


Fig. 2. Atomic force microscopy scan of the sample surface with a scanning field size of $30 \times 30 \mu\text{m}^2$: *a* – control sample; *b* – non-ME 1; *c* – non-ME 2; *d* – ME 5; *e* – ME 8; *f* – ME 10

In addition to radiation, the surfaces of ME and non-ME samples were exposed to products of the dissociative ionization of gas molecules ($\text{O}\cdot$, $\text{F}\cdot$, $\text{CF}_n\cdot$ and $\text{CO}\cdot$ radicals, where \cdot is the number of not coupled electrons of the outer shell) in vicinity of the anode wires of the MWPC [9]. Thus, a different morphological type of surface (terraced structures with isolated cells) was formed on the cathodes than on the control sample. As can be seen in Figs. 2*b*, *c*, non-ME samples were characterized by zones of segregation in addition to terraced structures.

Figures 2*d–f* (lower parts) show AFM scans of ME samples 5, 8 and 10. Most of their surface areas were subjected to erosion. Common to these samples are terraced structures similar to those found in non-ME samples (marked with white ovals in Figs. 2*d–f*). Changes in the surface morphology of ME samples were due to such radiation defects as blisters, craters, and finely dispersed structures characteristic of copper oxide Cu_2O . These structures are clearly visible in Figs. 2*d*, *e*. Both the foamy areas on the surface (see Fig. 2*d*) due to small blisters and the formation of craters caused by radiation (see Fig. 2*e*) do not have melting zones.

Zones of structural phase transitions (oxidation and melting) are clearly visible in Fig. 2*f*. The observed smoothing due to melting is distributed over image area of $30 \times 30 \mu\text{m}^2$, due apparently to the thermal action of high-density emission currents on the cathode copper foil. Surface melting can also occur in the copper foil along the trajectories of fast charged particles, which cause cascades and subcascades of moving vacancies and interstitial atoms. However, such effects at a relatively low intensity of irradiation ($R \approx 350 \text{ Hz} \cdot \text{cm}^{-2}$) should be point-localized [10].

At the same time, due to absorption by copper from the gas mixture of molecules containing oxygen, carbon and fluorine, the islands of dielectric oxide Cu_2O grow [2, 8] and nanocarbon and fluorocarbon films form [11, 12] on the cathode surface. The point emission of electrons is possible for such formations under the action of an electric field, which can heat their surfaces to the melting point. The inhomogeneity of the

distribution of emission points on the cathode could be due to the turbulence of the gas flow in the narrow gaps of the MWPC (5 mm) near the inlet and outlet of the gas mixture [2].

Figure 3 presents results of an analysis of the main characteristics of the surfaces of samples (roughness S and peak height differences Δh , both in nm). Data for four ME samples and three non-ME samples are given that depend on their coordinates along the Y axis. The surfaces of ME samples 7, 9 and 10 ($Y \approx 6$ cm, $Y \approx 15$ cm and $Y \approx 32$ cm, respectively) were examined at several points.

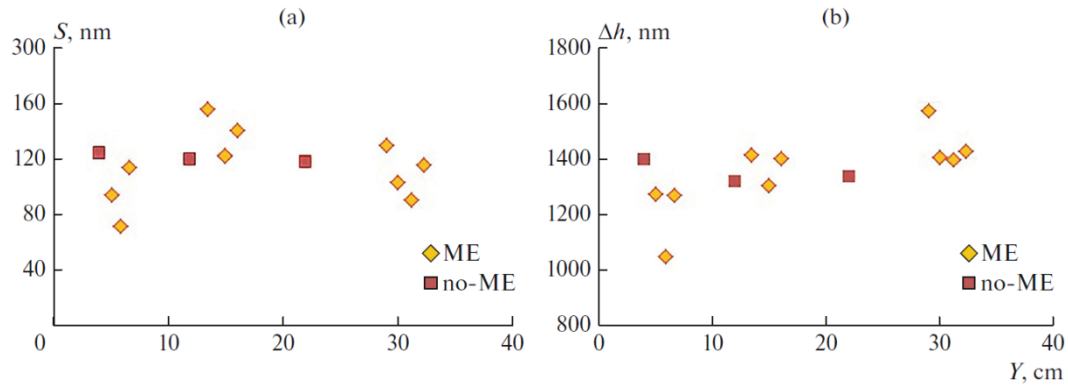


Fig. 3. Distribution of (a) roughness S and (b) peak heights Δh on the surface of ME samples and non-ME samples along the Y axes in and outside the zone of spontaneous currents

The roughness of the control sample surface was $S \approx 90$ – 100 nm, and the difference between peak heights at different points was $\Delta h \approx 1\,100$ – $1\,200$ nm, very close to the values in Fig. 3. The surface is rougher than that on the control sample in the zones on the Gap D plane, regardless of electron emission. The roughness varies in the range of $S \approx 100$ – 140 nm, and the difference between peak heights varies in the range of $\Delta h \approx 1\,300$ – $1\,450$ nm. This is apparently due to the plasma-chemical and radiation effects on the copper foils, which usually oxidizes the boundaries of crystallites and remove material from the surface [6].

Only the surface of ME sample seven is characterized by notable smoothing (see Fig. 1, $Y \approx 6$ cm) where the roughness and height of the peaks fall pointwise to $S \approx 70$ – 100 nm and $\Delta h \approx 1\,000$ – $1\,250$ nm, becoming comparable to the control sample. Electrons were apparently emitted precisely in the region where ME sample seven was taken. They heated the foil to the melting temperature locally and burned out peaks formed by radiation erosion [11, 12]. Analysis of the pore space of ME sample seven confirmed this assumption. Number n of pores in two areas ($30 \times 30 \mu\text{m}^2$) of AFM scanning of the sample almost doubles (from $n = 768$ to $n = 1\,327$), indicating high heterogeneity of surface erosion according to the type of blistering. The AFM scanning revealed a porous surface in the area with the most intense formation of pores, on which blisters could no longer form [13].

The AFM revealed new structural effects that could result in the spontaneous emission of electrons in the MWPCs. It was found that nanoscale carbon films are formed in the cavities and interstructural spaces of the copper foil of ME samples. Figure 4 (*upper part*) shows a fragment of an AFM scan of ME sample eight with a graphite-like film ~ 20 nm thick. The film is inside a cavity on the surface and has a characteristic structure similar to images of nanographite films obtained under laboratory conditions by condensing carbon from the gas phase [12]. Figure 4 (*lower part*) shows the current-voltage characteristic measured in the area where nanographite film is formed. A current-voltage characteristic with voltage U rising from -10 to $+10$ V is indicated by *red dots*. A current-voltage characteristic with voltage U falling from $+10$ to -10 V is shown by *blue dots*. The current hysteresis displays resistive switching, which is typical of many nanocarbon formations. The threshold value of the electric field strength for the emission of electrons in such structures is $E_t \approx 10 \text{ kV} \cdot \text{cm}^{-1}$ [14].

A nanocarbon film is uncontrollably and slowly formed on the copper foil of the MWPC cathode. This occurs in the electric field of the detector ($E_{\text{cathode}} \approx 5 \text{ kV} \cdot \text{cm}^{-1}$) with the gas mixture of $\text{Ar}/\text{CO}_2/\text{CF}_4$ at atmospheric pressure under prolonged exposure by the charged particles and processes of plasma-chemistry

interaction between the active radicals, ions, and copper. With AFM scanning, zones with a nanocarbon film are most often found near the walls of craters at the cathode.

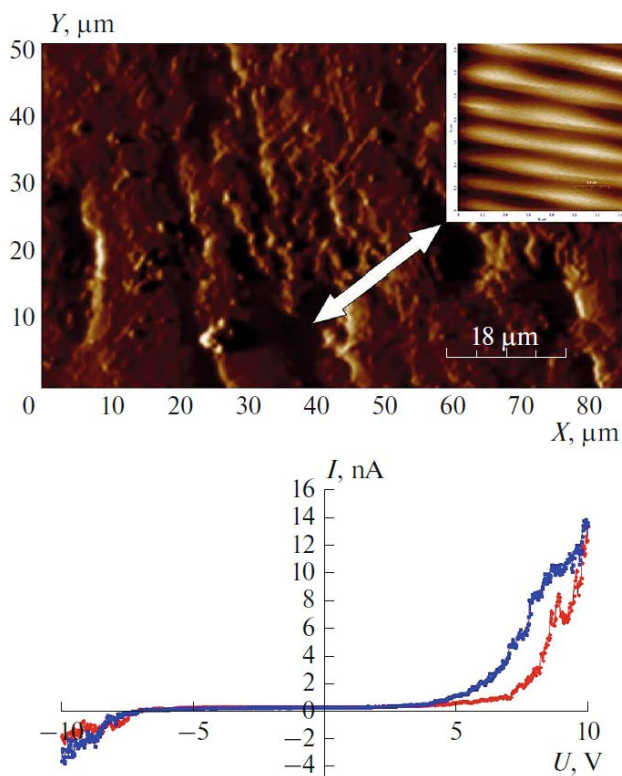


Fig. 4. An atomic force microscopy scan of ME sample eight with a scanning field size of $90 \times 90 \mu\text{m}^2$ (inset, $1.5 \times 1.5 \mu\text{m}^2$) is shown at the *top*. The current-voltage characteristic measured in the area of the nanographite film is shown *below*. The current-voltage characteristic upon raising voltage U from -10 to $+10$ V is represented by *red dots*. The current-voltage characteristic upon lowering voltage U from $+10$ to -10 V is given by *blue dots*

Our structural AFM-analysis of the MWPC cathode samples thus showed that the non-ME samples were characterized by a cellular structure with local zones of erosion. Radiation erosion was more pronounced in the ME samples. They were structurally heterogeneous, and their surfaces were smoothed as a result of melting. There were cascades of small craters (see Fig. 2e), and porous zones with many clearly visible small peaks and blisters. Nanosized carbon films were found at the boundaries of smoothed areas with loose defective areas, and in the cavities between microfibrils in the ME samples. The observed morphological types of the surface were due to structural phase transformations and thermal processes that occurred on cathode surfaces under the action of charged particles and in pointwise zones of electron emission [12].

Integrated Rutherford backscattering spectra (RBSes) were analysed layer-by-layer for all types of the samples in areas of $300 \times 300 \mu\text{m}^2$. The depth of penetration measured for oxygen and carbon in the samples was no greater than $2 \mu\text{m}$. The content of oxygen in near-surface layers ($\leq 0.4 \mu\text{m}$) was comparable for ME ($\sim 70\%$) and non-ME samples ($\sim 80\%$). On the other hand, the content of carbon in the ME samples ($\sim 15\%$) was three times higher than that in the non-ME samples ($\sim 5\%$). Graphite-like film formations on the surfaces of the ME samples are explained by their elevated carbon content (see Fig. 4). Another important difference between the samples was the presence of fluorine. In the RBS spectra of the ME samples, we detected fluorine at a level of $\sim 5\%$ in addition to carbon and oxygen, due to the high sensitivity of the procedure. We may therefore assume there were structures that contained fluorocarbon compounds CF_n on both cathodes surfaces in the MWPC.

Our results from studying samples *via* Raman spectroscopy were in good agreement with those from X-ray phase analysis. The oxide phase of Cu_2O and the phase of amorphous carbon were revealed on the analysed ME and non-ME surfaces by blowing the gas mixture through all four planes of the MWPC in succession. The gas flow thus redistributed active radicals in the working volume of the MWPC over all of the cathodes [2]. The presence of the Cu_2O oxide phase on the surface of the cathode in the MWPC of the LHCb muon detector agrees with results from studying detector prototypes. Laboratory tests of the MWPC

prototypes with an Ar/CO₂/CF₄ gas mixture have also established that Cu₂O was the main phase of the surface layers of cathode samples [6].

Copper oxide is a *p*-type semiconductor and, like all semiconductor materials, it is sensitive to the presence of defects and microimpurities. They result in local energy levels emerging in the bandgap and changes in such conductivity parameters as the concentration and mobility of carriers. The presence of Cu₂O oxide microgranules on the cathode surface may be the reason for the appearance of many centres of electron and photon emission with a wavelength $\lambda \approx 600$ nm at the electric field above a threshold of $E_t \geq 50$ kV · cm⁻¹ [8]. Due to the absorption of electrons in a cathode's material, however, the emission of electrons into the gas volume of the detector becomes impossible at a depth of ~ 1 μm. From the experience of observing ME in gas-discharge detectors, it is known that the dielectric on the cathode surface should be no more than several tens of nanometers thick for emission currents to appear [7]. Spontaneous currents due to Cu₂O granules are possible in the MWPC only if they form on the surface of a cathode in the form of micropeaks with an aspect factor (ratio of the height to the tip diameter) greater than 10 for the electric field on the cathode ($E_{\text{cathode}} \approx 5$ kV · cm⁻¹). The current of electrons through such a microobject heats the foil up to the melting point ($T_{\text{Cu}_2\text{O}} = 1235^\circ\text{C}$). The emission of electrons stops as a result of changes in the electrochemical properties of the material. The next possible reason for the ME is the emission of electrons by nanographite structures. The results revealed the condensation of carbon- and fluorine containing molecules on the cathode that were produced in the gas-discharge plasma near the anode wire. An example of such structures are nanographite films that form crystallites 1–2 μm tall. Since they are thin, the aspect ratios of these structures can be as great as 1000. The threshold value of the electric field for electron emission by nanographite films is $E_t \approx 10$ kV · cm⁻¹. This value of the electric field strength is easily achievable in an MWPC [11, 12].

The presence of fluorine and nanocarbon on the cathode surface can result in the formation of dielectric fluorocarbon compounds, which are a stable source of emission currents [14]. It is difficult to attribute definitely the nanostructures observed in the MWPC to one of the many models of low-threshold emission. To identify the reasons for the ME, however, it is important that almost all such nanostructures are characterized by electron emission.

4. Conclusion

The surface of a MWPC cathode from the LHCb experiment at the LHC was studied comprehensively for the first time in order to establish the reasons for spontaneous self-sustaining currents in the detector. Radiation erosion accompanied by the formation of copper oxide and nanosized carbon and fluorocarbon structures of high resistivity were revealed by the AFM, microprobes, X-ray diffractometry and Raman spectroscopy on the copper foil of the cathode. A characteristic feature of carbon and fluorocarbon nanostructures is the low threshold of electron emission. The threshold value of the electric field strength for nanostructures ($E_t \sim 10$ kV · cm⁻¹) is one fifth that of Cu₂O, and it can be reached on a cathode under the conditions of radiation damaging copper. Carbon and fluorocarbon nanostructures therefore seem to be the most realistic source of spontaneous currents in the MWPC.

References

1. L. Malter, Phys. Rev. **50**, 48 (1936).
2. F.P. Albicocco, L. Anderlini, M. Anelli *et al.*, JINST **14**, P11031 (2019).
3. H.H. Hansen, Int. J. Appl. Radiat. Isot. **34**, 1241 (1983).
4. S.B. Fisher, Radiat. Eff. Defects Solids **7**, 173 (1971).
5. D. Pfeiffer, G. Gorine, *et al.*, Nucl. Instrum. Meth. Phys. Res., Sect. A, **866**, 91 (2017).
6. M.E. Buzoverya, G.E. Gavrilov, O.E. Maev, Tech. Phys. **66** (2), 356 (2021).
7. G. Zhou, L. Wang, J.C. Yang, J. Appl. Phys. **97**, 063509 (2005).
8. R.E. Hurley, J. Phys. D: Appl. Phys. **10**, L195 (1979).
9. J. Va'Vra, Nucl. Instrum. Meth. Phys. Res., Sect. A **252**, 547 (1986).
10. V.A. Akat'ev, E.V. Metelkin, At. Energy **118** (2), 105 (2015).

11. A.N. Obraztsov, Al.A. Zakhidov, *Diamond Relat. Mater.* **13**, 1044 (2004).
12. A.N. Obraztsov, V.I. Kleshch, *J. Nanoelectron. Optoelectron.* **4**, 207 (2009).
13. M.I. Guseva, Yu.V. Martynenko, *Sov. Phys. Usp.* **24**, 996 (1981).
14. A.I. Ivanov, N.A. Nebogatikova, I.I. Kurkina, I.V. Antonova, *Semiconductors* **51** (10), 1306 (2017).

DATA ACQUISITION SYSTEM FOR THE EXPERIMENT “PROTON”

A.A. Vorobyev, **V.L. Golovtsov**, **N.V. Gruzinsky**, **P.A. Kravtsov**, **P.V. Neustroev**, **E.M. Spiridenkov**,
L.N. Uvarov, **A.A. Vasilyev**, **V.I. Yatsyura**

The “Proton” experiment uses the innovative *ep* elastic scattering method, which allows recording both recoil protons and scattered electrons with high accuracy and resolution, which leads to a completely new approach to measuring the proton radius.

The “Proton” set-up [1] includes two gaseous ionization detectors: an active hydrogen target in the form of an axial time-projection chamber (TPC) detecting recoil protons and a high precision forward tracker (FT) in the form of a set of multiwire proportional chambers with a cathode strip readout that registers scattered electrons. The FT is located behind the TPC in a separate volume of the same vessel, see Fig. 1.

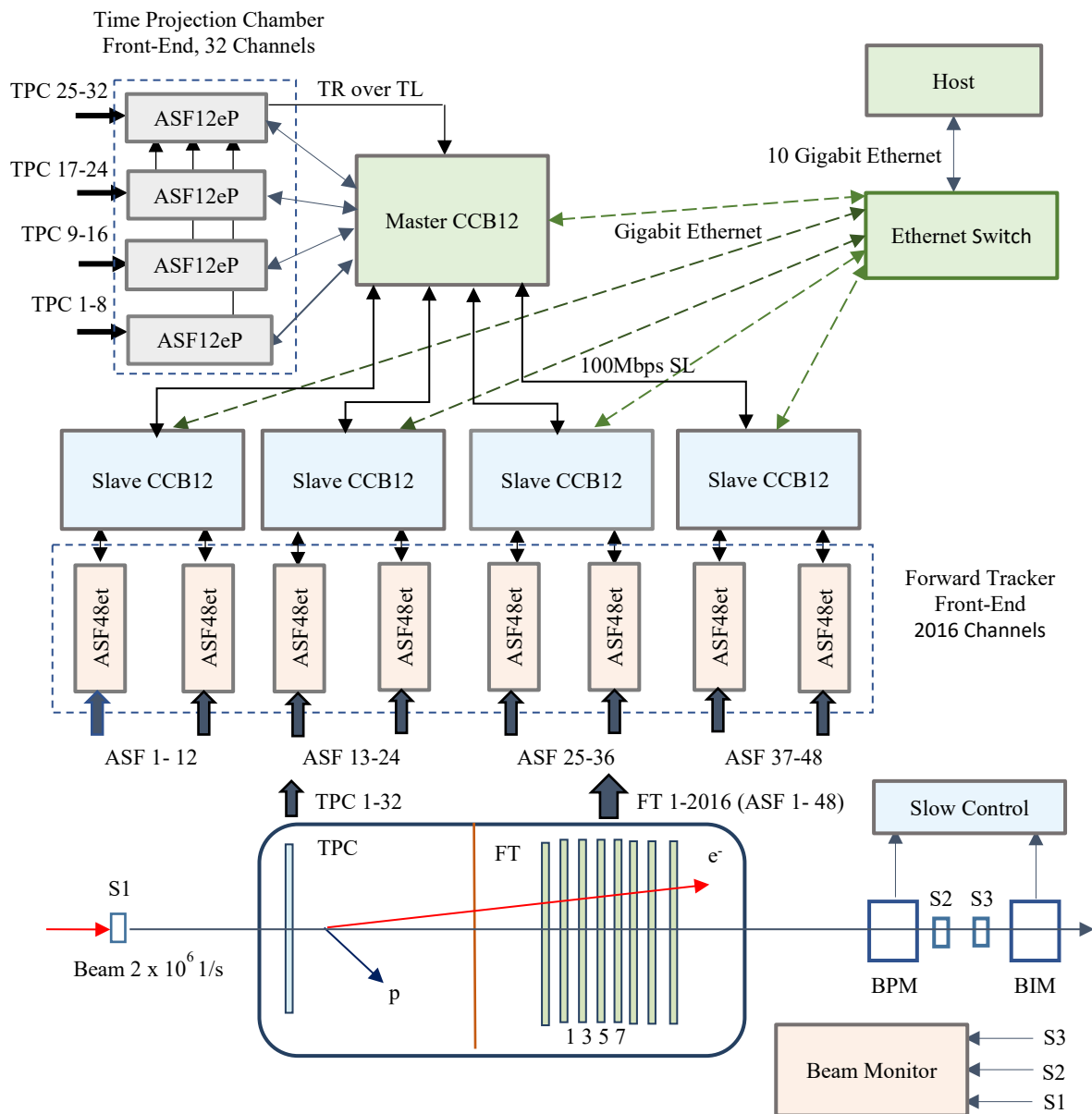


Fig. 1. Schematic view of the experimental set-up and the data acquisition system

The TPC anode is segmented into the central pad and eight concentric rings along the radius, some rings are subdivided into sectors. The total number of channels for the TPC anode readout reaches 32. The target parameters for the measurement are the energy of the recoil proton and the signal arrival time.

The FT consists of four pairs of chambers that measure the X and Y coordinates of the scattered electron track relative to the beam line. Each chamber is a symmetrical multiwire proportional chamber $600 \times 600 \text{ mm}^2$ in size with an anode plane (wires with a pitch of 3 mm) between two cathode planes (wires with a pitch of 0.5 mm). The cathode wires are orthogonal to the anode wires in one cathode plane (X or Y) and are inclined at an angle of 45° in the other cathode plane (U). Every five wires in the orthogonal cathode plane are grouped into strips. The strip in an inclined cathode plane consists of 100 wires. The number of signal channels in each chamber is $240 + 12 = 254$, which gives a total of 2016 channels for eight chambers. The target parameters for the measurement are the centre of gravity and the time of arrival of the cathode signal(s).

Beam monitoring is based on S1... S3 scintillation counters, a high-pressure ionization chamber as a beam intensity monitor (BIM) and a small proportional chamber as a beam position monitor (BPM). Knowing the number of beam electrons is necessary to determine the absolute cross section. The beam intensity is expected to be $2 \cdot 10^6$ electrons per second.

This article only deals with receiving events from the TPC and FT detectors and does not cover the electronics of the beam monitoring detectors. The detection of both the recoil proton and the scattered electron makes it possible to reconstruct the ep scattering event.

Using a flash analog-to-digital converter (flash ADC) is best suited to measure the target parameters of both detectors. The data acquisition system for the above two detectors has a tree-like architecture and is based on a configurable amplifier–shaper–flash (ASF) ADC, multichannel digitizer and a 12-port concentrator–control–board (CCB12). The CCB12 distributes the system clock and commands from the host computer to downstream devices over serial links (SL). The SL connects serial ports (SP) of the upstream and downstream devices and operates at 100 Mbps in both directions. A special class of broadcast commands addressed to the Master CCB12, such as “start operation”, “stop operation”, or generated by the Master CCB12, such as “trigger”, eventually reaches each device in the acquisition tree, causing them to work synchronously.

Registration of a recoil proton in any of the TPC channels causes a trigger request (TR) signal to be sent over the trigger link (TL) to the Master CCB12, the latter may distribute it as a “trigger” command.

Upon receiving a “trigger”, each channel of the TPC and FT digitizers generates a data block, containing event(s). An event is an array of flash ADC readings obtained as a result of digitizing the detector signal.

For offline event synchronization, each event in the data block is timestamped. The timestamp is a 44-bit binary counter that starts running in each device on the “start run” command. The counter overflow occurs after approximately 48 h. This makes the timestamp the unique identifier for the event. The CCB12 multiplexes twelve input 100 Mbps data streams into one and sends it to an Ethernet switch over Gigabit Ethernet. The switch communicates with the host *via* the 10 Gigabit Ethernet.

Digitizer. Two versions of the digitizer, called ASF12eP and ASF48et, serve the TPC and FT detectors, respectively. Both versions use the same ASF_48et main board design. It contains six flash ADC chips and programmable logic in the Spartan-6 LX field-programmable gate array (FPGA), see Fig. 2. For greater flexibility, the amplifiers and shapers are placed on a separate daughter board, which is connected to the input sockets on the main board.

The flash ADC chip is a 12-bit high-performance, low-power, octal channel analog devices ADS5282 ADC with a differential input voltage in the 2 V range and low-voltage differential signaling (LVDS) output. The input sampling rate can vary from 10 to 65 megasamples per second (MSPS). The output data latency is 12 sampling clock cycles. The serialized double data rate (DDR) outputs run at 6 times the input clock.

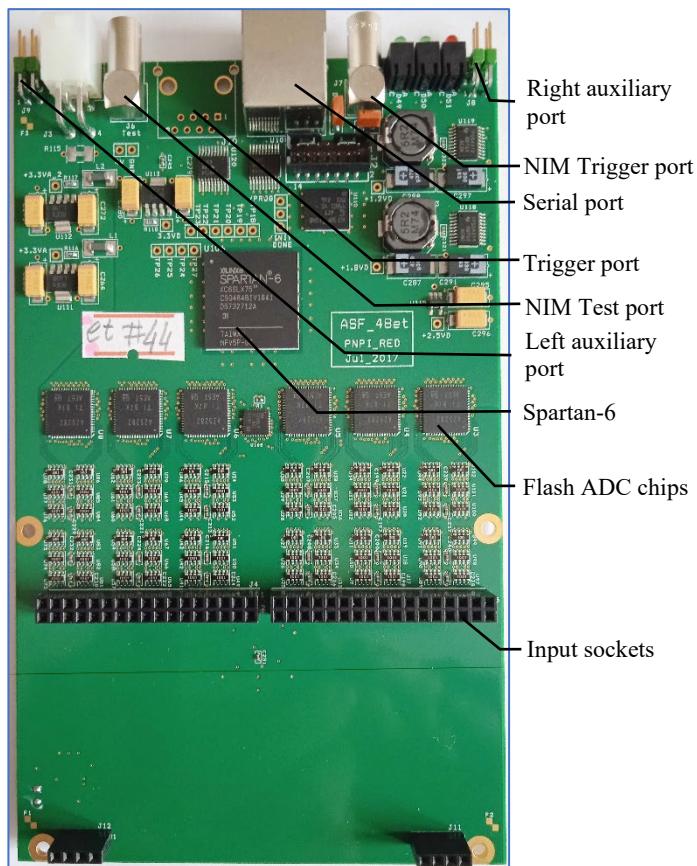


Fig. 2. ASF_48et close up

The Spartan-6 LX FPGA pinouts are 100% compatible across density in the same package. Thus, depending on the requirements, the ASF_48et board can be equipped with either the cheapest LX45 FPGA, or the more expensive LX75 and LX100 FPGAs, or the most expensive LX150 FPGA. All ports: SP for receiving commands and uploading data blocks, trigger port (TP) for sending TR to Master CCB12, NIM (NIM – current-based logic defined in nuclear instrumentation module standard) test port for receiving test signals, left and right auxiliary ports (LAP, RAP) for signal exchange between digitizers – are controlled *via* the FPGA. This data acquisition system does not use the NIM TP to receive external “trigger” signals. The signal standard for all ports except NIM is differential LVDS.

Concentrator. The CCB12 design is made as a main and daughter board, see Fig. 3. The main board has 12 SPs one upstream SP (USP) and TP. All ports use RJ45 connectors. The SLs connecting SPs or TPs of upstream and downstream devices are category 5e shielded patch cords. An inexpensive Spartan-3 FPGA on the main board controls all ports. The daughter board connects to the main board *via* a 96-pin connector. The daughter board is an off-shelf product TE0720-03-1CFA from Trenz Electronic GmbH. It integrates a Xilinx Zynq XC7Z020 system-on-chip (SoC), a Gigabit Ethernet transceiver, 1 GB DDR3 synchronous dynamic random access memory (DDR3 SDRAM), and 32 MB flash memory for configuration and operation. The SoC includes user-programmable resources: an Artix-7 FPGA and a dual-core ARM Cortex-A9 processor, on which all concentrator operation algorithms are built. The two versions of the concentrator, called Master CCB12 and Slave CCB12, use the same hardware but differ in firmware and processor codes.

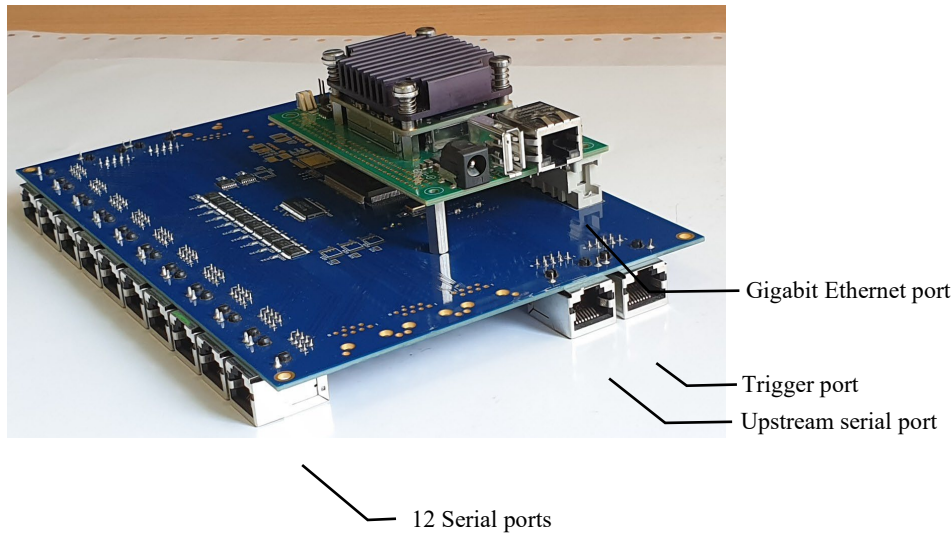


Fig. 3. Concentrator CCB12

ASF12eP digitizer. The ASF12eP digitizer collects data from the TPC. The TPC maximum drift time is $100\ \mu\text{s}$, but the spread of the signal arrival time from anode segments does not exceed $25\ \mu\text{s}$. To get a complete picture of the recoil proton track, the digitizers collect data from all segments of the anode in a $40\ \mu\text{s}$ window. The chosen $25\ \text{MHz}$ sampling rate is a compromise between obtaining optimal time resolution ($40\ \text{ns}$), the number of readings per “trigger” (typically 1 000 readings, but can be increased to 4 000 readings) and the expected “trigger” rate of $50\ \text{Hz}$. To further minimize the SL load and dead time, the number of channels has been reduced from a potentially available 48 to 12. Low-noise, charge-sensitive preamplifiers with a peaking time of $1\ \mu\text{s}$ have a noise level of $13\ \text{keV} + 0.5\ \text{keV/pF}$ and can measure TPC signals from $250\ \text{keV}$ up to $5\ \text{MeV}$.

The main board has a Spartan-6 LX100 FPGA. The logic for each digitizer channel includes:

- Deserializer of flash ADC serial output into a parallel word;
- 12-bit signal amplitude discriminator;
- 18-bit moving integrating window (MIW);
- 15-bit MIW discriminator;
- Pipeline delay to compensate for “trigger” latency;
- 8K word first-in-first-out (FIFO) memory that serves as the channel’s derandomizing buffer.

The MIW width can be up to 127 readings. The integrator works with the 11 most significant bits (MSB) of the flash ADC reading. On each sampling clock cycle, it adds a new reading and subtracts the earliest in time. The MIW discriminator compares the 15 MSB of the integrator with a threshold.

The outputs of the amplitude discriminator or MIW discriminator in any channel, or their coincidence, can be the source of the TR signal. TR is available at LAP or RAP. One of the four ASF12ep digitizers collects all TR *via* logical OR and sends them *via* TL to the TP of the Master CCB12, and the Master CCB12 broadcasts it as a “trigger” to all devices. Upon receiving a “trigger”, each channel of the digitizer generates an event with a timestamp corresponding to the time the “trigger” arrived. Events from all channels are combined into a common 32K word FIFO, which serves as a device derandomizing buffer and forms a single output data stream. Typically, TR generation is enabled for the second or third ring segments of the anode, *i. e.* delayed relative to the beginning of the track. To compensate for the delay, the event window typically begins $15\ \mu\text{s}$ before the “trigger” and ends $25\ \mu\text{s}$ after it, but can be adjusted over a wide range.

ASF48et digitizer. The ASF48et digitizer collects data from the FT. Any electron track found in the FT (outside the central dead zone of $2\ \text{cm}$) in the time window $100\ \mu\text{s}$ before the “trigger” signal could be the parent particle of the recoil proton. The digitizer is equipped with low-noise, charge-sensitive preamplifiers with a peaking time of $1\ \mu\text{s}$ and a noise level of $0.072\ \text{fC} + 0.0015\ \text{fC/pF}$.

The main board has a Spartan-6 LX75 FPGA. The logic for each digitizer channel includes:

- Deserializer of flash ADC serial output into a parallel word;
- Signal amplitude discriminator;

- Pipeline delay to compensate for “self-trigger” latency;
- 1K word memory as a ring buffer.

Each channel operates in self-triggered mode. Self-triggering causes the event to be stored in the ring buffer. Each event contains a timestamp corresponding to the time the “self-trigger” arrived and an array of flash ADC readings (typically 80 readings, but can be increased to 960 readings). The time position of the event is chosen to include both baseline and maximum amplitude readings. Both are used to find the centre of gravity (coordinate) of the scattered electron. Upon receiving a “trigger”, self-triggered events from all channels that occurred in the 100 μ s time window preceding the “trigger” are reloaded into a 16K word output FIFO to eventually form a single output data stream.

Master CCB12 and Slave CCB12 concentrator. The Master has a built-in trigger logic that receives TR signals from the ASF12eP digitizer and sends “triggers” to other devices in the acquisition tree. It assigns a timestamp to each received TR and marks it if it is used to generate a “trigger”. The “trigger” information constitutes the 13th data stream in addition to the 12 data streams coming from the SPs. The Master also distributes broadcast commands from the host to all downstream devices. It has different logic for the SP connected to the digitizer and the SP connected to the Slave, because it does not receive any data from the Slave, only its busy status, which is used in the trigger logic.

Both types of concentrators have the same logic for the SP connected to the digitizer. Two special commands “hold” and “resume” control the flow of data between digitizers and concentrators: “hold” causes the digitizer to stop sending data, and “resume” resumes normal data flow. The 16K word FIFO at the input of each SP serves as the channel’s derandomizing buffer. The FPGA logic reloads the data from the input FIFO to the 32K word output FIFO, splitting it into packets with headers and trailers. The header and trailer added to the packet contain overhead information such as header timestamp, packet number, SP number, number of kilo-words loaded into input and output FIFOs, trailer timestamp, and checksum. The processor forwards packets from the output FIFO to the host *via* Gigabit Ethernet.

The data acquisition system for the “Proton” experiment has been tested on cosmic rays.

References

1. A.A. Vorobyev *et al.* PNPI. High Energy Physics Division. Main Scientific Activities 2013–2018, 316–325 (2019).

HIGH-TEMPERATURE AND MASS-SEPARATOR METHODS FOR SELECTIVE PRODUCTION OF MEDICAL RADIONUCLIDES AT PROTON AND NEUTRON BEAMS

V.N. Pantelev, A.E. Barzakh, D.V. Fedorov, V.S. Ivanov, P.L. Molkanov, S.Yu. Orlov, M.D. Seliverstov

1. Introduction

Special pharmaceuticals, prepared on the basis of radionuclides, are very efficient tools for diagnostic and therapy of many kinds of different diseases. Presently, reactors on thermal neutrons and high current cyclotrons are utilized to this end. Regardless of the production method, the desired radionuclides should be separated from the irradiated target material and other undesired radionuclides. Generally, the so called “wet” radiochemical methods are used for extraction and purification of targeted medical radionuclides. However, these methods are accompanied by a large amount of liquid radioactive waste. Nevertheless, the problem of the isotope purification was successfully solved more than sixty years ago by building of special installations for nuclear physics studies – isotope separator on-line (ISOL) facilities working at beams of different projectile particles.

2. Mass-separator method

Shortly, the mass-separator method may be described as follows. At an ISOL installation, radioactive atoms are produced in an irradiated mass-separator target kept at a high temperature in a high vacuum. Then the atoms diffuse out of the target material and effuse as neutral atoms from the target container into the cavity of an ion source, where they are ionized. Finally, they form radioactive ion beams [1] after passing through a system of electrostatic lenses and a magnet analyser.

This method is usually applied for short-lived isotope production in nuclear physics experiments for study of exotic nuclei. The mass-separator method gives the possibility to produce very pure beams of radioisotopes. Another advantage of the mass-separator method is that several radioisotopes separated according to their mass numbers can be obtained and investigated simultaneously.

The mass separator can be applied for production of radionuclides in various modes:

- On-line mode (radionuclides are accumulated in the process of the target irradiation);
- Semi on-line mode (radionuclides are accumulated after the switching off the irradiating beam);
- Off-line mode (the target is irradiated separately and after that it is installed at the mass-separator).

In any case, certain requirements on the target material should be fulfilled. It should be a high-temperature resistant (to avoid destruction at a temperature of the targeted radionuclide evaporation) and should have a low vapor pressure ($< 10^{-4}$ mbar) at the working temperature to ensure a proper work of a high voltage system of the mass-separator. Provided these requirements are fulfilled, long-term operation of the mass-separator can be ensured with the efficiency of some radionuclide production up to 80%.

First experiments on the production of mass-separated medical radioisotopes were successfully carried out at the on-line mass-separator facility ISOLDE at CERN [2, 3]. These experiments have shown very promising prospects of the method, provided that it would be possible to increase significantly the activities of the obtained radionuclide samples. This can be achieved by using high current cyclotrons or high neutron-flux reactors.

3. High-temperature method of separation of the target material and the produced radionuclide

In case of non-compliance the above mentioned conditions for collection of long-lived radioisotopes with the half-lives of several tens of hours or more, a method of thermal pre-separation in vacuum of the target material and the selected radionuclides was proposed [4].

For this purpose, the difference in volatility of atoms of the desired radionuclide, the target material, and other produced radionuclides at a certain target temperature was used. In other words, the separation can be done if the target material and the atoms of targeted radionuclides have a considerable difference in the saturated vapour pressure in vacuum at a certain temperature. In general, this difference correlates with

the difference in enthalpy of adsorption on the surface of refractory metals from which the target containers are usually manufactured [5].

If the target material is much more volatile (has much higher vapour pressure) than the resulting radionuclide, it can be easily evaporated at a certain temperature from the target container into some cold ballast volume without loss of the resulting radionuclide. As it was demonstrated in our previous work, the radionuclide ^{82}Sr used for positron emission tomography (PET) diagnostics can be isolated from the binary compound of the RbCl target material with the efficiency better than 99% by heating it in a high vacuum for one hour [4, 6]. It was also shown that this principle works for separation of ^{82}Sr from metallic rubidium and a therapeutic radionuclide ^{67}Cu from a target made of metallic zinc [7].

These results show that the effect of thermal separation is universal regardless of whether the target substance is a molecular compound or it is in the natural metallic state. It is very important that the carrier-free radionuclide samples prepared by this method can be further utilized for isotopic separation using a mass-separator. This is necessary, when other radioisotopes of the selected element are present in the resulting sample.

Our previous work is related in general to the development of a thermal method for the separation of radionuclides obtained by irradiation of a target by protons of different energy [1, 4, 7, 8]. The main objective of the present work is to test experimentally whether this method could also be used to isolate the radionuclides produced in reactions with neutrons. For this purpose, ^{177}Lu which is the most promising radionuclide for the treatment of prostate tumors and $^{99\text{m}}\text{Tc}$, widely used for diagnostics, were selected. In the experiments, a metallic ytterbium target was used in order to obtain ^{177}Lu . For $^{99\text{m}}\text{Tc}$ production, the molybdenum oxide MoO_3 target was used.

4. Radioisotope complex ISOTOPE project

A detailed description of the ISOTOPE project which is constructed at the beam of high current cyclotron C-80 [9] can be found in Ref. [10]. Below its main features are presented.

The cyclotron C-80 with the proton beam energy 40–80 MeV and the intensity of 100 μA is designed to produce a wide spectrum of medical radionuclides for diagnostics and therapy. The use of three target stations will allow one to investigate and introduce different new methods of radionuclide production. They are the high-temperature separation method [1] and the mass-separator method, in which a specially constructed target is used [4]. A mass-separator with its target station will allow one for the production of isotopically separated medical radionuclides of a high purity, which will be implanted into corresponding collectors from which they can be easily extracted. Radionuclides which are planned for production at ISOTOPE are listed in Table 1. Additionally new methods are being developed for the following radionuclide production: ^{64}Cu , ^{67}Cu , ^{149}Tb , ^{177}Lu , ^{188}Re , ^{212}Pb , ^{212}Bi .

Table 1

Radionuclides planned for production at ISOTOPE

Radionuclide	Decay half-life, $T_{1/2}$
^{68}Ge	270.8 d
$^{82}\text{Sr}^*$	25.55 d
^{99}Tc	6 h
$^{111}\text{In}^*$	2.8 d
$^{123}\text{I}^*$	13.27 h
$^{124}\text{I}^*$	4.17 d
$^{223}\text{Ra}^*$	11.4 d
$^{224}\text{Ra}^*$	3.66 d
$^{225}\text{Ac}^*$	10 d

* Radioisotopes, which can be produced by means of a mass-separator.

5. High-temperature separation of lutetium radionuclides from an ytterbium target irradiated by protons and neutrons

^{177}Lu is considered to be a very efficient radionuclide for the prostate cancer therapy [11]. It can be produced by thermal neutrons in the $^{176}\text{Yb}(n, \gamma)^{177}\text{Yb} \rightarrow ^{177}\text{Lu}$ reaction. Usually, to extract ^{177}Lu from an irradiated ytterbium target, a complex radiochemical procedure, called “wet radiochemistry” is used. According to Ref. [5], ytterbium and lutetium are elements with very different enthalpy of adsorption on refractory metal surfaces – ~ 3.6 and ~ 6.6 eV, respectively. As is pointed out above, enthalpies of adsorption in general are in good correlation with the boiling points of the corresponding elements. In particular, this is confirmed for the couple ytterbium–lutetium with their boiling points of 1 194 and 3 393°C, respectively.

The first tests of a high-temperature method for separation of $^{171, 172}\text{Lu}$ from an ytterbium metal target were described in Ref. [12]. In that work, an ytterbium metal target was irradiated by a proton beam of the PNPI synchrocyclotron SC-1000 with a proton energy of 100 MeV. Such a beam was achieved by using a calibrated copper degrader [13] with remote change of its thickness.

For the neutron irradiation experiment for ^{177}Lu production, a neutron lead converter was used. The ytterbium target material was placed in a water tank, staying close to the neutron converter. The water tank with a metal ytterbium target is shown in Fig. 1. The target mass of metallic ytterbium for the experiment with neutron irradiation was about 100 mg. After three days of radiation cooling, the target was placed into a quartz vessel, which was inserted into a tungsten oven, heated by resistant heating at the vacuum test bench. The target material processing procedure was completely identical to that described in Ref. [12].



Fig. 1. The water tank used for slowing down of scattered neutrons. A metal ytterbium target is placed in a cylindrical channel inside the tank

During all the time of the target heating, the evaporated target material (metallic ytterbium) was collected in a special cooled volume. In the process of the target material evaporation, the oven temperature was kept in the interval of 800–900°C for the period of one hour in a high vacuum about 10^{-5} mbar.

In Figure 2a, the spectra with γ -lines of proton-irradiated ytterbium before (*black points*) and after (*red points*) the target heating in the quartz vessel are shown. The γ -line with the energy of 396 keV follows the ^{175}Yb ($T_{1/2} = 4.2$ d) β^- -decay. This line was used for calculation of the target material evaporation efficiency x , which can be expressed by the formula

$$x = (S_1^{\text{Yb}} - S_2^{\text{Yb}})/S_1^{\text{Yb}}, \quad (1)$$

where S_1^{Yb} – the γ -line intensity of ^{175}Yb before the irradiated sample heating; S_2^{Yb} – the intensity of the same γ -line after the sample heating.

The γ -line with the energy of 740 keV belongs to the ^{171}Lu ($T_{1/2} = 8.24$ d) β^+ -decay. A comparison of its intensity before and after heating shows what part of lutetium atoms remains in the vessel after heating. One can calculate the efficiency of lutetium isotope production ε using the following expression:

$$\varepsilon = S_2^{\text{Lu}}/S_1^{\text{Lu}},$$

where S_1^{Lu} – the γ -line intensity of ^{171}Lu before the irradiated sample heating; S_2^{Lu} – the intensity of the same γ -line after the sample heating.

In Figure 2b, the spectra with γ -lines of neutron irradiated ytterbium before (*black points*) and after (*red points*) target heating in a quartz vessel are shown. The γ -lines with the energies of 177 and 198 keV follow the ^{169}Yb ($T_{1/2} = 32$ d) β^+ -decay. These lines were used for monitoring of the target material evaporation. The γ -line with the energy of 208 keV belongs to the ^{177}Lu ($T_{1/2} = 6.73$ d) β^- -decay and shows what part of lutetium atoms remains in the vessel after heating.

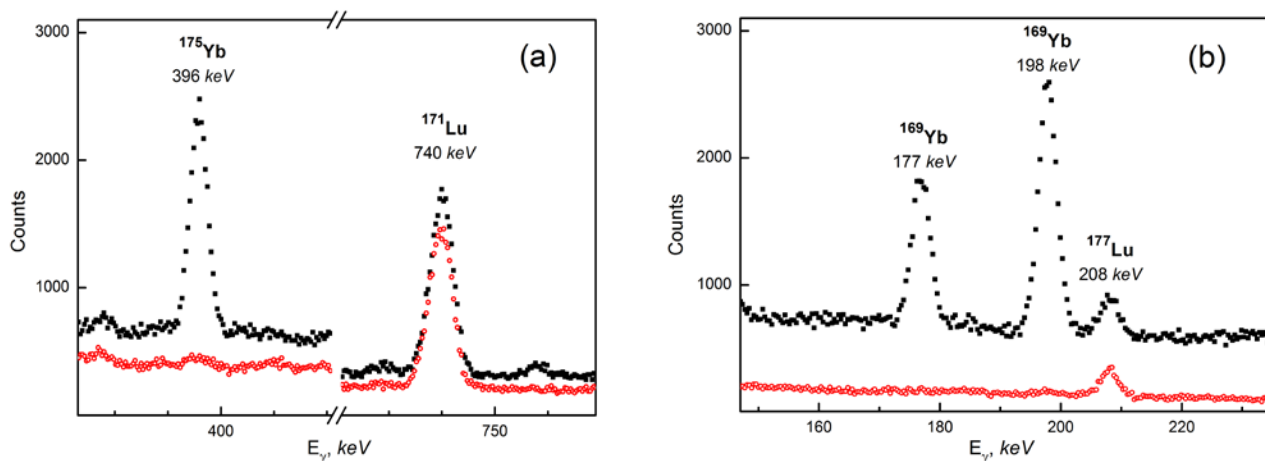


Fig. 2. Gamma spectra of the ytterbium target before (*black squares*) and after (*red open circles*) heating of the sample irradiated: *a* – by protons; *b* – by neutrons

The γ -lines intensities of the ytterbium and lutetium isotopes mentioned above are shown in Table 2. A comparison of the results of two experiments presented in Fig. 2 and Table 2 demonstrates that the method of thermal separation of lutetium isotopes does not depend on whether the required radionuclide are produced in the target material by protons or by neutrons.

Table 2

Gamma-lines intensities of the ytterbium and lutetium isotopes

Irradiation method	Protons (100 MeV)		Thermal neutrons	
	^{175}Yb	^{171}Lu	^{169}Yb	^{177}Lu
E_γ , keV	396	740	198	208
S_γ before heating	19 500	20 500	20 000	2 680
S_γ after heating*	870	19 940	300	2 060

* Corrections for S_γ after heating were introduced in accordance with decay half-lives.

The evaporation efficiency x for the Yb target material irradiated by protons and the production efficiency ε were determined as 0.96(1) and 0.97(2), respectively. For identical Yb target material irradiated by thermal neutrons these values were 0.99(1) and 0.77(7).

Despite the pronounced effect of efficient separation of lutetium isotopes produced by protons or neutrons from the metallic ytterbium target and relatively small statistical errors, the difference between the values of the production efficiency for different projectiles (protons or neutrons) is about 20%. This

discrepancy can be explained by a possible systematic error resulting from not precisely controlled procedure of the temperature rise while reaching the optimal temperature of the target material evaporation. In that case, if the temperature increases too rapidly, the desired radionuclides can be entrained by the flow of atoms of the target substance.

6. High-temperature separation of ^{99m}Tc from a molybdenum trioxide $^{99}\text{Mo}/^{99m}\text{Tc}$ target irradiated by protons and neutrons

The $^{99}\text{Mo}/^{99m}\text{Tc}$ radionuclide generator is the most widely used in diagnostic medicine. In the diagnostic procedures ^{99m}Tc ($T_{1/2} = 6.01$ h) is used. It is extracted from the generator containing the parent isotope ^{99}Mo ($T_{1/2} = 2.75$ d). The most common method for obtaining ^{99}Mo is the fission reaction of highly enriched ^{235}U with thermal neutrons. An alternative way is the method based on the application of a proton cyclotron. The mass of the target material MoO_3 for experiments with proton and neutron irradiation was about 200 mg. The molybdenum trioxide was irradiated by a proton beam of the PNPI synchrocyclotron SC-1000 with a proton energy of 100 MeV.

For the neutron irradiation of the molybdenum trioxide, a neutron lead converter was used. Similar to the experiment with Yb/Lu, the target material was placed into a water tank, staying close to the neutron converter (see Fig. 1). In each experiment, the irradiation time was about 24 h. The majority of isotopes produced by protons in a MoO_3 target have a fairly short life-time. Therefore, the cooling time of the irradiated target was only three hours. After that it was placed into a quartz vessel, which was inserted into a tungsten oven heated by resistant heating at the vacuum test bench. During all the time of the target heating, the evaporated target material MoO_3 was collected in a special cooled volume. During the target material evaporation, the oven temperature was kept in the interval of 600–800°C for the period of one hour in a high vacuum about 10^{-5} mbar.

The time interval between measurements of the spectra before and after target material heating was two hours. Corrections for isotope decay half-life were introduced when comparing the γ -lines intensities. In Figure 3a, the γ spectra of the proton irradiated molybdenum trioxide target before (*black points*) and after (*red points*) target heating in the quartz vessel are shown.

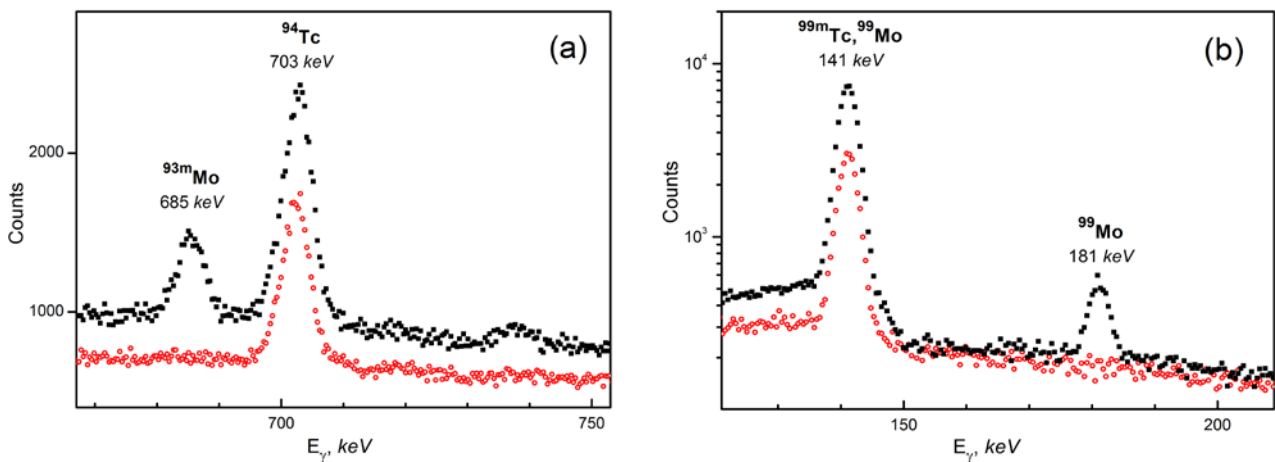


Fig. 3. Gamma spectra of the molybdenum trioxide target before (*black squares*) and after (*red open circles*) heating of the sample irradiated: *a* – by protons; *b* – by neutrons

In Figure 3a, the γ -line with the energy of 685 keV follows the ^{93m}Mo ($T_{1/2} = 6.85$ h) β^- -decay. This line was used for monitoring the target material evaporation. The part of the evaporated MoO_3 target material was calculated by the following formula:

$$x = (S_1^{\text{Mo}} - S_2^{\text{Mo}}) / S_1^{\text{Mo}}, \quad (3)$$

where S_1^{Mo} – the γ -line intensity of ^{93m}Mo before the target material heating; S_2^{Mo} – the intensity of the same γ -line after the sample heating.

The γ -line with the energy of 703 keV belongs to the ^{94}Tc ($T_{1/2} = 4.88$ h) β^- -decay, and a comparison of its intensity before and after heating shows what part of technetium atoms remains in the vessel after heating. One can calculate the efficiency of technetium isotope production using the following expression:

$$\varepsilon = S_2^{\text{Tc}}/S_1^{\text{Tc}},$$

where S_1^{Tc} – the γ -line intensity of ^{94}Tc before the target material heating; S_2^{Tc} – the intensity of the same γ -line after the sample heating.

In Figure 3b, the spectra of neutron irradiated molybdenum oxide before (*black points*) and after (*red points*) target heating are shown. The γ -line with the energy of 181 keV follows the ^{99}Mo ($T_{1/2} = 2.75$ d) β^- -decay. This line was used for monitoring the target material evaporation. The γ -line with the energy of 141 keV belongs to the ^{99m}Tc ($T_{1/2} = 6.01$ h) isomeric transition and shows what part of technetium atoms remains in the vessel after heating. The γ -lines intensities of the molybdenum and technetium isotopes mentioned above are presented in Table 3. A comparison of the results of two experiments presented in Fig. 3 and Table 3 demonstrates that the method of thermal separation of technetium isotopes does not depend on whether the required radionuclide are produced in the target material by protons or by neutrons.

Table 3

Gamma-lines intensities of the molybdenum and technetium isotopes

Irradiation method	Protons (100 MeV)		Thermal neutrons	
	^{93m}Mo	^{94}Tc	^{99}Mo	^{99m}Tc
E_γ , keV	685	703	181	141
S_γ before heating	7 450	24 600	2 800	64 300
S_γ after heating*	0	22 500	0	35 800

* Corrections for S_γ after heating were introduced in accordance with decay half-lives.

The evaporation efficiency x for the MoO_3 target irradiated by protons and the production efficiency ε were determined as 0.96(3) and 0.92(3), respectively. For the identical MoO_3 target material irradiated by thermal neutrons these values were 0.99(3) and 0.56(1).

Apparently, the difference between the production efficiency values for different projectiles (protons or neutrons) can be ascribed as in the case of Lu to the not precisely controlled procedure of temperature rise while reaching the optimal temperature of the target material evaporation. Another possibility of uncontrolled escape of technetium during the thermal injection from MoO_3 target is discussed in the next section.

7. Discussion

The goal of this work was to check the applicability of the method of thermal separation in vacuum of the desired isotopes from targets irradiated not only by protons but also by neutrons. For this purpose, the target materials were selected that ensure the production of radionuclides of lutetium and technetium both with proton and neutron beams. They were: metallic ytterbium for lutetium production and a binary molecular compound molybdenum oxide MoO_3 for technetium production.

It is natural to assume that in the case of a metal target the process of separation of the target substance and the produced radionuclides should not depend on how radionuclides are produced – using protons or neutrons, since both the target substance and the produced radionuclides are in the form of atoms. Therefore, it should be expected that at a significantly higher degree of volatility of the atoms of the target substance (ytterbium) with respect to the atoms of the generated lutetium (boiling points, respectively, 1 194°C and 3 393°C) a possibility arises to evaporate selectively the atoms of the target substance, while keeping the atoms of lutetium in the heated capsule. As it can be seen in Figures 2a and 2b, the thermal separation process is quite efficient, regardless of the method of obtaining lutetium from a metal ytterbium target.

A similar process occurs when a molecular compound is used as a target substance in the case of irradiation by protons. In this case, the molecular bonds are destroyed due to the bombardment of the target by protons with the energy of several tens of MeV and the produced nuclides are presented in the target as atoms rather than retain their molecular form. Therefore, the process of separation of the target substance (in this case MoO₃ with the boiling point 1 255°C) and the produced radionuclide technetium (with the boiling point 4 265°C) will proceed as efficiently, as in the case of the above-discussed lutetium.

A somewhat different situation may arise when a molecular compound is irradiated by neutrons. In this case, the destruction of the molecular bonds may not occur, as the recoil energies are commensurate with the binding energy of the molecule. This can lead to the formation of a new molecular compound, containing the produced radionuclide, with a high volatility, which will not allow the thermal separation of the target substance and the desired radionuclide. In the case of the target substance MoO₃, such a compound may be TcO₂, which has the boiling point about 1 100°C. Therefore, for each target substance in the form of a molecular compound (oxide, chloride, fluoride) preliminary experiments should be carried out to study the efficiency of production of the target material and the desired radionuclide, if they are produced by neutrons.

8. Conclusion

The present work shows that the method of thermal separation in vacuum can be used to isolate the produced radionuclides from the target substances irradiated not only with proton but also with neutron beams. The value of the efficiency of extraction of ¹⁷⁷Lu from the target of metallic ytterbium irradiated with neutrons is 77% with the efficiency of evaporation of the target substance being close to 100%. This value is somewhat different from the value of the efficiency of ¹⁷¹Lu extraction, obtained by its isolation from exactly the same target material irradiated by a proton beam. The reason for this can be insufficiently precisely controlled rate in the process of reaching the operating temperature of evaporation of the target substance.

The value obtained for the production efficiency of ^{99m}Tc from the MoO₃ target material irradiated with neutrons is about 56%. This value differs significantly from the value of the production efficiency $\varepsilon = 92\%$ of ⁹⁴Tc from the same target material irradiated by protons.

Another possible reason for this discrepancy, beside the mentioned above for the lutetium case, is the formation of the molecular compound TcO₂, which has a boiling point of about 1 100°C very close to that of the target material. In this case, some of technetium atoms included in the formed TcO₂ molecules will evaporate at the same rate as the molecules of the target substance. But it should be pointed out here that at this stage of the research this assumption requires additional experimental verification.

References

1. V.N. Panteleev *et al.*, Rad. Applic. **3**, 106 (2018).
2. G.J. Beyer, Hyperfine Interact. **129**, 529 (2000).
3. G.J. Beyer, T.J. Ruth, Nucl. Instrum. Meth. Phys. Res. B **204**, 694 (2003).
4. V.N. Panteleev *et al.*, Tech. Phys. **63**, 1254 (2018).
5. R. Kirchner, Nucl. Instrum. Meth. Phys. Res. B **26**, 204 (1987).
6. V.N. Panteleev *et al.*, RAD Proc. **2**, 43 (2017).
7. V.N. Panteleev *et al.*, Phys. Part. Nucl. **49**, 75 (2018).
8. V.N. Panteleev *et al.*, Rev. Sci. Instrum. **86**, 123510 (2015).
9. S.A. Artamonov *et al.*, PNPI. High Energy Physics Division. Main Scientific Activities 2007–2012, 332 (2013).
10. V.N. Panteleev *et al.*, PNPI. High Energy Physics Division. Main Scientific Activities 2007–2012, 278 (2013).
11. A.A. Shurinov *et al.*, Simpozium “Yadernaya Meditsina”: Sb. Tes. Docl., 18 (2019).
12. V.N. Panteleev *et al.*, RAP Conf. Proc. **1**, 1 (2019).
13. S.A. Artamonov *et al.*, PNPI. High Energy Physics Division. Main Scientific Activities 2013–2018, 6 (2019).

MODERNIZATION OF THE MEDICAL PROTON COMPLEX FOR STEREOTACTIC RADIOSURGERY AT NRC “KURCHATOV INSTITUTE” – PNPI

L.G. Vaganyan, A.A. Vasilev, D.L. Karlin, N.A. Kuzora, V.I. Maksimov, F.A. Pak, A.I. Khalikov

This paper is dedicated to the memory of professor Aleksey Alekseevich Vorobyov, who proposed in november 1971 to use a 1 GeV proton beam of the SC-1000 for clinical radiation therapy.

1. Introduction

Radiotherapy (stereotactic radiosurgery) using a proton beam of the synchrocyclotron SC-1000, was conducted from 1975 to 2013. It confirmed its viability and effectiveness, and received recognition in the scientific community. This article considers the method of proton therapy with 1 GeV beam energy based on the Medical Proton Complex (MPC) of the National Research Centre “Kurchatov Institute” – PNPI, created by the joint efforts of the PNPI and of the Russian Scientific Centre for Radiology and Surgical Technologies (RSC RST). The main results of the current activities of the Laboratory of Medical Physics of the Department of Medical Radiology of the PNPI on the modernization of the MPC, which consists in updating the material and technical base, expanding verification methods for quality assurance (QA) of dose planning and dose delivery for stereotactic radiosurgery using protons with an energy of 1 GeV at the PNPI, are presented. The modernization program will bring the treatment of oncological diseases in Gatchina to a new level.

Nowadays, thanks to technological advances of developed countries, radiation therapy has reached a qualitatively new level and has made a significant progress in terms of achieving the main aim, which is bringing the required dose to the therapeutic focus area while maintaining healthy tissues. About 40% of patients in Russia and up to 70% of patients in other developed countries receive at one stage or another the disease radiation treatment alone or in combination with other methods of cancer treatment. One of the most perspective and actively developing type of radiotherapy is proton beam therapy (PBT). The main advantage of using protons is a more efficient dose distribution within a target than with other types of radiation therapy.

Currently, there are more than 80 functioning PBT centres in the world [1], four proton therapy centres operating in Russia:

- A medical and technical complex in Dubna based on the Joint Institute for Nuclear Research phasotron, which accelerates protons to 660 MeV and protons are slowed down to 200 MeV for medical purposes;
- A proton complex at the A. Tsyba Medical Radiological Research Centre in Obninsk, opened in 2016 on the basis of a synchrotron with variable proton energy in the range from 70 to 250 MeV;
- The medical and diagnostic centre of the Sergey Berezin Medical Institute in Saint Petersburg, launched in 2017 on the basis of a Varian cyclotron with an energy of 250 MeV;
- A multicabin centre in Dimitrovgrad, launched in 2019 on the basis of an ion beam applications (IBA) cyclotron with an energy of 235 MeV.

2. Bragg peak method and on-through method

A typical depth dose distribution curve for a proton beam (Bragg ionization curve) in a tissue-equivalent medium (Fig. 1) has certain features. Depending on which part of the Bragg curve falls on the irradiation focus, there are two options for radiation therapy with proton beams: irradiation method using the Bragg peak (the method of stopping) and the method of irradiation with the plateau region (the “on-through” method). The last method is expedient to use for narrow beams. Protons up to 250 MeV are used when applying the Bragg peak method. Their range in biological tissues corresponds to the depth of the irradiated objects. A successful experience was gained in radiotherapy of patients with intracranial pathologies using higher energy protons in the USSR, which will be discussed in the article. The treatment of patients was started in 1975 in Gatchina (Leningrad region, Russia), at the Leningrad Nuclear Physics Institute (LNPI,

and PNPI nowadays). The radiation therapy was carried out by the “on-through” method with 1 GeV protons of the LNPI synchrocyclotron SC-1000 [2]. It is worth noting that the first experience of proton therapy at Berkeley was just the “on-through” method.

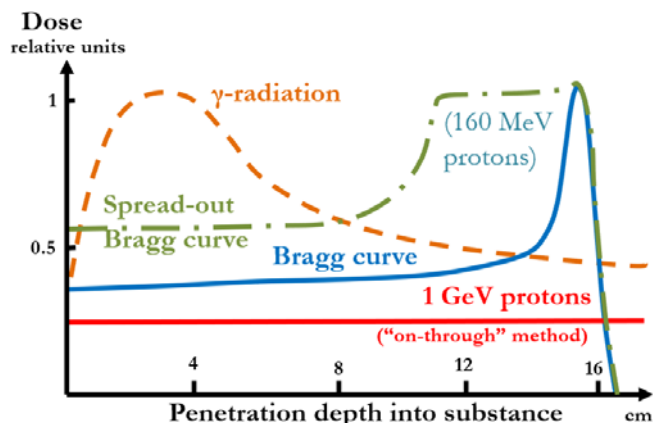


Fig. 1. Absorbed dose radiation distribution depending on the penetration depth into substance

The method of proton therapy using a beam of such energy is fundamentally different from other methods. There is no experience in the world practice of clinical use of beams of such energy in matters of their formation and dosimetry. The proton beam of the accelerator is monoenergetic and it has a small cross section. In order to enhance the effect in the irradiated tumor and to reduce the irradiation of healthy tissues, the technique of multifield irradiation from different directions is applied, which is implemented by rotating the irradiation stand relative to a monodirectional stationary beam.

The therapeutic installation (UPST) designed to implement the multifield irradiation technique in PNPI is shown in Fig. 2. The main elements of the UPST are a treatment table, a head fixation device (HFD) and an X-ray centralizer. The treatment table can rotate around the vertical axis (Z), passing through the isocentre of the installation by $\pm 40^\circ$. The HFD can perform pendulum movements at an angle of up to $\pm 36^\circ$ around the horizontal axis (X) perpendicular to the beam axis (Y). Both rocking axes, as well as the axis of the proton beam, intersect at one point, which is the isocentre of the UPST. At any rotation of the head fixation device and the treatment table, the object located in the isocentre of the UPST remains motionless. Thus, the proton beam is directed to the set-up isocentre (target centre) at different angles. The X-ray centralizer is a specially adapted X-ray diagnostic apparatus with the ability to rotate around the isocentre. It has two fixed positions: horizontal and vertical, which makes it possible to produce a lateral and frontal X-ray image, respectively, for precise targeting at the isocentre of the UPST.

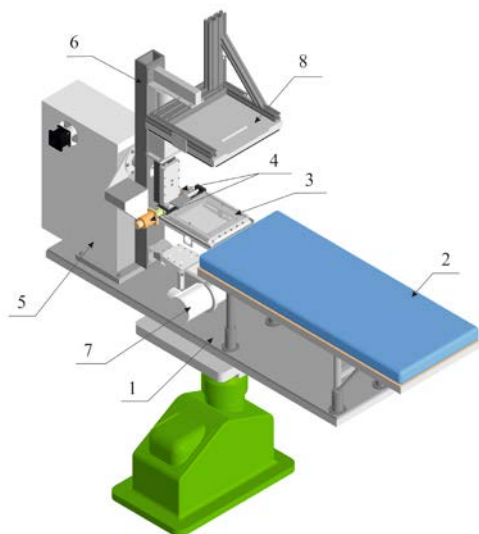


Fig. 2. Scheme of the installation of proton stereotaxic therapy: 1 – treatment table; 2 – treatment table deck; 3 – head fixation device; 4 – drives for movement of the deck of the HFD along the X and Y axes; 5 – HFD drive rack; 6 – rocker for rotation of the X-ray centralizer; 7 – X-ray monoblock; 8 – flat panel X-ray detector

The irradiation procedure begins with setting the initial position of the UPST: the HFD is set to -36° , the treatment table is set to -40° (depending on clinical requirements, other angles can be chosen). Simultaneously with switching on the beam, the movement of the UPST is started in accordance with the preset irradiation program. The HFD rotates from -36° to $+36^\circ$, after which the treatment table rotates to a fixed angle, depending on the planned number of passes (for example, 8° for 10 passes). This cycle of movement corresponds to one pass. Then the second pass begins: the HFD makes a reverse movement from $+36^\circ$ to -36° , the treatment table again turns to a fixed angle, *etc.* (Fig. 3) until the irradiation program is completed.

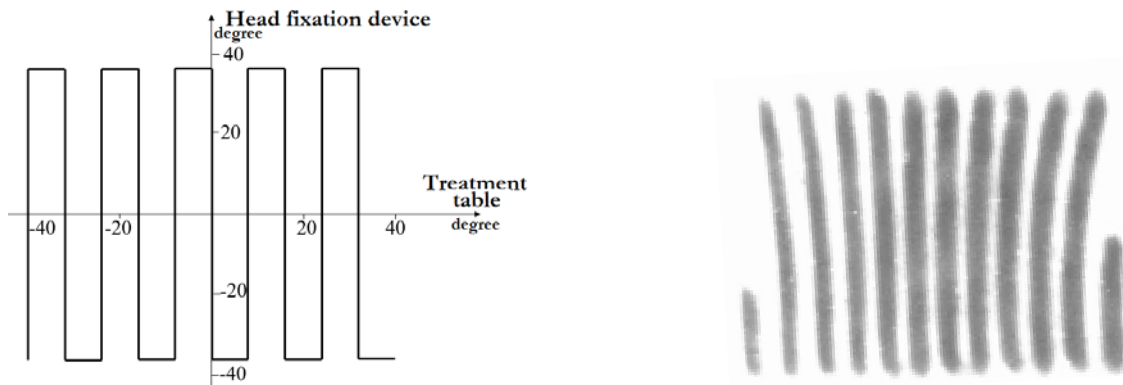


Fig. 3. Diagram of movement of the head fixation device and treatment table during 10 passes (*left*); radioautograph of a proton beam (*right*)

As a result, the beam describes a trajectory on the patient's head, shown in Fig. 4. The concentration of the dose at the desired point occurs due to the following factors:

- Changing the direction of the patient irradiation by slowly turning it in two planes relative to the beam axis;
- Focusing of the proton beam by quadrupole magnetic lenses to the irradiation point;
- Small angular scattering of protons with an energy of 1 GeV in the patient's body.

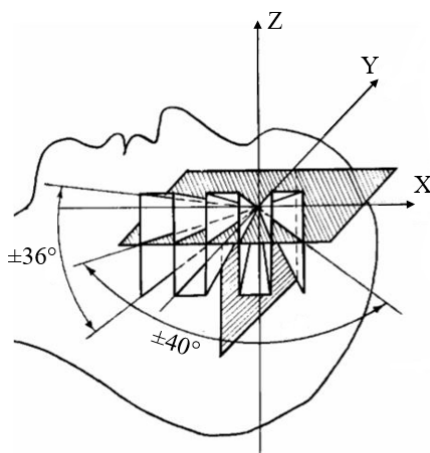


Fig. 4. Irradiation scheme. Direction of the proton beam passing through the centre of the target during stereotaxic irradiation using rotation of the stereotaxic proton therapy unit

Based on the results of clinical trials, it was found that the medical proton beam formed at the SC-1000 can be rationally used in the field of radioneurosurgery to affect small pathological areas of the brain (up to 2 cm) in order to destroy them. The main advantage of this method is the possibility of forming small dose fields with a high edge gradient, which makes it possible to concentrate the absorbed dose in the tumor with minimal radiation exposure of the surrounding tissues. Due to the high energy of the particles, the angular divergence of the 1 GeV proton beam is much smaller with the PBT than with the standard energy for PBT (using the Bragg peak), which simplifies the treatment planning. Using the gantry system is not provided due

to the high energy of protons: guide magnets would be too heavy and cumbersome, so the technique of rotating the object of irradiation on a special installation is used.

The first full-scale dosimetric and radiobiological studies to analyse the effectiveness and at the same time the safety of using 1 GeV proton beam of the SC-1000 for radiation therapy, as well as to determine the scope of its application, were carried out back in 1971–1974. By 2013, the proportion of patients receiving proton therapy from the RSC RST–PNPI was approximately 2% of the global number of patients treated in the world. Using of proton stereotactic therapy (radiosurgery) proved to be effective in the treatment of various brain diseases, especially pituitary adenomas and cerebrovascular malformations, as well as in adenohypophysis irradiation for palliative purposes in breast and prostate cancer [3]. After 40 years of successful experience in treating patients, studies conducted in 2013–2017 led to the decision on the advisability of upgrading the stereotaxic proton therapy (radiosurgery) unit to meet modern requirements and world standards in radiation therapy, as well as for UPST registration as a medical device and the resumption of medical activities. The key stages of the modernization were: updating the material and technical base and software, including the replacement of the X-ray centering complex, updating the clinical dosimetry system, creating an automated control system for the UPST, a system for dose-anatomical planning and expanding methods for verifying of exposure plans.

3. Modernization of the medical proton complex

3.1. Replacement of the main elements of the X-ray centralizer

The X-ray centralizer is an integral part of the UPST, which is necessary to point the irradiation focus at the isocentre of the UPST. Previously, a TURDE-19 X-ray machine manufactured in 1982 was used with an electron-optical converter (EOC) and an X-ray television installation, on the monitor of which the resulting image was displayed. The issue of replacing the old X-ray centralizer with a more modern one is long overdue. The obsolescence of the equipment was considered the main obstacle to the beginning of the formalization of the complex as a medical device. The main parts of the X-ray centralizer (the X-ray emitter, the power supply and EOC) were replaced in 2018 with new equipment that meets modern requirements for X-ray studies. The EOC device was replaced with a digital flat panel detector DFP 4343 (Fig. 5). The size of the active area of the detector is $430 \times 430 \text{ mm}^2$, the matrix resolution is 3072×3072 , and the pixel size is $140 \times 140 \text{ }\mu\text{m}^2$. For the new detector, a protective cover was made of plexiglass, and a radiopaque crosshair was applied, corresponding to the centre of the detector.

The updated X-ray centralizer based on a flat-panel detector surpasses the previously used one based on an image intensifier tube in most characteristics. The advantage is high spatial resolution, large dynamic range, high resistance to direct X-ray radiation, absence of spatial distortions and unevenness, insensitivity to magnetic fields, remote control, reduction of radiation exposure to staff. The high sensitivity of the flat panel detector makes it possible to obtain a high-quality image with a wide exposure range. In addition, it became possible to visualize small and low-contrast structures, which simplifies the procedure of laying the patient. Also, an automated workplace for the operator was organized to control the system and to work with the research results (Fig. 6). The digital format allows additional computer processing of the obtained images; the results of the study are stored in the system.



Fig. 5. X-ray centralizer in vertical position

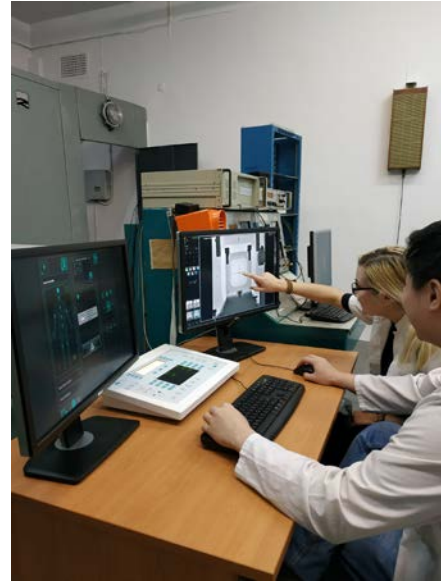


Fig. 6. Operator workstation

3.2. Update of the clinical dosimetry system

In 2018, the clinical dosimetry system was supplemented with a set of dosimetric equipment, which includes a Unidose^{weblin} PTW (Physikalisch-Technische Werkstätten) Freiburg GmbH T10021 single-channel dosimeter with built-in firmware for absolute dosimetry of therapeutic and diagnostic beams and ultrasmall PinPoint ionization chambers of the type TM31014 (0.015 cm³) and TM31015 (0.03 cm³). This device is included in the register of Rosstandart. The dose measurement range is from 200 μGy to 450 MGy, the dose rate being from 1.2 mGy/min to 7.5 kGy/min simultaneously in three measurement ranges. The dosimeter has the ability to correct readings by entering various corrections. Multiplication by correction factors is done automatically by the instrument. The device is easy to use. Setting up, adding and changing the necessary parameters of the device and detector for the study is rather simple. The device can be controlled remotely with a local personal computer *via* the Internet using the virtual network computing program.

Measurements of the dose of a proton beam with an energy of 1 GeV during the verification of the new system (using Unidose^{weblin}) were compared with the results of the existing equipment – thermoluminescence dosimetry (TLD) detectors. The analysis of the data showed that the difference in the dispensed dose does not exceed 5%, which indicates good agreement between the data. Figure 7 shows 2 Gy “dose binding” data using the chambers of clinical dosimeter Unidose^{weblin} and a comparison with the clinical dosimeter, type 27012, with hose ionization chamber, type 70107 (0.05 cm³). As can be seen from the diagrams, the differences in the absorbed dose for beams 1 and 2 cm in diameter do not exceed 5%. The difference in the dose at a narrow beam with a diameter of 8 mm arises due to different active volumes of the compared ionization chambers.

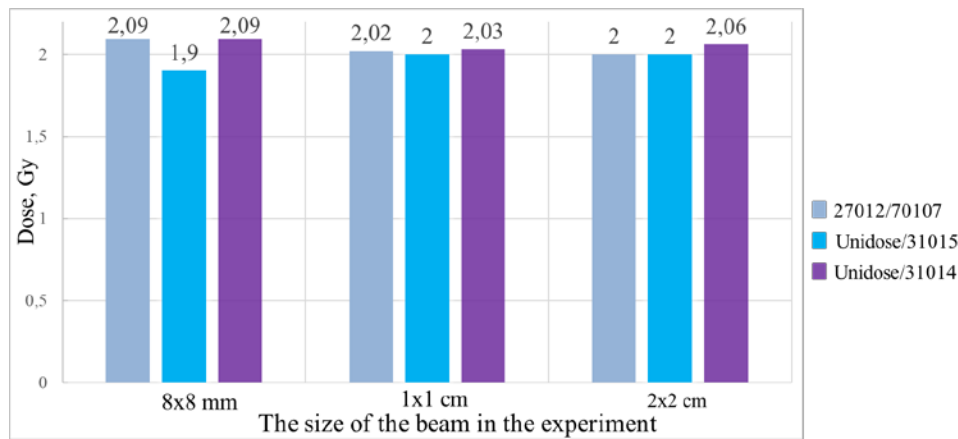


Fig. 7. Comparison of the “dose binding” using PTW Unidose^{webline} and clinical dosimeter type 27012

3.3. Replacement of the control system, and equipment layout

The third-generation UPST control scheme was created back in 1989. Accordingly, the existing element base has become obsolete over the years and cannot meet the current requirements for ensuring the quality of the proton therapy. In 2014–2016, in order to improve the exploitative characteristics (speed of movement, positioning accuracy) of the electromechanical units and elements of the UPST, unipolar stepper motors were replaced with bipolar ones, which made it possible to significantly improve the dynamic characteristics of the moved units of the UPST and to use the mode of reducing the step of the motors during their movement, which improves the smoothness of movement. Magnetic-modulatory sensors of angular displacements were replaced by optical multidigit sensors “angle-code”. This measure makes it possible to significantly improve the displacement measurement result and the overall safety of the obtained results. The replacement of the equipment required the development of a new hardware and software (see below). Two types of drivers and a power source for controlling the operation of bipolar stepper motors, three two-channel adapter-coordinator-distributors and a manual control panel for electromechanical units of the UPST were developed and manufactured. In order to respond promptly to emergency situations, the control drivers were moved in 2018 from the irradiation room to the control room. On the whole, the synchronization of the system has been simplified: two workstations have been merged into one; the UPST is controlled by a single program, which also receives data from ionization chambers and profilometers.

3.4. Creation of an automated control program for the installation of proton stereotaxic therapy

The development of a program for the automated control of the UPST was required in connection with the replacement of the hardware for controlling the drives of the treatment unit. The first version of the control program “Proton Therapy”, intended to control the patient irradiation system, was developed in 2015. This program was used in conjunction with the previously developed “Profilometer” program, designed to display the data obtained using multiwire proportional chambers that measure the spatial characteristics of the beam online during irradiation. The program “Proton Therapy” had two drawbacks:

- The forced use in conjunction with the “Profilometer” program installed at another workstation, as a result of which it became necessary to involve at least two operators to monitor the irradiation process;
- The development of the program was stopped at the testing stage.

To expand the capabilities of the first version of the program of the control, it was decided to rework it at a new level and to combine it with the program for monitoring the parameters of the proton beam. So, in 2019 a software was created for controlling the UPST with the function of controlling the parameters of the proton beam [4]. The program is designed to automate proton therapy and provides the following modes of operation:

- Manual control of five axes of movement of the UPST;

- Output of information about the beam parameters: beam profiles (size, position), background, statistical parameters, intensity;
- Calculation of the monitor unit per absorbed dose unit;
- Setting exposure parameters or loading patient exposure plans;
- Conducting irradiation according to the given algorithm;
- The ability to interrupt and continue the irradiation process;
- Display of complete information about the course of the irradiation process in the form of 3D animation, graphs, tables;
- Generating reports;
- Formation of daily logs of actions of the program and operator, the ability to view the log for any date;
- Editing and storage of the parameters of the movement of the elements of the UPST, setting the parameters for registration of the proton beam.

The developed program has a flexible and understandable interface (Fig. 8). It allows one to manage the UPST in the manual mode as efficiently as possible and to receive complete information about the state of the installation. There is full control over the beam parameters and the possibility of linking to the dose (“dose binding”). The beam profiles are controlled directly in the control program, and not at a separate station. These additions have increased the work efficiency and led to a reduction in the time spent on the commissioning. The irradiation process has become more understandable in terms of visual component and information content, which contributes to the standardization of treatment protocols. The control of the irradiation process (beam profiles) has become automated.

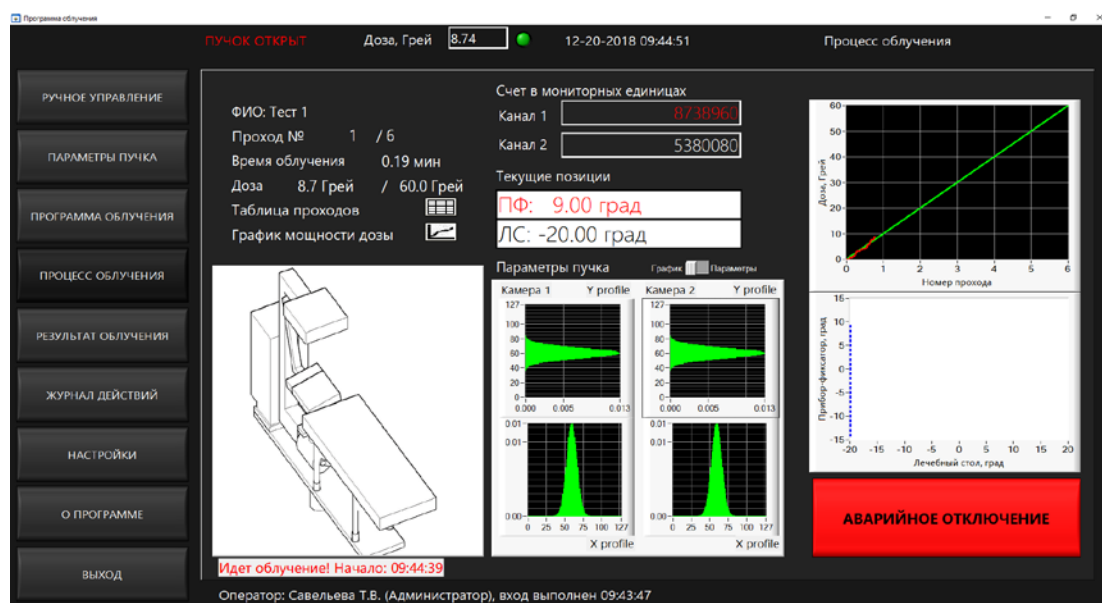


Fig. 8. Operating window of the stereotactic proton therapy unit control system

3.5. Development of a planning and verification system

A narrow proton beam with 1 GeV energy in combination with a stereotaxic irradiation method makes it possible to form strictly localized and concentrated dose fields. However, to realize this opportunity, it is necessary to carry out preliminary dose-anatomical planning of irradiation. At the first stage of proton therapy (1975–2013), irradiation planning was carried out manually according to experimental data. Dose distributions were obtained in a spherical phantom imitating the patient’s head using TLD detectors, which were placed in the phantom in two mutually perpendicular planes with a step of 5 mm in the central region and 10 mm at the periphery. In this way, several tens of isodose maps were obtained and analysed for various irradiation parameters, which were combined into an atlas of dose distributions. As a rule, due to the limited

shape and size of formations recommended for proton stereotaxic therapy with 1 GeV protons, the irradiation parameters in most cases did not change. The constructed isodose curves were plotted on a transparent film and superimposed on the magnetic resonance images of patients, performed in the frontal and sagittal planes, at the same scale. Then, the distance from the isocentre to the critical structures was determined. The measured distance was used to calculate the dose load on them. The areas of the target, and of the dose fields were calculated by simple arithmetic calculations. Manual scheduling is currently considered obsolete. Experimental data continue to be used, but only to verify the calculated dose distributions, and not as the main planning method.

The planning system and the verification system, along with the clinical dosimetry system, form the basis of radiotherapy quality assurance. The existing commercial software cannot be applied to the 1 GeV proton beam treatment method, since this method is unique and does not fit into the existing requirements. The work on the creation of a computerized treatment planning system (TPS) ProtoPlan, the algorithm for calculating the predicted dose of which is based on the Monte Carlo method with parameterization of integral properties, was started in 2018. The three-dimensional geometry of the TPS takes into account such features as:

- Energy of 1 GeV;
- Beam size of 6–10 mm at 50% isodose;
- Beam convergence and divergence;
- Lack of a gantry system;
- “On-through” irradiation;
- Change in linear energy transfer along the trajectory;
- Isocentric irradiation technique implemented with the help of the UPST;
- Scattering in the irradiated object;
- “Blurring: of the dose distribution due to secondary particles that are born in the process of interaction of protons with biological tissues.

Due to the uniqueness of the method of irradiation with 1 GeV protons, as well as the system of rotation of the irradiation area relative to the beam axis fixed in space, the main abilities of a non-standard proton therapy planning system became:

- Receiving data from diagnostic devices, support for the format of digital imaging and communications in medicine;
- Reconstruction of images from the original data set;
- Segmentation target volumes and organs at risk;
- Calculation of the absorbed dose from a given beam and its presentation in the form of two- and three-dimensional isodose distributions superimposed on anatomical images (Fig. 9);
- Construction of “dose-volume” histograms for targets and critical organs;
- Export of the irradiation plan to the control program of the UPST.

One of the complex tasks of the formation of the modern concept of the MPC, along with the planning system, is the verification of the calculated exposure plans. The verification system is designed to compare the actual dose that the patient will receive with the dose calculated in the planning system. This stage of radiation therapy allows to be sure of the exact implementation of the radiation plan and additionally check the correct operation of the planning system for various radiation parameters. The dose distribution measured during the implementation of the verification plan (QA-plan) is compared with the calculated dose distribution using the γ -analysis method, which is currently the global standard. This method combines two criteria:

- Comparison of the percentage difference between the calculated and measured dose values;
- Comparison of the smallest distance from the measurement point to the isodose surface of the calculated dose value corresponding to the measured value.

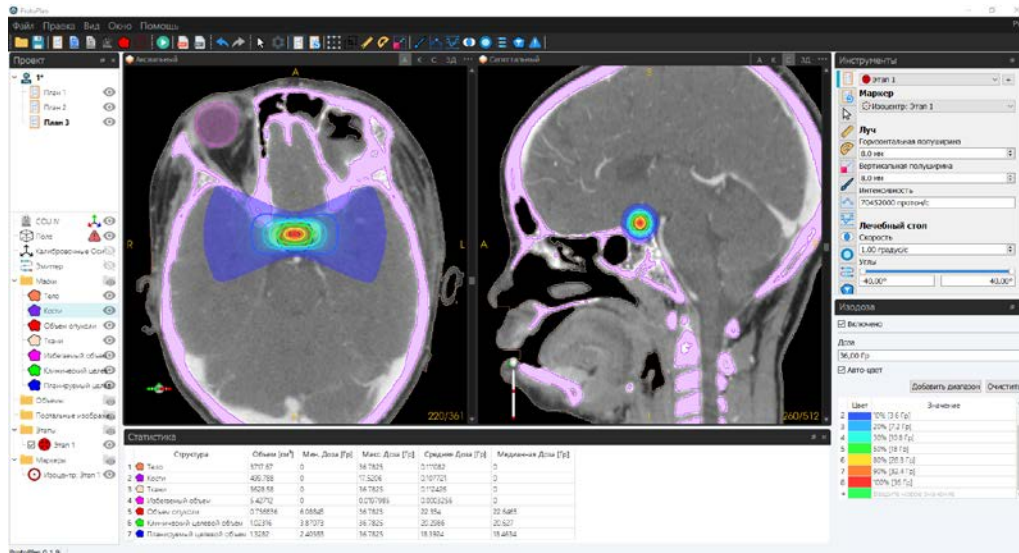


Fig. 9. Isodose curves superimposed on magnetic resonance images of patients in the frontal (*left*) and sagittal (*right*) planes obtained in ProtoPlan

Currently, the work is underway to build up a dosimetric phantom for verification, and a possibility of using radiochromic films as detectors for relative dosimetry is being considered. As a result, the commissioning of a system of planning and verification will make it possible to proceed to the registration of the UPST as a medical device and the resumption of medical activities.

4. Conclusion

On April 17, 2023 it will be 48 years since the start of treatment of patients with proton therapy based on the synchrocyclotron SC-1000. There is no doubt that the unique method of proton radiosurgery for brain diseases using 1 GeV protons should be used with maximum efficiency. To resume proton therapy, it is necessary to obtain a registration certificate for the UPST as a medical device. To this end, a program was launched to modernize the equipment in order to bring the MPC in line with modern quality requirements, as well as to improve the reliability of therapy based on the SC-1000.

As part of the modernization, the main elements of the MPC have been replaced with more modern analogues, including: an X-ray centering system, a clinical dosimetry system, a control system, and technical tests of the updated systems were carried out. The last stage of modernization, which made it possible to proceed to the registration of the UPST as a medical device, was the development of a system for dose-anatomical planning and verification of exposure plans. This stage was performed in 2021. By the end of 2022, all planned engineering and technical works have been completed to bring the MPC to modern standards. The proton therapy based on SC-1000 can now be resumed.

References

1. Particle Therapy Co-Operativ Group. <https://www.ptcog.ch>
2. N.K. Abrosimov *et al.*, J. Phys.: Conf. Ser. **41**, 424 (2006).
3. A.M. Granov *et al.*, Vopr. Onkol. **59**, 465 (2013).
4. M.R. Kolkhidashvili *et al.*, Preprint NRC “Kurchatov Institute” – PNPI 3040, 11 (2019).

CONTENTS

PREFACE	3
STATUS OF THE ACCELERATOR FACILITIES AT PNPI	
STATUS OF THE PNPI ACCELERATOR COMPLEX	
D.A. Amerkanov, S.A. Artamonov, E.M. Ivanov, L.A. Sukhorukov	6
ELEMENTARY PARTICLES PHYSICS	
HIGGS BOZON AND STANDARD MODEL STUDY WITH CMS AT THE LARGE HADRON COLLIDER	
A.A. Vorobyev, V.T. Kim, Yu.M. Ivanov, V.L. Golovtsov, E.V. Kuznetsova, P.M. Levchenko, A.Iu. Egorov, V.A. Murzin, V.A. Oreshkin, L.A. Shchipunov, I.B. Smirnov, D.E. Sosnov, V.V. Sulimov, L.N. Uvarov, S.A. Vavilov, S.S. Volkov, An.A. Vorobyev.....	16
OVERVIEW OF RECENT ATLAS RESULTS	
S.G. Barsov, A.E. Ezhilov, O.L. Fedin, V.T. Grachev, M.P. Levchenko, V.P. Maleev, Yu.G. Naryshkin, D. Pudzha, V.A. Schegelsky, V.M. Solovyev	26
EXPERIMENT LHCb AT THE LARGE HADRON COLLIDER	
G.D. Alkhazov, A.V. Andreyanov, N.F. Bondar, A.D. Chubykin, A.A. Dzyuba, P.V. Kravchenko, O.E. Maev, D.A. Maisuzenko, N.R. Sagidova, A.N. Solovyev, I.N. Solovyev, A.A. Vorobyev, N.I. Voropaev	36
BRIEF OVERVIEW OF SOME ALICE RESULTS IN 2019–2022	
V.V. Ivanov, A.V. Khanzadeev, E.L. Kryshen, M.V. Malaev, V.N. Nikulin, A.Yu. Ryabov, V.G. Ryabov, Yu.G. Ryabov, V.M. Samsonov, M.B. Zhalov	43
SEARCH FOR HEAVY RESONANCES DECAYING INTO A PAIR OF Z-BOZONS	
S.G. Barsov, A.E. Ezhilov, O.L. Fedin, M.P. Levchenko, V.P. Maleev, Yu.G. Naryshkin, V.A. Schegelsky, V.M. Solovyev, D. Pudza	50
MEASUREMENT OF TOP-QUARK PAIR SPIN CORRELATIONS	
S.G. Barsov, A.E. Ezhilov, O.L. Fedin, M.P. Levchenko, V.P. Maleev, Yu.G. Naryshkin, V.A. Schegelsky, V.M. Solovyev	58
MEASUREMENT OF THE TRANSVERSE MOMENTUM DISTRIBUTION OF DRELL–YAN LEPTON PAIRS IN PROTON–PROTON COLLISIONS AT $\sqrt{s} = 13$ TeV WITH THE ATLAS DETECTOR	
O.L. Fedin, V.P. Maleev, Yu.G. Naryshkin, V.A. Schegelsky, S.G. Barsov, V.M. Solovyev, A.E. Ezhilov, M.P. Levchenko, D. Pudzha	65
DIJETS WITH LARGE RAPIDITY SEPARATION AT CMS AS A PROBE FOR BFKL EFFECTS	
A.Iu. Egorov, V.T. Kim, G.E. Gavrilov, V.L. Golovtsov, Yu.M. Ivanov, E.V. Kuznetsova, V.A. Murzin, V.A. Oreshkin, I.B. Smirnov, D.E. Sosnov, V.V. Sulimov, L.N. Uvarov, S.S. Volkov, A.A. Vorobyev	71
PNPI STUDY OF RARE DECAYS OF B^0 AND B_s^0 MESONS IN THE LHCb EXPERIMENT	
G.D. Alkhazov, A.V. Andreyanov, N.F. Bondar, A.D. Chubykin, A.A. Dzyuba, P.V. Kravchenko, O.E. Maev, D.A. Maisuzenko, N.R. Sagidova, A.N. Solovyev, I.N. Solovyev, A.A. Vorobyev, N.I. Voropaev	79

HEAVY BARYONS AT LHCb G.D. Alkhazov, A.V. Andreyanov, N.F. Bondar, A.D. Chubykin, A.A. Dzyuba, P.V. Kravchenko, O.E. Maev, D.A. Maisuzenko, N.R. Sagidova, A.N. Solovyev, I.N. Solovyev, A.A. Vorobyev, N.I. Voropaev	86
FIRST MEASUREMENT OF DIFFRACTIVE PROTON–NUCLEUS COLLISIONS WITH CMS AT THE LARGE HADRON COLLIDER E.V. Kuznetsova, D.E. Sosnov, V.T. Kim, S.A. Nasybulin, G.E. Gavrilov, V.L. Golovtsov, Yu.M. Ivanov, V.A. Murzin, V.A. Oreshkin, I.B. Smirnov, V.V. Sulimov, L.N. Uvarov, S.S. Volkov, A.A. Vorobyev	94
ULTRAPERIPHERAL NUCLEAR COLLISIONS IN ALICE AT THE LARGE HADRON COLLIDER V.A. Guzey, V.V. Ivanov, A.V. Khanzadeev, E.L. Kryshen, M.V. Malaev, V.N. Nikulin, A.Yu. Ryabov, V.G. Ryabov, Yu.G. Ryabov, V.M. Samsonov, M.B. Zhalov	98
THE HADRONIC PHASE LIFETIME DURING THE EVOLUTION OF EXTREME STATES OF MATTER IN COLLISIONS OF ULTRARELATIVISTIC NUCLEI AT THE LARGE HADRON COLLIDER V.V. Ivanov, A.V. Khanzadeev, E.L. Kryshen, M.V. Malaev, V.N. Nikulin, A.Yu. Ryabov, V.G. Ryabov, Yu.G. Ryabov, V.M. Samsonov, M.B. Zhalov	104
GENERALIZATION OF SUDAKOV FORM FACTOR FOR SKEWED KINEMATIC REGIME V.T. Kim.....	108
BENT CRYSTALS FOR SPS AND LARGE HADRON COLLIDER BEAMS Yu.M. Ivanov, A.S. Denisov, Yu.A. Gavrikov, B.L. Gorshkov, M.A. Koznov, L.P. Lapina, L.G. Malyarenko, V.I. Murzin, L.F. Pavlova, V.V. Skorobogatov, L.A. Vaishnena.....	111
PRECISION MEASUREMENT OF THE MUON CAPTURE RATE ON DEUTERON, PRELIMINARY RESULT OF THE MUSUN EXPERIMENT V.A. Ganzha, K.A. Ivshin, P.V. Kravchenko, P.A. Kravtsov, A.N. Solovyev, I.N. Solovyev, A.A. Vasilyev, A.A. Vorobyov, N.I. Voropaev, M.E. Vznuzdaev	121
HIGH-PRECISION DECAY ENERGY OF ^{187}Re FOR RESEARCH IN FUNDAMENTAL PHYSICS S.A. Eliseev, P.E. Filianin, Yu.N. Novikov	126
LONGITUDINAL DOUBLE-SPIN ASYMMETRIES IN SEMI-INCLUSIVE DEEP INELASTIC SCATTERING OF ELECTRONS AND POSITRONS BY PROTONS AND DEUTERONS S.L. Belostotski, G.E. Gavrilov, A.A. Izotov, P.V. Kravchenko, S.I. Manaenkov, Yu.G. Naryshkin, V.V. Vikhrov	129
STUDY OF THE PRODUCTION OF NEGATIVELY CHARGED PIONS IN pn COLLISIONS AT THE BEAM MOMENTA BETWEEN 1 140 AND 1 670 MeV/c V.V. Sarantsev, S.G. Sherman, V.A. Nikonov, A.V. Sarantsev.....	133
PNPI PARTICIPATION IN THE LHC DETECTORS UPGRADE	
CMS ENDCAP MUON SYSTEM UPGRADE A.A. Vorobyev, V.T. Kim, Yu.M. Ivanov, A.Iu. Egorov, G.E. Gavrilov, V.L. Golovtsov, E.V. Kuznetsova, V.A. Murzin, V.A. Oreshkin, I.B. Smirnov, D.E. Sosnov, V.V. Sulimov, L.N. Uvarov, S.S. Volkov	140

UPGRADE PROGRAMME OF THE ATLAS DETECTOR AT THE LARGE HADRON COLLIDER
 S.G. Barsov, O.L. Fedin, A.E. Ezhilov, M.P. Levchenko, V.P. Maleev, Yu.G. Naryshkin,
 D. Pudzha, V.A. Schegelsky, V.M. Solovyev148

UPGRADE PROGRAMME OF THE LHCb DETECTOR AT THE LARGE HADRON COLLIDER
 G.D. Alkhazov, N.F. Bondar, B.V. Bochin, A.D. Chubykin, V.V. Chulikov, S.A. Gets, A.A. Dzyuba,
 D.S. Ilyin, S.N. Kotryakhova, V.S. Kozlov, O.E. Maev, N.R. Sagidova, A.A. Vorobyev155

NUCLEAR AND ATOMIC PHYSICS

SEARCH FOR MUON CATALYZED $d^3\text{He}$ FUSION
 V.D. Fotev, V.A. Ganzha, K.A. Ivshin, P.V. Kravchenko, P.A. Kravtsov, E.M. Maev, A.V. Nadtochy,
 A.N. Solovev, I.N. Solovyev, A.A. Vasilyev, A.A. Vorobyov, N.I. Voropaev, M.E. Vznuzdaev166

OBSERVATION OF A NEW PHENOMENON
 OF THE HIGHLY EXCITED LONG-LIVED ATOMIC ISOMERS
 S.A. Eliseev, P.E. Filianin, Yu.N. Novikov178

STUDY OF THE STRUCTURE OF LIGHT EXOTIC NUCLEI BY PROTON ELASTIC SCATTERING
 IN INVERSE KINEMATICS USING THE ACTIVE TARGET IKAR
 G.D. Alkhazov, A.V. Dobrovolsky, A.G. Inglessi, A.V. Khanzadeev, G.A. Korolev,
 L.O. Sergeev, A.A. Vorobyov, V.I. Yatsyura182

LOOKING FOR THE ELECTRON BRIDGE IN $^{229\text{m}}\text{Th}$
 A.V. Popov, Yu.I. Gusev, T.V. Koneva, Yu.V. Nechiporenko, Yu.N. Novikov190

SHAPE-STAGGERING EFFECT IN MERCURY NUCLEI
 A.E. Barzakh, D.V. Fedorov, P.L. Molkanov, V.N. Pantelev, M.D. Seliverstov196

SHELL EFFECT AND ODD-EVEN STAGGERING IN CHARGE RADII
 AROUND THE $N = 126$ SHELL CLOSURE
 A.E. Barzakh, D.V. Fedorov, P.L. Molkanov, V.N. Pantelev, M.D. Seliverstov204

HYPERFINE ANOMALY IN GOLD AND MAGNETIC MOMENTS OF $I^\pi = 11/2^-$ GOLD ISOMERS
 A.E. Barzakh, D.V. Fedorov, P.L. Molkanov, V.N. Pantelev, M.D. Seliverstov,
 Yu.A. Demidov, M.G. Kozlov211

LARGE SHAPE STAGGERING IN NEUTRON-DEFICIENT Bi ISOTOPES
 A.E. Barzakh, D.V. Fedorov, P.L. Molkanov, V.N. Pantelev, M.D. Seliverstov, L.V. Skripnikov,
 A.V. Oleynichenko, A.V. Zaitsevskii217

STUDY OF NUCLEON CORRELATIONS IN NUCLEI
 BY THE INCLUSIVE (p, p') -REACTION AT 1 GeV
 O.V. Miklukho, V.A. Andreev, G.V. Fedotov, A.A. Izotov, A.Yu. Kisselev, N.G. Kozlenko,
 D.V. Novinskiy, A.V. Shvedchikov, S.S. Volkov, A.A. Zhdanov224

μSR STUDIES OF MULTIFERROICS AND FERROLIQUIDS
 AT THE NRC "KURCHATOV INSTITUTE" – PNPI
 A.L. Getalov, E.N. Komarov, S.A. Kotov, G.V. Shcherbakov, S.I. Vorob'ev229

LABORATORY BALL LIGHTNING–PLASMOID – NEW TYPE OF THE GAS DISCHARGE
 G.D. Shabanov, A.G. Krivshich239

NEW PROJECTS

IRINA PROJECT AT THE REACTOR PIK V.N. Pantelev, A.E. Barzakh, D.V. Fedorov, P.L. Molkanov, M.D. Seliverstov	250
AMBER – A NEW FACILITY AT THE CERN SPS A.A. Dzyuba, A.G. Inglessi, K.A. Ivshin, E.M. Maev, O.E. Maev, A.N. Solovyev, I.N. Solovyev, A.A. Vassiliev, A.A. Vorobyev, M.E. Vznuzdaev	254
THE SPASCHARM EXPERIMENT AT THE ACCELERATOR U-70 (IHEP, PROTVINO) V.A. Andreev, A.B. Gridnev, N.G. Kozlenko, V.S. Kozlov, V.A. Kuznetsov, D.V. Novinsky, V.I. Tarakanov, V.S. Temirbulatov	262
SHiP: SEARCH FOR HIDDEN PARTICLES V.T. Kim, E.V. Kuznetsova, O.L. Fedin, G.E. Gavrilov, V.L. Golovtsov, N.V. Gruzinskiy, S.A. Nasybulin, V.P. Maleev, L.N. Uvarov, V.I. Yatsyura, A.V. Zelenov	271
PNPI IN THE MPD PROJECT AT NICA O.L. Fedin, D.A. Ivanishchev, A.V. Khanzadeev, L.M. Kochenda, D.O. Kotov, P.A. Kravtsov, E.L. Kryshen, M.V. Malaev, A.Yu. Ryabov, V.G. Ryabov, Yu.G. Ryabov, V.M. Samsonov, M.B. Zhalov	280
SPD EXPERIMENT AT NICA: POLARIZED AND UNPOLARIZED STRUCTURE OF THE PROTON AND DEUTERON V.T. Kim, E.V. Kuznetsova, S.G. Barsov, S.A. Bulanova, O.L. Fedin, G.E. Gavrilov, V.L. Golovtsov, A.K. Kiryanov, V.P. Maleev, S.A. Nasybulin, D.E. Sosnov, L.N. Uvarov, A.V. Zelenov	286
ENGINEERING DESIGN OF THE RICH AND MUCH DETECTORS FOR THE CBM EXPERIMENT AT FAIR D.A. Ivanishchev, A.V. Khanzadeev, N.M. Miftakhov, V.N. Nikulin, E.V. Roshchin, A. Riabov, Yu.G. Ryabov, G.V. Rybakov, V.M. Samsonov, O.P. Tarasenkova, D.V. Tyts	294
STATUS OF THE FORWARD TIME-OF-FLIGHT DETECTOR FOR THE PANDA EXPERIMENT AT GSI S.L. Belostotski, G.V. Fedotov, A.A. Izotov, S.I. Manaenkov, O.V. Miklukho, V.A. Stepanov, D.O. Veretennikov, S.S. Volkov, A.A. Zhdanov	303
PNPI IN THE R ³ B PROJECT AT FAIR G.D. Alkhazov, V.A. Andreev, A.Y. Arutyunova, A.V. Dobrovolsky, V.L. Golovtsov, D.S. Ilyin, A.G. Inglessi, V.V. Ivanov, A.V. Khanzadeev, G.A. Korolev, A.G. Krivshich, E.M. Maev, D.A. Maysuzenko, A.V. Nadtochiy, E.V. Roschin, V.V. Sarantsev, L.N. Uvarov, S.S. Volkov, V.I. Yatsyura, A.A. Zhdanov	312
CONCEPTUAL PROJECT OF THE PROTON BEAM LINES IN THE NUCLEAR MEDICINE COMPLEX OF THE “KURCHATOV INSTITUTE” – PNPI D.A. Amerkanov, S.A. Artamonov, E.M. Ivanov, V.I. Maximov, V.A. Tonkikh	321

METHODICAL AND APPLIED RESEARCH

INSTRUMENT BASE OF SYSTEMS FOR DIAGNOSTICS AND TRANSPORTATION OF PROTON AND NEUTRON BEAMS FOR RADIATION TESTING OF ELECTRONICS AT THE 1 GeV SYNCHROCYCLOTRON OF PNPI D.A. Amerkanov, S.A. Artamonov, A.S. Vorobyov, G.I. Gorkin, E.M. Ivanov, S.V. Kosyanenko, O.V. Lobanov, V.G. Muratov, V.V. Pashuk, O.A. Shcherbakov, V.A. Tonkikh, V.S. Anashin, A.E. Kozyukov, P.A. Chubunov	326
ABSOLUTE PROTON BEAM MONITOR BASED ON AN IONIZATION CHAMBER WITH A TRANSVERSE ELECTRIC FIELD D.A. Amerkanov, E.M. Ivanov, N.A. Ivanov, O.V. Lobanov, V.V. Pashuk	330
IMPORTANT FOCUSING PROPERTIES OF THE MAGNETIC STRUCTURE OF ISOCHRONOUS CYCLOTRONS WITH HIGH SPIRALING ANGLE OF THE POLE TIPS D.A. Amerkanov, S.A. Artamonov, E.M. Ivanov, G.A. Riabov, V.A. Tonkikh.....	332
CALCULATION AND OPTIMIZATION OF HIGH-ENERGY BEAM TRANSFER LINES BY THE MONTE CARLO METHOD D.A. Amerkanov, S.A. Artamonov, E.M. Ivanov, G.A. Riabov, V.A. Tonkikh.....	337
THE CALCULATION METHOD AND OPTIMIZATION OF A PROTON BEAM LINE WITH COLLIMATORS BY USING COURANT–SNYDER FORMALISM D.A. Amerkanov, S.A. Artamonov, E.M. Ivanov, V.A. Tonkikh.....	341
STRATEGY OF EQUIPPING THE PIK REACTOR EXPERIMENTAL STATIONS WITH DETECTION SYSTEMS A.G. Krivshich, D.S. Ilyin	344
PROTON ARM SPECTROMETER FOR THE R ³ B SET-UP AT FAIR G.D. Alkhazov, V.A. Andreev, V.L. Golovtsov, D.S. Ilyin, A.G. Inglessi, V.Yu. Ivanov, N.N. Filimonova, L.M. Kochenda, P.A. Kravtsov, A.G. Krivshich, D.A. Maysuzenko, A.V. Nadtochiy, I.N. Parchenko, S.S. Volkov, L.N. Uvarov, V.I. Yatsyura.....	354
HIGH VOLTAGE POWER SUPPLY FOR THE PROTON ARM SPECTROMETER OF THE R ³ B EXPERIMENT AT FAIR S.V. Bondarev, V.L. Golovtsov, N.V. Gruzinsky, N.B. Isaev, E.A. Lobachev, L.N. Uvarov, V.I. Yatsyura, S.S. Volkov	364
COMPREHENSIVE STUDY OF A PROPORTIONAL CHAMBER CATHODE'S SURFACE AFTER ITS OPERATION IN AN EXPERIMENT AT THE LARGE HADRON COLLIDER G.E. Gavrilov, A.A. Dzyuba, O.E. Maev	366
DATA ACQUISITION SYSTEM FOR THE EXPERIMENT "PROTON" A.A. Vorobyev, V.L. Golovtsov, N.V. Gruzinsky, P.A. Kravtsov, P.V. Neustroev, E.M. Spiridenkov, L.N. Uvarov, A.A. Vasilyev, V.I. Yatsyura	373
HIGH-TEMPERATURE AND MASS-SEPARATOR METHODS FOR SELECTIVE PRODUCTION OF MEDICAL RADIONUCLIDES AT PROTON AND NEUTRON BEAMS V.N. Panteleev, A.E. Barzakh, D.V. Fedorov, V.S. Ivanov, P.L. Molkanov, S.Yu. Orlov, M.D. Seliverstov	378

MODERNIZATION OF THE MEDICAL PROTON COMPLEX
FOR STEREOTACTIC RADIOSURGERY AT NRC “KURCHATOV INSTITUTE” – PNPI
L.G. Vaganyan, A.A. Vasilev, D.L. Karlin, N.A. Kuzora, V.I. Maksimov, F.A. Pak, A.I. Khalikov385

CONTENTS394

High Energy Physics Division
MAIN SCIENTIFIC ACTIVITIES
2018–2022

Отпечатано в издательско-полиграфическом отделе
НИЦ «Курчатовский институт» – ПИЯФ
на Kopica Minolta AccurioPrint C4065

188300, Гатчина Ленинградской обл., мкр. Орлова роща, д. 1
Зак. 364, тир. 40, уч.-изд. л. 50; 27.09.2023.